Porphyrinoid dyes for photodynamic anticancer and antimicrobial therapy treatments

A thesis submitted in fulfilment of the requirements for the degree of

DOCTOR OF PHILOSOPHY

at

Rhodes University

By

Rodah Cheruto Soy

February 2023

Dedication

This dissertation is dedicated to my dear husband, Denis Magero, and our daughter Judith Aloo Magero, and in loving memory of my late father-in-law, Mr Benedict Opondo Magero Gumo. Special thanks to you, Denis, for your love, support, and sacrifices you made for us throughout my PhD studies. To my lovely daughter Judith, you basically spent all these years without a mum; you gave me a reason to push on; you are the best thing that ever happened to us. To my late father-in-law, Khuka Ben, I will eternally cherish your unconditional love and support. I know you would have been proud of my achievement; may your soul rest in eternal peace!

Acknowledgment

I am deeply indebted to my supervisor Prof. John Mack for his invaluable guidance, patience, understanding, and advice throughout my PhD studies. It was a great pleasure and honor working with you, Prof. Mack; I truly admire your work ethic. I am also grateful to my co-supervisor, Distinguished Prof Nyokong, for her invaluable support, advice, and hard work instilled in us, which will come in handy in life. Special thanks also go to Prof. Xu Liang of Jiangsu University in the People's Republic of China for collaborative research work. I also thank Dr Edith Amuhaya of USIU-Africa and Mr James Oyim for hosting me in Kenya during a research visit.

Many thanks to Dr Jonathan Britton and Ms Gail Cobus for their administrative support. Special thanks to Dr Balaji Babu for his guidance, kindness, and friendship. It was a great honor to work with great minds like Dr David Oluwole, Dr Njemuwa Nwaji, Dr Edith Dube, Dr Pinar Sen, Dr Refilwe Matshitse, Dr Donovan Mafukidze, Dr Nnaemeka Nnaji, and Dr Yolande Openda. Mr Somila Dingiswayo and Mr Samuel Shabangu cheered me up; they fondly referred to me as "dada," meaning sister. I also acknowledge the support from all the members of the S22 laboratory at Rhodes University for making my PhD journey so memorable.

Special thanks to my family for your love, prayers, and support. Namely, Denis Magero and Judith Aloo, my parents, William and Grace Soi, my lovely siblings Ben, Japheth, David, and Joyce, and nieces, Tzuri, Nayna, and Eliyana, and my in-laws (the Gumos); Judith Walubengo and Pius Magero Gumo.

I gratefully acknowledge the financial support extended toward my PhD studies by the Organization for Women in Science for the Developing World (OWSD) in partnership with Rhodes University in the form of a PhD fellowship scholarship. It has made my dream come true.

All the Glory be to God for the great things He has done in my life. To this far, I must acknowledge that God the Father. You are my Ebenezer and Jehovah Jireh.

Abstract

The search for alternative therapies and non-toxic photosensitizer drugs that can efficiently generate cytotoxic reactive oxygen species for biomedical applications, such as in alternative photodynamic therapy (PDT) for cancer treatment and photodynamic antimicrobial chemotherapy (PACT) for drug-resistant bacteria treatment is on the rise. Nevertheless, the lack of photosensitizer dyes that absorb light strongly within the therapeutic window (620−850 nm) that can locally target the tumor and bacterial cells and generate singlet oxygen efficiently are some of the main challenges in PDT and PACT treatment. This study sought to address the challenges that impede PDT and PACT from realizing their full potential by synthesizing a series of *meso*-aryltetrapyrrolic photosensitizer dyes that absorb light within the therapeutic window. These include *meso*-tetraarylporphyrin (Por), A_3-type *meso*-triarylcorrole (Cor), *meso*-tetraarylchlorin (Chl), and N-confused *meso*-tetraarylporphyrin (NCP) dyes with 4-thiomethylphenyl (**1**), thien-3-yl (**2**), thien-2-yl (**3**), 5-bromo-thien-2-yl (**4**), 4-methoxyphenyl (**5**), 3-methoxyphenyl (**6**), 4-hydroxyphenyl (**7**) and 4-hydroxy-3-methoxyphenyl (**8**) *meso*-aryl rings. Por, Cor, Chl and NCP dyes and and their Ga(III), P(V), In(III) and/or Sn(IV) complexes with **1**-**8**, **1**-**4**, **5**-**8** and **5** *meso*-aryl rings were studied, along with two A_2B-type Ga(III) *meso*-triarylcorroles with pentafluorophenyl rings at the A_2 positions and 3,6-di-*t*-butyl-9H-carbazole (**9**) or *N*-butyl-4-carbazole (**10**) rings at the B position that were prepared in the laboratory of Prof. Xu Liang of Jiangsu University in the People's Republic of China. The carbazole nitrogen of **10**-GaCor was quaternized at Rhodes University with ethyl iodide to form a cationic species (**10**-GaCor-Q) for PDT and PACT activity studies.

The structures of the synthesized dyes were confirmed using UV-visible absorption and ^{1}H NMR spectroscopy, and MALDI-TOF-mass spectrometry. **1**-**4**-InPor In(III) porphyrins, **1**-**4**-P^{V}Cor, **1**-**4**-GaCor A_3 P^{V} and Ga^{III} corrole dyes were also conjugated to gold nanoparticles (AuNPs) and silver nanoparticles (AgNPs) *via* sulfur-gold and sulfur-silver affinities. The successful conjugation of the dyes onto the nanoparticles to form dye-AuNP or dye-AgNP nanoassemblies was confirmed using transmission electron microscopy (TEM), energy dispersive X-ray (EDX) spectroscopy, X-ray powered diffraction (XRD), and (X-ray photon spectroscopy) XPS. The photophysicochemical, photostability, and lipophilicity properties of the dyes and their PDT and PACT activities were investigated, and the structure-property relationships were analyzed. This was accomplished by analyzing the changes in the properties of the dyes due to the *meso*-aryl substituents, central ions, molecular symmetry, and heavy atom effects. Time-dependent-density functional theory (TD-DFT) calculations were also used to further probe the electronic and optical spectroscopic properties of the dyes.

The analysis of the photophysicochemical, photostability, and lipophilicity data for the synthesized dyes demonstrated that there are inherent structure-property relationships for the dyes studied. The TD-DFT calculations also assisted in rationalizing the observed optical spectroscopic data for the dyes. The introduction of different *meso*-aryl substituents resulted in minor absorption spectral changes on the parent structures of the dyes due to their inductive and mesomeric effects, while the insertion of Ga(III), In(III), and Sn(IV) electropositive metal centers resulted in marked red shifts of the B bands due to favorable interactions with the porphyrin or porphyrinoid ligand core. The lower symmetries of the corrole, chlorin, and N-confused porphyrin dyes resulted in enhanced absorption properties within the therapeutic

window relative to porphyrins. The heavy atom effect from the Ga(III), In(III), and Sn(IV) central ions, the *meso*-aryl groups, and the external heavy atom effect from the AuNPs and AgNPs significantly reduced the fluorescence quantum yield values of the dyes resulting in high singlet oxygen quantum yields. The dye complexes also exhibited properly balanced lipophilic properties and high photostabilities. The P(V) ion of the A_3 P^V corrole dyes reduced the aggregation effects, enhanced cellular uptake, and lowered the lipophilicity values relative to the A_3 Ga^{III} corrole dyes. The porphyrin and porphyrinoid complexes studied exhibited relatively low *in vitro* dark cytotoxicity toward MCF-7 cancer cells, which is enhanced for AuNP nanoconjugates of **1**-InPor, **1**-**3**-P^VCor, and **1**-**3**-GaCor. The dyes also have low *in vitro* dark cytotoxicity toward planktonic and biofilm cells of *S. aureus* and *E. coli*. The complexes also exhibited favorable PDT and PACT activities toward MCF-7 cancer cells, and planktonic and biofilm *S. aureus* and *E. coli* bacteria due to their high singlet oxygen quantum yields. AuNP and AgNP nanoconjugates of **1**-**4**-InPor, **1**-**4**-P^VCor, and **1**-**4**-GaCor exhibited enhanced PDT and PACT activities due to the favorable synergistic effects of nanoparticles. The PDT and PACT activities of A_3 P^V corrole dyes and the nanoconjugates of **1**-**4**-P^VCor are slightly higher than those of A_3-type Ga^{III} corroles and their nanoconjugates due to decreased aggregation effects and enhanced PS drug uptake. The cationic **10**-GaCor-Q species also exhibit favorable PDT and PACT activities in contrast to the neutral **9**-**10**-GaCor dyes due to enhanced PS drug penetration into the tumor or bacteria cells. The complexes also exhibited high Log_{10} reduction values for planktonic *S. aureus* suggesting that the dyes are highly efficient PS dyes. The activities of the complexes toward planktonic *E. coli* bacteria are moderate except for **10**-GaCor-Q, **2**-**4**-P^VCor-AgNPs, and **5**-**8**-SnChl chlorins exhibiting relatively favorable activity with > 3 Log_{10} $CFU.mL^{-1}$ values. The dyes also exhibit moderate

activities toward the *S. aureus* and *E. coli* biofilm cells, which are lower than for the planktonic cells, as shown by their lower Log_{10} reduction values. The data demonstrate that the low symmetry corrole, chlorin, and N-confused porphyrin complexes that absorb light strongly within the therapeutic window have significantly enhanced PDT and PACT activities relative to their porphyrin analogs.

Table of Contents

List of Figures

List of Schemes

List of Tables

List of Abbreviations

AgNPs	Silver nanoparticles
AuNPs	Gold nanoparticles
ALA	5-Aminolevulinic acid
B3LYP	Becke-3-parameter, Lee-Yang-Parr
$BF_3{\cdot}OEt_2$	Boron trifluoride diethyl etherate
CAM-B3LYP	Coulomb attenuated-B3LYP
Ce_6	Chlorin e6
CFU	Colony-forming unit
DDQ	2,3-Dichloro-5,6-dicyano-*p*-benzoquinone
DFT	Density Functional Theory
DMEM	Dulbecco's modified eagle medium
DPBS	Dulbecco's phosphate buffer saline
DPBF	1,3-Diphenylbenzofuran
DPM	Dipyrromethene
EDX	Energy dispersive X-ray
EPR	Enhanced permeability and retention
FCS	Fetal calf serum
FDA	Food and Drugs Administration of USA
Ga^{III}TPCor	Ga(III) *meso*-triphenylcorrole
H_2TPP	*Meso*-tetraphenylporphyrin free-base ligand

H_2TPChl	*Meso*-tetraphenylchlorin free-base ligand
H_3TPCor	*Meso*-triphenylcorrole free-base ligand
HOMO	Highest occupied molecular orbital
IC_{50}	Half-maximal inhibitory concentration
IC	Internal conversion
InTPP	Chloroindium (III) *meso*-tetraphenylporphyrin
IRF	Instrument response function
ISC	Intersystem crossing
IUPAC	International Union of Pure and Applied Chemistry
LED	Light emitting diode
LUMO	Lowest unoccupied molecular orbital
MALDI	TOF-MS Matrix-assisted laser desorption ionization-time of flight-mass spectroscopy
MCF-7	Michigan Cancer Foundation-7 breast cancer cell line
MCD	Magnetic circular dichroism
MO	Molecular orbital
MSA	Methanesulfonic acid
MTT	3-(4,5-Dimethylthiazol-2-yl)-2,5-diphenyl-2H-tetrazolium bromide
NCP	N-Confused porphyrin
NIR	Near Infrared
NMR	Nuclear magnetic resonance
OD	Optical density

PACT	Photodynamic antimicrobial chemotherapy
PBS	Phosphate buffer saline
PDT	Photodynamic therapy
PS	Photosensitizer
P^{V}TPCor	P(V) *meso*-triphenylcorrole
ROS	Reactive oxygen species
TCSPC	Time-correlated single photon counting
TD-DFT	Time dependent-density functional theory
TEM	Transmission electron microscopy
TEA	Triethylamine
TFA	Trifluoroacetic acid
TLC	Thin layer chromatography
UV-vis	Ultraviolet-visible spectroscopy
XPS	X-ray photon spectroscopy
XRD	X-ray powered diffraction
ZnTPP	Zinc(II) 5,10,15,20-*meso*-tetraphenylporphyrin

List of symbols

Abs	Absorbance
ΔA	Change in absorbance
ε	Molar extinction coefficient
t	Time
h	Hours
min	Minutes
s	Seconds
ns	Nanoseconds
λ	Wavelength
nm	Nanometres
α	Alpha position carbon
β	Beta (peripheral) position carbon
m/z	Mass-to-charge ratio
e^-	Electron
S_0	Singlet ground state
S_n	Singlet-excited state
T_n	Triplet-excited state
$^1O_2$	Singlet oxygen
$^3O_2$	Molecular ground state triplet oxygen
τ_F	Fluorescence lifetime
τ_T	Triplet lifetime
ϕ_Δ	Singlet oxygen quantum yield
ϕ_F	Fluorescence quantum yield

CHAPTER ONE

Introduction

This chapter provides the general introduction to the dissertation research work. This includes the problem statement, aims, objectives, and a brief literature review on the synthesis, photophysicochemical properties, and singlet oxygen applications of porphyrinoid dyes.

1.0 Introduction

The research described in this thesis involves the facile synthesis and an investigation of the trends in the spectroscopic properties of a series of tetrapyrrolic macrocycle dyes that include porphyrins and porphyrin analogs, such as corroles, chlorins, and N-confused porphyrins. The porphyrin analogs absorb light more strongly at the red end of the visible light region compared to their porphyrin analogs. The theoretical studies guided the choice of the dyes, the rational selection of *meso*-aryl substituents and core functionalization with metal and P(V) ions, and the identification of trends in their photophysicochemical properties. The potential utility of the photosensitizer (PS) dyes for the photodynamic therapy (PDT) of cancer and photoinactivation of bacteria by photodynamic antimicrobial chemotherapy (PACT) was assessed. In addition, the effect of nanoparticles on the photophysicochemical properties of the dyes was also investigated for porphyrin and corrole derivatives consisting of sulfur atoms on their *meso*-aryl substituents. These dyes were conjugated to gold and silver nanospheres noncovalently through S-Au and S-Ag affinities to form nanoassemblies with enhanced PDT and PACT activities.

1.1 Problem statement

The public health sector is currently facing a myriad of problems related to terminal ailments, such as cancer and the emergence of antibiotic-resistant infectious diseases due to bacteria 'superbugs'. The latter issue will result in significant additional morbidity and mortality in the decades ahead if alternative approaches are not developed due to the slow rate of preparing new antibiotics for clinical use. Therefore, scientists need to address these problems by developing novel, safe, and affordable cancer treatment techniques, such as PDT and PACT, to address antibiotic resistance by developing novel photosensitizer dyes for use in these alternative

protocols [1–8]. Photodynamic therapy has long gained prominence as a promising minimally non-invasive cancer treatment protocol involving non-toxic light-absorbing chromophore/photosensitizer dyes, light of appropriate wavelength, singlet oxygen, and reactive oxygen species (ROS) in the selective destruction of tumor cells [1–5,9–16]. The PDT technique involves systematic administration of a photosensitizer dye that is selectively localized in the target tumor region followed by irradiation with laser light of appropriate wavelength to elicit a series of photochemical reactions that produce the cytotoxic singlet oxygen and ROS that kill the target tumor cells. This process also induces immunological responses [1–6,9,12–16].

PACT is a closely related technique to PDT, which uses the same basic principle to inactivate or kill microbial cells, bacteria, viruses, fungi, and other infections [7,8,17–24]. During PACT, inactivation occurs by destroying the outer membrane of microbes [7,8,18–24]. The nature of the bacteria species and the porosity of their cytoplasmic outer membrane primarily influence the photosensitizer drug penetration into the inner membranes and the efficiency of bacteria inactivation [7,8,18–24]. It is also important to note that while bacteria grow in both biofilms and as planktonic cells, most microbes persist in nature in the former since biofilms attach to surfaces [20,23,25–27]. Planktonic cells are free-living (free-floating) microorganisms suspended in the liquid phase, whereas biofilms are microorganism aggregates or communities mainly embedded in self-produced extracellular polymer matrix adhered to surfaces or tissues [23,25–27]. The polymeric matrix secures the bacteria in the biofilm against adverse environmental conditions, enabling the bacteria to reproduce and survive more readily. For this reason, biofilms exhibit dramatically decreased susceptibility toward antimicrobial agents, biocides, and immune systems [20,23,25–27]. Moreover, biofilms are of great public health concern since they are the

most difficult bacteria to treat and cause major chronic infections [20,23,25–27]. This research study, therefore, sought to investigate the PACT activities of the synthesized photosensitizer dyes against both planktonic cells and biofilms of Gram-(+) *Staphylococcus aureus* and Gram-(−) *Escherichia coli* bacteria strains.

The photosensitizer dye drugs widely used today in PDT treatment, including those in clinical trials, are typically porphyrin-based dyes [1–3,15,18,28–35]. However, these porphyrin-based dyes have yet to fulfill their full potential since they absorb relatively weakly in the therapeutic window (620−850 nm) and allow weak penetration of light to deep-seated tumors; therefore, these drugs are mostly suitable for use in the treatment of superficial or topical tumors [1–3,15,18,31–35]. Although the other clinically approved PDT drugs belonging to the phthalocyanine dye class absorb strongly in the low-energy region, they are prone to aggregation and are usually not readily soluble in an aqueous environment, thus limiting their efficacy [36,37]. For decades, the main bottleneck has been the search for highly efficient photosensitizer drugs for use in PDT and PACT with favorable photophysicochemical properties within the therapeutic window, where auto-fluorescence, including light scattering absorption by water, tissues, and cells are minimized [2–4,12–15,18]. Recent studies have shown that porphyrin-based analog dyes, such as corroles, chlorins, and N-confused porphyrins, that absorb light relatively strongly in the near-infrared region are better candidates for use in PDT than porphyrins, since they enable improved light penetration into the deep-seated tumors and hence result in enhanced PDT activity [34,38–44].

One of the approaches for fine-tuning the stability and photophysicochemical properties of porphyrins and porphyrin analog dyes to suit various applications is the introduction of heavy

atoms, such as metal ions or halogen atoms, into the macrocycle core or onto *meso*-aryl groups [45–49]. Heavy central atoms, such as gallium, indium, and tin, enhance the forbidden spin-orbit coupling process to populate the triplet excited states and enhance the generation of singlet oxygen, which is believed to be the chief cytocidal agent during PDT and PACT [45-47,49,50]. Previous studies have also shown that insertion of Group 15 non-metal ions, such as phosphorous P(V) ion, into the porphyrin macrocycle core, also improves the solubility properties of dyes in an aqueous environment resulting in improved cellular uptake and biodistribution of the drugs. The presence of two axial ligands decreases aggregation from the π-π stacking effect of dye molecules [51–55]. For these reasons, gallium, indium, Sn(IV), and P(V) ions were selected as central atoms for the synthesized dyes in this study. The choice of *meso*-aryl groups of the porphyrin-based macrocycles also significantly influences the photophysicochemical properties of the dyes and bioactivities. For instance, incorporating *meso*-aryl groups with heteroatoms, such as sulfur, nitrogen, and halogen atoms, improves the binding affinity of the drug for the tissues and microbe cell walls [56–60]. For these reasons, derivatives with *meso*-aryl rings that provide favorable anticancer, antifungal, antibiotic, and antioxidant properties, such as thienyl, carbazole, pentafluorophenyl, hydroxy, methoxy, and methylthiophenyl groups, were selected as the *meso*-aryl groups for the synthesized dyes in this study.

The lack of selective delivery and specificity of photosensitizer dye toward cancer cells and microbial cells remains one of the challenges impeding PDT and PACT from realizing their potential utility [2-4,12-14,22,24,61]. Conjugation of the dyes with nanoparticles to form nano-assemblies has been identified as one of the best strategies for addressing these problems due to the favorable functional properties of nano-assemblies [2–4,12–14,17,22,32,62–69], including

high stability, small size, tune-ability, high surface area, and specificity that allow specific target localization and selective accumulation of the dye in tumor tissues due to the enhanced permeability and retention effect [2–4,13,17,22,62–70]. Gold and silver metallic nanoparticles (MNPs) have been reported to exhibit anticancer and antimicrobial properties, respectively [22,62,65,69,71–73]. For this reason, this study also considered the conjugation of *meso*-thienyl and *meso*-methylthiophenyl dye derivatives with gold and silver nanospheres *via* non-covalent sulfur-gold and sulfur-silver affinities.

Therefore, this research study mainly sought to address challenges related to PDT and PACT by preparing porphyrin and NIR absorbing porphyrin analogs, such as corroles, chlorins, and N-confused porphyrins as novel photosensitizer dyes by using relatively facile synthesis methods that can be easily scaled up. The nanoparticles were also incorporated to enhance drug delivery and selectivity toward the MCF-7 breast cancer cell line, and planktonic and biofilm microbial cells of *Escherichia coli* and *Staphylococcus aureus*.

The specific objectives of the study were:

i. To synthesize and characterize novel functionalized porphyrins and their structural analogs.
ii. To evaluate the photophysical and photochemical properties of novel functionalized porphyrins and their structural analogs.
iii. To prepare nanoparticle conjugates of the novel functionalized porphyrins and their structural analogs
iv. To evaluate the utility of the dyes and conjugates prepared in (i) and (iii) for PDT and PACT applications against human cancer cell lines and various bacteria.

1.2 Porphyrin and porphyrin analogs

Porphyrin and porphyrin analog derivatives are an important class of tetrapyrrolic macrocycles dye. They have been a major focus of research for centuries in wide-ranging fields, such as biomedicine, biology, and chemistry, due to their unique photophysicochemical, redox, and optical properties [35,47,48,74]. Furthermore, the naturally occurring metalloporphyrinoid ligand derivatives, such as chlorophyll, Vitamin B12 complex, heme (**Figure 1.1**), bacteriochlorophyll, and cytochromes play key roles in biochemical processes, bio-metabolism, and enzymatic catalysis [74,75].

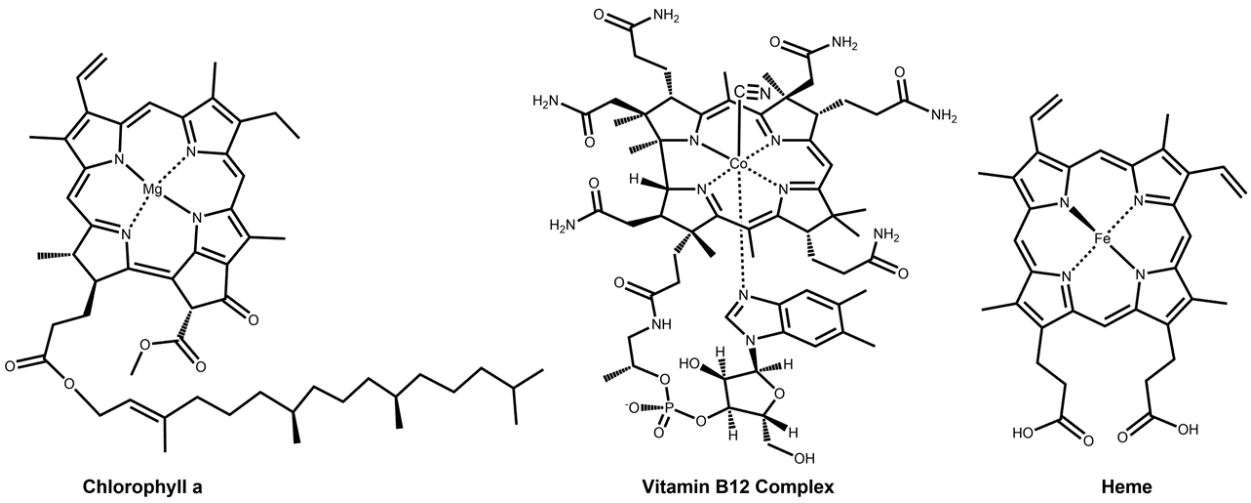

Figure 1.1: Naturally occurring porphyrinoids.

The photochemistry, electrochemistry, aromaticity, chemical and physical stabilities, spectroscopic, and ligand binding properties of these natural porphyrinoids, have inspired the rational design and synthesis of porphyrins and porphyrin analogs, such as corroles, chlorins, and N-confused porphyrins (**Figure 1.2**) for applications in wide-ranging fields [74,76,77]. These include their use as photosensitizer dyes in photoelectric devices, in catalytic reactions, for harvesting energy in solar cells, in optical imaging, oxygen transport, biosensors, bioimaging, and

as diagnostic and therapeutic agents in biomedical processes, such as PDT and PACT [3,31,34,39,76,78–83].

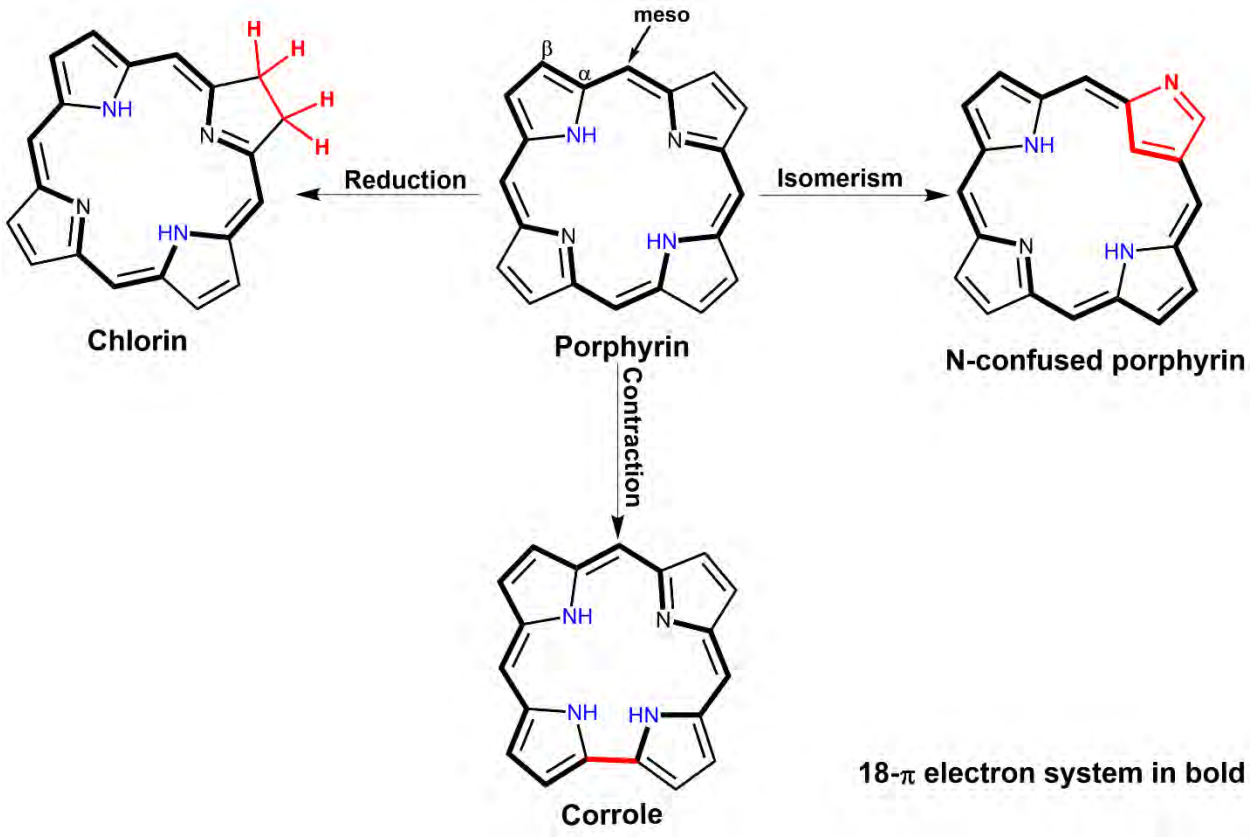

Figure 1.2: Porphyrin and porphyrin analog structures.

1.2.1 Porphyrin history and nomenclature

Porphyrins are tetrapyrrolic pigments well known for their importance in natural structures. They gained a high profile in molecular dye chemistry as pigments of life that play a key role in catalytic processes that involve porphyrins in coenzymes or proteins [74,75]. Porphyrins have been explored for decades in various fields, with significant research in a biomedical context dating to the early 1840s when hemoglobin was chemically treated with concentrated sulfuric acid to obtain iron-free hematin [84]. However, inaccuracies surrounding the vagueness of the

technique rendered the whole process problematic. In the late 1860s, Thudichum purified the iron-free hematin and named it “cruentine” due to its reddish fluorescence [85]. In 1871, Stockvis and Hoppe-Seyler described its spectrum and named it ‘hematoporphyrin’ due to the ‘blood purple’ color [86]. The intense absorption band for hemoglobin at 400 nm was first described in 1883 by Soret and is still often referred to as the Soret band [87], while the structure of porphyrins as a tetrapyrrole macrocycle linked by four methine bridges was first correctly proposed by Küster in 1912 [88]. However, the scientific community did not widely accept the proposed structure until 1929, when Fischer and Ziele confirmed it definitively after their successful syntheses of haem, octamethylporphyrin, and the type I, II, and III isomers of etioporphyrin from pyrrolic starting materials [89].

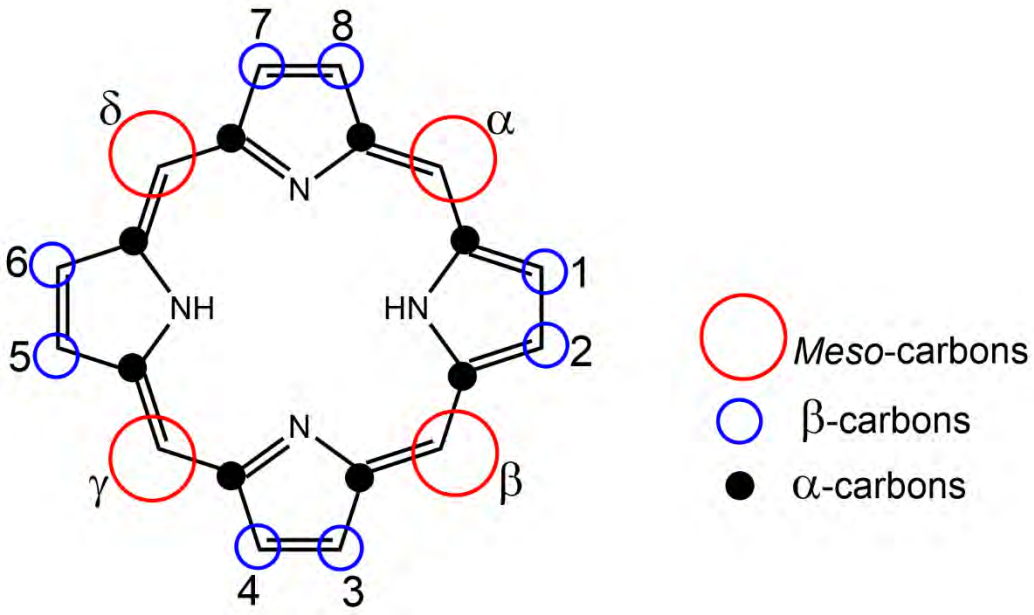

Figure 1.3: Porphine nomenclature and numbering according to the Fischer system.

Hans Fischer contributed significantly to porphyrin research. He also developed a classical nomenclature system for porphyrinoids based on assigning trivial names to new porphyrin

ligands and a numbering system [90,91]. According to this naming system, the methine bridges carbons (α, β, γ, and δ) were assigned as the *meso*-positions, and the outer pyrrole carbons as *beta* (β) position with the four pyrrolic rings labeled capital letters A, B, and C and D [90,91] units, but some carbon atoms of the porphyrin skeleton were unidentified (**Figure 1.3**). In 1979, the complexities in naming porphyrins with the Fischer system led the *International Union of Pure and Applied Chemistry (IUPAC)* and the *"International Union of Biochemistry (IUB)* to establish a systematic naming system for porphyrins and related tetrapyrrolic compounds in which every atom in the ring was numbered including the inner nitrogen atoms (**Figure 1.4**). This IUPAC method has proven helpful for communication of results across various fields and eased the complexity of accurately naming porphyrinoid compounds [92].

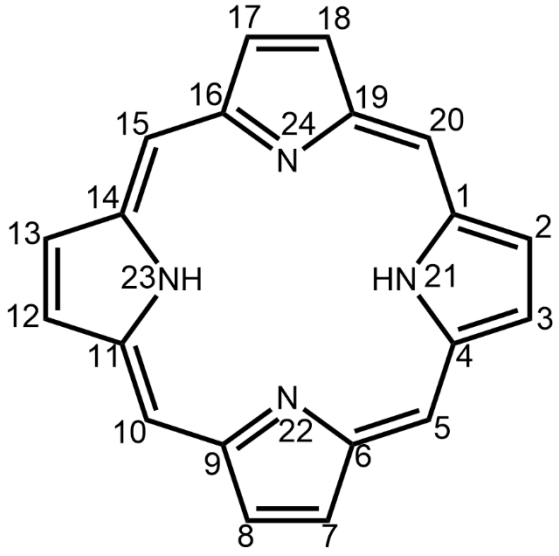

Figure 1.4: Porphine numbering system according to the IUPAC system.

The parent porphyrin structure is a planar heteroaromatic macrocycle with D_{2h} symmetry that consists of four pyrrole rings connected by methylene bridges to form a heteroaromatic 16 atom 18-π electron system on the inner ligand perimeter (**Figure 1.2**) [48,74]. The carbons of the

pyrrole moieties are often labeled α and β, depending on their relative proximity to the core nitrogen atoms. Two NH protons are aligned in an opposite arrangement in the inner core. The ligand is hence dianionic and can coordinate a wide range of central ions, mainly metal ions, to form complexes.

Porphyrins readily undergo various electrophilic substitution reactions mainly at the *meso*-positions due to their aromaticity, since these carbon atoms experience high electron density [74]. For this reason, many synthetic porphyrins and porphyrin analog derivatives are formed through *meso*-aryl electrophilic substitutions [74,93,94]. Since the porphyrin parent structure (**Figure 1.2**) is planar, coordination to axial ligands from both sides of the molecular plane is facilitated, when the oxidation state of the central ion is greater than two, such as is the case with Sn(IV) and P(V) [48,95]. Axial ligation of porphyrins and their derivatives can be beneficial since it decreases the aggregation of molecules [95] and facilitates further tailoring and functionalization of compounds to enhance their suitability for various applications or chemical reactions [51,54,95–98]. In general, porphyrin and its derivatives can also be modified through functionalization at the core, *meso*, and *beta* positions of the rings with various substituent groups to suit various applications (**Figure 1.2**) [48,74,77].

1.2.2 Porphyrin Synthetic methodologies

Developments in porphyrin synthesis have long been fuelled by the ever-increasing demand for their use in many fields, focusing on more efficient, greener, and facile procedures that yield high amounts of products. The aromaticity of porphyrins enables them to readily undergo various electrophilic substitutions involving different substituent groups [74,93,94]. This has been exploited for many years in porphyrin synthesis research and remains one of the most studied

reactions involving porphyrins and their derivatives. For instance, several synthetic techniques have explored electrophilic substitutions at the *meso*-positions (the 5,10,15,20-positions of the ring), since electrophilic substitutions can readily occur at these positions. These include popular synthetic methods, such as the Rothemund, Alder-Longo, and Lindsey reactions, which are each described in depth below.

Reactions involving the β-pyrrolic carbons (i.e. the 2,3,7,8,12,13,17,18-positions) have also been studied for modifying porphyrins with different substituents [74,94]. Modifications at the β-positions exert larger steric and electronic effects on the porphyrin ring relative to those at the *meso*-aryl positions. For this reason, the β-substituents are known to induce non-planarity in the porphyrin ring in a manner that can regulate the photophysicochemical features of the tetrapyrrolic structures to resemble their photosynthetic counterparts, such as coenzyme F430 and P-450 and Vitamin B12. The modifications at the β-pyrrole carbons yield compounds with lower symmetry, such as chlorins and bacteriochlorins, that are closely related to the naturally occurring porphyrin derivatives and hence gained considerable attention facilitating further progress in porphyrin synthesis research [74,77,94]. Since this thesis covers porphyrins and porphyrin analog derivatives, such as corroles, chlorins, and N-confused porphyrins that exhibit lower symmetry with strong absorption properties in the lower energy near-infrared (NIR) region, this section mainly focuses on synthetic techniques for porphyrins, and subsequent sections will deal with the NIR absorbing porphyrin derivatives.

1.2.2.1 Rothemund method

Tetraarylporphyrin synthesis protocols evolved over several decades, with Rothemund in 1935 pioneering a major synthesis procedure for symmetric free-base *meso*-substituted porphyrins.

The reaction involved an acid-catalyzed pyrrole and benzaldehyde condensation in methanol solution under anaerobic conditions at high temperatures (100°C) in a sealed tube [99]. Low yields of tetraphenylporphyrin (TPP) products of *ca.* 4% were obtained using this approach. Later in 1939, Rothemund modified the reaction conditions by heating the reaction mixture at 200°C in the sealed tubes to obtain various *meso*-substituted porphyrins at *ca.* 10% yield. In an effort to obtain much higher yields, he later modified the reaction conditions by heating the sealed tubes in the presence of pyridine at a high temperature (220°C) for 48 h to yield 11% of the TPP, as shown in **Scheme 1.1** [100].

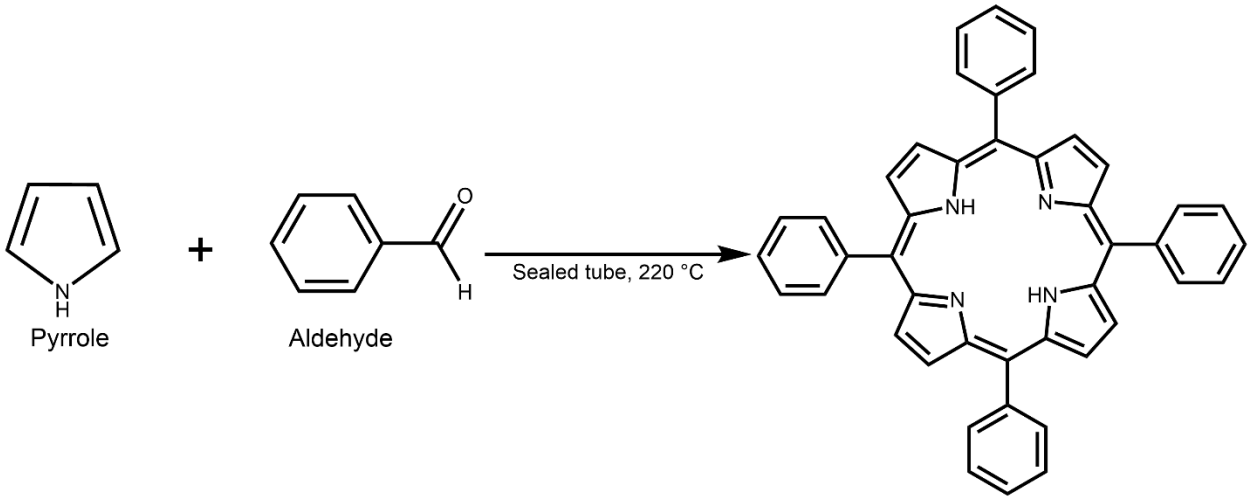

Scheme 1.1: Rothemund method for porphyrin synthesis [99].

1.2.2.2 Adler-Longo method

Alder-Longo and co-workers refined the Rothemund method to involve milder reaction conditions for synthesizing a wider range of *meso*-substituted symmetrical porphyrins [101,102]. The method involved refluxing equimolar quantities of pyrrole and benzaldehyde in propionic acid for about 30 min at 140°C under open atmospheric conditions to obtain a reddish-brown solution (**Scheme 1.2**). The reaction mixture was first left to cool down slowly to room

temperature, followed by filtration to obtain the product. After filtration, the product was washed using cold methanol and then hot water to yield purple crystals at *ca.* 20% yield. The relatively high yields obtained for TPP provided the possibility of large-scale production of *meso*-tetraaryl porphyrins [101,102]. However, the harsh acidic and high-temperature reaction conditions limit the potential scope of the Alder-Longo method; particularly, in synthesizing porphyrins from many sensitive aldehydes, since they hardly react with pyrrole under these conditions. In addition, recovering some porphyrin products from the reaction mixture can be problematic due to their solubility in propionic acid [74,93,103]. Regardless of the challenges faced, the refined Alder-Longo procedure remains one of the prominent protocols for efficiently synthesizing various symmetrical and asymmetrical porphyrins *via* the statistical condensation approach [103].

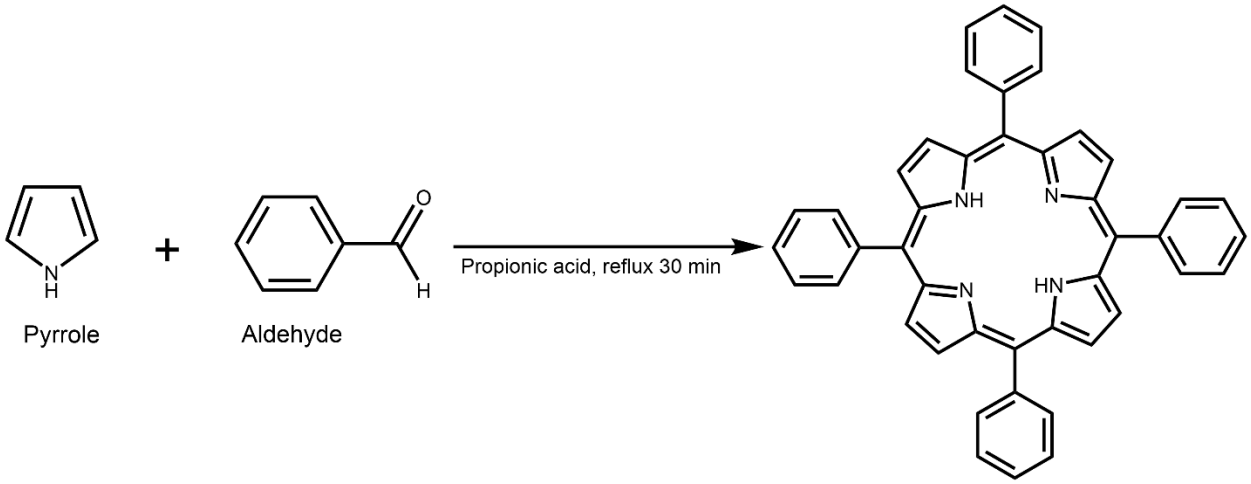

Scheme 1.2: Adler-Longo method for porphyrin synthesis [101,102].

1.2.2.3 Lindsey's method

In the early 1980s, Lindsey and co-workers developed a milder protocol after gaining a comprehensive knowledge and understanding of the sequential phases involved in the biosynthesis of porphyrins [104,105]. The approach involved two sequential reaction steps at

room temperature. The first step involved a condensation reaction of equimolar concentrations of an aldehyde and pyrrole in a very dilute solution of dry DCM in the presence of a mild acid catalyst, preferably trifluoroacetic acid (TFA) or BF_3·etherate (≈ 10^3 M), to form an unstable porphyrinogen intermediate (**Scheme 1.3**). The second step was an oxidation step in which the porphyrinogen was oxidized to a stable porphyrin product in the presence of an oxidant, usually *p*-chloranil or 2,3-dichloro-5,6-dicyano-1,4-benzoquinone (DDQ), to obtain an up to 50% product yield depending on the aldehydes used.

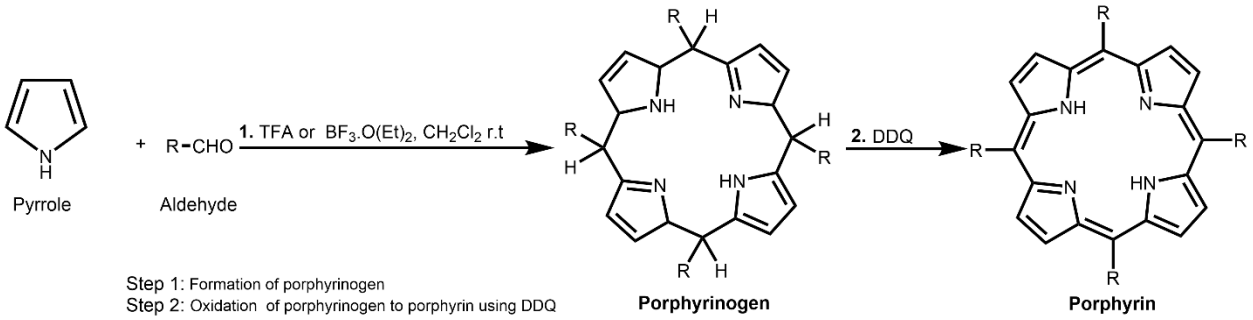

Scheme 1.3: Lindsey method for porphyrin synthesis [104].

Lindsey's strategy significantly broadened the scope for using very sensitive aldehydes for symmetric and asymmetric porphyrin synthesis [105]. However, for better yields, very dilute concentrations of the starting materials (pyrrole and aldehyde) (10^{-2}) are needed to minimize the competitive formation of pyrromethene oligomers and favor the formation of the porphyrinogen. Hence, for large-scale synthesis, large amounts of chlorinated solvents (CH_2Cl_2 or $CHCl_3$) must be handled, which can be challenging [106]. Despite these challenges, Lindsey's strategy essentially upgraded the previous porphyrin synthesis protocols and afforded many previously unreported *meso*-tetraarylporphyrins in good yields. It has also paved the way for

further improvements of the reaction conditions and, therefore, the product yields in porphyrin and porphyrin derivative syntheses [106].

1.3 Porphyrin analog derivatives

In recent years, porphyrin-based research has focused on developing structurally modified low-symmetry porphyrin analogs with enhanced properties, such as core contracted porphyrinoids, hydro-porphyrins, and *iso*-porphyrins, such as corroles, chlorins, and N-confused porphyrins [107–109]. These structural modifications result in remarkable changes in the porphyrin photophysical, ion-coordination, optical, redox, and catalytic properties. Thus, making them potentially suitable for a wide range of applications, such as use as catalysts and as photosensitizers in optoelectronics and biomedical applications [107–109]. Therefore, this section reviews the various applications and syntheses of the structural analogs of the porphyrins that were studied, i.e. corroles, chlorins, and N-confused porphyrins.

1.3.1 Corroles

The study of corroles has made significant progress over the past few decades. Corroles are tetrapyrrolic macrocycles with a single methylene bridge from the porphyrin framework removed [110–115]. However, unlike the parent porphyrins macrocycle, the direct pyrrole-pyrrole linkage within the LX_3 *mer*-macrocycle structure results in a smaller binding pocket and lower symmetry (**Figure 1.2**). Nevertheless, an electron-rich 18 π-system is still maintained on the inner ligand perimeter [110–114].

Corroles have a similar macrocyclic cavity to that of corrins since one of the methylene bridges of the porphyrin system is missing in their structure [110,112,113,116]. Therefore, they are

tetrapyrrolic macrocycles structurally related to the cobalt-chelating corrin in Vitamin B12, shown in **Figure 1.1**. Novel corroles consequently facilitate a biomimetic approach for aquacobalamin (Vitamin B12) [76]. However, corroles are more electron-rich due to their aromatic 18 π-electron systems [76,110,112–114,116,117]. The corrole core coordination is comprised of three NH protons and one imino nitrogen (**Figure 1.2**). Hence, it is a trianionic chelating ligand capable of stabilizing metal ions in unusually high oxidation states [46,110–114,116,117]. These properties have led to applications in wide-ranging fields that include catalysis [118–120], solar cells [121,122], photovoltaic cells [123,124], bioimaging [55,125], biosensors [126], and phototherapy techniques [39,127–131].

1.3.1.1 Corroles Synthesis methods

The history of synthetic corroles dates back to 1965 and the initial research of Johnson and Kay [132]. However, due to limited scope for substitution and low yields, research into corrole synthesis and their use in porphyrinoid chemistry was restricted for a long time. A highly improved facile synthesis of *meso*-substituted corroles was developed in 1999 by Gross *et al.* and Paolesse *et al.* [133,134]. Their methods exploited the condensation of aryl aldehydes with pyrroles with improved product yields, which in most cases involves the extension of substitutional scope compared to the original methods [110,111]. These synthetic methods revolutionized the development of corrole chemistry since they attracted considerable attention from researchers active in the tetrapyrrolic macrocycle field and facilitated research on applications in a wide range of fields, including catalysis and photomedicine. Since then, significant progress has been made in refining the reaction conditions for the preparation of *meso*-substituted corroles.

For instance, significant advances have also been made in the preparation of low symmetry derivatives and the coordination chemistry of corroles, including new methods, such as pacman-type multicorrole systems, which are analogous to the *pacman*-porphyrins and hangman corroles [110,135]. These advances have resulted in a rich corrole coordination chemistry. Since corroles are trianionic ligands, they favor coordination by central ions in higher oxidation states, and this has attracted interest in various fields [46,49,112,136]. For example, in catalysis, corroles are used in isolating high-valent multiply bonded central ions, such as manganese(v) oxo that can epoxidate olefins, manganese(V) imide complexes, iron(IV) corroles capable of mediating olefin aziridination, and chromium(V) and chromium(VI) nitride complexes [112,136,137].

1.3.1.1.1 The first synthesis Approach: Johnson and Kay

Johnson and Kay first described a corrole synthesis approach in 1965, in which 1,19-dideoxybiladiene-ac hydrobromides (1',8'-dideoxybiladiene-ac hydrobromides) were suspended in methanol [132]. Thereafter, the solution was treated with aqueous sodium acetate, irradiated with a 200 W bulb, and left for 10 min to complete cyclization (**Scheme 1.4**). However, this synthetic approach was tedious since the synthesis of intermediate materials involved multiple steps. Also, it resulted in low yields and limited scope for peripheral substitution patterns beyond β-alkylated derivatives [110].

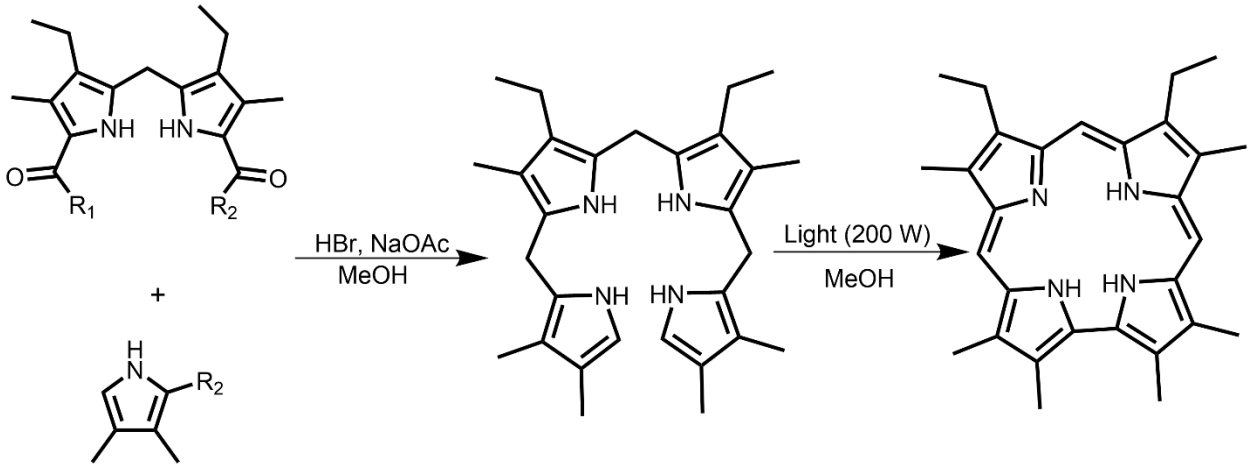

Scheme 1.4: Corrole synthesis approach reported by Johnson and Kay [132].

1.3.1.1.2 The direct corrole synthesis methods

The direct corrole synthesis approach was developed independently by Gross *et al.* and Paolesse *et al.*, in 1999, and has garnered the attention of many researchers resulting in an increasing number of reports on corrole synthesis [133,134]. Paolesse and coworkers 1999 reported a 'one-pot' corrole synthesis method (**Scheme 1.5a**). This approach is primarily a refined Rothemund method involving the reaction of pyrrole and benzaldehyde (mole ratio 3:1) in acetic acid to yield a mixture of porphyrinoid product macrocycles, which include corroles and porphyrins. The major drawback of this method is the production of porphyrin side products in nearly the same amount as the desired corroles products at quite low yields (*ca.* 5%) [110].

On the other hand, in 1999, Gross and coworkers reported a solvent-free approach in which a solid support, such as Florisil®, silica, or alumina, is used [134] (**Scheme 1.5b**). This involves heating equimolar quantities of pyrrole and aldehyde for several hours to yield a black tar-like product. This is then washed with dry dichloromethane and oxidized with DDQ in the presence of air. However, the yield is usually only between 8−11%.

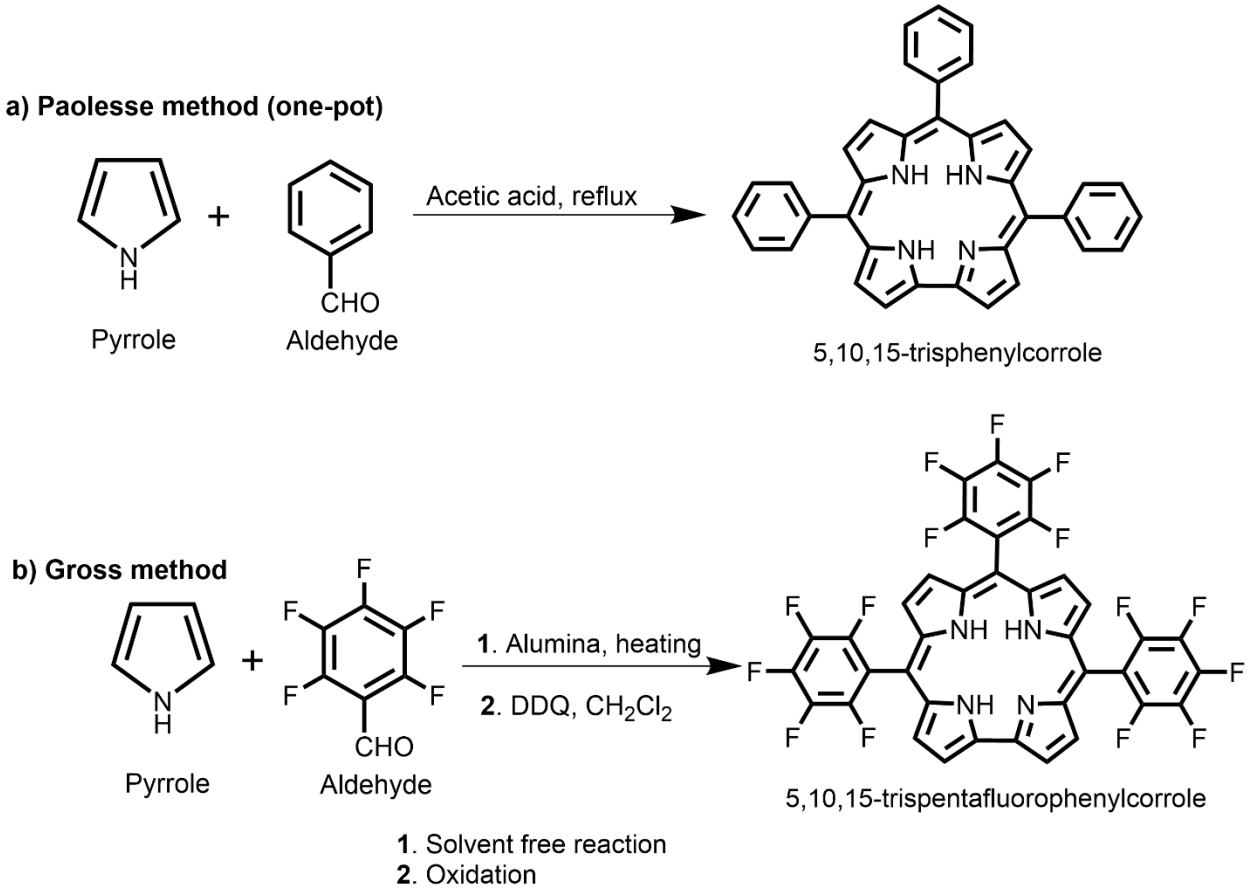

Scheme 1.5: The first direct corrole synthesis approaches [133,134].

In general, the molecular basis of the direct *meso*-A_3 triarylcorrole synthesis approaches remains the same despite the differences in methodology (**Scheme 1.5**). These approaches involve two independent steps, as shown in **Scheme 1.6**. In the first step, pyrrole and aldehyde derivatives are reacted in an acid-catalyzed electrophilic substitution reaction [133,134]. This results in a mixture of aldehyde-pyrrole polymers of varying lengths with alternating pyrrole and aldehyde subunits. The second step involves the oxidative closure of the polymers to form a ring by pyrrole-pyrrole coupling. This was followed by aromatization that led to various macrocycles similar in length to the tetrapyrrane chains produced in the first step [110,133,134]. The oxidation process involves using 2,3-dichloro-5,6-dicyano-1,4-benzoquinone (DDQ) or *p*-chloranil (tetrachloro-1,4-

benzoquinone) in chloroform or dichloromethane. The desired polymer for corrole synthesis is obtained through the condensation of four pyrroles and three aldehyde subunits (i.e. a bilane or tetrapyrrane) [133,134].

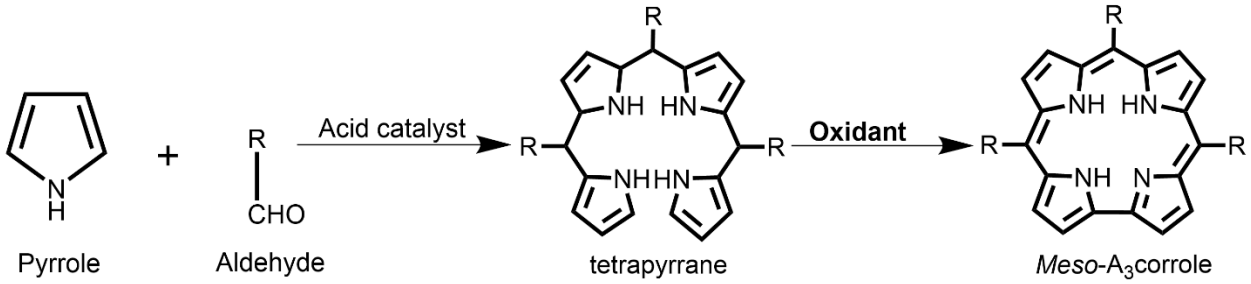

Scheme 1.6: Direct *meso*-A_3 triarylcorrole synthesis [138].

Gryko and coworkers subsequently reported major improvements to the direct corrole synthesis approach [138–142]. They developed an efficient 'one-pot' synthetic approach for A_3 *meso*-substituted corroles using a water:methanol solvent system in the presence of 0.1 M catalytic HCl (**Scheme 1.7a**). The reaction involved the condensation of dilute aldehydes (5 mmol) and pyrrole (10 mmol) starting materials, resulting in intermediate products. These are primarily the dipyrromethane intermediate, consisting of two pyrrole units linked by a methine bridge, which is soluble in the solvent system, and an insoluble bilane product that tends to precipitate, which effectively halted the reaction at this stage. The bilane products were then isolated and oxidized to form a corrole macrocycle. This reaction led to a decrease in the yields of porphyrins and other side products formed. Gryko and Koszarna reported yields of between 13−56% [138,140,141]. It was found that a higher corrole yield could be obtained using *p*-chloranil instead of DDQ.

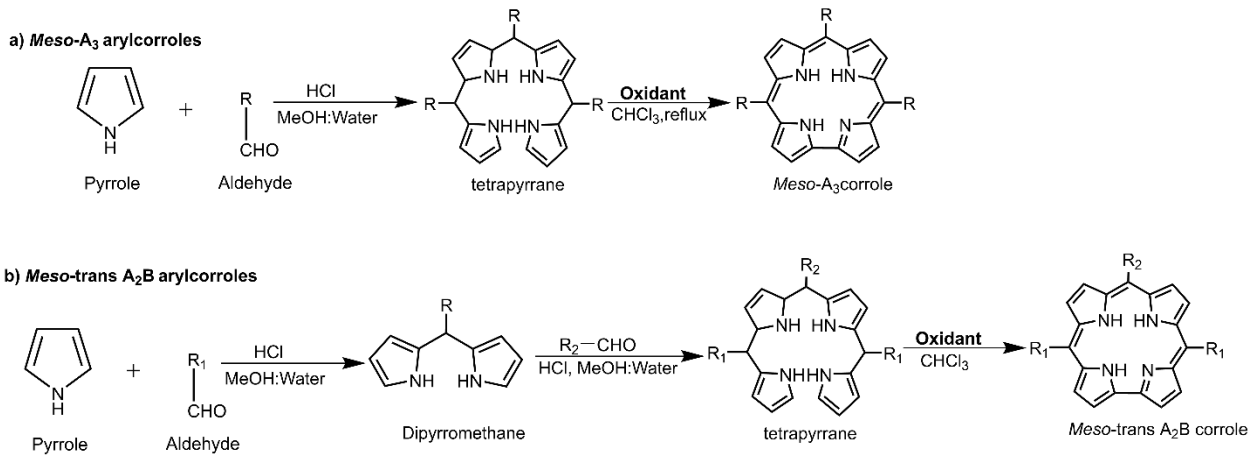

Scheme 1.7: Preparation of A_3 and *trans*-A_2B *meso*-arylcorroles by the Gryko and Koszarna method [141].

In 2006, Gryko and Koszarna reported optimized reaction conditions for efficiently synthesizing a series of A_3 *meso*-triarylcorroles and *trans*-A_2B corroles in unprecedentedly high yields [141]. The synthesis approach for *trans*-A_2B *meso*-triarylcorroles synthesis is similar to the previously described *meso*-A_3 triarylcorrole synthesis with slight modifications (**Scheme 1.7b**). This involves three reactions steps: the first step is an acidic catalyzed condensation of pyrrole (10 mmol) and aldehyde (5 mmol) in a 0.1 M HCl methanol:water (1:1) solution at room temperature for 1 h to form a dipyrromethane. This is followed by an acid-catalyzed condensation reaction of the dipyrromethane (1 mmol) and a second aldehyde (0.5 mmol) in a 0.1 M HCl methanol:water (1:1) solution at room temperature for 1 h to yield a tetrapyrrane. The last step involves the tetrapyrrane ring closure in the presence of an oxidant to form a *trans*-A_2B *meso*-triarylcorrole in yields of between 15−50% [141]. In general, the Gryko and Koszarna synthesis methods are still the commonly preferred approaches for obtaining A_3 and A_2B *meso*-aryl corroles in good yields from a wide range of aldehydes with both electron-withdrawing and -donating properties.

1.3.2 Chlorins

Chlorins are dihydroporphyrin macrocycle derivatives that have gained considerable significance in porphyrinoid research due to their unique photophysical properties that have been exploited in both biological and material applications [143–146]. The chlorin structure is similar to those of porphyrins and the naturally occurring chlorophyll pigment (**Figure 1.1**). However, unlike porphyrins, there is a single reduced peripheral pyrrole double bond (**Figure 1.2**). A chlorin is formed due to the saturation of the β,β'-pyrrolic double bond, and further saturation of these bonds results in the formation of an isobacteriochlorin or bacteriochlorin [144–146]. These reduced porphyrin derivatives and their metal complexes exhibit low symmetry properties; C_{2v} for the metallochlorin and D_{4h} for the metalloporphyrin with strong absorption properties in the red region of the electromagnetic spectrum. Notably, the 18 π-electron system of dihydroporphyrins and tetrahydrophyrins is not altered with the reduction of these double bonds [144–146]. However, the spectral properties of a chlorin macrocycle can be altered significantly depending on the nature and substitution patterns of the β- and/or *meso*-substituents [145,146].

In essence, variations in the chemical structures are associated with the introduction of functional groups that catalyze various chemical reactions for naturally occurring chlorin derivatives [144–146]. These variations include changes in the oxidation states and the differences associated with metals or substituents on the outer periphery of the tetrapyrroles. As a result, the structure of chlorins and their functions are altered, such as interactions with the surrounding protein, hydrogen bonding, covalent bonding, and electrostatic interactions. For instance, this is evident with prosthetic groups that consist of iron centers that play crucial roles in oxygen transport and storage, including electron transfer processes [144–146].

Chlorins have been studied for applications in wide-ranging fields, such as photomedicine, catalysis, molecular photonics, conversion of solar energy in dye-sensitized solar cells, and molecular imaging [145–147]. They are also preferred photosensitizer dyes for PDT since they exhibit intense absorption bands between 630−670 nm in the therapeutic window in contrast with their metal porphyrin analogs. A majority of the porphyrinoid-based PDT drugs that are FDA-approved or in clinical trials are chlorin-based. For example, *m*-tetra(hydroxyphenyl)chlorin (Foscan®), tin ethyl etiopurpurin (Purlytin®), and N-aspartyl chlorin *e6* (Talaporfin sodium®) [1,9,148]. Therefore, due to their favorable properties, most chlorin derivative research has focused on how naturally occurring chlorophylls are isolated, how biosynthetic tetrapyrrolic compounds can be derived, how porphyrins can be reduced to chlorins and on total synthesis from their antecedents [145,146].

1.3.2.1 Chlorin synthesis methods

1.3.2.1.1 One-flask synthesis of chlorins from porphyrins

Calvin and co-workers reported the isolation of *meso*-tetraphenylchlorin (H_2TPChl) as a by-product of the intended synthesis of H_2TPP by the Rothemund method [149–151]. This involved a modification reaction after introducing zinc acetate to the vessel, which led to the easy isolation of the TPP and TPChl zinc chelates after column chromatography. In 1952, Dorough and Huennekens improved the isolation of H_2TPChl and also reported and characterized nine of its metal chelates [152] (**Scheme 1.8**). The free-base TPChl was obtained after the zinc chlorin formed was treated with hydrochloric acid to convert it to the corresponding free-base compound. This approach is disadvantageous because the chromatographic process of isolating the chlorin from the mixture with the porphyrin is highly tedious [146]. However, this was the

method of choice for synthesizing chlorins before Whitlock's method of reducing porphyrins using diimide was reported [153].

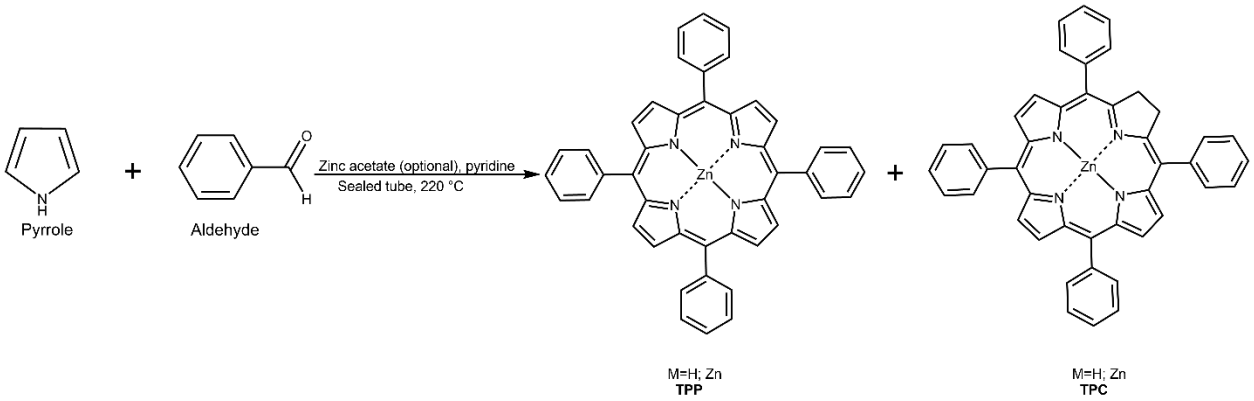

Scheme 1.8: Dorough and Huennekens' improved one-flask synthesis of *meso*-tetraphenylchlorin [152].

1.3.2.1.2 *De novo* synthetic routes to chlorins

The *de novo* synthetic approach was first developed by Battersby *et al.* in 1988 to synthesize C-methylated hydroporphyrin macrocycles, including chlorin and bonellin [154,155]. The characteristic chlorin π-system is locked in by the presence of a geminal dimethyl group in the pyrroline ring, where adventitious oxygen-mediated hydrogenation is blocked. It involves the self-condensation reaction of a western half (2,3,4,5-tetrahydro-1,3,3-trimethyldipyrrin) and an eastern half (9-bromodipyrromethane-1-carboxaldehyde or 9-bromodipyrromethane-1-carbinol) to form hydrobilin followed by metal-mediated oxidative cyclization (**Scheme 1.9**). Chlorins with one (5- or 10-) or two (5,10-) *meso*-substituents are obtained from the use of substituted analogs of the western and eastern halves and allow the synthesis of chlorin derivatives with diverse substituents at the β-pyrrole positions [156]. However, the use of substituted precursors involving the western and eastern halves does not provide access to the

15- and 20- positions. Nevertheless, this can still be achieved through the further derivatization of the intact chlorin [146,156].

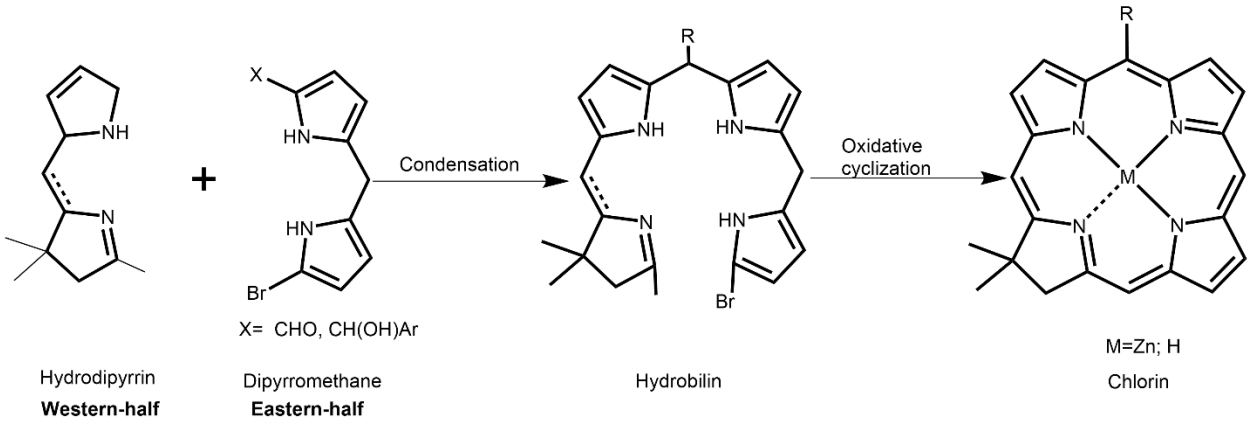

Scheme 1.9: *De novo* synthesis of chlorins [156].

1.3.2.1.3 Hydrogenation of Porphyrins

Porphyrins are 'cryptoolefinic' due to the presence of peripheral double bonds and hence can undergo olefinic reactions, which is unusual for π-systems that are highly aromatic [74,145]. These reactions involve the reduction of diimide and the OsO_4-mediated dihydroxylation of *meso*-aryl porphyrins to form the corresponding chlorins [145]. Whitlock's approach involved the generation of diimide to reduce porphyrins into chlorins [153]. The reaction proceeded through the generation of diimide from the thermal decomposition of *p*-toluenesulfonyl hydrazide in the presence of solvents or bases, such as pyridine, picoline, and sodium carbonate. The mixture was then treated carefully with oxidants, such as DDQ or *p*-chloranil, which converted tetrahydroporphyrins to chlorin (or bacteriochlorin and isobacteriochlorin) (**Scheme 1.10**). However, this process is tedious as it involved separating a complex mixture of porphyrins, chlorins, and bacteriochlorins.

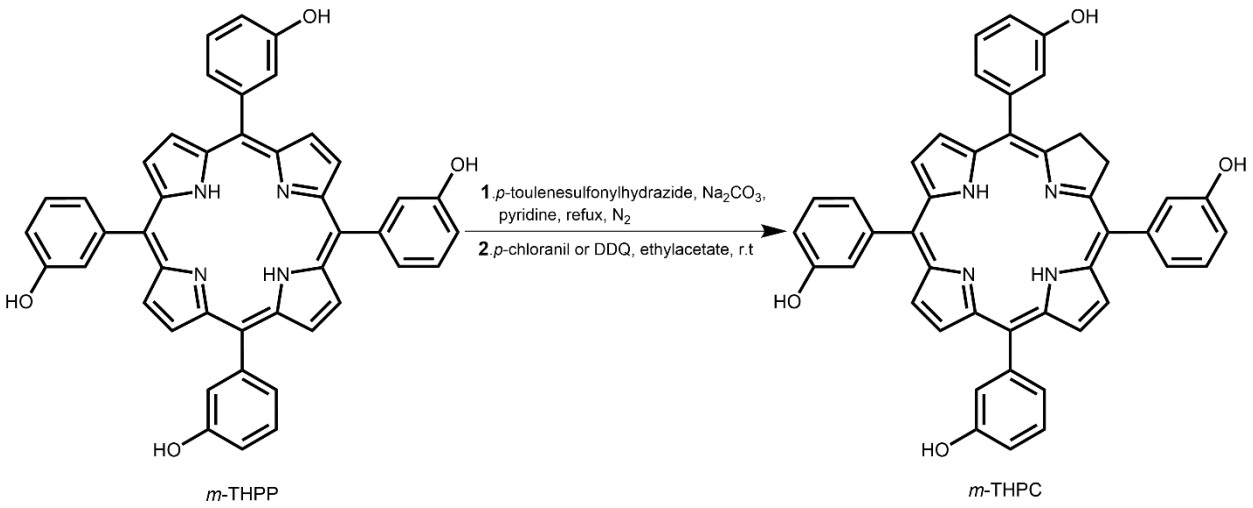

Scheme 1.10: Whitlock's approach for preparing *m*-THPC [153].

Milder reaction conditions were reported by Pereira *et al.* in 2010 by preparing chlorins and bacteriochlorins in the absence of solvents and bases. This reaction involved heating a mixture of porphyrin with *p*-$TsNHNH_2$ in a ratio of 1:30 in an evacuated Schlenk tube up to 140°C. This reaction resulted in a favorable yield of bacteriochlorins of approximately 84%. Moreover, Pereira *et al.* investigated the selective dehydrogenation of bacteriochlorin to the corresponding chlorin using Fenton's reagent (H_2O_2 and catalytic $FeCl_3$) [157,158].

In addition in 2010, Nascimento *et al.* also reported a much-improved hydrogenation approach that involved a two-step microwave synthesis (**Scheme 1.11**). In a similar manner to Whitlock's reaction conditions, the first step involved the treatment of porphyrin with *p*-$TsNHNH_2$ leading to the formation of a bacteriochlorin or a chlorin, and very rarely, the porphyrin. The second step involved the oxidation of the bacteriochlorin to the chlorin using manganese (IV) oxide. This method resulted in a high yield of chlorin since MnO_2 is a heterogeneous catalyst. Purification and isolation were hence much more efficient, clean, and eco-friendly [159].

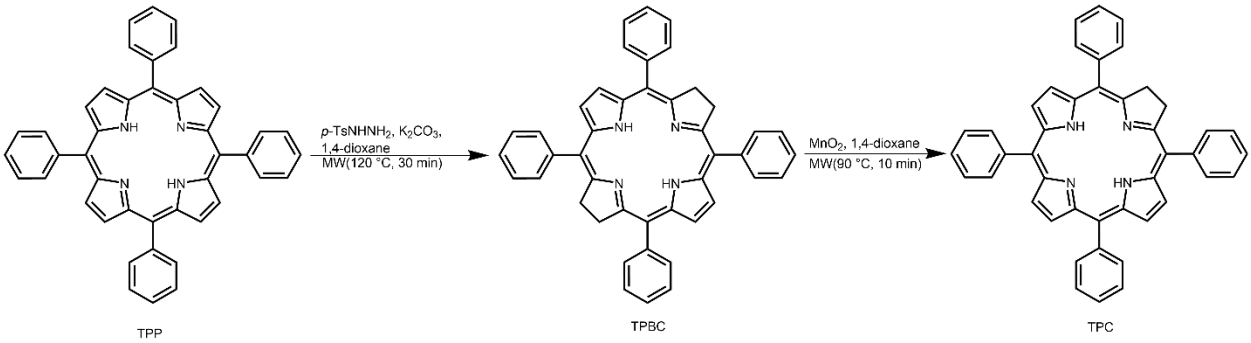

Scheme 1.11: Microwave-assisted synthesis of chlorin (Nascimento and co-workers) [159].

1.3.3 N-confused porphyrins

N-confused porphyrins are true isomers of porphyrins, unlike chlorins, corroles, and other porphyrin analogs. Compared to other porphyrins, N-confused porphyrins (**Figure 1.2**) have at least one of the four pyrrole nitrogen atoms facing outwards, while a CH moiety is located in the central cavity of the macrocycle [160–165]. In 1994, research groups in Poland and Japan first reported 5,10,15,20-tetraaryl-2-aza-21-carbaporphyrin (N-confused porphyrin) [166,167]. The rich metal ion coordination chemistry of this ligand resulted from its ability to stabilize metals in unusually high oxidation states. The ease of formation of metal-carbon bonds by the inner CH moiety of N-confused porphyrins facilitates the synthesis of several other unusual organometallic complexes [160,163–165].

The presence of internal and external nitrogen atoms, together with the inner CH moiety, facilitates the formation of inner and outer coordination complexes and supramolecular structures [161,163–165,168]. Over the past few decades, the chemistry of N-confused porphyrins has grown vastly. This has led to the preparation of several new types of N-confused porphyrin analogs and the exploitation of their metal-coordination properties [164,165]. Core modification of the N-confused porphyrin ligand so that either one or two pyrrole nitrogen are

replaced by other heteroatoms, including O, Se, and S, has led to the formation of core-modified confused porphyrins [162] and the formation of the unusual metal complexes involving weak metal-heteroatom bonds that have interesting properties [160,162,163,165].

1.3.3.1 N-confused porphyrin synthesis methods

1.3.3.1.1 One-flask N-confused porphyrin synthesis

In 1994, two independent research groups led by Chmielewski *et al.* and Furuta *et al.* reported the synthesis of N-confused porphyrin (NCP) [166,167]. They identified free-base NCP as a byproduct of one-flask porphyrin syntheses in low yields obtained under modified reaction conditions based on acid-catalyzed condensation of pyrrole and benzaldehyde. The report by Chmielewski *et al.* (**Scheme 1.12a**) led to the preparation of the 5,10,15,20-tetra(*p*-tolyl)-2-aza-21-carbaporphyrin (H_2NCTTP) after an excess of pyrrole and 4-methylbenzaldehyde were mixed in dichloromethane, and the reaction was catalyzed by BF_3·etherate [166]. The mixture was stirred for one hour in an inert atmosphere and then oxidized with *p*-chloranil. The crude mixture was then separated with chromatography, and a yield of 4% was obtained for H_2NCTTP. Furuta and co-workers synthesized NCP by replacing the conventional use of propionic acid with *tert*-BuOH/CH_2Cl_2 and concentrated HBr (**Scheme 1.12b**) [167]. The process involves mixing pyrrole and benzaldehyde and stirring in the dark at room temperature for two days. This was followed by oxidization with chloranil. Subsequent chromatographic separation led to a yield of 5-7% for H_2NCTPP. These synthetic procedures inherently resulted in a mixture of the NCP target compound at low yields and a normal porphyrin at higher yields. However, in 1999, Geier and Lindsey reported an improved yield of *meso*-tetraphenyl-N-confused porphyrin (TP-NCP) (35%)

as a ubiquitous byproduct of one-flask porphyrin syntheses by using methanesulfonic acid (MSA) as a catalyst [169].

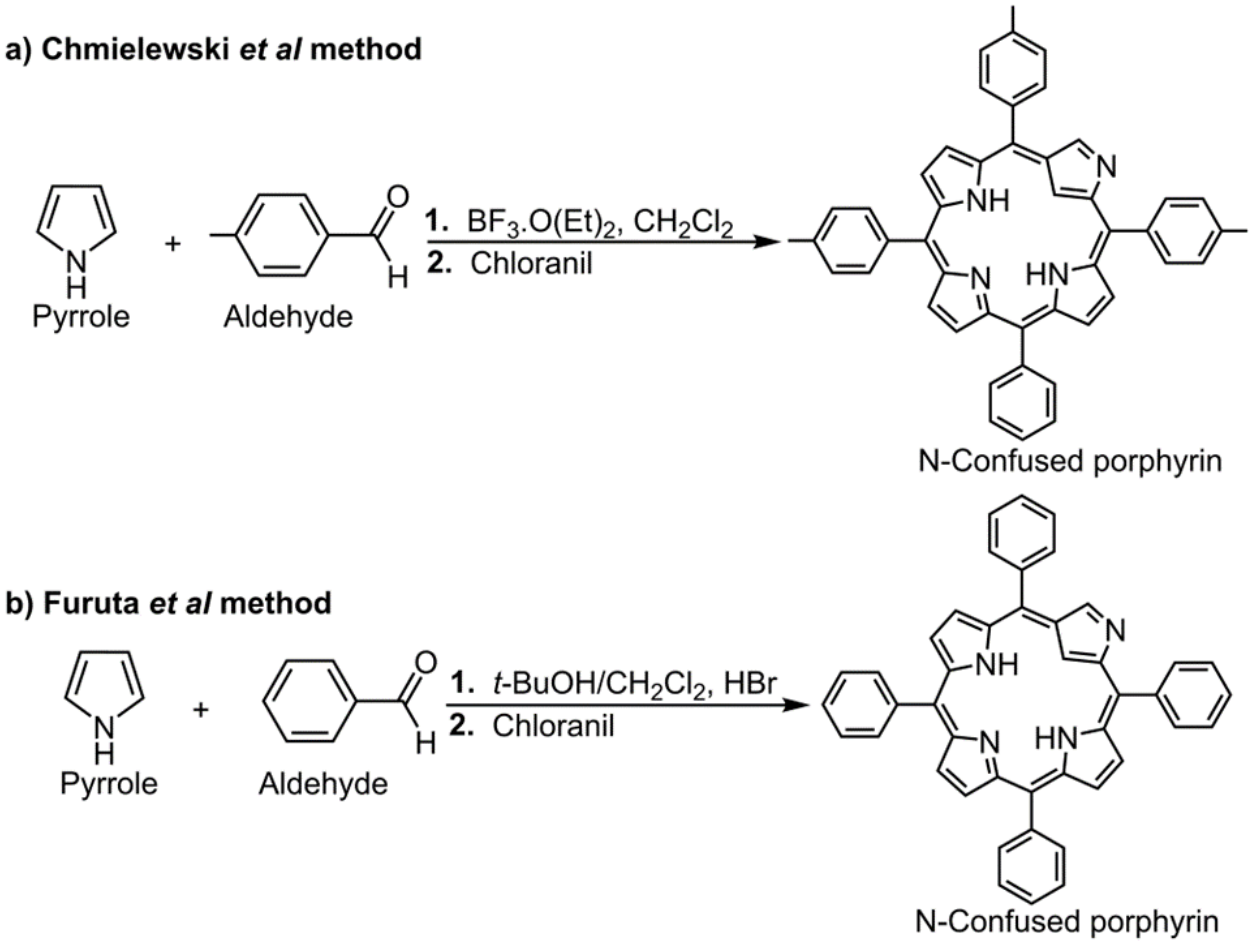

Scheme 1.12: One-flask N-confused porphyrin syntheses a) Chmielewski method [166] b) Furuta method [167].

1.3.3.1.2 An improved one-flask synthesis of N-confused porphyrin

Geier and Lindsey reported improved two-step, one-flask conditions for the synthesis of free-base N-confused porphyrin (H_2NCTPP) (**Scheme 1.13**) [169]. This involved the reaction of pyrrole (10 mM) and benzaldehyde (10 mM) in dichloromethane, followed by the addition of methanesulfonic acid (MSA) (7 mM). The mixture was stirred for 30 min, followed by oxidization

using DDQ. Thereafter, the acid was quenched by adding triethylamine (TEA) to the reaction mixture. Subsequent column chromatography separation on alumina led to a highly improved yield of 35% (800 mg) of H_2NCTPP.

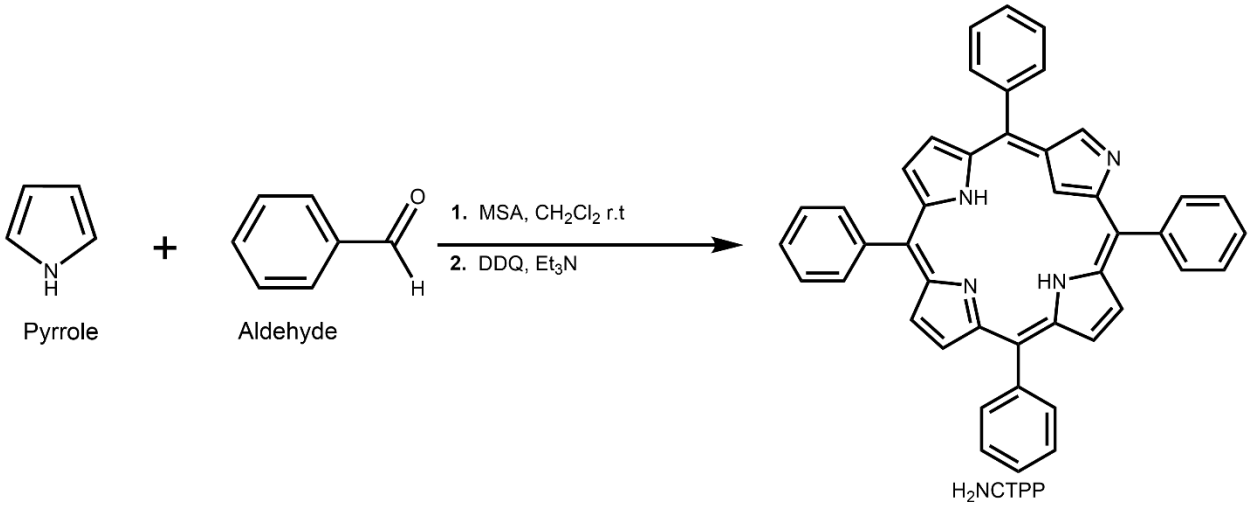

Scheme 1.13: Synthesis of H_2NCTPP using Geier and Lindsey's procedure [169].

Geier and Lindsey's method contributed significantly to the synthesis and coordination chemistry of N-confused porphyrins (NCPs) since it facilitated the synthesis of a wide range of NCPs bearing diverse substituents that are coordinated to various metal ions. However, synthesizing NCPs with electron-withdrawing groups, such as pentafluorophenyls, is challenging using this approach since this method affords very low yields (< 0.1%).

1.3.3.1.3 Stepwise synthetic approach for pentafluorophenyl)-N-confused porphyrin

There has been ongoing interest in the preparation and study of *tetrakis*(pentafluorophenyl)-N-confused porphyrin (C_6F_5–NCP) due to the significance of the strongly electron-withdrawal property of pentafluorophenyl substituent. However, very low yields (< 0.1%) were obtained for C_6F_5–NCP using the one-flask Lindsey reaction method since the reaction resulted in the preferential formation of ring-expanded porphyrins. Following this, Furuta and co-workers

reported a stepwise synthesis of C_6F_5–NCP in 2003 (**Scheme 1.14**) using the Friedel-Crafts reaction of the corresponding dipyrromethane to obtain a carbinol N-confused perfluorophenyl substituted dipyrromethene [170]. This reaction was followed by an acid-catalyzed condensation with a normal dipyrromethene and subsequent oxidation of the mixture using DDQ to obtain a 21% yield of C_6F_5-NCP. This stepwise reaction procedure afforded several C_6F_5-NCP metal complexes and established research on their chemistry. However, limiting factors to this approach include the need for greater synthetic expertise compared to the one-flask method and the time-consuming procedure of this method [171].

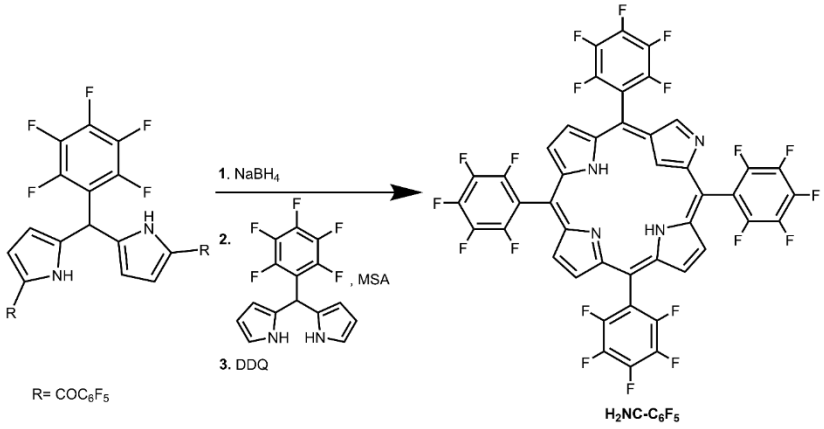

Scheme 1.14: Stepwise synthesis of N-confused porphyrin (C_6F_5-NCP) bearing perfluorophenyl groups reported by Furuta and co-workers [170].

1.4 Optical properties of porphyrins and porphyrin analogs

Porphyrins and porphyrin analogs exhibit intense colors due to the absorption bands in the 400−800 nm range of the electromagnetic spectrum that arise from their highly conjugated 18-π electron systems [74,77]. A normal porphyrin typically exhibits a very intense absorption band (B band) between 400−450 nm and weaker absorption bands (Q bands) between 500−700 nm [48,74]. Typical ground-state absorption spectra for *meso*-aryl substituted metalloporphyrins and

the metalloporphyrin analogs studied (i.e. corrole, chlorin, and N-confused porphyrin complexes) are provided in **Figure 1.5**.

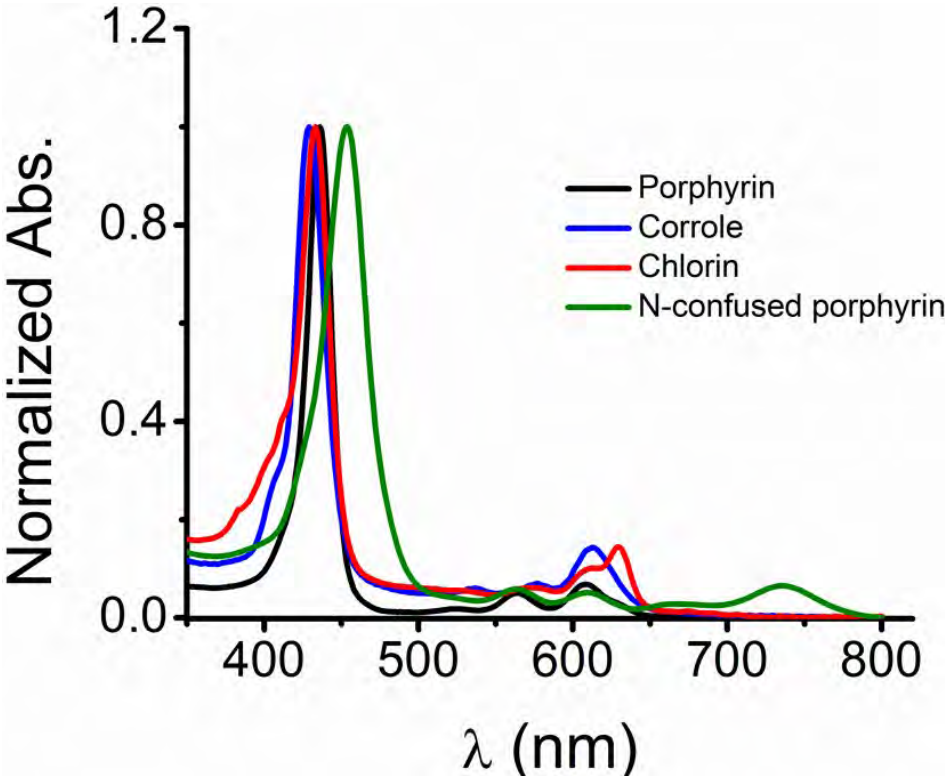

Figure 1.5: Normalized ground-state absorption spectra for typical Sn(IV) porphyrin (black), Ga(III) corrole (blue), Sn(IV) chlorin (red), and Sn(IV) N-confused porphyrin (green) complexes in DMSO.

The electronic absorption properties of the porphyrins and porphyrin analogs studied in this thesis can be conceptualized using Gouterman's 4-orbital and Michl's perimeter models [172-175]. A theoretical model describing the electronic absorption spectra for tetrapyrrolic compounds, including porphyrins, reduced porphyrins (chlorins and isobacteriochlorin), and phthalocyanines, was described by Gouterman in the early 1960s based on a four-frontier molecular orbital approach [172]. According to this model, porphyrin electronic absorption spectra arise from the transitions between four frontier molecular orbitals (MOs) derived from

the doubly-degenerate HOMO and LUMO of a parent $C_{16}H_{16}^{2-}$ parent hydrocarbon, which has M_L values of ±4 and ±5 associated with the presence of four and five angular nodal planes, respectively (**Figure 1.6**)[172].

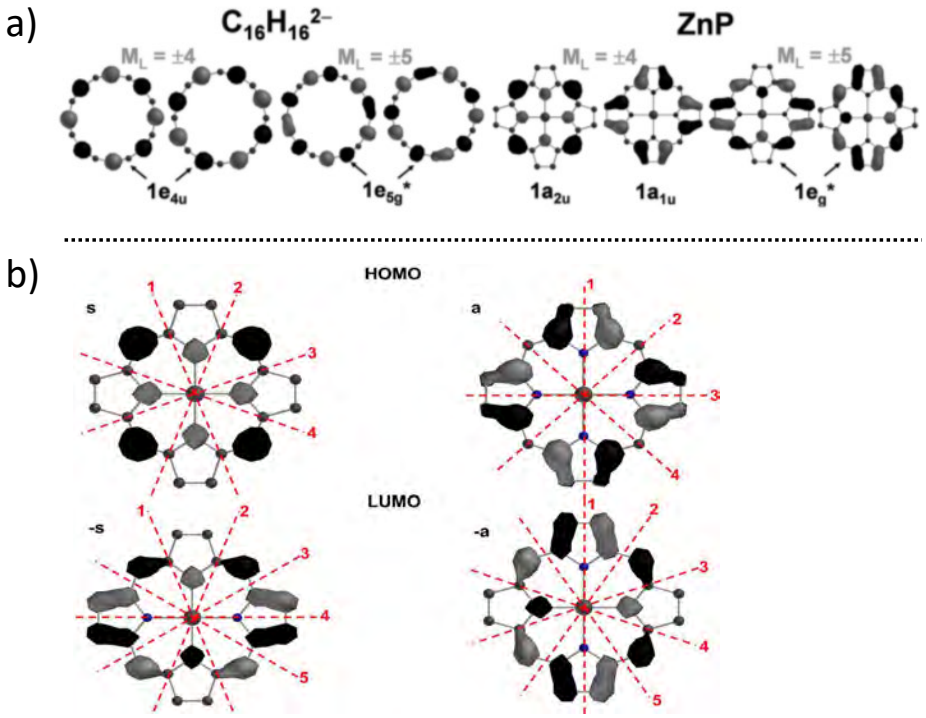

Figure 1.6: a) The parent $C_{16}H_{16}^{2-}$ inner ligand and the four frontier MOs; b) angular nodal patterns for zinc tetraphenylporphyrin (ZnTPP) of the **a**, **s**, **-a**, and **-s** MOs of Michl's perimeter model. Reproduced with permission from Reference [109]. Copyright © American Chemical Society 2017.

The parent 16 atom 18 π-electron inner ligand perimeter ($C_{16}H_{16}^{2-}$) of the porphyrin ring consists of π-MOs arranged in an M_L = 0, ±1, ±2, ±3, ±4, ±5, ±6, ±7, 8 sequence in ascending energy terms due to the angular nodal properties [109]. Michl developed 4N+2 and 4N perimeter models for assigning the frontier π-MOs derived from the HOMO and LUMO of the parent perimeters of aromatic, anti-aromatic, and nonaromatic π-systems [173]. The π-MOs with angular nodal planes

that lie on the *y*-axis are designated as the **a** and **-a** MOs, while those with large MO coefficients on the *y*-axis are referred to as the **s** and **-s** MOs in this context (**Figure 1.6 b**).

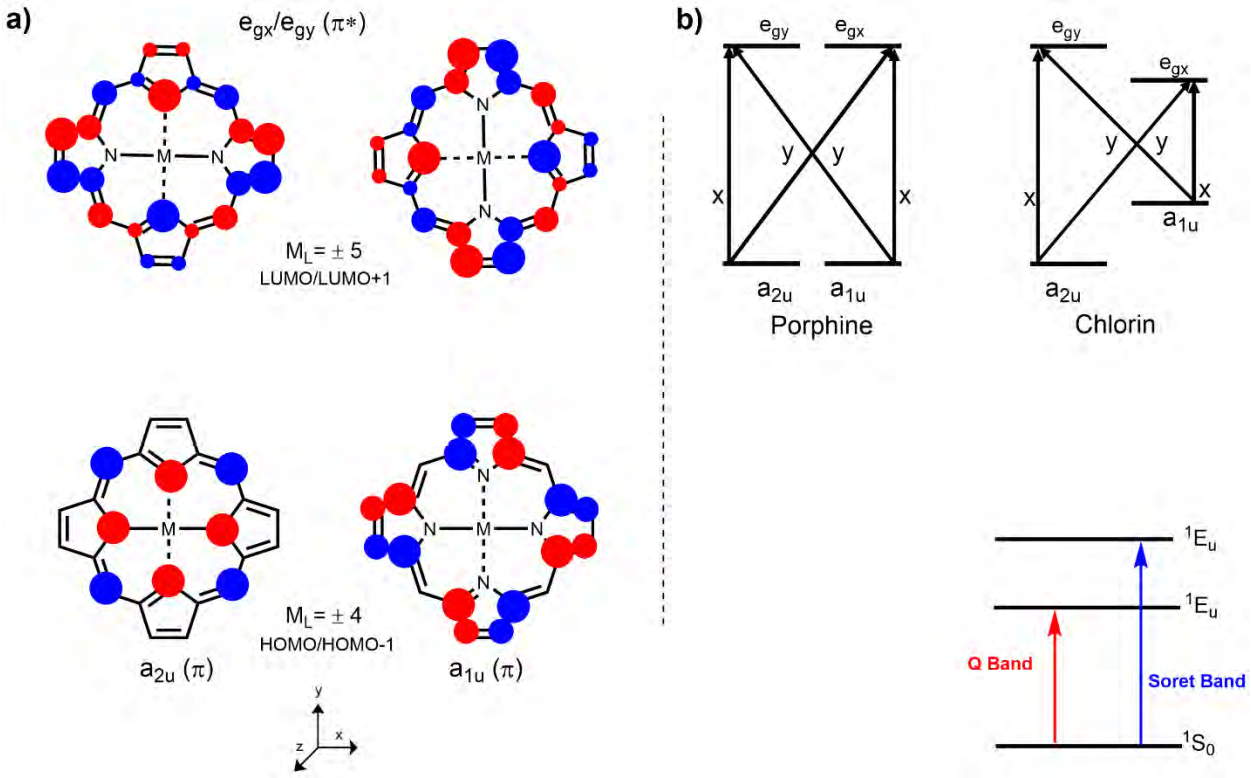

Figure 1.7: a) The four frontier molecular orbitals of porphyrin by Gouterman. b) The energy levels and electronic transitions for porphyrins.

Gouterman's 4-orbital model predicts that the HOMO level of porphyrins arising from the $C_{16}H_{16}^{2-}$ parent perimeter is non-degenerate ($1a_{1u}$ and $1a_{2u}$ or **a** and **s**, respectively) while the LUMO level ($1e_g$* or **-a** and **-s**) is degenerate. The HOMO and LUMO levels of metalloporphyrins with D_{4h} symmetry have M_L values of ±4 and ±5 angular nodal properties, respectively, regardless of which metal ions and peripheral substituents are introduced [172], (**Figure 1.7 a**). Gouterman's 4-orbital model predicted that the intense Soret band ($S_0 \rightarrow S_2$) arises from the allowed B transition ($\Delta M_L = \pm 1$) at high energy in the blue region of the visible and the weaker Q band ($S_0 \rightarrow S_1$) arises from

the forbidden Q transition ($\Delta M_L = \pm 9$) in the lower energy red region (**Figure 1.6b**). The Q bands of porphyrins are forbidden due to the near degeneracy of the $1a_{1u}$ and $1a_{2u}$ MOs: this results in the cancellation of the electric dipole moments transitions from the nearly equal contributions transitions from the $1a_{2u} \rightarrow 1e_g^*$ and $1a_{2u} \rightarrow 1e_g^*$ one-electron transitions (**Figure 1.7b**) [172].

Peripheral substitution and decreased symmetry result in significant changes in the optical properties of porphyrins, corroles, chlorins, N-confused porphyrin, and other porphyrin derivatives [48,109,174] (**Figure 1.5**) In general, structural modifications with *meso* or β substituents or changes in symmetry result in significant perturbations to the relative energies of the four-frontier MOs and this modifies the electronic structure and optical properties [109,176,177], since the lifting of the degeneracies of the frontier MOs results in a mixing of the allowed and forbidden properties of the B and Q bands. The various structural modifications of the porphyrin ligand that are required to form corrole, chlorins, and N-confused porphyrin complexes hence result in an intensification of the Q band [109]. This makes these PS dyes favorable candidates for biomedical singlet oxygen related applications, such as PDT, that require the PS dye to absorb light strongly in the therapeutic window (620−850 nm) [44,174,175].

The theoretical section in Chapter 10 will provide a more detailed discussion to provide a deeper understanding of the effect of these structural modifications on the four frontier orbitals of the tetrapyrrolic macrocycles that were studied.

1.5 Photophysicochemical properties of porphyrins and porphyrin analogs

Porphyrins and porphyrin analogs undergo photophysicochemical processes that are the key to determining their suitability for use as photosensitizer dyes in various fields, such as PDT and

PACT [46,48,76]. These properties are fundamentally derived from the different electronic transition states of the dye molecules following the absorption of a photon. These processes can be more clearly visualized using a Jablonski diagram (**Figure 1.8**). When a PS dye is irradiated with light of appropriate wavelength, it absorbs an incident photon and is photoexcited from the ground state (S_0) to the unoccupied molecular orbital S_n, corresponding to the amount of light energy transferred [178,179]. This is followed by several rapid relaxation mechanisms of the excited states to the short-lived lowest vibrational level S_1 through the internal conversion process (IC). From the S_1 excited state, the molecule (^{1}PS) either decays rapidly to the ground state by emitting a photon following Kasha's rule through fluorescence or by nonradiative decay [178,179]. According to Kasha's rule, fluorescence occurs exclusively at the lowest vibrational level of the S_1 state, which means that fluorescence emission spectra and quantum yields are usually independent of the excitation wavelength [180].

The S_1 singlet-excited state can also undergo a spin-forbidden process called intersystem crossing to the long-lived T_1 triplet-excited state (^{3}PS). The T_1 state can decay back to the S_0 ground state by emitting a photon *via* phosphorescence or transfer energy to ground state molecular dioxygen ($^3O_2$) and other radicals to form singlet oxygen ($^1O_2$) by a Type II mechanism. Electron transfer by a Type I mechanism results in the formation of reactive oxygen species (ROS) [179]. The processes that arise after photoexcitation can be quantified with quantum yields. A quantum yield provides a measure of process efficiency in terms of a ratio of the number of times the process occurs per photon absorbed [179]. In this study, four photophysical and photochemical processes related to the fluorescence quantum yields (Φ_F), fluorescence lifetimes (τ_F), singlet oxygen quantum yields (Φ_Δ), and triplet lifetimes(τ_T) were measured and analyzed.

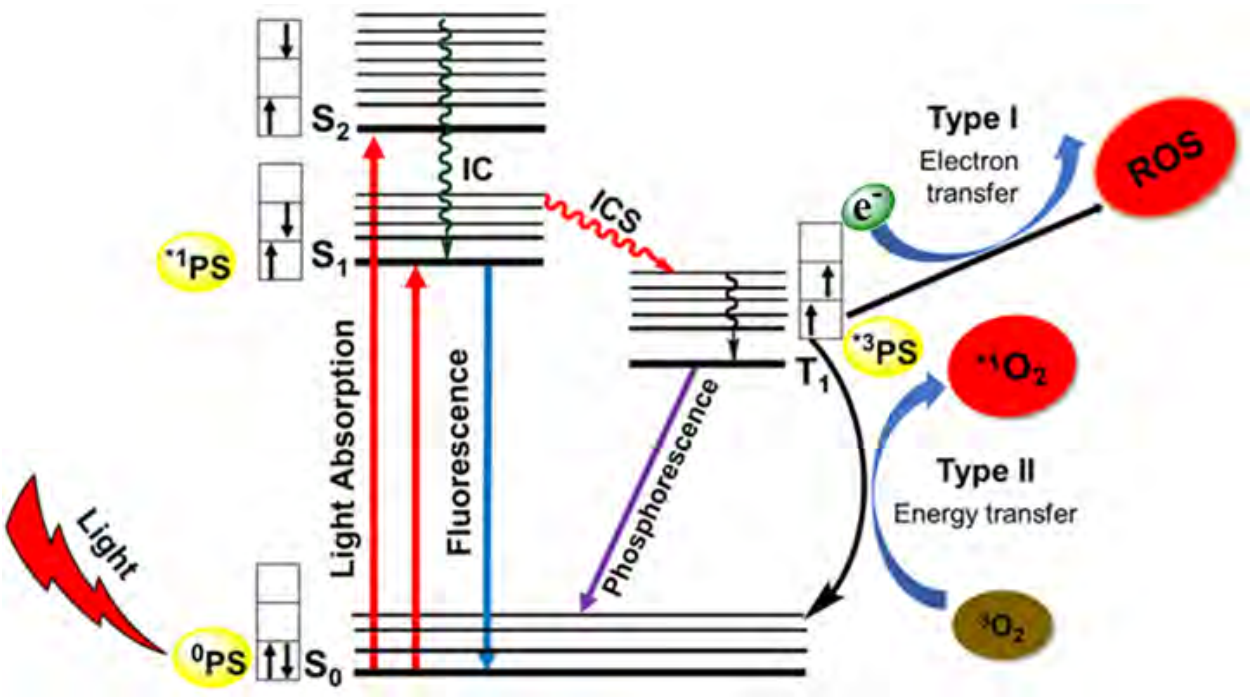

Figure 1.8: A Jablonski diagram illustrating the photophysicochemical processes of a PS dye upon photoexcitation: absorption, fluorescence, internal conversion (IC), intersystem crossing (ICS), triplet excited state (T1), and phosphorescence.

1.5.1 Fluorescence quantum yields and lifetimes

Fluorescence occurs when a fluorophore compound is photoexcited with the light of a certain wavelength with photons emitted at a specific wavelength range over a defined range, typically 10^{-6} to 10^{-8} seconds [178]. Porphyrins and porphyrin analogs exhibit fluorescent characteristics due to their highly conjugated 18-π electron systems and rigid structures. The fluorescence spectra of these compounds are primarily mirror images of their $S_0 \rightarrow S_1$ absorption bands in the 600−800 nm range, following Kasha's rule [76,178], as previously discussed. The two most important fluorescent properties of a fluorophore that determine its suitability for use in various applications are its fluorescent quantum yield (Φ_F) and lifetime (τ_F).

The fluorescent quantum yield (Φ_F) provides a measure of the efficiency of a fluorophore in emitting a photon by providing the ratio of the number of photons emitted to the number of photons absorbed. It is also defined as the ratio of the intrinsic radiative rate constant (K_r) to the sum of all rate constants (K_r) for all the processes involved in the depopulation of the S_1 excited state, as described in Equation 1.1.

$$\Phi = \frac{K_r}{K_r + K_{nr}} \quad \textbf{(1.1)}$$

Where K_r is the radiative rate constant, and K_{nr} is the sum of rate constants of internal conversion and intersystem crossing to the triplet state.

The fluorescence quantum yields of porphyrins and porphyrin analogs vary significantly depending on the structure, nature of coordination central ion, and the *meso* and peripheral substituents. The incorporation of heavy atoms, such as metals and halides, is known to lower the yields, among other factors, such as the solvent used, pH, aggregation, and temperature [181–184]. The Φ_F values are usually determined by using a comparative method. This is accomplished by comparing the integrated area of a sample fluorescence curve with that of a known standard excited at the same wavelength under the same experimental conditions [185] as described in Equation 1.2:

$$\Phi_F = \Phi_{F(std)} \frac{F.A_{std}.\eta^2}{F_{std}.A.\eta^2_{std}} \quad (1.2)$$

Where $\Phi_{F(std)}$ denotes the fluorescence quantum yield of the standard, F and F_{std} are the areas under the fluorescence curve for the sample and the standard, respectively; A and A_{std} represent the absorbance of the sample and the standard at the excitation wavelength and η^2 and $\eta^2{}_{std}$ are

the refractive indices of the solvent used for the sample and the standard, respectively. In this study, zinc(II)tetraphenylporphyrin (ZnTPP) in DMSO (Φ_F = 0.037) was used as the standard.

Fluorescence lifetime (τ_F) values provide the average amount of time a fluorophore spends in the S_1 excited state before relaxing back to the S_0 ground state *via* the emission of a photon. Fluorescence lifetimes can be determined by measuring the decay in fluorescence intensity as a function of time after populating the excited molecules uniformly with a brief pulse of light. The decay in fluorescence intensity is described as a function of time by an exponential function in Equation 1.3:

$$I(t) = I(o).e^{-t/\tau} \quad \textbf{(1.3)}$$

Where I(t) denotes the fluorescence intensity measured at time t, I(o) is the initial intensity observed immediately after excitation, and τ is the fluorescence lifetime.

Therefore, the fluorescence lifetime (τ_F) is defined as the time for the decay of 1/e (approximately 37%) of the initial fluorescence intensity. It is also defined as the reciprocal of the sum of rate constants for all the processes involved in the S_1 excited state depopulation, as described in Equation 1.4:

$$\tau_F = \frac{1}{K_r + K_{nr}} \quad \textbf{(1.4)}$$

Where K_r is the radiative rate constant, and K_{nr} is the sum of rate constants of processes' internal conversion and intersystem crossing to the triplet state.

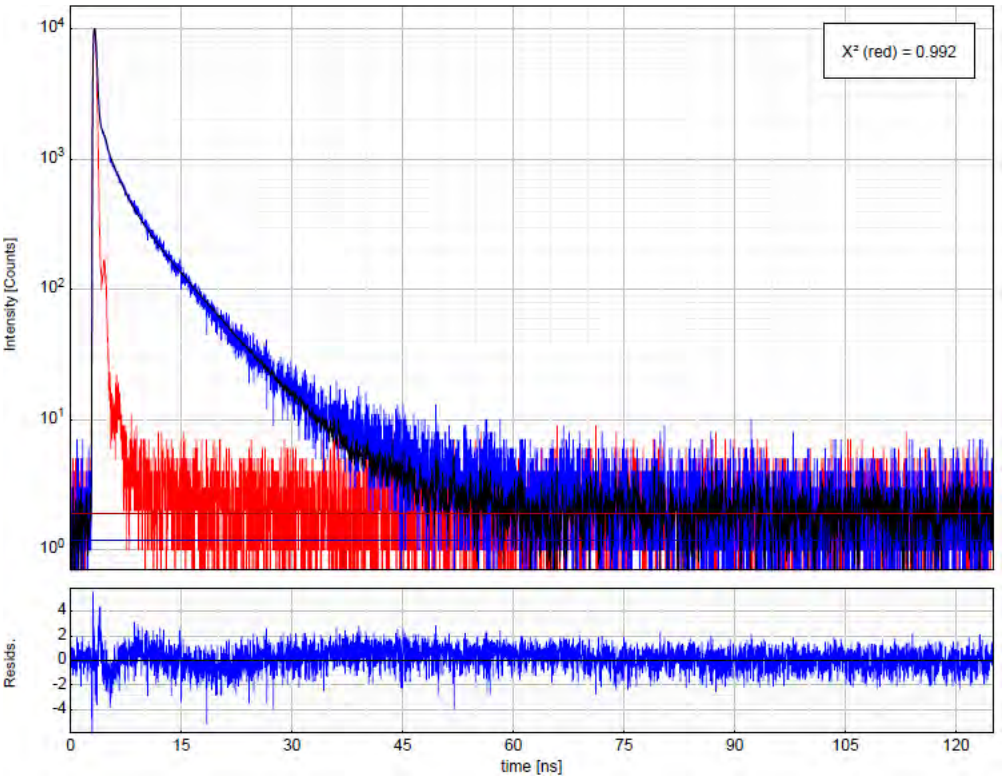

Figure 1.9: A typical fluorescence decay curve (blue), reduced χ^2 fitting (black), residuals (lower panel blue), and instrument response function (IRF) (red) for a porphyrinoid in DMSO.

However, if emission were only a decay process, the lifetime would be defined as a natural or radiative lifetime (τ_0). The radiative lifetime (τ_0) is the inverse of the radiative constant $\tau_o = K_r{}^{-1}$. It is longer than the fluorescence lifetime (τ_F) and is related to fluorescence quantum yield as described in Equation 1.5.

$$\tau_0 = \frac{\tau_F}{\Phi_F} \qquad (\mathbf{1.5})$$

Where τ_0 denotes the radiative lifetime, τ_F is the fluorescence lifetime, and Φ_F is the fluorescence quantum yield.

The τ_F values are usually measured using the time-correlated photon counting technique (TCSPC) by analyzing fluorescence emission decay curves through deconvoluted exponential fitting

(**Figure 1.9**). Research studies have shown that the τ_F values for porphyrin and porphyrin analog derivatives vary significantly, ranging from 0.1−20 ns depending on their core ion and their *meso* and peripheral structural modification chemistry [183,186,187].

1.5.2 Triplet lifetimes

The therapeutic activity of a PS dye for PDT and PACT use depends to a large extent on its ability to populate the T_1 triplet excited state and induce the cytotoxic Type I and Type II species after photon absorption [1,3,13,14,46,47]. Longer lifetimes for the T_1 state increase the probability of collisions with an $^3O_2$ molecule and consequently increase the generation of $^1O_2$. This largely depends on the spin-orbit coupling interactions that enhance and optimize the spin-forbidden ISC process to the T_1 state, which can be enhanced by incorporating heavy atoms. Since the heavy atom effect favors ISC to the T_1 state, it simultaneously lowers the rate of the fluorescence process [14,46,47]. For porphyrins and porphyrin analog derivatives, triplet lifetimes range from a few microseconds to milliseconds with a drastic decrease observed in the presence of heavy atoms [46,183]. The triplet excited state absorption and lifetime properties of a PS dye can be measured by the laser flash photolysis technique. The triplet lifetimes were obtained by exponential fittings of the triplet decay curves.

1.5.3 Singlet oxygen quantum yields

$^1O_2$ is the chief cytocidal agent crucial for inducing a cascade of biochemical reactions that result in cell death by apoptosis or necrosis in phototherapeutic applications [3,4,8,13–15,17]. It is produced when a PS molecule in the T_1 excited state transfers energy efficiently to $^3O_2$. As

discussed previously, the heavy atom effect enhances the rate of ISC to the triplet manifold and hence facilitates the efficient generation of singlet oxygen [3,14,15,46].

The singlet oxygen quantum yield (Φ_Δ) measures the quantitative efficiency of a PS dye in generating the reactive singlet oxygen species after photoexcitation. A comparative chemical method is often used to quantify the amount of reactive oxygen species generated by a molecule upon photoirradiation. This method involves using a chemical reagent, such as 3-diphenylisobenzofuran (DPBF), that scavenges or quenches singlet oxygen species in organic solutions. When a singlet oxygen quencher is added to a PS dye solution, it reacts with the singlet oxygen produced upon photoexcitation to form a degraded product, as illustrated in **Figure 1.10**. This results in a change in the intensity of the main absorption band of the quencher, which can be monitored at fixed time intervals with a UV-visible absorption spectrometer. The singlet oxygen yield (Φ_Δ) of a PS sample can be quantified using a comparative method as described in Equation (1.6):

$$\Phi_\Delta = \Phi_{\Delta std}.\frac{m.F^{std}}{m^{std}.F} \qquad (\mathbf{1.6})$$

Where $\Phi_{\Delta std}$ is the singlet oxygen quantum yield of the standard (5,10,15,20 *meso*-tetraphenylporphyrin H_2TPP = 0.52 in DMSO [188], or Rose Bengal RB = 0.76 in DMSO [189]); m and m^{std} are the rates of photodegradation of DPBF (at *ca.* 418 nm) by the sample and standard respectively; and F and F^{std} are the absorption correction factors of the sample and the standard. The concentration of DPBF was kept constant for the sample, and the standard and the experiments were performed under the same experimental conditions in terms of the solvent, excitation wavelength, and optical densities.

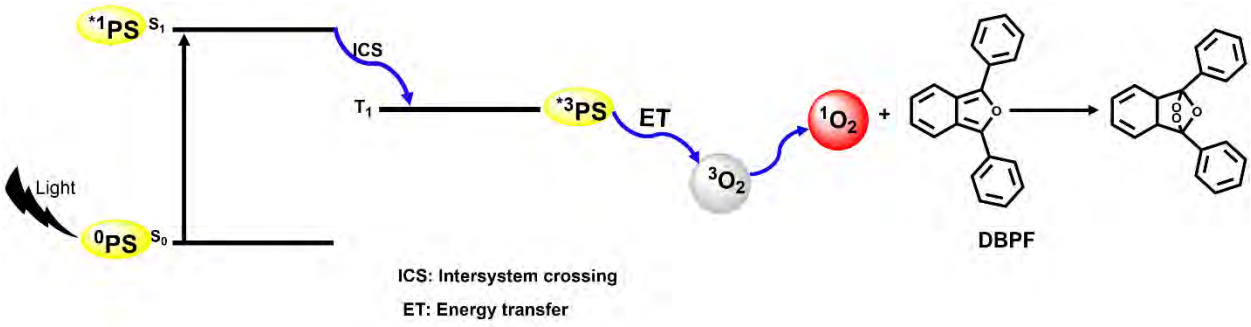

Figure 1.10: The photoexcitation and photochemical production of singlet oxygen mechanism by a dye and subsequent reaction with the DPBF quencher.

1.5.4 Photostabilities of the dyes

The photostability of a PS dye is an important property that determines its efficiency for use in many fields. A PS dye undergoes an irreversible loss of its photosensitizing properties after photobleaching and photodegradation [14,190–192]. These processes occur *via* two main mechanisms: oxygen-dependent and oxygen-independent mechanisms. Oxygen-dependent photobleaching mechanism is common for porphyrinoid dyes. Since this class of dyes finds application in many fields, such as artificial photosynthesis, photocatalysis, dye-sensitized solar cells, and PDT and PACT, in each case, their mode of action involves photoinduced processes derived from the triplet manifold [190–192]. Oxygen-dependent photobleaching involves oxidative photodegradation processes in which a PS dye self-degrades while generating $^1O_2$. During PDT and PACT, a PS dye usually generates $^1O_2$ and may undergo self-oxidative photobleaching. This can result in unwanted side products that can cause complications and reduce PDT and PACT efficacy [14,190–192]. Therefore, a suitable photosensitizer for PDT and PACT should be highly photostable. Research studies have established that the photostabilities of the dyes primarily depend on their chemical structural properties, among other factors [190–

192]. In this study, the photostabilities of the dyes were measured on a UV-visible spectrometer by monitoring the changes in their absorption spectral features upon photoirradiation under the same conditions used for the PDT and PACT activity studies.

1.6 Application of porphyrin and porphyrin analog dyes

1.6.1 Photodynamic therapy

PDT has emerged as a minimally invasive clinical cancer treatment technique, in contrast to the conventional cancer treatments, such as surgery, radiotherapy, and chemotherapy that are characterized by harmful side effects, including indiscriminate destruction of both healthy and tumor cells [1–6,12–16]. PDT involves the administration of a photosensitizer dye that selectively localizes in the targeted tumor cells, which upon irradiation with harmless light of appropriate wavelength (preferably 620−850 nm therapeutic window for deeper tissue penetration), initiates a series of photochemical reactions. These photochemical reactions occur when the photoexcited photosensitizer dye in the T_1 state interacts with the intracellular molecules to produce Type I and Type II reaction products that are cytotoxic to tumor cells [1–6,12–16].

Type I products are produced when the photosensitizer interacts with the biological substrates, such as lipids, nucleic acids, and proteins, *via* electron or hydrogen transfer to form a pair of free radical species of the photosensitizer and corresponding biomolecule [1–6,12–15]. When the free radicals are in an oxygenated environment, they interact with $^3O_2$ through a direct electron transfer to form superanion radicals and other ROS, that induce oxidative stress to the tumor cells and thus kill them. In contrast, Type II reactions involve the T_1 state transferring its energy

to $^3O_2$ to form $^1O_2$, the principal cytotoxic agent responsible for tumor cell destruction during PDT [1–6,12–16].

In essence, PDT treatment efficiency depends on the photophysical and photochemical properties of the photosensitizer dye, particularly their enhanced capability to undergo ISC to the triplet excited and initiate the photochemical processes [1–6,12–16]. Research studies have established that an ideal photosensitizer for PDT use should exhibit high photostability, selectivity to tumor cells, enhanced solubility in biological media, absorption properties in the therapeutic window, enhanced ISC, high triplet quantum yields and long-lived triplet excited state, high singlet oxygen quantum yield, minimal dark cytotoxicity, and enhanced biocompatibility [1–6,12–16]. However, a photosensitizer that meets all these ideal requirements has yet to be obtained, and therefore PDT has yet to fulfill its potential. There is an ongoing research focus on the search for new photosensitizer dyes that exhibit the desired properties, particularly strong absorption properties in the NIR region for deeper penetration into deep-seated tumors, high singlet oxygen quantum yields, and selectivity toward tumor cells [1–6,9,12–16]. In recent decades, porphyrin analog dyes, such as corroles, chlorins, and N-confused porphyrins that exhibit enhanced absorption properties in the red-visible end of the electromagnetic spectrum have gained considerable attention in this context [9,39,44,148].

1.6.1.1 Porphyrins and porphyrin analog derivatives used as PDT drugs

For decades, porphyrin-based dyes have been studied extensively for PDT [1–6,9–16]. For example, the first-generation PDT drug approved for clinical use was Photofrin®, a complex porphyrins oligomer consisting of monomeric hematoporphyrin units linked by ether and ester bonds. However, it suffered from significant drawbacks, such as relatively weak absorption at the

red end of the visible region. This implies that a high concentration of dye has to be administered during PDT treatment, resulting in slow clearance from the human body, and thus, prolonged periods of light-sensitization of patient skin due to its PDT efficiency. In addition, although its monomeric units have a Φ_{Δ} value of 0.64, this significantly decreases to less than 0.15 in aqueous biological media due to aggregation, and there is poor selectivity toward tumor cells [1–6,9,12–16,31,34]. These drawbacks inspired the development of second-generation photosensitizer dyes characterized by improved purity and strong absorption in the therapeutic region. These include porphyrin analogs, such as chlorins, phthalocyanine, naphthalocyanine, purpurins, and texaphyrin derivatives [1–6,9–16]. **Table 1.1** highlights some of the porphyrin-based drugs that are clinically approved or in clinical trials for PDT treatment use. However, second-generation PDT drugs also exhibited limitations, such as low solubility and poor selectivity toward tumor cells, leading to the development of third-generation photosensitizer drugs [1–6,9,12–16].

Third-generation PDT photosensitizer drugs typically consist of second-generation drugs grafted with specific target agents, which enhance drug stability, solubility, selectivity, and bioaccumulation in the tumor tissues. These drug formulations also often consist of photosensitizer dyes conjugated with nanoparticles or nanocarriers, such as metallic nanoparticles, quantum dots, liposomes, micelles, polymers, and dendrimers, including biomolecules, such as peptides, antibodies, amino acids, and carbohydrates incorporated through conjugation or encapsulation to target specific tumor tissues [1–6,9,12–16]. The majority of the third-generation photosensitizers are at the developmental stage and have shown superior performance compared to the second-generation photosensitizers. For example, studies have shown that Ce_6 photosensitizer conjugated to gold nanoparticles (AuNPs) exhibits improved ROS

generation by 1.6-fold compared to Ce_6 alone [193]. The study also showed that further modification of AuNP-Ce_6 with PEGylated-lactoferrin (Lf-PEG) enhanced oral absorption and targeted the glioblastoma multiforme (GBM) cancer. The *in vivo* studies on an orthotopic mice model showed improved bioavailability of 7.3 ± 1.2% and that the amount of Ce_6-AuNP-Lf targeted to GBM was as high as 11.8 ± 2.1 μg/kg after drug administration. PDT treatment was much improved due to the favorable effect of AuNPs and GBM targeting [193].

Table 1.1: Selected porphyrin and porphyrin analog PDT drugs approved or in clinical trials.

	Drug	**Active drug**	λ (nm)	**Description**	**Cancer targeted**	**Refs**
First-generation	Photofrin®	HpD	630	Porphyrin oligomer but with limited tissue penetration and prolonged skin photosensitivity of patients after treatment.	Lung, endobronchial, esophageal, adenocarcinoma, and brain cancer	[1,10,11,16,194–196]
Second generation	Foscan®	*m*-THPC	652	Chlorin derivative, but with side-effects, such as pain and headaches, including photosensitivity.	Head, neck, pancreatic, and breast cancer	[1,10,11,197–199]
Second generation	Visudyne®	Verteporfin BDP	690	Chlorin derivative derived from Protoporphyrin IX, which allows deeper light penetration but with prolonged photosensitivity and pain due to treatment side-effects.	Age-related macular degeneration	[1,11,200,201]
Second generation	Purlytin®	Pururin	660	Sn(IV) chlorin-based photosensitizer, which is highly effective for short-term therapy sessions. However, it exhibits dark cytotoxicity, photosensitivity, and	Chest wall metastasis, Kaposi sarcoma, and metastasis of breast cancer	[1,10,14,16,194,202]

				poor stability in aqueous solutions		
Second generation	Laserphyrin®	Talaporfin-mono-L-aspartyl-chlorin	664	Chlorin derivative with improved therapeutic efficiency. However, it exhibits skin photosensitivity.	Head, neck, liver, prostate, metastasis, colorectal neoplasm	[3,10,16,203]
Second generation	Levulan®	ALA-protoporphyrin IX	630	It converts to protoporphyrin IX in cells upon administration but has low activity and requires longer treatment periods.	Skin, actinic keratosis, bladder,	[3,10,194,204]
Second generation	Photosens®	Sulfonated Al phthalocyanine	676	A phthalocyanine derivative with sulfonate groups that improve intracellular localization and excretion from tissues, but its use is limited by aggregation at high concentrations.	Endobronchial and coetaneous lesions, lip, tongue, head, and neck	[11,205,206]
Second generation	Radachlorin	Ce_6	662	It is a complex mixture of three chlorins which is highly effective but photosensitive.	Skin cancer, lung carcinoma, early oesophageal, liver, cervical cancer	[3,207,208]

Since many photosensitizer drugs approved for PDT use are porphyrin-based macrocycles, porphyrins, corroles, chlorins, and N-confused porphyrins that can be structurally modified and easily functionalized to be suitable for PDT use are promising candidates in this context. In this research work, *meso*-aryl porphyrins and porphyrin analogs that include corroles, chlorins, and N-confused porphyrins were core functionalized with P(V), Ga(III), and In(III) metal ions. Part of this work on the PDT activities of chloroindium (III) porphyrins, pyridyl gallium(III), and dihydroxy phosphorous(V) A_3 *meso*-triarylcorroles and their gold nanoconjugates has already been published, including research on A_2B type Ga(III) *meso*-triarylcorroles [174,209,210]. These photosensitizers and the gold nanoconjugates exhibited favorable PDT activities due to the

enhanced singlet oxygen generation related to the heavy atom effect from In(III) and Ga(III) metal ions. In addition, P(V) A_3 *meso*-triarylcorrole derivatives exhibited improved cellular uptake due to limited PS aggregation, which enhanced their PDT activities despite their low singlet oxygen quantum yields relative to the corresponding Ga(III) A_3 *meso*-triarylcorroles [174]. The studies also demonstrated that the incorporation of gold-nanoconjugates results in enhanced PDT activity due to the favorable properties of these nanosystems.

1.6.2 Photodynamic antimicrobial therapy

PACT is a phototherapy modality that uses the same basic principle as PDT in the photoinactivation of microbes [7,8,16–23]. During PACT, as in PDT, the photosensitizer is photoexcited with the light of a specific wavelength to populate the T_1 excited state and elicit photochemical reactions that include the generation of $^1O_2$ and other ROS that kill microbial cells [7,8,16–23]. The nature and type of bacteria species, particularly their outer membrane, determines the type of photosensitizer and photoirradiation wavelength to be used during PACT [7,8,16–23]. A favorable photosensitizer for PACT use should exhibit similar ideal properties to those previously described for PDT use.

However, the need for a PS dye to absorb light strongly in the therapeutic window is not a major criterion, particularly in addressing superficial infections, which require light power in the milliwatts range rather than in the tens of watts [24,211–213]. This is in contrast to an ablative therapy, such as PDT, that requires light of longer wavelength for efficient photoactivity. Therefore, light in the visible or ultraviolet range can yield efficient phototoxic reactions that result in oxidative damage to bacteria cell walls. In contrast, the light in the red-visible end of the electromagnetic spectrum is ideal for deep-tissue bacterial infections, including bacteria biofilms,

which require light of longer wavelength for deeper penetration and efficient photoinactivation [7,24,211–213].

During PACT, an ideal photosensitizer dye should exhibit an opposite charge to the bacterial cell wall for effective drug penetration and photoinactivation due to the favorable electrostatic interactions [18,19]. Typically, neutral, anionic, or cationic photosensitizer dyes are effective in destroying Gram-(+) bacteria, such as *Staphylococcus aureus* (*S. aureus*) since the Gram-(+) outer membrane (**Figure 1.11a**) consists of a relatively porous peptidoglycan layer and lipoteichoic acid, which eases the penetration of the photosensitizer drug [18,19,21,23]. However, Gram-(−) bacteria (**Figure 1.11b**), such as *Escherichia coli* (*E. coli*), consist of a size-exclusion porin outer membrane with an inner phospholipid and an outer negatively charged lipopolysaccharide membrane, which envelops the thin peptidoglycan layer creating an effective permeability barrier that restricts the penetration of many photosensitizer dyes [18,19,21,23]. Gram-(−) bacteria are mainly inactivated by cationic photosensitizer dyes, which can electrostatically interact with the outer layer, or by molecules that can disorganize the Gram-(−) permeability barrier [18,21,23].

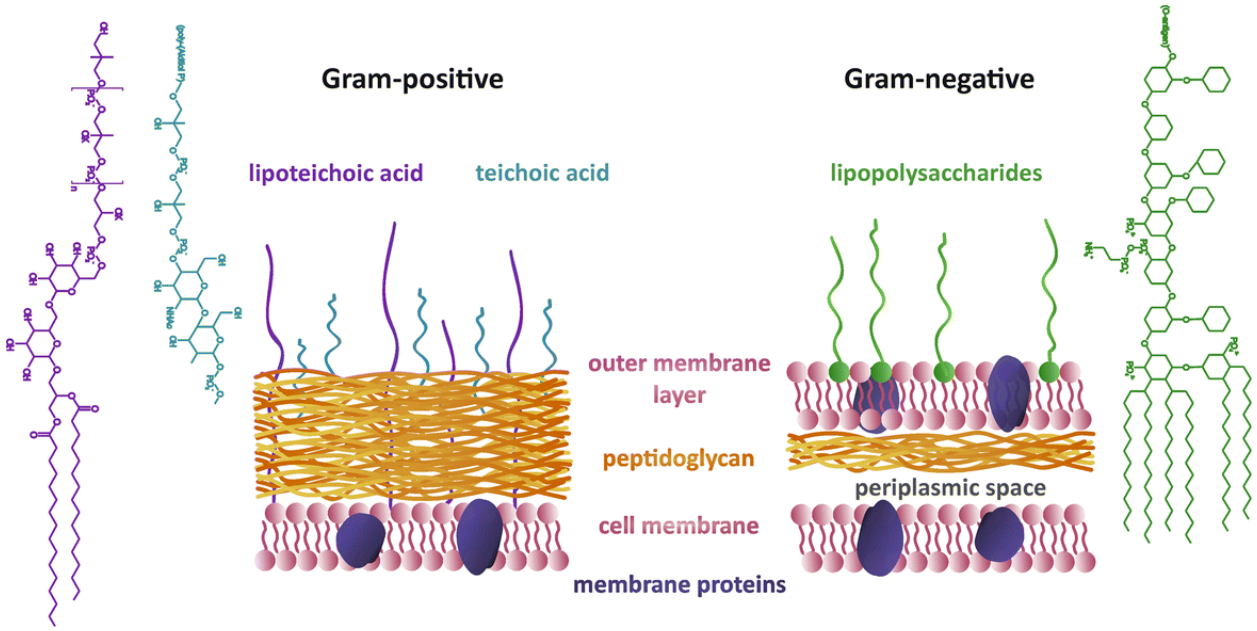

Figure 1.11: a) A comparison of Gram-(−) and b) Gram-(+) outer membrane. Reproduced with permission from Reference [214]. Copyright © Springer 2019.

As previously described, bacteria exist in nature as planktonic cells and biofilms, with the latter noted to cause deadly infections. Planktonic bacteria strains are free-floating microbes mainly suspended in water or on hydrophilic surfaces. Their gene pattern expression differs distinctly from the corresponding biofilm bacteria strains since they lack the outer coating (glycocalyx matrix) [20,23,25–27]. Therefore, they are more vulnerable to antibacterial agents than the corresponding biofilm bacteria. On the other hand, biofilm bacteria are surface adherent bacteria enclosed in a protective matrix coating composed of numerous sugars and are highly resilient and adaptive to the prevailing environment. They exhibit unique and effective organization, interaction, and coordination among their occupants, with enhanced survival and propagation capabilities under adverse environmental conditions. The sticky outer matrix shields the biofilm bacteria from physical stress and can withstand nutrient deprivation, pH shifts, oxygen radicals, disinfectants, and antibiotics, unlike planktonic organisms [20,23,25–27]. For this reason, many

chronic infectious diseases resistant to antimicrobial agents are related to biofilms [20,23,25–27].

For decades, many research studies have demonstrated that porphyrins and porphyrin analogs are promising photosensitizers for use in PACT against both planktonic and biofilm bacteria [18,28–30,214]. This class of dyes is versatile and can be easily modified at the *meso*-positions and the core to enhance ISC and generate high singlet oxygen quantum yields [46,48,74,77]. The porphyrins, corroles, chlorins, and N-confused porphyrins studied were rationally selected, and structure-property relationships related to their PACT activities were investigated. The effect of nanoparticles on their PACT activities was also assessed in the context of the porphyrin and corrole derivatives with sulfur atoms on their *meso*-aryl substituents, which facilitate conjugation to silver nanoparticles.

1.6.3 Enhancement of porphyrin and porphyrin analog properties

Nanoparticles, such as those of noble metals, such as gold and silver, including metal alloys, among other nanomaterials, are promising strategies for enhancing the properties of systems for wide-ranging applications in phototherapy [62–73,83,193,212]. This is due to their inherent favorable properties, such as specificity, stability, tuneability, biocompatibility, low toxicity, and bioaccumulation. The size and shape-dependent surface plasmon resonance (SPR) effect of MNPs enables efficient absorption and conversion of light energy to generate heat in photothermal therapy (PTT) [24,62–69,71,72,193]. The PTT effect causes irreversible cell damage by loosening the cell membranes and denaturing proteins through heat dissipation, destroying the diseased tissues [13,22,62,63,66,72].

Moreover, MNPs, such as gold and silver nanoparticles, are known to exhibit antitumor and antimicrobial properties and to also facilitate the selective accumulation of the drugs in the targeted tissues through the enhanced permeability and retention (EPR) effect [13,22,24,62–66,69,71,73]. This enables the selective accumulation of molecules of higher molecular weights in the target diseased tissues due to abnormal hypervascularization in the cancerous and inflamed tissues. Since the diseased tissues exhibit poor lymphatic drainage, the nanoparticles are retained in the targeted sites after internalization due to the inability of the tumors or inflamed tissues to renew and clean interstitial fluids. Therefore, the EPR effect enables drugs to passively and selectively target cancer tumors and infected tissue sites [70,215].

Besides the nano-scale benefits, functionalization of photosensitizer dyes with MNPs improves their stability and photophysicochemical properties [5,13,22,65,216,217] since they enhance the rate of ISC to the triplet manifold and thus increase the generation of signet oxygen due to the heavy atom effect [216,217]. This enhances the PDT and PACT activities by reducing their minimum inhibitory concentration [22,63]. Moreover, they can deliver oxygen and generate oxygen *in situ* in hypoxic tumor environments enhancing the PDT effect [68]. In addition, the conjugation of gold and silver nanoparticles through the self-assembly mechanism inherently protects the dyes from photobleaching by covering the reactive sites during the self-quenching singlet oxygen generation [218]. Therefore, synergistic therapeutic effects are achieved in the case of nanoassemblies with improved PDT and PACT activities compared to the dyes alone.

Since gold and silver exhibit a very strong affinity for sulfur, compounds containing sulfur atoms can be easily conjugated [219] to form powerful nanoassemblies entities for tumor and infection targeting. In this research study, porphyrin and corrole derivatives with *meso*-thienyl and -

methylthiophenyl substituents were conjugated to gold and silver nanoparticles, and their PDT and PACT activities were assessed.

1.7 Thesis outline

This thesis primarily focuses on the synthesis, characterization, and evaluation of the photophysicochemical properties of porphyrins and their analogs, such as include corroles, chlorins, and N-confused porphyrins. It consists of four major sections: the introduction, the experimental section, the results and discussion, and lastly, the conclusion and future outlook of the research study.

Chapter 1 provides the introduction to the thesis and focuses on the background of the study and the problems being addressed. It provides details on the background to using porphyrins and their analogs as photosensitizer dyes and their nanoparticle conjugation, including the commonly used synthetic methodologies, their fundamental photophysicochemical properties, and their application as photosensitizer drugs for use in PDT and PACT treatment protocols.

Chapter 2 provides the experimental section, including descriptions of the instrumentation, materials, and experimental procedures.

Chapters 3 to 11 represent the results and discussion sections and describe the synthesis and characterization of the synthesized dyes, their optical and photophysicochemical properties, PDT and PACT activities, theoretical studies, conclusions, and future outlook for the work described.

Chapter 3 describes the synthesis and structural characterization of the dyes and nanoparticle conjugates.

Chapters 4 and 5 describe the optical and photophysicochemical properties of the various photosensitizer dyes.

Chapters 6 to 9 provide the results and discussion related to the singlet oxygen applications. Chapter 6 focuses on the PDT and PACT properties of porphyrin derivatives, while Chapters 7 to 9 focus on those of the corroles, chlorins, and N-confused porphyrins studied, respectively.

Chapter 10 provides a theoretical study of the photosensitizer dyes that makes use of molecular modeling.

Lastly, Chapter 11 provides the conclusions and future outlook for the study.

CHAPTER TWO

Experimental

This chapter details the materials and instruments used, the synthetic procedures, and characterization methods for the dyes including the protocols followed for the *in vitro* PDT and PACT activity experiments.

2.0 Experimental section

This chapter details the materials and instrumentation used and describes the experimental procedures for the synthesis and characterization of all the photosensitizer dyes, along with the protocols for the *in vitro* dark cytotoxicity, PDT, and PACT studies.

2.0 Materials

All the solvents, chemicals, and reagents used in this work were of analytical grade quality and were purchased from commercial suppliers and used as received unless otherwise stated.

2.0.1 Solvents

Solvents used include chloroform, methanol, petroleum ether, tetrahyrofuran, acetone, pyridine, acetonitrile, and toluene. All of these were obtained from Sigma-Aldrich. Ethyl acetate, dichloromethane (DCM), dimethylformamide (DMF), and dimethylsulfoxide (DMSO) were purchased from Merck. Type II Millipore water was collected from an ELGA, Veolia water Purelab, flex system (Marlow, UK). Deuterated dimethysulfoxide (DMSO-d_6) and chloroform ($CDCl_3$) were obtained from Sigma-Aldrich

2.0.2 Chemicals and Reagents

Aromatic aldehydes, bases, and acid catalysts, including the oxidizing agents and salts used for porphyrins, porphyrin analogs, silver, and gold nanospheres synthesis that include: benzaldehyde, 4-methylthiobenzaldehyde, 3-thiophenecarboxyaldehyde, 2-thiophenecarboxaldehyde, 5-bromo-2-thiophenecarboxaldehyde, 3-methoxybenzaldehyde, 4-methoxybenzaldehyde, 4-hydroxybenzaldehyde, 4-hydroxy-3-methoxybenzaldehyde, pyrrole, *p*-chloranil, propionic acid, oleylamine, methanesulfonic (MSA), trimethylamine (TEA), 2,3-

dichloro-5,6-dicyano-1,4-benzoquine(DDQ), *p*-toluenesulfonhydrazide, potassium carbonate, hydrochloric acid (36%), anhydrous sodium sulfate, glacial acetic acid, sodium acetate, silver(III) nitrate, gold(III) chloride trihydrate, indium (III) chloride, gallium(III) chloride, phosphorus(V) oxychloride, tin(II) chloride dihydrate and 5,10,15,20-tetraphenylporphyrinato zinc(II) (ZnTPP) were purchased from Sigma-Aldrich. In addition, 1,3-diphenylisobenzofuran (DPBF), which is used as a singlet oxygen scavenger, was obtained from Sigma-Aldrich.

Chemicals and reagents used for cellular uptake, *in vitro* dark cytotoxicity, and PDT studies, such as Triton-100 X, ethylenediaminetetraacetic acid (EDTA), Dulbecco's phosphate-buffered saline (DPBS), trypan blue, Dulbecco's modified Eagle's media (DMEM) and trypsin were obtained from Sigma-Aldrich. Cultures of epithelial MCF-7 breast cancer cells line were purchased from Cellonex. The MTT assay was purchased from Sigma-Aldrich. Neutral red cell proliferation reagent (WST-1), 100 mg mL^{-1} penicillin-100-ug.mL^{-1}-streptomycin-amphoteric B mixture and 10% (v/v) heat-inactivated fetal calf serum (FCS) were purchased from Lonza (Biowest).

The crystal violet assay and tryptic soy broth were purchased from Sigma-Aldrich for the PACT studies. Agar bacteriological BBL Muller Hinton broth and nutrient agar were purchased from Merck and prepared according to the manufacturer's specifications. *Staphylococcus aureus* (ATCC 25923) and *Escherichia coli* (ATCC 25922) were obtained from Davies Diagnostics and Microbiologics, respectively. Phosphate buffer saline (PBS 10 mM, pH 7.4) was prepared following the standard procedure using 137 mM NaCl, 10 mM $NaHPO_4$, 2.7 mM KCl, and 1.8 mM KH_2PO_4 in 1 L of type II Millipore water.

2.1 Equipment

- The ground state UV-visible absorption spectra were measured on Shimadzu UV-2550 and Thermo Fischer Scientific™ Evolution™ 350-UV-Vis spectrophotometers.
- Fluorescence spectra were recorded on a Varian Eclipse spectrofluorometer.
- ^{1}H NMR spectra were measured on the Bruker Avance II 600 MHz and AMX 400 MHz NMR spectrometers using tetramethylsilane or the solvent residual as the internal standard.
- Mass spectrometry (MS) data were recorded on a Bruker AutoFLEX III Smartbeam MALDI-TOF operated in the positive ion mode with a α-cyano-4-hydroxycinnamic acid matrix and a 354 nm nitrogen laser as the ionizing source.
- Magnetic circular dichroism (MCD) spectra were recorded on a Chirascan plus spectrodichrometer equipped with a 1 tesla permanent magnet by using both parallel and antiparallel fields and subtracting a solvent baseline. The conventions of Piepho and Schatz are followed in the description of the sign of the MCD signal and the definition of the Faraday terms [220].
- Fluorescence lifetimes were obtained from a time-correlated single photon counting setup (TCSPC) (FluoTime 300, Picoquant® GmbH) with a diode laser (LDH–P–485, Picoquant® GmbH, 44 ps pulse width, 20 MHz repetition rate). The fluorescence signal was detected at the magic angle with a Peltier-cooled photomultiplier tube (PMT) (PMA-C 192-N-M, Picoquant GmbH) module and integrated electronics (PicoHarp 300E, Picoquant GmbH). The instrument response function (IRF) was measured by scattering with a Ludox solution (DuPont). The data were analyzed using the in-built FluoFit software (Picoquant GmbH), with the error in the decay times estimated by support plane analysis.

- Triplet state lifetimes were measured using an Edinburgh instruments LP980 spectrometer and pump beams of between 420−434 nm provided by an Ekspla NT-342B laser fitted with an OPO. The Soret band absorbance of the sample solutions was maintained at *ca.* 1.5 in nitrogen-saturated DMSO by degassing for 20 min before the triplet excitation and absorbance measurement at 500 nm. The triplet state decay curves were fitted exponentially using OrginPro 9 software, and transient curves provided the maximum triplet absorption detection wavelength.
- The photodegradation of DPBF in DMSO solution was used to quantify the singlet oxygen quantum yields based on a comparative method. The source of irradiation was a Spectra-Physics® Primoscan OPO (GWU Lasertechnik Vertiebsges, mbH) pumped with a Spectra-Physics Quanta-Ray Lab Nd:YAG laser at the crossover between the sample and the standard (Rose Bengal or 5,10,15,20-tetraphenylporphyrin (H_2TPP)).
- Nanoparticle and nanoconjugate morphologies were assessed using a Zeiss Libra model 120 transmission electron microscope (TEM) operated at 100 kV. TEM micrographs were processed with the iTEM software package.
- X-ray diffraction (XRD) data were obtained from a Bruker D8 Discover diffractometer equipped with a Lynx Eye Detector using Cu Kα radiation (1.5405 Å, nickel filter). Data were recorded over the 2θ = 5 to 100° range at a scan rate of 1° min^{-1}, a filter time constant of 2.5 s per step, and a slit width of 6 nm. The samples were placed on a zero-background silicon wafer slide. X-ray diffraction data were analyzed using Eva (evaluation fitting curve) software with baseline subtraction performed on each diffraction pattern

by subtracting a spline fitted to the curve background and the full-width at half maximum values obtained in this study.

- The qualitative elemental composition of the nanoparticles and the nanoconjugates were estimated on an energy-dispersive X-ray (EDX) spectrometer consisting of an Inca Penta FET coupled with a Vaga Tescam operated at 20 kV.
- X-ray photoelectron spectroscopy (XPS) spectra were recorded on an AXIS Ultra DLD with an Al monochromatic anode equipped with a charge neutralizer supplied by Kratos Analytical. The following parameters were set: the operating pressure was kept low at 5 × 10^{-9} torr, the emission current was 10 mA, and the anode (HT) was set at 15 kV. A hybrid lens was used, and the resolution was set at 160 eV pass energy in slot mode to acquire scans, while for XPS wide scans, the emission current was set at 12.5 mA, the anode (HT) at 15 kV, and the resolution maintained at 160 eV using a hybrid lens in the slot mode. The resolution was changed to an 80 eV pass energy in the slot mode for high-resolution scans. A nonlinear least squares fitting procedure was used to resolve chemically distinct species. The C_{1s} binding energy (BE) of 285 eV was used to align the core level BEs.
- Theoretical calculations were performed using the Gaussian 09 software package with an intel/Linux cluster hosted in the CSIR's Centre for High-Performance Computing in Cape Town, South Africa [221]. Geometry optimizations were performed using the B3LYP functional with 6-31G(d) basis sets. The optimized B3LYP geometries were then used to carry out TD-DFT calculations using the CAM-B3LYP functional since it has a long-range correction [222]. For cases in which TD-DFT calculations would not converge with 6-31G(d) basis sets, SDD basis sets were consistently used [223]. The Chemcraft software

program was used to generate simulated spectra with a fixed bandwidth at 2000 cm^{-1} [224]. Avogadro was used to visualize the molecular orbitals [225].

- The MCF-7 cancer cells were cultured in 75 cm^3 vented flasks (Porvair) in a humidified atmosphere incubator with *ca.* 5% CO_2 at 37°C (Heal Force).
- The MCF-7 cancer cells were routinely examined on a Zeiss AxioVert.A1 fluorescence LED inverted microscope under phase contrast viewing.
- Thorlabs M595L3, M625L3, and M660L3 light-emitting diode (LEDs) with irradiance values of 160, 240, and 280 $mW.cm^{-2}$ at 595, 625, and 660 nm, respectively, were mounted onto the housing of a Modulight 7710-680 medical laser system were used to illuminate 96 well tissue culture plates (127.76 × 85.48 mm).
- Cell viability values were determined by measuring the absorbance of WST-1 cell proliferation neutral red reagent (Roche) at 450 nm or by carrying out the MTT assay at 540 nm on a Synergy 2 multi-diode microplate reader (BioTek).
- The cellular uptake of each drug was determined by measuring the fluorescence intensities through excitation of the photosensitizer dye at their B band maxima on a Synergy 2 multi-diode microplate reader (BioTek).
- The sterilization of all the materials and equipment used in bacteria culturing, such as glassware, Eppendorf tubes, test tubes, agar, nutrient broth, and PBS, was carried out with a China medical device RAU-530D autoclave.
- The incubation of bacteria culture suspensions and agar plates was carried out in a thermostatic oven equipped with a shaker.

- The optical density (OD) values of the bacteria cultures were measured with a Ledect 96 microplate reader from Labxim products.
- The homogenization of bacteria culture suspensions was performed on a Pro VSM-3 Labplus Vortex mixer.
- Bacteria pellets were harvested from the bacteria culture suspensions with a Merck Eppendorf 5810 centrifuge.
- PACT studies were performed with Thorlabs M595L3, M625L3, and M660L3 LEDs at 595, 625, and 660 nm mounted onto the housing of a Modulight 7710-680 medical laser system to illuminate 24 or 96 well tissue culture plates (127.76 × 85.48 mm).
- The colony-forming unit (CFU/mL) values were determined on a Scan 500® series Automatic Colony Counter from Healthcare Technologies.
- Bacteria biofilm biomass quantification was carried out with the crystal violet assay by measuring absorbance values at 590 nm on a Synergy 2 multi-diode microplate reader (BioTek).

2.2 Synthesis methods

2.2.1 Porphyrin synthesis

Free-base porphyrin ligands and their chloroindium(III) and dichloro Sn(IV) porphyrin complexes, including the 5,10,15,20-*meso*-tetraphenylporphyrin (H_2TPP) control compound and its chloroindium(III) porphyrin complex (InTPP), were synthesized following literature techniques [102,226–229].

2.2.1.1 Synthesis of free-base porphyrins

The free-base porphyrin ligands (**1**-**8**-Por and H_2TPP control) have been reported previously [102,230–237]. In this study, they were prepared by following the Alder-Longo method [102] (**Scheme 2.1a**). 5,10,15,20-*Meso*-tetra(4-methylthiophenyl)porphyrin (**1**-Por) was synthesized using 4-methylthiobenzaldehyde (1.142 g, 7.5 mmol) in 500 mL propionic acid. The mixture was warmed, and freshly distilled pyrrole (0.502 g, 7.5 mmol) was added for 5 min. The reaction mixture was brought to reflux for 2 h and thereafter allowed to cool down to room temperature and filtered to obtain the product. The filter cake was thoroughly washed first with warm water, followed by cold methanol to remove the black tar and propionic acid. The product was purified using silica gel column chromatography and CH_2Cl_2/petroleum ether (1:3) eluent to afford **1**-Por. Yield: 2.3 g (36%). ^{1}H NMR (400 MHz, $CDCl_3$) δ 8.87 (s, 2H), 8.49 (d, *J* = 9.3 Hz, 6H), 8.13 (d, *J* = 7.7 Hz, 6H), 7.83 (d, *J* = 8.0 Hz, 4H), 7.63 (d, *J* = 7.7 Hz, 6H), 2.80 (s, 3H), 2.76 (s, 9H), -2.79 (s, 2H). UV-vis (DMSO): λ_{max} nm (log ε) 425 (5.61), 519 (4.25), 556 (4.10), 596 (3.78), 650 (3.90). MS (MALDI TOF): Calcd. m/z 798.20; observed: 799.69 $[M+H]^+$ [230].

2-**8**-Por and H_2TPP control free-base porphyrin ligands were synthesized in a similar manner described for **1**-Por (**Scheme 2.1a**).

5,10,15,20-*Meso*-tetra(thien-3-yl)porphyrin (**2**-Por) was obtained in 33% yield. ^{1}H NMR (400 MHz, $CDCl_3$) δ 8.98 (s, 6H), 8.62 (s, 2H), 8.44 (d, *J* = 3.0 Hz, 1H), 8.39 (d, *J* = 4.9 Hz, 1H), 8.03 (d, *J* = 4.1 Hz, 3H), 8.00 (d, *J* = 4.8 Hz, 3H), 7.95 (dd, *J* = 4.9, 3.0 Hz, 1H), 7.74 (dd, *J* = 4.8, 3.0 Hz, 3H), -2.72 (s, 2H). UV-vis (DMSO): λ_{max} nm (log ε) 421(5.25), 518 (4.23), 557(4.08), 598 (4.10), 652 (3.90). MS (MALDI TOF): Calcd. m/z 638.07; observed: 638.51 $[M]^+$ [232].

5,10,15,20-*Meso*-tetra(thien-2-yl)porphyrin (**3**-Por) was obtained in 31% yield. ^{1}H NMR (400 MHz, $CDCl_3$) δ 8.97 (s, 8H), 7.85 (d, *J* = 2.3 Hz, 4H), 7.79 (d, *J* = 5.3 Hz, 4H), 7.46 – 7.43 (m, 4H), -2.71 (s, 2). UV-vis (DMSO): λ_{max} nm (log ε) 423(5.41), 518 (4.76), 555(4.63), 598 (4.50), 650 (4.27). MS (MALDI TOF): Calcd. m/z 638.07; observed: 639.52 $[M+H]^+$ [184,231,233].

5,10,15,20-*Meso*-tetra(5-bromothien-2-yl)porphyrin (**4**-Por) was obtained in 28% yield. ^{1}H NMR (400 MHz, $CDCl_3$) δ 9.11 (s, 8H), 7.66 (d, *J* = 3.6 Hz, 4H), 7.49 (d, *J* = 3.6 Hz, 4H), -2.77 (s, 2H). UV-vis (DMSO): λ_{max} nm (log ε) 431(5.55), 524 (4.51), 567(4.29), 613 (4.11), 660 (3.93). MS (MALDI TOF): Calcd. m/z 954.42; observed: 955.26 $[M+H]^+$ [233].

5,10,15,20-*Meso*-tetra(4-methoxyphenyl)porphyrin (**5**-Por) was obtained in 43% yield. ^{1}H NMR (400 MHz, $CDCl_3$) δ 8.86 (s, 8H), 8.13 (d, *J* = 8.5 Hz, 8H), 7.29 (d, *J* = 8.5 Hz, 8H), 4.10 (s, 12H), -2.75 (s, 2H). UV-vis (DMSO): λ_{max} nm (log ε) 424(5.22), 519 (3.69), 556 (3.56), 595(3.20), 650 (3.42). MS (MALDI TOF): Calcd. m/z 734.29; observed: 735.15 $[M+H]^+$ [230,236].

5,10,15,20-*Meso*-tetra(3-methoxyphenyl)porphyrin (**6**-Por) was obtained in 41% yield. ^{1}H NMR (400 MHz, $CDCl_3$) δ 8.89 (s, 8H), 7.84 – 7.78 (m, 8H), 7.65 (t, *J* = 7.9 Hz, 4H), 7.34 (d, *J* = 8.3 Hz, 4H), 3.99 (s, 12H), -2.80 (s, 2H). UV-vis (DMSO): λ_{max} nm (log ε) 420 (5.21), 515 (3.88), 548(3.46), 590 (3.36), 645 (3.32). MS (MALDI TOF): Calcd. m/z 734.29; observed: 734.61 $[M]^+$ [236].

5,10,15,20-*Meso*-tetra(4-hydroxyphenyl)porphyrin (**7**-Por) was obtained in 37% yield. ^{1}H NMR (400 MHz, DMSO-d_6) δ 9.95 (s, 4H), 8.86 (s, 8H), 8.00 (d, *J* = 8.4 Hz, 8H), 7.20 (d, *J* = 8.4 Hz, 8H), -2.89 (s, 2H). UV-vis (DMSO): λ_{max} nm (log ε) 425 (5.56), 520 (4.29), 560 (4.24), 595 (3.97), 651 (3.92). MS (MALDI TOF): Calcd. m/z 678.23; observed: 679.25 $[M+H]^+$ [184,234–238].

5,10,15,20-*Meso*-tetra(4-hydroxy-3-methoxyphenyl)porphyrin (**8**-Por) was obtained in 35% yield. ^{1}H NMR (400 MHz, DMSO-d_6) δ 9.51 (s, 4H), 8.91 (s, 8H), 7.77 (s, 4H), 7.59 (d, *J* = 7.6 Hz, 4H), 7.21 (d, *J* = 7.9 Hz, 4H), 3.90 (s, 12H), -2.87 (s, 2H). UV-vis (DMSO): λ_{max} nm (log ε) 428 (5.56), 521 (4.28), 560(4.18), 596 (3.80), 651(3.95). MS (MALDI TOF): Calcd. m/z 798.27; observed: 799.12 $[M+H]^+$ [237,238].

The 5,10,15,20-*Meso*-tetra(phenyl)porphyrin H_2TPP control compound was obtained in 43% yield. ^{1}H NMR (400 MHz, $CDCl_3$) δ 8.85 (s, 8H), 8.22 (d, *J* = 6.9 Hz, 8H), 7.76 (d, *J* = 7.1 Hz, 12H), -2.77 (s, 2H). UV-vis (DMSO): λ_{max} nm (log ε) 417 (5.24), 513 (3.80), 551(3.43), 589 (3.20), 644(3.36). MS (MALDI TOF): Calcd. m/z 614.25; observed: 615.12 $[M+H]^+$ [102,230].

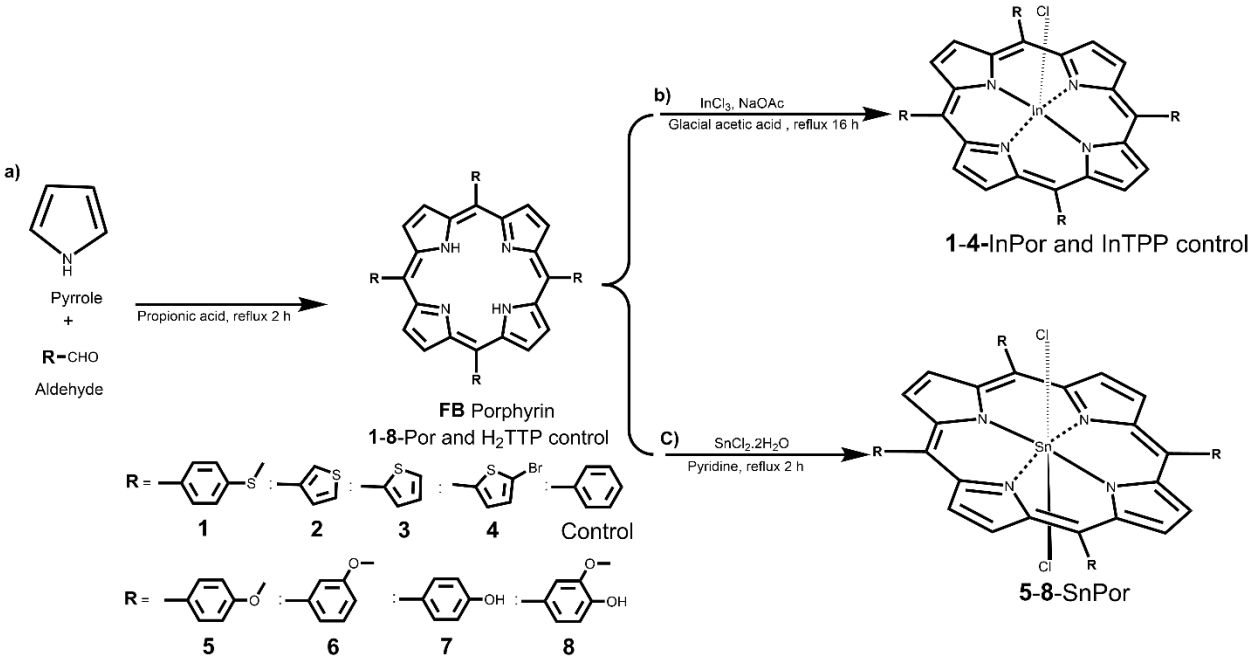

Scheme 2.1: a) Synthesis of **1**-**8**-Por and the H_2TPP control and their corresponding b) **1**-**4**-InPor and the InTPP complex and c) **5**-**8**-SnPor Sn(IV) complexes.

2.2.1.2 Synthesis of chloroindium(III) porphyrin complexes

The chloroindium(III) *meso*-tetrakisporphyrin complexes were synthesized by following modified literature methods [226,227] (**Scheme 2.1b**). Chloroindium(III) *meso*-5,10,15,20-tetraphenylporphyrin (InTPP) was synthesized as a control complex as described in the literature [226,227]. The synthesis of the **1**-InPor and **3**- InPor In(III) porphyrin complexes has been reported previously [209]. **2**-InPor and **4**-InPor were synthesized in a similar procedural manner to **1-** and **3**-InPor. For the preparation of chloroindium(III) 5,10,15,20-*meso*-tetra(thien-3-yl)porphyrin (**2**-InPor), **2**-Por (97 mg, 0.152 mmol) was dissolved in 20 mL of glacial acetic acid, and sodium acetate (250 mg, 3.05 mmol) was added, stirred and heated to reflux at 100°C. $InCl_3$ salt (93 mg, 0.42 mmol) was added in excess to the reaction mixture and refluxed further for 16 h. The reaction progress was monitored by UV-visible absorption spectroscopy and thin-layer chromatography (TLC) until completion. The reaction mixture was cooled to room temperature, and water was added to induce precipitation. The precipitate was filtered and washed with warm Millipore water several times. After washing, the crude product was dissolved in 9:1 $CHCl_3$/methanol and dried *in vacuo*. After removing the organic solvents, the product was purified using silica gel column chromatography with 9:1 $CHCl_3$/methanol eluent to afford **2**-InPor green-purple solid. Yield: 85 mg (88%). ^{1}H NMR (600 MHz, DMSO-d_6) δ 9.10 (s, 8H), 8.38 (s, 4H), 8.10 (d, J = 3.0 Hz, 4H), 8.06 (d, J = 4.3 Hz, 4H). UV-vis (DMSO): λ_{max} nm (log ε) 430 (5.19), 563 (3.84), 607(3.72). MS (MALDI TOF): Calcd. m/z 786.30; observed: 786.13 $[M-Cl]^+$.

Chloroindium(III) 5,10,15,20-*meso*-tetra(4-methylthiophenyl)porphyrin (**1**-InPor) was obtained in 96.6% yield. ^{1}H NMR (600 MHz, DMSO-d_6) δ 9.01 (m, 6H, Ar-H), 8.33 (m, 4H, Ar-H), 8.18 (m, 7H, Ar-H), 7.75 (m, 7H, Ar-H), 2.77 (m, 9H, CH_3), 2.09 (m, 3H, CH_3). UV-vis (DMSO): λ_{max} nm (log

ε) 435 (5.07), 568 (3.06), 612 (3.55). MS (MALDI TOF): calcd. *m/z* 946.82; observed 946.06 $[M-Cl]^+$ [209].

Chloroindium(III) 5,10,15,20-*meso*-tetra(thien-2-yl)porphyrin (**3**-InPor) was obtained in 97.6% yield. ^{1}H NMR (600 MHz, DMSO-d_6) δ_H ppm 9.18 (m, 7H, Ar-H), 8.31 (m, 5H, Ar-H), 8.21–7.98 (m, 4H, Ar-H), 7.66 (d, *J* = 3.4 Hz, 4H, Ar-H). UV-vis (DMSO): λ_{max} nm (log ε) 438 (5.50), 570 (2.51), 618 (1.88). MS (MALDI TOF): calcd. *m/z* 786.93; observed 786.51 $[M-Cl]^+$ [209].

Chloroindium(III) 5,10,15,20-*meso*-tetra(5-bromo-thien-2-yl)porphyrin (**4**-InPor) was obtained in 83% yield. ^{1}H NMR (600 MHz, DMSO-d_6) δ 9.28 (s, 8H), 7.92 (d, *J* = 3.0 Hz, 4H), 7.79 (d, *J* = 3.5 Hz, 4H). UV-vis (DMSO): λ_{max} nm (log ε) 441 (5.44), 572 (4.45), 619(4.27). MS (MALDI TOF): Calcd. m/z 1102.68; observed: 1101.52 $[M-Cl]^+$.

Chloroindium(III) 5,10,15,20-*meso*-tetraphenylporphyrin (InTPP) was obtained in 92.6% yield. ^{1}H NMR (400 MHz, DMSO-d_6) δ 9.07 (s, 4H), 8.97 (s, 4H), 8.29 (d, *J* = 6.3 Hz, 8H), 7.90 (d, *J* = 7.9 Hz, 12H). UV-vis (DMSO): λ_{max} nm (log ε) 428 (5.10), 561 (3.66), 601(3.60). MS (MALDI TOF): calcd. *m/z* 763.00; observed 762.89 $[M-Cl]^+$ [226,227].

2.2.1.3 Synthesis of dichlorotin(IV) porphyrin complexes

The **5**-**8**-SnPor Sn(IV) *meso*-tetraporphyrin complexes were synthesized by following modified literature methods [228,229] (**Scheme 2.1c**). **5**-Por (152 mg, 0.207 mmol) was dissolved in dry pyridine, and $SnCl_2{\cdot}2H_2O$ (98 mg, 0.43 mmol) was added, stirred, and heated to reflux for 2 h. The reaction progress was monitored by UV-visible absorption spectroscopy and thin-layer chromatography (TLC). The reaction mixture was allowed to cool down to room temperature, and Millipore water was added to induce precipitation. The precipitate was filtered, and the filter

cake was washed severally with warm 1% HCl-Millipore water to remove the excess salt. The crude product was dissolved in $CHCl_3$ and dried *in vacuo*. The product residue was purified using silica gel column chromatography with 9:1 $CHCl_3$/methanol eluent to afford **5**-SnPor solid. Yield: 128 mg (84%). ^{1}H NMR (400 MHz, $CDCl_3$) δ 9.25 (s, 8H), 8.25 (d, *J* = 8.5 Hz, 8H), 7.37 (d, *J* = 8.6 Hz, 8H), 4.14 (s, 12H). UV-vis (DMSO): λ_{max} nm (log ε) 431 (5.17), 568 (3.81), 612 (3.99). MS (MALDI TOF): Calcd. m/z for $[M]^+$ = 922.11, $[M-Cl]^+$= 887.15; observed: 888.20 $[M-Cl+H]^+$.

6-**8** SnPor Sn(IV) porphyrin complexes were synthesized in a similar manner to the procedure described for **5**-SnPor (**Scheme 2.1c**).

6-SnPor was obtained in 78% yield. ^{1}H NMR (400 MHz, $CDCl_3$) δ 8.91 (s, 8H), 7.88 – 7.78 (m, 8H), 7.67 (t, *J* = 7.8 Hz, 4H), 7.36 (d, *J* = 8.3 Hz, 4H), 4.01 (s, 12H). UV-vis (DMSO): λ_{max} nm (log ε) 429 (5.30), 558 (4.02), 601 (3.73). MS (MALDI TOF): Calcd. m/z for $[M]^+$ = 922.11, $[M-Cl]^+$= 887.15; observed: 888.15 $[M-Cl+H]^+$.

7-SnPor was obtained in 83% yield.^{1}H NMR (400 MHz, DMSO-d_6) δ 10.00 (s, 4H), 8.92 (s, 8H), 8.05 (d, *J* = 8.3 Hz, 8H), 7.26 (d, *J* = 8.3 Hz, 8H). UV-vis (DMSO): λ_{max} nm (log ε) 441 (5.21), 567 (3.93), 615 (4.03). MS (MALDI TOF): calcd. *m/z* for $[M]^+$ = 866.05, $[M-Cl]^+$= 831.09; observed: 831.42 $[M-Cl]^+$.

8-SnPor was obtained in 86% yield. ^{1}H NMR (400 MHz, DMSO-d_6) δ 9.57 (s, 4H), 8.97 (s, 8H), 7.84 (s, 4H), 7.65 (d, *J* = 7.7 Hz, 4H), 7.28 (d, *J* = 7.9 Hz, 4H), 3.96 (s, 12H). UV-vis (DMSO): λ_{max} nm (log ε) 445 (5.30), 572 (3.97), 620 (4.15). MS (MALDI TOF): calcd. *m/z* for $[M]^+$ = 986.10, $[M-Cl]^+$= 951.12; observed: 952.16 $[M-Cl+H]^+$.

2.2.2 Corrole synthesis

The *meso*-aryl A_3 free-base corroles, namely: 5,10,15-tri-4-methylthiophenyl- (**1**-Cor), 5,10,15-trithien-3-yl- (**2**-Cor), 5,10,15-trithien-2-yl (**3**-Cor) and 5,10,15-tri-5-bromo-thien-2-yl- (**4**-Cor) including their Ga(III) and P(V) complexes were synthesized following reported literature procedures [141,239,240] (**Scheme 2.2**). 5,10,15-triphenylcorrole (H_3TPCor) and its P(V) and Ga(III) A_3 *meso*-triarylcorrole complexes (P^VTPCor, Ga^{III}TPCor) were also synthesized as control compounds following modified literature methods [141,241,242] (**Scheme 2.2**). The synthesis of **1**-**3** A_3 P(V) and Ga(III) corrole complexes has already been published in the literature [174]. In this study, asymmetric A_2B *meso*-triarylcorroles were obtained through collaborative work with Prof. Xu Liang's group at Jiangsu University in China. Our collaborators synthesized A_2B *meso*-triaryl free-base corroles (**9**-Cor and **10**-Cor) and their Ga(III) corrole complexes (**9**-GaCor and **10**-GaCor). In this thesis work, the received Ga(III) corrole complexes (**9**-**10**-Cor) were modified by alkylating with iodoethane to successfully obtain **10**-GaCor-Q, but alkylation of **9**-GaCor was unsuccessful (**Scheme 2.3**). The results from this collaborative research work have also already been reported [210].

2.2.2.1 Synthesis of free-base A_3 *meso*-triarylcorroles

Free-base corroles were synthesized in this study by following the Gryko method [141]. During the synthesis of 5,10,15-tri-4-methylthiophenylcorrole (**1**-Cor), 4-methylthiobenzaldehyde (5 mmol) was dissolved in an acid-catalyzed solution of 1:1 v/v methanol/H_2O (400 mL) and conc. HCl (4.25 mL). Pyrrole (10 mmol) was added to the reaction mixture and stirred at room temperature in the dark for 3 h to form pink bilane precipitates. The precipitate was extracted using $CHCl_3$ and washed four times with Millipore water. The organic phase was dried over

anhydrous sodium sulfate and concentrated to 150 mL, and *p*-chloranil oxidant (1 g) was added in excess, and the solution was refluxed for 1 h. The reaction mixture was cooled down to room temperature and filtered. The filtrate was dried *in vacuo* and flash-column-chromatographed on silica gel with CH_2Cl_2 as the eluent. The organic solvent was evaporated, and the product was purified twice on a silica gel column with 1:3 CH_2Cl_2/petroleum ether elute to afford the target compound **1**-Cor solid. Yield: 831 mg (25%). UV-vis (DMSO): λ_{max} nm (log ε) 422 (5.17), 574 (3.93), 641 (4.12). MS (MALDI TOF): Calcd. m/z 664.18; observed: 665.54 $[M+H]^+$ [141].

2-**4**-Cor and H_3TPCor control were synthesized in a similar manner to that described for **1**-Cor (**Scheme 2.2a**).

5,10,15-Trithien-3-ylcorrole (**2**-Cor) was obtained in 21% yield, UV-vis (DMSO): λ_{max} nm (log ε) 424 (5.30), 594 (4.02), 645 (3.73). MS (MALDI TOF): Calcd. m/z 544.09; observed: 544.40 $[M]^+$ [141].

5,10,15-Trithien-2-ylcorrole (**3**-Cor) was obtained in 23% yield. UV-vis (DMSO): λ_{max} nm (log ε) 425 (5.06), 587 (4.15), 647 (4.43). MS (MALDI TOF): calcd. *m/z* 544.09; observed 544.31 $[M^+]$ [141]

5,10,15-Tri-5-bromo-thien-2-ylcorrole (**4**-Cor) was obtained in 18% yield. ^{1}H NMR (400 MHz, $CDCl_3$) δ 7.98 (s, 2H), 7.64 (s, 4H), 7.52 (d, *J* = 3.3 Hz, 2H), 7.15 (d, *J* = 1.8 Hz, 4H), 7.03 (d, *J* = 4.1 Hz, 2H). UV-vis (DMSO): λ_{max} nm (log ε) 430 (5.04), 660 (3.51), 731 (3.22). MS (MALDI TOF): calcd. *m/z* 777.82; observed 779.34 $[M+H]^+$.

5,10,15-Triphenylcorrole (H_3TPCor) was obtained in 28% yield. UV-vis (DMSO): λ_{max} nm (log ε) 426 (5.53), 582 (4.60), 642 (4.72). MS (MALDI TOF): calcd. *m/z* 526.22; observed 526.55 $[M]^+$ [141].

2.2.2.2 Synthesis of dihydroxy P(V) A_3 *meso*-triarylcorroles

The synthesis of A_3 *meso* triaryl P(V) corroles (**1**-**3**-P^VCor) and P^VTPCor control has already been reported in the literature [174,239]. Dihydroxyphosphorus(V) 5, 10, 15 *meso* tri[5-bromo-thien-2yl] corrole (**4**-P^VCor) was synthesized following a previously reported procedure [174]. **4**-Cor free-base corrole (61 mg, 0.078 mmol) in dry pyridine (10 mL) was stirred under an inert environment and heated to 60°C, followed by a dropwise addition of $POCl_3$ (0.6 mL, 2.38 mmol) for 5 min. The reaction mixture was brought to reflux at 100°C for 12 h. The reaction progress was regularly monitored by UV-visible absorption spectroscopy and thin-layer chromatography (TLC). After 12 h, the reaction vessel was allowed to cool down to room temperature, and Millipore water was added. The crude product was extracted from the reaction mixture solution using $CHCl_3$ and washed several times with 10% HCl Millipore water solution to remove residual pyridine and dried *in vacuo*. The product residue was purified by basic alumina column chromatography with 9:1 dichloromethane/methanol eluent to afford target compound **4**-P^VCor as a purple-green solid. Yield: 45 mg (75%).^{1}H NMR (600 MHz, $CDCl_3$) δ 8.10 (d, *J* = 11.3 Hz, 2H), 7.96 (d, *J* = 9.9 Hz, 4H), 7.76 (d, *J* = 9.3 Hz, 2H), 7.63 (d, *J* = 8.7 Hz, 2H), 7.47 (d, *J* = 5.6 Hz, 2H), 7.17 (d, *J* = 8.4 Hz, 2H). UV-vis (DMSO): λ_{max} nm (log ε) 419 (5.35), 568 (4.19), 612 (4.51). MS (MALDI TOF): Calcd. m/z 839.77; observed: 840.25 $[M-2OH+H]^+$.

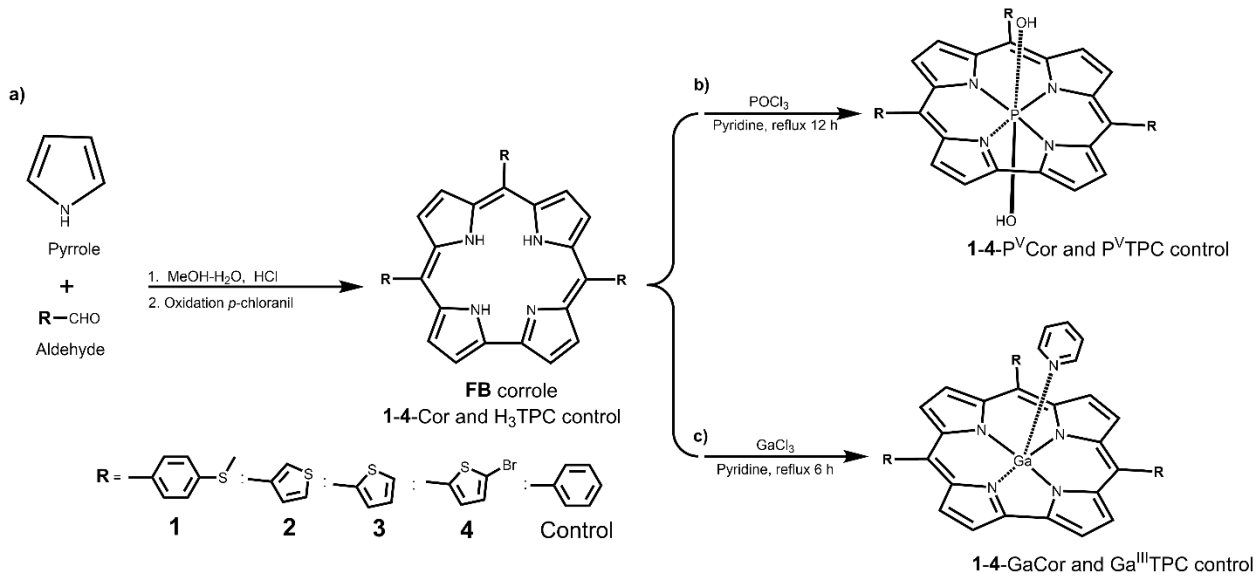

Scheme 2.2: a) Synthesis of **1**-**4**-Cor and the H_3TPCor control and b) **1**-**4**-P^{V}Cor and the P^{V}TPCor control, and c) **1**-**4**-GaCor and the Ga^{III}TPCor control.

Dihydroxyphosphorus(V) 5,10,15-*meso*-tri[4-(methylthio)phenyl]corrole (**1**-P^{V}Cor) was obtained in 80% yield, ^{1}H NMR (600 MHz, $CDCl_3$) δ 9.14 (s, 1H), 9.07 (s, 1H), 8.09 (d, *J* = 8.2 Hz, 1H), 7.79 (d, *J* = 9.3 Hz, 1H), 7.60 (d, *J* = 7.8 Hz, 3H), 7.47 (d, *J* = 9.3 Hz, 4H), 7.17 (s, 2H), 7.05 (d, *J* = 9.7 Hz, 3H), 5.73 (d, *J* = 7.6 Hz, 4H), 1.96 (s, 9H, CH_3). UV-vis (DMSO): λ_{max} nm (log ε) 419 (5.71), 568 (4.63), 612 (4.98). MS (MALDI TOF): Calcd. m/z 726.13; observed: 727.01 $[M-2OH+H]^{+}$ [174].

Dihydroxyphosphorus(V) 5,10,15-*meso*-trithien-3-ylcorrole (**2**-P^{V}Cor) was obtained in 78% yield. ^{1}H NMR (600 MHz, $CDCl_3$) δ 8.96 (s, 1H), 7.88 (s, 1H), 7.77 (d, *J* = 7.3 Hz, 9H), 7.45 (d, *J* = 5.3 Hz, 2H), 7.05 (d, *J* = 6.6 Hz, 1H), 5.74 (d, *J* = 6.4 Hz, 3H). UV-vis (DMSO): λ_{max} nm (log ε) 423 (5.60), 562 (4.62), 611 (4.79). MS (MALDI TOF): Calcd. m/z 606.04; observed: 607.32 $[M-2OH+H]^{+}$ [174].

Dihydroxyphosphorus(V) 5,10,15-*meso*-trithien-2-ylcorrole (**3**-P^{V}Cor) was obtained in 82% yield. ^{1}H NMR (600 MHz, $CDCl_3$) δ 8.73 (s, 6H), 8.23 (d, *J* = 7.6 Hz, 3H), 7.77 (s, 6H), 7.07 (d, *J* = 8.8 Hz,

1H), 6.74 (d, *J* = 8.8 Hz, 1H). UV-vis (DMSO): λ_{max} nm (log ε) 427 (5.63), 573 (4.49), 614 (4.62). MS (MALDI TOF): Calcd. m/z 606.04; observed: 606.24 $[M-2OH]^+$ [174].

Dihydroxyphosphorus(V) 5,10,15-*meso*-triphenylcorrole (P^VTPCor) was obtained in 85% yield. UV-vis (DMSO): λ_{max} nm (log ε) 425 (5.78), 572 (4.54), 620 (4.78). MS (MALDI TOF): calcd. *m/z* 588.17; observed 589.47 $[M-OH+H]^+$ [239].

2.2.2.3 Synthesis of Ga(III) A_3 *meso*-triarylcorroles

Since we have also reported the synthesis of A_3 *meso* triaryl Ga(III) corroles (**1**-**3**-GaCor, in this section, the synthesis of Gallium(III) 5,10,15-tri-[5-bromo-thien-2-yl]corrole (pyridyl) (**4**-GaCor) is described following a similar reported procedure [174]. **4**-Cor free-base corrole (54 mg, 0.064 mmol) was dissolved in dry pyridine (15 mL), and excess $GaCl_3$ (270 mg, 1.58 mmol) was added and stirred under an inert environment. The reaction mixture was brought to reflux at 120°C for 6 h. The reaction progress was monitored regularly by TLC and UV-visible absorption spectroscopy until completion. After 6 h, the reaction vessel was cooled to room temperature, and organic solvents evaporated *in vacuo*. The crude product was purified using basic alumina column chromatography and 3:1 dichloromethane/methanol eluent to afford the target compound **4**-GaCor. Yield: 43 mg (79%). ^{1}H NMR (600 MHz, $CDCl_3$) δ 8.28 (d, *J* = 8.9 Hz, 2H), 8.12 (d, *J* = 11.1 Hz, 2H), 7.97 (d, *J* = 4.2 Hz, 4H), 7.85 (d, *J* = 5.7 Hz, 2H), 7.36 (d, *J* = 11.0 Hz, 4H), 7.19 (d, *J* = 5.2 Hz, 2H), 7.04 (d, *J* = 6.9 Hz, 1H), 6.82 (d, *J* = 11.5 Hz, 2H). MS (MALDI TOF): Calcd. m/z 922.76; observed: 923.39 $[M-Py]^+$.

Gallium(III) 5,10,15-tri-[4-(methylthio)phenyl]corrole(pyridyl) (**1**-GaCor) was obtained in 86% yield. ^{1}H NMR (600 MHz, $CDCl_3$) δ 8.52 (d, *J* = 7.3 Hz, 2H), 7.93 (d, *J* = 7.6 Hz, 1H), 7.86 (d, *J* = 8.2

Hz, 2H), 7.64 (s, 5H), 7.45 (d, *J* = 7.1 Hz, 10H), 7.19 (s, 2H), 7.05 (d, *J* = 6.6 Hz, 2H), 5.74 (s, 1H), 2.10 (s, 9H, CH_3). UV-vis (DMSO): λ_{max} nm (log ε) 429 (5.42), 581 (4.89), 615 (4.94). MS (MALDI TOF): Calcd. m/z 809.12; observed: 810.29 $[M-Py+H]^+$ [174].

Gallium(III) 5,10,15-*meso*-trithien-3-ylcorrole(pyridyl) (**2**-GaCor) was obtained in 82% yield. ^1H NMR (600 MHz, $CDCl_3$) δ 9.28 (d, *J* = 4.2 Hz, 2H), 9.21 (s, 2H), 9.11 (s, 1H), 8.06 (s, 3H), 8.03 (s, 2H), 7.89 (s, 2H), 7.75 (d, *J* = 7.3 Hz, 4H), 7.52 (d, *J* = 4.6 Hz, 1H), 7.03 (d, *J* = 7.8 Hz, 2H), 6.40 (d, *J* = 5.4 Hz, 3H). UV-vis (DMSO): λ_{max} nm (log ε) 429 (5.48), 559 (4.01), 616 (4.30). MS (MALDI TOF): Calcd. m/z 689.03; observed: 689.23 $[M-Py]^+$ [174].

Gallium(III) 5,10,15-*meso*-trithien-2-ylcorrole(pyridyl) (**3**-GaCor) was obtained in 82% yield. ^1H NMR (600 MHz, $CDCl_3$) δ 9.29 (s, 7H), 9.11 (s, 1H), 8.90 (s, 1H), 7.95 (d, *J* = 3.4 Hz, 4H), 7.87 (d, *J* = 6.0 Hz, 5H), 7.51 (d, *J* = 2.1 Hz, 4H). UV-vis (DMSO): λ_{max} nm (log ε) 433 (5.35), 578 (4.16), 622 (3.84). MS (MALDI TOF): Calcd. m/z 689.03; observed: 689.60 $[M-Py]^+$ [174].

Gallium(III) 5,10,15-*meso*-tri-phenylcorrole(pyridyl) (Ga^{III}TPCor) was obtained in 83% yield. UV-vis (DMSO): λ_{max} nm (log ε) 432 (5.40), 567 (4.47), 622 (4.52). MS (MALDI TOF): calcd. *m/z* 671.16; observed 671.47 $[M-Py]^+$ [242].

2.2.2.4 Synthesis of A_2B *meso*-triarylcorroles

9-**10**-Cor *meso* triaryl A_2B free-base corrole ligands and their Ga(III) complexes were synthesized by following literature procedures [141,240]. 5-Pentafluorophenyldipyrromethane (DPM) (**Scheme 2.3a**) was prepared by using the Rohand method as described in the literature [243].

2.2.2.4.1 Synthesis of free-base A_2B *meso*-triarylcorroles

A_2B *meso* triaryl free-base corroles were synthesized in a stepwise manner using an acid-catalyzed condensation reaction of the appropriate dipyrromethane with 9-(4-formylphenyl)-3,6-di-*t*-butyl-9H-carbazole (**2**) or *N*-butyl-4-carbazole-3-carboxaldehyde (**3**) followed by an oxidation reaction using DDQ to form the **9**-**10**-Cor free-base corrole ligands (**Scheme 2.3b**).

The synthesis of *meso*-10-(3,6-di-*t*-butyl-9H-carbazole)-5,15-dipentafluorophenylcorrole (**9**-Cor) was carried out using DPM (6.0 mmol, 1.87 g) dissolved in 140 mL freshly distilled dry CH_2Cl_2. 9-(4-Formylphenyl)-3,6-di-*t*-butyl-9H-carbazole carboxaldehyde (**2**) was added to the mixture and stirred in the dark under an inert argon environment at room temperature for 20 min. TFA (0.54 mmol, 40 µL) was added to catalyze the reaction, and the mixture was allowed to stir for a further 4.5 h. Thereafter, the reaction mixture was diluted to 600 mL by adding CH_2Cl_2, and the oxidant was added in excess and stirred for 0.5 h. The reaction mixture was filtered and dried *in vacuo*, and the crude product was purified using silica gel column chromatography and 1:1 CH_2Cl_2: hexane (v:v)) eluent afford the target compound **9**-Cor. Yield: 302 mg (17%); ^{1}H NMR (600 MHz, $CDCl_3$) δH 9.05 (d, *J* = 6 Hz, 2H), 8.78 (d, *J* = 6 Hz, 2H), 8.70 (d, *J* = 12 Hz, 2H), 8.51 (s, 2H), 8.35−8.30 (m, 2H), 8.18 (d, *J* = 2.4 Hz, 2H), 7.91 (d, *J* = 0.6 Hz, 2H), 7.70−7.68 (m, 2H), 7.59−7.53 (m, 2H), 1.46 (s, 18H). UV-vis (CH_2Cl_2): λ_{max} nm (log ε) 417 (5.07). High-resolution ESI-MS: Calcd. m/z 982.29; observed: 982.30 $[M-H]^+$ [210].

Meso-10-(*N*-butyl-4-carbazole)-5,15-dipentafluorophenylcorrole (**10**-Cor) was synthesized in a similar manner to the procedure described for **9**-Cor to afford a 21% yield. ^{1}H NMR (600 MHz, $CDCl_3$) δ_H 9.12 (d, *J* = 6 Hz, 2H), 8.88 (d, *J* = 2.4 Hz, 1H), 8.75 (d, *J* = 6 Hz, 4H), 8.69−8.68 (m, 2H), 8.29−8.18 (m, 2H), 7.59−7.57 (m, 2H), 4.58-4.54 (m, 2H), 1.25 (s, 9H). UV-vis (CH_2Cl_2): λ_{max} (log ε)

414 (5.16). High-resolution ESI-MS (negative): Calcd. m/z 850.20; observed: 850.20 $[M-H]^-$ [210].

2.2.2.4.2 Synthesis of A_2B *meso* triaryl Ga(III) corroles

Gallium(III) *meso*-(10-3,6-di-*t*-butyl-9H-carbazole)-5,15-dipentafluorophenylcorrole(pyridyl) was prepared using **9**-Cor free-base corrole (98 mg, 0.1 mmol) dissolved in dry pyridine (20 mL) and excess $GaCl_3$ (176 mg, 1 mmol) was added. The mixture was stirred and refluxed at 140°C (**Scheme 2.3c**). After the reaction completion, the reaction vessel was cooled down to room temperature and organic solvents evaporated *in vacuo*, and the residual crude product was purified using silica gel chromatography and 1:1 dichloromethane/hexane eluent to give the target compound **9**-GaCor. Yield: 64 mg (58%); ^{1}H NMR (600 MHz, $CDCl_3$) δ_H 9.27 (d, *J* = 6 Hz, 2H), 8.98 (d, *J* = 6 Hz, 2H), 8.98 (d, *J* = 6 Hz, 2H), 8.92 (d, *J* = 6 Hz, 2H), 8.84 (s, 2H), 8.34 (d, *J* = 12 Hz, 2H), 7.96 (d, *J* = 6 Hz, 2H), 7.77 (d, *J* = 12 Hz, 2H), 7.63 (d, *J* = 2.4 Hz, 2H), 6.69 (d, *J* = 12 Hz, 1H), 3.74 (m, 4H), 1.46 (s, 18H). UV-vis (DMSO): λ_{max} (log ε) 423 (5.30), 574 (4.24); 600 (4.39). MS (MALDI TOF): Calcd. m/z 1128.24; observed: 1128.25 $[M-Py]^+$ [210].

Gallium(III) *meso*-10-(N-butyl-4-carbazole)-5,15-dipentafluorophenylcorrole(pyridyl) was synthesized using **10**-Cor in a similar manner described for **9**-GaCor (**Scheme 2.3b**) to yield 60% of the target compound. ^{1}H NMR (600 MHz, $CDCl_3$) δ_H 9.25 (d, *J* = 6 Hz, 2H), 8.87 (d, *J* = 6 Hz, 2H), 8.85 (s, 1H), 8.84 (d, *J* = 6 Hz, 4H), 8.81 (d, *J* = 4.2 Hz, 4H), 8.23-8.21 (m, 2H), 8.15 (d, *J* = 6 Hz, 2H), 7.72 (d, *J* = 6 Hz, 2H), 7.60-7.56 (m, 2H),7.27 (s, 1H), 6.69 (t, *J* = 12 Hz, 2H), 5.90 (t, *J* = 6 Hz, 2H), 4.56 (t, *J* = 12 Hz, 2H), 1.59 (s, 1H). UV-vis (DMSO): λ_{max} (log ε) 424 (5.45), 576 (4.47); 602 (4.53). MS (MALDI TOF): Calcd. m/z 997.15; observed: 997.55 $[M-Py]^+$ [210].

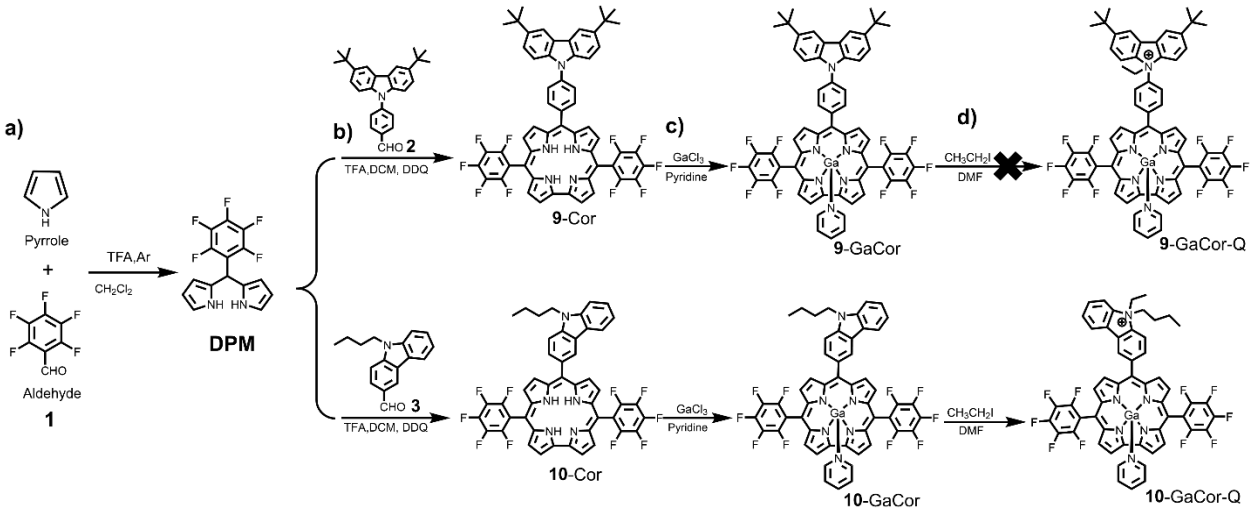

Scheme 2.3: a) Synthesis of 5-pentafluorodipyrromethane (**DPM**), b) the **9**-**10**-Cor A_2B meso-triaryl free-base corroles, and c) the corresponding **9**-**10**-GaCor gallium(III) corroles including d) the alkylated **9**-**10**-GaCor gallium(III) corrole complexes.

2.2.2.4.3 Synthesis of alkylated A_2B *meso* triaryl Ga(III) corroles

For the synthesis of gallium(III) *meso*-10-(9-butyl-9-ethyl-9H-carbazol-9-ium)-5,15-dipentafluorophenylcorrole(pyridyl), **10**-GaCor (32 mg, 0.032 mmol) was dissolved in dry DMF (10 mL), and excess iodoethane (0.1 mL, 12 mmol) was added. The mixture was stirred and refluxed at 60°C for 24 h under an inert N_2 environment (**Scheme 2.3d**). The reaction vessel was cooled to room temperature, and cold diethyl ether was added to induce the precipitation of **10**-GaCor-Q. The precipitate was filtered, washed thoroughly with diethyl ether, and dried to afford the **10**-GaCor-Q target compound. Yield: 25 mg (78%); ^{1}H NMR $(CD_3)_2CO$, 600 MHz) δ 9.34 (d, *J* = 3.9 Hz, 2H), 9.04 (d, *J* = 4.3 Hz, 2H), 8.97 (d, *J* = 3.5 Hz, 2H), 8.92 (s, 1H), 8.85 (d, *J* = 4.4 Hz, 2H), 8.27 (t, *J* = 7.4 Hz, 2H), 7.94 (d, *J* = 8.2 Hz, 1H), 7.73 (d, *J* = 8.5 Hz, 2H), 7.55 (t, *J* = 7.8 Hz, 1H), 7.24 (t, *J* = 7.3 Hz, 2H), 7.05 (s, 1H), 6.29 (s, 2H), 4.68 (t, *J* = 7.1 Hz, 2H), 3.44 (s, 2H), 1.62 (dd, *J* = 15.2, 7.5 Hz, 3H), 1.42 (s, 1H), 1.29 (d, *J* = 9.9 Hz, 1H), 1.20 (s, 2H), 1.07 (t, *J* = 7.4 Hz, 3H). UV-vis (DMSO): λ_{max}

(log ε) 423 (5.18), 575 (4.16); 602 (4.31). MS (MALDI TOF): Calcd. m/z 1027.20; observed: 1027.12 $[M]^+$ [210].

The synthesis of gallium(III) *meso*-10-(3,6-di-tert-butyl-9-ethyl-9-phenyl-9H-carbazol-9-ium)-5, 15- dipentafluorophenylcorrole (pyridyl) (**9**-GaCor-Q) was attempted in a similar manner to that described for **10**-GaCor-Q, but the reaction was unsuccessful (**Scheme 2.3d**).

2.2.3 Chlorin synthesis

2.2.3.1 Synthesis of free-base chlorins

Free-base chlorins (**5**-**8**-Chl) were synthesized following a procedure described in the literature [153] (**Scheme 2.4**). 5,10,15,20-tetrakis(4-methoxyphenyl)chlorin (**5**-Chl) previously reported [244] was synthesized in this study using **5**-Por (74 mg, 1 mmol) was dissolved in dry pyridine (40 mL), and K_2CO_3 (8 mmol) was added and stirred. The mixture was then refluxed in an inert nitrogen environment, and the same amount of *p*-toluenesulfonyl hydrazide (4 mmol) was added at 3 h intervals for 12 h. The reaction progress was monitored regularly using TLC and UV-visible absorption spectroscopy and stopped when porphyrin peaks disappeared, and the reduced bacteriochlorin peak started becoming stronger at 730 nm. The reaction mixture was cooled down to room temperature, extracted with $CHCl_3$, washed three times with 0.1M HCl solution, and lastly with Millipore water to remove pyridine and salts. The organic layer was dried over anhydrous sodium sulfate salt, and *p*-chloranil was added until the band at 730 nm disappeared. The mixture was filtered, and the organic solvent was evaporated. The crude product was purified by using silica gel chromatography with 3:1 CH_2Cl_2/petroleum ether eluent to afford the **5**-Chl target compound as a purple solid. Yield: 32 mg (43%). ^{1}H NMR (600 MHz, $CDCl_3$) δ 8.58 (d,

J = 4.6 Hz, 2H), 8.52 (d, *J* = 8.4 Hz, 2H), 8.47 (s, 1H), 8.44 (s, 1H), 8.19 (d, *J* = 4.6 Hz, 2H), 8.01 (d, *J* = 8.2 Hz, 4H), 7.77 (d, *J* = 8.1 Hz, 6H), 7.52 (d, *J* = 6.6 Hz, 4H), 4.16 (s, 4H), 4.06 (s, 6), 4.04 (s, 6H), -1.42 (s, 2H). UV-vis (DMSO): λ_{max} (log ε) 424 (5.02), 522 (3.90), 551 (3.85), 597 (3.65), 651 (4.06). MS (MALDI TOF): Calcd. m/z 736.30; observed: 737.38 $[M+H]^+$.

6-**8**-Chl free-base chlorin ligands were synthesized in a similar manner to that described for **5**-Chl (**Scheme 2.4**).

5,10,15,20-Tetra(3-methoxyphenyl)chlorin (**6**-Chl) was obtained in 41% yield. ^{1}H NMR (400 MHz, $CDCl_3$) δ 8.62 (d, *J* = 4.7 Hz, 2H), 8.46 (d, *J* = 3.9 Hz, 2H), 8.23 (d, *J* = 4.7 Hz, 2H), 7.71 (d, *J* = 7.6 Hz, 4H), 7.55 (d, *J* = 4.0 Hz, 2H), 7.35 (d, *J* = 2.3 Hz, 2H), 7.33 (d, *J* = 2.3 Hz, 2H), 7.22 (d, *J* = 2.3 Hz, 3H), 7.20 (d, *J* = 2.6 Hz, 3H), 4.19 (s, 4H), 3.94 (s, 12H), -1.48 (s, 2H). UV-vis (DMSO): λ_{max} nm (log ε) 420 (5.07), 515 (3.77), 549 (3.51), 596 (3.22), 651 (4.00). MS (MALDI TOF): Calcd. m/z 736.30; observed: 737.43 $[M+H]^+$.

5,10,15,20-Tetra(4-hydroxyphenyl)chlorin (**7**-Chl) [236,245] was obtained in 37% yield. ^{1}H NMR (400 MHz, DMSO-d_6) δ 9.87 (s, 2H), 9.75 (s, 2H), 8.86 (s, 2H), 8.59 (d, *J* = 5.2 Hz, 2H), 8.19 (d, *J* = 5.2 Hz, 2H), 8.00 (d, *J* = 8.4 Hz, 2H), 7.76 (d, *J* = 9.2 Hz, 1H), 7.62 (d, *J* = 5.0 Hz, 4H), 7.57 (d, *J* = 3.5 Hz, 2H), 7.47 (d, *J* = 8.6 Hz, 1H), 7.38 (d, *J* = 11.0 Hz, 2H), 7.20 (d, *J* = 8.7 Hz, 4H), 4.12 (s, 4H), -1.57 (s, 2H). UV-vis (DMSO): λ_{max} nm (log ε) 426 (5.11), 524 (3.93), 556 (3.92), 599 (3.39), 650 (4.27). MS (MALDI TOF): Calcd. m/z 680.24; observed: 681.38 $[M+H]^+$.

5,10,15,20-Tetra(4-hydroxy-3-methoxyphenyl)chlorin **8**-Chl was obtained in 35% yield. ^{1}H NMR (400 MHz, DMSO-d_6) δ 9.52 (s, 4H), 8.66 (d, *J* = 5.1 Hz, 2H), 8.38 (s, 2H), 8.25 (d, *J* = 5.1 Hz, 2H), 7.58 (d, *J* = 8.2 Hz, 4H), 7.51 (d, *J* = 8.3 Hz, 4H), 7.14 (d, *J* = 4.2 Hz, 4H), 4.20 (s, 4H), 3.83 (d, *J* = 7.7

Hz, 12H), -1.57 (s, 2H).UV-vis (DMSO): λ_{max} nm (log ε) 428 (5.05), 520 (3.93), 560 (3.83), 601 (3.93), 653 (4.01). MS (MALDI TOF): Calcd. m/z 800.28; observed: 801.43 $[M+H]^+$.

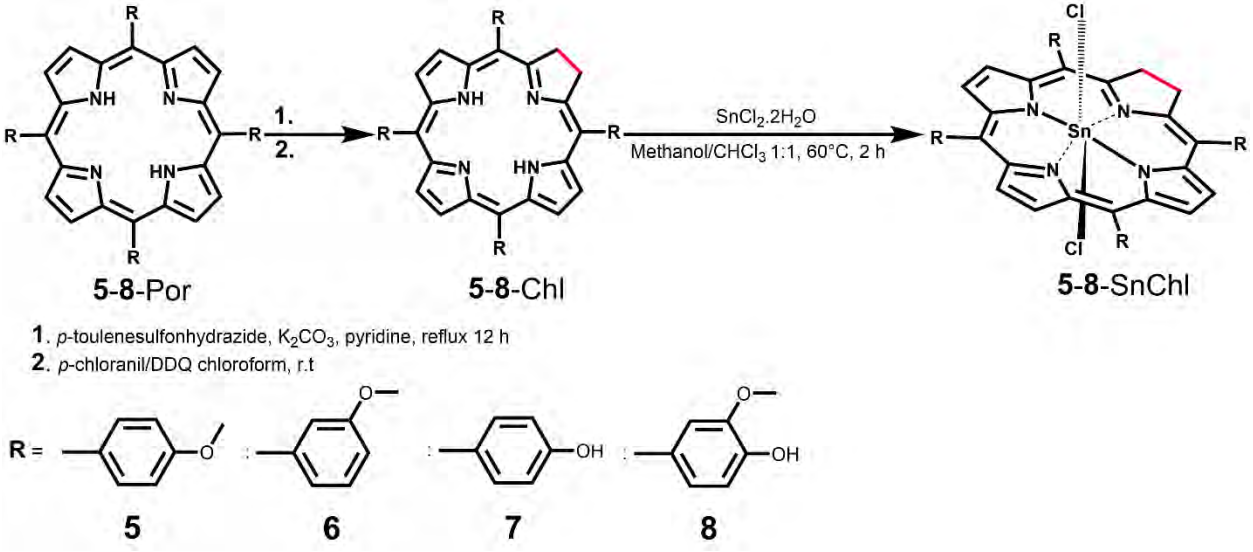

Scheme 2.4: Synthesis of **5**-**8**-Chl and the **5**-**8**-SnChl complexes.

2.2.3.2 Synthesis of Sn(IV) chlorins

For the preparation of dichlorotin(IV) 5,10,15,20-tetra(4-methoxyphenyl)chlorin, **5**-Chl (45 mg, 0.06 mmol) was dissolved in 15 mL dry $CHCl_3$/methanol solution (1:1 v/v) and warmed. $SnCl_2{\cdot}2H_2O$ (98 mg, 0.43 mmol) was added, and the reaction mixture was brought to reflux for 12 h (**Scheme 2.4**). The reaction progress was monitored using TLC and UV-visible absorption spectroscopy. The reaction mixture was cooled to room temperature, and organic solvents were evaporated. The residual crude product was purified on a neutral alumina column chromatography and CH_2Cl_2/MeOH (7:1 v/v) eluent to afford the target compound **5**-SnChl as green crystals. Yield: 33 mg (74%). ^{1}H NMR (400 MHz, $CDCl_3$) δ 8.32 (d, *J* = 2.4 Hz, 2H), 8.23 (d, *J* = 8.7 Hz, 2H), 8.17 (d, *J* = 4.6 Hz, 2H), 8.03 (d, *J* = 2.3 Hz, 2H), 8.01 (d, *J* = 2.3 Hz, 4H), 7.80 (d, *J* = 2.2 Hz, 2H), 7.14 (d, *J* = 2.6 Hz, 4H), 7.12 (d, *J* = 2.5 Hz, 4H), 4.13 (s, 4H), 4.06 (s, 6H), 4.02 (s, 6H).

UV-vis (DMSO): λ_{max} nm (log ε) 433 (5.07), 572 (3.76), 608 (3.65), 629 (4.06). MS (MALDI TOF): Calcd. m/z for $[M]^+$ = 924.13, $[M\text{-}Cl]^+$= 889.16; observed: 890.11 $[M-Cl+H]^+$.

6-**8**-SnChl Sn(IV) chlorin complexes were synthesized in a similar manner to the procedure described for **5**-SnChl (**Scheme 2.4**).

Dichlorotin(IV) 5,10,15,20-tetra(3-methoxyphenyl)chlorin (**6**-SnChl) was obtained in a 77% yield. ^{1}H NMR (400 MHz, $CDCl_3$) δ 8.65 (d, *J* = 5.1 Hz, 2H), 8.57 (d, *J* = 9.0 Hz, 2H), 8.20 (d, *J* = 5.2 Hz, 2H), 7.81 (d, *J* = 8.0 Hz, 2H), 7.58 (d, *J* = 8.1 Hz, 4H), 7.45 (d, *J* = 7.3 Hz, 4H), 7.16 (d, *J* = 6.7 Hz, 2H), 7.10 (d, *J* = 9.7 Hz, 2H), 4.37 (s, 4H), 3.95 (s, 12H).UV-vis (DMSO): λ_{max} nm (log ε) 430 (5.23), 564 (3.96), 602 (4.03), 627 (4.12). MS (MALDI TOF): Calcd. m/z for $[M]^+$ = 924.13, $[M-Cl]^+$= 889.16; observed: 889.16 $[M-Cl]^+$.

Dichlorotin(IV) 5,10,15,20-tetra(4-hydroxyphenyl)chlorin (**7**-SnChl) was obtained in 65% yield.^{1}H NMR (400 MHz, DMSO-d_6) δ 9.05 (s, 2H), 8.84 (s, 2H), 8.38 (d, *J* = 4.9 Hz, 2H), 8.18 (d, *J* = 4.3 Hz, 2H), 8.13 (d, *J* = 7.5 Hz, 2H), 8.07 (s, 2H), 8.00 (d, *J* = 5.2 Hz, 2H), 7.96 (d, *J* = 2.8 Hz, 2H), 7.64 (d, *J* = 8.8 Hz, 4H), 7.23 (d, *J* = 6.3 Hz, 2H), 7.17 (d, *J* = 8.6 Hz, 2H), 7.11 (d, *J* = 8.2 Hz, 2H), 4.14 (s, 4H). UV-vis (DMSO): λ_{max} nm (log ε) 438 (5.11), 576 (3.79), 613 (3.99), 629 (4.16). MS (MALDI TOF): calcd. *m/z* for $[M]^+$ = 868.07, $[M-Cl]^+$= 833.09; observed: 834.11 $[M-Cl+H]^+$.

Dichlorotin(IV) 5,10,15,20-tetra(4-hydroxy-3-methoxyphenyl)chlorin (**8**-SnChl) was obtained in 72% yield. ^{1}H NMR (400 MHz, DMSO-d_6) δ 9.68 (s, 4H), 8.71 (d, *J* = 4.7 Hz, 2H), 8.22 (d, *J* = 5.1 Hz, 2H), 8.04 (d, *J* = 10.4 Hz, 2H), 7.79 (d, *J* = 9.6 Hz, 4H), 7.68 (d, *J* = 14.2 Hz, 4H), 7.13 (d, *J* = 8.7 Hz, 4H), 4.19 (s, 4H), 3.94 (s, 12H). UV-vis (DMSO): λ_{max} nm (log ε) 439 (5.05), 575 (3.95), 615 (4.19),

630 (4.36). MS (MALDI TOF): calcd. *m/z* for $[M]^+$ = 988.11, $[M-Cl]^+$= 953.14; observed: 953.48 $[M-Cl]^+$.

2.2.4 N-confused porphyrin synthesis

2.2.4.1 Synthesis of free-base 5,10,15,20-tetrakis(4-methoxyphenyl)-2-azaporphyrin

The free-base N-confused porphyrin ligand was prepared following a procedure described in the literature [169]. Dilute equimolar pyrrole and 4-methoxybenzaldehyde (5 mmol) in dry CH_2Cl_2 (1 L) were stirred at room temperature, and a catalytic amount of MSA (230 uL, 3.5 mmol) was added dropwise for 5 min (**Scheme 2.5**). The reaction mixture was further stirred for 30 min, and excess DDQ (5.13 mmol, 1.2 g) oxidant was added and stirred for 2 min. The reaction was subsequently quenched by TEA (1 mL), and the reaction mixture was filtered with a basic alumina pad. The filtrate was evaporated, and the crude product was column chromatographed on basic alumina with 1:4 CH_2Cl_2/hexane eluent and subsequently washed with dilute HCl to afford the target compound **5**-NCP as a purple solid. Yield: 425 mg (12%). ^{1}H NMR (600 MHz, $CDCl_3$): δ 8.94 (d, *J* = 4.7 Hz, 1H), 8.88 (d, *J* = 4.6 Hz, 1H), 8.68 (s, 1H), 8.58 (d, *J* = 4.7 Hz, 1H), 8.53 (d, *J* = 10.0 Hz, 3H), 8.32 (d, *J* = 8.4 Hz, 2H), 8.26 (d, *J* = 8.4 Hz, 2H), 8.06 (m, 4H), 7.40 (d, *J* = 8.4 Hz, 4H), 7.28 (m, 4H), 4.10 (s, 3H), 4.09 (s, 6H), 4.07 (s, 3H). UV-vis (DMSO): λ_{max} nm (log ε) 444 (5.11), 550 (3.84), 640 (4.05), 700 (4.13), 778 (3.50). MS (MALDI TOF): Calcd. m/z 734.29; observed: 735.44 $[M+H]^+$.

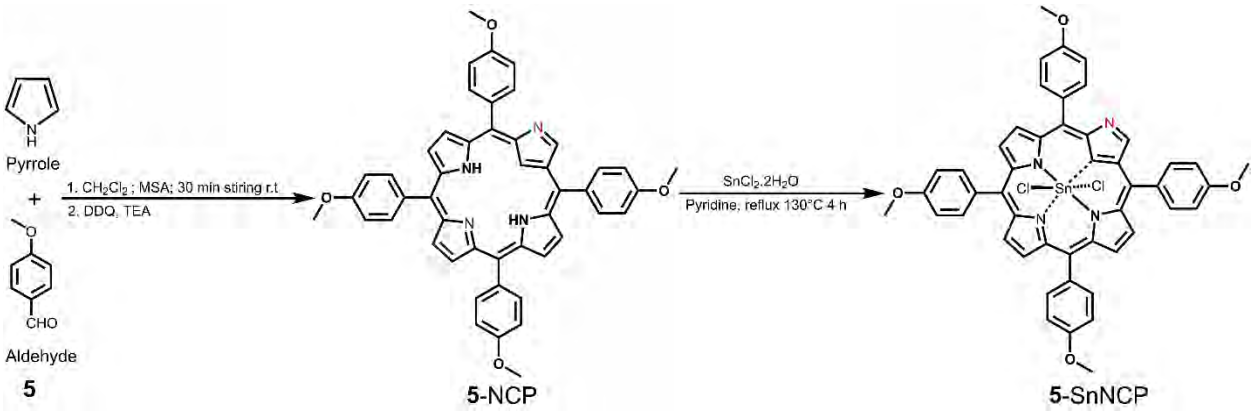

Scheme 2.5: Synthesis of **5**-NCP and **5**-SnNCP.

2.2.4.2 Synthesis of Sn(IV) 5,10,15,20-tetrakis(4-methoxyphenyl)-2-azaporphyrin

5-NCP (75 mg, mmol) in dry pyridine was warmed, and $SnCl_2 \cdot 2H_2O$ (98 mg, 10 mmol) was added and refluxed for 4 h under an N_2 atmosphere (**Scheme 2.5b**). The reaction progress was regularly monitored using TLC and UV-visible absorption spectroscopy. The reaction mixture was cooled down to room temperature and dried *in vacuo*. The residual crude product was purified on a neutral alumina column chromatography and CH_2Cl_2/MeOH (10:1 v/v) eluent. The product was then subsequently washed with dilute HCl to afford the target compound **5**-SnNCP green solid. Yield: 58 mg (77%). ^{1}H NMR (600 MHz, $CDCl_3$) : ^{1}H NMR (600 MHz,) δ 10.77 (s, 1H), 8.80 (s, 1H), 8.50 (d, *J* = 5.1 Hz, 1H), 8.41 (d, *J* = 4.9 Hz, 1H), 8.26 (d, *J* = 3.2 Hz, 2H), 8.14 (d, *J* = 3.0 Hz, 2H), 7.91 (m, 6H), 7.84 (d, *J* = 8.0 Hz, 2H), 7.19 (m, 6H), 7.09 (d, *J* = 8.2 Hz, 2H), 4.03 (s, 9H), 3.80 (s, 3H).UV-vis (DMSO): λ_{max} nm (log ε) 454 (5.18), 562 (3.90), 608 (4.04), 667 (3.30), 733 (3.96). MS (MALDI TOF): Calcd. m/z for $[M]^+$ = 922.11, $[M-Cl]^+$= 887.15; observed: 887.54 $[M-Cl]^+$.

2.2.5 Gold and silver nanoparticles synthesis

Oleylamine-capped gold and silver nanoparticles were synthesized following the previously described literature procedure [246]. Gold(III)chloride trihydrate (50 mg, 0.15 mmol) was

dissolved in oleylamine (2 mL), oleic acid(1 mL), and toluene (2 mL) and then quickly injected into a refluxing solution of oleylamine (2 mL) and toluene (45 mL) (**Scheme 2.6a**). The reaction progress was monitored using UV-visible absorption spectroscopy until the color of the reaction mixture changed from yellow to red wine. After 20 min, the heating was stopped, the solution was cooled, and methanol/isopropanol 1:1(100 mL) was added to induce the precipitation of gold nanoparticles. The product was recovered through centrifugation at 15000 rpm for 15 min. The product was washed three times with methanol and centrifuged to yield a grey solid (45%, sizes ~ 10-15 nm).

For AgNP synthesis, silver nitrate (50 mg, 0.3 mmol) was dissolved in oleylamine (2.5 mL) and oleic acid (1 mL) (**Scheme 2.6b**). The mixture solution was added into refluxing diphenyl ether (10 mL) under an inert environment and refluxed for a further 5 h. The progress of the reaction was monitored using UV-visible absorption spectroscopy until the color changed to dark brown. After 5 h, the reaction was stopped, cooled to room temperature, and methanol was added to induce precipitation. The product was recovered through centrifugation at 15000 rpm for 15 min, followed by washing three times using methanol and centrifuging to yield a yellow-brown solid (52%, size *ca.* 10 nm).

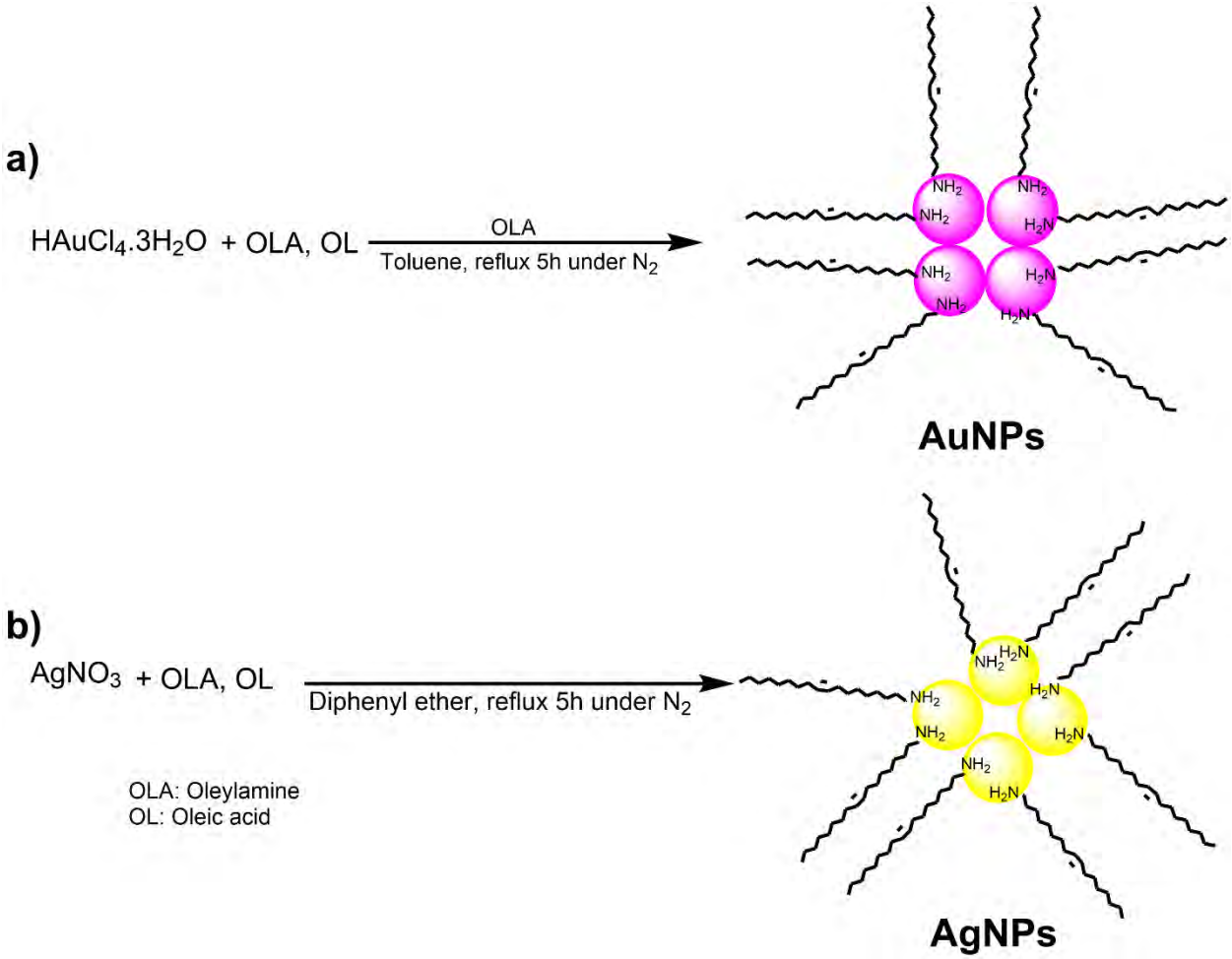

Scheme 2.6: Synthesis of oleylamine capped a) gold and b) silver nanospheres.

2.2.5.1 Functionalization of porphyrinoid complexes with gold and silver nanoparticles

1-**4**-InPor chloroindium porphyrins, **1**-**4**-P^{V}Cor, and **1**-**4**-GaCor were conjugated to gold and silver nanoparticles *via* self-assembly following a previously reported procedure [247,248]. Briefly, each complex (10 mg) was dissolved in chloroform(5 mL) and added to a refluxing solution of toluene (10 mL). Then the oleylamine-capped gold (AuNPs) or silver (AgNPs) nanoparticles (4 mg in toluene 2 mL) solution was quickly injected into the reaction vessel and refluxed further for 4 h (**Scheme 2.7**). The reaction mixture was cooled down to room temperature and stirred further for 24 h to enhance efficient ligand exchange on the binding sites of complexes on the AuNP or

AgNP nanoparticle surfaces. The nanoconjugates were obtained by precipitation using methanol and centrifugation at 5000 rpm for 10 min. The products were washed and centrifuged three times to remove any unreacted complex and dried.

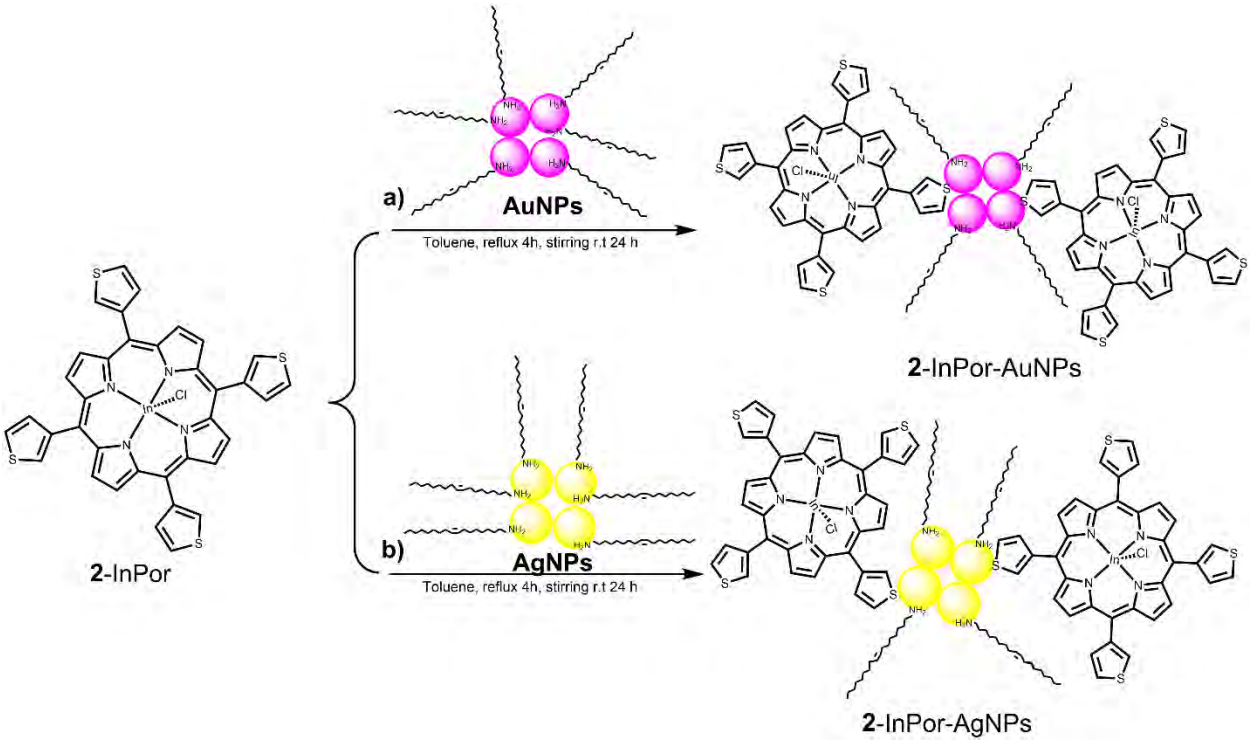

Scheme 2.7: Synthesis of a) **2**-InPor-AuNPs and b) **2**-InPor-AgNPs as representative nanoconjugates.

2.3 Photostability

The photostabilities of the photosensitizer dyes were studied by monitoring the UV-visible absorption spectra of the samples upon irradiation with a 595, 625, or 660 nm Thorlabs LED for 30 min. The sample solutions were prepared in 1% DMSO-H_2O in the dark. Their Soret band absorbance was maintained at *ca.* 1 and the solutions were transferred into the quartz UV-cells (1 × 1 cm) and sealed tightly. Photoirradiation was carried out with Thorlabs LEDs mounted onto the housing of a Modulight 7710-680 medical laser system, with the reaction progress monitored

by measuring the UV-visible absorption spectroscopy on a Thermo Fischer Scientific™ Evolution™ 350-UV-Vis spectrophotometer at 15 min time intervals. The studies were also performed as earlier described in 1% DMSO/DMEM culture media solutions at 7.4 pH for complexes **3**-P^{V}Cor, **3**-GaCor, and their **3**-P^{V}Cor-AuNP and **3**-GaCor-AuNP nanoconjugates as representative examples to aid the comparison of 1% DMSO/H_2O solutions studies with the physiological conditions [174]. The photobleaching rates of the dyes were calculated from the observed change in the absorption intensities with irradiation time and are presented as percentage values (**Table 5.4**).

2.4 Lipophilicity

The lipophilicity tests were carried out in triplicate for each dye complex studied by using the "shake-flask" method [249]. The sample solutions were prepared using 0.5 mg of each dye complex dissolved in 10 mL of dry $CHCl_3$. For each 3 mL $CHCl_3$ solution of the complex, the absorbance at the Soret band maxima (A_o) was measured. 3 mL of Millipore water was then added to each 3 mL $CHCl_3$ solution, followed by the stirring of the mixture at room temperature for 4 h. Thereafter, the mixture was centrifuged at 5000 rpm for 10 min to allow the separation of the water and $CHCl_3$ phases. Then the absorbance of the $CHCl_3$ layer (A_f) was measured for each complex mixture, with the value for the water phase determined from the difference between the initial (A_o) and final (A_f) of the dye complex in $CHCl_3$. The partition coefficient values (Log $P_{o/w}$) for the complexes in $CHCl_3$:H_2O were derived using Equation 2.1 [249].

$$P_{octanol} = [1.343 + \text{Log } P_{chloroform}] / 1.126 \quad (2.1)$$

2.5 PDT studies

2.5.1 MCF-7 cells culturing

The MCF-7 cells were cultured as previously described [250] in Dulbecco's modified Eagles' medium (DMEM) containing 4.5 $g.L^{-1}$ glucose with L-glutamine and phenol red. The media was supplemented with 10% (v/v) heat-inactivated fetal calf serum (FCS) and 5% 100 unit mL^{-1} penicillin 100 $\mu g.mL^{-1}$ streptomycin amphotericin B. The cells were grown in a T75 cm^2 vented flask (Porvair) and incubated in a humidified 5% CO_2 atmosphere at 37°C until 80% confluence was achieved. The cells were rinsed with Dulbecco's modified phosphate buffer saline (DPBS) before routine standard trypsinization during subculturing and cell harvesting. The trypsinized cells were treated with trypan blue dye exclusion assay (0.40% trypan blue solution), and a hemocytometer was used to count viable cells. The cells were seeded in 96-well plates at a density of 10000 cells/well in supplemented red-phenol DMEM medium and incubated under a humidified 5% CO_2 for 24 h at 37°C to enable cell attachment to the wells. The attached cells were then rinsed twice using 100 µL DPBS, and subsequently, 100 µL of the drugs (the studied compounds) in the DMEM medium were administered over gradient concentration ranges. The drug stock solutions were prepared in DMSO since they are insoluble in aqueous media. After dilution, appropriate drug aliquot volumes were prepared in DMEM media such that the highest gradient concentrations consisted of < 1% (v/v) DMSO. The control cells were supplemented with DMEM medium alone, with the effect of DMSO on the cells investigated by incubating the cells in 1% (v/v) DMSO-DMEM media. The plates were then re-incubated for 24 h in the dark for further studies that include *in vitro* dark cytotoxicity and PDT activity studies, including cellular uptake studies.

2.5.2 *In vitro* dark and light studies

The MCF-7 cancer cells treated with the different drug concentrations were rinsed thrice with 100 µL DPBS to remove any residual drug, as described in Section 2.6.1. DMEM media with no red phenol was added. For i*n vitro* dark cytotoxicity studies, the drug-treated cells were not photoirradiated, while for light studies, the treated cells were photoirradiated with a Thorlabs LED (M595L3, M625L3, or M660L3) mounted onto a Modulight 7710-680 medical laser system housing at 595, or 625, or 660 nm based on the Q band maxima of the drugs administered. The excitations of the PS dyes were performed in the red region of the electromagnetic spectrum since the dyes used in this work are intended for use in the treatment of deep-seated infected soft tissues and tumors [251,252].

The Thorlabs M595L3 LED was used for 20 min photoirradiations of cells treated with the A_2B *meso*-triarylcorrole series (**9**-**10**-GaCor and **10**-GaCor-Q) for 20 min, and a Thorlabs M625L3 LED was used for 10 min photoirradiations of cells treated with the chloroindium porphyrin series. It was also used for photoirradiation of cells treated with **5**-**8**-SnPor and the A_3 *meso*-triarylcorrole dyes series (**1**-**3**-GaCor, **1**-**3**-P^VCor, and their **1**-**3**-GaCor-AuNP and **1**-**3**-P^VCor-AuNP nanoconjugates) for 20 min. Both Thorlabs M625L3 and M660L3 LEDs were used for 20 min photoirradiations of cells treated with **5**-Por, **5**-SnPor, **5**-**8**-Chl, **5**-**8**-SnChl, **5**-NCP, and **5**-Sn-NCPs. The DMEM media was replaced with red phenol, and the cells were further incubated for 24 h. Routine examination of the cells and imaging was performed with a Zeiss AxioVert.A1 Fluorescence LED inverted microscope. Cell viabilities were determined using the WST-1 and MTT assay protocols following the manufacturer's specifications by measuring the absorbances of the assays at 450 and 540 nm, respectively, on a Synergy 2 multi-mode microplate reader (BioTek®).

All the experiments were carried out in triplicate, with the data analyzed statistically using the student T-test and ANOVA. The percentage cell viabilities were calculated as the percentage ratio of the absorbance of the drug-treated cells against the untreated controls [250], as described in Equation 2.2.

$$\%\ \text{Cell Viability} = \frac{\text{Absorbance of samples at 450 (or 540) nm}}{\text{Absorbance of control at 450 (or 540) nm}} \times 100 \qquad (2.2)$$

Since the IC_{50} value is another important parameter for determining drug efficacy, it was calculated for the dyes by nonlinear regression analysis using GraphPad Prism 5. During *in vitro* PDT studies, the IC_{50} value provides a half-maximal inhibitory concentration of a photosensitizer dye for inhibiting the growth or killing 50% of cancer cells after drug incubation and light treatment. Error bars represent the standard deviation (n = 3).

2.6 Cellular uptake

Cellular uptake profiles for the dyes were determined with MCF-7 cancer cells already attached to the 96-well plates (cell density 10^4 cells/well during seeding, as described in Section 2.6.1). The cells were treated with three gradient concentrations of the dyes and were incubated for 24 h. Optimum cellular uptake was evident after 24 h of drug incubation [253]. The three gradient concentrations of the drugs were considered since cellular uptake is a function of PS concentration, with the lowest concentrations known to exhibit minimal cellular uptake and the highest concentrations known to exhibit relatively low uptake due to an altered transport mechanism [254,255]. The treated cells were washed thrice with 100 µL DPBS to remove residual PS drugs and lyzed with 100 mL of 30% Triton X-100 in DMSO. The accumulated drugs inside the cells were assessed on a Synergy 2 multi-diode microplate reader (BioTek) by measuring the

fluorescence intensities of each drug (dye) at λ_{max} wavelength. The experiments were carried out in triplicate, and the data were analyzed statistically with a student T-test and ANOVA. Error bars represent the standard deviation (n = 3).

2.7 PACT studies

The PACT activities of the photosensitizer dyes were carried out with planktonic and biofilms cells of Gram-(+) *S. aureus* (ATCC® 25923™) and Gram-(−) *E. coli* bacteria (ATCC®, 25922™) strains. Photoinactivation experiments were performed as described in the literature with slight modifications [256]. The viable bacteria colonies were estimated using the direct viable colony count method and an indirect crystal violet staining assay. The planktonic bacteria cells were estimated using the direct method only by counting the viable colonies formed on the agar plates using a bacteria counter, as described previously in the literature [256]. Both the viable colony count and indirect methods were used for viable biofilm cells [257]. The crystal violet assay was used to quantify the biofilm biomass indirectly by measuring the absorbance intensity at 590 nm on a Synergy 2 multi-diode microplate reader (BioTek). The PS dye stock solutions were first prepared in DMSO since they were insoluble in PBS alone with the appropriate drug aliquots volumes prepared to 1% (v/v) DMSO-PBS solution after serial dilution. Photoinactivation experiments were carried out in the dark and after irradiation with a Thorlabs LED (M595L3, M625L3, or M660L3) mounted onto a Modulight 7710-680 medical laser system housing. The Thorlabs LED chosen for photoirradiation depended primarily on the Q band maxima of the dye drugs administered. For all *in vitro* dark cytotoxicities and photoinactivation activity studies of the dyes against both the planktonic and biofilm cells of *S. aureus* and *E. coli* bacteria strains, the

effect of PS dye drug concentrations with a fixed fluence (light) dosage and the effect of fluence rate with a fixed drug dye concentration dosage were investigated.

2.7.1 Planktonic bacteria culturing

S. aureus and *E. coli* bacteria strains were grown anaerobically on the agar plates to obtain colonies of each strain by following the manufacturer's specifications. A single colony of each bacterial strain was inoculated into 5 mL of freshly prepared Lura nutrient broth. The culture mixture was vortexed and incubated at 37°C with agitation (*ca.* 200 rpm) in a shaker rotary incubator for 18 and 48−72 h for *S. aureus* and *E. coli*, respectively. Aliquots from each bacteria culture mixture were taken regularly to measure their optical densities until the bacterial growth reached a mid-logarithmic phase (OD 620 nm, *ca.* 0.6-0.8). The bacteria pellets were then harvested through centrifugation for 15 min at 3000 rpm and washed three times with PBS to remove residual nutrient broth. The bacteria pellets were resuspended in 4 mL PBS and further diluted to 1:1000 (v/v) in PBS to obtain the working bacteria culture stock solutions.

The viable colonies count of the freshly prepared *S. aureus* and *E. coli* bacteria cultures were determined by serial dilution of the bacteria culture stock solutions by factors of 10^{-4}, 10^{-5}, 10^{-6}, 10^{-7}, 10^{-8}, and 10^{-9}. A 100 µL aliquot of each sample solution was aseptically inoculated on the agar plates in triplicates and incubated for 24 h at 37°C to determine the optimum bacteria count. The viable bacteria colonies were counted on a Scan 500® series Automatic Colony Counter. The optimized bacteria solutions ranging from 2.78−3.01 × 10^8 CFU/mL and 1.62−2.01 × 10^8 CFU/mL for *S. aureus* and *E. coli*, respectively, were used in the subsequent studies.

2.7.2 *In vitro* dark and light photoinactivation of planktonic bacteria

The experimental procedure followed for sample preparation for *in vitro* dark and light studies of the dyes for photoinactivation of planktonic *S. aureus* and *E. coli* bacteria strains was the same. For time-dependence studies, a 5 mL bacteria suspension (10^8 CFU/mL) of *S. aureus* or *E. coli* in 1% DMSO/PBS solution was incubated with the dye drug (of appropriate concentration) at 37°C in a rotary shaking incubator at 200 rpm for 30 min in the dark. Half (2.5 mL) of the drug-incubated bacteria suspension was transferred into a 24-well plate for light studies, and the remaining half (2.5 mL) was kept in another 24-well plate in the dark for *in vitro* dark cytotoxicity studies. For light studies, the drug-treated bacteria suspensions were irradiated with an M595L3, M625L3, or M660L3 Thorlabs LED mounted onto a Modulight 7710-680 medical laser system housing. This facilitates excitation at 595, 625, or 660 nm, respectively, over different time intervals. For bacteria suspensions treated with chloroindium (III) porphyrin series (**1**-**4**-InPor and their **1**-**4**-InPor-AgNP nanoconjugates), the studies were carried out at 2.5 and 15 μg/mL against *S. aureus* and *E. coli*, respectively. Photoirradiations were performed with a Thorlabs M625L3 LED at 15 min time intervals for 75 min. In contrast, bacteria suspensions treated with the A_3 P^V and Ga^{III} corrole series (**1**-**4**-GaCor, **1**-**4**-P^VCor, and their **1**-**4**-GaCor-AgNPs and **1**-**4**-P^VCor-AgNP nanoconjugates) were studied at 0.5 and 2.5 μg/mL against *S. aureus*, and at 10 μg/mL against *E. coli* bacteria. The photoirradiations were performed with a Thorlabs M625L3 LED. The *S. aureus* and *E. coli* bacteria suspensions were treated with 0.5 μg/mL and 10 μg/mL of the A_3 P^V and Ga^{III} corrole series, respectively. The photoirradiation treatments were carried out over 15, 30, 60, 90, and 120 min intervals, and 5, 15, 30, 45, 60, and 75 min intervals for *S. aureus* suspensions treated with 2.5 μg/mL of the dye series. In contrast, for A_2B Ga^{III} corrole series (**9**-**10**-GaCor and **10**-

GaCor-Q) dye drugs against *S. aureus* bacteria, two concentrations of 0.5 and 2.5 μM were used and 10 μM was used against *E. coli* bacteria with photoirradiations at different time intervals using a Thorlabs M595L3 LED. For the A_2B Ga^{III} corrole dye series, photoirradiations were carried out at 15, 30, 60, 90, and 120 min against *S. aureus* and *E. coli* suspensions treated with 0.5 and 10 μM of dye series, respectively, and 5, 15, 30, 45, 60, 75 min for *S. aureus* suspensions treated with 2.5 μM of the dyes, while for the porphyrins, chlorins, and N-confused porphyrin free-base ligands (**5**-**8**-Por, **5**-**8**-Chl, and **5**-NCP) and their Sn(IV) complexes (**5**-**8**-SnPor, **5**-**8**-SnChl, and **5**-SnNCP), a 1 μM of the dye was administered against *S. aureus* and 5 μM against *E. coli* bacteria. For *S. aureus* and *E. coli* suspensions treated with the Sn(IV) porphyrin dye series, the photoirradiation treatments were carried out over 5, 10, 15, 30, 45, 60 and 75 min intervals using a Thorlabs M625L3 LED, while for the bacteria suspension treated with **5**-Por, **5**-SnPor, **5**-**8**-Chl, **5**-**8**-SnChl, **5**-NCP and **5**-SnNCP, M625L3 and M660L3 Thorlabs LEDs were used for photoirradiations over 5, 10, 15, 30, 45, 60 and 75 min intervals.

After light and dark treatments at the considered time intervals, a 100 μL aliquot of the samples was aseptically inoculated on the agar plate and incubated at 37°C for 18 h. The viable bacteria colonies were counted on a Scan 500® series Automatic Colony Counter to determine CFU/mL values. The controls were *S. aureus* and *E. coli* bacteria suspensions (10^8 CFU/mL) without the PS dye drug. The cell survival fractions were calculated by comparing the drug-treated bacteria with the control. The Log_{10} reductions were calculated using Equation 2.3. All the experiments were performed in three independent triplicates, and data were analyzed statistically using student T-test and ANOVA.

Log reduction = Log (A) − Log (B) (2.3)

Where A and B represent the number of viable colonies (CFU/mL) of bacteria for the untreated and treated samples, respectively.

Prior to time-dependence studies, the effect of gradient concentrations of the dyes was analyzed at fixed light (fluence) doses to establish the optimal concentrations. For bacteria suspensions treated with chloroindium (III) porphyrin series (**1**-**4**-InPor and their **1**-**4**-InPor-AgNP nanoconjugates), concentration studies were carried out at 1, 1.5, 2, 2.5, and 5 μg/mL against *S. aureus* and 2.5, 5, 10, 15, and 20 μg/mL against *E. coli* with the photoirradiations performed with a Thorlabs M625L3 LED for 60 min. For the bacteria suspensions treated with the A_3 P^V and Ga^{III} corrole dyes series (**1**-**4**-GaCor, **1**-**4**-P^VCor, and their **1**-**4**-GaCor-AgNP and **1**-**4**-P^VCor-AgNP nanoconjugates), studies were carried out at 0.5, 1, 2, 2.5, 5 μg/mL gradient concentrations against *S. aureus*, and 2.5, 5, 10, 15, and 20 μg/mL against *E. coli* with the photoirradiations performed with a Thorlabs M625L3 LED for 60 min. For the A_2B Ga^{III} corrole dye series (**9**-**10**-GaCor and **10**-GaCor-Q), the dyes were administered at 0.5, 1, 2, 2.5, and 5 μM concentrations against *S. aureus* and 2.5, 5, 10, 15, and 20 μM against *E. coli* with the photoirradiation treatments performed with a Thorlabs M595L3 LED for 60 min. For bacteria suspensions treated with Sn(IV) porphyrins, chlorins and N-confused porphyrin dye complexes (**5**-**8**-SnPor, **5**-**8**-SnChl, and **5**-Sn-NCP) gradient concentrations of 0.5, 1, 1.5, 2, 2.5, 5 μM were administered against *S. aureus*, and 1, 2.5, 5, 10, and 15 μM against *E. coli* with photoirradiation carried out for 45 min using a Thorlabs M625L3 LED.

2.7.3 Biofilm bacteria culturing

The freshly prepared planktonic *S. aureus* and *E. coli* bacteria cultures (prepared as described in Section 2.7.1) were diluted to 1×10^6 CFU/mL in Tryptic Soy Broth (TBS). The TBS-supplemented bacteria cultures (200 µL/well) were seeded into the 96-well plates and incubated anaerobically under static conditions at 37°C with 5% CO_2 for 24 and 72 h for *S. aureus* and *E. coli*, respectively, to form the *S. aureus* and *E. coli* single-species bacteria biofilms. The wells with media alone provided the negative controls. After incubation, the culture media was discarded, and the wells were gently rinsed two times with PBS to remove the residual TBS and the non-adherent planktonic bacteria cells. The plates were air-dried at room temperature for 30 min to fix the adherent cells.

The biofilm bacteria biomass was quantified with a crystal violet assay. A 150 µL/well aliquot of 0.1% (w/v) crystal violet assay was used to stain the biofilm-coated wells for 15 min at room temperature. The crystal violet assay was then discarded, and the wells were washed three times using 200 µL PBS/well to remove the residual dye. 150 µL/well PBS was again added to the stained wells, and the absorbance values of well solutions were measured at 590 nm on a Synergy 2 multi-mode microplate reader (BioTek®). All the experiments were carried out in triplicate, and the Z-score method was used to identify outlier values. Non-outlier values were used to calculate the average biofilm formed. The average negative control value was subtracted from the obtained biofilms absorbance data, and the data were provided as mean absorbance ± standard deviation. Biofilms were considered to be formed when the absorbance value at 590 nm was three times the standard deviation of the negative control mean absorbance [258]. All the experimental data were analyzed statistically with a student T-test and ANOVA.

Viable cell counts of the single species *S. aureus* and *E. coli* biofilms were also estimated by using the viable colony count method. The biofilms formed in the 96-well plates were solubilized by adding 200 µL/well of PBS and sonicating the plates vigorously for 10 min, followed by scraping of the wells to dislodge the adherent cells. The resultant well suspension was vortexed to homogenize the solution and serial diluted 10-fold times, and a 100 µL aliquot of the diluted sample was then aseptically inoculated on the agar plate in triplicates followed by incubation at 37°C for 18 h. The viable colonies count (CFU/mL) was carried out on a Scan 500® series Automatic Colony Counter. All the experimental data were analyzed statistically with a student T-test and ANOVA.

2.7.4 *In vitro* dark and light photoinactivation of biofilm cells

Initially, experiments were carried out to study the effect of dye concentration on inhibiting the growth of the single-species biofilms of *S. aureus* and *E. coli* strains (grown as described in Section 2.7.2). For these concentration studies, the single species biofilms of *S. aureus* and *E. coli* strains were incubated with 100 µL/well aliquots of the dye series at various concentrations for 30 min. For light studies, the drug-incubated 96-well plates biofilms were photoirradiated with a 595, 625, or 660 nm Thorlabs LED for 30 min. For the dark studies, the drug-treated plates were kept in the dark (in the absence of photoirradiation) for 30 min to determine the dark cytotoxicities of the drugs. For the chloroindium (III) porphyrin dye series (**1**-**4**-InPor and their **1**-**4**-InPor-AgNP nanoconjugates), concentration studies were carried out at 25, 50, 100, 150, and 250 µg/mL of the dye against both single-species biofilms of *S. aureus* and *E. coli* strains and photoirradiations were performed with an M625L3 Thorlabs LED. For the A_3 P^V and Ga^{III} corrole dye series (**1**-**4**-GaCor, **1**-**4**-P^VCor and their **1**-**4**-GaCor-AgNP and **1**-**4**-P^VCor-AgNP nanoconjugates), gradient

concentrations of 15, 30, 60, 120, and 240 μg/mL of the dye drugs were used to treat the single species *S. aureus* and *E. coli* biofilm strains with the photoirradiations performed with an M625L3 Thorlabs LED. For the A_2B Ga^{III} corrole dye series (**9**-**10**-GaCor and **10**-GaCor-Q), the single species *S. aureus* and *E. coli* biofilms strains were treated with 15, 30, 60, 120, and 240 μM of the dye series and the photoirradiations were performed with an M595L3 Thorlabs LED. For free-base ligands of porphyrins (**5**-**8**-Por), chlorins (**5**-**8**-Chl), and N-confused porphyrin (**5**-NCP) and their Sn(IV) complexes (**5**-**8**-SnPor, **5**-**8**-SnChl, and **5**-Sn-NCP), the single species *S. aureus* and *E. coli* biofilms were treated with the drugs concentrations of 25, 50, 100 and 200 μM. The photoirradiations were performed with an M625L3 Thorlabs LED for the porphyrin series (**5**-**7** Por, **5**-**7** SnPor) with both M625L3 and M660L3 Thorlabs LEDs used for **5**-Por and **5**-SnPor, the chlorins (**5**-**8**-Chl, **5**-**8**-SnChl), and the N-confused porphyrin (**5**-NCP, **5**-SnNCP) series. The controls were the biofilm-coated wells with PBS media alone (untreated biofilms). After the dark and light treatments, the supernatant liquid was discarded, and the wells were gently rinsed with PBS. The biofilms cell densities were then quantified using crystal violet assay by measuring the absorbance of the assay at 590 nm on a Synergy 2 multi-mode microplate reader (BioTek®) and also by using the viable colony count method as previously described in Section 2.7.3.

For time-dependence studies, the single species *S. aureus* and *E. coli* biofilms bacteria were treated, respectively, with 50 and 100 μg/mL of the chloroindium (III) porphyrin series (**1**-**4**-InPor and their **1**-**4**-InPor-AgNP nanoconjugates). Photoirradiations were carried out with a Thorlabs M625L3 LED at 15 min time intervals for 75 min. For the A_3 P^V and Ga^{III} corroles dye series (**1**-**4**-GaCor, **1**-**4**-P^VCor, and their **1**-**4**-GaCor-AgNP and **1**-**4**-P^VCor-AgNP nanoconjugates), 30 and 60 μg/mL of the dyes were used to treat *S. aureus* and *E. coli* biofilms, respectively. Photoirradiations

were performed over 15, 30, 60, 90, and 120 min intervals using a Thorlabs M625L3 LED. 30 and 60 μM of the A_2B Ga^{III} corrole (**9**-**10**-GaCor and **10**-GaCor-Q) dye series were used against *S. aureus* and *E. coli* biofilm bacteria, respectively, followed by photoirradiations over 15, 30, 60, 90, 120 min time intervals. For free-base ligands of porphyrins, chlorins, and N-confused porphyrin (**5**-**8**-Por, **5**-**8**-Chl, and **5**-NCP) and their Sn(IV) complexes (**5**-**8**-SnPor, **5**-**8**-SnChl, and **5**-Sn-NCP), 25 and 50 μM of the dyes were administered against *S. aureus* and *E. coli* biofilms bacteria, respectively. The photoirradiations were performed over 15, 30, 45, 60, and 75 min intervals with a Thorlabs M625L3 LED. Thorlabs M625L3 and M660L3 LEDs were used for biofilms treated with **5**-Por, **5**-SnPor, **5**-**8**-Chl and **5**-**8**-SnChl, and **5**-NCP and **5**-SnNCP. The ability of the dyes to inhibit the single species *S. aureus* and *E. coli* biofilms were quantified using crystal violet assay and viable colonies count methods as previously described, and the data were compared with the controls. All the experiments were performed with three independent triplicates and compared with the control, and data were analyzed statistically with a student T-test and ANOVA.

2.7 PACT studies

The PACT activities of the photosensitizer dyes were carried out with the planktonic and biofilms cells of Gram-(+) *S. aureus* (ATCC® 25923™) and Gram-(−) *E. coli* bacteria (ATCC®, 25922™) strains. Photoinactivation experiments were performed as described in the literature with slight modifications [256,259,260]. The viable bacteria colonies were estimated using the direct viable colony count and an indirect method using a crystal violet staining assay. The planktonic bacteria cells were estimated using the direct method only by counting the viable colonies formed on the agar plates using a bacteria counter, as described previously in the literature [256,259,260], while for biofilms cells, both the viable colony count and the indirect methods were used

[210,214,261,262]. The crystal violet assay was used to quantify the biofilm biomass indirectly by measuring the absorbance intensity at 590 nm on a Synergy 2 multi-diode microplate reader (BioTek). The PS dye drug stock solutions were first prepared in DMSO since they were insoluble PBS alone with the appropriate drug aliquots volumes prepared to 1% (v/v) DMSO-PBS solution after serial dilution. Photoinactivation experiments were carried out in the dark, and after photoirradiation with an M595L3, M625L3, or M660L3 Thorlabs LED mounted onto a Modulight 7710-680 medical laser system housing. The Thorlabs LED chosen for photoirradiation depended primarily on the Q band maxima of dye drugs administered. For all *in vitro* dark cytotoxicity and photoinactivation activity studies of the dyes against both the planktonic and biofilm cells of *S. aureus* and *E. coli* bacteria strains, the effect of PS dye drug concentrations with a fixed fluence (light) dosage and the effect of fluence rate with a fixed drug dye concentration dosage were investigated.

2.7.1 Planktonic bacteria culturing

S. aureus and *E. coli* bacteria strains were grown anaerobically on the agar plates to obtain colonies of each by following the manufacturer's specifications. A single colony of each bacterial strain was inoculated into a 5 mL freshly prepared Lura nutrient broth. The culture mixture was vortexed and incubated at 37°C with agitation (*ca.* 200 rpm) in a shaker rotary incubator for 18 and 48−72 h for *S. aureus* and *E. coli*, respectively. Aliquots from the bacteria culture mixtures were taken regularly to measure their optical densities until the bacterial growth reached a mid-logarithmic phase (OD 620 nm, *ca.* 0.6−0.8). The bacteria pellets were then harvested through centrifugation for 15 min at 3000 rpm and washed three times with PBS to remove residual

nutrient broth. The bacteria pellets were resuspended in 4 mL PBS and further diluted to 1:1000 (v/v) in PBS to obtain the working bacteria culture stock solutions.

The viable colonies count of the freshly prepared *S. aureus* and *E. coli* bacteria cultures were determined by serial dilution of the bacteria culture stock solutions by factors of 10^{-4}, 10^{-5}, 10^{-6}, 10^{-7}, 10^{-8}, and 10^{-9}. A 100 µL aliquot of each sample solution was aseptically inoculated on the agar plates in triplicates and incubated for 24 h at 37°C to determine the optimum bacteria count. The viable bacteria colonies were counted on a Scan 500® series Automatic Colony Counter. Optimized bacteria solutions of colony-forming units (CFU/mL) ranging from 2.78−3.01 × 10^8 CFU/mL and 1.62−2.01 × 10^8 CFU/mL for *S. aureus* and *E. coli,* respectively, were used in the subsequent studies.

2.7.2 *In vitro* dark and light photoinactivation of planktonic bacteria

The experimental procedure followed for sample preparation for *in vitro* dark and light studies of the dyes for photoinactivation of planktonic *S. aureus* and *E. coli* bacteria strains was the same. For time-dependence studies, a 5 mL bacteria suspension (10^8 CFU/mL) of *S. aureus* or *E. coli* bacteria strains in 1% DMSO/PBS solution was incubated with appropriate concentrations of the porphyrinoid dye drugs at 37°C in a rotary shaking incubator at 200 rpm for 30 min in the dark. Half (2.5 mL) of the drug-incubated bacteria suspension was transferred into a 24-well plate for light studies, and the remaining half (2.5 mL) was kept in another 24-well plate in the dark for *in vitro* dark cytotoxicity studies.

For light studies, the drug-treated bacteria suspensions were irradiated with M595L3, M625L3 or M660L3 Thorlabs LEDs mounted onto a Modulight 7710-680 medical laser system housing. This

facilitates excitation at 595, 625, or 660 nm, respectively, over different time intervals. For bacteria suspensions treated with chloroindium (III) porphyrin series (**1**-**4**-InPor and their **1**-**4**-InPor-AgNP nanoconjugates), the studies were carried out at 2.5 and 10 μg/mL against *S. aureus* and *E. coli*, respectively. Photoirradiations were carried out with a Thorlabs M625L3 LED at 15 min time intervals for 75 min. For bacteria suspensions treated with A_3 P^V and Ga^{III} corrole dyes series (**1**-**4**-GaCor, **1**-**4**-P^VCor, and their **1**-**4**-GaCor-AgNP and **1**-**4**-P^VCor-AgNP nanoconjugates), the studies were carried out at 0.5 and 2.5 μg/mL against *S. aureus* and at 10 μg/mL against *E. coli* bacteria with the photoirradiations performed over different time intervals with a Thorlabs M625L3 LED. For *S. aureus* and *E. coli* bacteria, suspensions were treated with 0.5 μg/mL and 10 μg/mL of the A_3 P^V and Ga^{III} corroles dye series, respectively. The photoirradiation treatments were carried out over 15, 30, 60, 90, and 120 min time intervals and 5, 15, 30, 45, 60, and 75 min for *S. aureus* suspensions treated with 2.5 μg/mL of the dye series.

For the A_2B Ga^{III} corrole series (**9**-**10**-GaCor and **10**-GaCor-Q) studies against *S. aureus* bacteria, two concentrations of 0.5 and 2.5 μM were used, and 10 μM was used against *E. coli* bacteria. Photoirradiations were performed over different time intervals with a Thorlabs M595L3 LED. 15, 30, 60, 90, and 120 min intervals were studied against *S. aureus* and *E. coli* suspensions treated with 0.5 and 10 μM of dye series, respectively, while 5, 15, 30, 45, 60, and 75 min intervals were studied for *S. aureus* suspensions treated with 2.5 μM of the dyes.

For the porphyrins, chlorins, and N-confused porphyrin free-base ligands (**5**-**8**-Por, **5**-**8**-Chl, and **5**-NCP) and their Sn(IV) complexes (**5**-**8**-SnPor, **5**-**8**-SnChl, and **5**-Sn-NCP), 1 μM of the dye was administered against *S. aureus* and 5 μM against *E. coli* bacteria suspensions. For *S. aureus* and *E. coli* suspensions treated with Sn(IV) porphyrin dye series, the photoirradiation treatments

were carried out over 5, 10, 15, 30, 45, 60, and 75 min intervals using a Thorlabs M625L3 LED. For the bacteria suspensions treated with **5**-Por, **5**-SnPor, **5**-**8**-Chl, **5**-**8**-SnChl, **5**-NCP, and **5**-SnNCP, both Thorlabs M625L3 and M660L3 LEDs were used for photoirradiation at 5, 10, 15, 30, 45, 60, and 75 min intervals.

After light and dark treatments at the considered time intervals, a 100 µL aliquot of the samples was aseptically inoculated on the agar plate and incubated at 37°C for 18 h. Viable bacteria colonies were counted with a Scan 500® series Automatic Colony Counter to determine colony-forming unit (CFU/mL) values. The controls were *S. aureus* and *E. coli* bacteria suspensions (colony-forming units 10^8 CFU/mL) with no PS dye drug. The cell survival fractions were calculated by comparing the drug-treated bacteria with the control. The Log_{10} reductions were calculated using Equation 2.4:

$$\text{Log reduction} = \text{Log (A)} - \text{Log (B)} \quad (2.4)$$

Where A and B represent the number of viable colonies (CFU/mL) of bacteria for the untreated and treated samples, respectively. All the experiments were carried out in three independent triplicates, and data were analyzed statistically using student T-test and ANOVA.

Prior to time-dependence studies, the effect of gradient concentrations of the dyes was analyzed at fixed light (fluence) to establish the optimal concentrations. For bacteria suspensions treated with chloroindium (III) porphyrin series (**1**-**4**-InPor and their **1**-**4**-InPor-AgNP nanoconjugates), concentration studies were carried out at 1, 1.5, 2, 2.5, and 5 µg/mL against *S. aureus* and 2.5, 5, 10, 15, and 20 µg/mL against *E. coli* through irradiations with a Thorlabs M625L3 LED for 60 min.

For the bacteria suspensions treated with the A_3 P^V and Ga^{III} corrole dyes series (**1**-**4**-GaCor, **1**-**4**-P^VCor, and their **1**-**4**-GaCor-AgNPs and **1**-**4**-P^VCor-AgNP nanoconjugates) 0.5, 1, 2, 2.5, 5 µg/mL gradient concentrations were administered against *S. aureus*, and 2.5, 5, 10, 15, and 20 µg/mL against *E. coli* with photoirradiations performed with a Thorlabs M625L3 LED for 60 min. For the A_2B Ga^{III} corrole dye series (**9**-**10**-GaCor and **10**-GaCor-Q), the dyes were administered at 0.5, 1, 2, 2.5, and 5 µM concentrations against *S. aureus* and 2.5, 5, 10, 15, and 20 µM against *E. coli* with photoirradiation treatments performed with a Thorlabs M595L3 LED for 60 min. For bacteria suspensions treated with Sn(IV) porphyrins, chlorins and N-confused porphyrin dye complexes (**5**-**8**-SnPor, **5**-**8**-SnChl, and **5**-Sn-NCP) gradient concentrations of 0.5, 1, 1.5, 2, 2.5, and 5 µM were administered against *S. aureus*, and 1, 2.5, 5, 10, and 15 µM against *E. coli* with photoirradiation carried out for 45 min using a Thorlabs M625L3 LED.

2.7.3 Biofilm bacteria culturing

The freshly prepared planktonic *S. aureus* and *E. coli* bacteria cultures (prepared as described in Section 2.7.1) were diluted to 1×10^6 CFU/mL in Tryptic Soy Broth (TBS). The TBS-supplemented bacteria cultures (200 µL/ well) were seeded into the 96-well plates and incubated anaerobically under static conditions at 37°C with 5% CO_2 for 24 and 72 h for *S. aureus* and *E. coli*, respectively, to form *S. aureus* and *E. coli* single-species bacteria biofilms. The wells with media alone provided the negative controls. After incubation, the culture media was discarded, and the wells were gently rinsed two times with PBS to remove the residual TBS and the non-adherent planktonic bacteria cells. The plates were air-dried at room temperature for 30 min to fix the adherent cells.

The biofilm bacteria biomass was quantified using the crystal violet assay. 150 µL/well aliquot of 0.1% (w/v) crystal violet assay was used to stain the biofilm-coated wells for 15 min at room

temperature. The crystal violet assay was then discarded, and the wells were washed three times using 200 µL PBS/well to remove the residual dye. 150 µL/well of PBS was again added to the stained wells, and the absorbance of well solutions was measured at 590 on a Synergy 2 multi-mode microplate reader (BioTek®). All the experiments were carried out in triplicate, and the Z-score method was used to identify outlier values. Non-outlier values were used to calculate the average biofilm formed. The average negative control value was subtracted from the obtained biofilms absorbance data, and the data were provided as mean absorbance ± standard deviation. Biofilms were considered to have formed when the absorbance value at 590 nm was three times the standard deviation of the negative control mean absorbance [258]. All the experimental data were analyzed statistically using a student T-test and ANOVA.

Viable cell counts for the single species *S. aureus* and *E. coli* biofilms were also estimated with the viable colony count method. The biofilms formed in the 96-well plates were solubilized by adding 200 µL/well of PBS and sonicating the plates vigorously for 10 min, followed by scraping of the wells to dislodge the adherent cells. The resultant well suspension was vortexed to homogenize the solution and serial diluted 10-fold times, and a 100 µL aliquot of the diluted sample was then aseptically inoculated on the agar plate in triplicates followed by incubation at 37°C for 18 h. The viable colonies count (CFU/mL) was carried out on a Scan 500® series Automatic Colony Counter. All the experimental data were analyzed statistically with a student T-test and ANOVA.

2.7.4 *In vitro* dark and light photoinactivation of biofilm cells

Initially, the effect of the various dye concentrations on inhibiting the growth of the single-species biofilms of *S. aureus* and *E. coli* strains (grown as described in Section 2.7.2) experiments were

carried out. For these concentration studies, the single species biofilms of *S. aureus* and *E. coli* strains were incubated with 100 µL/well aliquots of the dye series at various concentrations for 30 min. For light studies, the drug-incubated 96-well plates biofilms were photoirradiated with a Thorlabs LED (595, 625, or 660 nm) for 30 min, while for the dark studies, the drug-treated plates were kept in the dark (in the absence of irradiation) for 30 min to determine the dark cytotoxicities of the drugs. For the chloroindium (III) porphyrin dye series (**1**-**4**-InPor and their **1**-**4**-InPor-AgNP nanoconjugates), concentration studies were carried out at 25, 50, 100, 150, and 250 µg/mL of the dye against both single-species biofilms of *S. aureus* and *E. coli* strains. Photoirradiations were carried out with an M625L3 Thorlabs LED. For the A_3 P^V and Ga^{III} corrole dye series (**1**-**4**-GaCor, **1**-**4**-P^VCor and their **1**-**4**-GaCor-AgNPs and **1**-**4**-P^VCor-AgNP nanoconjugates), gradient concentrations of 15, 30, 60, 120 and 240 µg/mL of the dye drugs were used to treat the single species *S. aureus* and *E. coli* biofilm strains with the photoirradiation performed with an M625L3 Thorlabs LED. For the A_2B Ga^{III} corrole dye series (**9**-**10**-GaCor and **10**-GaCor-Q), the single species *S. aureus* and *E. coli* biofilms strains were treated with 15, 30, 60, 120, and 240 µM of the dye series and the photoirradiations were performed with an M595L3 Thorlabs LED. For free-base ligands of porphyrins (**5**-**8**-Por), chlorins (**5**-**8**-Chl), and N-confused porphyrin (**5**-NCP) and their Sn(IV) complexes (**5**-**8**-SnPor, **5**-**8**-SnChl, and **5**-SnNCP, the single species *S. aureus* and *E. coli* biofilms were treated with the drugs concentrations of 25, 50, 100 and 200 µM). For this Sn(IV) dye series, the photoirradiations were performed with an M625L3 Thorlabs LED for the porphyrin series (**5**-**7** Por, **5**-**7** SnPor) with both M625L3 and M660L3 Thorlabs LEDs used for **5**-Por and **5**-SnPor, the chlorins (**5**-**8**-Chl, **5**-**8**-SnChl), and the N-confused porphyrin (**5**-NCP, **5**-SnNCP) series. The controls were the biofilm-coated wells with PBS media

alone (untreated biofilms). After the dark and light treatments, the supernatant liquid was discarded, and the wells were gently rinsed with PBS. The biofilm cell densities were then quantified using crystal violet assay by measuring the absorbance of the assay at 590 nm on a Synergy 2 multi-mode microplate reader (BioTek®) and also by using the viable colony count method as previously described in Section 2.7.3.

For time-dependence studies, the single species *S. aureus* and *E. coli* biofilms bacteria were treated with 50 and 100 μg/mL of the chloroindium (III) porphyrin series (**1**-**4**-InPor and their **1**-**4**-InPor-AgNP nanoconjugates), respectively. Irradiations were carried out with a Thorlabs M625L3 LED at 15 min time intervals for 75 min. In contrast, the A_3 P^V and Ga^{III} corrole series (**1**-**4**-GaCor, **1**-**4**-P^VCor, and their **1**-**4**-GaCor-AgNP and **1**-**4**-P^VCor-AgNP nanoconjugates), 30 and 60 μg/mL of the dyes were used to treat *S. aureus* and *E. coli* biofilms, respectively. Photoirradiations were carried out over 15, 30, 60, 90, and 120 min intervals with a Thorlabs M625L3 LED. 30 and 60 μM of the A_2B Ga^{III} corrole (**9**-**10**-GaCor and **10**-GaCor-Q) dye series were used against *S. aureus* and *E. coli* biofilms bacteria, respectively, followed by photoirradiation over 15, 30, 60, 90, and 120 min intervals.

For the free-base ligands of porphyrins, chlorins, and the N-confused porphyrin (**5**-**8**-Por, **5**-**8**-Chl, and **5**-NCP) and their Sn(IV) complexes (**5**-**8**-SnPor, **5**-**8**-SnChl, and **5**-SnNCP), 25 and 50 μM of the dyes were administered against *S. aureus* and *E. coli* biofilms, respectively. Photoirradiations were carried out over 15, 30, 45, 60, and 75 intervals with a Thorlabs M625L3 LED. Both Thorlabs M625L3 and Thorlabs M660L3 LEDs were used for biofilms treated with **5**-Por, **5**-SnPor, **5**-**8**-Chl, and **5**-**8**-SnChl, and **5**-NCP and **5**-SnNCP. The ability of the dyes to inhibit the single species *S. aureus* and *E. coli* biofilms were quantified using the crystal violet assay and viable colonies count

methods as previously described, and the data were compared with the controls. All the experiments were performed with three independent triplicates and compared with the control, and data were analyzed statistically with a student T-test and ANOVA.

2.8 Concluding remarks

The target *meso*-aryl porphyrin, corrole, chlorin, and N-confused porphyrin dyes were synthesized using different facile synthetic protocols. Since **1**-**4**-InPor, **1**-**4**-P^{V}Cor, and **1**-**4**-GaCor corrole dyes contain sulfur atoms on their *meso*-aryl groups, these dyes were conjugated to AuNPs and AgNPs *via* S−AuNPs and S−AgNPs affinities to form nanoassemblies. The experimental procedures used during characterization, optical spectroscopic studies, and photophysicochemical properties evaluation of dyes, nanoparticles, and nanoconjugates have been outlined. The protocols followed during the culturing of planktonic and biofilm cells of *S. aureus* and *E. coli* bacteria species and MCF-7 cancer cells, including cellular uptake, *in vitro* dark toxicity, and phototoxicities during the PACT and PDT activity studies, have also been described.

RESULTS AND DISCUSSION

The results discussed in this thesis have been published in peer-reviewed journals.

1. **Soy R**, Babu B, Mack J, Nyokong T. The Photodynamic Anticancer and Antibacterial Activity Properties of a Series of *meso*-Tetraarylchlorin Dyes and Their Sn (IV) Complexes. *Molecules*, 2023;28(10):4030. 10.3390/molecules28104030
2. **Soy R.C.**, Babu B., Mack J. Nyokong, T. The photodynamic activities of the gold nanoparticle conjugates of phosphorus (V) and gallium (III) A3 *meso*-triarylcorroles. *Dyes and Pigments*, 2021;194:109631. 10.1016/j.dyepig.2021.109631
3. **Soy R.C**, Babu B., Oluwole D. O., Nwaji N., Oyim J., Amuhaya E, Prinsloo E., Mack J., Nyokong. Photophysicochemical properties and PDT activity of chloroindium (III) tetraarylporphyrins and their gold nanoparticle conjugates. *J Porphyrins Phthalocyanines*, 2019; 23:34-45. 10.1142/9789811223556_0014
4. Niu Y., Guo Y., Zhu W., **Soy R.C**, Babu B. Mack J.* Tebello Nyokong, Haijun Xu* and Xu Liang*. Ga^{III}triarylcorroles with Push-Pull Substitutions: Synthesis, Electronic Structure and Biomedical Applications. *Dalton Trans.*, 2022,51, 10543-10551. 10.1039/D2DT01262F.

The following additional publications are from the collaborative research studies conducted during the doctoral studies.

1. Nnaji N, **Soy R**, Ikala YO, Nyokong T. Phthalocyanines as corrosion inhibitors. In Smart Anticorrosive Materials 2023p, p. 365-400. Elsevier.

2. Liang X., Pan Z.Y., Guo W., Mack J., **Soy R.**, Nyokong T., Zhang Q.C., Zhu W. Regulating the Single-Molecule Conductance of Corroles by the Substituents on the B-Site. *J Phys Chem C* 2022, 126, 50, 21476–21481. 10.1021/acs.jpcc.2c07140
3. Sen P., **Soy R.,** Mgidlana S., Mack J., Nyokong, T. Light-driven antimicrobial therapy of palladium porphyrins and their chitosan immobilization derivatives and their photophysical-chemical properties. *Dyes and Pigments*, 2022;203:110313. 10.1016/j.dyepig.2022.110313
4. Liang X., Pan Z.Y., Guo W., Mack J., **Soy R**., Nyokong T., Zhang Q.C., Zhu W. Regulating the Single-Molecule Conductance of Corroles by the Substituents on the B-Site. *J. Phys. Chem. C*, 2022; 126, 50, 21476-21481. 10.1021/acs.jpcc.2c07140
5. Dube E., **Soy R.C.**, Shumba M., Nyokong T. Photophysicochemical behaviour of phenoxy propanoic acid functionalised zinc phthalocyanines when grafted onto iron oxide and silica nanoparticles: Effects in photodynamic antimicrobial chemotherapy. *Journal of Luminescence.* 2020; 234:117939. 10.1016/j.jlumin.2021.117939
6. Babu B., **Soy R.C.**, Mack J., Nyokong T. Non-aggregated lipophilic water-soluble tin porphyrins as photosensitizers for photodynamic therapy and photodynamic antimicrobial chemotherapy. *New J Chem*. 2020;44(26):11006-12. 10.1039/D0NJ01564D
7. Shabangu S.M., Babu B., **Soy R.C.**, Oyim J., Amuhaya E., Nyokong T. Susceptibility of Staphylococcus aureus to porphyrin-silver nanoparticle mediated photodynamic antimicrobial chemotherapy. *Journal of Luminescence*, 2020;222:117158. 10.1016/j.jlumin.2020.117158

8. Shabangu S.M., Babu B., **Soy R.C.**, Managa M., Sekhosana E. K., Nyokong T. Photodynamic antimicrobial chemotherapy of asymmetric porphyrin-silver conjugates toward photoinactivation of Staphylococcus aureus. *J Coord. Chem.*, 2020;73(4):593-608. 10.1080/00958972.2020.1739273
9. Tang W., Qiu Y., Li X., **Soy R.C.**, Mack J., Nyokong T., Liang X. pH-Dependent Electrochemically Catalyzed Oxygen Reduction Behaviors of o-Substituted Co (III) Corroles. *Macroheterocycles*. 2020;13(2):156-62. 10.6060/mhc200183l
10. Zhang X., Wang Y., Wen J., Zhu W., Mack J., **Soy R.C.**, Nyokong T., Liang X. *Meso*- and axially-modified IrIIItriarylcorroles with tunable electrocatalytic properties. *Dyes Pigments*. 2020;175:108124. 10.1016/j.dyepig.2019.108124
11. Qin M., Zhang Z., Zhu W., Mack J., **Soy R.C.**, Nyokong T., Liang X. Modulation of the optical properties of chiral porphyrin dimers by introducing bridged chiral amide-bonds. *J. Porphyrins Phthalocyanines*. 2021;25(01):37-46. 10.1142/S1088424620500492
12. Lian X., Qin X., Li M., Zhang X., Mack J., **Soy R.C.**, Nyokong T. and Zhu W. Modulation of the Supramolecular Chirality Properties of Bio-inspired Chiral Porphyrin Dimers. *Dyes Pigments*, 2019;171:107637. 10.1016/j.dyepig.2019.107637
13. Gu T., Tao J., Zhu W., Mack J., **Soy R.C.**, Nyokong T., Xu H., Li M. and Liang X.. Co(II)Tetraphenyltetraphenanthroporphyrin@MWCNTs: Enhanced ππ Interaction for Robust Electrochemical Catalysis. *New J. Chem.*, 2019;43(26):10631-6. 10.1039/C9NJ01707K

14. Yuan X., Li M., Meng T., Mack J., **Soy R.C.**, Nyokong T., Zhu W., Xu H. and Liang X. Fused-Ring-Expanded Rubyrins: Effect of Core-Modification with Group 16 Heteroatoms and Fused-ring Expansion. *Dyes Pigments*, 2018;158:188-94. 10.1016/j.dyepig.2018.05.045

CHAPTER THREE

Synthesis and Characterization of Porphyrinoid Dyes

This chapter details the synthesis and characterization of the porphyrinoid dyes.

3.0 Synthesis and characterization of the dyes and nanoconjugate derivatives

This chapter details the synthesis and characterization of porphyrin and porphyrin analog dyes. The synthesized dyes have been structurally characterized using nuclear magnetic resonance (NMR) spectroscopy and MALDI-TOF MS. This chapter also describes the synthesis of gold and silver nanoparticles and their dye nanoconjugates, and their characterization by powder X-ray diffraction, transmission electron microscopy, and energy dispersive electron microscopy.

Different facile synthesis approaches have been used in this work to obtain the target free-base porphyrin and porphyrin analog dyes. These methods primarily involve acid-catalyzed condensation reactions of pyrrole with the appropriate aldehydes under specified conditions to obtain the target dyes. Some of the synthesized free-base porphyrins (**5**-**8**-Por) were also structurally modified on one of their pyrrole rings using the reductive amination method to obtain the target free-base chlorin dyes (**5**-**8**-Chl). The synthesized free-base dyes were further functionalized at the cores with indium(III), Sn(IV), or gallium(III)) metal chloride salts or phosphoryl oxychloride ($POCl_3$) to obtain the target coordinated dye complexes. Inserting coordination atoms into porphyrin and porphyrin analog core cavities enhances the photophysicochemical properties (see Chapters 4 and 5). The synthetic schemes for all the synthesized dyes series and their complexes have been presented in Chapter 2 (**Schemes 2.1-2.6**).

The optical spectra obtained during structural characterization of the synthesized dyes series and those of the nanoparticles and nanoconjugates are not included in this chapter, but a few selected sets of spectra are provided as representative examples. In addition, some of the spectral data (^{1}H NMR and MS) for the dyes are provided in the Appendix. The facile synthetic

approaches used in this work yielded the target porphyrins and porphyrin analog dyes in good yields. These methods readily allowed facile scaling up of the target dyes. In addition, the design of dyes, particularly the choice of *meso*-aryl groups and central coordination ions and the structural modification of the porphyrin ligand to form porphyrin analogs, was motivated by the need to obtain dyes with favorable photophysicochemical properties (see Chapter 4) suitable for use in PDT and PACT applications (see Chapters 5-9).

3.1 Synthesis and characterization of porphyrins and their Indium (III) and Sn(IV) complexes

The free-base porphyrin ligands (**1**-**8**-Por and H_2TPP control) have been reported previously [102,230–237] and were synthesized in this work following the well-established Adler-Longo method[101]. This method involves an acid-catalyzed condensation reaction of the pyrrole with an appropriate aldehyde under reflux conditions (**Scheme 2.1a**). The aromatic aldehydes used during the synthesis of the porphyrins consisted of 4-methylthiophenyl (**1**), 3-thiophene (**2**), 2-thiophene (**3**), 5-bromo-2-thiophene (**4**), 4-methoxyphenyl (**5**), 3-methoxyphenyl (**6**), 4-hydroxyphenyl (**7**), and 3-hydroxy-4-methoxyphenyl (**8**) commonly known as vanillin and phenyl group for the control compounds. The synthesized **1**-**8**-Por dyes contain sulfur or oxygen heteroatoms that result in favorable physicochemical properties, such as red shifts of the major absorption bands to longer wavelengths. After silica-gel chromatographic purification, the target free-base porphyrin dye products were obtained at moderately high yields (≥ 30%).

In(III) or Sn(IV) metal ions were inserted into the cores of the synthesized free-base porphyrin dyes (**1**-**8**-Por and H_2TPP control) as shown in **Scheme 2.1b** for **1**-**4**-Por and H_2TPP control and **Scheme 2.1c** for **5**-**8**-Por. The synthesis and structural characterization of **1**-InPor and **3**-InPor was

reported previously [209]. **Figure 3.1** give the molecular structures for **4**-Por, **4**-InPor, **8**-Por, and **8**-SnPor as representative examples of the synthesized porphyrins in this work.

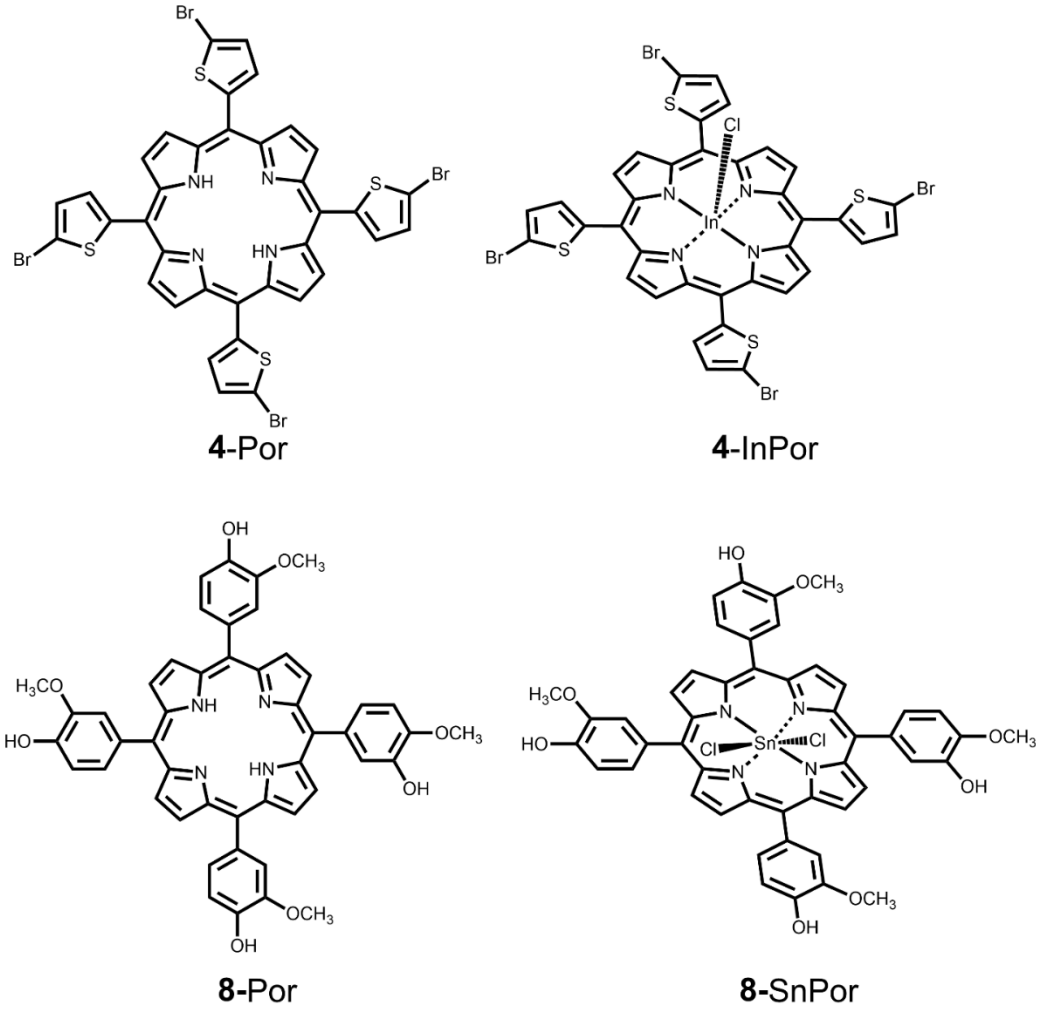

Figure 3.1: Molecular structures of porphyrin dyes.

The synthesized porphyrin dyes were successfully structurally characterized using ^{1}H NMR spectroscopy and MALD-TOF MS spectrometry. The ^{1}H NMR spectra for **1**-**8**-Por, H_2TPP, InTPP, **2** and **4**-InPor, and **5**-**7**-SnPor are also provided in **Figure 3.2** and **Figures A1**-**A7** in the Appendix. **Figures 3.2** provides the ^{1}H NMR spectra for the **4**-Por, **4**-InPor, **8**-Por, and **8**-SnPor complexes as representative examples of the synthesized dyes. It shows the spectroscopic changes related to

the chemical transformations, which occur upon insertion of In(III) or Sn(IV) ions into the free-base porphyrin dyes (**4**-Por, **8**-Por) cavities to afford the target In(III) and Sn(IV) porphyrin complexes (**4**-InPor, **8**-SnPor).

The anticipated protons signals for the synthesized porphyrins can be readily assigned. The chemical shifts between 7.00−9.30 ppm can be assigned to the aromatic protons from the β-pyrrole positions and the *meso*-aryl substituents. In general, the β-pyrrolic protons appear mainly as singlets at slightly higher frequencies than the *meso*-aryl protons. The hydroxy (OH) protons from the *meso*-aryl substituent groups also appear at higher frequencies between 9.50−10.00 ppm as singlet signals (**Figures 3.2b** and **A 6-7**) for the **7**-**8**-porphyrin dyes. The methyl (CH_3) protons from the *meso*-aryl substituent groups lie between 4.14−2.76 ppm at the aliphatic region as singlet signals for **1**-Por, **5**-**6**-Por, **8**-Por dyes and their corresponding In(III) or Sn(IV) complexes (**Figures 3.2b**, **A 1a**, **A 4-5** and **A 7**). The NH protons for the free-base porphyrin dyes (**1**-**8**-Por and H_2TPP) lie between −2.89 to −2.71 ppm in the negative low frequency region as singlet signals. These protons disappeared upon insertion of In(III) or Sn(IV) ions into the free-base porphyrins cores (**1**-**8**-Por) to obtain the corresponding In(III) or Sn(IV) porphyrin complexes (**Figures 3.2** and **A 2**-**7**). This confirms the successful synthesis of the In(III) and Sn(IV) metalloporphyrin complexes.

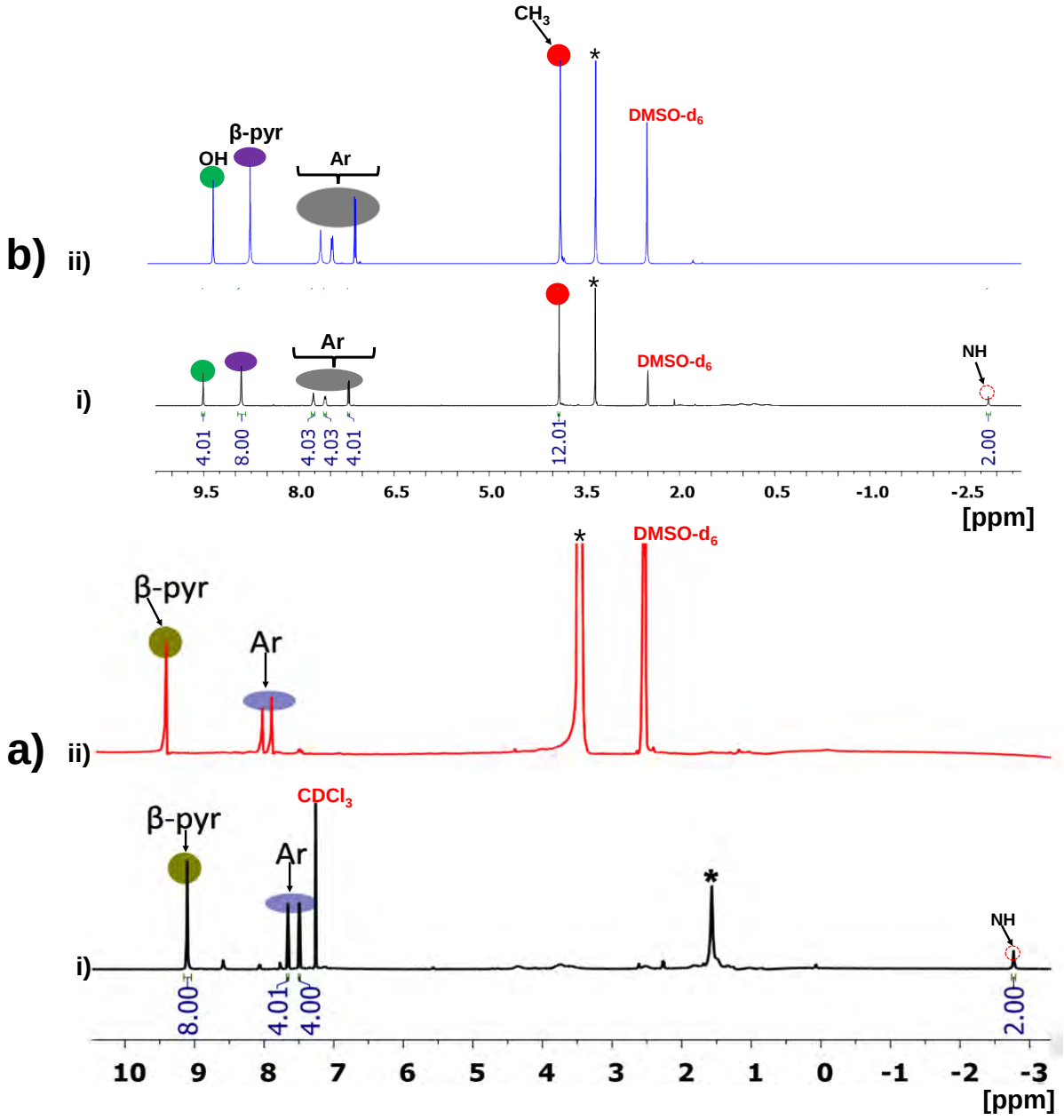

Figure 3.2: ^{1}H NMR spectra for a) i) **4**-Por, ii) **4**-InPor, and b) i) **8**-Por and ii) **8**-SnPor and black* asterisks highlight the residual water peak.

MALDI-TOF mass spectroscopic analysis also identified the anticipated parent ion peaks for the synthesized porphyrin dyes. The MS data are in close agreement with the theoretical masses and are consistent with the target structures. The MALDI-TOF data for **1**-**8**-Por and H_2TPP porphyrin

dyes and their In(III) and Sn(IV) porphyrin complexes are provided in **Figures A8-16** in the Appendix. The MS data for **1**-**8**-Por and H_2TPP free-base porphyrin dyes show mainly $[M+H]^+$ or $[M]^+$ molecular ion species, while for In(III) and Sn(IV) porphyrin complexes, the spectra exhibit $[M-Cl + H]^+$ or $[M-Cl]^+$ ion peaks. However, for Indium (III) porphyrin complexes, $[M+H]^+$ or $[M]^+$ ions (**Figures A 8b-A 12b**) are observed as intense peaks due to the loss of chloride ions suggesting that the chloride axial ligands are labile. For Sn(IV) porphyrin complexes, a similar trend is also observed with the intense molecular ion peaks exhibiting $[M-Cl+H]^+$ or $[M-Cl]^+$ species, which correspond to the loss of one chloride ion.

3.2 Synthesis and characterization of corrole dyes and their P(V) and Ga(III) complexes.

The A_3 and A_2B *meso*-triarylcorroles were prepared by following literature methods [141]. Since the synthesis and characterization of **1**-**3** *meso*-triaryl A_3 P(V) and Ga(III) corrole complexes [174] and also for **5**-**6** A_2B *meso*-triarylcorrole complexes have already been published [210], only a summary in this context is presented.

3.2.1 Synthesis and characterization of A_3 *meso*-triarylcorrole dyes and their P(V) and Ga(III) complexes.

Meso-triaryl A_3 free-base corroles were synthesized following the optimized Gryko method [141], as shown in **Scheme 2.2a**. P(V) and Ga(III) corrole complexes were prepared by reacting the appropriate free-base corrole ligands (**1**-**4**-Cor and H_3TPCor) with P(V) or Ga(III) salts to afford the target **1**-**4**-P^VCor, **1**-**4**-GaCor, P^VTPCor and Ga^{III}TPCor corrole complexes (**Scheme 2.2b**-**c**). The molecular structures for **4**-Cor, **4**-P^VCor, and **4**-GaCor are provided in **Figure 3.3** as representatives for the synthesized A_3 *meso*-triaryl corroles.

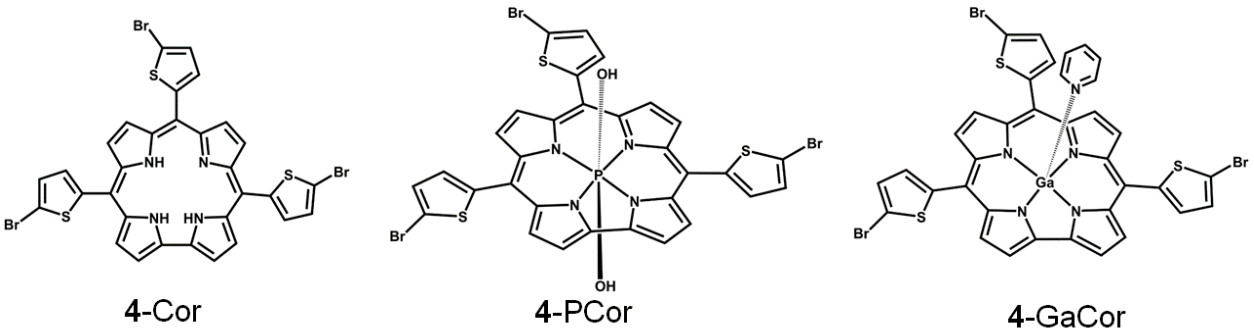

Figure 3.3: Molecular structures of A_3 *meso*-triarylcorrole dyes.

^{1}H NMR spectra and MALDI-TOF MS data confirmed the structures and purity of the synthesized A_3 *meso*-triarylcorrole dyes (**Figures 3.4** and **A 17-21**). The ^{1}H NMR spectra for **4**-Cor, **4**-P^{V}Cor, and **4**-GaCor are provided in **Figures 3.4** and **A 17** as examples of the synthesized A_3 *meso*-triarylcorrole dyes. The anticipated protons can be readily assigned for the corrole dyes. The ^{1}H NMR spectra for **4**-Corrole dyes show chemical shifts between 7.00−8.28 ppm for the 14 aromatic protons. The peaks for the eight β-pyrrolic protons lie at slightly higher frequencies than the six protons from the *meso*-triaryl groups (**Figures 3.4** and **A 17**).

The MALDI-TOF MS data also revealed the anticipated parent ion peaks and confirmed the structures of the target corrole dyes. The MS spectra for **4**-Cor, **4**-P^{V}Cor and **4**-GaCor exhibit $[M+H]^+$, $[M-2OH+H]^+$, and $[M-Py]^+$ parent molecular ion peaks species, respectively (**Figures A 20**-**21**). The MS values are in close agreement with the theoretical masses of the dyes. However, **4**-P^{V}Cor and **4**-GaCor corrole complexes exhibit $[M-OH+H]^+$ and $[M]^+$ species as the intense molecular ion peaks due to the loss of the hydroxyl and pyridyl axial ligands, respectively (**Figure A 18**). This suggests that the hydroxyl and pyridyl axial ligands are labile for the dihydroxy P(V) and pyridyl Ga(III) corrole complexes, a trend consistently similar to the previously reported MS data for **1**-**3**-P^{V}Cor and **1**-**3**-GaCor corrole dyes [174].

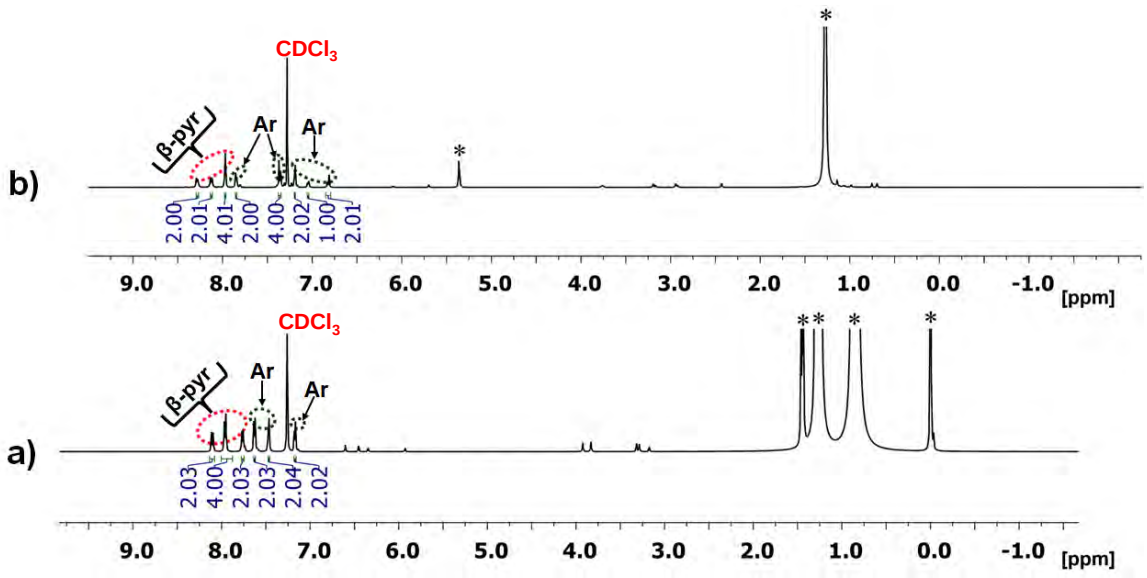

Figure 3.4: ^{1}H NMR spectra for a) **4**-P^{V}Cor and b) **4**-GaCor. Black asterisks highlight the residual water peak and solvent impurities.

3.2.2 Synthesis and characterization of A_2B *meso*-triarylcorrole dyes and their Ga(III) complexes.

Meso triaryl A_2B free-base corroles (**9**-**10**-Cor) were synthesized following literature methods [141,243]. **9**-**10**-GaCor Ga(III) corrole complexes were prepared by inserting the Ga(III) ion into the central cavity of the **9**-**10**-Cor free-base corrole dyes (**Scheme 2.3c**). The synthesized **9**-**10**-GaCor Ga(III) corrole complexes were alkylated on their carbazole moiety with ethyl iodide to afford the **10**-GaCor-Q quaternized derivative, but an attempt to quaternize **9**-GaCor was unsuccessful. **Figure 3.5** provides the molecular structures for **9**-GaCor, **10**-GaCor, and **10**-GaCor-Q *meso* triaryl A_2B Ga(III) corroles.

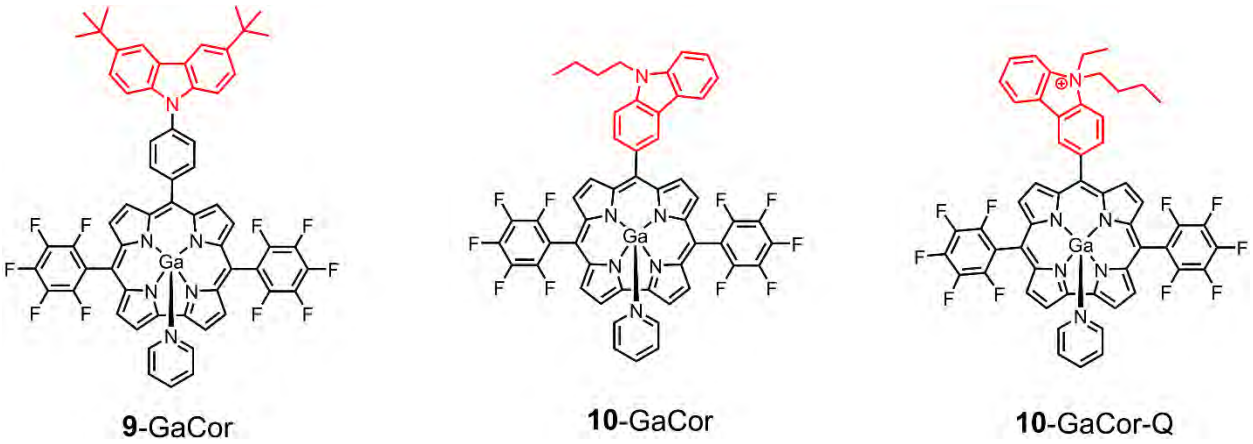

Figure 3.5: Molecular structures of A_2B *meso*-triarylcorrole dyes.

^{1}H NMR and MALDI-TOF MS spectroscopic data confirmed the structures and purity of the synthesized **5**-**6** A_2B *meso*-triarylcorroles. The anticipated protons can be readily assigned. The ^{1}H NMR spectra for **9**-GaCor, **10**-GaCor, and its quaternized **10**-GaCor-Q species are shown in **Figures A21**-**22** as representatives for the synthesized A_2B *meso*-triarylcorrole dyes. The chemical shifts that lie at 8.83−9.27 ppm for **9**-GaCor can be assigned to the eight-β-pyrrolic protons. The *meso*-aryl protons derived from the benzo and carbazole moieties lie between 8.27−8.37 ppm and 7.63−7.96 ppm, respectively, while the proton peaks at 3.73 and 6.69 ppm can be assigned to the pyridyl axial ligand and the peak at 1.50 ppm can be assigned to the tert-butyl groups attached to the carbazole moiety [210].

In a similar manner, the protons for **10**-GaCor and **10**-GaCor-Q can be readily assigned. The chemical shifts at 8.81−9.34 ppm can be assigned to the eight-β-pyrrolic protons and carbazole *meso*-aryl protons resonating at 7.55−8.79 ppm. The pyridyl axial ligands protons lie between 6.29−7.24 ppm, and butyl protons for **10**-GaCor and both butyl and ethyl protons for **10**-GaCor-Q lie between 1.07−4.68 ppm. The MS data also confirmed the structures of the target A_2B *meso*-triarylcorrole dyes. The MS data show strong $[M-Py]^+$, $[M-Py]^+$, and $[M]^+$ parent molecular ion

peaks species for **9**-GaCor, **10**-GaCor, and **10**-GaCor-Q, respectively (**Figures A 23**-**24**) [210]. The MS data closely agree with the theoretical masses of the dyes.

3.3 Synthesis and characterization of chlorin dyes and their Sn(IV) complexes.

The target **5**-**8**-Chl free-base chlorins were synthesized from **5**-**8**-Por free-base porphyrins starting materials by reducing one of their β-pyrroles using the Whitlock diimide reduction method [153] (**Scheme 2.4a**). **5**-**8**-Chl free-base chlorin dyes were metalated using $SnCl_2 \cdot 2H_2O$ salt to afford the target **5**-**8**-SnChl complexes at relatively high yields (**Scheme 2.4b**). **Figure 3.5** provides the molecular structures of **5**-Chl and **8**-Chl and their Sn(IV) chlorin complexes as representatives for the synthesized chlorin dyes.

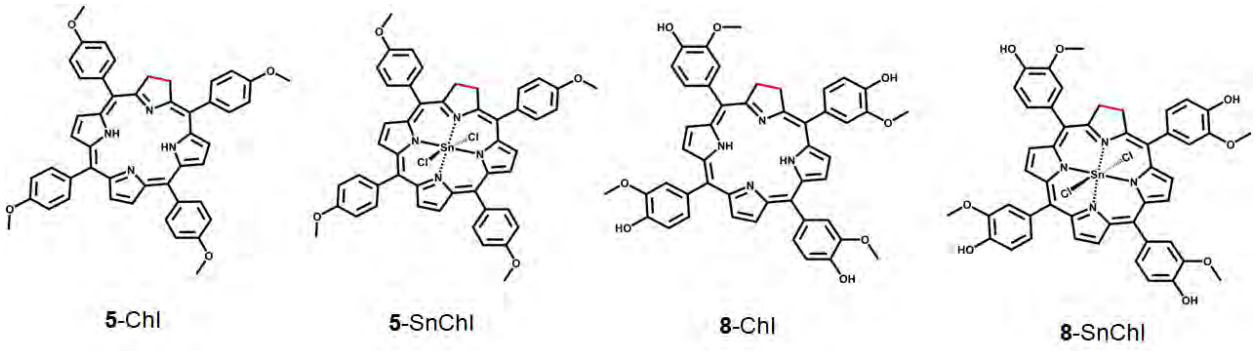

Figure 3.6: Molecular structures of chlorin dyes.

The ^{1}H NMR and MALDI-TOF MS data confirmed the structures of the target chlorin dyes (**Figures 3.6** and **A 22**-**28**). The anticipated protons signals for the synthesized chlorin dyes can be readily assigned in a similar manner to their porphyrin parent structures (**5**-**8**-Por**)**. **Figure 3.6** give the ^{1}H NMR spectra for the porphyrin starting material (**5**-Por), free-base chlorin (**5**-Chl), and its Sn(IV) chlorin complex (**5**-SnChl) as a representative set. It shows the chemical shift changes associated with the reduction of one of the peripheral pyrrole bonds of porphyrin dye (**5**-Por) during the

synthesis of corresponding chlorin (**5**-Chl). It also gives the spectral changes related to the insertion of the Sn(IV) ion into the free-base chlorin core to form the **5**-SnChl complex. The ^{1}H NMR spectra for the **6**-**8**-Chl and their corresponding **6**-**8**-SnChl complexes are provided in **Figures A22**-**24** in the Appendix.

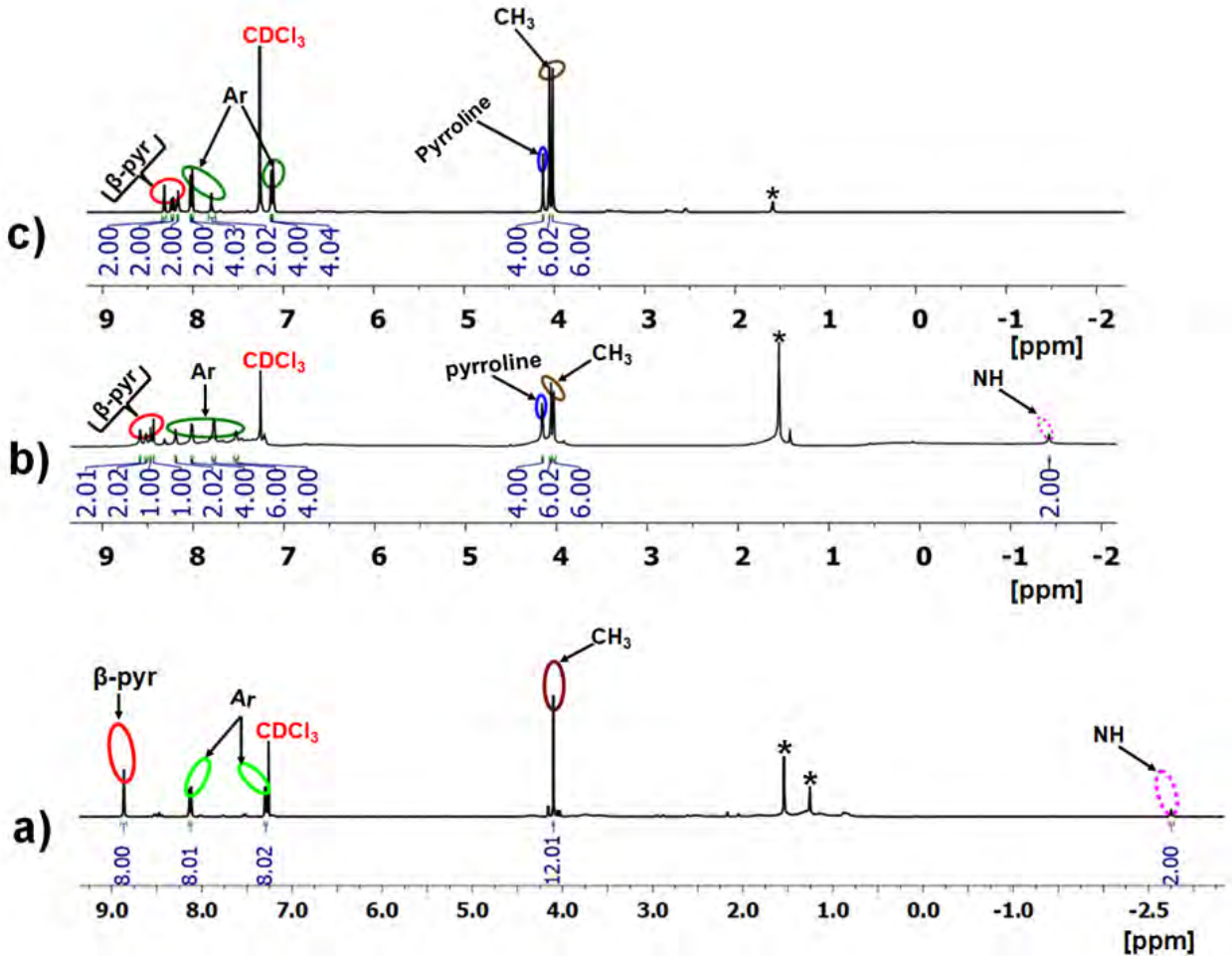

Figure 3.7: ^{1}H NMR spectra for a) **5**-Por and b) **5**-Chl and c) **5**-SnChl and black* asterisk highlight the residual water peak and solvent impurities.

The chemical shifts at 8.00−8.71 ppm can be readily assigned to the 6 protons from the β-pyrrole positions, while the aromatic protons from the *meso*-aryl groups lie at 7.00−8.00 ppm at slightly lower frequencies than the β-pyrrole protons (**Figure 3.6**). The hydroxy (OH) protons from the

meso-aryl substituent groups lie at higher frequencies, 8.84−10.00 ppm for **7**-**8**-Chl and the **7**-**8**-SnChl complexes (**Figures A 23**-**24**). The methyl (CH_3) protons from the *meso*-aryl substituent groups lie between 3.83−4.07 ppm at the aliphatic region for **5**-**6**-Chl and **8**-Chl and their corresponding Sn(IV) chlorin complexes (**Figures 3.6**, **A 22** and **A 24**). The characteristic four pyrroline protons for chlorin dyes lie between 4.12−4.37 ppm as singlet signals (**Figures 3.6b**-**c** and **A 22**-**24**). These proton peaks confirm the synthesis of chlorin dyes from their parent porphyrin structures [159,263]. Singlet peaks for the two NH core protons for **5**-**8**-Chl lie between −1.42 to −1.57 ppm at the negative low-frequency region. However, upon insertion of Sn(IV) ions into the free-base chlorin dyes (**5**-**8**-Chl) cavities, the two NH protons disappeared for **5**-**8**-SnChl Sn(IV) complexes (**Figures 3.6** and **A 22**-**24**). This confirms the successful synthesis of **5**-**8**-SnChl complexes.

MALDI-TOF mass data confirmed the structures for the target chlorin dyes. The anticipated parent ion peaks are observed, which agree closely with the theoretical masses of chlorin dyes. The MALDI-TOF data for **5**-**8**-Chl and their **5**-**8**-SnChl complexes are provided in **Figures A25**-**28**. The MS data for **5**-**8**-Chl free-base chlorin dyes exhibit mainly $[M+H]^+$ or $[M]^+$ molecular ion species, while the **5**-**8**-SnChl complexes exhibited $[M-Cl+H]^+$ or $[M-Cl]^+$ parent peak species due to the loss of a chloride ion in a similar manner to the **5**-**8**-SnPor Sn(IV) complexes.

3.4 Synthesis and characterization of N-confused porphyrin and its Sn(IV) complex.

Free-base N-confused porphyrin **5**-NCP was synthesized in this study by following the Lindsey method [169] (**Scheme 2.5a**). The corresponding **5**-SnNCP complex was also prepared by inserting Sn(IV) ion into the **5**-NCP core using $SnCl_2 \cdot 2H_2O$ salt (**Scheme 2.5b**). **Figure 3.7** give the molecular structures of the synthesized **5**-NCP, **5**-SnNCP complex, and its **5**-SnPor isomer.

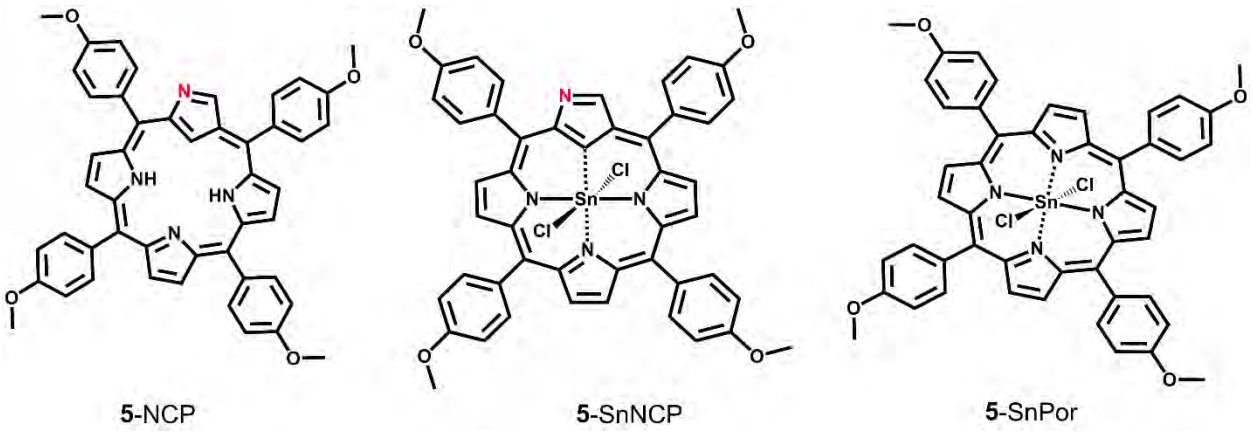

Figure 3.8: Molecular structures of N-confused porphyrins and a porphyrin isomer.

The structures of the synthesized **5**-NCP and **5**-SnNCPs were confirmed using ^{1}H NMR spectra and MS spectroscopic data. The anticipated protons can be assigned in the ^{1}H NMR spectra. **Figure 3.8** give the ^{1}H NMR spectra for **5**-NCP and **5**-SnNCP. The chemical shift at 10.77 ppm downfield is the characteristic N-confused porphyrin outer NH proton (**Figure 3.8b**). This proton appears downfield since it is deshielded due to the ring current generated by the π-macrocycle. However, this peak was not observed for the free-base **5**-NCP (**Figure 3.8a**). This is due to the lower prominence of the N-confused porphyrin tautomer with an NH proton in the chloroform solvent used during the ^{1}H NMR analysis, since it mainly exists in highly polar solvents such as DMSO or DMF [168]. The seven β-pyrrole protons also appear at higher frequencies between 8.14−8.80 ppm. The *meso*-aryl substituent protons appear in a similar manner to those of **5**-porphyrins previously characterized. The chemical shifts between 7.00−8.32 ppm and 3.80−4.10 ppm can be assigned to the *meso*-aryl aromatic and methyl protons, respectively.

The MALDI-TOF MS data also showed the anticipated parent ion peaks and confirmed the structures of the target N-confused porphyrin dyes (**Figure A 29**). The MS data trends are similar to those of previously characterized **5**-porphyrin isomers with **5**-NCP free-base N-confused

porphyrin dye exhibiting $[M+H]^+$ molecular ion species and $[M-Cl]^+$ species for **5**-SnNCP Sn(IV) N-confused complex dyes.

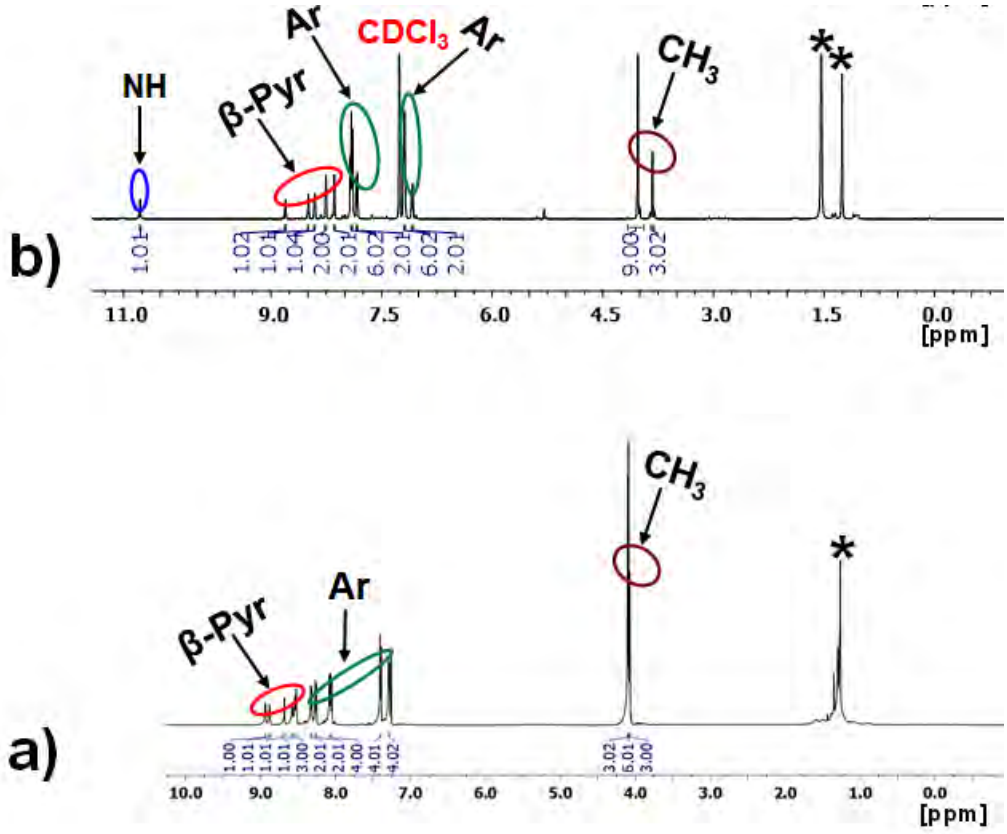

Figure 3.9: ^{1}H NMR Spectra for a) **5**-NCP and b) **5**-SnNCP and black* asterisk highlight the residual water peak and solvent impurities.

3.5 Synthesis and characterization of gold and silver nanoparticles and their dye nanoconjugates.

Gold and silver nanoparticles were synthesized following literature methods [246,248]. In this study, porphyrin and corrole dye complexes (**1**-**4**-InPor, **1**-**4**-P^{V}Cor, and **1**-**4**-GaCor), which consist of sulfur atoms on their *meso*-aryl substituents, were conjugated to AuNPs and AgNPs through the ligand exchange method. This was followed by self-assembly through sulfur-gold and sulfur-

silver affinities [246,264] to afford the dye-AuNP or dye-AgNP nanoassemblies (**Scheme 2.6**). The shape and sizes of AuNPs or AgNPs, including their conjugation with the dyes, were confirmed by TEM, XRD, EDX, and XPS spectroscopy. The loading ratios of porphyrin or corrole dyes to AgNPs or AuNPs were estimated using UV-visible absorption spectroscopy. Since the diameter of a porphyrin or corrole molecule is less than 1 nm and those of AuNPs and AgNPs are > 9 nm, more than one porphyrin or corrole complex is anticipated to be attached to the surfaces of AgNPs or AuNPs. The loading ratios of dye to MNPs are likely to significantly influence the photophysicochemical properties of the dye-nanoconjugates [265]. Since we previously reported the characterization of **1**-InPor-AuNPs, **1**-**3**-P^{V}Cor-AuNPs, and **1**-**3**-GaCor-AuNPs gold [174,209], in this section, a few selected dye-AuNP or dye-AgNP nanoconjugates are discussed as representative examples.

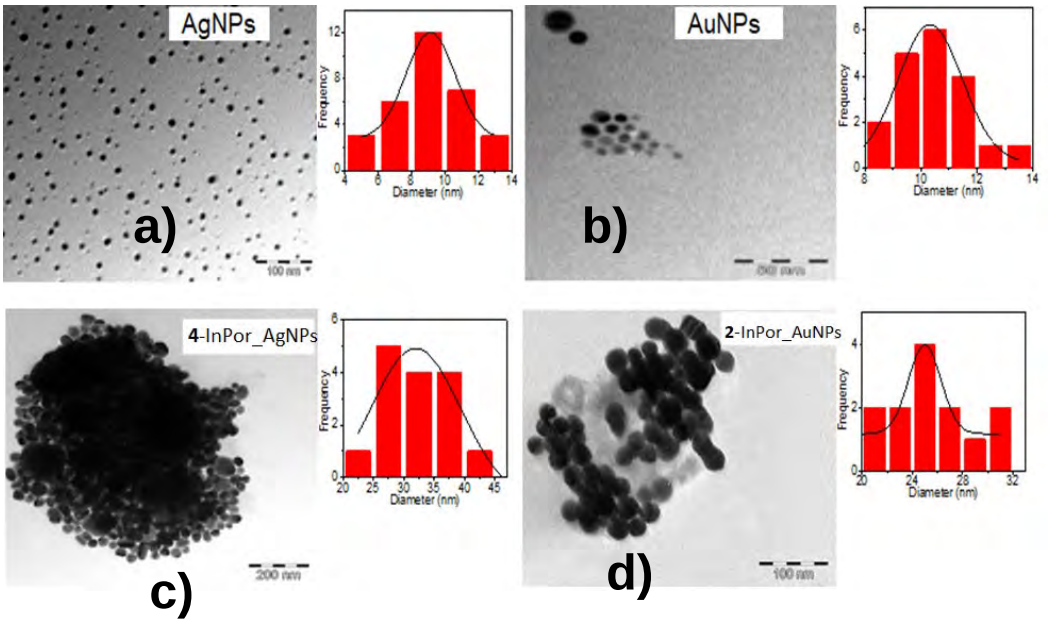

Figure 3.10: Representative TEM micrographs for a) AuNPs, b) AgNPs, c) **4**-InPor-AgNPs, and d) **2**-InPor-AuNPs with size distribution histograms as insets.

TEM analysis data show that the synthesized nanoparticles are monodispersed and spherical in shape, with average diameter sizes of 9.1 and 10.5 nm for AgNPs and AuNPs, respectively. However, upon conjugating the dyes to AuNP or AgNP nanoparticles, the average diameter sizes of nanoparticles increased. For example, to 23.1 and 25.3 nm for **4**-InPor-AgNPs and **4**-InPor-AuNPs, respectively (**Figure 3.10**) with the formation of clusters or aggregates due to π-π stacking effects resulting from the interaction of dyes molecules on the adjacent nanoparticles [246]. The EDX spectra of AuNPs, **2**-InPor-AuNPs, **4**-P^{V}Cor-AuNPs, AgNPs, **4**-InPor-AgNPs, and **4**-P^{V}Cor-AgNPs are provided as representative examples in **Figure A 32**. The EDX analysis data confirmed the elemental composition of the AuNP and AgNP nanoparticles. The anticipated peaks based on the elemental compositions of the dye complexes, along with additional Au or Ag atom peaks, are observed for the nanoconjugates.

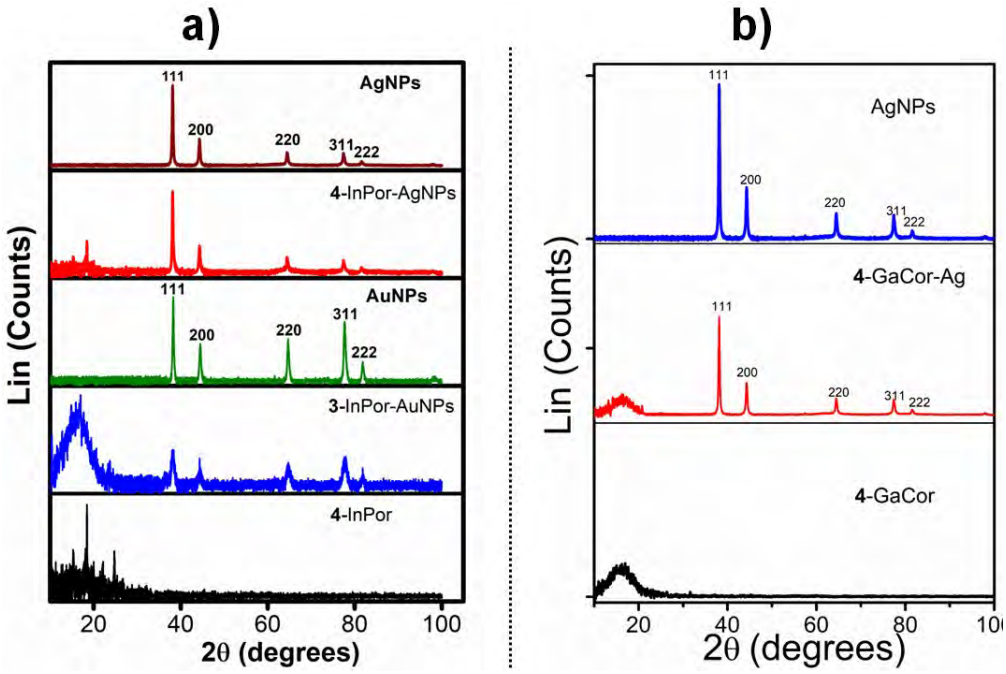

Figure 3.11: Representative X-ray diffractograms of a) AgNPs, **4**-InPor-AgNPs, AuNPs, **3**-InPor-AuNPs, and **4**-InPor b) AgNPs, **4**-GaCor, and **4**-GaCor-AgNPs.

XRD analysis data showed the anticipated well-defined crystalline peaks at 2Θ = 38.5, 44.8, 65.1. 77.9, and 82.5°, which correspond to the 111, 200, 220, 311, and 222 planes of the face-centered-cubic structure of metallic AuNPs or AgNPs (**Figure 3.11**). Peak broadening between 10 and 20° was observed for the dye complexes alone (for example, **4**-InPor and **4**-GaCor in **Figure 3.11**), which is typical for coordinated amorphous porphyrinoids [266]. Peak broadening between 10 and 20° and attenuated crystalline peaks for AuNPs or AgNPs were observed for the nanoconjugates, confirming conjugate formation.

XPS analysis was also used to assess the chemical composition of the porphyrinoid complexes, AuNPs or AgNPs, and their nanoconjugates. For example, the XPS survey spectra for **1**-P^{V}Cor, **1**-P^{V}Cor-AuNPs, and AuNPs showed the anticipated elements in their anticipated binding energy ranges. For instance, the XPS spectrum for **1**-P^{V}Cor showed P (133.2 eV), S (160.8 eV), C (282.5 eV), N (398.1 eV), and O (529.2 eV) peaks, while for AuNPs, the Au peaks appeared at 83.9, 334.1, 352.5, and 547.2 eV, with C (282.1 eV) and O (532.8 eV) peaks also observed from the oleic acid and oleylamine capping agents. For the nanoconjugate (**1**-P^{V}Cor-AuNPs), the anticipated elements; P (134.4 eV), S (163.1 eV), C (283.8 eV), N (398.8 eV) and O (530.7 eV) peaks arising from the **1**-P^{V}Cor dye were observed including Au (82.3, 334.0 and 351.2 eV) peaks from the AuNP nanoparticles [174].

The core-level high-resolution XPS spectra of S2p showed the anticipated interactions, particularly self-assembly interactions between the porphyrinoid dyes containing *meso*-aryl sulfur atoms bonded to AuNPs or AgNPs surfaces through Au-S or Ag-S bonds. For instance, the deconvolution of the S2p peak of **1**-P^{V}Cor (**Figure 3.12 b**) resulted in two typical subpeaks at 161.3 and 162.5 eV corresponding to unbound C−S 2p3/2 and partially oxidized sulfur 2p1/2 species

bonds, respectively [267]. However, upon conjugation, the deconvoluted S2p spectrum of the **1**-P^{V}Cor-AuNP nanoconjugate (**Figure 3.12** c) contains three distinct subpeaks at 161.7, 163.1 and 165.6 eV corresponding to unbound C−S 2p3/2, partially oxidized 2p1/2 and S−Au, respectively [174]. The presence of the S-Au peak provides direct spectroscopic evidence for the successful participation of dye sulfur atoms in conjugation with gold nanoparticles.

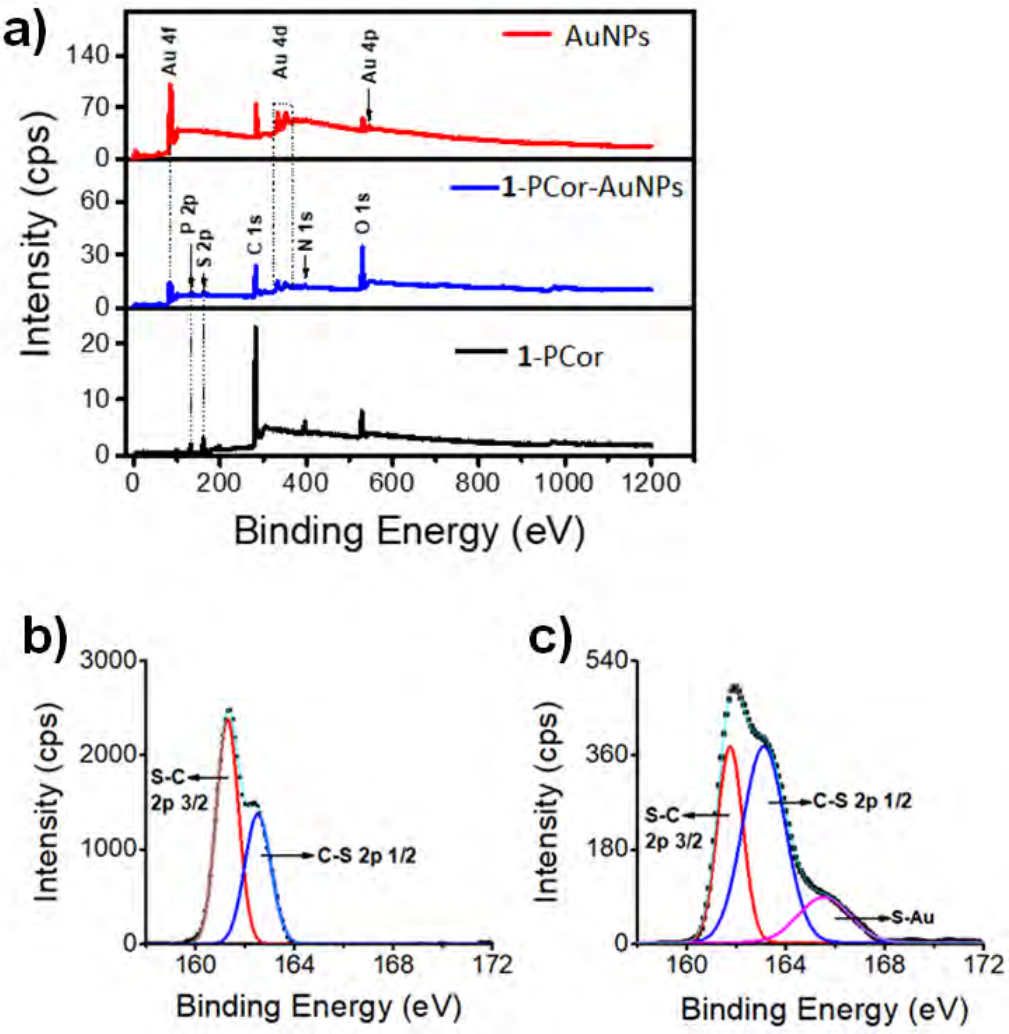

Figure 3.12: Representative XPS spectra a) wide scan survey spectra for **1**-P^{V}Cor, **1**-P^{V}Cor-AuNPs, and AuNPs, and b) high-resolution S2p spectra of **1**-P^{V}Cor and c) **1**-P^{V}Cor-AuNPs [174].

3.6 Concluding remarks

A series of A_4 *meso*-tetraarylporphyrin, A_3 and A_2B *meso*-triarylcorroles, A_4 *meso*-tetraarylchlorin, and A_4 N-confused *meso*-tetraarylporphyrin dyes were successfully synthesized, and their structures were confirmed by ^1H NMR spectroscopy, and MALDI-TOF MS. AgNPs and AuNPs including their porphyrin and corrole dye nanoconjugates were fully characterized using TEM, EDX spectroscopy and XRD, and XPS.

CHAPTER FOUR

Optical Spectroscopic Properties of the Dyes

This chapter discusses the optical spectroscopic properties of the dyes studied investigated by the UV-visible absorption, fluorescence, and magnetic circular dichroism (MCD) spectroscopic techniques.

4.0 Introduction

The porphyrin and porphyrin analog dyes were rationally selected by incorporating *meso*-aryl substituents that consist of electron-donating (rings with nitrogen, sulfur, and oxygens) or electron-withdrawing (rings with fluorines) groups. The P(V) ion or In(III), Sn(IV), and Ga(III) metal ions were inserted into the cores of the dyes to obtain complexes with favorable photophysicochemical properties. The effects of the *meso*-aryl and core substituents on the optical properties of the dyes, including symmetry modifications in the context of corroles, chlorins, and N-confused porphyrin dyes, are evaluated. The effects of nanoparticles on the optical properties of **1**-**4**-InPor and **1**-**4**-*meso*-triaryl P(V) and Ga(III) corroles are also analyzed. A favourable photosensitizer for PDT and PACT should absorb light strongly at the low energy region of the electromagnetic spectrum in the therapeutic window to allow the penetration of light into deep-seated diseased cells [2,3,16,18]. In this study, the optical properties of the dyes determined the excitation wavelength ranges used during PDT and PACT irradiation studies.

All the electronic ground state main absorption (λ_{abs}), emission (λ_{em}), and MCD spectra of the dyes studied obtained during optical spectroscopic analysis are not presented in this chapter. Only a few representative sets are provided as examples. Some of the optical spectra of the dyes are also provided in the Appendix. The theoretical calculations (see Chapter 10) will further elucidate the effects of structural modification on the optical properties of studied porphyrin and porphyrin analog dyes in the context of Gouterman's four-frontier orbital and Michl's perimeter models.

4.1 Optical properties of porphyrin dyes

The porphyrin dyes in this study contain six or five-membered *meso*-aryl substituent groups and are core coordinated to In(III) or Sn(IV) heavy metal ions. **1**-**4**-Por and H_2TPP control porphyrin dyes are coordinated to In(III) ion and **5**-**8**-Por to the Sn(IV) ion. The *meso*-aryl substituents of **1**-**4**-Por dyes contain sulfur heavy atoms, while **4**-Por also has bromines. *Meso*-phenyl groups were used for the control compounds (H_2TPP and InTPP) (**Scheme 2.1**), and the *meso*-aryl substituents of **5**-**8**-Por contain oxygen heteroatom (**Scheme 2.1**). The sulfur atoms of **1**-**4**-InPor dyes also provided sites for functionalization with AuNPs or AgNPs through the self-assembly *via* ligand exchange interactions to form the corresponding **1**-**4**-InPor-AuNP or **1**-**4**-InPor-AgNP nanoassemblies. The AuNP or AgNP metallic nanoparticles are also known for enhancing absorption bands and also induce the external heavy atom effects [248]. Since the optical properties of **1**-InPor, **3**-InPor, and the **1**-InPor AuNP nanoconjugate were reported previously [209], a summary is provided in this context.

4.1.1 Ground state electronic absorption and emission properties of porphyrin ligands and their In(III) and Sn(IV) complexes

The porphyrin dyes studied have the typical intense Soret bands in the blue region (*ca.* 400 nm) and four weak Q bands in the low energy region, which collapsed into two for the coordinated In(III) and Sn(IV) complexes (**Figures 4.1**-**4.3** and **A 36**-**39**). This is due to the change in the D_{2h} molecular symmetry to the increased full square symmetry D_{4h} for metalloporphyrins [35,48]. **Table 4.1** summarizes the optical properties of the porphyrin dyes studied in DMSO, while the solvatochromic absorption data in 1% DMSO/H_2O and $CHCl_3$ solvents are provided in **Table A.1** in the Appendix.

As anticipated, the main absorption bands of **1**-**4**-Por are red shifted relative to those of the *meso*-phenyl control compounds (**Table 4.1**). This is due to the favorable mesomeric effects from the electron-donating sulfur atoms of the *meso*-aryl substituents [184]. In addition, there are significant red shifts in the main spectral bands of porphyrin derivatives with *meso*-thien-2-yl (**3**) and *meso*-5-bromo-thien-2-yl (**4**) rings relative to those with *meso*-thien-3-yl (**2**), and *meso*-4-methylthiophenyl (**1**) groups. This is due to the favorable mesomeric interactions between the *meso*-thien-2-yl derivatives with the porphyrin core, since they lack *ortho*-hydrogens and can easily rotate [268,269] (see Chapter 10 for detailed discussion). There are also red shifts of the main spectral bands of porphyrin derivatives with *para*-substituted *meso*-4-methoxyphenyl (**5**), -4-hydroxyphenyl (**7**), and -4-hydroxy-3-methoxyphenyl (**8**) rings in contrast to those with *meta* substituted *meso*-3-methoxyphenyl (**6**) groups. This is related to the inductive and mesomeric interactions between the porphyrin core and the *meso*-aryl groups [184] (see Chapter 10).

The Soret bands of the In(III) (**1**-**4**-InPor, InTPP) and Sn(IV) (**5**-**8**-SnPor) metalloporphyrins in DMSO are consistently red shifted by approximately *ca.* 9 and 12 nm, respectively, relative to those of their corresponding free-base ligands (**Table 4.1**). This is due to the changes in the geometries and delocalized π-electron densities of porphyrins upon replacing the two core amino (NH) hydrogens with the electropositive In(III) and Sn(IV) ions [184,270]. This results in red shifts of the main absorption bands [270].

There are no significant solvatochromic effects on the main absorption bands of the porphyrin dyes studied, but slight dependence on solvent polarity is evident with red shifts observed from $CHCl_3$ < DMSO solvent. However, in 1% DMSO/H_2O, there is band broadening in the main absorption spectra of the free-base porphyrin ligands in contrast to those of chloroindium(III)

and dichlorotin(IV) porphyrin complexes (as shown in **Figure A.37** as an example). This is likely due to aggregation effects, which are reduced for In(III) and Sn(IV) porphyrin complexes by chloro and dichloro axial ligation. This aggregation effect is an undesirable property, since it inhibits the absorption of light and sublocalization of the dye in the lipid-aqueous biological environment of the cells and hence lowers the PDT and PACT activities of the dyes [3,6,14].

The emission spectra of the porphyrin dyes studied (**Figures 4.1** and **A 36**) are typical of porphyrin dyes with two emission bands that are mirror images of the Q band absorption peaks [48,270]. The emission spectra of In(III) and Sn(IV) porphyrin complexes are blue-shifted in contrast to those of their corresponding free-base ligands due to the rigid D_{4h} structures of metalloporphyrin dyes [270]. As anticipated, the trends in the emission spectra of the porphyrin dyes studied correspond closely to those observed in the UV-visible absorption spectra. For instance, there are evident red shifts in the emission spectra of *meso*-thien-2-yl (**3**) and *meso*-5-bromo-thien-2-yl (**4**) derivatives relative to those of the *meso*-thien-3-yl (**2**), -4-methylthiophenyl (**1**) and -phenyl control compounds (H_2TPP, InTPP) (**Table 4.1**). The emission profiles of *meso*-4-methoxyphenyl (**5**), -4-hydroxyphenyl (**7**), and -4-hydroxy-3-methoxyphenyl (**8**) porphyrin derivatives are also red shifted in contrast to *meso*-3-methoxyphenyl (**6**) dyes in a similar manner to the UV-visible absorption properties (**Figure 4.1**, **Table 4.1**).

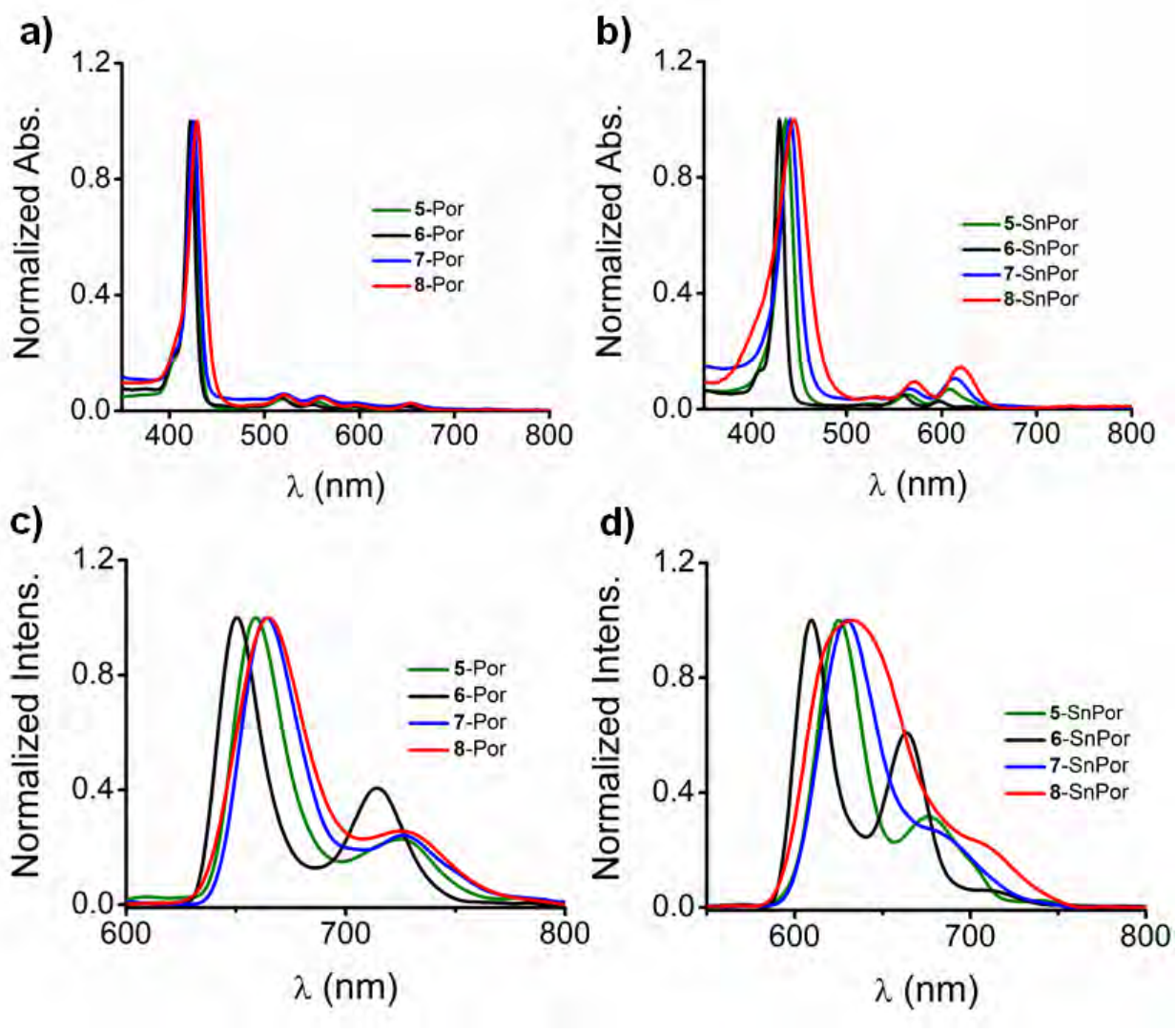

Figure 4.1: UV-visible absorption spectra of the porphyrin dyes and their Sn(IV) complexes (a) **5**-Por (green), **6**-Por (black), **7**-Por (blue), and **8**-Por (red); (b) **5**-SnPor (green), **6**-SnPor (black), **7**-SnPor (blue), and **8**-SnPor (red) in DMSO. Fluorescence spectra of the dyes are provided at the bottom (c-d) with the same color lines used in the corresponding absorption spectra.

4.1.2 MCD properties of porphyrins

Magnetic circular dichroism (MCD) is a powerful tool for analyzing the nature of the electronic perturbations in the π-systems [173,220]. It is an essential tool for probing the ground state and

excited state electronic degeneracies and geometries of porphyrins and porphyrinoid macrocycles, since it provides electronic structural information that cannot otherwise be easily obtained from the ground state absorption spectra alone [174,271]. The MCD spectra are characterized by three spectral features: the $\mathcal{A}_1$, $\mathcal{B}_0$, and $\mathcal{C}_0$ Faraday terms. The $\mathcal{A}_1$ term arises from transitions to orbitally degenerate excited states, while the $\mathcal{B}_0$ term is observed for transitions between non-degenerate ground and excited states transitions, and the $\mathcal{C}_0$ term is temperature-dependent and is associated with orbitally degenerate ground state transitions [220,271,272].

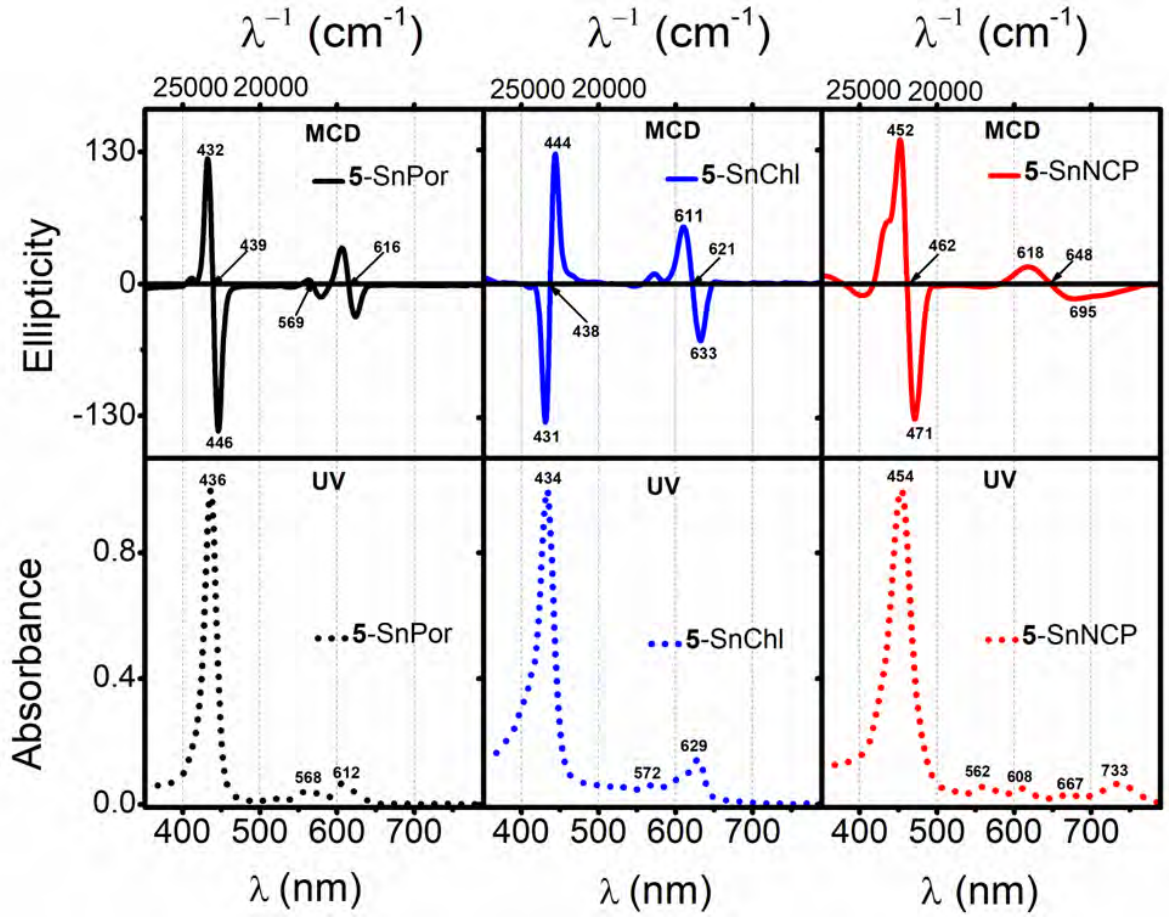

Figure 4.2: MCD spectra (top) and absorption spectra (bottom) of **5**-SnPor (black), **5**-SnChl (blue), and **5**-SnNCP (red) in DMSO.

The MCD spectra of In(III) and Sn(IV) porphyrin dyes (**Figures 4.2** and **A 37**) consist of intense Faraday $\mathcal{A}_1$ terms with negative to positive sign patterns in ascending energy that are typical of four-fold symmetry transitions of metalloporphyrins [271,272]. The cross-over-points on the MCD spectra of porphyrin complexes are closely aligned to B and Q absorption band maxima (**Figures 4.2** and **A 37**). The −/+ sign patterns observed on the MCD spectra of the studied In(III) and Sn(IV) porphyrin dyes are consistent with the predicted ΔHOMO > ΔLUMO trend (in the context of Michl's perimeter model, ΔHOMO refers to the energy gap between the **a** and **s** MOs, while ΔLUMO refers MOrefers to that between the **-a** and **-s** MOs), since a normal metalloporphyrin has degenerate LUMO MOs. This is also confirmed by TD-DFT calculations of the dyes (See Chapter 10).

4.2 Electronic absorption and emission properties of the 1-4-InPor-AuNP and 1-4-InPor-AgNP conjugates

The absorption and emission spectra of the In(III) porphyrin AuNP or AgNP nanoconjugates resemble those of their **1**-**4**-InPor parent porphyrins (as shown in **Figure 4.3** as examples). The surface plasmon resonance (SPR) bands of AuNPs and AgNPs lie at 535 and 413 nm, respectively (**Figure A 38**). However, these SPR bands are not clearly defined in the absorption spectra of **1**-**4**-InPor-AuNPs and **1**-**4**-InPor-AgNPs conjugates. However, the band broadening and enhancement in the B and Q band regions, respectively, provide evidence for the successful conjugation of the porphyrin dyes to the nanoparticles [273]. **Table 4.1** summarizes the optical spectroscopic data and the estimated loading ratios of porphyrin complexes to nanoparticles (μg of porphyrin/ mg of NP) of the studied **1**-**4**-InPor-AgNP and **1**-**4**-InPor-AuNP nanoconjugates in DMSO, while the

solvatochromic absorption data of **1**-**4**-InPor-AgNP and **1**-**4**-InPor-AuNP nanoconjugates in $CHCl_3$, and 1% DMSO/H_2O are summarized in **Table A 1** in the Appendix.

The trends in the main absorption spectral features of **1**-**4**-InPor-AuNP and **1**-**4**-InPor-AgNP nanoconjugates in $CHCl_3$, DMSO, 1% DMSO/H_2O vary significantly with blue shifts, or red shifts or no change in contrast to those of their corresponding **1**-**4**-InPor complexes (**Figure A 39**). This could be related to the different refractive indices of the solvents, the close-packing, and varied orientations of the porphyrin molecules on the SPR of the AuNPs or AgNPs [248,274]. The trends in the emission profiles of the studied **1**-**4**-InPor-AuNP and **1**-**4**-InPor-AgNP conjugates in DMSO are consistent with those in their absorption spectra (**Figure 4.3**).

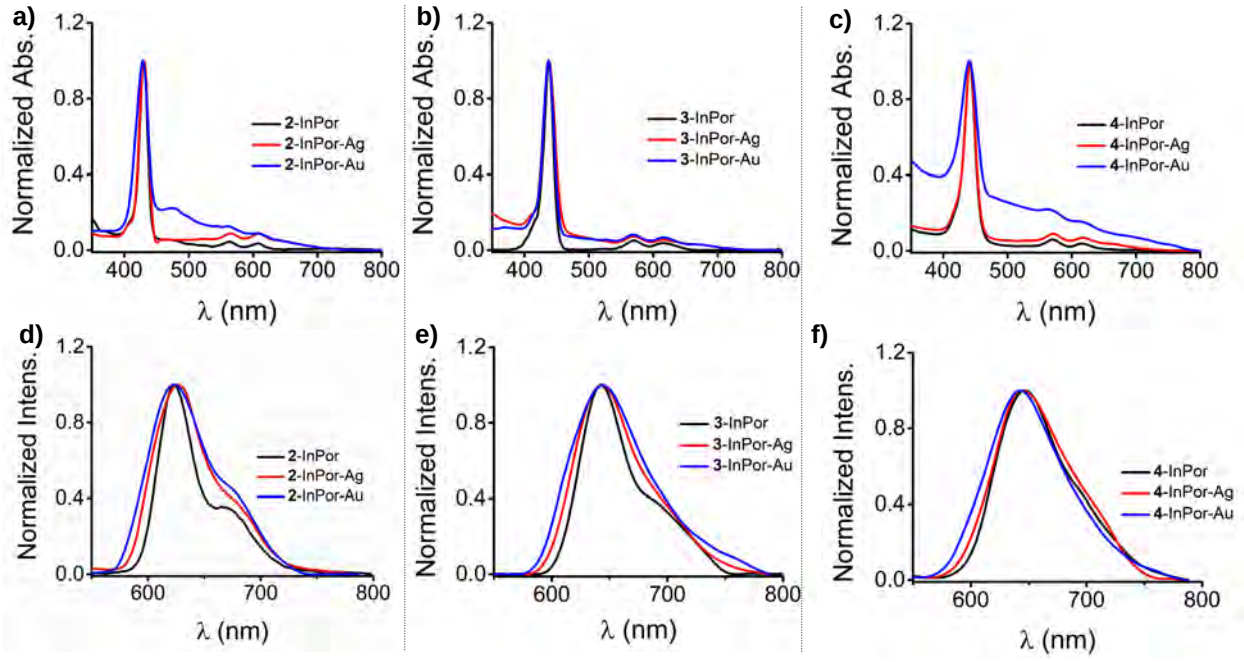

Figure 4.3: UV-visible absorption spectra of a) **2**-InPor (black), **2**-InPor-AgNPs (red), and **2**-InPor-AuNPs (blue); b) **3**-InPor (black), **3**-InPor-AgNPs (red), and **3**-InPor-AuNPs (blue); c) **4**-InPor (black), **4**-InPor-AgNPs (red), and **4**-InPor-AuNPs (blue) in DMSO. Fluorescence

spectra of the porphyrin dyes and nanoconjugates are provided at the bottom (d-f) with the same line types used for the corresponding absorption spectra.

Table 4.1: The optical absorption and emission properties of the H_2TPP and InTPP control compounds, **1**-**8**-Por, **1**-**4**-InPor, **5**-**8**-SnPor, **1**-**4**-InPor-AuNPs and **1**-**4**-InPor-AgNPs porphyrin nanoconjugates in DMSO.

Sample	**λ_{Abs}** (nm)			**λ_{em}** (nm)	**SPR**	**Size** (nm)	**P loading** (μg/mg NP)
	B	Q_{01}	Q_{00}				
H_2TPP	418	514, 549	590, 647	654, 715	---	---	---
1-Por	424	518, 556	596, 650	660, 721	---	---	---
2-Por	421	518, 557	593, 652	661, 725	---	---	---
3-Por	425	520, 557	598, 650	671, 730	---	---	---
4-Por	431	524, 567	613, 660	674, 737	---	---	---
InTPP	428[a]	561[a]	601[a]	609, 660[a]	---	---	---
1-InPor	435[a]	566[a]	609[a]	625, 670[a]	---	---	---
2-InPor	430	563	607	623, 670	---	---	---
3-InPor	438[a]	573[a]	618[a]	643, 703[a]	---	---	---
4-InPor	441	572	620	646, 724	---	---	---
AgNPs	---	---	---	---	403	9.1	---
AuNPs	---	---	---	---	535	10.5	---
1-InPor-AgNPs	433	564	606	619, 665	422	22.8	24
1-InPor-AuNPs	429[a]	573[a]	618[a]	617, 663[a]	523[a]	26.0[a]	30[a]
2-InPor-AgNPs	430	565	609	626, 680	420	27.7	20
2-InPor-AuNPs	429	561	607	623, 677	532	23.4	19
3-InPor-AgNPs	438	569	616	644, 707	426	21.8	18
3-InPor-AuNPs	437	570	618	645, 719	528	21.2	15
4-InPor-AgNPs	442	571	620	645, 726	424	23.1	16
4-InPor-AuNPs	440	569	619	643, 723	533	25.3	13

5-**8**-Por and their **5**-**8**-SnPor porhyrin complexes

5-Por	424	519, 556	595, 650	659, 726	---	---	---
6-Por	420	515, 548	590, 645	650, 714	---	---	---
7-Por	425	520, 560	595, 651	664, 726	---	---	---
8-Por	428	521, 560	596, 653	665, 726	---	---	---
5-SnPor	438	568	612	625, 678	---	---	---
6-SnPor	429	558	602	610, 664	---	---	---
7-SnPor	441	567	615	630, 680	---	---	---
8-SnPor	445	572	620	634, 712	---	---	---

[a]Optical data obtained from [209]

4.3 Optical properties of corrole dyes

The studied A_3 *meso*-triaryl corrole dye series are coordinated to P(V) and Ga(III) ions (**Scheme 2.2**). They have *meso*-aryl substituents that are identical to those of previously described **1**-**4**-Por dyes, and their control compounds also consist of *meso*-phenyl groups (H_3TPCor, P^VTPCor, Ga^{III}TPCor). Since **1**-**4**-Cor corrole dyes contain sulfur atoms on their *meso*-aryl substituents, their P(V) and Ga(III) complexes are conjugated to AuNPs and AgNPs. This was achieved *via* S-Au or S-Ag affinities to form the corrole dye-AuNP and corrole dye-AgNP nano-assemblies (**1**-**4**-P^VCor-AuNPs, **1**-**4**-GaCor-AuNPs, **1**-**4**-P^VCor-AgNPs, and **1**-**4**-GaCor-AgNPs). The A_2B *meso*-triarylcorroles (**Scheme 2.4**), on the other hand, are coordinated to Ga(III) ion (**9**-GaCor, **10**-GaCor), and **10**-GaCor corrole dye was successfully quarternized with ethyl iodide to form **10**-GaCor-Q. The *meso*-aryl substituents of A_2B *meso*-triarylcorrole dyes have push-pull properties, since they consist of electron-withdrawing pentafluorophenyl rings at the A_2 positions and electron-donating carbazole moieties at the B position. Since the optical properties of **1**-**3**-P^VCor and **1**-**3**-GaCor A_3 *meso*-triaryl P(V) and Ga(III) corroles and their AuNP nanoconjugates, including the Ga(III) A_2B

meso-triaryl corroles, have been reported in the literature [174,210], only a summary is provided in this Chapter.

4.3.1 Ground state electronic absorption and emission properties of corroles

The absorption spectra of the studied A_3 and A_2B *meso*-triaryl corrole dyes (**Figures 4.4**-**4.6**) are typical of corroles with intense Soret bands at *ca.* 400 nm and weaker Q bands at *ca.* 500−800 nm [112,275]. The Q bands of corrole dyes are slightly more intense due to lower symmetry arising from the introduction of a direct-pyrrole-pyrrole bond to the parent porphyrin structures [46,112,136,275] (see Chapter 10). **Table 4.2** summarizes the optical properties of the studied A_3 and A_2B *meso*-triaryl corrole dyes in DMSO, and **Tables A 2**-**3** in the Appendix provides the solvatochromic absorption data.

There are significant red shifts in the main absorption bands of **1**-**4**-GaCor A_3 *meso*-triaryl Ga(III) corroles in contrast to the corresponding **1**-**4**-P^VCor P(V) corrole complexes in DMSO (**Table 4.2**). This is due to favorable coupling interactions between the delocalized π-π electron system of the corrole ring and electropositive Ga(III) ion, which lowers the electronic transitions energies resulting in the observed red shifts [174].

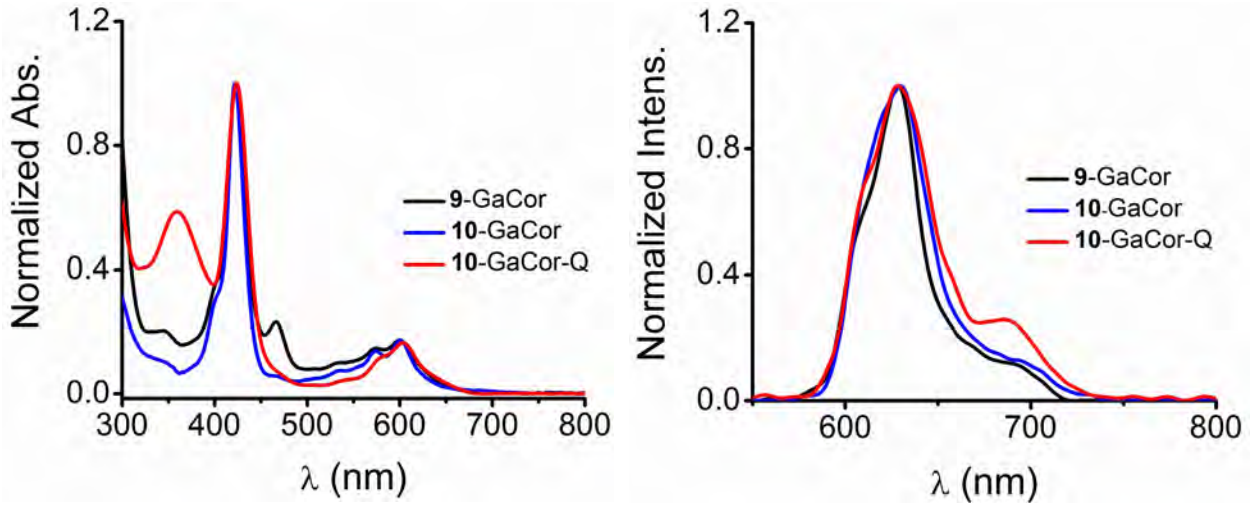

Figure 4.4: a) UV-visible absorption spectra of the A_2B *meso*-triaryl Ga(III) corroles **9**-GaCor (black), **10**-GaCor (blue), and **10**-GaCor-Q (red) in DMSO. b) Fluorescence spectra of the dyes with the same color lines used for the corresponding absorption spectra. Reproduce with permission from Reference [210].

The introduction of different A_3 and A_2B *meso*-aryl substituents results in minor spectral changes to the absorption properties relative to the parent *meso*-phenylcorrole control compounds (H_3TPCor, P^VTPCor, Ga^{III}TPCor) due to their inductive and mesomeric effects (**Table 4.2**). The trends in the absorption spectra related to the *meso*-aryl substituents of the A_3 *meso*-triaryl corrole series (**1**-**4**-Cor, **1**-**4**-P^VCor, and **1**-**4**-GaCor) are consistent with those of the corresponding **1**-**4**-Por dyes (discussed earlier in **Section 4.1.1**). For instance, B and Q bands of *meso*-thienyl-2-yl derivatives (**3**-**4**-Cor, **3**-**4**-P^VCor, and **3**-**4**-GaCor) are significantly red shifted relative to those of *meso*-methylthiophenyl (**1**), -thien-3-yl (**2**) and the -phenyl control compounds in a similar manner to **3**-**4**-Por and **3**-**4**-InPor analogs. Since *meso*-thien-2-yl derivatives (**3**, **4**) lack *ortho* hydrogens and can easily rotate, they interact favorably with the corrole core due to more

effective mesomeric effects [174,268,269]. This results in the observed red shifts of the main absorption bands of dyes (**Table 4.2**) (see Chapter 10 for detailed discussion).

There are also minor changes in the main absorption spectra of A_2B *meso*-triaryl Ga(III) corroles (**9**-**10**-GaCor and **10**-GaCor-Q) in DMSO due to push and pull mesomeric effects from the electron-withdrawing *meso*-aryl groups at the A_2 positions and the electron donating *meso*-aryl group at the B position. Since these dyes have very similar structures, the variations in their absorption properties are minimal [210] (**Figure 4.4**, **Tables 4.2** and **A 2**). In addition, the introduction of cationic ethyl iodide to the carbazole moiety of **10**-GaCor *meso*-aryl ring to form **10**-GaCor-Q has a negligible effect on the UV-visible absorption spectrum of the dye (**Figure 4.4**).

There are minimal solvatochromic effects on the main absorption bands of the studied A_3 *meso*-triarylcorrole dyes, with slight red shifts observed due to solvent polarity $CHCl_3$ < DMSO solvent. There is band broadening of the Q and B bands of free-base corrole ligands (H_3TPCor, **1**-**4**-Cor) and Ga(III) corrole complexes (**1**-**4**-GaCor) relative to those of their corresponding P(V) complexes (P^VTPCor, **1**-**4**-P^VCor) in 1% DMSO/H_2O solvent (as shown in **Figure A 41** as an example). This can be attributed to aggregation effects that are reduced in the context of P(V) corrole complexes (P^VTPCor and **1**-**4**-P^VCor) by their dihydroxy axial ligands [174]. This aggregation is an undesirable property that limits the absorption of light and sublocalization of the dye in the lipid-aqueous biological environment of the cells, hence lowering the PDT and PACT activities of the dyes [1,3,15].

However, there are significant solvatochromic effects on the B bands of A_2B *meso*-triaryl Ga(III) corroles in non-polar solvents. In highly polar solvents, there is no significant correlation in this regard related to the interaction with the core ligand (**Table A 2**-**3**) [210]. The Q and B bands of

these A_2B *meso*-triaryl Ga(III) corroles in 1% DMSO/H_2O solvent also exhibit slight band broadening due to the minor aggregation effects (**Figure A 41**).

The emission spectra of the studied A_3 and A_2B *meso*-triaryl corroles are typical of corrole dyes [275]. They contain two emission bands derived from the first excited state decay associated with Q_{00} electronic transition at higher energy and Q_{01} vibrational features on a Kasha's rule basis [180]. The emission bands of A_3 and A_2B *meso*-triaryl P(V) and Ga(III) corrole complexes are blue-shifted in comparison to those of corresponding free-base corrole dyes due to their rigid structures [174,210]. As anticipated, the shifts in the emission spectra of the corrole dyes studied are closely related to their UV-visible absorption properties. For example, there are red shifts on the emission spectra of *meso*-thien-2-yl (**3**) and *meso*-5-bromo-thien-2-yl (**4**) corrole derivatives relative to those of *meso*-4-methylthiophenyl (**1**), *meso*-thien-3-yl (**2**), and the *meso*-phenyl control compounds (H_3TPCor, P^{V}TPCor, Ga^{III}TPCor) (**Table 4.4**)[174]. There are also minor differences in the emission spectra of A_2B *meso*-triaryl Ga(III) corroles in DMSO (**Figure 4.4**, **Table 4.4**). This is closely related to the trends in the absorption spectra since these A_2B *meso*-triaryl Ga(III) corrole dyes have very similar structures [210].

Table 4.2: Absorption and emission parameters of A_3 *meso*-triaryl free-base and their P^V and Ga^{III} complexes, AgNP and AuNP nanoconjugates of A_3 **1**-**4**-P^VCor and **1**-**4**-GaCor corroles and A_2B *meso*-triaryl Ga(III) corroles in DMSO.

A_3 *meso*-triaryl corroles							
Sample	**λ_{Abs} (nm)**			**SPR**	**Size** (nm)	**C loading** (μg/mg NP)	**λ_{em} (nm)**
	B	Q_{01}	Q_{00}				
H_3TPCor	426[b]	582[b]	642[b]	---	---	---	667, 732[b]
1-Cor	422[b]	574[b]	641[b]	---	---	---	662, 725[b]
2-Cor	424[b]	594[b]	645[b]	---	---	---	663, 725[b]
3-Cor	425[b]	587[b]	647[b]	---	---	---	680, 755[b]
4-Cor	430	660	731	---	---	---	675, 768
1-P^VCor	419[b]	570[b]	611[b]	---	---	---	619, 676[b]
2-P^VCor	423[b]	562[b]	611[b]	---	---	---	623, 698[b]
3-P^VCor	427[b]	573[b]	614[b]	---	---	---	631, 708[b]
4-P^VCor	429[b]	574[b]	615[b]	---	---	---	633, 724[b]
1-GaCor	429[b]	581[b]	615[b]	---	---	---	639, 702[b]
2-GaCor	429[b]	559[b]	616[b]	---	---	---	632, 728[b]
3-GaCor	433[b]	578[b]	622[b]	---	---	---	657, 740[b]
4-GaCor	435	560	621	---	---	---	661, 739
P^VTPCor	425[b]	574[b]	612[b]	---	---	---	630, 708[b]
Ga^{III}TPCor	430[b]	567[b]	622[b]	---	---	---	654, 719[b]
AgNPs	---	---	---	403	9.1	---	---
AuNPs	---	---	---	535[b]	10.5[b]	---	---
1-P^VCor-AgNPs	422	567	612	422	22.2	26	619, 679
1-P^VCor-AuNPs	419[b]	569[b]	609[b]	538[b]	22.2[b]	42[b]	616, 674[b]
2-P^VCor-AgNPs	422	565	607	400	31.2	29	623, 720
2-P^VCor-AuNPs	427[b]	575[b]	614[b]	542[b]	29.4[b]	34[b]	632, 714[b]
3-P^VCor-AgNPs	426	565	611	426	26.1	29	623, 715
3-P^VCor-AuNPs	430[b]	577[b]	624[b]	540[b]	22.3[b]	27[b]	637, 701[b]
4-P^VCor-AgNPs	432	566	617	426	24.4	25	642, 732
4-P^VCor-AuNPs	425	571	609	541	20.2	26	638, 725
1-GaCor-AgNPs	428	581	624	428	29.3	22	637, 722
1-GaCor-AuNPs	429[b]	580[b]	620[b]	541[b]	21.2[b]	24[b]	640, 725[b]
2-GaCor-AgNPs	433	567	622	433	31.5	22	657, 752

2-GaCor-AuNPs	430 [b]	564 [b]	622 [b]	537 [b]	25.9 [b]	18 [b]	642, 721 [b]
3-GaCor-AgNPs	433	566	624	433	32	19	652, 737
3-GaCor-AuNPs	432 [b]	564 [b]	617 [b]	530 [b]	29.0 [b]	14 [b]	640, 703 [b]
4-GaCor-AgNPs	433	558	616	417	28.5	22	654, 754
4-GaCor-AuNPs	434	566	626	536	25.3	17	673, 730
A_2B *meso*-triaryl Ga(III) corroles							
9-GaCor	423 [c]	574 [c]	604[c]	---	---	---	630, 694[c]
10-GaCor	422[c]	573 [c]	602[c]	---	---	---	629, 691[c]
10-GaCor-Q	424 [c]	578 [c]	600 [c]	---	---	---	630, 688[c]

Optical parameters reproduced from References [b][174] and [c][210].

4.3.2 MCD properties of corroles

The MCD spectra of the studied A_3 and A_2B *meso*-triaryl corrole complexes have oppositely signed coupled pairs of B_0 Faraday terms with +/− sign sequence in ascending energy terms in contrast with the A_0 terms observed for four-fold symmetrical metalloporphyrin (**Figure A 38**). The +/− sign sequence is consistent with the ΔHOMO < ΔLUMO trend predicted by TD-DFT calculations of the corrole complexes studied (see Chapter 10). This pattern is consistent with those of low-symmetry porphyrin analogs previously reported by Mack and co-workers [175,271].

4.3.3 Electronic absorption and emission properties of the AgNP and AuNPs conjugates of 1-4-P^VCor and 1-4-GaCor P(V) and Ga(III) A_3 *meso*-triaryl corroles

Table 4.2 summarizes the optical parameters and the estimated loading ratios of dye to nanoparticle of the AgNP and AuNP nanoconjugates of the P(V) and Ga(III) A_3 *meso*-triaryl corroles studied. The dye/nanoparticle loading capacity is higher for P(V) corroles than their Ga(III) corroles counterparts. This can be attributed to the favorable combination of hydrogen bonding interactions from the dihydroxy axial ligands of P(V) corroles and π-π stacking effect [276,277] with the AgNPs or AuNPs. Higher dye/nanoparticle loadings can influence the

photophysicochemical, PDT, and PACT activity properties of the P(V) corrole nanoconjugates, as reported previously for **1**-**3**-P^{V}Cor-AuNPs [174].

Figure 4.6 provide the absorption and emission spectra of **4**-P^{V}Cor-AgNP, **4**-P^{V}Cor-AuNP, **4**-GaCor-AgNP, and **4**-GaCor-AuNP nanoconjugates as representative examples. The SPR bands of AgNPs and AuNPs at 413 and 535 nm, respectively, are not clearly defined in the UV-visible absorption spectra of the corrole nanoconjugates (**Figure 4.6**). However, band enhancement is evident in the Q band region and band broadening in the B band regions of the AgNPs and AuNPs corrole nanoconjugates, which confirms the successful conjugation of P(V) and Ga(III) A_3 *meso*-triarylcorrole complexes (**1**-**4**-P^{V}Cor and **1**-**4**-GaCor) to AgNPs or AuNPs.

Various absorption spectral features are observed for the AgNP and AuNP nanoconjugates of the P(V) and Ga(III) A_3 *meso*-triarylcorroles studied in $CHCl_3$, DMSO, 1% DMSO/H_2O. There are blue shifts, red shifts, or no change in contrast to those of their corresponding P(V) or Ga(III) corrole complexes (**1**-**4**-P^{V}Cor or **1**-**4**-GaCor). This could be attributed to the close-packing and varied orientations of corrole molecules on the SPR of the AuNPs or AgNPs and differences in the refractive indices of the solvents [248,274]. The trends in the emission properties of the studied A_3 P(V) and Ga(III) corroles and **1**-**4**-AgNP or -AuNP nanoconjugates are consistent with those in the UV-visible absorption spectra.

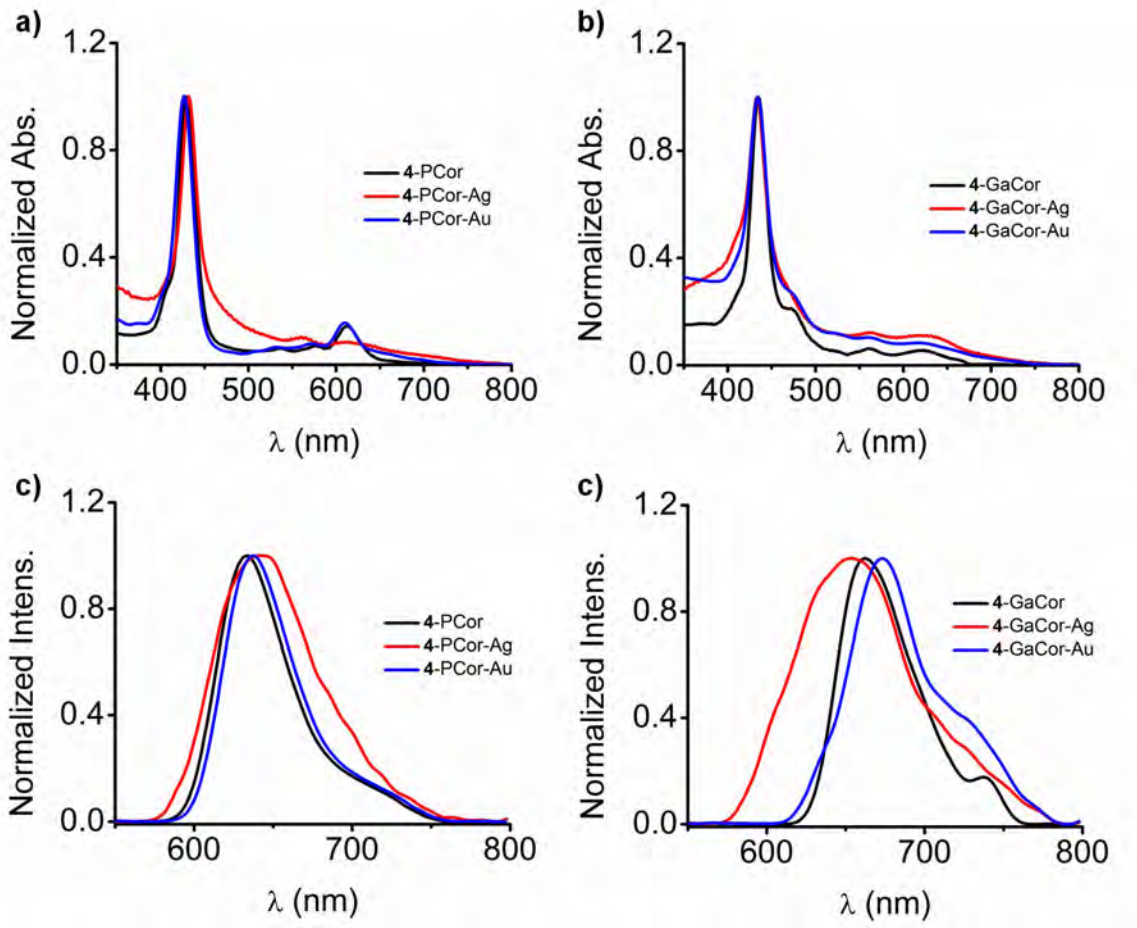

Figure 4.5: UV-visible absorption spectra of a) **4**-P^{V}Cor (black), **4**-P^{V}Cor-AgNPs (red), and **4**-P^{V}Cor-AuNPs (blue); b) **4**-GaCor (black), **4**-GaCor-AgNPs (red), and **4**-GaCor-AuNPs (blue) in DMSO. Fluorescence spectra of the corrole dyes, silver, and gold nanoconjugates are provided at the bottom (c-d) with the same line types used for the corresponding absorption spectra.

4.4 Optical properties of chlorin dyes

This section details the optical properties of **5**-**8**-Chl A$_4$ *meso*-tetra aryl chlorins and their Sn(IV) chlorin complexes. Since the **5**-**8**-Chl dyes studied have identical *meso*-aryl substituents and Sn(IV) central ion with **5**-**8**-Por dyes and also **5**-NCP, the changes in the optical properties across these dye series can be directly compared.

4.4.1 Ground state electronic absorption and emission properties of chlorins

The ground state absorption spectra of the studied A_4 *meso*-tetraaryl chlorins are typical of chlorin dyes with intense B bands at *ca.* 400 nm and a set of four Q bands at low energy region with a characteristic slightly more intense Q band at *ca.* 650 nm in contrast to the parent porphyrin dyes [145] (**Figure 4.7a**). For Sn(IV) chlorins (**5**-**8**-SnChl), there are red shifts in the B bands, and the four Q bands of free-base ligands collapsed into two with the characteristic slightly more intense Q band blue shifting to *ca.* 630 nm (**Figure 4.7b**). The slightly more intense Q band arises from hydrogen reduction on one of the peripheral β-β pyrrole double bonds of the parent porphyrin ring to form a low symmetry chlorin dye [50,145] (see Chapter 10). **Table 4.3** summarizes the optical properties of the chlorin dyes studied, including those of their paporphyrins and N-confused porphyrin analogs in DMSO. The solvatochromic absorption data in $CHCl_3$ and 1% DMSO/H_2O of the chlorins studied are provided in **Table A 4** in the Appendix.

The trends in absorption properties of the chlorins studied are closely related to those observed for their porphyrin analogs (**5**-**8**-Por and **5**-**8**-SnPor) described previously in **Section 4.1.1**. For instance, there are also minor absorption spectral changes due to inductive and mesomeric effects from the *meso*-aryl substituents of the chlorins studied (**5**-**8**-Chl, **5**-**8**-SnChl). The absorption spectra of *meso*-4-methoxyphenyl (**5**), *meso*-4-hydroxyphenyl (**7**), and *meso*-4-hydroxy-3-methoxyphenyl (**8**) chlorin derivatives are red shifted in contrast to those of *meta*-substituted *meso*-3-methoxyphenyl (**6**) chlorin dyes. This is due to more favorable mesomeric interactions between the chlorin core and *meso*-phenyl groups with *para*-substituents [184] (see Chapter 10).

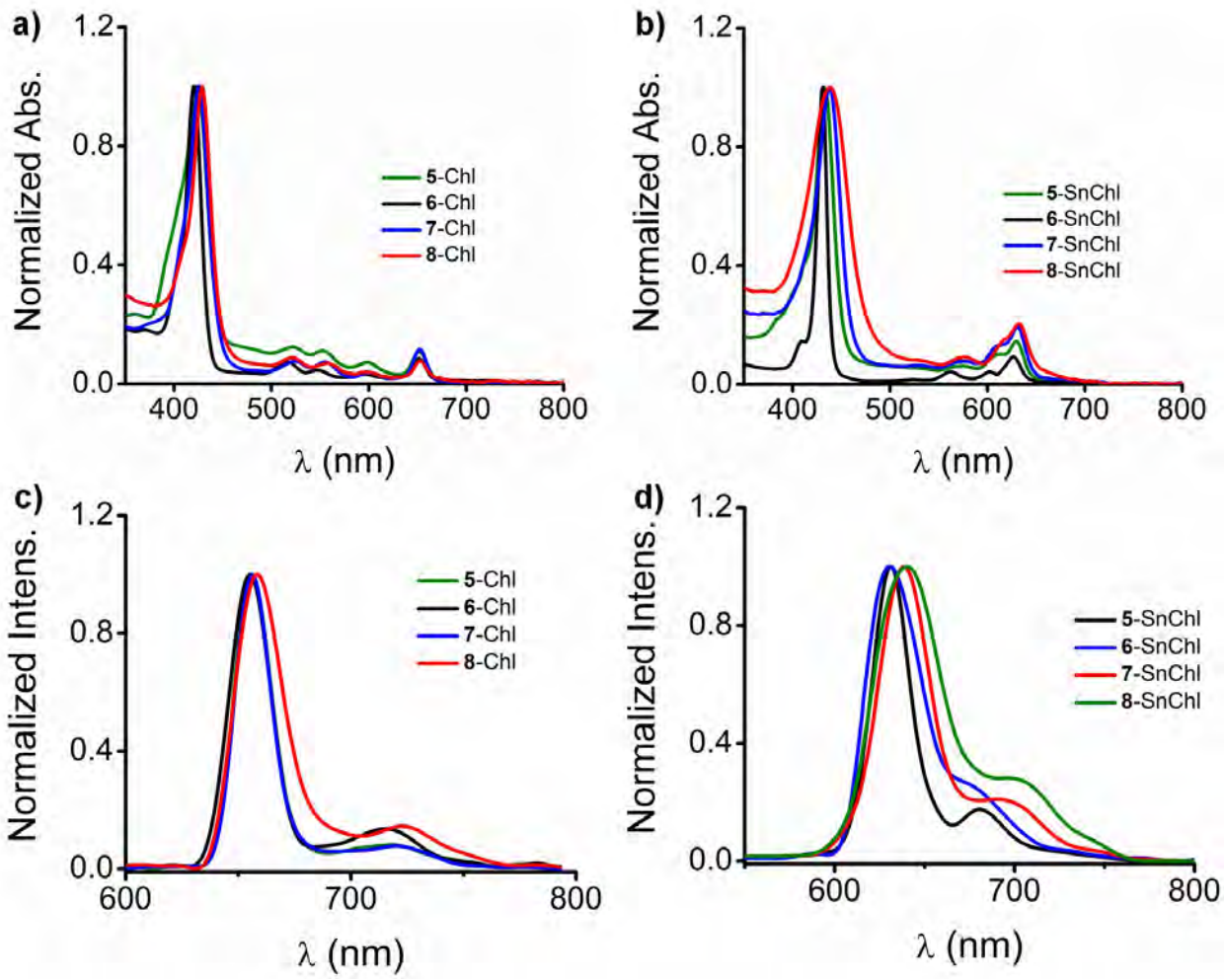

Figure 4.6: UV-visible absorption spectra of the chlorin dyes and their Sn(IV) complexes (a) **5**-Chl (green), **6**-Chl (black), **7**-Chl (blue), and **8**-Chl (red); (b) **5**-SnChl (green), **6**-SnChl (black), **7**-SnChl (blue), and **8**-SnChl (red) in DMSO. Fluorescence spectra of the dyes are provided at the bottom (c-d) with the same color lines used for the corresponding absorption spectra.

The main absorption bands of the chlorin dyes studied exhibit minor solvatochromic effects with a slight dependence on solvent polarity, as evidenced by slight red shifts from $CHCl_3$ < DMSO. There are band broadening on the absorption spectra of the free-base chlorins in 1% DMSO/H_2O solvent in contrast to those of dichlorotin(IV) chlorin complexes (as shown in **Figure A 41**). This is

likely related to aggregation effects in the context of free-base chlorins, which are probably decreased by the dichloro axial ligands of Sn(IV) chlorin complexes.

The chlorins studied have two-band emission profiles typical of chlorin dyes [145]. The emission spectra of Sn(IV) chlorins are blue shifted in contrast to free-base chlorins due to the introduction of the Sn(IV) ion resulting in rigid planar structures. The trends in the emission profiles of the chlorin dyes studied correspond closely to those in the UV-visible absorption spectra, with red shifts observed for **5**-Chl, **7**-Chl, and **8**-Chl derivatives in contrast to **6**-Chl (**Figure 4.1**, **Table 4.3**).

4.4.2 MCD properties of chlorins

The MCD spectra of Sn(IV) chlorin complexes have B_0 Faraday terms with a +/− sign pattern in ascending energy terms (**Figure 4.2** and **Figure A 42**). This is due to the low symmetry of the chlorin arising from hydrogen reduction of the β-β peripheral pyrrole ring of the parent porphyrin resulting in a loss of degeneracy of the MOs derived from the LUMO of the parent hydrocarbon perimeter as described by Michl [173]. As anticipated, the +/− sign sequence is consistent with ΔHOMO < ΔLUMO predicted in the TD-DFT calculations of **5**-**8**-SnChl (see Chapter 10). It also affirms the significant intensification of the Q bands of Sn(IV) chlorins in contrast to those of their **5**-**8**-SnPor analogs due to the mixing of allowed and forbidden properties when ΔHOMO ≠ ΔLUMO. The MCD spectral features of the chlorin dyes studied agree with those reported for low-symmetry porphyrin analogs [109,174,271].

Table 4.3: Absorption and emission parameters of A_4 *meso*-tetraaryl porphyrins (**5**-**8**-Por, **5**-**8**-SnPor), chlorins (**5**-**8**-Chl, **5**-**8**-SnChl), and N-confused porphyrin dyes (**5**-NCP, **5**-SnNCP) and their Sn(IV) complexes in DMSO.

Porphyrins				
Sample		λ_{Abs} (nm)		λ_{em} (nm)
	B	Q_{01}	Q_{00}	
5-Por	424	519, 556	595, 650	659, 726
6-Por	420	515, 548	590, 645	650, 714
7-Por	425	520, 560	595, 651	664, 726
8-Por	428	521, 560	596, 653	665, 726
5-SnPor	438	568	612	625, 678
6-SnPor	429	558	602	610, 664
7-SnPor	441	567	615	630, 680
8-SnPor	445	572	620	634, 712
SnTPP	427[d]	562[d]	602[d]	---- ----
Chlorins				
5-Chl	424	522, 551	597, 651	656, 720
6-Chl	420	515, 549	596, 651	655, 717
7-Chl	426	524, 556	599, 650	656, 721
8-Chl	428	520, 560	601, 653	658, 724
5-SnChl	433	572	608, 629	631, 682
6-SnChl	430	564	602, 627	630, 679
7-SnChl	438	576	613, 629	639, 698
8-SnChl	439	575	615, 630	641,704
N-confused porphyrins				
5-NCP	444	550, 640	700, 778	775, 843
5-SnNCP	454	562, 608	667, 733	731, 838

[d] Absorption data of **SnTPP** control in DMSO are from Reference [44].

4.5 Optical properties of N-confused porphyrin dyes

This section details the optical properties of *meso*-tetra aryl N-confused porphyrin (**5**-NCP) and its Sn(IV) N-confused porphyrin complex (**5**-SnNCP). The changes in the optical properties of the studied N-confused porphyrin dyes (**5**-NCP and **5**-SnNCP) are contrasted with those of their porphyrin isomers (**5**-Por and **5**-SnPor) and chlorin analogs (**5**-Chl and **5**-SnChl), since these dye series have identical *meso*-aryl groups and Sn(IV) core centers. **Table 4.3** summarizes the optical properties of the studied N-confused porphyrin in DMSO, and **Table A 4** in the Appendix gives the solvatochromic absorption data of the N-confused porphyrin dyes in benzene, $CHCl_3$, and 1% DMSO/H_2O.

4.5.1 Ground state electronic absorption properties and emission properties of N-confused porphyrins

The ground state spectra of the studied N-confused porphyrin dyes (**5**-NCP, **5**-SnNCP) have significantly red shifted intense B bands and weaker Q bands at longer wavelengths in contrast to those of their porphyrin isomers (**5**-Por, **5**-SnPor) and chlorin analogs (**5**-Chl, **5**-SnChl) (**Figure 4.8**). This results from low symmetry effects upon isomerization of **5**-Por dyes to form N-confused dyes by inversion of inner pyrrole nitrogen to the outer ring [44,160,167] (see Chapter 10). The Q bands of N-confused porphyrin dyes lie deep into the therapeutic window NIR region (**Figure 4.8**, **Table 4.3**).

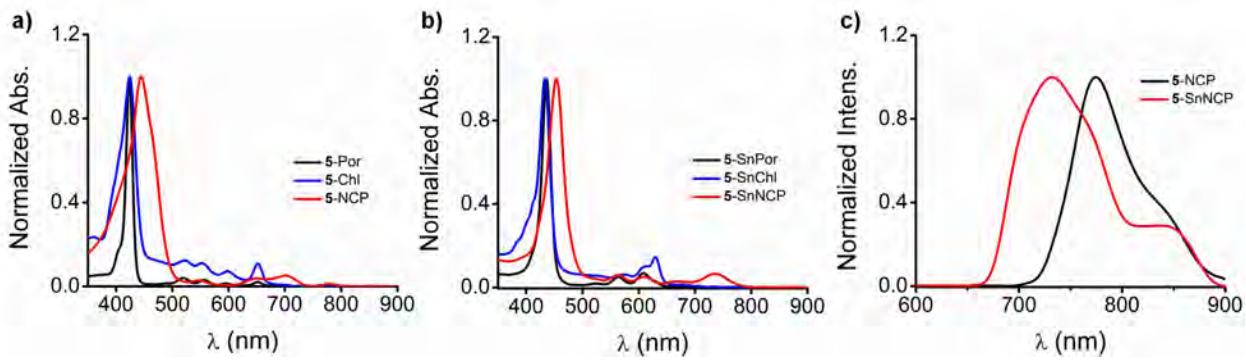

Figure 4.7: (a-b) UV-visible absorption spectra of (a) free-base ligands **5**-Por (black), **5**-Chl (blue), and **5**-NCP (red); (b) Sn(IV) complexes with the same color lines used for the corresponding free-base ligands. c) Fluorescence spectra of N-confused porphyrin dyes **5**-NCP (black) and **5**-SnNCP (red).

The studied N-confused porphyrin dyes also exhibit solvatochromic absorption spectral features in both polar and non-polar solvents due to their tautomeric properties (**Table A 4**), since in hydrogen bond-forming polar solvents, the outer NH of N-confused porphyrin tautomer is highly stabilized [278]. However, in 1% DMSO/H_2O solvent, there is band broadening in absorption bands of **5**-NCP free-base ligand in contrast to its **5**-SnNCP dichlorotin(IV) complex (as shown in **Figure A.41**). This is due to undesirable aggregation effects that are likely decreased by the dichloro axial ligands of **5**-SnNCP Sn(IV) complex.

There are significant red shifts of one of the Q bands of the NCP dyes in non-polar solvents, such as benzene, into the deep NIR region at *ca.* 759 nm and 809 nm for **5**-NCP and **5**-SnNCP, respectively, compared to polar solvents. This has a direct implication on the sub-localization of the dye in the aqueous or non-polar lipid components of the cells and the light absorption properties of the dye during PDT and PACT [44]. The emission spectra of the studied N-confused porphyrin dyes are also significantly red shifted relative to those of their corresponding porphyrin

isomers and chlorins analogs (**Figure 4.8c**, **Table 4.3**). This trend is consistent with their UV-visible absorption profiles.

4.5.2 MCD properties of N-confused porphyrin

The MCD spectra of the **5**-SnNCP complex (**Figure 4.2**) consist of a pseudo-A_o term that is typical of a normal metalloporphyrin when ΔHOMO > ΔLUMO. This is consistent with TD-DFT calculations of **5**-SnNCP (see Chapter 10). However, it has been reported that MCD spectral features of NCP dyes are remarkably complex depending on the different variables involved [279,280]. For instance, the predominance of various tautomeric forms of NCP dyes determines the MCD sign pattern with protonation of outer NH, resulting in a reversal to ΔHOMO < ΔLUMO by a simple protonation [279,280]. These reports further showed that when the outer NH of the NCP dye is methylated for Ni(II) N-confused porphyrin, the ΔHOMO < ΔLUMO is observed. The MCD sign pattern for the methylated species is not easily reversed by simple deprotonation in contrast to the NH derivative [279,280].

4.6 Concluding remarks

The spectral changes due to the structure-property relationships related to the *meso*-aryl substituents, the central ion, and symmetry effects were carefully analyzed. The inductive and mesomeric effects from different *meso*-aryl substituents resulted in minor spectral changes. In the context of free-base ligands, the insertion of more electropositive central ions into porphyrin or porphyrin analog ligand cores resulted in significant red shifts of the B bands due to more favorable interactions with the macrocycles cores. For symmetry reasons, major spectral changes are evident with an intensification of Q bands in the therapeutic window observed for the chlorin and corrole dyes. Also, the isomerization of porphyrin to low symmetry N-confused porphyrin

resulted in significant red shifts of the B and Q bands of the dyes, with the Q bands lying deep in the therapeutic window. The broadening and band enhancement in the B and Q band region are evident upon conjugation of **1**-**4**-InPor and **1**-**4**-*meso*-triaryl P(V) and Ga(III) corroles to gold or silver nanoparticles. The trends in the optical properties of the dyes have a direct impact on the light-absorbing properties of the dye during PDT and PACT studies (Chapters 6-9), since a favorable PS for PDT and PACT should absorb light strongly deep in the therapeutic window.

CHAPTER FIVE

Photophysicochemical Properties of the Dyes

This chapter details the photophysicochemical, photostability, and lipophilicity properties of the porphyrin and porphyrin analog dyes studied to investigate the suitability of the dyes for use in PDT and PACT singlet oxygen applications.

5.0 Photophysicochemical properties of porphyrin and porphyrin analog dyes.

The photophysicochemical properties of the studied porphyrins, corroles, chlorins, and N-confused porphyrin dyes were evaluated to determine the suitability of the dyes for use as PS dyes in PDT and PACT singlet oxygen applications (Chapters 6-9). These photophysicochemical properties include fluorescence quantum yield (ϕ_F), fluorescence lifetime (τ_F), triplet lifetimes (τ_T), and singlet oxygen quantum yields (ϕ_Δ). The heavy atom effect is anticipated in the context of porphyrin and porphyrin analog dyes with sulfur and bromine atoms on their *meso*-aryl groups, metal ion centers, and conjugation to AuNPs and AgNPs. The heavy atom effect decreases the rate of fluorescence and enhances ISC to the triplet manifold resulting in higher singlet oxygen yields [46,115,181–184]. The photostabilities of the dyes studied and lipophilicities of the dye complexes are also discussed. Since these properties also have a direct implication on the sub-localization of the dyes in bacteria or tumor cells and the photodegradation behavior of the PS dye during PDT and PACT treatments [177,237]. The dyes studied are anticipated to exhibit favorable photophysicochemical properties, such as high photostabilities and balanced lipophilicities, and have high singlet oxygen quantum yields resulting in improved PDT and PACT activities (see Chapters 6-9). Since the photophysicochemical properties of **1**-InPor, **3**-InPor, and **1**-InPor AuNPs conjugate [209], A_3 *meso*-triaryl corroles (H_3TPCor, **1**-**3**-Cor, P^VTPCor, Ga^{III}TPCor, **1**-**3**-P^VCor, **1**-**3**-GaCor, **1**-**3**-P^VCor-AuNP and **1**-**3**-GaCor-AuNP nanoconjugates) [174] and A_2B *meso*-triaryl corroles (**9**-**10**-GaCor and **10**-GaCor-Q) [210] have already been published, a summary is provided in this context.

5.1 Photophysicochemical properties of porphyrin dyes

The photophysicochemical properties of H_2TPP and **1**-**4**-Por free-base porphyrins and their In(III) porphyrin complexes (InTPP, **1**-**4**-InPor), **1**-**4**-InPor-AgNP and **1**-**4**-InPor-AuNP nanoconjugates including **5**-**8**-Por and their Sn(IV) complexes (**5**-**8**-SnPor) in DMSO are summarized in **Table 5.1**.

The fluorescence quantum yield values (Φ_F) were obtained using a comparative method [185]. The methylthiophenyl and thienyl *meso*-aryl substituted porphyrins (**1**-**4**-Por, **1**-**4**-InPor) have low Φ_F values due to the heavy atom effect from the sulfur atoms. The In(III) and Sn(IV) porphyrin complexes also exhibit lower Φ_F values than those of their corresponding free-base porphyrin ligands (**Table 5.1**), since the heavy atom effect from In(III) and Sn(IV) metal ions quenches the fluorescence. A further reduction in the Φ_F values is evident for **1**-**4**-InPor-AgNPs and **1**-**4**-InPor-AgNPs relative to the corresponding dye complexes. This is due to the external heavy atom effects from AgNPs and AuNPs.

The fluorescence lifetimes (τ_F) values were also determined by exponential fitting of the fluorescence decay curves. The trends in the τ_F values of the studied porphyrins are consistent with their Φ_F values. For instance, the free-base porphyrin ligands (H_2TPP, **1**-**8**-Por) have higher τ_F values in the range of 1.21−7.02 ns in contrast to those of their corresponding In(III) and Sn(IV) porphyrin complexes, which lie at 0.24−1.13 ns range (**Table 5.1)**. This is due to the heavy atom effects of the In(III) and Sn(IV) ions. A further decrease in τ_F values is observed for **1**-**4**-InPor-AgNPs and **1**-**4**-InPor-AuNPs (**Table 5.1**) due to the external heavy atom effect from metallic AgNPs and AuNPs.

The transient absorption spectra and triplet state decay curves in DMSO of the porphyrin dyes studied were obtained using laser photolysis experiments (as shown in **Figure A 43** as examples).

Generally, the transient spectra of the studied porphyrin and porphyrin analog dyes exhibit broad spectra at 450−550 nm associated with triplet-triplet transitions (T_1-T_n) with ground state depletion also observed in the B and Q band regions (**Figure A 43**). The τ_T values of the studied porphyrin dye series vary significantly. For instance, H_2TPP and **1**-**4**-Por free-base porphyrin dyes have shorter triplet lifetimes in contrast to those of the In(III) porphyrin complexes due to their structural flexibility (**Table 5.1**). A further decrease in τ_T values is also observed for the **1**-**4**-InPor-AgNP and **1**-**4**-InPor-AuNP nanoconjugates due to combined heavy atom effects from sulfur atoms and AgNPs or AuNPs. However, **5**-**8**-Por have longer triplet lifetimes than the corresponding Sn(IV) complexes (**Table 5.1**). This could be due to the heavy atom effect in the context of Sn(IV) porphyrin complexes.

The Φ_Δ values of the studied porphyrins were determined using a chemical method by monitoring the rate of photodegradation of DBF singlet oxygen quencher (as shown in **Figure 5.1 a**, as an example). The Φ_Δ values for the free-base porphyrin dyes (H_2TPP, **1**-**8**-Por) ranged from 0.54−0.60. These values are lower than those of their corresponding In(III) and Sn(IV) porphyrin dyes, which lie in the 0.61−0.72 range. Since In(III) and Sn(IV) ions are heavy atoms, they enhance intersystem crossing to the triplet state, resulting in increased singlet oxygen production. There is also a further increase in the Φ_Δ values for **1**-**4**-InPor-AgNP and **1**-**4**-InPor-AgNP nanoconjugates in the 0.68−0.81 range in contrast to those of the corresponding dye complexes (**Table 5.1**). This is probably due to the external heavy atom effect of the AgNPs and AuNPs.

The photostabilities of the porphyrin dyes studied in 1% DMSO/H_2O were determined using UV-Visible spectroscopy by monitoring changes in the B band absorption intensities of dyes upon irradiation with laser light for 30 min. The photostabilities of free-base porphyrin dyes (*ca.* 15%)

are lower than those of their corresponding In(III) and Sn(IV) complexes, since they lack the stabilization effect at their frontier π-MOs from the high valent central metal ions. In contrast, **1**-**4**-InPor-AgNP and **1**-**4**-InPor-AuNP nanoconjugates have higher photostabilities than the corresponding **1**-**4**-InPor dyes (**Table 5.1**). This is due to the protective nature of AgNPs and AuNPs for effectively binding sulfur atoms, which protects the reactive sites of dye during singlet oxygen generation processes. Ideally, PS dyes must be stable under PDT or PACT conditions. However, the PS tends to undergo self-destructive oxidative photodegradation processes when generating singlet oxygen during PDT or PACT experiments resulting in unwanted harmful side products, which lower the PDT and PACT activities of the dyes [190–192].

The lipophilicities were determined by the shake-flask method [249]. The lipophilicities values of In(III) and Sn(IV) porphyrin complexes are provided in **Table 5.2.** A compound with Log P values between 0−5 has the proper balance in the localization of the drug in the aqueous and lipophilic regions of the cells with better cellular absorption, permeation, and biodistribution [281]. The Log $P_{o/W}$ values for In(III) porphyrins (InTPP, **1**-**4**-InPor) lie in the 2.0−2.50 range, while those of Sn(IV) porphyrin complexes (**5**-**8**-SnPor) lie between 1.07−1.58. These lipophilicity values suggest that Sn(IV) porphyrin complexes are less lipophilic than In(III) dyes. This can be attributed to the dichloro axial ligands of the Sn(IV) ion in contrast to the chloro axial ligand of In(III) porphyrins. The axial ligands can minimize aggregation effects at higher concentrations of the Sn(IV) porphyrin dyes resulting in enhanced cellular uptake and bioaccumulation in the cells[174].

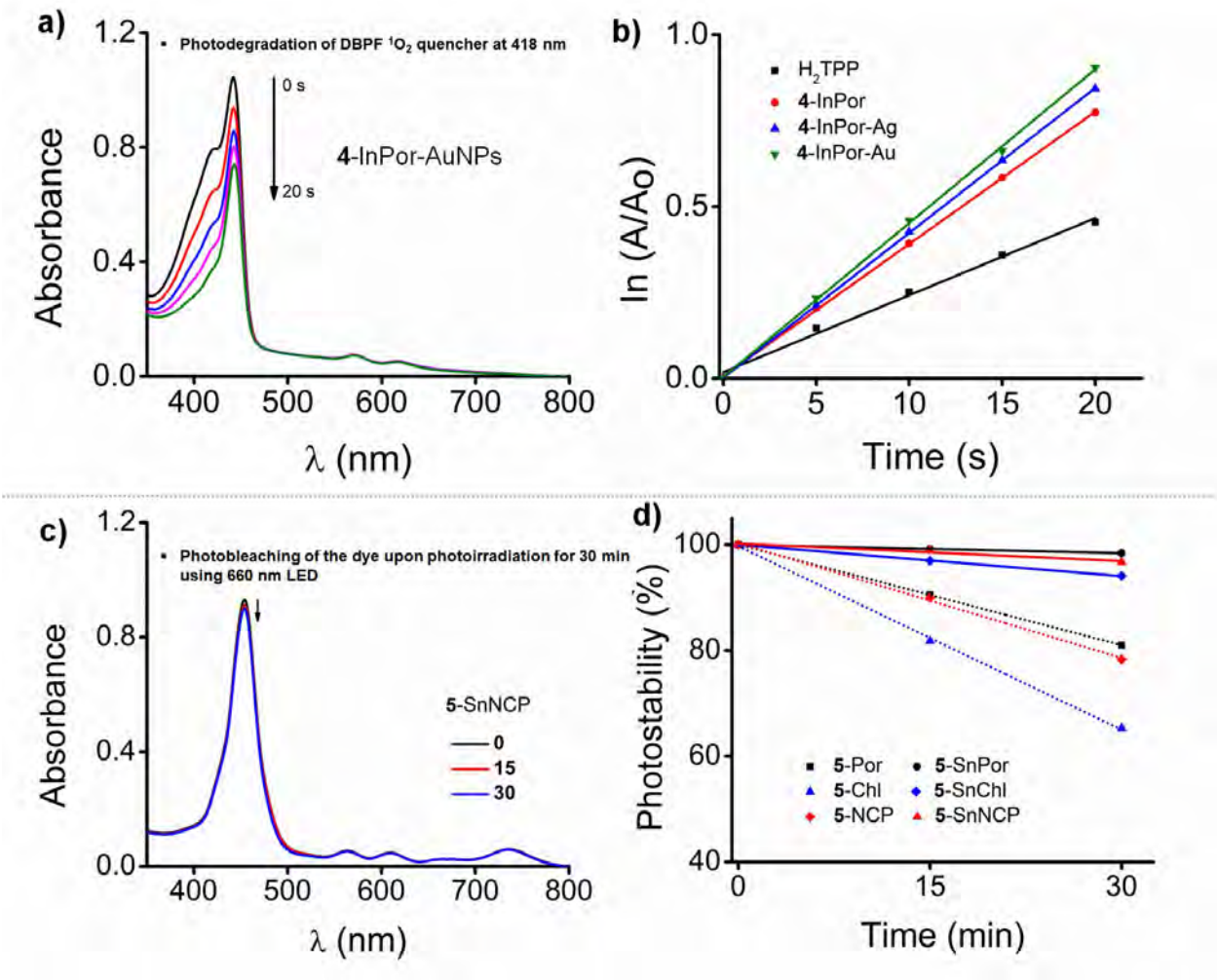

Figure 5.1: a) UV-visible absorption spectra of **4**-InPor-AuNPs in DMSO showing the photodegradation of DPBF singlet oxygen quencher at 418 nm for 20 s. b) Plot of change in the absorbance of DPBF against photoirradiation time for H_2TPP standard, **4**-InPor, **4**-InPor-AgNPs, and **4**-InPor-AuNPs. c) UV-visible absorption spectra of **5**-SnNCP in 1% DMSO/H_2O upon irradiation for 30 min with 660 nm LED; d) Plot of change in the absorbances of **5**-Por, **5**-SnPor, **5**-Chl, **5**-SnChl, **5**-NCP, and **5**-SnNCP dyes with time when photoirradiated with 660 nm LED for 30 min at 15 min time-interval.

Table 5.1: Photophysicochemical and photostability properties of free-base A_4 *meso*-tetraaryl free-base porphyrins, In(III) and Sn(IV) porphyrins and **1**-**4**-InPor-AgNP and **1**-**4**-InPor-AuNP nanoconjugates.

Sample	Φ_F ± 0.02	τ_F (ns) ± 0.01	τ_T (μs) ± 0.01	Φ_Δ ± 0.01	Photostability (%)
H_2TPP	0.065	7.02	20	0.54	85
1-Por	0.051	4.18	17	0.55	84
2-Por	0.036	3.08	18	0.57	82
3-Por	0.034	2.91	15	0.58	84
4-Por	0.016	1.21	11	0.6	80
InTPP	0.026[a]	1.13[a]	262	0.61[a]	95
1-InPor	0.01[a]	0.51[a]	267	0.63[a]	94
2-InPor	0.013	0.42	175	0.65	96
3-InPor	0.007[a]	0.44[a]	146	0.68[a]	96
4-InPor	0.006	0.28	25	0.72	95
1-InPor-AgNPs	0.008	0.42	199	0.68	97
1-InPor-AuNPs	0.005	0.41	86	0.7	98
2-InPor-AgNPs	0.007	0.34	68	0.72	97
2-InPor-AuNPs	0.006	0.32	21	0.7	98
3-InPor-AgNPs	0.005	0.32	47	0.74	98
3-InPor-AuNPs	0.006	0.28	19	0.73	99
4-InPor-AgNPs	0.004	0.2	16	0.77	97
4-InPor-AuNPs	0.005	0.19	14	0.81	98
A_4 *meso*-tetraaryl porphyrins and Sn(IV) complexes					
5-Por	0.043	5.33	239	0.57	81
6-Por	0.041	5.26	278	0.57	82
7-Por	0.039	4.71	239	0.55	79
8-Por	0.037	4.12	224	0.59	75
5-SnPor	0.023	0.65	198	0.67	97
6-SnPor	0.018	0.67	205	0.65	98
7-SnPor	0.015	0.45	193	0.65	95
8-SnPor	0.017	0.24	184	0.68	94

[a] Data reproduced from Reference [209].

Table 5.2: Water partition coefficient values (Log Po/w) of the studied A_4 *meso*-tetraaryl In(III) and Sn(IV) porphyrins.

A_4 *meso*-tetraaryl In(III) porphyrins	
Sample	**Log $P_{o/w}$ (± 0.01)**
InTPP	2.5
1-InPor	2.42
2-InPor	2.23
3-InPor	2.21
4-InPor	2.07
A_4 *meso*-tetraaryl Sn(IV) porphyrins	
5-SnPor	1.51
6-SnPor	1.58
7-SnPor	1.07
8-SnPor	1.21

5.2 Photophysicochemical properties of corrole dyes

The photophysicochemical properties of the studied A_3 and A_2B *meso*-triaryl corroles, including those of AgNP and AuNP nanoconjugates of **1**-**4**-P^{V}Cor and **1**-**4**-GaCor corrole dyes in DMSO, are summarized in **Table 5.3**. The Φ_F values of the A_3 free-base corroles (H_3TPCor, **1**-**4**-Cor) are comparable to those of their corresponding P(V) complexes (P^{V}TPCor, **1**-**4**-P^{V}Cor), since P(V) corroles are highly fluorescent [54,55,119,174]. The A_3 Ga(III) corroles (Ga^{III}TPCor, **1**-**4**-GaCor), on the other hand, have lower Φ_F values due to Ga(III) ion heavy atom effect [46,115,174]. A further reduction in Φ_F values is also evident for the AgNP and AuNP nanoconjugates of the A_3 **1**-**4**-P^{V}Cor and **1**-**4**-GaCor dyes due to the external heavy atom effect [174], while for A_2B *meso*-triaryl Ga(III) corrole dyes, the Φ_F values are comparable since the dyes have closely related structures [210]. The Φ_F values for A_2B Ga(III) corroles are higher than those of A_3 Ga(III) corroles. This is likely due to the presence of highly fluorescent carbazole moieties [282,283].

The fluorescence parameter values for the A_3 free-base corroles and their P^V corrole complexes are broadly comparable (**Table 5.3**). As would normally be anticipated based on high Φ_F values, A_3 free-base corroles and their A_3 P^V corroles have longer τ_F values (**Table 5.3**). In contrast, those of A_3 and A_2B Ga(III) complexes are shorter due to the heavy atom effect [174,210]. There is a further decrease in the τ_F values for the AgNP and AuNP nanoconjugates of the A_3 **1**-**4**-P^VCor and **1**-**4**-GaCor dyes in contrast to those of the corrole complexes alone due to the external heavy atom effect [174].

The triplet lifetimes (τ_T) values of A_3 and A_2B *meso*-triaryl corroles vary significantly due to several different factors. This is consistent with the observed trends for porphyrin dyes discussed earlier. For instance, A_3 free-base corroles have shorter triplet lifetimes due to their flexible structures, which can enhance nonradiative decay processes [174]. The A_3 Ga(III) corroles also exhibit shorter triplet lifetimes relative to their A_3 P(V) counterparts due to the heavy atom effect (**Table 5.3**). The AgNP and AuNP nanoconjugates of **1**-**4**-P^VCor and **1**-**4**-GaCor dye exhibit shorter triplet lifetimes due to the combined heavy atom effects from the metallic nanoparticles and sulfur atoms on the *meso*-aryl substituents of the dyes [174]. On the other hand, the τ_T values (the values in brackets in **Table 5.3**) of the A_2B *meso*-triaryl Ga(III) corroles are comparable in the presence of oxygen (in unpurged solutions). However, in N_2 purged solutions, the τ_T values of **9**-GaCor and **10**-GaCor are high in contrast to the quaternized **10**-GaCor-Q dye [210]. This is due to the high sensitivity of quaternized dye to the changes in solution conditions [284].

The Φ_Δ values for A_3 free-base corroles are low (**Table 5.3**). This is normally anticipated for highly fluorescent compounds, since these processes are competitive [46]. On the other hand, the A_3 Ga(III) corroles have higher Φ_Δ values than those of their A_3 P(V) corrole counterparts. The Φ_Δ

values of A_2B Ga(III) corroles are also high and comparable among the dyes in this series due to their broadly similar structural properties [210]. The heavy atom effect in the context of A_3 and A_2B Ga(III) corroles likely enhanced ISC to triplet resulting in increased singlet oxygen generation [46,174]. There is also a further increase in the Φ_Δ values of AgNP and AuNP nanoconjugates of A_3 **1**-**4**-P^VCor and **1**-**4**-GaCor P(V) and Ga(III) corroles in contrast to those of the parent complexes alone. This is due to the external heavy atom effects [174], while the Φ_Δ values for the A_2B Ga(III) corroles are comparable, since the dyes have very similar structures [210].

The rate of photobleaching of the studied A_3 and A_2B *meso*-triarylcorrole dyes was determined in 1% DMSO/H_2O and also under physiological conditions in 1% DMSO/DMEM cell culture media solution for A_3 **3**-PVCor and **3**-GaCor and their **3**-PVCor-AuNP and **3**-GaCor-AuNP nanoconjugates. The photostability values of the corroles are summarized in **Table 5.3**. The difference in the rates of photobleaching for **3**-P^VCor and **3**-GaCor and their **3**-P^VCor-AuNPs and **3**-GaCor-AuNP nanoconjugates are negligible in 1% DMSO/H_2O and under physiological conditions (**Table 5.3** in brackets).

The A_3 free-base corrole dyes have lower photostabilities (*ca.* 20%) than the corresponding P(V) and Ga(III) complexes. This is due to the lack the stabilization effect at the frontier π-MOs of free-base corrole from the high valent central ions, which can limit the photodegradation processes [174]. The A_3 and A_2B Ga(III) corroles have slightly higher photostability values than A_3 P(V) corroles due to their greater structural rigidity. A further increase in photostability is evident for AgNP and AuNP nanoconjugates of A_3 **1**-**4**-P^VCor and **1**-**4**-GaCor corrole dyes (**Table 5.3**). This is due to the protective effects of the AgNPs and AuNPs, which bind effectively to sulfur atoms and protect the reactive sites of the dye from self-degradation during singlet oxygen generation.

The lipophilicities values of A_3 and A_2B *meso*-triaryl corrole complexes (**Table 5.4**) are within the optimal 0−5 lipophilic balance range for drugs [281]. The Log $P_{o/W}$ values for A_3 P(V) porphyrin complexes are slightly lower than those of their Ga(III) counterparts. This suggests that A_3 P(V) complexes are less lipophilic. This can be attributed to the dihydroxy axial ligands of the P(V) ion in contrast to the pyridyl axial ligand in the context of A_3 Ga(III) corroles [174]. The lipophilicity value of positively charged **10**-GaCor-Q is also less than those of uncharged **9**-**10**-GaCor A_2B *meso*-triarylcorrole dyes. The dihydroxy axial ligands of A_3 P(V) corroles and positive charge for **10**-GaCor-Q can minimize aggregation effects at higher concentrations of the dyes and enhance cellular uptake in the bacteria and tumor cells [174,210].

Table 5.3: Photophysicochemical and photostability properties of A_3 and A_2B *meso*-triaryl corroles, including the AgNP and AuNP nanoconjugates of **1**-**4**-P^{V}Cor and **1**-**4**-GaCor.

A_3 *meso*-triaryl corroles					
Sample	**Φ_F** ± 0.02	**τ_F** (ns) ± 0.01	**τ_T** (µs) ± 1	**Φ_Δ** ± 0.01	**Photostability** (%)
H_3TPCor	0.11	6.26	16	0.28	69
1-Cor	0.086	3.5	14	0.3	64
2-Cor	0.041	3.37	13	0.32	75
3-Cor	0.035	3.25	13	0.35	79
4-Cor	0.031	2.32	11	0.40	76
P^{V}TPCor	0.042	3.95	155	0.41	77
1-P^{V}Cor	0.052	3.6	188	0.42	78
2-P^{V}Cor	0.042	3.28	92	0.44	82
3-P^{V}Cor	0.036	3.1	92	0.47	84 (85.9)
4-P^{V}Cor	0.027	2.72	79	0.59	79
Ga^{III}TPCor	0.034	3.26	37	0.57	85
1-GaCor	0.041	3.08	46	0.6	85
2-GaCor	0.037	2.74	34	0.63	88
3-GaCor	0.032	2.62	33	0.69	89(89.4)
4-GaCor	0.018	2.07	27	0.72	82
1-P^{V}Cor-AgNPs	0.036	2.67	108	0.47	92
1-P^{V}Cor-AuNPs	0.027	2.2	122	0.49	98
2-P^{V}Cor-AgNPs	0.031	2.46	49	0.52	90
2-P^{V}Cor-AuNPs	0.021	2.02	83	0.47	99

3-P^{V}Cor-AgNPs	0.028	2.25	60	0.49	91
3-P^{V}Cor-AuNPs	0.014	1.82	48	0.51	94(93.8)
4-P^{V}Cor-AgNPs	0.018	1.66	38	0.63	91
4-P^{V}Cor-AuNPs	0.011	1.29	44	0.67	94
1-GaCor-AgNPs	0.026	1.85	22	0.64	97
1-GaCor-AuNPs	0.025	1.93	25	0.67	97
2-GaCor-AgNPs	0.023	1.99	23	0.68	98
2-GaCor-AuNPs	0.017	1.73	26	0.72	99
3-GaCor-AgNPs	0.019	1.84	21	0.69	95
3-GaCor-AuNPs	0.008	1.48	27	0.74	97(96.5)
4-GaCor-AgNPs	0.012	1.12	19	0.75	96
4-GaCor-AuNPs	0.01	0.87	14	0.73	98
A_2B *meso*-triaryl corroles					
9-GaCor	0.071	1.63	255 (33)	0.66	92
10-GaCor	0.073	1.54	193 (48)	0.67	94
10-GaCor-Q	0.062	1.74	42 (26)	0.64	91

Data reproduced from References [174] and [210]. Data for **4**-Cor, **4**-P^{V}Cor, and **4**-GaCor, and the AgNP nanoconjugates of **1**-**4**-P^{V}Cor, and **1**-**4**-GaCor, including AuNP nanoconjugates of **4**-P^{V}Cor and **4**-GaCor have not been reported previously.

Table 5.4: Water partition coefficient values (Log $P_{o/w}$) of the studied A_3 *meso*-triaryl P(V) and Ga(III) corroles, including A_2B *meso*-triaryl Ga(III) corroles.

A_3 *meso*-triaryl P^{V} and Ga^{III} corroles	
P^{V}TPCor	1.31
1-P^{V}Cor	1.27
2-P^{V}Cor	1.1
3-P^{V}Cor	1.04
4-P^{V}Cor	0.91
GaTPC	2.01
1-GaCor	1.87
2-GaCor	1.83
3-GaCor	1.76
4-GaCor	1.61
A_2B *meso*-triaryl Ga^{III} corroles	
9-GaCor	1.74
10-GaCor	1.44
10-GaCor-Q	1.01

5.3 Photophysicochemical properties of chlorin dyes

The photophysicochemical properties of the studied A_4 *meso*-tetraaryl chlorins in DMSO are summarized in **Table 5.5**. The free-base chlorins (**5**-**8**-Chl) have higher fluorescence quantum yield (Φ_F) values and longer fluorescence lifetimes (τ_F) (**Table 5.5**) that are slightly higher than those of their parent **5**-**8**-Por analogs (**Table 5.1**). This is consistent with the reported fluorescence trends of chlorin dyes related to their flexible structural changes [285–287]. The Φ_F and τ_F values of **5**-**8**-Chl decreased significantly on metalation of the dyes to **5**-**8**-SnChl complexes due to the Sn(IV) ion heavy atom effect [50].

The triplet lifetime (τ_T) values of free-base chlorins (**5**-**8**-Chl) are also longer than those of their corresponding Sn(IV) chlorins (**5**-**8**-SnChl). This is due to the heavy atom effect in the context of Sn(IV) chlorin complexes [50]. The free-base chlorins (**5**-**8**-Chl) have relatively high Φ_Δ values that lie in the 0.59−0.62 range and are comparable to those of their parent porphyrins (**Table 5.1**, **Table 5.5**). This can likely be attributed to effective quenching processes in the transfer of energy by the triplet state of chlorin dyes to molecular oxygen [286]. The Φ_Δ values of **5**-**8**-SnChl, on the other hand, are higher than those of the free-base chlorins due to the heavy atom effect [50].

The photostabilities in 1% DMSO/H_2O solutions of the chlorins studied are summarized in **Table 5.5**. The free-base chlorins have low photostability values (*ca.* 35%) in contrast to those of their parent porphyrin dyes and their Sn(IV) chlorin complexes (**Table 5.5**). This is due to the flexible structural properties of free-base chlorins since they lack the stabilization effect at the frontier π-MOs from a high valent metal ion [145]. The photostabilities of Sn(IV) chlorins are higher and comparable to those of their Sn(IV) porphyrin analogs. This is due to their greater structural rigidity and the heavy atom effect [50].

The lipophilicities values of Sn(IV) chlorin dyes lie at 1.0−1.4 (**Table 5.6**) and are comparable to those of their Sn(IV) porphyrin analogs (**Table 5.2**). These values lie in the optimal lipophilic balance range for drugs [281]. The lipophilicities values obtained suggest that Sn(IV) chlorin complexes are less lipophilic. This can be attributed to the dichloro axial ligands of the Sn(IV) ion, in a similar manner to those of their Sn(IV) porphyrin analogs. The dichloro axial ligands can minimize aggregation effects at higher concentrations of the dyes and enhance cellular uptake [174,210].

Table 5.5: Photophysicochemical and photostability properties of **5**-**8**-Chl and **5**-NCP and their Sn(IV) complexes.

A_4 *meso*-tetraaryl chlorins					
Sample	**Φ_F** ± 0.02	**τ_F** (ns) ± 0.01	**τ_T** (μs) ± 1	**Φ_Δ** ± 0.01	**Photostability** (%)
5-Chl	0.121	6.25	181	0.61	65
6-Chl	0.084	6.56	188	0.59	67
7-Chl	0.098	5.76	189	0.58	64
8-Chl	0.074	5.6	111	0.62	63
5-SnChl	0.018	0.67	87	0.71	94
6-SnChl	0.015	0.75	85	0.7	96
7-SnChl	0.014	0.35	96	0.69	90
8-SnChl	0.012	0.28	81	0.74	88
A_4 *meso*-tetraaryl N-confused porphyrins					
5-NCP	0.012	1.23	166	0.26	78
5-SnNCP	0.007	0.22	108	0.85	96

Table 5.6: Water partition coefficient values (Log $P_{o/w}$) of the A_4 *meso*-tetraaryl Sn(IV) chlorins and N-confused porphyrin.

Sn(IV) A_4 *meso*-tetraaryl chlorins	
5-SnChl	1.44
6-SnChl	1.39
7-SnChl	0.96
8-SnChl	1.09
Sn(IV) A_4 *meso*-tetraaryl N-confused porphyrin	
5-SnNCP	1.27

5.4 Photophysicochemical properties of N-confused porphyrin dyes

The photophysicochemical properties of the studied A_4 *meso*-tetraaryl N-confused porphyrin dyes in DMSO are summarized in **Table 5.5**. The free-base N-confused porphyrin (**5**-NCP) has a very low fluorescence quantum yield (Φ_F) and a shorter fluorescence lifetime (τ_F) than its **5**-Por isomer (**Table 5.1**) and **5**-Chl counterpart (**Table 5.5**). The observed fluorescence behavior is normally anticipated for N-confused porphyrin dyes due to the inversion of the inner NH to the outer ring of a porphyrin isomer [165]. A further reduction in the Φ_F and τ_F values is observed for the **5**-SnNCP complex due to the heavy atom effect. The triplet lifetimes (τ_T) for **5**-NCP and its Sn(IV) complex (**5**-SnNCP) are longer (**Table 5.5**). This is anticipated to enhance the generation of singlet oxygen and hence, the suitability of the dyes as photosensitizer dyes for PDT and PACT use.

In contrast, the obtained Φ_Δ value is significantly lower for **5**-NCP free-base N-confused porphyrin (**Table 5.5**) than that of its **5**-Por isomer (**Table 5.1**) and **5**-Chl counterpart (**Table 5.5**). This anomalous behavior of **5**-NCP is consistent with the reported Φ_Δ values of free-base N-confused porphyrins [44,288–290]. This can be attributed to the enhanced intramolecular vibrational

relaxation processes arising from higher degrees of freedom in free-base N-confused porphyrin structure, which competitively dissipates the singlet oxygen generation processes [289]. On the other hand, the Φ_Δ value of **5**-SnNCP is unusually high relative to those of its Sn(IV) porphyrin isomer (**5**-SnPor) (**Table 5.1**) and chlorin (**5**-SnChl) analog (**Table 5.5**). This is due to the heavy atom effect and enhanced structural rigidity for **5**-SnNCP, which results in enhanced ISC to the triplet excited state and effective conversion of molecular oxygen to generate a high amount of singlet oxygen [44].

The photostability values of **5**-NCP and **5**-SnNCP in 1% DMSO/H_2O are provided in **Table 5.5**. The values obtained show that the NCP dyes studied are photostable. The photostability value of **5**-NCP (*ca.* 22%) is comparable to that of its **5**-Por isomer (**Table 5.1**). This value is lower than that of the **5**-SnNCP Sn(IV) complex (**Table 5.5**). This is due to the flexible structural features of the free-base NCP ligand since it lacks the high valent metal ion, which can result in an enhanced stabilization effect at the frontier π-MOs. There is a high photostability value for **5**-SnNCP, which is comparable to that of its **5**-SnPor isomer (**Table 5.1**). This high value is due to the heavy atom effect of the Sn(IV) ion and the greater structural rigidity of the dye, which decreases the photobleaching processes.

The lipophilicities value of **5**-SnNCP lies at 1.27. This value is within the 0−5 optimal lipophilic balance range and slightly lower than that of its **5**-SnPor isomer (**Table 5.2**) and **5**-SnChl counterpart (**Table 5.5**). This suggests that the **5**-SnNCP complex is less lipophilic. This could be due to its characteristic inverted inner amine (NH) to the outer perimeter of the porphyrin ring, which can minimize aggregation effects at higher dye concentrations and enhance cellular uptake and bioaccumulation in the aqueous and lipophilic regions of the cells.

5.5 Concluding remarks

The trends in the photophysicochemical, photostability, and lipophilicity properties of the studied porphyrin and porphyrin analog dyes are inherently dependent on their structural modification properties related to the *meso*-aryl substituents, the central ion, symmetry effects, and heavy atom effects. The heavy atom effect from the *meso*-aryl groups, core coordination ion, and external heavy atom effect from AuNP and AgNP significantly decreases the fluorescence parameter values resulting in high singlet oxygen quantum yields. The studied dye complexes are highly photostable with properly balanced lipophilic properties. The photophysicochemical, photostability, and lipophilic values of dyes are anticipated to have a direct impact on the PDT and PACT activities of the dyes (see Chapters 6-9).

CHAPTER SIX

Singlet Oxygen Applications of Porphyrin Dyes

This chapter discusses the *in vitro* PDT and PACT activities of porphyrin dyes toward MCF-7 breast cancer cells and planktonic and biofilm cells of *S. aureus* and *E. coli* bacteria to analyze their suitability for use as photosensitizer dyes in PDT.

6.0 Introduction

The porphyrin dyes studied in this work are neutral PS dyes. The effects of structural modifications related to the different *meso*-aryl groups, In(III) and Sn(IV) coordination ions, and nanoparticle conjugation (AgNPs and AuNPs) effects in the context of **1**-**4**-InPor on the PDT and PACT activities of porphyrin dyes are closely examined. It is anticipated that the porphyrin dyes in this work will exhibit favorable PDT and PACT activities, since they have relatively high ϕ_Δ values > 0.55, relatively high photostabilities > 70%, and properly balanced lipophilicity values.

6.1 PDT and PACT activities of In(III) porphyrin dyes

The PDT activities of **1**-InPor, **3**-InPor, and **1**-InPor-AuNP nanoconjugate have already been reported [209], and a summary is provided in this context. **1**-**4**-InPor and their AgNP and AuNP nanoconjugates were used as PS dyes for PACT studies.

6.1.1 *In vitro* PDT cytotoxicity studies of In(III) porphyrins

Figure 6.1 provides the dark cytotoxicity and phototoxicity plots of MCF-7 cancer cells treated with **1**-InPor, **3**-InPor, and **1**-InPor-AuNP conjugates over a 3−40 μg.mL^{-1} concentration range in the dark and under 10 min illumination at a fixed light dose of 144 J.cm^{-2} from a 625 nm Thorlabs LED. **Table 6.1** provides a summary of the IC_{50} values and phototoxicity index (PI) ratios of **1**-InPor, **3**-InPor, and the **1**-InPor-AuNP nanoconjugate dyes, including cell viability values in the dark and after illuminations at 40 μg.mL^{-1} of the dyes. Ideally, a favorable PS dye for PDT use must exhibit high cytocidal activities upon illumination with either no or minimal cytocidal activities in the absence of illumination (dark) [3–5]. Dark cytotoxicity is one of the undesirable features of PS dyes used in PDT, since it results in indiscriminate cytocidal activities toward both healthy and cancerous cells [3–5].

The IC_{50} values of **1**-InPor, **3**-InPor, and **1**-InPor-AuNP conjugates are > 40 μg.mL^{-1} in the dark (**Table 6.1**). However, **3**-InPor exhibited some dark cytotoxicity with cell viabilities ≥ 49% at the highest concentration (40 μg.mL^{-1}) of the dye (**Figure 6.1**, **Table 6.1**). The cell viabilities of **1**-InPor increased upon conjugation to AuNPs to form **1**-InPor-AuNP nanoconjugate, from ≥67% to ≥ 89% at the highest concentration (40 μg/mL). This suggests that conjugation of the dye to AuNPs significantly lowered the dark cytotoxicity [209]. Generally, the *in vitro* dark cytotoxicity activities of **1**-InPor, **3**-InPor, and **1**-InPor-AuNPs suggest that these dyes are relatively innocuous toward MCF-7 cancer cells in the dark [209].

1-InPor, **3**-InPor, and **1**-InPor-AuNPs under illumination have relatively low IC_{50} values, high PI > 3.3, and low cell viability values ≤ 21% (at higher dye concentration) (**Figure 6.1**, **Table 6.1**). This suggests that the studied In(III) porphyrin dyes have favorable PDT activities, possibly due to their high ϕ_Δ values. Interestingly, the PDT activity of the **1**-InPor-AuNP nanoconjugate is significantly enhanced relative to that of the parent **1**-InPor dye. This is demonstrated by the much lower IC_{50} and cell viability values, including a higher PI ratio for the **1**-InPor-AuNP nanoconjugate. This is due to the favorable synergistic effects of the AuNPs that include higher ϕ_Δ values, enhanced drug delivery properties, and the enhanced permeability and retention effect [209].

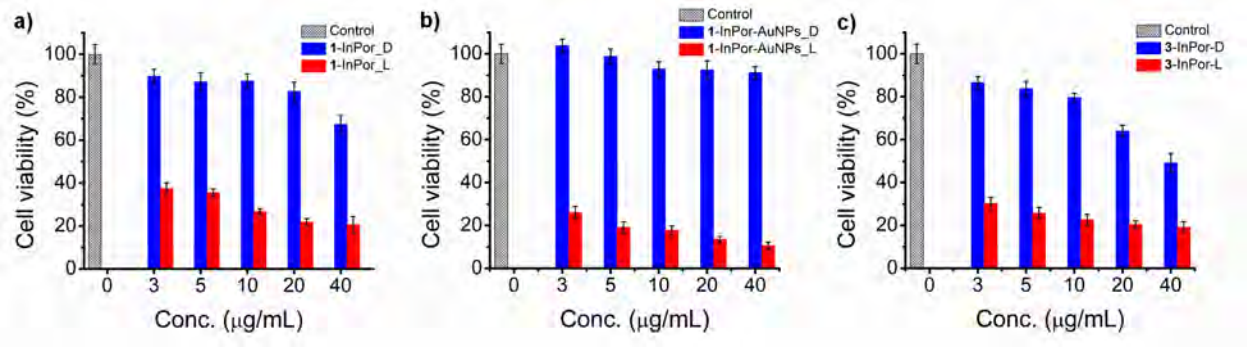

Figure 6.1: Percentage cell viabilities in the dark (blue) and after illumination for 10 min (red) upon treatment with 3–40 μg/mL of **1**-InPor, **1**-InPor-AuNPs, and **3**-InPor dyes. Reproduced with permission from Reference [209]. Copyright © World Scientific 2019.

Table 6.1: IC_{50}, PI, and cell viability values for **1**-InPor, **3**-InPor, and **1**-InPor-AuNPs against MCF-7 cancer cells.

Sample	IC_{50} (μg/mL)		PI[d]	Cell viability (%) at 40 μg.mL^{-1}	
	Dark[a]	Light[b]		Dark[a]	Light[b]
1-InPor	> 40	15.1	3.30	67	21
1-InPor-AuNPs	> 40	8.78	5.69	89	11
3-InPor	> 40	11.4	4.38	49	19

[a] 24 h incubation dark cytotoxicity data, [b]phototoxicity data against MCF-7 cancer cell line upon exposure to a Thorlabs 625 nm LED (240 mW.cm^{-2}, 10 min). [d]PI = phototoxic index (dark and light IC_{50} values toxicity ratio). Reproduced from Reference [209].

6.1.2 *In vitro* PACT cytotoxicity studies of In(III) porphyrins on the planktonic and biofilm cells of *S. aureus* and *E. coli* bacteria.

1-**4**-InPor and their AgNP (**1**-**4**-InPor-AgNPs) and AuNP (**1**-**4**-InPor-AuNPs) nanoconjugates exhibited minor dark toxicities toward the planktonic and biofilm cells of *S. aureus* and *E. coli* (as shown in **Figures A 44** and **Figure 46** in the Appendix as examples). These dyes also showed significant cytotoxic activities toward the planktonic and biofilm cells of *S. aureus* and *E. coli* bacteria after illumination with a PS dye. This shows that singlet oxygen is indeed the main

cytocidal agent that inactivates the planktonic and biofilm cells of *S. aureus* and *E. coli* bacteria during PACT, as anticipated in the context of tetrapyrrolic macrocycle PS dyes, such as porphyrins [7,18,23].

6.1.2.1 *In vitro* PACT activities of In(III) porphyrins on planktonic *S. aureus* and *E. coli* bacteria

The concentration optimization study results showed that **1**-**4**-InPor In(III) porphyrin dyes have higher PACT activities toward *S. aureus* at lower concentrations than is the case with *E. coli* (**Figure A 45**). This trend is normally anticipated in the context of neutral PS dyes, such as **1**-**4**-InPor. Neutral PS dyes are not as effective in inactivating Gram-(−) bacteria species, such as *E. coli*, in contrast *to S. aureus*, due to an effective negatively charged double layer permeability barrier of Gram-(−) bacteria that restricts the penetration of many dyes [18,21,23]. 2.5 $\mu g.mL^{-1}$ for *S. aureus* and 10 $\mu g.mL^{-1}$ for *E. coli* were then used in the time-dependent studies to provide a comparison of the PACT activities of **1**-**4**-InPor and their AgNP and AuNP nanoconjugates. **Table 6.2** summarizes the time-dependent Log_{10} reduction values and cell survival values for In(III) porphyrin dyes (**1**-**4**-InPor) and their AgNP (**1**-**4**-InPor-AgNPs) and AuNP (**1**-**4**-InPor-AuNPs) nanoconjugates toward planktonic and biofilm cells of *S. aureus*, and *E. coli* after 75 min irradiation at 625 nm with an M625L3 Thorlabs LED.

After illumination, **1**-**4**-InPor PS dyes exhibited favorable PACT activities toward *S. aureus* with high log reduction values in the range of 4.28−7.69 Log10 $CFU.mL^{-1}$ after 75 min illumination (**Figure 6.2**, **Table 6.2**). The PACT activities of **1**-**4**-InPor dyes against planktonic *S. aureus* were significantly enhanced upon conjugation to AgNPs (**1**-**4**-InPor-AgNPs) and AuNPs (**1**-**4**-InPor-AuNPs). This is demonstrated by the higher Log_{10} reduction values observed at shorter irradiation times (**Table 6.2**). The *meso*-thienyl porphyrins and their nanoconjugates (**2**-**4**-InPor, **2**-**4**-InPor-

AgNPs, **2**-**4**-InPor-AuNPs) also performed better by completely eradicating the planktonic *S. aureus* colonies at shorter irradiation times than for the *meso*-methylthiophenylporphyrins and their nanoconjugates (**1**-InPor, **1**-InPor-AgNPs, **1**-InPor-AuNPs) (**Table 6.2**). This is due to the higher ϕ_Δ values for the nanoconjugates and the favorable synergistic effects of AgNPs and AuNPs that enhance the microbial activity of the dyes [22,73,291], including the antimicrobial activities of thienyl derivatives [60]. The AgNPs and AuNPs alone did not exhibit significant PACT activities toward planktonic *S. aureus* and *E. coli* species with < 0.4 Log_{10} reduction values.

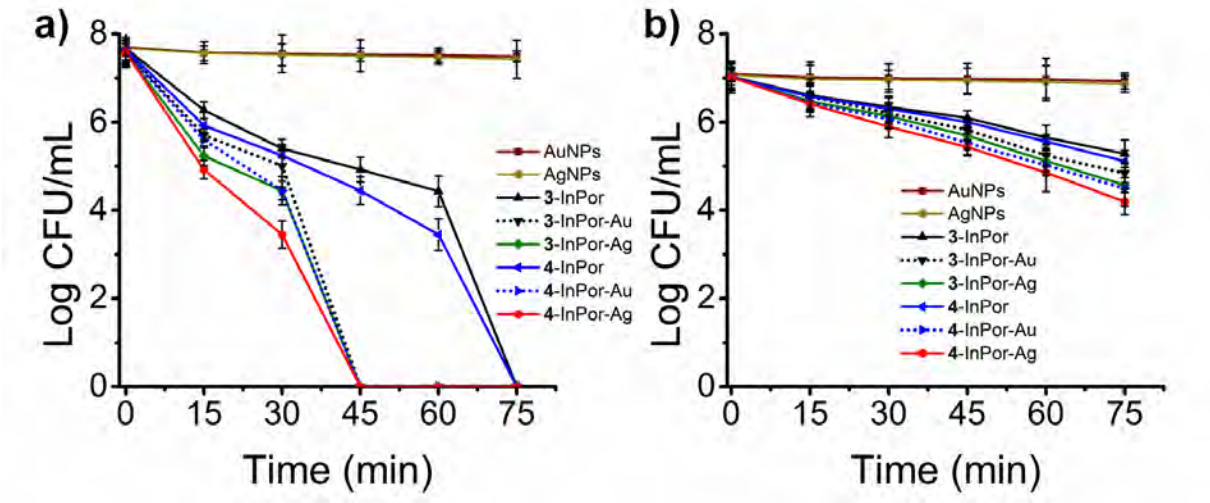

Figure 6.2: Log CFU.mL^{-1} plots of planktonic cells of a) *S. aureus* and b) *E. coli* upon treatment with gradient concentrations of AuNPs, AgNPs, **3**-**4**-InPor In(III)porphyrin dyes and their AgNP and AuNP nanoconjugates after 75 min irradiation at 625 nm with a Thorlabs M625L3 LED (240 mW.cm^{-2}).

In marked contrast, the **1**-**4**-InPor dyes have low Log_{10} reduction values for photoinactivation of *E. coli* in the range of 1.40−1.90, with ≥ 95% cell inactivation and ≤ 5% cell survival (**Figure 6.2b**, **Table 6.2**). This is anticipated since **1**-**4**-InPor are neutral PS dyes and are ineffective toward Gram-(−) bacteria due to the permeability barrier effects that restrict the PS drug penetration

[18,21]. The PACT activities of the **1**-**4**-InPor dyes were enhanced upon conjugation to AgNPs and AuNPs, resulting in moderate Log_{10} reduction values of 2.0−2.86 range, which denote ≥ 99% cell reduction and ≤ 1% cell survival (**Table 6.2**). These values are slightly lower than the optimal 3 Log_{10} value (99.9% cell reduction). According to the FDA of the USA, a molecular dye with > 3 Log_{10} CFU.mL^{-1} is classified as an efficient antimicrobial agent [292].

Table 6.2: Log reduction and cell viability values for In(III) porphyrin dyes against planktonic cells of *S. aureus* and *E. coli* in 1% DMSO/PBS after illumination at 625 nm with a Thorlabs M625L3 LED (240 mW.cm^{-2}).

	S. aureus			***E. coli***		
Sample	**Conc. μg.mL^{-1}**	**Log_{10} reduction**	**Cell survival (%)**	**Conc. μg.mL^{-1}**	**Log_{10} reduction**	**Cell survival (%)**
1-InPor	2.5	4.28 @75[a]	< 0.01	10	1.4	3.91
2-InPor	2.5	7.69 @75	0	10	1.73	1.85
3-InPor	2.5	7.69 @75	0	10	1.78	1.68
4-InPor	2.5	7.69 @75	0	10	1.9	1.28
AgNPs-alone	2.5	0.40 @75	0	10	0.21	63.8
1-InPor-AgNPs	2.5	7.69 @60	0	10	2.01	0.99
2-InPor-AgNPs	2.5	7.69 @45	0	10	2.44	0.37
3-InPor-AgNPs	2.5	7.69 @45	0	10	2.5	0.32
4-InPor-AgNPs	2.5	7.69 @45	0	10	2.86	0.14
AuNPs-alone	2.5	0.20 @75	0	10	0.17	68.4
1-InPor-AuNPs	2.5	7.69 @60	0	10	1.91	1.24
2-InPor-AuNPs	2.5	7.69 @45	0	10	2.14	0.72
3-InPor-AuNPs	2.5	7.69@45	0	10	2.21	0.6
4-InPor-AuNPs	2.5	7.69@45	0	10	2.5	0.31

[a] Illumination time in minutes used to achieve the Log_{10} reduction value is provided after the @ character.

6.1.2.2 *In vitro* PACT activities of In(III) porphyrins on the biofilms of *S. aureus* and *E. coli* bacteria

The concentration-dependence studies were performed over a 25−250 μg.mL^{-1} concentration range against *S. aureus* and *E. coli* biofilms followed by 30 min irradiation at 625 nm with a Thorlabs M625L3 LED (light dose of 432 J.cm^{-2}). The viable cells were quantified using the crystal

violet assay (**Figure 6.3a-b**). The **1**-**4**-InPor and their AgNP (**1**-**4**-InPor-AgNPs) and AuNP (**1**-**4**-InPor-AuNPs) nanoconjugates exhibited significant photoinactivation effects at higher concentrations of the dyes. 50 $\mu g.mL^{-1}$ of the dyes for *S. aureus* biofilms and 100 $\mu g.mL^{-1}$ of the dyes for *E. coli* biofilms were identified as the optimal concentrations for further use during time-dependent studies, since, at these concentrations, the illumination with the dyes resulted in ≤ 50% viable cells. These concentrations are higher than those used against the planktonic bacteria due to the lower susceptibility of biofilm bacteria species to the antimicrobial agents, since they have the polymeric matrix that secures the bacteria against adverse conditions and antimicrobial agents [25–27].

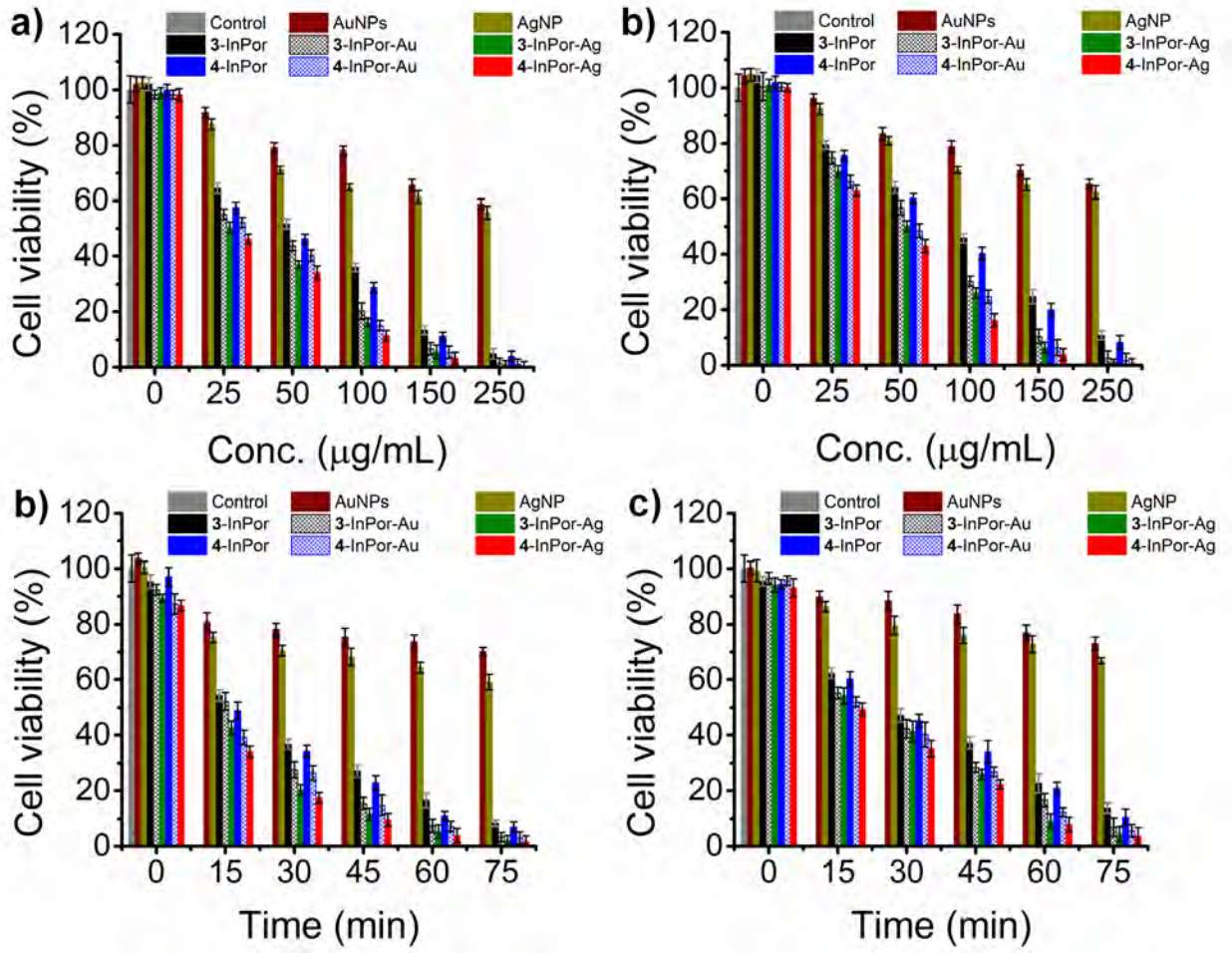

Figure 6.3: The cell viability (%) plots for biofilm cells of a) *S. aureus* and b) *E. coli* on treatment with gradient concentrations of AuNPs, AgNPs, **3**-**4**-InPor, and their AgNP and AuNP nanoconjugates after 30 min illumination at 625 nm with a Thorlabs M625L3 LED (240 $mW.cm^{-2}$) with quantification of viable cells carried out with the crystal violet stain. The cell viability plots of biofilm cells of c) *S. aureus* and d) *E. coli*, after treatment with c) 50 $\mu g.mL^{-1}$, and d) 100 $\mu g.mL^{-1}$, of AuNPs, AgNPs, **3**-**4**-InPor, and their AgNP and AuNP nanoconjugates after 75 min illumination at 625 nm with a Thorlabs M625L3 LED (240 $mW.cm^{-2}$). Viable cells were estimated using the viable colony count method.

Table 6.3 provides a summary of time-dependent Log_{10} reduction values and cell survival values for **1**-**4**-InPor and their AgNP (**1**-**4**-InPor-AgNPs) and AuNP (**1**-**4**-InPor-AuNPs) nanoconjugates after 75 min illumination. The PACT activities of **1**-**4**-InPor against biofilm cells of *S. aureus* and *E. coli* are relatively low in contrast to those of the planktonic bacteria. For instance, the Log reduction values for *E. coli* biofilms < 1 Log_{10} $CFU.mL^{-1}$ and those for *S. aureus* biofilms treated *meso*-thienyl porphyrins (**2**-**4**-InPor) are slightly higher ≥ 1 Log_{10} $CFU.mL^{-1}$ (**Figure 6.3b-c**, **Table 6.3**). Upon conjugation of **1**-**4**-InPor to AgNPs and AuNPs, the PACT activities of dyes were significantly enhanced against S*. aureus* and *E. coli* biofilms. This is demonstrated by moderate Log_{10} reduction values of ≥ 1 Log_{10} $CFU.mL^{-1}$ and ≤ 10% cell survival after 75 min irradiation reduction (**Table 6.3**). This is due to higher ϕ_{Δ} values and the enhanced synergistic action of nanoconjugates, such as favorable drug delivery and enhanced cellular uptake, which result in enhanced PACT action [22,291,293]. The AgNPs and AuNPs alone did not exhibit significant PACT activities toward the biofilm cells of *S. aureus* and *E. coli* species with < 0.2 Log_{10} reduction values.

Table 6.3: Log reduction and cell viability values for In(III) porphyrin dyes against biofilm cells of *S. aureus* and *E. coli* in 1% DMSO/PBS after illumination for 75 min at 625 nm with a Thorlabs M625L3 LED (240 mW.cm^{-2}).

	S. aureus			***E. coli***		
Sample	**Conc. μg.mL^{-1}**	**Log$_{10}$ reduction**	**Cell survival (%)**	**Conc. μg.mL^{-1}**	**Log$_{10}$ reduction.**	**Cell survival (%)**
1-InPor	50	0.79	16.3	100	0.61	24.4
2-InPor	50	1.00	10.0	100	0.8	15.8
3-InPor	50	1.07	8.4	100	0.86	13.9
4-InPor	50	1.16	7.0	100	0.92	12.0
AgNPs-alone	50	0.22	59.2	100	0.16	66.8
1-InPor-AgNPs	50	1.36	4.3	100	1.1	8.3
2-InPor-AgNPs	50	1.57	2.7	100	1.28	5.2
3-InPor-AgNPs	50	1.65	2.2	100	1.37	4.4
4-InPor-AgNPs	50	1.78	1.6	100	1.44	3.6
AuNPs-alone	50	0.15	70.2	100	0.12	73.1
1-InPor-AuNPs	50	1.25	5.6	100	1.02	9.3
2-InPor-AuNPs	50	1.41	3.9	100	1.11	7.7
3-InPor-AuNPs	50	1.47	3.4	100	1.16	6.9
4-InPor-AuNPs	50	1.51	3.1	100	1.24	5.7

6.2 PDT and PACT activities of Sn(IV) porphyrins

The PDT and PACT activities of **5**-**8**-Por free-base porphyrin ligands and their **5**-**8**-SnPor were assessed against MCF-7 cancer cells and the planktonic and biofilm cells of *S. aureus* and *E. coli* species.

6.2.1 *In vitro* PDT cytotoxicity studies of Sn(IV) porphyrins

The *in vitro* dark cytotoxicity and PDT activities of **5**-**8**-Por and **5**-**8**-SnPor dyes toward MCF-7 cancer cells were investigated over 0.39−25 μM gradient concentration of the drugs. **Figure 6.4** provides the cytotoxicity plots for MCF-7 cancer cells upon treatment with the gradient concentrations of **6**-**8**-SnPor dyes in the dark and under illumination at 625 nm with a Thorlabs M625L3 LED with a light dose of 288 J.cm^{-2} as representative examples. **Table 6.4** provides a

summary of IC_{50}, phototoxicity index (PI), and cell viability values in the dark and after illumination at the highest concentration (25 µM) of **5**-**8**-Por and **5**-**8**-SnPor dyes. **5**-**8**-Por and **5**-**8**-SnPor dyes exhibited IC_{50} > 25 µM values in the dark, with ≥ 70% viable cells at the highest concentrations (25 µM) of the PS dyes (**Figure 6.4**, **Figure A 47**, **Table 6.4**). This suggests that **5**-**8**-Por and **5**-**8**-SnPor have minimal dark cytotoxicity effects and are relatively innocuous toward MCF-7 cancer cells in the absence of illumination. For this reason, **5**-**8**-Por and **5**-**8**-SnPor are promising PS dye candidates for use in PDT

As would be anticipated based on their high ϕ_Δ values, **5**-**8**-SnPor exhibited enhanced PDT activities with IC_{50} values ≤ 16.5 µM, PI > 1.5, and low cell viability values ≤ 26.8% at 25 µM (**Figure 6.4**, **Table 6.4**). In contrast, **5**-**8**-Por free-base porphyrins have low PDT activities toward MCF-7 cancer cells under illumination at a fixed light dose of 280 $J.cm^2$, in contrast to **5**-**8**-SnPor (**Table 6.4**). This is demonstrated by their higher IC_{50} values of ≤ 24.7 µM, slightly lower phototoxicity indices > 1, and higher cell viability values of ≤ 46.5% at 25 µM

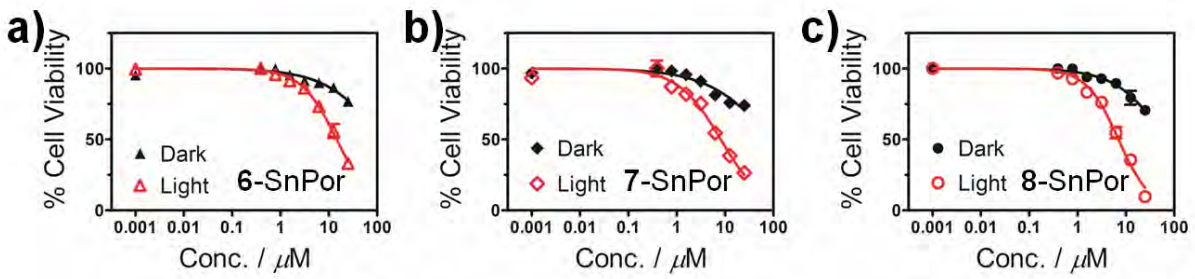

Figure 6.4: Cytotoxicity plots of MCF-7 cancer cells in the dark (black line) and under illumination (red line) with M625L3 Thorlabs LED at 625 for 20 min for a) **6**-SnPor, b) **7**-SnPor and c) **8**-SnPor.

The effects of different *meso*-aryl substituents on the PDT activities of **5**-**8**-Por and **5**-**8**-SnPor dyes are also evident, with higher PDT activities observed for *meso*-vanillic derivatives (**8**-Por, **8**-SnPor)

as well as -4-hydroxyphenyl derivatives (**7**-Por, **7**-SnPor) in contrast to *meso*-methoxyphenyl derivatives (**5**-**6**-Por and **5**-**6**-SnPor). This could be due to the reported anticancer properties of vanillic and phenolic derivatives [294–296].

Table 6.4: IC_{50}, PI, and cell viability values for **5**-**8**-Por and **5**-**8**-SnPor dyes against MCF-7 cancer cells.

	IC_{50} (μM)		PI[c]	Cell viability (%) at Conc. 25 μM	
Sample	**Dark[a]**	**Light[b]**		**Dark[a]**	**Light[b]**
5-Por	> 25	24.7	< 1	89.7	46.5
6-Por	> 25	23.6	1.1	87.5	44.5
7-Por	> 25	18.1	1.4	77.3	38.9
8-Por	> 25	17.8	1.4	71.2	32.7
5-SnPor	> 25	14.7	1.7	83.1	26.8
6-SnPor	> 25	16.5	1.5	76.8	24.1
7-SnPor	> 25	11.2	2.2	73.9	22.4
8-SnPor	> 25	7.1	3.5	70.6	18.7

[a] 24 h incubation dark cytotoxicity data, [b]phototoxicity data against MCF-7 cancer cell line upon exposure to a Thorlabs 625 nm LED 240 $mW.cm^{-2}$, 20 min). [c]PI = phototoxic index (dark and light IC_{50} values toxicity ratio).

6.2.2 *In vitro* PACT cytotoxicity studies of Sn(IV) porphyrins on the planktonic and biofilm cells of *S. aureus* and *E. coli* bacteria.

5-**8**-Por and their **5**-**8**-SnPor have minor dark cytotoxicity activities toward planktonic and biofilm cells of *S. aureus* and *E. coli* species (**Figure A 48**-**50**).

6.2.2.1 *In vitro* PACT activities of Sn(IV) porphyrins on planktonic *S. aureus* and *E. coli* bacteria

1 μM for *S. aureus* and 5 μM for *E. coli* were identified as the optimal concentrations of the dyes (**Figure A 48**) for use during time-dependent studies. **Table 6.5** summarizes the time-dependent Log_{10} reduction values and cell survival values for **5**-**8**-Por and their **5**-**8**-SnPor dyes toward planktonic and biofilm cells of *S. aureus*, and *E. coli* after 75 min irradiation at 625 nm with

M625L3 Thorlabs LED. **5**-**8**-Por and their **5**-**8**-SnPor dyes have favorable PACT activities toward planktonic *S. aureus* with high Log_{10} reduction values of 7.62 at 75 min (**Figures 6.5**, **Table 6.5**). **5**-**8**-SnPor dyes have higher PACT activities toward planktonic *S. aureus* than the corresponding **5**-**8**-Por free-base ligands (**Figure 6.5**). This is demonstrated by the complete eradication of *S. aureus* colonies at a shorter irradiation time of 30 min with high Log_{10} reduction values of 7.62 (**Figure 6.5a**, **Table 6.5**). This is due to their high ϕ_Δ values because of the heavy atom effect associated with the Sn(IV) ion of the Sn(IV) porphyrins.

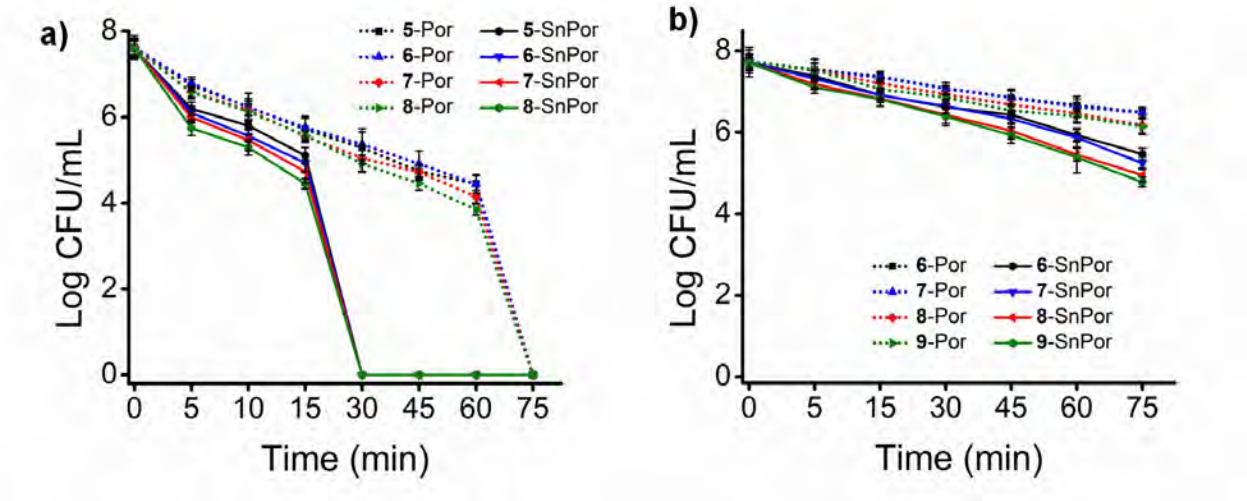

Figure 6.5: Log $CFU.mL^{-1}$ plots of planktonic cells of a) *S. aureus*, and b) *E. coli* upon treatment with a) 1 µM and b) 5 µM of **5**-**8**-Por and **5**-**8**-SnPor dyes after 75 min irradiation at 625 nm using an M625L3 Thorlabs LED (240 $mW.cm^{-2}$).

In contrast, the **5**-**8**-Por free-base porphyrins have low Log_{10} reduction values for *E. coli* in the 1.22−1.58 Log_{10} range, which denotes ≥ 94% cell inactivation and ≤ 6% cell survival (**Figure 6.5b**, **Table 6.5**), while **5**-**8**-SnPor have moderate Log_{10} reduction values ≥ 2.4 Log_{10} $CFU.mL^{-1}$, with > 99% cell reduction and ≤ 0.4% cell survival. This is due to the high ϕ_Δ values for **5**-**8**-SnPor dyes.

The effects of different *meso*-aryl substituents of the PACT activities of dyes also showed that *meso*-4-hydroxyphenyl and -4-hydroxy-3-methoxyphenylporphyrins (**7**-**8**-Por, **7**-**8**-SnPor) have higher PACT activities against planktonic *S. aureus* and *E. coli* bacteria in contrast to the *meso*-methoxyphenylporphyrins (**5**-**6**-Por, **5**-**6**-SnPor) (**Figure 6.5**). This could be due to the vanillic and hydroxyphenyl moieties that can interact slightly better with the *S. aureus* and *E. coli* cell wall resulting in enhanced drug penetration [295,297]. Overall, the low Log_{10} reduction values for **5**-**8**-Por and **5**-**8**-SnPor for the planktonic *E. coli*, in contrast to planktonic *S. aureus*, are normally anticipated in the context of neutral PS dyes, since neutral PS dyes are not very effective in the inactivation of *E. coli* due to the permeability barrier that restricts the penetration of uncharged dyes [18,21].

6.2.2.2 *In vitro* PACT activities of Sn(IV) porphyrins on the biofilms of *S. aureus* and *E. coli* bacteria

For concentrations studies, 25−200 μM gradient concentrations of **5**-**8**-Por and **5**-**8**-SnPor dyes were used to treat the biofilm cells of *S. aureus* and *E. coli* followed by 30 min illumination with a Thorlabs M625L3 LED (240 $mW.cm^{-2}$). Viable cells were quantified using the Crystal violet stain (**Figure 6.6a**-**b**, **Figure A 49c**-**d**). Since **5**-**8**-SnPor dyes exhibited enhanced PACT toward the biofilm cells, lower concentrations of 25 μM of the dyes for *S. aureus* biofilms and 50 μM for *E. coli* biofilms were identified as optimal concentrations for further use during time-dependent studies.

As normally anticipated based on the higher ϕ_Δ values, the Log_{10} reduction values for *S. aureus* and *E. coli* biofilms treated with **5**-**8**-SnPor dyes are slightly higher than those of the corresponding **5**-**8**-Por free-base ligands (**Table 6.5**). These values lie in the 1.40−1.98 Log_{10}

CFU.mL^{-1} range, which denotes ≥ 96% cell reduction and ≤ 4% cell survival (**Figure 6.6c**-**d**, **Figure A 50c**-**d**, **Table 6.5**). This suggests that **5**-**8**-SnPor dyes have moderate PACT activities against the biofilm cells of *S. aureus* and *E. coli*. Nonetheless, these values are less than those observed for the planktonic *S. aureus* and *E. coli* species, since biofilms are less susceptible to antimicrobial agents due to their extracellular polymeric matrix [25–27].

The effect of different *meso*-aryl groups is consistent with those observed in the context of planktonic *S. aureus* and *E. coli* species. The *meso*-4-hydroxyphenyl and -4-hydroxy-3-methoxyphenylporphyrins (**7**-**8**-Por, **7**-**8**-SnPor) have slightly higher PACT activities toward *S. aureus* and *E. coli* biofilms in contrast to *meso*-methoxyphenyl derivatives (**5**-**6**-Por, **5**-**6**-SnPor) (**Figure 6.5**). This is demonstrated by their slightly higher Log_{10} reduction and lower cell survival values (**Figure 6.5**, **Figure 6.6**, **Figure A 49-50c**-**d**, **Table 6.5**). This can be attributed to the favorable interactions from the vanillic and phenolic groups of the PS dyes with the biofilm cells, which can result in slightly enhanced drug penetration and cellular uptake [295,297].

Table 6.5: Log reduction and cell survival values for planktonic and biofilm cells of *S. aureus* and *E. coli* upon treatment with **5**-**8**-Por and their **5**-**8**-SnPor dyes in 1% DMSO/PBS after illumination at 625 nm with a Thorlabs M625L3 LED (240 mW.cm^{-2}).

	S. aureus					***E. coli***					
	Planktonic cells		**Biofilm**			**Planktonic cells**			**Biofilm**		
Sample	**Conc. µM**	**Log_{10} reduction**	**Conc. µM**	**Log_{10} reduction**	**Cell survival (%)**	**Conc. µM**	**Log_{10} reduction**	**Cell survival (%)**	**Conc. µM**	**Log_{10} reduction**	**Cell survival (%)**
5-Por	1	7.62 @75[a]	25	0.74	18.0	5	1.22	6.0	50	0.79	16.1
6-Por	1	7.62 @75	25	0.78	16.5	5	1.25	5.6	50	0.82	15.1
7-Por	1	7.62 @75	25	0.91	12.4	5	1.54	2.9	50	0.96	10.9
8-Por	1	7.62 @75	25	0.89	12.9	5	1.58	2.7	50	0.97	10.8
5-SnPor	1	7.62 @30	25	1.40	4.0	5	2.40	0.4	50	1.49	3.3
6-SnPor	1	7.62 @30	25	1.55	2.8	5	2.47	0.3	50	1.58	2.6
7-SnPor	1	7.62 @30	25	1.94	1.1	5	2.76	0.2	50	1.77	1.7
8-SnPor	1	7.62 @30	25	1.98	1.1	5	2.94	0.1	50	1.73	1.8

[a] Illumination time in minutes used to achieve the Log_{10} reduction value is provided after the @ character.

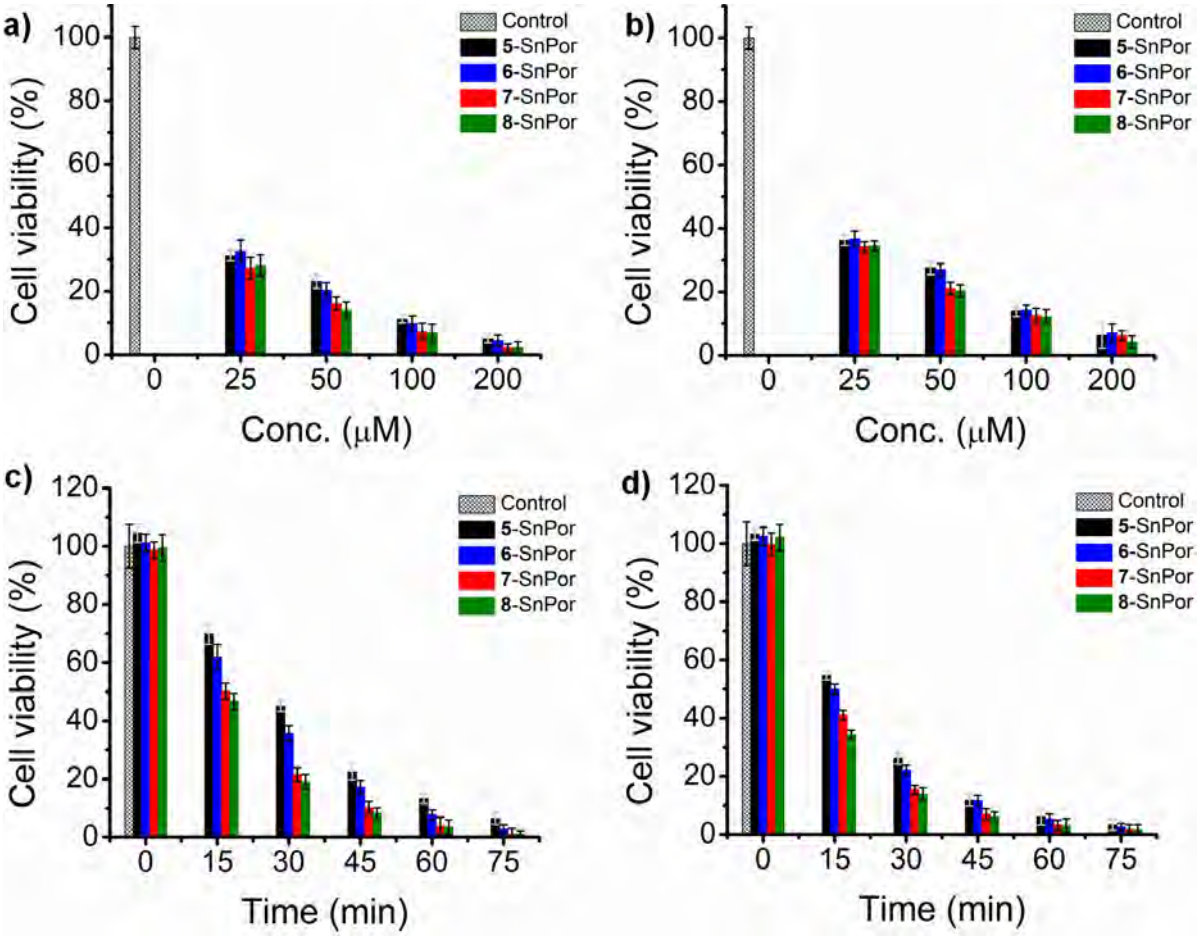

Figure 6.6: The cell viability plots for biofilm cells of a) *S. aureus* and b) *E. coli* upon treatment with gradient concentrations of **5**-**8**-SnPor after 30 min illumination at 625 nm with a Thorlabs M625L3 LED (240 $mW.cm^{-2}$) with cells quantification by crystal violet stain. c-d) The cell viability plots of biofilm cells of c) *S. aureus* and d) *E. Coli*, upon treatment with c) 25 µM, and d) 50 µM of **5**-**8**-SnPor after 75 min illumination at 625 nm with a Thorlabs M625L3 LED (240 $mW.cm^{-2}$) and viable colonies were estimated using viable colony count method.

6.3 Concluding remarks

The PDT and PACT activities of the porphyrins studied are highly dependent on the ϕ_Δ values of the dyes. The In(III) and Sn(IV) porphyrin dyes exhibited favorable PDT and PACT activities since they have high ϕ_Δ values. Conjugation of **1**-InPor to AuNPs results in enhanced PDT activity of **1**-InPor-AuNPs, significantly lowering undesirable dark cytotoxicity. Conjugation of **1**-**4**-InPor dyes to AgNPs and AuNPs also enhanced the PACT activities of the dye nanoconjugates against planktonic and biofilm cells of *S. aureus* and *E. coli*. This is due to the favorable synergistic effects of the AuNPs and AgNPs, which enhance drug penetration and cellular uptake.

CHAPTER SEVEN

Singlet Oxygen Applications of Corrole Dyes

The *in vitro* PDT and photodynamic antimicrobial therapy activities of corrole dyes against MCF-7 breast cancer cells and planktonic and biofilm cells of *S. aureus* and *E. coli* bacteria are discussed in-depth to analyze the suitability of the dyes for use as photosensitizers in PDT.

7.0 Introduction

The A_3 and A_2B *meso*-triarylcorrole dyes used during PDT and PACT treatment are neutral PS dyes except for **10**-GaCor-Q, which is positively charged. The effects of different *meso*-aryl groups, the P(V) and Ga(III) central ions, and conjugation with AuNPs and AgNPs on the PDT and PACT activities of **1**-**4**-P^VCor and **1**-**4**-GaCor were assessed. During PDT and PACT studies, illuminations of A_3 and A_2B *meso*-triarylcorrole dyes were performed at 625 and 595 nm using Thorlabs M625L3 (240 mW.cm^2) and Thorlabs M595L3 (250 mW.cm^2) LEDs, respectively.

7.1 PDT and PACT activities of A_3 P^V and Ga^{III} corrole dyes

Since the PDT activities of the H_3TPCor, P^VTPCor, and Ga^{III}TPCor control compounds, **1**-**3**-Cor free-base corrole ligands, **1**-**3**-P^VCor and **1**-**3**-GaCor dyes including **1**-**3**-P^VCor-AuNP and **1**-**3**-GaCor-AuNP nanoconjugates against MCF-7 cancer cells have already been reported [174], a summary is provided in this context. The PACT activities of **1**-**4**-P^VCor and **1**-**4**-GaCor and their AgNP nanoconjugates (**1**-**4**-P^VCor-AgNPs, **1**-**4**-GaCor-AgNPs) against the planktonic and biofilm cells of *S. aureus* and *E. coli* species are also discussed in this chapter.

7.1.1 Cellular uptake and *in vitro* PDT cytotoxicity studies of A_3 P^V and Ga^{III} corroles against MCF-7 cancer cells

The cellular uptake studies of the A_3 *meso*-triarylcorrole dyes were performed by measuring the fluorescence intensities of MCF-7 cancer cells after 24 h incubation with 6.25, 12.5, and 50 μg.mL^{-1} of A_3 P^V and Ga^{III} corrole dyes (**Figure 7.1**). The A_3 P^V corrole dyes exhibited slightly higher fluorescence intensities than their A_3 Ga^{III} corrole counterparts, with AuNP nanoconjugates exhibiting lower fluorescence intensities than those of the corrole dyes alone (**Figure 7.1a-c**). Since the analogous sets of A_3 P^V and Ga^{III} corrole dyes have comparable fluorescence quantum yields (**Table 5.3**), the observed trends suggested that P^V corroles have slightly enhanced cellular

uptake relative to their A_3 Ga^{III} corrole counterparts [174]. This could be due to the dihydroxy axial ligands of the P(V) ion in contrast to the pyridyl axial ligands A_3 Ga(III) corroles, which enhance uptake and reduce aggregation effects at higher concentrations of the dyes [174].

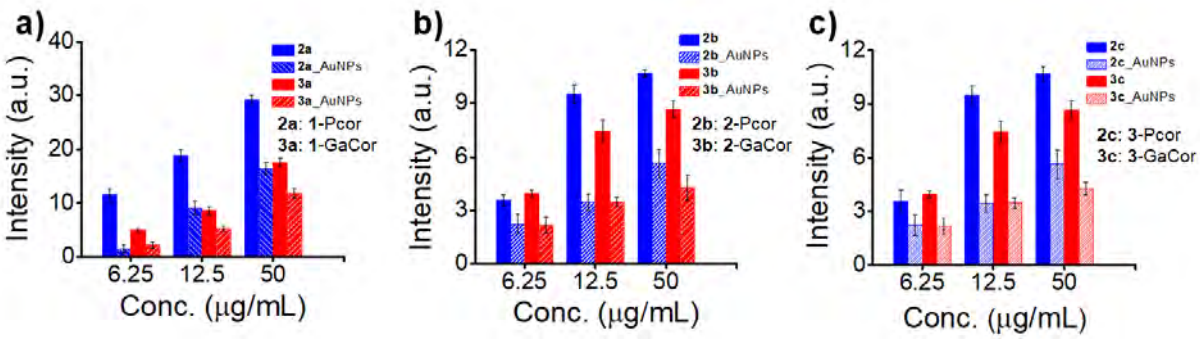

Figure 7.1: Fluorescence intensity plots for MCF-7 cancer cells after 24 h incubation with **1**-**3**-P^{V}Cor and **1**-**3**-GaCor and their **1**-**3**-P^{V}Cor-AuNP and **1**-**3**-GaCor-AuNP nanoconjugates. Reproduced with permission from Reference [174]. Copyright © Elsevier 2021.

The *in vitro* dark cytotoxicity and PDT activities of the H_3TPCor, P^{V}TPCor, and Ga^{III}TPCor control compounds, **1**-**3**-Cor free-base corrole ligands, **1**-**3**-P^{V}Cor and **1**-**3**-GaCor dyes including **1**-**3**-P^{V}Cor-AuNPs and **1**-**3**-GaCor-AuNPs conjugates toward MCF-7 cancer cells were investigated over a 1.56−50 μg.mL^{-1} gradient concentration range of the PS drugs. **Table 7.1** provides a summary of IC_{50}, phototoxicity index (PI) in the dark and after illumination for the H_3TPCor, P^{V}TPCor, and Ga^{III}TPCor control compounds, **1**-**3**-Cor free-base corrole ligands, **1**-**3**-P^{V}Cor and **1**-**3**-GaCor dyes including **1**-**3**-P^{V}Cor-AuNPs and **1**-**3**-GaCor-AuNPs conjugates. **Figure 7.2** provide MCF-7 cell morphologies for the control and after treatment with 50 μg.mL^{-1} of corrole PS drugs in the dark and under illumination with a Thorlabs M625L3 LED, while **Figure 7.3** provides the cytotoxicity plots for MCF-7 cancer cells upon treatment with the gradient concentrations of **3**-P^{V}Cor and **3**-

GaCor dyes and their **3**-P^{V}Cor-AuNP and **3**-GaCor-AuNP nanoconjugates at a fixed light dose of 288 J.cm^{-2} as representative examples.

The IC_{50} values for the A_3 *meso*-triarylcorrole photosensitizers in the dark are IC_{50} > 50 μg.mL^{-1} (**Table 7.1**). Therefore, the dyes have minor dark cytotoxicity effects, which are further reduced upon conjugation of **1**-**3**-P^{V}Cor and **1**-**3**-GaCor corrole dyes to AuNPs [174]. The spindle-like cell morphologies of MCF-7 cancer cells treated with AuNP nanoconjugates in the dark are similar to those of the control compounds (**Figure 7.2**). This also provides further evidence for minimal dark cytotoxicity effects for the A_3 P^{V} and Ga^{III} corrole AuNP nanoconjugates. The studied A_3 *meso*-triarylcorroles are relatively innocuous toward MCF-7 cancer cells in the absence of illumination and are hence potential candidates for use as PS dyes in PDT [174].

The free-base A_3 *meso*-triarylcorroles have relatively low PDT activities in contrast to those of their A_3 P^{V} and Ga^{III} corroles, as demonstrated by their higher IC_{50} values > 28.4 μg.mL^{-1} (**Table 7.1**). This is normally anticipated based on their low ϕ_{Δ} values. In marked contrast, A_3 P^{V} and Ga^{III} corrole dyes have low IC_{50} values (IC_{50} < 11.7 μg.mL^{-1}) due to their higher ϕ_{Δ} values [174]. The PDT activities of the A_3 P^{V} corroles are enhanced relative to the analogous Ga^{III} corrole counterparts, as shown by their slightly lower IC_{50} values and higher PI indices (**Table 7.1**). This can be attributed to the competitive processes that result in the inefficient quenching of the triplet state of Ga^{III} corroles by the molecular oxygen in the cancer cells region [174].

The PDT activities of **1**-**3**-P^{V}Cor-AuNP and **1**-**3**-GaCor-AuNP nanoconjugates are also enhanced relative to those of the dyes alone, as demonstrated by lower IC_{50} values and higher PI indices (**Figure 7.3**, **Table 7.1**) [174]. The MCF-7 cells treated with 50 μg.mL^{-1} AuNP nanoconjugates shrunk significantly after illumination (**Figure 7.2**). This also demonstrates the enhanced PDT

activities of the A_3 AuNP nanoconjugates. This could be due to the high ϕ_Δ values for the A_3 P^V and Ga^{III} corrole AuNP nanoconjugates combined with the favorable synergistic effects of AuNPs, such as enhanced drug delivery and the enhanced retention permeability effect [174].

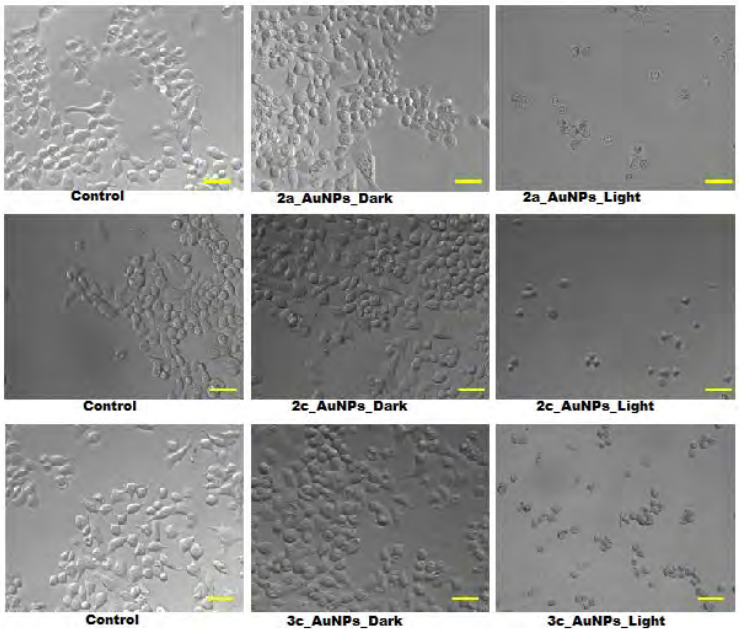

Figure 7.2: MCF-7 cancer cells morphologies for the control compounds and after treatment with 50 µg.mL^{-1} of **1**-P^VCor-AuNPs, **3**-P^VCor-AuNPs, and **3**-GaCor-AuNPs in the dark and under illumination with a Thorlabs M625L3 (240 mW.cm^2, 20 min). (Scale bar: 200 µm). Reproduced with permission from Reference [174]. Copyright © Elsevier 2021.

Overall, P^VTPCor, **1**-**3**-P^VCor A_3 P^V corroles, and the **1**-**3**-P^VCor-AuNPs conjugates have higher PDT activities than their Ga^{III} counterparts. This can most likely be associated with the dihydroxy axial ligands on the P(V) ion, which slightly enhance the uptake, biodistribution, and bioaccumulation of the dyes due to reduced aggregation effects at higher concentrations of the dyes [174].

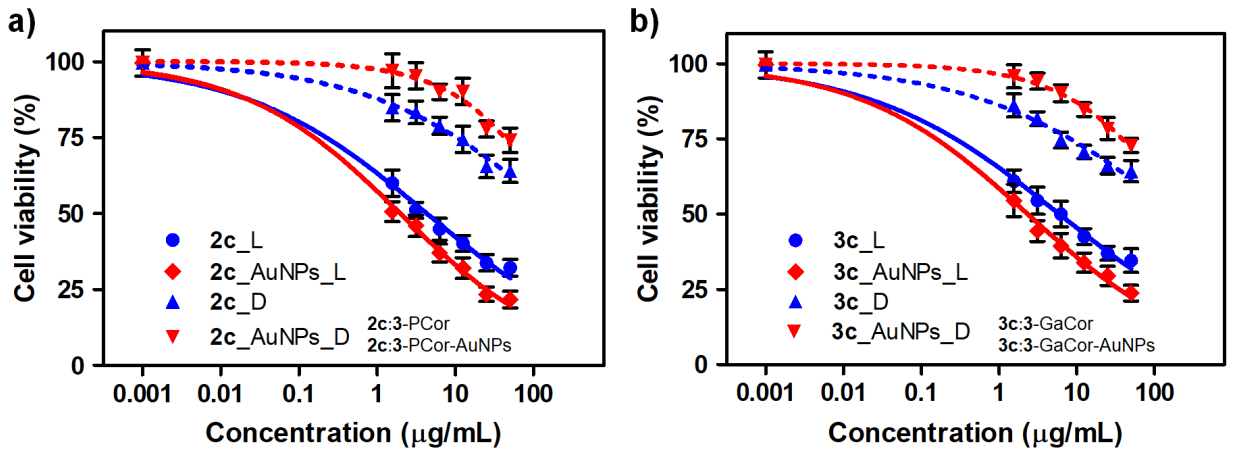

Figure 7.3: Cytotoxicity plots of MCF-7 cancer cells treated with gradient concentrations of a) **3**-P^{V}Cor, **3**-P^{V}Cor-AuNPs, and b) **3**-GaCor, **3**-GaCor-AuNPs in the dark (_D) and under illumination (_L) with a M625L3 Thorlabs LED. Reproduced with permission from Reference [174]. Copyright © Elsevier 2021.

Table 7.1: IC_{50} and PI values for **1**-**3**-P^{V}Cor, **1**-**3**-GaCor, and their **1**-**3**-P^{V}Cor-AuNP and **1**-**3**-GaCor-AuNP nanoconjugates against MCF-7 cancer cells.

	IC_{50} (μg/mL)		PI[d]
Sample	**Dark[b]**	**Light[c]**	
H_3TPCor	> 50	49.4	> 1.0
1-Cor	> 50	44.9	> 1.1
2-Cor	> 50	32.2	> 1.6
3-Cor	> 50	28.4	> 1.8
1-P^{V}Cor	> 50	7.1	> 7.1
2-P^{V}Cor	> 50	4.7	> 10.6
3-P^{V}Cor	> 50	4.2	> 11.9
1-GaCor	> 50	8.3	> 6.0
2-GaCor	> 50	5.6	> 8.9
3-GaCor	> 50	5.2	> 9.6
P^{V}TPCor	> 50	9.9	> 5.1
Ga^{III}TPCor	> 50	11.7	> 4.3
1-P^{V}Cor-AuNPs	> 50	3.4	> 14.7
2-P^{V}Cor-AuNPs	> 50	2.7	> 18.5
3-P^{V}Cor-AuNPs	> 50	2.4	> 20.8
1-GaCor-AuNPs	> 50	4.3	> 11.6
2-GaCor-AuNPs	> 50	3.5	> 14.3
3-GaCor-AuNPs	> 50	3.1	> 16.1

[a]24 h incubation dark cytotoxicity data, [b]phototoxicity data against MCF-7 cancer cell line upon exposure to a Thorlabs 625 nm LED (240 $mW.cm^{-2}$, 20 min). [c]PI = phototoxic index (dark and light IC_{50} values toxicity ratio). Data are reproduced from Reference [174].

7.1.2 *In vitro* PACT cytotoxicity studies of A_3 P^V and Ga^{III} corroles on the planktonic and biofilm cells of *S. aureus* and *E. coli* bacteria.

1-**4**-P^VCor and **1**-**4**-GaCor, **1**-**4**-P^VCor-AgNP and **1**-**4**-GaCor-AgNP nanoconjugates have minor dark cytotoxicity activities toward planktonic and biofilm cells of *S. aureus* and *E. coli* species (**Figures A 51**-**53**).

7.1.2.1 *In vitro* PACT cytotoxicity studies of A_3 P^V and Ga^{III} corroles on the planktonic *S. aureus* and *E. coli* bacteria.

Optimal concentrations of 0.5 and 2.5 $\mu g.mL^{-1}$ for *S. aureus* and 10 $\mu g.mL^{-1}$ for *E. coli* were identified for use during time-dependent studies of **1**-**4**-P^VCor and **1**-**4**-GaCor and their AgNP nanoconjugates (**Figure A 51c**-**d**). **Figure 7.4** provides the Log $CFU.mL^{-1}$ plots for **3**-**4**-P^VCor, **3**-**4**-GaCor corroles and their AgNP nanoconjugates against planktonic *S. aureus* and *E. coli* upon treatment with 0.5 and 2.5 $\mu g.mL^{-1}$ of the dyes for *S. aureus* and 10 $\mu g.mL^{-1}$ of the dyes for *E. coli*, as representative examples. **Table 7.2** summarizes the time-dependent Log_{10} reduction and cell survival values for **1**-**4**-P^VCor, **1**-**4**-GaCor, and their AgNP nanoconjugates, including AgNPs alone toward planktonic cells of *S. aureus* and *E. coli* after 75 or 120 min illumination at 625 nm with a Thorlabs M625L3 LED.

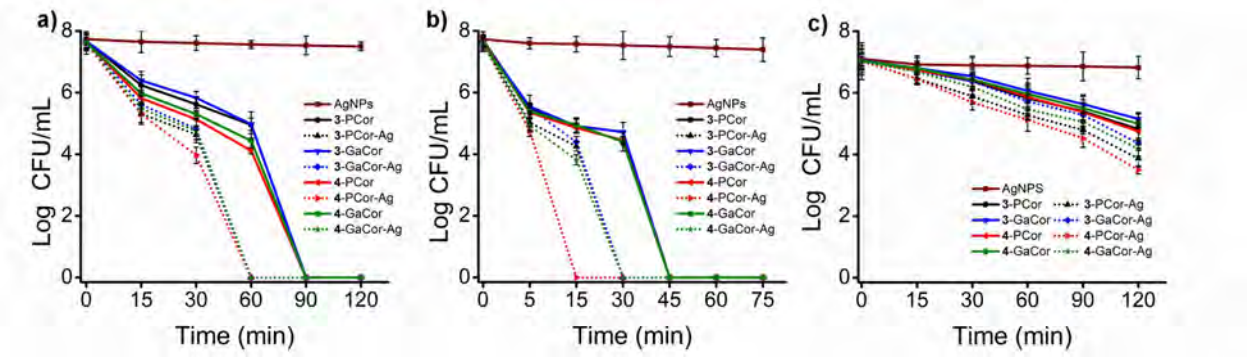

Figure 7.4: Log CFU.mL^{-1} plots of planktonic cells of a-b) *S. aureus*, and c) *E. coli* upon treatment with a) 0.5 µg.mL^{-1}, b) 2.5 µg.mL^{-1} and c) 10 µg.mL^{-1} of AgNPs, **3**-**4**-P^{V}Cor, **3**-**4**-GaCor A_3 P^{V} and Ga^{III} corrole dyes and their AgNP nanoconjugates after a) 120 min b) 75 min and c) 120 min irradiation at 625 nm using an M625L3 Thorlabs LED (240 mW.cm^{-2}).

1-**4**-P^{V}Cor and **1**-**4**-GaCor have favorable PDT activities against planktonic *S. aureus*, as demonstrated by their high Log_{10} reduction values (**Figure 7.5a**-**b**), **Table 7.2**). For example, the Log_{10} reduction values for planktonic *S. aureus* treated with 0.5 µg.mL^{-1} of A_3 P^{V} and Ga^{III} corrole dyes are greater than the optimal Log_{10} CFU.mL^{-1} = 3 value after 120 min illumination. This was anticipated based on their relatively high ϕ_{Δ} values. The PACT activities of **1**-**4**-P^{V}Cor and **1**-**4**-GaCor were further enhanced by increasing the concentration of the dyes to 2.5 µg.mL^{-1}. This is demonstrated by high Log_{10} reduction values with complete eradication of *S. aureus* colonies after illumination for short periods (**Table 7.2**). This suggests that the studied A_3 P^{V} and Ga^{III} corroles are efficient PS dyes for the inactivation of *S. aureus* at very low concentrations of the dyes.

In marked contrast, **1**-**4**-P^{V}Cor, and **1**-**4**-GaCor corrole dyes exhibited low PACT activities toward planktonic *E. coli* with low Log_{10} reduction values that lie in the 1.49−2.45 Log_{10} range, with ≤ 3.21% cell survival after 120 min illumination. This trend was anticipated for the neutral **1**-**4**-

P^{V}Cor, and **1**-**4**-GaCor dyes, since Gram-(−) *E. coli* has *an* effective permeability barrier that restricts uncharged dyes, such as the neutral PS dyes from penetrating the cells [18,21,23]. Nevertheless, **1**-**4**-P^{V}Cor have slightly enhanced PACT activities toward both planktonic *S. aureus* and *E. coli* species in compared to their A_3 Ga^{III} corrole counterparts (**Figure 7.5**). This trend is consistent with the previously reported PDT behavior of the dyes [174]. This can most likely be attributed to the favorable effects of dihydroxy axial ligands of P(V) ion, which enhance the uptake of the PS dyes by reducing aggregation effects and thus enhancing the cytotoxic effects of the dyes [174].

The AgNPs alone exhibited minor PACT effects toward planktonic *S. aureus* and *E. coli* (**Figure 7.5**, **Table 7.2**). In contrast, the PACT activities of **1**-**4**-P^{V}Cor, and **1**-**4**-GaCor against planktonic *S. aureus* and *E. coli* were enhanced upon the conjugation of the dyes to AgNPs. This is demonstrated by the higher Log_{10} reduction values for the AgNP nanoconjugates with complete eradication of *S. aureus* colonies at shorter illumination periods than with the dyes alone (**Table 7.2**), due to the higher ϕ_{Δ} values for AgNP nanoconjugates combined with the synergistic action of AgNPs, such as enhanced drug delivery and enhanced cellular uptake that result in enhanced PACT cytotoxic action [22,73,291].

The different *meso*-aryl substituents of **1**-**4**-P^{V}Cor, and **1**-**4**-GaCor corroles also have minor effects on the PACT activities of the dyes. For example, the *meso*-thienyl corroles (**2**-**4**-P^{V}Cor, **2**-**4**-GaCor) and their AgNP nanoconjugates (**2**-**4**-P^{V}Cor-AgNPs, **2**-**4**-GaCor-AgNPs) have enhanced PACT activities against planktonic *S. aureus* and *E. coli* than the methylthiophenyl derivatives (**1**-P^{V}Cor, **1**-GaCor, **1**-P^{V}Cor-AgNPs, **1**-GaCor-AgNPs). This is demonstrated by their slightly higher Log_{10} reduction values, which result in the complete eradication of *S. aureus* colonies at a shorter

illumination time (**Table 7.2**). This trend is also consistent with the data obtained for their **1**-**4**-InPor analogs (**2**-**4**-InPor). The favorable PACT performance of A_3 *meso*-thienyl corroles could be due to the antimicrobial properties of thienyl derivatives [60].

Table 7.2: Log reduction and cell survival values for **1**-**4**-P^{V}Cor, **1**-**4**-GaCor, and their **1**-**4**-P^{V}Cor-AgNP and **1**-**4**-GaCor-AgNP nanoconjugates against planktonic *S. aureus*, and *E. coli* cells after irradiation at 625 nm using an M625L3 Thorlabs LED (240 mW.cm^{-2}).

	S. aureus				***E. Coli***	
Sample	**Log_{10} reduction at 0.5 μg.mL^{-1}**	**Cell survival (%) at 0.5 μg.mL^{-1}**	**Log_{10} reduction at 2.5 μg.mL^{-1}**	**Cell survival (%) at 2.5 μg.mL^{-1}**	**Log_{10} reduction at 10 μg.mL^{-1}**	**Cell survival (%) at 10 μg.mL^{-1}**
1-P^{V}Cor	3.48 @120	0.03	7.71 @60	0	1.73	1.88
2-P^{V}Cor	7.71 @90	0	7.71@45	0	2.14	0.72
3-P^{V}Cor	7.71 @90	0	7.71@45	0	2.27	0.53
4-P^{V}Cor	7.71 @90	0	7.71@45	0	2.45	0.36
1-GaCor	3.16 @120	0.07	7.71 @60	0	1.49	3.21
2-GaCor	7.71 @120	0	7.71@45	0	1.84	1.46
3-GaCor	7.71 @90	0	7.71@45	0	1.94	1.15
4-GaCor	7.71 @90	0	7.71@45	0	2.10	0.79
AgNPs	0.29 @120	61.6	0.32@75	47.7	0.27	53.8
1-P^{V}Cor-AgNPs	7.71 @90	0	7.71 @45	0	2.49	0.31
2-P^{V}Cor-AgNPs	7.71 @60	0	7.71@30	0	3.06	0.09
3-P^{V}Cor-AgNPs	7.71 @60	0	7.71@30	0	3.23	0.06
4-P^{V}Cor-AgNPs	7.71 @60	0	7.71@15	0	3.60	0.02
1-GaCor-AgNPs	7.71 @90	0	7.71 @45	0	2.31	0.48
2-GaCor-AgNPs	7.71 @60	0	7.71 @30	0	2.67	0.22
3-GaCor-AgNPs	7.71 @60	0	7.71@30	0	2.73	0.19
4-GaCor-AgNPs	7.71 @60	0	7.71@30	0	2.90	0.13

[a] Illumination time in minutes used to achieve the Log_{10} reduction value is provided after the @ character.

7.1.2.2 *In vitro* PACT cytotoxicity studies for A_3 P^{V} and Ga^{III} corroles against biofilms of *S. aureus* and *E. coli* bacteria.

Optimal concentrations of 50 μg.mL^{-1} of the dyes for *S. aureus* biofilms and 100 μg.mL^{-1} for *E. coli* biofilms were used during the time-dependent studies of **1**-**4**-P^{V}Cor, and **1**-**4**-GaCor corroles and their AgNP nanoconjugates (**Figure 7.5a-b**). **1**-**4**-P^{V}Cor have slightly higher Log_{10} reduction values and lower cell survival toward *S. aureus* and *E. coli* biofilm cells than their Ga^{III} corrole counterparts (**Figure 7.5** and **Table 7.3**). For instance, *meso*-thienyl P^{V} corroles (**2**-**4**-P^{V}Cor) have ≥ 1 Log_{10} values with ≥ 90% cell reduction and ≤ 10% cell survival (**Table 7.3**). This suggests that

1-**4**-P^{V}Cor have slightly enhanced PACT activities against biofilm cells of *S. aureus* and *E. coli* species in contrast to their Ga^{III} counterparts. This trend is consistent with the observed PACT behavior of the dyes against the planktonic *S. aureus* and *E. coli* species. This is likely associated with decreased aggregation effects and enhanced drug uptake in the context of the A_3 P^{V} corroles due to the dihydroxy axial ligands of the P(V) ion [174].

The PACT activities of **1**-**4**-P^{V}Cor and **1**-**4**-GaCor corrole dyes were also slightly enhanced against *S. aureus* and *E. coli* biofilms upon conjugation to AgNPs. This is demonstrated by moderate Log_{10} reduction values of ≥ 1 Log_{10} $CFU.mL^{-1}$ and ≤ 10% cell survival after 120 min illumination (**Table 7.3**). This can be attributed to the higher ϕ_{Δ} values for AgNP nanoconjugates and enhanced synergistic action AgNPs, such as favorable drug delivery and enhanced cellular uptake, which result in enhanced PACT activity [22,291,293]. In contrast, the PACT activity of AgNPs alone toward the biofilm cells of *S. aureus* and *E. coli* species is relatively minor, as demonstrated by the < 0.2 Log_{10} reduction values, which denote ≤ 62.5% cell survival.

Overall, the Log_{10} reduction values for the biofilms treated with A_3 P^{V} and Ga^{III} corroles are much lower than those of the planktonic *S. aureus* and *E. coli* bacteria discussed earlier. This trend is normally anticipated since biofilm bacteria are less susceptible to antimicrobial agents due to the

extracellular polymeric matrix, which secures the bacteria cells and thus restricts drug penetration [25-27].

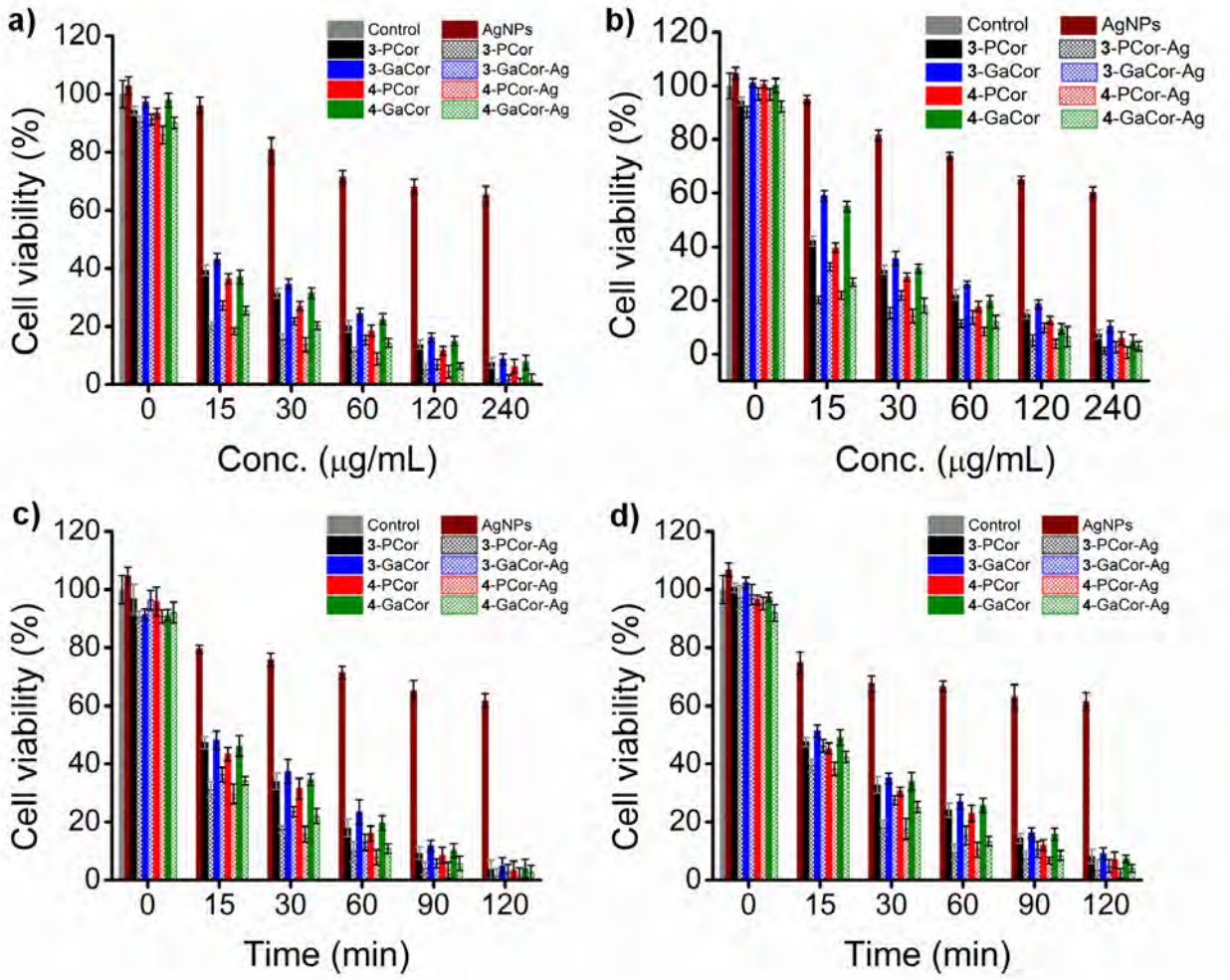

Figure 7.5: The cell viability plots for biofilm cells of a) *S. aureus* and b) *E. coli* upon treatment with gradient concentrations of **3**-**4**-P^{V}Cor, **3**-**4**-GaCor, and their AgNP nanoconjugates after 30 min illumination at 625 nm with a Thorlabs M625L3 (240 mW.cm^{-2}) LED with viable cells quantified by crystal violet stain. c-d) The cell viability plots of biofilm cells of c) *S. aureus* and d) *E. Coli*, upon treatment with c) 50 μg.mL^{-1}, and d) 100 μg.mL^{-1} of **3**-**4**-P^{V}Cor, **3**-**4**-GaCor, and their AgNP nanoconjugates after 120 min illumination at 625 nm

with a Thorlabs M625L3 (240 mW.cm^{-2}) with viable colonies were estimated using the viable colony count method.

Table 7.3: Log reduction and cell survival values for **1**-**4**-P^{V}Cor, **1**-**4**-GaCor A_3 P^{V} and Ga^{III} corrole dyes, and their **1**-**4**-P^{V}Cor-AgNPs and **1**-**4**-GaCor-AgNP and -AgNP nanoconjugates in 1% DMSO/PBS against biofilm cells of *S. aureus* and *E. coli* after 120 min illumination at 625 nm with a Thorlabs M625L3 (240 mW.cm^{-2}) LED.

	***S. aureus* biofilms**		***E. Coli* biofilms**	
Sample	**Log_{10} reduction at 30 μg.mL^{-1}**	**Cell survival (%) at 30 μg.mL^{-1}**	**Log_{10} reduction at 60 μg.mL^{-1}**	**Cell survival (%) at 60 μg.mL^{-1}**
1-P^{V}Cor	1.15	7.04	0.88	13.18
2-P^{V}Cor	1.36	4.24	1.01	9.80
3-P^{V}Cor	1.41	3.74	1.07	8.22
4-P^{V}Cor	1.49	3.27	1.16	6.97
1-GaCor	0.95	11.12	0.73	18.51
2-GaCor	1.27	5.37	1.00	10.02
3-GaCor	1.30	4.96	1.04	9.19
4-GaCor	1.40	3.94	1.09	7.37
AgNPs	0.21	61.71	0.20	62.50
1-P^{V}Cor-AgNPs	1.47	3.31	1.20	6.20
2-P^{V}Cor-AgNPs	1.70	1.98	1.42	3.83
3-P^{V}Cor-AgNPs	1.83	1.48	1.44	3.39
4-P^{V}Cor-AgNPs	1.87	1.36	1.51	2.34
1-GaCor-AgNPs	1.34	4.55	1.11	7.71
2-GaCor-AgNPs	1.52	3.01	1.26	5.53
3-GaCor-AgNPs	1.56	2.75	1.32	4.82
4-GaCor-AgNPs	1.60	2.55	1.37	4.06

7.2 PDT and PACT activities of A_2B Ga^{III} corrole dyes

The PDT and PACT activities of **9**-**10**-GaCor and **10**-GaCor-Q against MCF-7 cancer cells, planktonic and biofilm cells of *S. aureus* and *E. coli* species have already been reported [210], so a summary is provided in this context. Since the A_2B Ga^{III} corrole dyes have similar structural features and

photophysicochemical properties (**Table 5.2**), the effects of push and pull and cationic species in the context of **10**-GaCor-Q on the PDT and PACT activities of dyes can be carefully analyzed.

7.2.1 Cellular uptake and *in vitro* PDT cytotoxicity studies of A_2B Ga^{III} corroles against MCF-7 cancer cells

The cellular uptake studies for **9**-**10**-GaCor and **10**-GaCor-Q were performed by measuring the fluorescence intensities of MCF-7 cells after 24 h incubation with 10 µM of the dyes (**Figure 7.6a**). Since the A_2B Ga^{III} corrole dyes have similar fluorescence quantum yields (**Table 5.2**), the higher fluorescence intensity observed for **10**-GaCor-Q demonstrated enhanced uptake relative to those of the **9**-**10**-GaCor dyes (**Figure 7.6a**) [210].

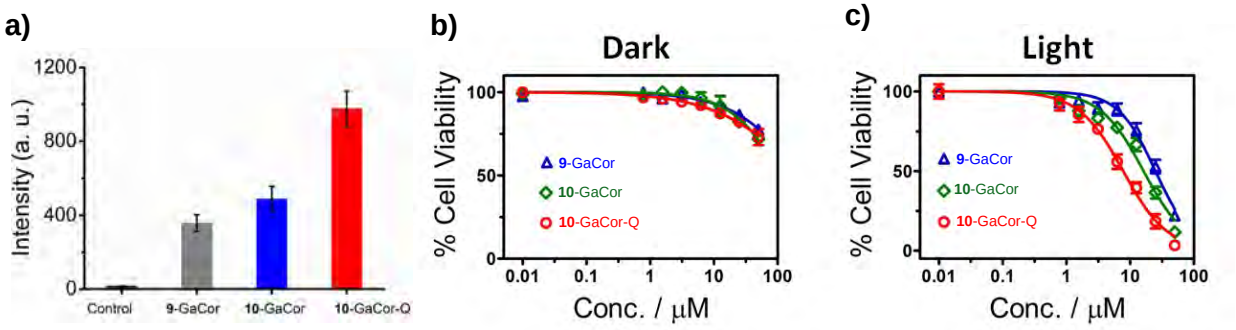

Figure 7.6: a) Fluorescence intensity plots for MCF-7 cancer cells after 24 h incubation with 10 µM of **9**-**10**-GaCor and **10**-GaCor-Q. b-c) Cytotoxicity plots of MCF-7 cancer cells treated with gradient concentrations of **9**-**10**-GaCor and **10**-GaCor-Q a) in the dark b) under illumination with a M595L3 Thorlabs LED. Reproduced with permission from Reference [210]. Copyright © Royal Society of Chemistry 2022.

The *in vitro* dark cytotoxicity and PDT activities of **9**-**10**-GaCor and **10**-GaCor-Q against MCF-7 cancer cells were investigated over 0.7–50 µM gradient concentrations of the dyes. **Table 7.4** provides a summary of the IC_{50} and phototoxicity index (PI) values in the dark and after illumination for **9**-**10**-GaCor and **10**-GaCor-Q. **Figure 7.6b-c** gives the cytotoxicity plots for the

MCF-7 cancer cells treated with 0.7−50 µM gradient concentrations of **9**-**10**-GaCor and **10**-GaCor-Q b) in the dark and c) under illumination for 20 min at a fixed light dose of 300 J.cm^{-2} from the M595L3 Thorlabs LED.

9-**10**-GaCor and **10**-GaCor-Q dyes have minor dark cytotoxicity effects, as demonstrated by high IC_{50} values > 50 µM in the dark (**Figure 7.6b**, **Table 7.4**). This suggests that the A_2B Ga^{III} corrole are innocuous toward MCF-7 cancer cells in the absence of illumination and are favorable candidates for use as PS dyes in PDT [210]. **10**-GaCor-Q also exhibited enhanced PDT activity, as shown by its lower IC_{50} value of < 7.8 µM under illumination in contrast to **9**-**10**-GaCor. This was expected based on higher cellar uptake of **10**-GaCor-Q by MCF-7 cells since it has cationic species [210]. This confirms that positively-charged PS dyes have enhanced cellar uptake and, consequently, phototherapeutic effects [2,3,15].

Table 7.4: IC_{50} and PI values for **9**-**10**-GaCor and **10**-GaCor-Q against MCF-7 cancer cells.

Sample	IC_{50} (µM) dark	IC_{50} (µM) light	PI (dark/light)
9-GaCor	> 50	24.8	> 2.01
10-GaCor	> 50	16.2	> 3.09
10-GaCor-Q	> 50	7.8	> 6.45

Reproduced from Reference [210].

7.2.2 *In vitro* PACT cytotoxicity studies of A_2B Ga^{III} corroles on the planktonic and biofilm cells of *S. aureus* and *E. coli* bacteria.

9-**10**-GaCor and **10**-GaCor-Q exhibited minor dark cytotoxicity toward planktonic and biofilm cells of *S. aureus* and *E. coli* species [210]. The concentration optimization studies results identified 0.5 and 2.5 µM of A_2B Ga^{III} corrole dyes against planktonic *S. aureus* and 10 µM for *E. coli* as optimal concentrations for use during time-dependant studies. **Figure 7.7** provides the Log

CFU.mL^{-1} plots for planktonic a-b) *S. aureus* and c) *E. coli* upon treatment with 0.5 and 2.5 µM of **9**-**10**-GaCor and **10**-GaCor-Q for *S. aureus* and 10 µM for *E. coli*, while **Figure 7.8** provides the cell viability plots for the biofilm cells of a, c) *S. aureus* and b, d) *E. coli* upon treatment with a-b) 15−240 µM gradient concentrations of A_2B Ga^{III} corrole dyes after 30 min illumination at 595 nm with a Thorlabs M625L3 LED (250 mW.cm^{-2}) with viable cells quantified by crystal violet stain. **Figure 7.8 c-d)** provides the time-dependent cell viability plots upon treatment with 30 µM and d) 60 µM of the dyes after 120 min illumination at 595 nm with a Thorlabs M595L3 LED (250 mW.cm^{-2}), and viable cells were estimated using viable colony count method. **Table 7.5** provides a summary of time-dependent Log_{10} reduction values and cell survival values of **9**-**10**-GaCor and **10**-GaCor-Q toward planktonic cells of *S. aureus* and *E. coli* after 75 or 120 min illumination at 595 nm with a Thorlabs M595L3 LED, while **Table 7.6** summarizes time-dependent Log_{10} reduction and cell survival values for biofilm cells of *S. aureus* and *E. coli* treated with **9**-**10**-GaCor and **10**-GaCor-Q after 120 min illumination at 595 nm with a Thorlabs M595L3 LED.

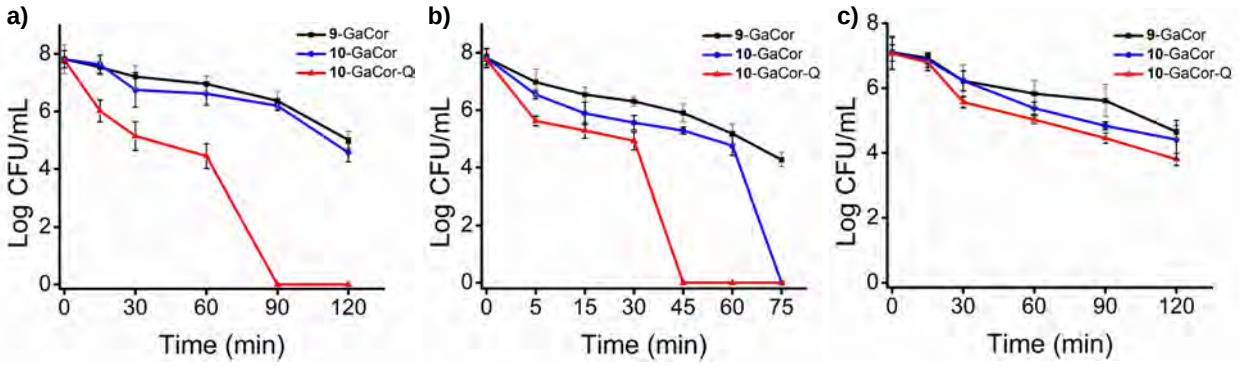

Figure 7.7: Log CFU.mL^{-1} plots of planktonic cells of a-b) *S. aureus* and c) *E. coli* upon treatment with a) 0.5 µM, b) 2.5 µM and c) 10 µM of **9**-**10**-GaCor and **10**-GaCor-Q after a) 120 min b) 75 min and c) 120 min irradiation at 595 nm using a Thorlabs M595L3 LED (250

mW.cm^{-2}). Reproduced with permission from Reference [210]. Copyright © Royal Society of Chemistry 2022.

The **9**-**10**-GaCor neutral PS dyes have relatively favorable PACT activities against planktonic *S. aureus* at 2.5 µM of the dyes with > 3 Log_{10} CFU.mL^{-1} log reduction values (**Figure 7.7b**, **Table 7.5**). **9**-**10**-GaCor also exhibited moderate PACT activities against planktonic *E. coli*. This is demonstrated by Log_{10} reduction values in the 2.40−2.65 range, which denotes ≥ 99% cell reduction and ≤ 0.4% cell survival [210]. As anticipated, its cationic species, **10**-GaCor-Q, exhibited enhanced PACT activities toward planktonic *S. aureus* and *E. coli* species compared to the non-quaternized **9**-**10**-GaCor dyes. This is demonstrated by the higher Log_{10} reduction values of 7.78 Log_{10} CFU.mL^{-1} for *S. aureus* with complete eradication of colonies at lower concentration of the dye (0.5 µM) after illumination for shorter periods than was necessary with **9**-**10**-GaCor dyes (**Figure 7.7a**) [210]. The Log_{10} reduction value for **10**-GaCor-Q against planktonic *E. coli* is 3.26 Log_{10} CFU.mL^{-1}, which denotes ≤ 0.06% cell survival or 99.94% cell reduction (**Table 7.5**). This value meets the optimal > 3 Log_{10} CFU.mL^{-1} requirement for an antimicrobial agent. This suggests that **10**-GaCor-Q is an efficient PS dye for the photoinactivation of both *S. aureus* and *E. coli* [210].

Table 7.5: Log reduction and cell survival values for **9**-**10**-GaCor and **10**-GaCor-Q in 1% DMSO/PBS against planktonic cells of *S. aureus* and *E. coli* after illumination at 595 nm with a Thorlabs M595L3 (250 mW.cm^{-2}) LED.

	S. aureus				***E. coli***	
Sample	**Log_{10} reduction at 0.5 µM**	**Cell survival (%) at 0.5 µM**	**Log_{10} reduction at 2.5 µM**	**Cell survival (%) at 2.5 µM**	**Log_{10} reduction at 10 µM**	**Cell survival (%) at 10 µM**
9-GaCor	2.79 @120[a]	0.16	3.66 @75	0.03	2.40	0.40
10-GaCor	3.23 @120	0.06	7.78 @60	0	2.65	0.23
10-GaCor-Q	7.78 @90	0	7.78 @45	0	3.26	0.06

[a] Illumination time in minutes for the Log_{10} reduction value is provided after the @ character. Reproduced from Reference [210].

9-**10**-GaCor and **10**-GaCor-Q exhibit significant PACT activities toward the biofilm cells of *S. aureus* and *E. coli* upon treatment with 15−240 µM gradient concentration of the dyes followed by illumination at a fixed dose light of 450 J.cm^{-2} [210]. Lower concentrations of 30 µM for *S. aureus* and 60 µM for *E. coli* were identified as the optimal concentrations for use during time-dependant studies (**Figure 7.8a-b**). The PACT activity of **10**-GaCor-Q against *S. aureus* and *E. coli* biofilms is higher than those of the non-quaternized **9**-**10**-Cor dyes (**Figure 7.7c-d**, **Table 7.6**). This is demonstrated by higher Log_{10} reduction values that lie at 2 Log_{10}, which denote ≥ 99% cell reduction and ≤ 0.9% cell survival for *S. aureus* and 1.1 Log_{10} for *E. coli*, which denotes 91.8% cell reduction and ≤ 8.2% cell survival (**Table 7.6**). These values suggest that **10**-GaCor-Q has moderate PACT activities toward the biofilm cells *S. aureus* and *E. coli* [210]. This was anticipated for the cationic species of **10**-GaCor-Q, which can enhance penetration of the drug into the biofilm cells in contrast to the neutral PS dyes [210].

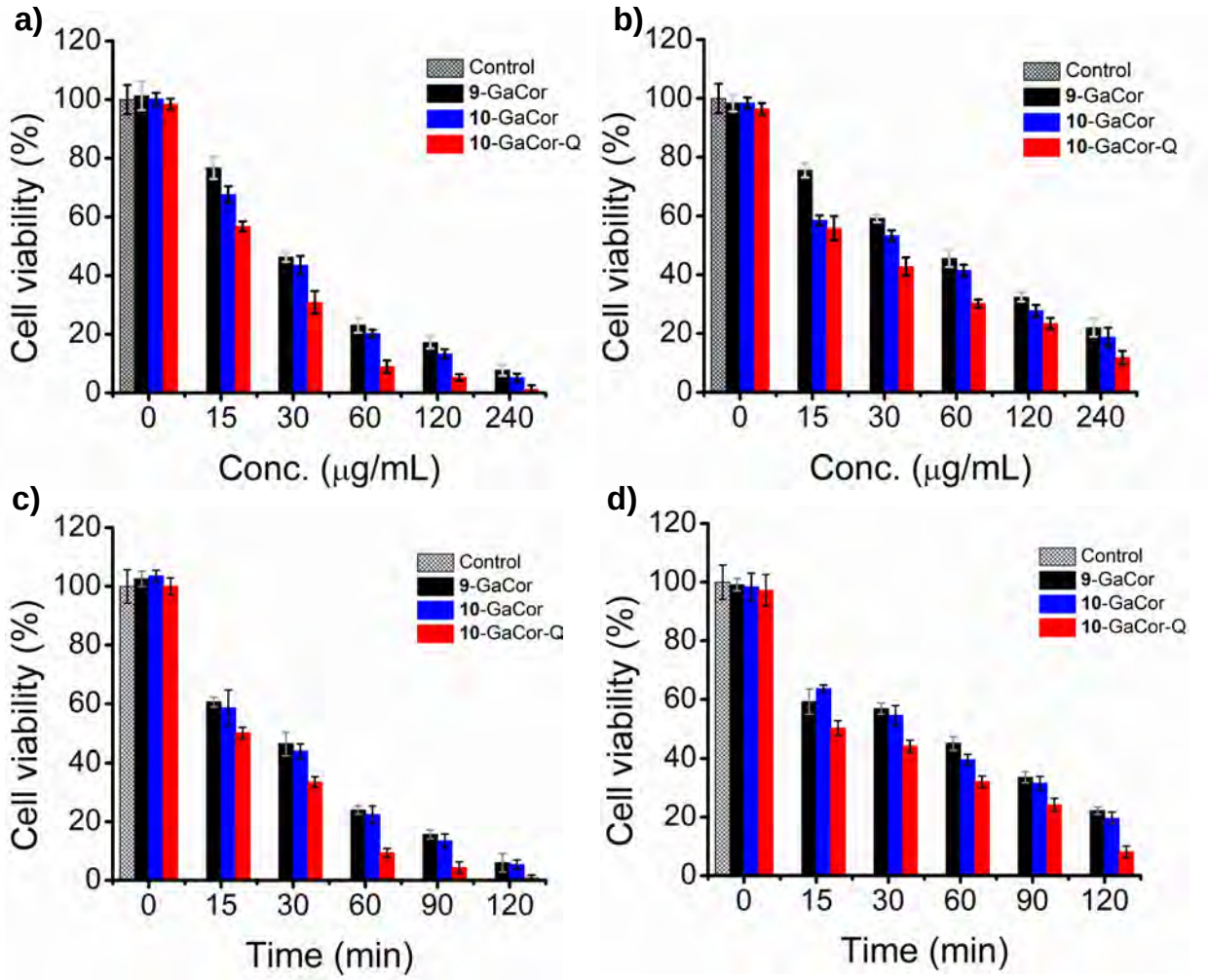

Figure 7.8: The cell viability plots for biofilm cells of a) *S. aureus* and b) *E. coli* upon treatment with gradient concentrations of **9**-**10**-GaCor and **10**-GaCor-Q after 30 min illumination at 595 nm with a Thorlabs M595L3 LED (250 $mW.cm^{-2}$) with viable cells quantified by crystal violet stain. c-d) The cell viability plots of biofilm cells of c) *S. aureus* and d) *E. Coli*, upon treatment with c) 30 μM, and d) 60 μM of **9**-**10**-GaCor and **10**-GaCor-Q after 120 min illumination at 625 nm with 595 nm with a Thorlabs M595L3 LED (250 $mW.cm^{-2}$) with viable colonies estimated using the viable colony count method. Reproduced with permission from Reference [210]. Copyright © Royal Society of Chemistry 2022.

Table 7.6: Log reduction and cell survival values for **9**-**10**-GaCor and **10**-GaCor-Q in 1% DMSO/PBS against biofilm cells of *S. aureus* and *E. coli* after 120 min illumination at 595 nm with a Thorlabs M595L3 LED (250 mW.cm^{-2}).

	S. aureus		***E. coli***	
	Log_{10} reduction	**Cell survival (%)**	**Log_{10} reduction**	**Cell survival (%)**
Sample	**at 30 μM**		**at 60 μM**	
9-GaCor	1.22	6.0	0.65	22.2
10-GaCor	1.27	5.4	0.71	19.6
10-GaCor-Q	2.02	0.9	1.10	8.2

Reproduced from Reference [210].

7.3 Concluding remarks

A_3 P^V corrole dyes exhibited more favorable PDT and PACT activities than A_3 Ga^{III} corroles. This is most likely due to the dihydroxy axial ligands of the P(V) ion, which decrease aggregation effects and enhance cellular uptake of the PS dyes. The PDT activities of **1**-**3**-P^VCor and **1**-**3**-GaCor were significantly enhanced upon conjugation to AuNPs. In a similar manner, conjugation of **1**-**4**-P^VCor and **1**-**4**-GaCor to AgNPs enhanced the PACT activities of the dyes. This is due to the favorable synergistic effects of AuNPs and AgNPs, such as higher ϕ_Δ values, enhanced cellular uptake of PS drug, and the enhanced permeability retention effect, among others. The presence of a cationic species for **10**-GaCor-Q also enhanced the PDT and PACT activities of the dye in contrast to the neutral **9**-**10**-GaCor A_2B Ga^{III} corroles, since the cationic charge enhances the penetration of the PS drug into the tumor or bacteria cells resulting in enhanced cytotoxic effects.

CHAPTER EIGHT

Singlet Oxygen Applications of Chlorin Dyes

The *in vitro* PDT and PACT activities of chlorin dyes against MCF-7 breast cancer cells and planktonic and biofilm cells of *S. aureus* and *E. coli* bacteria are discussed to analyze the suitability of the dyes for use as photosensitizers.

8.0 Introduction

The chlorin dyes used in this work are neutral PS dyes. The illumination of chlorin PS dyes during PDT and PACT studies were performed at 625 and 660 nm within the therapeutic window at the red end of the visible region of the electromagnetic spectrum. The effects of different *meso*-aryl groups that include *meso*-4-methoxyphenyl (**5**), -3-methoxyphenyl (**6**), -4-hydroxyphenyl (**7**), and -4-hydroxy-3-methoxyphenyl (**8**) on the PDT and PACT activities of the dyes are carefully analyzed. The effects of the Sn(IV) ion on the PDT and PACT activities of **5**-**8**-SnChl is also examined. Since the chlorin dyes have relatively high ϕ_Δ values > 0.58, they are anticipated to exhibit favorable PDT and PACT activities.

8.1 *In vitro* PDT cytotoxicity studies of chlorins against MCF-7 cancer cells

Figure 8.1 and **Figure A 54** in the appendix provide the cytotoxicity plots of MCF-7 cancer cells in the dark and under 20 min illumination at 625 and 660 nm from Thorlabs M625L3 and M660L3 LEDs upon treatment with gradient concentrations of **6**-**8**-Chl and **6**-**8**-SnChl. **Table 8.1** provides a summary of IC_{50}, phototoxicity index (PI), and cell viability values of **5**-**8**-Chl and **5**-**8**-SnChl in the dark and under illumination. **5**-**8**-Chl and **5**-**8**-SnChl have IC_{50} values > 25 μM in the dark and ≥ 70% viable cells at 25 μM of the dyes. This suggests that **5**-**8**-Chl and **5**-**8**-SnChl are relatively innocuous toward MCF-7 cancer cells in the absence of illumination. This suggests that the chlorin dyes studied are promising candidates for use as PS dyes in PDT.

During the PDT studies, fixed light doses of 280 and 336 J.cm^2 were used to illuminate chlorin dyes at 625 and 660 nm, respectively. The PDT results demonstrate that illumination of **5**-**8**-Chl and **5**-**8**-SnChl at 660 nm resulted in enhanced PDT activities relative to illumination at 625 nm (**Table 8.1**). This could be due to the reported favorable effects of stronger absorption of light by

a PS dye at longer wavelength deep into the therapeutic window, since it can readily penetrate into the tissues resulting in enhanced phototherapy effects [50,211,212].

5-**8**-Chl free-base chlorins also exhibited relatively favorable PDT activities (**Table 8.1**) relative to the parent **5**-**8**-Por dyes discussed earlier (**Table 6.4**). For example, **5**-**8**-Chl have relatively low IC_{50} values of ≤ 18.8 μM, PI > 1.1, and low cell viability values of ≤ 38.1% at 25 μM after illumination at 625 nm with significantly lower IC_{50} values of ≤ 13.9 μM after illumination at 660 nm (**Table 8.1**). As would be anticipated based on their high ϕ_Δ values and stronger absorption in the NIR region, **5**-**8**-SnChl outperformed their **5**-**8**-Chl free-base chlorin ligands and their **5**-**8**-SnPor analogs (**Table 8.1**). For instance, **5**-**8**-SnChl have IC_{50} values of ≤ 1.5 μM, PI > 16.7, and low cell viability values of ≤ 5.8% at 25 μM of the dyes upon illumination at 660 nm (**Figure 8.1**, **Table 8.1**).

The PDT activity trends due to the different *meso*-aryl substituents of **5**-**8**-Chl and **5**-**8**-SnChl are consistent with those of their parent porphyrin dyes (**5**-**8**-Por, **5**-**8**-SnPor) discussed earlier (**Table 6.4**). For example, *meso*-vanillic chlorin derivatives (**8**-Chl, **8**-SnChl) followed by phenolic chlorins (**7**-Chl, **7**-SnChl) have significantly higher PDT activities than the *meso*-methoxyphenylchlorins (**5**-**6**-Chl and **5**-**6**-SnChl). This trend can be attributed to the anticancer properties of vanillic and phenolic derivatives [294–296]. Overall, chlorins outperformed their parent porphyrin dyes. This can be attributed to the stronger absorption properties of chlorin dyes in the therapeutic window, among other unknown favorable effects.

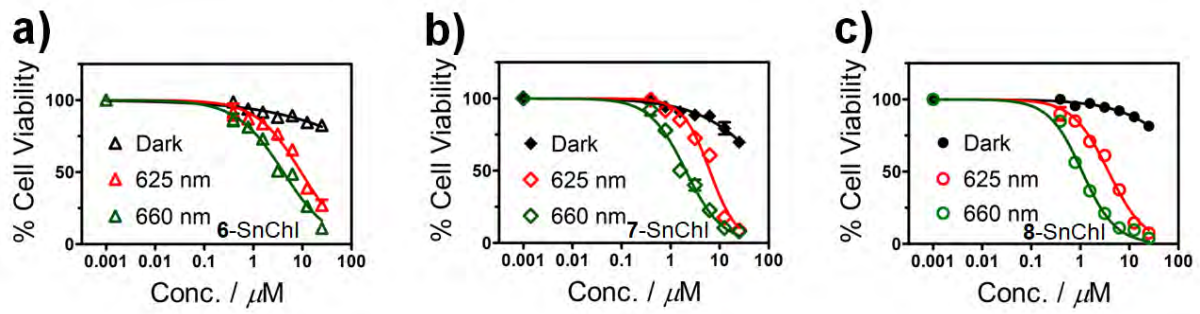

Figure 8.1: Cytotoxicity plots of MCF-7 cancer cells in the dark (black line) and under illumination for 20 min at 625 nm (red line) and 660 nm (green) with M625L3 and M660L3 Thorlabs LEDs, respectively, upon treatment with gradient concentrations of a) **6**-SnChl, b) **7**-SnChl and c) **8**-SnChl.

Table 8.1: IC_{50}, PI, and cell viability values for **5**-**8**-Chl and **5**-**8**-SnChl against MCF-7 cancer cells.

				PI[c]		Cell viability (%)		
		IC_{50} (μM)				at 25 μM		
		Light[b]				Light[b]		
Sample	**Dark[a]**	**625 nm**	**660 nm**	**625 nm**	**660 nm**	**Dark[a]**	**625 nm**	**660 nm**
5-Chl	> 25	18.8	13.9	1.3	1.8	85.2	38.1	31.9
6-Chl	> 25	16.8	12.3	1.5	2.0	86.0	37.7	28.9
7-Chl	> 25	12.1	9.4	2.1	2.7	81.2	34.7	26.7
8-Chl	> 25	10.8	6.1	2.3	4.1	75.8	28.2	23.1
5-SnChl	> 25	6.1	1.4	4.1	17.9	84.2	9.5	5.5
6-SnChl	> 25	7.4	1.5	3.4	16.7	82.4	9.2	5.8
7-SnChl	> 25	4.3	1.1	5.8	22.7	70.7	8.8	4.3
8-SnChl	> 25	3.8	1.0	6.6	24.8	81.5	7.6	3.2

[a] 24 h incubation dark cytotoxicity data, [b]phototoxicity data against MCF-7 cancer cell line upon exposure to Thorlabs M625L3 (240 $mW.cm^{-2}$, 20 min) and M660L3 (280 $mW.cm^{-2}$, 20 min) LEDs. [c]PI = phototoxic index (dark and light IC_{50} values toxicity ratio).

8.2 *In vitro* PACT cytotoxicity studies of chlorins on the planktonic and biofilm cells of *S. aureus* and *E. coli* bacteria.

5-**8**-Chl free-base chlorins and their **5**-**8**-SnChl have minor dark cytotoxicity activities toward planktonic and biofilm cells of *S. aureus* and *E. coli* species (as shown in **Figures A 55**-**56** as examples). The PDT and PACT results for the chlorin dyes showed that the photoexcitation of dyes at 660 nm resulted in enhanced PDT and PACT effects in contrast to illumination at 625 nm (**Tables 8.1-8.3**). This confirms the previous reports that light in the red end of the electromagnetic spectrum deep into the therapeutic window can readily penetrate into tissues resulting in enhanced phototherapy effects [44,177,211,212].

8.2.1 *In vitro* PACT cytotoxicity studies of chlorins on the planktonic cells of *S. aureus* and *E. coli* bacteria

Optimal concentrations of 1 μM for *S. aureus* and 5 μM for *E. coli* were used during time-dependent studies for **5**-**8**-Chl and **5**-**8**-SnChl. These concentrations are comparable to those of the **5**-**8**-Por and **5**-**8**-SnPor analogs discussed earlier (Chapter 6). **Table 8.3** summarizes the time-dependent Log_{10} reduction values and cell survival values for **5**-**8**-Chl and **5**-**8**-SnChl toward planktonic cells of *S. aureus* and *E. coli* after 75 min irradiations at 625 and 660 nm with M625L3 and M660L3 Thorlabs LEDs respectively.

5-**8**-Chl free-base chlorins exhibited favorable PACT activities toward planktonic *S. aureus* with high Log_{10} reduction values after 45 min illumination, while **5**-**8**-SnChl have higher PACT activities toward planktonic *S. aureus* than those of the **5**-**8**-Chl free-base ligands. This is demonstrated by the complete eradication of planktonic *S. aureus* colonies after 15 min illumination for **5**-**8**-SnChl and also 10 min for **7**-**8**-SnChl at 660 nm (**Figure 8.2**, **Table 8.2**), due to the high ϕ_Δ values for **5**-**8**-SnChl that are related to the presence of the heavy Sn(IV) ion.

5-**8**-Chl free-base chlorin ligands also exhibit moderate Log_{10} reduction values under illumination at 660 nm for planktonic *E. coli* in the 2.01−2.65 range after illumination for 75 min, which denotes ≥ 99% cell reduction and ≤ 0.9 cell survival. This contrasts with the favorable performance **5**-**8**-Chl exhibited toward planktonic *S. aureus*. This trend is nevertheless anticipated in the context of neutral PS dyes toward Gram-(−) *E. coli*, since *E. coli* bacteria have a permeability barrier, which restricts PS dyes from penetrating the cells [18,21]. On the other hand, **5**-**8**-SnChl exhibited favorable PACT activities toward planktonic *E. coli* with higher Log_{10} reduction values of ≥ 3.10 after 75 min illumination with Thorlabs M625L3 and M660L3 LEDs (**Table 8.2**). These values are greater than the optimal ≥ 3 Log_{10} (99.9% cell reduction) guideline and ≤ 0.1% cell survival for antimicrobial agents. This suggests that **5**-**8**-SnChl can be efficient PS dyes for the eradication of planktonic *E. coli*.

The effects of different *meso*-aryl substituents on the PACT activities of the chlorin dyes against planktonic *S. aureus* and *E. coli* are consistent with those observed for their porphyrin analogs (**5**-**8**-Por, **5**-**8**-SnPor). The *meso*-4-hydroxyphenyl (**7**-Chl, **7**-SnChl) and -4-hydroxy-3-methoxyphenylchlorins (**8**-Chl, **8**-SnChl) have slightly higher PACT activities than the *meso*-methoxyphenylchlorins (**5**-**6**-Chl, **5**-**6**-SnChl) (**Figure 8.2**, **Table 8.2**). This can be attributed to the hydrophilic vanillic and phenolic *meso*-aryl groups of the chlorin PS dyes, which can interact favorably with the planktonic *S. aureus* and *E. coli* cell wall resulting in slightly enhanced PS penetration and cellular uptake [295,297]. Overall, the PACT activities of chlorin dyes toward planktonic *S. aureus* and *E. coli* at 625 nm are higher than those of the **5**-**8**-Por and **5**-**8**-SnPor dyes discussed earlier. This suggests that there could be other unknown favorable properties for chlorin dyes that enhance their PACT activities.

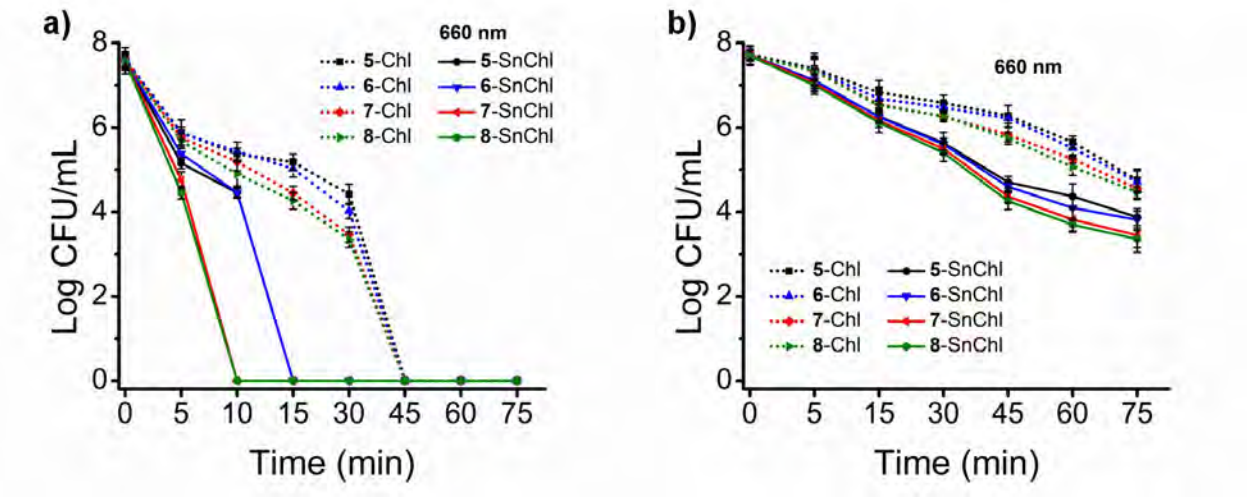

Figure 8.2: Log CFU.mL^{-1} plots of planktonic cells of a) *S. aureus* and b) *E. coli* upon treatment with a) 1 µM and b) 5 µM of **5**-**8**-Chl and **5**-**8**-SnChl after 75 min irradiation at 660 nm using an M660L3 Thorlabs LED (280 mW.cm^{-2}, 75 min).

Table 8.2: Log reduction and cell survival values for chlorin dyes against planktonic cells of *S. aureus* and *E. coli* in 1% DMSO/PBS after illumination at 625 and 660 nm with Thorlabs M625L3 (240 mW.cm^{-2}) and M660L3 (280 mW.cm^{-2}) LEDs.

Sample	*S. aureus*		*E. coli*			
	625 nm	660 nm	625 nm		660 nm	
	Log reduction	Log reduction	Log reduction	Cell survival (%)	Log reduction	Cell survival (%)
5-Chl	7.62 @45[a]	7.62 @45	1.92	1.20	2.01	0.86
6-Chl	7.67 @45	7.67 @45	1.96	1.10	2.20	0.62
7-Chl	7.67 @45	7.67 @45	2.10	0.87	2.47	0.32
8-Chl	7.67 @45	7.67 @45	2.30	0.50	2.65	0.22
5-SnChl	7.62 @15	7.62 @15	3.10	0.04	3.69	0.01
6-SnChl	7.67 @15	7.67 @15	3.50	0.03	3.90	0.01
7-SnChl	7.67 @15	7.67 @10	3.72	0.02	4.24	0.01
8-SnChl	7.67 @15	7.67 @10	3.87	0.01	4.36	< 0.01

[a] Illumination time in minutes for the Log_{10} reduction value is provided after the @ character.

8.2.2 *In vitro* PACT cytotoxic activities of chlorins on the biofilms of *S. aureus* and *E. coli* bacteria

The optimal concentrations of **5**-**8**-Chl and **5**-**8**-SnChl used during the time-dependent studies were 25 µM for *S. aureus* biofilms and 50 µM for *E. coli* biofilms (**Figure 8.3**). The Log_{10} reduction values for *S. aureus* and *E. coli* biofilms are ≥ 1 Log_{10} with ≥ 90% cell reduction and ≤ 10% cell survival (**Table 8.3**). These Log_{10} reduction values are much lower than those observed against the planktonic *S. aureus* and *E. coli* bacteria. This is normally anticipated in the context of *S. aureus* and *E. coli* biofilms, since biofilms are less susceptible to antimicrobial agents due to their self-securing polymeric matrix, which restricts drug penetration [25–27]. The photoexcitation of chlorin dyes at 660 nm resulted in slightly higher Log_{10} reduction values for *S. aureus* and *E. coli* biofilms than those obtained with 625 nm irradiation (**Table 8.3**). This observation agrees with previous reports, which explained that NIR illumination faciltates deeper penetration of light into the tissue resulting in enhanced PACT activities [50,211,212].

The *meso*-4-hydroxyphenyl and -4-hydroxy-3-methoxyphenylchlorins (**7**-**8**-Chl, **7**-**8**-SnChl) exhibited slightly higher PACT activities toward biofilm cells of *S. aureus* and *E. coli* than *meso*-methoxyphenylchlorins (**5**-**6**-Chl, **5**-**6**-SnChl) (**Table 8.3**). This could be associated with favorable interactions between the hydrophilic vanillic and phenolic groups of the chlorin dyes and the biofilm cells, resulting in slightly enhanced drug penetration and cellular uptake [297]. As anticipated based on their high ϕ_Δ values, the Log_{10} reduction values for **5**-**8**-SnChl are slightly higher toward biofilm cells of *S. aureus* and *E. coli* in contrast to the **5**-**8**-Chl free-base ligands (**Table 8.3**).

Table 8.3: Log reduction and cell survival values for chlorin dyes against biofilm cells of *S. aureus* and *E. coli* in 1% DMSO/PBS after illumination for 75 min with Thorlabs M625L3 (240 $mW.cm^{-2}$) and M660L3 (280 $mW.cm^{-2}$) LEDs.

Sample	***S. aureus* biofilm cells**				***E. coli* biofilm cells**			
	625 nm		**660 nm**		**625 nm**		**660 nm**	
	Log reduction	**Cell survival (%)**	**Log reduction**	**Cell survival (%)**	**Log reduction**	**Cell survival (%)**	**Log reduction**	**Cell survival (%)**
5-Chl	1.03	9.3	1.30	5.0	1.10	8.7	1.20	6.3
6-Chl	1.20	6.7	1.30	4.5	1.13	7.5	1.26	5.5
7-Chl	1.25	5.7	1.42	3.8	1.18	6.6	1.37	4.3
8-Chl	1.30	4.8	1.46	3.4	1.23	5.8	1.38	4.1
5-SnChl	1.70	2.0	2.00	1.0	1.64	2.3	1.72	1.9
6-SnChl	1.76	1.7	2.20	0.6	1.77	1.7	2.10	0.9
7-SnChl	1.86	1.4	2.34	0.5	1.92	1.1	2.37	0.6
8-SnChl	1.88	1.3	2.40	0.4	1.94	1.2	2.25	0.4

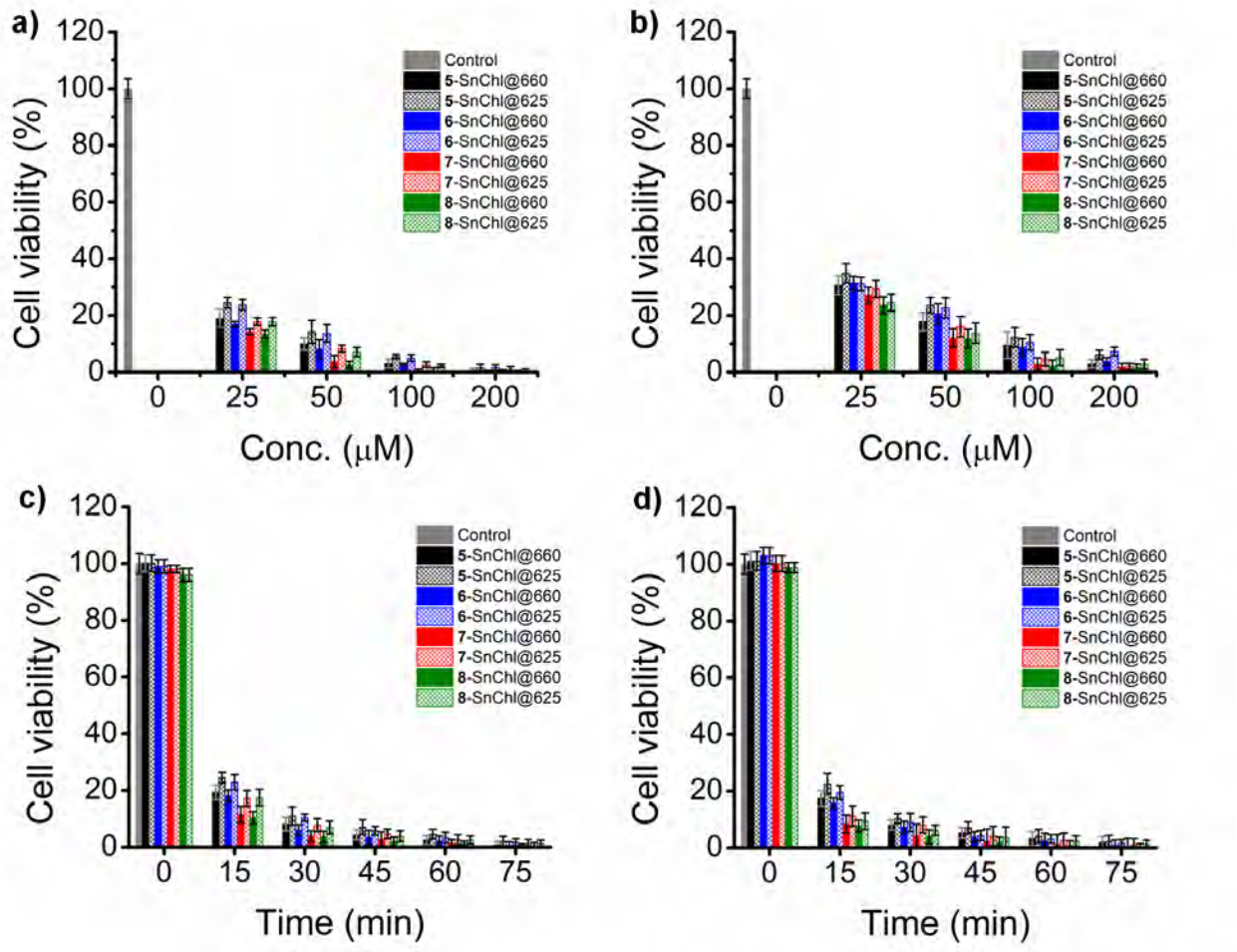

Figure 8.3: The cell viability plots for biofilm cells of a) *S. aureus* and b) *E. coli* upon treatment with gradient concentrations of **5**-**8**-SnChl after 30 min illumination at 625 and 660 nm with Thorlabs M625L3 (240 mW.cm^{-2}) and M660L3 (280 mW.cm^{-2}) LEDs with cell quantification by crystal violet stain. c-d) The cell viability plots of biofilm cells of c) *S. aureus* and d) *E. Coli*, upon treatment with c) 25 μM, and d) 50 μM of **5**-**8**-SnChl after 75 min illumination at 625 and 660 nm with Thorlabs M625L3 (240 mW.cm^{-2}) and M660L3 (240 mW.cm^{-2}) LEDs. Viable colonies were estimated by the viable colony count method.

8.3 Concluding remarks

The photoexcitation of chlorin dyes at 660 nm at the red end of the electromagnetic spectrum resulted in enhanced PDT and PACT activities. The chlorin PS dyes have favorable PDT and PACT activities that are significantly enhanced relative to those of their porphyrin analogs. This is probably due to their high singlet oxygen quantum yields, which favorably enhance the PDT and PACT activities of the chlorin dyes.

CHAPTER NINE

Singlet Oxygen Applications of N-confused Porphyrin Dyes

This chapter discusses the *in vitro* PDT and PACT activities of N-confused porphyrin dyes against MCF-7 breast cancer cells and planktonic and biofilm cells of *S. aureus* and *E. coli* bacteria to analyze the suitability of the dyes for use as photosensitizers in PDT.

9.0 Introduction

The N-confused porphyrin dyes (**5**-NCP, **5**-SnNCP) in this study are neutral PS dyes that consist of *meso*-4-methoxyphenyl groups that are comparable to those of **5**-Por and **5**-SnPor, **5**-Chl and **5**-SnChl. Illuminations were performed at 625 and 660 nm during PDT and PACT studies in the red region of the visible and deeper into the therapeutic window. The effect of the Sn(IV) ion on the PDT and PACT activities of the NCP dyes is assessed. The PDT and PACT activities of **5**-NCP and **5**-SnNCP dyes are consistently compared with those of their porphyrin isomers (**5**-Por, **5**-SnPor) and chlorin (**5**-Chl, **5**-SnChl) analogs. It is anticipated that the NCP dyes studied will have favorable PDT and PACT activities, since **5**-SnNCP dye has an unusually high ϕ_Δ value.

9.1 *In vitro* PDT activities of N-confused porphyrins on MCF-7 cancer cells

The *in vitro* dark cytotoxicity and PDT activities of **5**-NCP and **5**-SnNCP dyes and their porphyrin isomers (**5**-Por, **5**-SnPor) and chlorin analogs (**5**-Chl, **5**-SnChl) toward MCF-7 cancer cells were investigated over gradient drug concentrations in the 0.39−25 μM range. **Figure 9.1** provides the cytotoxicity graphs for MCF-7 cancer cells treated with gradient concentrations of **5**-SnNCP, **5**-SnPor, and **5**-SnChl in the dark and under 20 min illumination at 625 and 660 nm with Thorlabs LEDs. Fixed light doses of 288 and 336 J.cm^{-2} were used for illuminations at 625 and 660 nm, respectively. **Table 9.1** provides a summary of IC_{50}, phototoxicity index (PI), and cell viability values in the dark and after illumination at 25 μM for **5**-NCP, **5**-SnNCP, **5**-Por, **5**-SnPor, **5**-Chl, and **5**-SnChl. **5**-NCP and **5**-SnNCP dyes have IC_{50} values > 25 μM in the dark, with ≥ 81% viable cells at 25 μM of the dyes. This suggests that **5**-NCP and **5**-SnNCP NCP dyes and their porphyrin isomers and chlorin analogs are relatively innocuous toward MCF-7 cancer cells in the absence of

illumination with minor dark cytotoxicity properties. Therefore, these dyes are promising PS dye candidates for use in PDT.

The PDT results for the N-confused porphyrin dyes showed that illumination at 660 nm resulted in enhanced PDT effects in contrast to illumination at 625 nm (**Figure 9.1**, **Figure A 57**, **Table 9.1**). This confirms the previous reports that light in the therapeutic window can readily penetrate into the tissues resulting in enhanced phototherapy effects [44,177,211,212]. Nevertheless, due to its low ϕ_Δ value, **5**-NCP dye exhibited low PDT activity toward MCF-7 cancer cells under illumination at both 625 and 660 nm. This is shown by the high IC_{50} values > 25 µM, a PI < 1, and higher cell viability values of ≤ 56.5% at 25 µM under illumination at 660 nm (**Table 9.1**). In contrast, **5**-SnNCP Sn(IV) NCP exhibited enhanced PDT activity with IC_{50} values ≤ 1.6 µM, PI > 15.6, and low cell viability values ≤ 6.7% at 25 µM for illumination under 660 nm (**Figure 9.1**, **Table 9.1**). **5**-SnNCP outperformed its **5**-SnPor isomer with a comparable PDT activity to that of its **5**-SnChl counterpart (**Table 9.1**). This is due to its exceptionally high ϕ_Δ value and photon absorption properties deep within the therapeutic window.

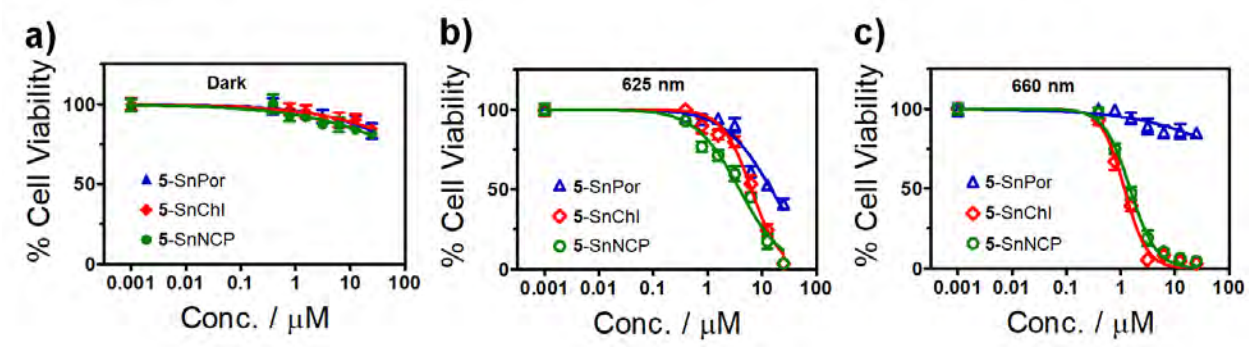

Figure 9.1: Cytotoxicity plots of MCF-7 cancer cells in a) the dark and b-c) under illumination for 20 min at b) 625 nm with M625L3 (240 $mW.cm^{-2}$) LED and at c) 660 nm M660L3 (280

mW.cm^{-2}) Thorlabs LEDs, respectively, upon treatment with gradient concentrations of **5**-SnPor (blue), **5**-SnChl (green) and **5**-SnNCP (red) dyes.

Table 9.1: IC_{50}, PI, and cell viability values for **5**-NCP and **5**-SnNCP and their porphyrin isomers (**5**-Por, **5**-SnPor) and chlorin analogs (**5**-Chl, **5**-SnChl) against MCF-7 cancer cells.

	IC_{50} (μM)			PI[c]		Cell viability (%) at 25 μM		
		Light[b]					Light[b]	
Sample	Dark[a]	625 nm	660 nm	625 nm	660 nm	Dark[a]	625 nm	660 nm
5-Por	> 25	24.7	> 25	< 1	< 1	89.7	46.5	49.4
5-Chl	> 25	> 25	12.4	13.9	1.1	85.2	38.1	31.9
5-NCP	> 25	> 25	> 25	< 1	< 1	87.2	75.8	56.5
5-SnPor	> 25	14.7	22.5	1.7	1.1	83.1	26.8	40.7
5-SnChl	> 25	6.1	1.4	4.1	17.9	84.2	9.5	5.5
5-SnNCP	> 25	4.8	1.6	5.2	15.6	81.4	8.1	6.7

[a] Dark cytotoxicity data 24 h incubation, [b] phototoxicity data against MCF-7 cancer cell line upon exposure to Thorlabs 625 (240 mW.cm^{-2}, 20 min) and 660 nm (280 mW.cm^{-2}, 20 min) LEDs. [c]PI = phototoxic index (dark and light IC_{50} values toxicity ratio).

9.2 *In* vitro cytotoxic activities of N-confused porphyrin dyes on the planktonic and biofilm cells of *S. aureus* and *E. coli*

The N-confused porphyrin dyes (**5**-NCP, **5**-SnNCP) have minor dark cytotoxicity activities toward planktonic and biofilm cells of *S. aureus* and *E. coli* species (**Figures A 54**-**55**). The illumination of NCP PS dyes at 660 nm resulted in enhanced photocytotoxicity activities of the dyes toward planktonic and biofilm cells of *S. aureus* and *E. coli* in contrast to illumination at 625 nm (**Tables 8.2-8.3**). This suggests that illumination at the red end of the visible region in the therapeutic window can enhance the phototherapeutic effect since the light can readily penetrate deeply into the tissues [44,211,212].

9.2.1 *In vitro* PACT activities of N-confused porphyrins on the planktonic cells of *S. aureus* and *E. coli* bacteria

Optimal concentrations of 1 μM for *S. aureus* and 5 μM for *E. coli* were identified for use during the time-dependent studies of NCP dyes in a similar manner to their porphyrin isomers (**5**-Por, **5**-SnPor) and chlorin analogs (**5**-Chl, **5**-SnChl). **5**-NCP free-base ligand exhibits low Log_{10} reduction values for planktonic *S. aureus* and *E. coli* (**Table 9.2**). This shows that **5**-NCP has low PACT activity toward the planktonic *S. aureus* and *E. coli* in contrast to the **5**-Por isomer and its **5**-Chl counterpart (**Figure 9.2**, **Table 9.2**). The low PACT activity for **5**-NCP dye is due to its low ϕ_Δ value resulting in a low phototherapeutic effect.

In marked contrast, inserting a Sn(IV) ion into **5**-NCP to form **5**-SnNCP resulted in enhanced PACT activity with high Log_{10} reduction values for planktonic *S. aureus* and moderate values for planktonic *E. coli* species. For instance, **5**-SnNCP completely eradicated the planktonic *S. aureus* after illumination for 15 min (**Figure 9.2b**, **Table 9.2**). The PACT activities of **5**-SnNCP toward planktonic *S. aureus* and *E. coli* are lower than its **5**-SnChl counterpart and much more favourable than those of its **5**-SnPor isomer (**Table 9.2**). This is due to its unusually high ϕ_Δ value, which results in enhanced cytotoxic effects. **5**-NCP and **5**-SnNCP dyes have low Log_{10} reduction values for planktonic *E. coli* in contrast to the higher values for *S. aureus*, as would be anticipated for neutral PS dyes (**Table 9.2**), since neutral PS dyes are not as effective as positively charged PS dyes in inactivating Gram-(−) *E. coli* due to the doubled layered permeability barrier of *E. coli* that restricts the penetration of PS dyes [18,21].

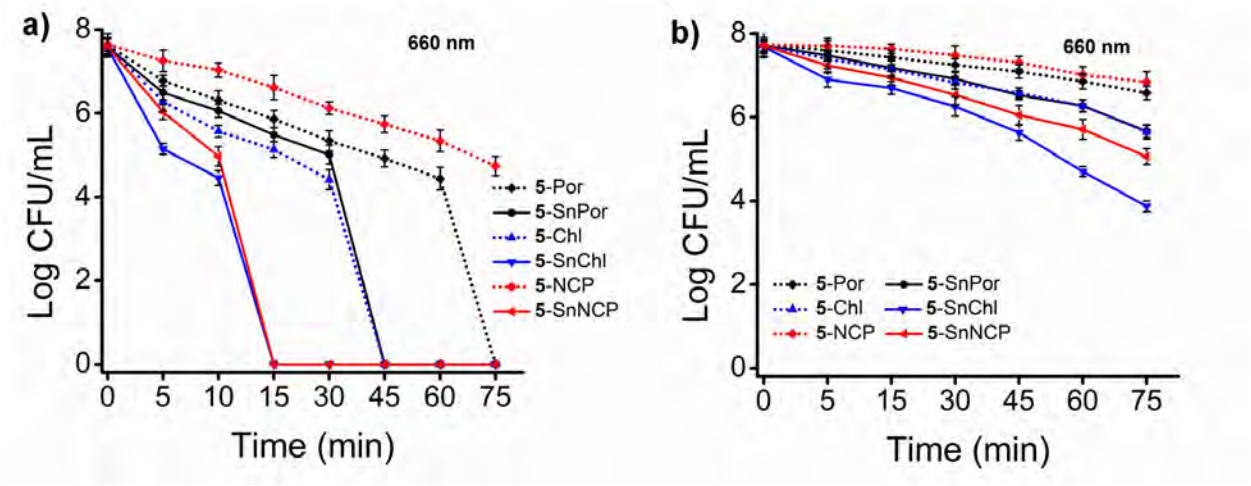

Figure 9.2: Log CFU.mL^{-1} plots of planktonic cells of a) *S. aureus* and b) *E. coli* upon treatment with a) 1 µM and b) 5 µM of **5**-Por, **5**-Chl, **5**-NCP, **5**-SnPor, **5**-SnChl, and **5**-SnNCP dyes after 75 min irradiation at 660 nm using an M660L3 Thorlabs LED (280 mW.cm^{-2}).

Table 9.2: Log reduction and cell survival values for planktonic cells of *S. aureus* and *E. coli* upon treatment with **5**-NCP and **5**-SnNCP dyes, including their porphyrin and chlorin analogs in 1% DMSO/PBS after illumination at 625 and 660 nm with Thorlabs M625L3 (240 mW.cm^{-2}, 75 min) and M660L3 (280 mW.cm^{-2}, 75 min) LEDs.

	S. aureus		***E. coli***			
	625 nm	**660 nm**	**625 nm**		**660 nm**	
Sample	**Log reduction**	**Log reduction**	**Log reduction**	**Cell survival (%)**	**Log reduction**	**Cell survival (%)**
5-Por	7.62 @75[a]	7.62 @45	1.22	6.0	1.13	7.4
5-Chl	7.62 @45	7.62 @45	1.92	1.20	2.01	0.86
5-NCP	2.00 @75	2.48@75	0.76	17.1	0.88	13.3
5-SnPor	7.62 @30	7.62 @45	2.40	0.40	2.01	0.90
5-SnChl	7.62 @15	7.62 @15	3.10	0.04	3.69	0.01
5-SnNCP	7.62 @30	7.62 @15	2.40	0.39	2.90	0.12

[a] Illumination time in minutes for the Log_{10} reduction value is provided after the @ character.

9.2.2 *In vitro* PACT activities of N-confused porphyrins on the biofilms of *S. aureus* and *E. coli* bacteria

Optimized concentrations of 25 μM were used for *S. aureus* biofilms and 50 μM was used for *E. coli* biofilms during the time-dependent studies for **5**-NCP and **5**-SnNCP in a similar manner to their porphyrin isomers (**5**-Por, **5**-SnPor) and chlorin analogs (**5**-Chl, **5**-SnChl). **5**-NCP and **5**-SnNCP have slightly higher Log_{10} reduction values for *S. aureus* and *E. coli* biofilms after illuminations at 660 nm in contrast to those at 625 nm (**Table 9.3**). This confirms the previous reports that illuminations that allow deeper penetration into tissue results in enhanced phototherapy effects [44,50,211,212].

The Log_{10} reduction values for biofilms of *S. aureus* and *E. coli* upon treatment with **5**-NCP and **5**-SnNCP are low in contrast to those obtained for planktonic bacteria. This is expected for biofilms, since they have a polymeric matrix that secures the biofilms from the cytocidal effects of antimicrobial agents [25–27]. **5**-NCP exhibits very low Log_{10} reduction values for *S. aureus* and *E. coli* biofilms in contrast to **5**-Por and **5**-Chl (**Figure 9.3**, **Table 9.3**). This could be due to the low ϕ_Δ value of **5**-NCP. On the other hand, **5**-SnNCP exhibits higher PACT activities toward the biofilm cells of *S. aureus* and *E. coli* in contrast to its **5**-NCP free-base ligand and **5**-SnPor isomer (**Table 9.3**). The activities of **5**-SnNCP are closely comparable to those of **5**-SnChl. This is due to the high ϕ_Δ value for **5**-SnNCP dye.

Table 9.3: Log reduction and cell survival values for biofilm cells of *S. aureus* and *E. coli* upon treatment with **5**-NCP and **5**-SnNCP dyes, including their porphyrin and chlorin analogs in 1% DMSO/PBS after illumination for 75 min at 625 and 660 nm with Thorlabs M625L3 (240 mW.cm^{-2}, 75 min) and M660L3 (280 mW.cm^{-2}, 75 min) LEDs.

Sample	*S. aureus* biofilm cells				*E. coli* biofilm cells			
	625 nm		660 nm		625 nm		660 nm	
	Log_{10} reduction	Cell survival (%)	Log_{10} reduction	Cell survival (%)	Log_{10} reduction	Cell survival (%)	Log_{10} reduction	Cell survival (%)
5-Por	0.74	18.0	0.69	20.5	0.79	16.1	0.63	23.4
5-Chl	1.03	9.3	1.30	5.0	1.10	8.7	1.20	6.3
5-NCP	0.34	45.8	0.46	34.6	0.31	49.4	0.42	37.8
5-SnPor	1.35	4.0	1.20	6.5	1.49	3.3	1.22	6.0
5-SnChl	1.70	2.0	2.00	1.0	1.64	2.3	1.72	1.9
5-SnNCP	1.34	4.5	1.58	2.6	1.40	4.0	1.63	2.4

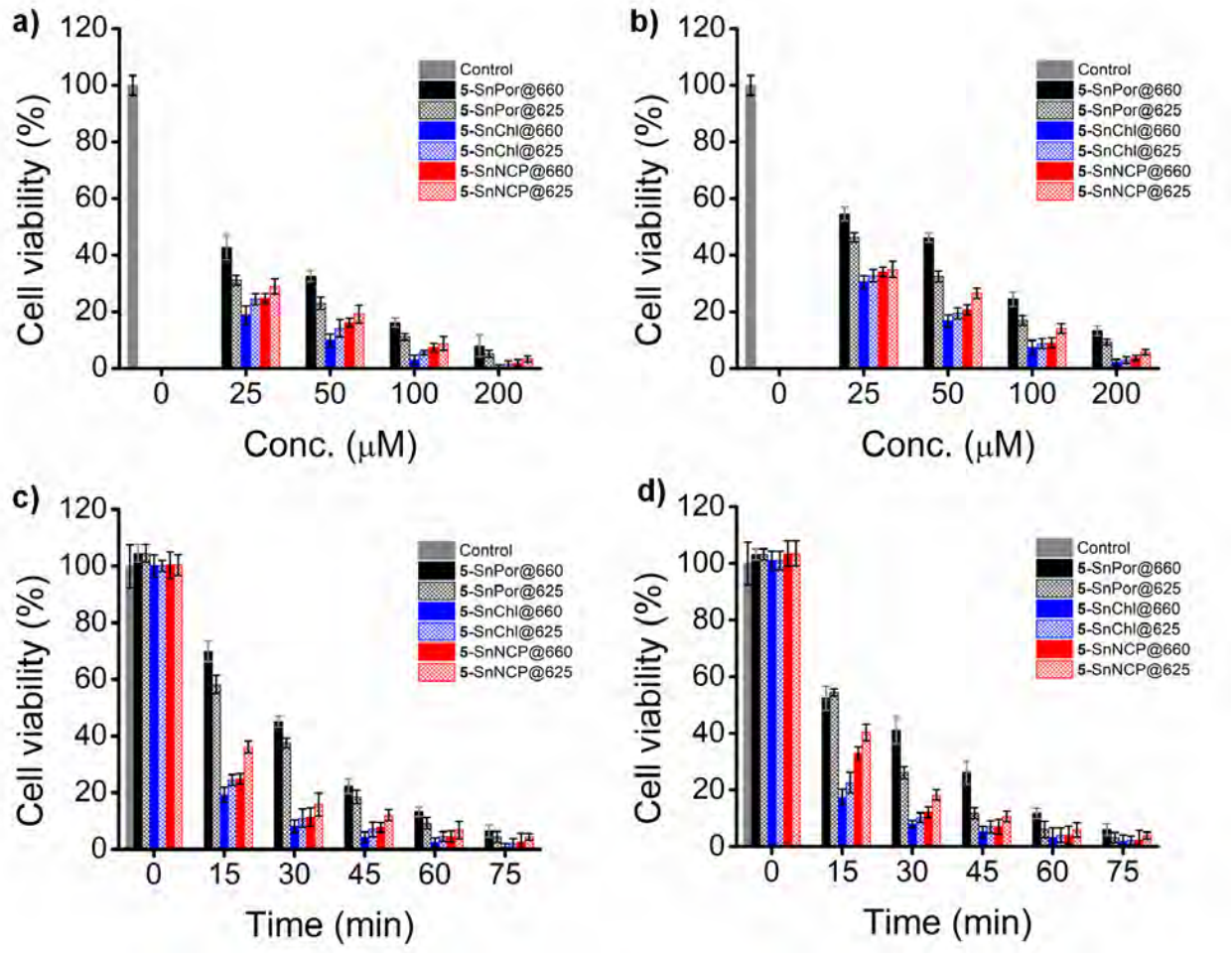

Figure 9.3: The cell viability plots for biofilm cells of a) *S. aureus* and b) *E. coli* upon treatment with gradient concentrations of **5**-SnNCP, **5**-SnPor, and **5**-SnChl after 30 min illumination at 625 and 660 nm with Thorlabs M625L3 (240 mW.cm^{-2}) and M660L3 (280 mW.cm^{-2}) LEDs with cells quantification by crystal violet stain. c-d) The cell viability plots of biofilm cells of c) *S. aureus* and d) *E. Coli*, upon treatment with c) 25 μM, and d) 50 μM of **5**-SnNCP, **5**-SnPor, and **5**-SnChl after 75 min illumination at 625 and 660 nm with Thorlabs M625L3 (240 mW.cm^{-2}) and M660L3 (280 mW.cm^{-2}) LEDs. Viable colonies were estimated by using the viable colony count method.

9.3 Concluding remarks

5-SnNCP exhibited favorable PDT and PACT activities based on its exceptionally high ϕ_Δ in contrast to its **5**-NCP free-base ligand and **5**-SnPor isomer. The NCP dyes have higher PDT and PACT activities upon illumination at 660 nm rather than 625 nm. **5**-SnNCP is a promising PS drug for use in PDT and PACT treatments and merits further in depth study.

CHAPTER TEN

Molecular Modeling Calculations of the Dyes

This chapter details the theoretical molecular modeling studies of porphyrins, corroles, chlorins, and N-confused porphyrin dyes.

10.0 Introduction

This chapter provides an in-depth analysis of the electronic structures of the dyes studied and predicts their optical properties trends by examining the structure-property relationships. This was accomplished by carrying out geometry optimization and time-dependent density functional theory (TD-DFT) theoretical calculations. TD-DFT has emerged as an indispensable theoretical tool for obtaining valuable data that successfully predict several key features of molecules in the excited state, such as vibronic coupling, charge transfer, optical and photophysicochemical properties [109,272,298]. The TD-DFT data in this study are conceptualized using Gouterman's 4-orbital and Michl's perimeter models (discussed in Chapter 1, **Section 1.4**). The main focus of this chapter is to investigate the trends in the main spectral features of structurally related porphyrins and porphyrin analog dyes arising from changes in the energies of the four frontier π-MOs due to coordination ion at the core, the *meso*-aryl substituents or symmetry-related effects relative to the parent porphyrin core. This is done by analyzing changes in the angular nodal patterns and relative energies of the **a**, **s**, **-a**, and **-s** frontier MOs, and changes in the magnitudes of the HOMO−LUMO gaps of the dyes. The key goal of the project is to red shift (bathochromic shift) and intensify the Q bands of the dyes in the therapeutic window for their potential use as PS dyes in PDT and PACT applications. The TD-DFT calculations are also used to confirm the observed MCD sign patterns, since they are a function of the relative arrangement of the four frontier π-MOs [272]. This helps to validate the accuracy of the calculations.

10.1 Computational Methods

All the theoretical calculations involving the optimization of molecular geometries of the dyes were performed using the Becke-3-parameter, Lee-Yang-Parr (B3LYP) exchange-correlation

functional of the Gaussian 09 software package with either 6-31G(d) or SDD basis sets. SDD basis sets were preferred since they offer reasonable approximations for porphyrin, corroles, chlorins, and N-confused porphyrin complexes containing heavy atoms, such as Ga(III), In(III), and Sn(IV) metals [223]. **Figure A 61** shows the optimized B3LYP-SDD geometries as representative examples of the studied porphyrins, corroles, chlorins, and N-confused porphyrin dyes. The In(III) and Ga(III) ions lie above the porphyrin macrocycle in a slightly domed conformation (as shown in **Figures A 61 a and b**). In contrast, the P(V) ion of corrole complexes and the Sn(IV) ion of the porphyrin, chlorin, and N-confused porphyrin complexes lie in-plane with the porphyrin or porphyrinoid cores resulting in slightly distorted square-planar conformations (**Figure A 61b** and **c**). This is consistent with previously reported conformations for P(V) and Ga(III) corroles [174]. The optimized B3LYP geometries of the dyes were then used to carry out TD-DFT calculations using the Coulomb-attenuated B3LYP (CAM-B3LYP) functional with SDD basis sets. The CAM-B3LYP functional was used since it incorporates an increasing fraction of Hartree-Fock (HF) exchange parameters as the interelectronic separation increases to provide a long-range correction [222].

10.2 Molecular modeling of In(III) and Sn(IV) porphyrin dyes

Modeling calculations were carried out for **1**-**4**-InPor and **5**-**8**-SnPor, and their In(III) and Sn(IV) 5,10,15,20-*meso*-tetraphenylporphyrin parent complexes (InTPP and SnTPP). For the porphyrin dyes studied, TD-DFT calculations predict the effects of structural modifications on the optical properties of the parent porphyrins ((Cl)InTPP and SnTPP) mainly due to the different *meso*-aryl substituents and metal centers (In(III), Sn(IV)). The simulated TD-DFT spectra of the complexes can be readily accounted for in the context of Gouterman's 4-orbital model [172] (**Figure 1.7**).

This model describes how the intense B bands and weak Q bands of porphyrin arise from the electronic transitions in the four frontier π-MOs of the 16-atom 18-π electron parent $C_{16}H_{16}^{2-}$ cyclic polyene of the porphyrin ring with M_L = ±4 or ±5 angular nodal properties [172]. The four frontier π-MOs are readily assigned as the **a**, **s**, **-a**, and **s** MOs by following Michl's perimeter model so that the electronic structures of dyes of differing symmetries can be readily compared [173]. Since the HOMO and LUMO MOs have M_L values ±4 and ±5 angular nodal properties, the electronic transitions between the nearly degenerate **a** and **s** HOMO (a_{1u} and a_{2u}) and the degenerate **-a** and **-s** LUMO ($1e_g$) MOs give rise to the intense allowed B bands (ΔM_L = ±1) and relatively weak forbidden Q bands (ΔM_L = ±9) of normal porphyrins (**Figures 10.1, 10.2, 10.7** and **10.9**).

The electronic transitions and TD-DFT absorption spectra of In(III) and Sn(IV) porphyrins are summarized in **Table A 5** in the Appendix. The angular nodal patterns of the HOMO−LUMO MOs of In(III) porphyrins are shown in **Figure 10.1**, while **Figure 10.2** shows the simulated TD-DFT spectra, π-MOs, and HOMO−LUMO gap energies of the In(III) porphyrin dye series. **Figures 10.6**-**10.8** contrast and compare the angular nodal patterns of the frontier π-MOs, calculated TD-DFT spectra, and HOMO−LUMO gap energies of **5**-**8**-SnPor and their **5**-**8**-SnChl and **5**-SnNCP analogs and the SnTPP parent complex.

Since the theoretical calculations for InTPP, **1**-InPor, and **3**-InPor have already been reported [209], a summary is provided in this context. The **a**, **s**, **-a**, and **-s** MOs of **1**-**4**-InPor are largely stabilized relative to those of the parent (Cl)InTPP for In(III) porphyrin series (as shown in **Figure 10.1** and **Figure 10.2b**). This is due to the inductive effects from the electron-donating sulfur atoms of the **1**-**4** *meso*-aryl groups, which result in slight red shifts on the main spectral bands of

the dyes. There are also marked red shifts on the main spectral bands of *meso*-thien-2-yl (**3**-InPor) and *meso*-5-bromo-thien-2-yl porphyrin derivatives (**4**-InPor) in contrast to those of *meso*-thien-3-yl (**2**-InPor) and *meso*-4-methylthiophenyl (**1**-InPor) and the parent (Cl)InTPP *meso*-tetraphenylporphyrin (**Figure 10.3**). This is due to the lack of *ortho*-H and β-H steric hindrance resulting in easier rotation of the *meso*-thien-2-yl groups and, thus, more effective mesomeric interactions between the *meso*-thien-2-yl groups and the porphyrin core [268,269,299]. The **s**, **-a**, and **-s** MOs are more stabilized than the **a** MOs for the *meso*-thien-2-yl derivatives (**3**-**4**-InPor), since they have larger MO coefficients at the *meso*-positions (**Figure 10.2**). This results in a slight narrowing of the HOMO−LUMO gaps, which is consistent with the observed red shifts in the simulated TD-DFT (**Figure 10.2a**, **Table A2**) and experimental UV-visible absorption spectra of the dyes (**Table 4.1**).

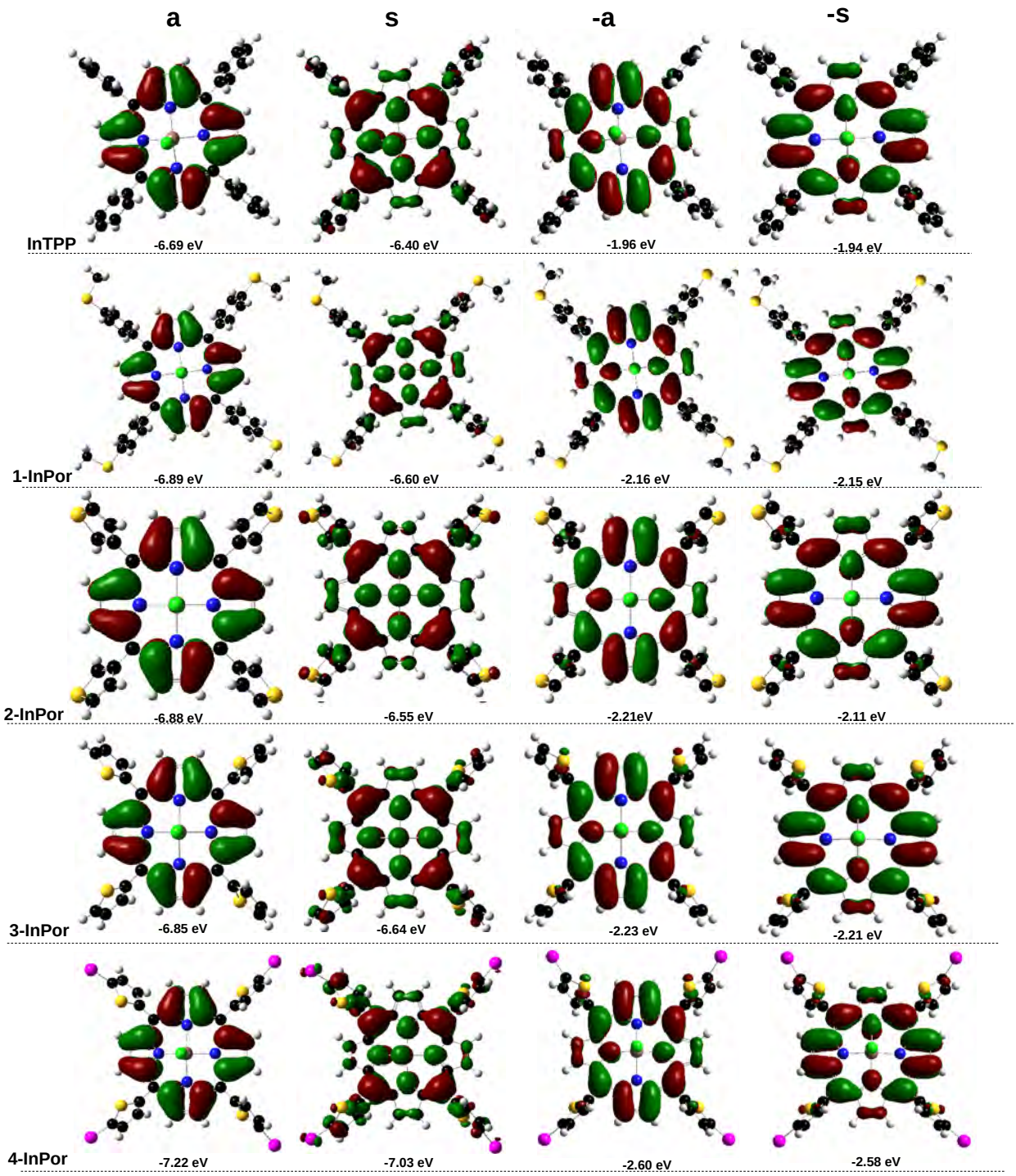

Figure 10.1: Angular nodal patterns and energies of **a**, **s**, **-a**, and **-s** MOs of the parent InTPP and **1**-**4**-InPor.

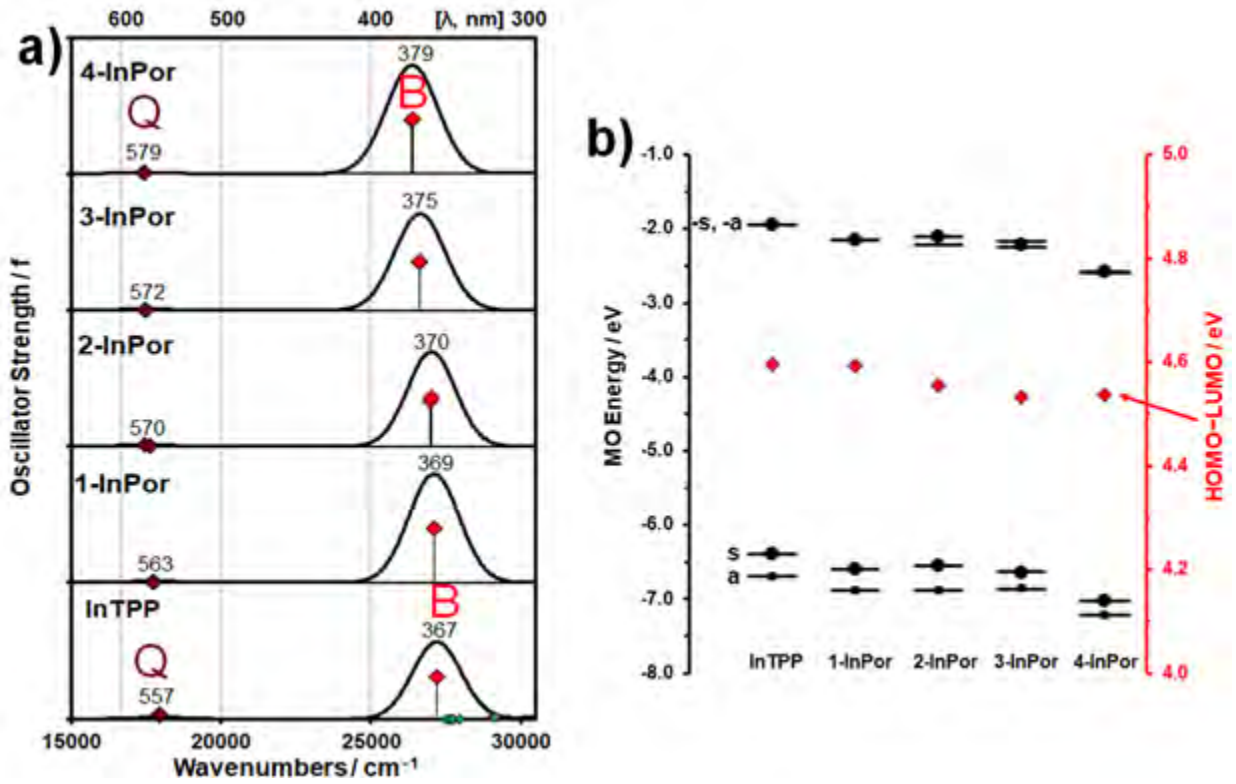

Figure 10.2: a) TD-DFT spectra for InTPP and **1**-**4**-InPor at the CAM-B3LYP/SDD level. The Q bands are highlighted with maroon and B bands in red diamonds. The Chemcraft software package was used to generate the simulated TD-DFT spectra at a fixed bandwidth of 2000 cm^{-1}. b) Molecular orbital energies of InTPP and **1**-**4**-InPor at the CAM-B3LYP/SDD level. The red diamonds highlight the average HOMO−LUMO gap energies obtained by taking into account the **a**, **s**, **-a**, and **-s** MOs, and are plotted against a secondary axis. Small black squares highlight the occupied MOs **s**, and larger black circles denote the **s** and **-s** MOs.

The **a**, **s**, **-a**, and **-s** MOs of **5**-SnPor and **7**-**8**-SnPor are stabilized, and they have smaller MO coefficients at the *meso*-carbons relative to the parent SnTPP structure. This is due to the favorable inductive effects arising from the *meso*-4-methoxyphenyl (**5**), *meso*-4-hydroxyphenyl (**7**), and *meso*-4-hydroxy-3-methoxyphenyl (**8**) *meso*-aryl groups. This results in a slight narrowing

of HOMO−LUMO gaps and red shifts on the spectral bands of the dyes. However, the **s** MO of **6**-SnPor is destabilized in contrast to those of its corresponding *para*-methoxyphenylporphyrin isomer (**5**-SnPor), **7**-**8**-SnPor, and SnTPP control. This results in a slightly larger HOMO−LUMO gap for **6**-SnPor and hence, the observed blue shifts in its spectral bands.

In general, there are relatively minor changes in the main spectral and electronic structures of the parent (Cl)InTPP and SnTPP porphyrins upon introducing different *meso*-aryl groups to **1**-**4** and **5**-**8**. There are also minor changes in the frontier orbital energies of **1**-**4**-InPor and **5**-**8**-SnPor relative to those of the (Cl)InTPP and SnTPP parent complexes (**Figures 10.3** and **10.5**). The slight red shifts observed are due to the favorable inductive effects from the electron-donating *meso*-aryl substituents. The interaction of the **s** MO with the electropositive Sn(IV) central ion for **5**-**8**-SnPor complexes is significant, since it has larger MO coefficients at the nitrogen pyrrole in contrast to the In(III) ion for **1**-**4**-InPor (**Figures 10.6** and **10.8**). The ΔHOMO (difference in the energies of the **a** and **s** MOs) values of the studied In(III) and Sn(IV) porphyrin dyes (**1**-**4**-InPor and **6**-**8**-SnPor) are much greater than ΔLUMO (difference in the energies of the **–a** and **-s** MOs) values (**Figures 10.3** and **10.9**). This trend is consistent with the observed MCD spectra of In(III) and Sn(IV) porphyrin and the sign patterns from −/+ in ascending energy and also with the observed UV-visible absorption spectral bands (see Chapter 4 Section **4.1.1**).

10.3 Molecular modeling of P(V) and Ga(III) corrole dyes

Since the TD-DFT calculations for Ga(III) corroles did not always reach completion at the CAM-B3LYP/6-31G(d) level of theory, the SDD basis set functional was consistently used during TD-DFT calculations of all the P(V), and Ga(III) A_3 and A_2B triaryl corroles studied. The TD-DFT calculations predict the optical properties related to the changes in energies of the four frontier π-MOs due

to symmetry effects arising from introducing a direct pyrrole-pyrrole bond to form corrole dyes from the porphyrin core [128]. The effects of different electron-donating and electron-withdrawing *meso*-aryl substituents, and the P(V) and Ga(III) central ions, on the spectral properties of the corrole dyes studied were also closely examined. Since the theoretical calculations for the parent P^{V}TPCor, Ga^{III}TPCor, Ga^{III}TPFPC, **1**-**3**-P^{V}Cor, **1**-**3**-GaCor, and **9**-**10**-GaCor have already been reported [174,210], a summary is provided in this context.

Table A 5 in the Appendix summarizes the calculated TD-DFT spectral band wavelengths, oscillator strengths, and electronic transitions of the corroles studied. **Figure 10.3** shows the angular nodal patterns of the **a**, **s**, **-a**, and **-s** MOs of P^{V}TPCor, **4**-P^{V}Cor, Ga^{III}TPCor, **4**-GaCor, Ga^{III}TPFPC, and **10**-GaCor corroles as representative examples for the A_3 and A_2B *meso*-triaryl P(V) and Ga(III) corrole complexes. The simulated TD-DFT spectra of A_3 *meso*-triaryl P(V) and Ga(III) corrole complexes are depicted in **Figure 10.4**, and the MO energies and HOMO−LUMO energies are provided in **Figure 10.5**, while those of the previously reported **9**-**10**-GaCor [210] are provided in **Figure 10.6**.

The calculated Q and B bands of the studied A_3 and A_2B *meso*-triaryl corrole dyes can be interpreted in the context of Gouterman's 4-orbital model (**Figure 1.7**) using the four frontier π-MOs associated with the 15 atom 18-electron $C_{15}H_{15}^{3-}$ parent hydrocarbon of the corrole ring as discussed previously for porphyrin dyes. For symmetry reasons, corrole complexes (C_{2v}) lack the four-fold symmetry due to the loss of methine bridge in contrast to metalloporphyrins (D_{4h}) [114]. This results in a lifting of the degeneracy of the **-a** and **-s** MOs (**Figures 10.3**, **10.5**, and **A 42**) and the mixing of the forbidden Q band and allowed B band properties of the corrole dyes, which results in a slight intensification of the Q bands relative to the parent porphyrins.

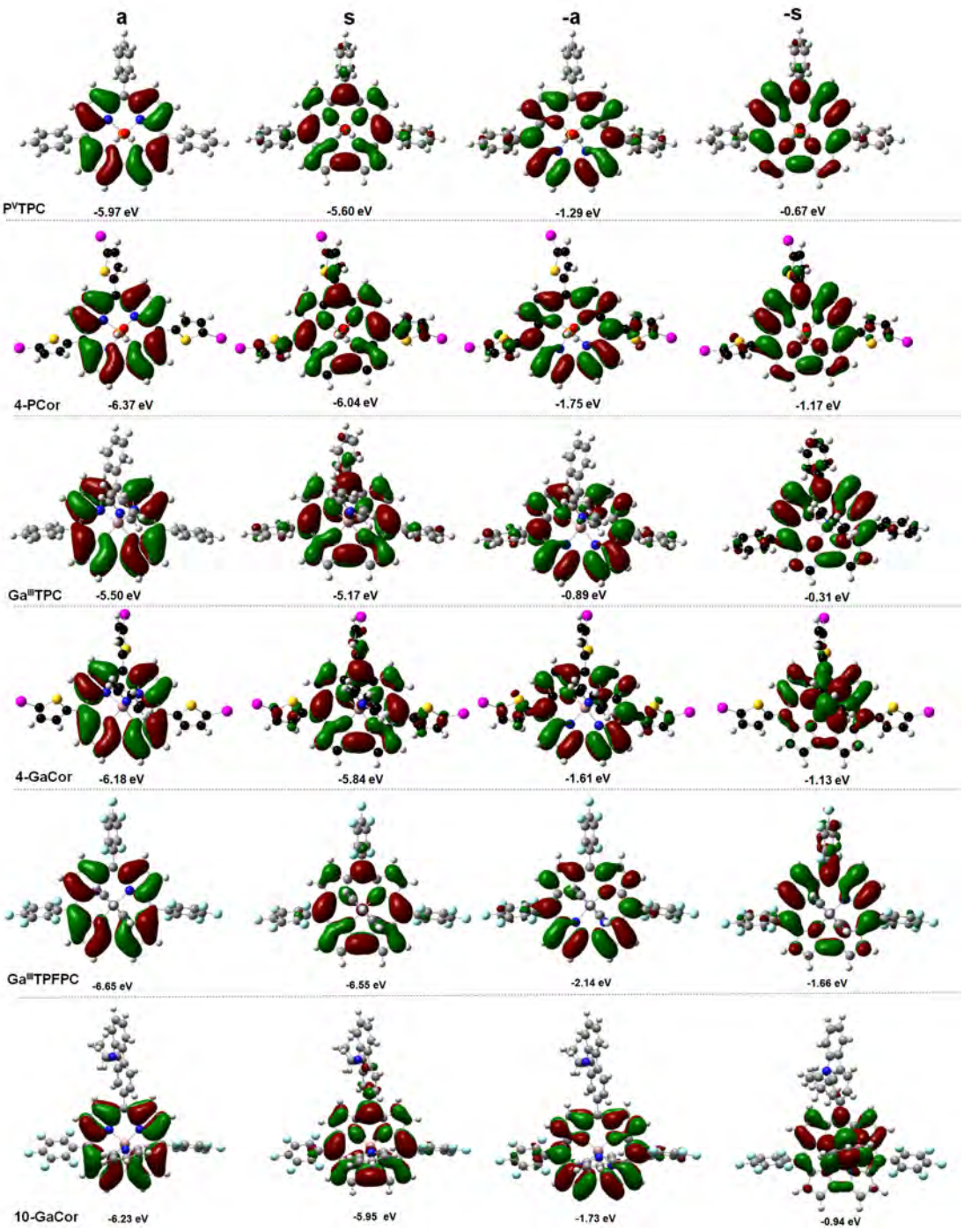

Figure 10.3: Angular nodal patterns of and energies of **a**, **s**, **-a**, and **-s** MOs of P^{V}TPCor, **4**-P^{V}Cor, **4**-GaCor, Ga^{III}TPFPC, and **10**-GaCor corroles.

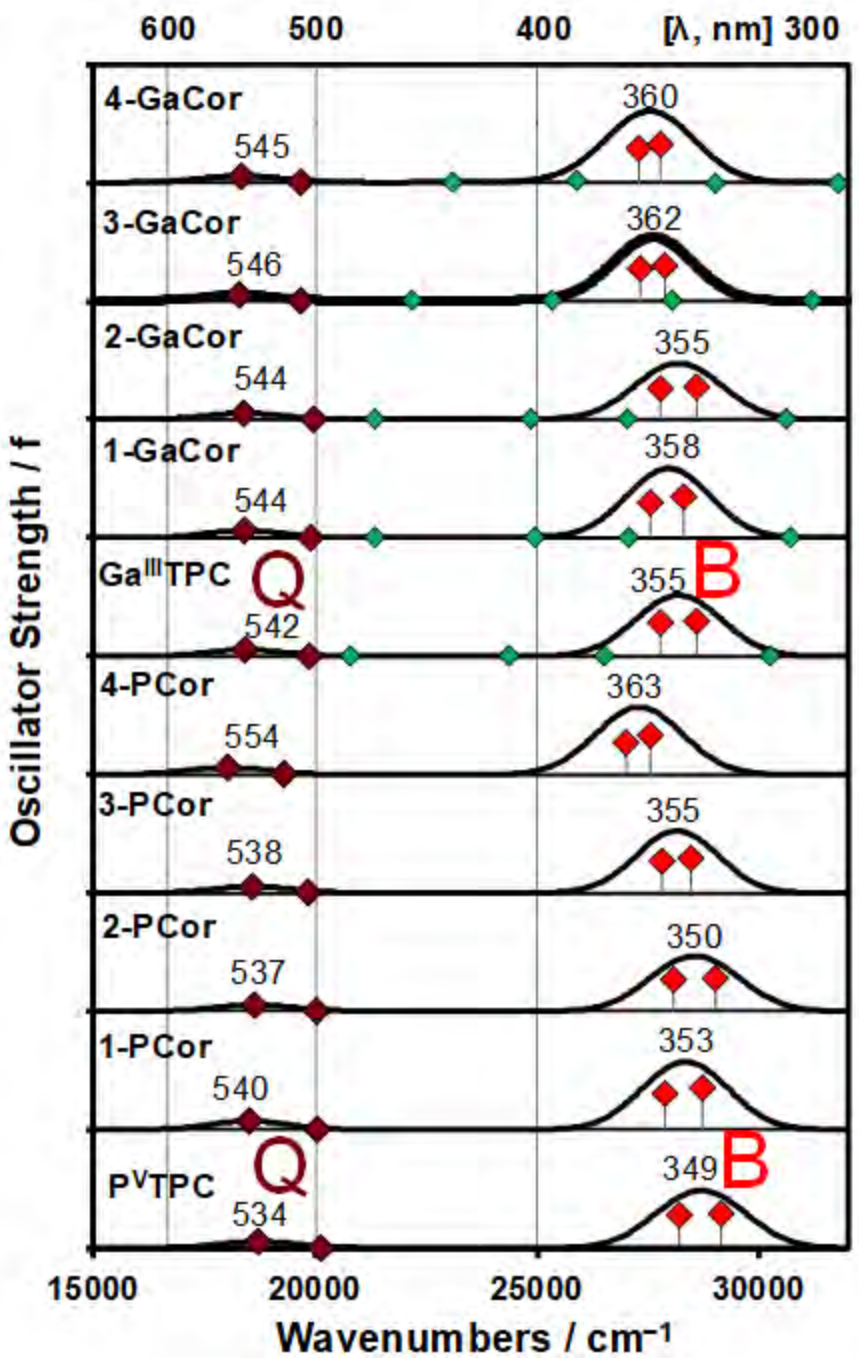

Figure 10.4: TD-DFT spectra for P^{V}TPCor, **1**-**4**-P^{V}Cor, Ga^{III}TPCor, and **1**-**4**-GaCor at the CAM-B3LYP/SDD level of theory. The Q bands are highlighted with maroon and B bands in red diamonds. The simulated TD-DFT spectra were generated using the Chemcraft software package at a fixed bandwidth of 2000 cm^{-1}.

The calculated main spectral bands of **1**-**4**-GaCor are more red shifted than those of the corresponding **1**-**4**-P^{V}Cor P(V) corroles (**Figure 10.5**). This could be due to more effective interactions of the **s** MOs with the more electropositive Ga(III) central ion due to larger MO coefficients at the pyrrole nitrogen. This results in a minor narrowing of HOMO−LUMO gaps resulting in the observed red shifts [174].

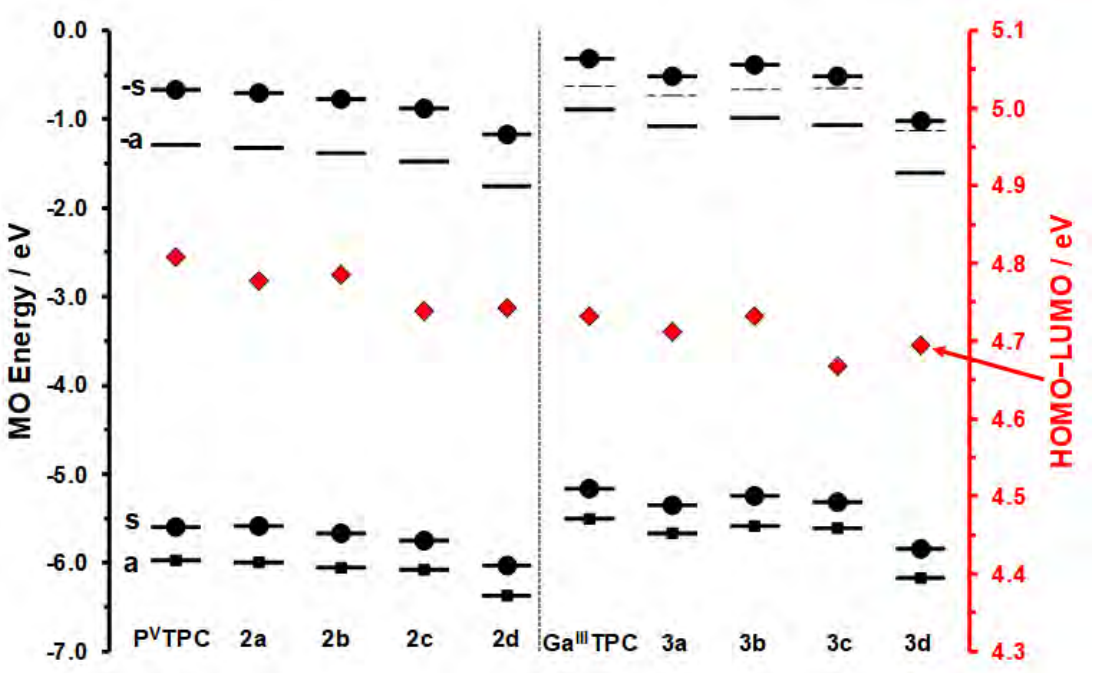

Figure 10.5: Molecular orbital energies of P^{V}TPCor, **1**-**4**-P^{V}Cor (**2a**-**d**), Ga^{III}TPCor, **1**-**4**-GaCor (**3a**-**d**) at the B3LYP/SDD level of theory. The average HOMO−LUMO gap energies plotted against a secondary axis are highlighted by red diamonds. Occupied MOs are highlighted with small black squares, and black circles denote the **s** and **-s** MOs. The MO energies for the axial pyridyl rings are highlighted with dashed lines.

The changes of the energies of the frontier π-MOs energies due to the inductive and mesomeric effects arising from the different *meso*-aryl substituents of **1**-**4**-P^{V}Cor and **1**-**4**-Ga in contrast to

the parent *meso*-phenyl structures (P^{V}TPCor and Ga^{III}TPCor) result in minor spectral changes (**Figure 10.4**). This trend is consistent with those for **1**-**4**-InPor discussed previously. There are also red shifts in the main spectral bands of *meso*-thien-2-yl derivatives (**3**-**4**-P^{V}Cor and **3**-**4**-GaCor) relative to those of *meso*-methylthiophenyl (**1**), *meso*-thien-3-yl (**2**), and parent *meso*-phenyl structures (P^{V}TPCor, Ga^{III}TPCor). This is due to more effective mesomeric interactions between the *meso*-thien-2-yl derivatives with the corrole core [174], which is consistent with those of their corresponding **3**-**4**-InPor complexes that were previously discussed. The **s**, **-a**, and **-s** MOs of *meso*-thien-2-yl derivatives (**3**-**4**-P^{V}Cor and **3**-**4**-GaCor) are more stabilized than the **a** MOs due to larger MO coefficients at the *meso*-carbons (**Figure 10.4**). This results in a minor narrowing of the HOMO−LUMO gaps and, consequently, the observed red shifts in the simulated spectral bands in the TD-DFT spectra are consistent with the observed UV-visible absorption spectra (**Table 4.2**).

There are also relatively minor spectral changes for the **9**-**10**-GaCor A_2B triaryl Ga(III) corroles due to push-pull effects arising from the electron-withdrawing *meso*-pentafluorophenyl groups at the A_2 positions and the electron-donating carbazole moieties at the B position (**Figure 10.6**). Due to inductive effects, the electron-withdrawing groups at the A_2 positions largely stabilize the frontier MOs of **9**-**10**-GaCor relative to the parent Ga^{III}TPCor. In contrast, the electron-donating carbazole groups destabilize the **s** and **-s** MOs of **9**-**10**-GaCor, which have larger MO coefficients at the *meso*-positions than the parent *meso*-tripentafluorophenylcorrole due to mesomeric effects (Ga^{III}TPFPC) [210]. In general, the ΔLUMO values are greater than ΔHOMO values for the studied A_3 and A_2B *meso*-triaryl P(V) and Ga(III) corroles, which is consistent with the +/− sign patterns arranged in ascending energy in the MCD spectra (**Figure A 38**). The calculated TD-DFT spectra of

all the corrole dyes studied are generally consistent with the observed UV-visible absorption spectra (**Table 4.2**).

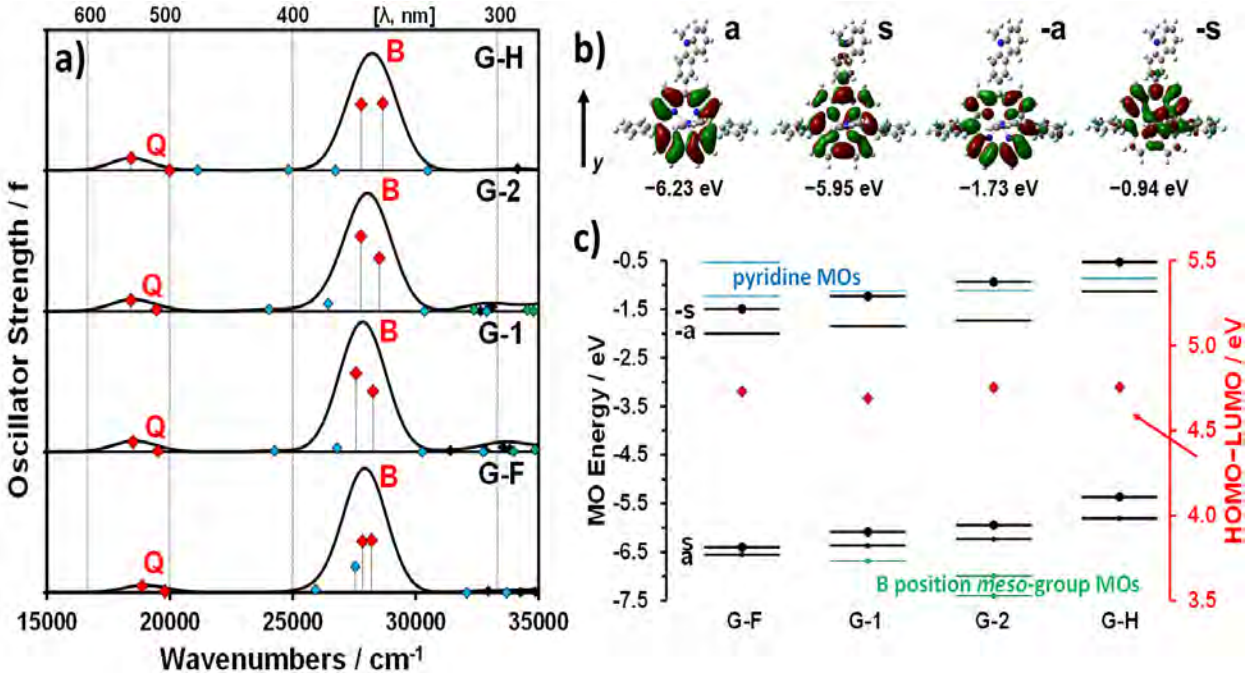

Figure 10.6: a) Calculated TD-DFT spectra for the parent structures Ga^{III}TPFPC (**G-F**), Ga^{III}TPCor (**G-H**), and **9**-**10**-GaCor (**G-1** and **G-2**) at the CAM-B3LYP/SDD level. The Q and B bands are highlighted with red diamonds, while blue and green diamonds are used for transitions into MOs localized on the axial pyridine ligand and out of MOs localized on the B position *meso*-aryl group, respectively. The Chemcraft software package was used to generate the simulated TD-DFT spectra at a fixed bandwidth of 2000 cm^{-1}. b) Angular nodal patterns of **a**, **s**, **-s**, **-a** frontier MOs of **10**-GaCor. **c)** Molecular orbital energies of Ga^{III}TPFPC (**G-F**), Ga^{III}TPCor (**G-H**), and **9**-**10**-GaCor (**G-1** and **G-2**) at the CAM-B3LYP/SDD level of theory. The red diamonds highlight the average HOMO−LUMO gap energies obtained by taking into account the **a**, **s**, **-a**, and **-s** MOs, and are plotted against a secondary axis. Blue and green lines are used for the MOs localized on the axial pyridine ligand and the B position

meso-aryl group, respectively. Small black or green squares denote occupied MOs in this context, while small black squares highlight the occupied MOs, and larger black circles denote the **s** and **-s** MOs. Reproduce from Reference [210]. Copyright © Royal Society of Chemistry 2022.

10.4 Molecular modeling of the Sn(IV) chlorins and Sn(IV) N-Confused dye

Theoretical calculations were also carried out for **5**-**8**-SnChl and **5**-SnNCP. The TD-DFT spectral properties of the chlorins and N-confused porphyrin dyes can be described in the context of Gouterman's 4-orbital model (**Figure 1.7**) associated with the four frontier π-MOs of the 16-atom 18-π electron parent $C_{16}H_{16}^{2-}$ hydrocarbon of the porphyrin ring as previously described for porphyrin dyes [172]. The TD-DFT calculations for the **5**-**8**-SnChl and **5**-SnNCP dye series successfully predict trends related to the changes in the main spectral features of the dyes due to structural modifications arising from symmetry effects and the *meso*-aryl substituents.

Figure 10.7 shows the angular nodal patterns of the **a**, **s**, **-a**, and **-s** MOs of the parent SnTPP, **5**-SnPor, **5**-SnChl, and **5**-SnNCP as representative examples for Sn(IV) porphyrin, chlorin, and N-confused porphyrin dyes. The angular nodal patterns of HOMO−LUMO MOs of **6**-**8**-SnPor and **6**-**8**-SnChl are also shown in **Figure A 62** in the Appendix.

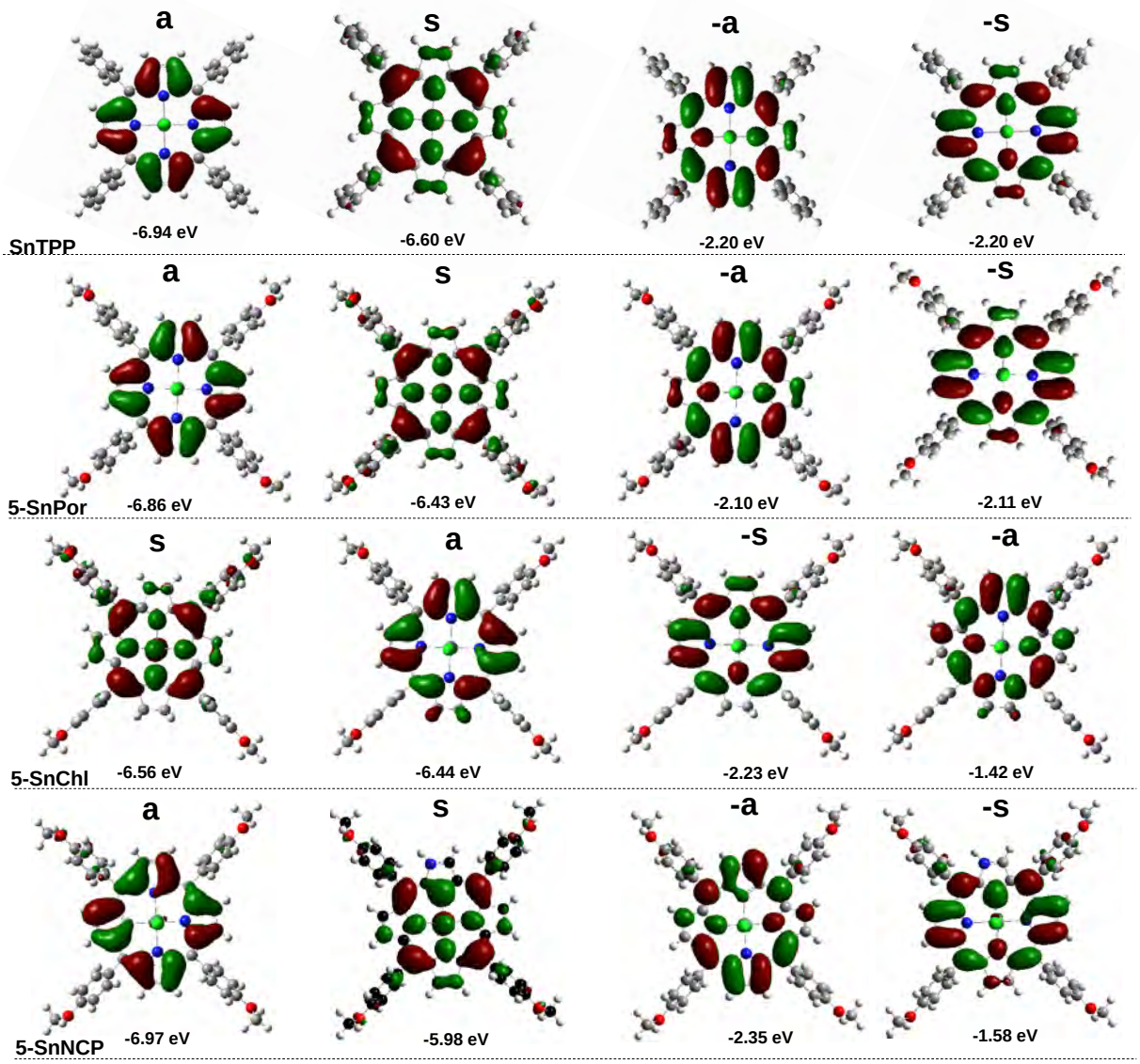

Figure 10.7: Angular nodal patterns of and energies of **a**, **s**, **-a**, and **-s** MOs of the parent SnTPP, **5**-SnPor, **5**-SnChl, and **5**-SnNCP.

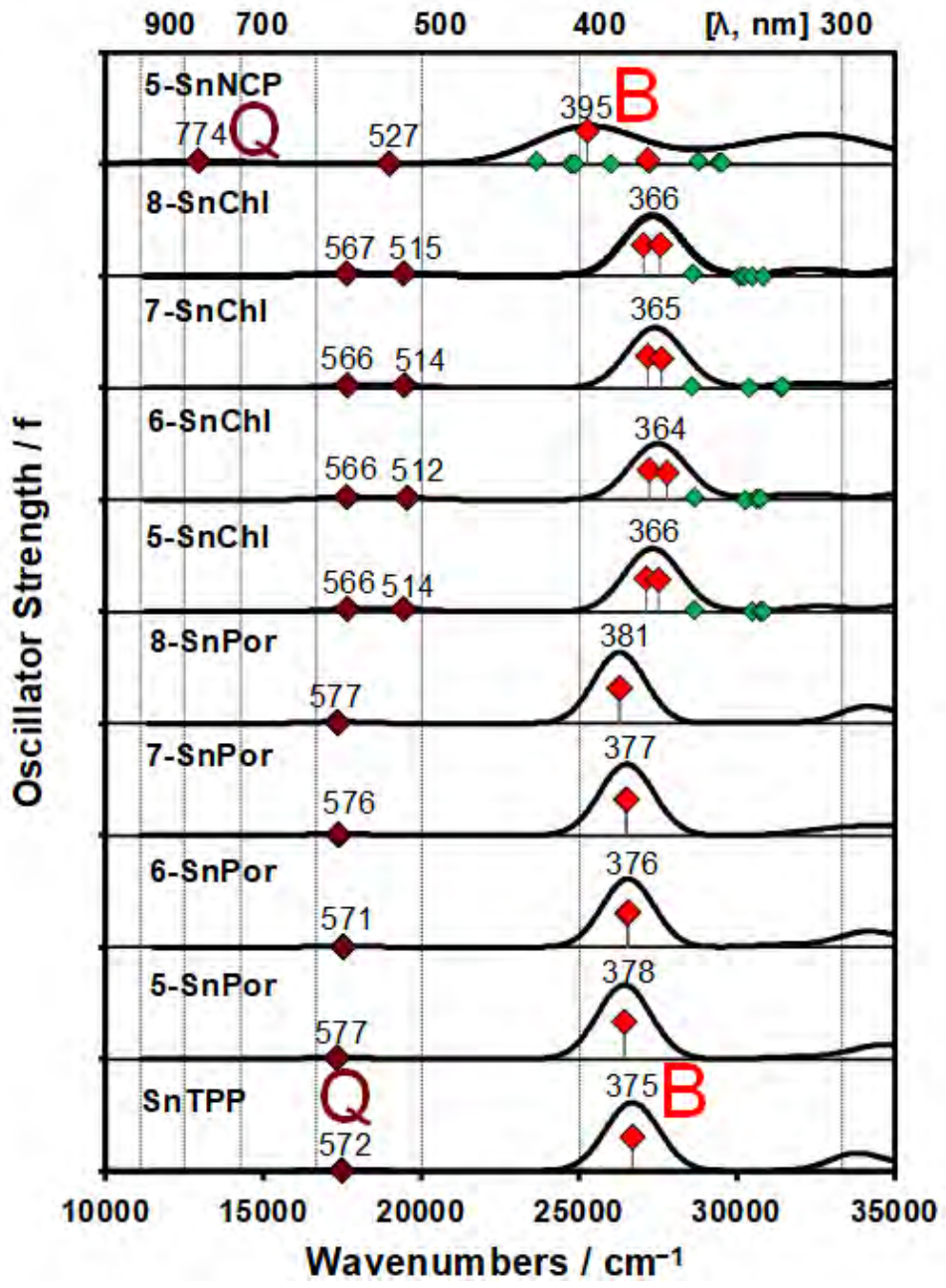

Figure 10.8: TD-DFT spectra for SnTPP, **5**-**8**-SnPor, **5**-**8**-SnChl, and **5**-SnNCP at the CAM-B3LYP/SDD level of theory. The Q and B bands are highlighted with maroon and red diamonds, respectively. The Chemcraft software package was used to generate the simulated TD-DFT spectra at a fixed bandwidth of 2000 cm^{-1}.

The calculated TD-DFT spectra of the studied Sn(IV) porphyrin (**5**-**8**-SnPor), chlorin (**5**-**8**-SnChl), and N-confused porphyrin (**5**-SnNCP) complexes are shown in **Figure 10.8**, and a summary of their MO energies and HOMO−LUMO energies are provided in **Figure 10.9**. The calculated TD-DFT spectral band wavelengths, oscillator strengths, and electronic transitions of the studied Sn(IV) porphyrins, chlorins, and N-confused porphyrins are summarized in **Table A 5** in the Appendix.

The structural modifications that result from the reduction of one of the peripheral pyrrole bonds of the porphyrin ring or inversion of one of the inner nitrogen atoms to the outer perimeter of the pyrrole ring gives rise to low symmetry chlorins and N-confused porphyrins [44,50]. Therefore, for symmetry reasons, metallochlorins (**5**-**8**-SnChl) and metallo-N-confused porphyrin (**5**-SnNCP) lack the characteristic four-fold symmetry of metalloporphyrin (D_{4h}) dyes [109,172] (as shown in **Figures 10.7**, **10.9** and **Figure A 42**).

The degeneracy of the **-a** and **-s** MOs of **5**-**8**-SnChl is lifted since the **-s** MOs have larger MO coefficients at the reduced peripheral β-pyrrole bond in contrast to their porphyrin analogs (**5**-**8**-SnPor) and the SnTPP model complex (**Figure 10.9**). This splitting of the **-a** and **-s** MOs energies and the mixing of forbidden Q band and allowed B band properties of **5**-**8**-SnChl results in the observed intensification of the Q bands relative to those of their corresponding **5**-**8**-SnPor (**Figures 4.6** and **4.7**). However, the average HOMO−LUMO gaps of **5**-**8**-SnChl are slightly larger than those of the corresponding **5**-**8**-SnPor complexes (**Figure 10.9**). This results in the observed minor blue shifts in their main spectral bands (**Figure 10.8**, **Table A 5**).

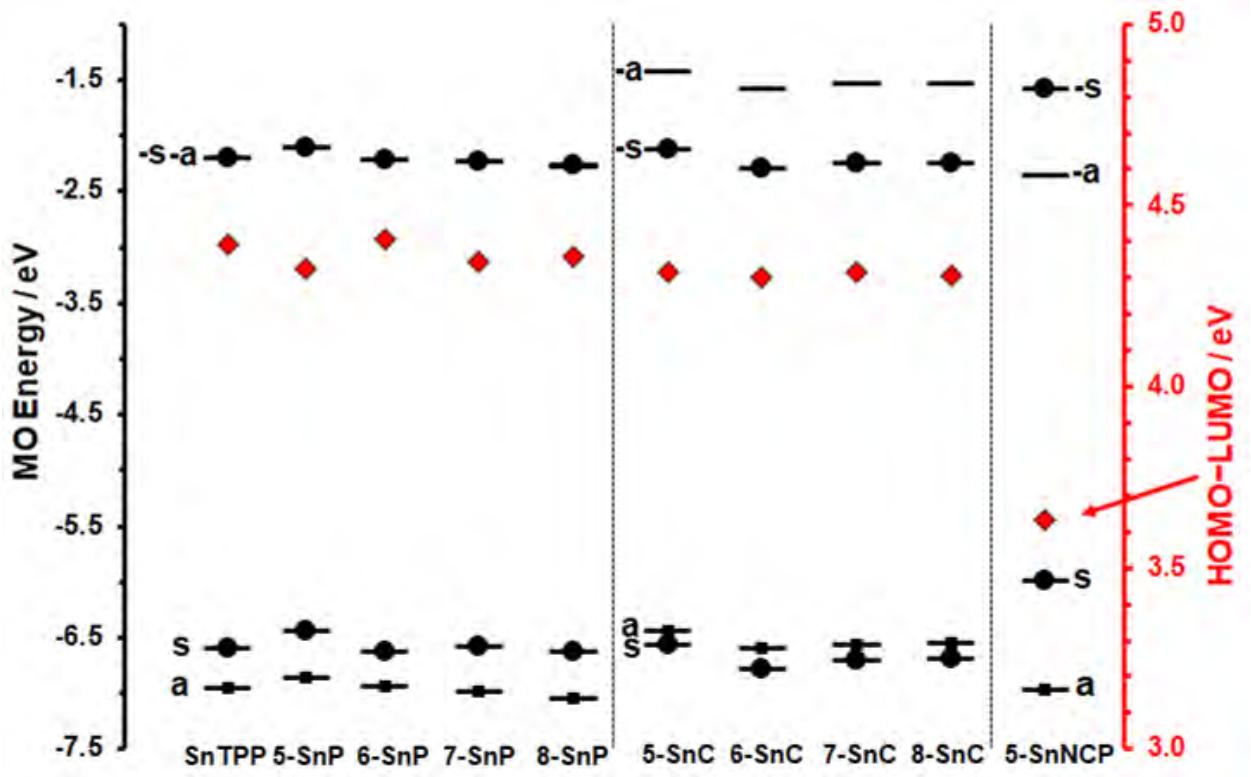

Figure 10.9: Molecular orbital energies of SnTPP, **5**-**8**-SnPor, **5**-**8**-SnChl, and **5**-SnNCP at the B3LYP/SDD level of theory. The red diamonds highlight the HOMO−LUMO gap energies and are plotted against a secondary axis. Occupied MOs are highlighted with small black squares, and black circles denote the **s** and **-s** MOs.

The **s** and **-s** MOs of **5**-SnNCP are destabilized since there are large MO coefficients on the carbon that replaces the inner pyrrole ring nitrogen of the **5**-SnPor isomer and SnTPP model complex (**Figures 10.7** and **10.9**). The **-a** MO is stabilized due to a large MO coefficient on the confused pyrrole nitrogen (**Figure 10.9**). **5**-SnNCP has a narrower HOMO−LUMO gap (**Figure 10.9**) than its **5**-SnPor isomer and the SnTPP model complex. This results in marked red shifts of the main spectral bands of the dye (**Figures 4.8c** and **10.8**, **Table 4.3**). The *meso*-aryl substituents result in minor changes in the main spectral features of **5**-**8**-SnChl and **5**-SnNCP, which are consistent with those of the corresponding **5**-**8**-SnPor dyes. The **s** MOs of **5**-SnChl and **7**-**8**-SnChl are destabilized

and have smaller MO coefficients relative to the SnTPP model complex due to favorable mesomeric interactions with the chlorin core. This results in a minor narrowing of the HOMO−LUMO gaps and red shifts in the main spectral bands of the dyes. However, the **s** MO of **6**-SnChl is destabilized compared to those of its corresponding **5**-SnChl isomer and the SnTPP parent complex, which results in a slightly larger HOMO−LUMO value and the observed blue shifts in the spectral bands of the dye.

In general, the ΔLUMO values of **5**-**8**-SnChl are larger than the ΔHOMO values, in contrast to those of the corresponding **5**-**8**-SnPor dyes (**Figure 10.9**). This theoretical observation is consistent with +/− sign patterns in ascending energy in the MCD spectra of **5**-**8**-SnChl (**Figure 4.2**, and **Figure A 42**). The ΔHOMO > ΔLUMO trend for **5**-SnNCP is also consistent with the sign sequence observed for its **5**-SnPor isomer, but the ΔHOMO and ΔLUMO values for **5**-SnNCP are larger. This is consistent with the MCD spectra of **5**-SnNCP, which consists of −/+ sign patterns arranged in ascending energy terms for the Q and B bands (**Figure 4.2**).

10.5 Concluding remarks

TD-DFT theoretical calculations predicted the structure-property relationships of the porphyrin, corrole, chlorin, and N-confused porphyrin dye complexes studied due to the different *meso*-aryl substituents and coordination core ions, and the effects of molecular symmetry. Introducing different *meso*-aryl substituents on the parent structures resulted in minor spectral changes due to their inductive and mesomeric effects, while the insertion of electropositive metal centers, such as Ga(III), In(III), and Sn(IV), into the cores of the dyes resulted in marked red shifts of the B bands due to favorable interactions with the porphyrin or porphyrinoid ligand core. The changes in the main spectral features of chlorin, corrole, and N-confused porphyrin dyes for symmetry

reasons are very significant, with strong absorption properties predicted in the therapeutic window in contrast to the parent porphyrin. The simulated TD-DFT spectra and changes in the ΔLUMO and ΔHOMO energies of the frontier MOs of the dyes studied are consistent with the observed UV-visible absorption and MCD spectra (discussed in **Chapter 4**).

CHAPTER ELEVEN

Conclusions and Recommendations for Further Studies

This chapter provides concluding remarks and recommendations for further studies.

11.0 Conclusions

This study mainly focussed on the synthesis and characterization of *meso*-aryl tetrapyrrolic dyes that include porphyrins, corroles, chlorins, and N-confused porphyrins that have favorable photophysicochemical properties as PS dyes for use in PDT and PACT. These dyes were successfully synthesized using facile synthetic approaches that mainly involved acid-catalyzed condensation reactions of different aromatic aldehydes with pyrrole under the specified conditions. The synthetic approaches used readily allow the scaling up of yields. In this work, the key focus was to identify structure-property relationships, particularly on the optical and photophysicochemical features of the synthesized dyes that determine the suitability of the dyes for use in PDT and PACT treatments. The structural modifications considered include the introduction of different *meso*-aryl substituents, core functionalization with metals (Ga(III), In(III), and Sn(IV)) and P(V) ions, and the reduction of lower symmetry in the context of the corroles, chlorins, and N-confused porphyrin dyes.

The *meso*-aryl groups of the synthesized tetrapyrrolic dyes contain heteroatoms, such as sulfur, nitrogen, and halides, that are known to enhance the binding affinities of the PS drugs to tissues. These *meso*-aryl groups used include methylthiophenyl (**1**), thienyls (**2**-**4**), carbazoles (**9**-**10**-GaCor), pentafluorophenyl (**9**-**10**-GaCor), methoxyphenyl (**5**-**6**), phenolic (**7**), and vanillic (**8**) rings. *Meso*-phenyl rings were used in model complexes and as control compounds. The insertion of heavy metal ions into the cores of the dyes and halides on the *meso*-aryl groups red shifted the main spectral bands of the dyes and enhanced the intersystem crossing to the triplet excited states. This resulted in the enhanced generation of singlet oxygen as demonstrated by the higher ϕ_{Δ} values for these complexes relative to those of the free-base ligands and also enhanced the

photostabilities of the dyes, while the insertion P(V) ion lowered the lipophilicity values of the dyes and enhanced the uptake of PS dyes by the cells.

Since **1**-**4**-InPor, **1**-**4**-P^{V}Cor, and **1**-**4**-GaCor have sulfur atoms on their *meso*-aryl substituents, they were conjugated to AuNPs and AgNPs through self-assembly *via* sulfur-gold and sulfur-silver affinities to afford the dye-AuNP or dye-AgNP nanoassemblies. Conjugation of the dyes to AgNPs and AuNPs significantly enhanced the photostabilities, ϕ_{Δ} values of the dyes due to the external heavy atom effect, and PS drug uptake. The introduction of a cationic charge to **10**-GaCor afforded a cationic **10**-GaCor-Q species with lower lipophilicity and enhanced PS dye uptake. On the other hand, the lower symmetry of the corroles, chlorins, and N-confused porphyrins resulted in enhanced absorption properties within the therapeutic window at the red end of the visible region and into the NIR. This addressed the inherent weak absorbance of the porphyrin dyes at the red end of their UV-visible absorption spectra.

The studied porphyrins, corroles, chlorins, and N-confused porphyrins exhibited minor dark cytotoxicity activities toward MCF-7 cancer cells, planktonic and biofilm cells of *S. aureus* and *E. coli* species and significant cytotoxicity effects after illumination. This is desirable for PS dyes used in PDT and PACT treatments. Since the synthesized dyes are mainly neutral PS dyes, the PACT activities of the dyes toward planktonic *E. coli* are generally lower than those for planktonic *S. aureus*. This is anticipated since neutral PS dyes are not as effective as cationic dyes in the photoinactivation of Gram-(−) bacteria species, such as *E. coli*, due to the permeability barriers of Gram-(−) bacteria species, which restrict the penetration of uncharged PS dyes. The PACT activities of the studied porphyrin and porphyrin analog PS dyes toward biofilm cells of *S. aureus* and *E. coli* are also lower due to the lower susceptibility of biofilm bacteria to the antimicrobial

agents since they have a polymetric matrix that secures the microbes. This is demonstrated by the lower Log_{10} reduction values for the biofilms compared to those obtained for the planktonic bacteria cells.

The effect of incorporating different *meso*-aryl groups into the porphyrin and porphyrin analog dyes on the PDT and PACT activities of the dyes is relatively minor. Nonetheless, the thienyl derivatives of In(III) porphyrin (**2**-**4**-InPor) and A_3 P^V and Ga^{III} corrole dyes (**2**-**4**-P^VCor, **2**-**4**-GaCor) and their nanoconjugates have slightly enhanced PDT and PACT activities in contrast to the *meso*-methylthiophenyl derivatives and phenyl control compounds. Also, the *meso*-vanillic and phenolic porphyrins (**7**-**8**-Por, **7**-**8**-SnPor) and chlorins (**7**-**8**-Chl, **7**-**8**-SnChl) exhibited slightly enhanced PDT and PACT activities relative to the *meso*-methoxy derivatives (**5**-**6**-Por, **5**-**6**-SnPor, **5**-**6**-Chl, and **5**-**6**-SnChl). This could be due to the previously reported anticancer and antimicrobial activities of thienyl, vanillic and phenolic derivatives. The push-pull effects from the electron-withdrawing *meso*-pentafluorophenyl groups and electron-donating *meso*-carbazole group for A_2B Ga^{III} corroles also enhanced the PDT and PACT activities of these dyes. The introduction of cationic species on the *meso*-carbazole moiety for **10**-GaCor-Q significantly improved the PDT and PACT activities. This is shown by the lower IC_{50} value against MCF-7 cancer cells, higher log reduction values for planktonic *S. aureus* and *E. coli* that are in the > 3−7.78 Log_{10} $CFU.mL^{-1}$ range, and > 1 Log_{10} $CFU.mL^{-1}$ for the biofilm bacteria. This is related to the enhanced uptake of **10**-GaCor-Q.

The insertion of In(III), Ga(III), and Sn(IV) metal ions into the porphyrin and porphyrin analog dye cores also enhanced PDT and PACT activities of the metal complexes toward MCF-7 cancer cells and planktonic *S. aureus* relative to the corresponding free-base ligands. This is demonstrated by

the low IC_{50} values for the complexes against MCF-7 cancer cells and higher log reduction values in the > 3−7.6 Log_{10} range for planktonic *S. aureus*, which denote > 99.9% cell reduction or complete eradication colonies. This is due to their enhanced generation of cytotoxic singlet oxygen, as shown by higher ϕ_Δ values for the metal complexes. The P(V) ion of the A_3 P^V corrole dyes exhibited enhanced PDT and PACT activities relative to their A_3 Ga^{III} corrole counterparts. This is most likely due to the dihydroxy axial ligands of the P(V) ion, which decrease aggregation effects at higher concentrations of the dyes and enhance uptake by the MCF-7 cancer cells and bacteria cells.

Conjugation of **1**-InPor, **1**-**3**-P^VCor, and **1**-**3**-GaCor to AuNPs significantly decreased the dark cytotoxicity activities of the nanoconjugates against MCF-7 cancer cells. This is demonstrated by the higher cell viabilities for the dye-AuNP nanoconjugates relative to the corresponding dye complexes alone. The AuNP nanoconjugates also exhibited enhanced PDT activities, as demonstrated by the lower IC_{50} values and cell viabilities for MCF-7 cancer cells than is observed with the complexes alone.

In a similar manner to the **1**-**4**-InPor-AuNPs and AgNP nanoconjugates, **1**-**4**-P^VCor and **1**-**4**-GaCor exhibited enhanced PACT activities toward planktonic and biofilm cells of *S. aureus* and *E. coli* species, as shown by their higher log reduction values > 7.6 Log_{10} $CFU.mL^{-1}$ with complete eradication of *S. aureus* colonies. **3**-**4**-P^VCor-AgNP nanoconjugates are relatively efficient PS dyes against planktonic *E. coli* species, as demonstrated by their log reduction values > 3 Log_{10} $CFU.mL^{-1}$. Since the biofilm bacteria are less susceptible to antimicrobial agents, conjugation of the dyes to AuNPs or AgNPs resulted in moderate PACT activities with > 1 Log_{10} $CFU.mL^{-1}$. The improved PDT and PACT activities of the nanoconjugates in contrast to the dyes alone are due to

the favorable synergistic effects of AuNPs and AgNPs, such as enhanced ϕ_Δ values, cellular uptake, and the enhanced permeability and retention effect.

The lower symmetry of the A_3 P^V and Ga^{III} corroles, Sn(IV) chlorins, and Sn(IV) N-confused porphyrin dyes also resulted in enhanced PDT and PACT activities relative to those of their porphyrin analogs. This is due to the enhanced absorption of light within the therapeutic window, which facilitates penetration of light into deep-seated cancer and bacteria cells. Also, illumination of chlorins and N-confused porphyrin photosensitizers at 660 nm using a Thorlabs M660L3 LED (280 $mW.cm^{-2}$) resulted in enhanced PDT and PACT activities of the dyes relative to 625 nm illumination from a Thorlabs M625L3 LED (240 $mW.cm^{-2}$). This is due to the significant absorbance by the dyes in the red region of the visible, deep into the therapeutic window, which results in enhanced penetration of light into the MCF-7 cells, and the planktonic and biofilm cells of *S. aureus* and *E. coli*.

Interestingly, the neutral **5**-**8**-SnChl also have very favorable PDT and PACT activities against the MCF-7 cell line, and biofilm and planktonic *S. aureus* and *E. coli* bacteria compared to their **5**-**8**-SnPor and **5**-SnNCP analogs. This is demonstrated by their lower IC_{50} and cell viability values for MCF-7 cells, as well as the complete eradication of the planktonic *S. aureus* after illumination for short periods and higher log reduction values for *E. coli* that are > 3 Log_{10} $CFU.mL^{-1}$. The unusually enhanced phototoxicity effects for **5**-**8**-SnChl, particularly toward Gram-(−) bacteria species, warrants further in-depth investigation.

11.1 Future recommendations

The *in vitro* studies in this work confirmed that low symmetry porphyrin analogs, such as corroles, chlorins, and N-confused porphyrins, have enhanced absorption properties within the

therapeutic window with favorable light penetration into tissues, which results in improved PDT and PACT activities relative to porphyrin dyes. *In vivo* studies are warranted to further elucidate the efficiency of the porphyrin analog dyes. In addition, further modification and functionalization strategies are necessary to improve the optical and photophysicochemical properties of the dyes. This includes:

- Exploration of solubility strategies, such as the introduction of cationic species such as quaternary ammonium moieties, axial ligation with water-soluble derivatives, including core-functionalization of the dyes with hexadentate coordination ions, such as P(V), Sn(IV), and Si(IV), that introduce axial ligands from above and below the porphyrin ring. In addition, encapsulation of PS drugs using micelles and liposomes can enhance the solubility properties of the drug. These solubility strategies can reduce aggregation effects and enhance drug penetration into the cell, uptake, biodistribution, and bio-availabilities of the dyes.
- The introduction of different functional groups on the β-β pyrrole bonds of chlorin dyes can also be explored, such as hydrolyzation strategies to further enhance the optoelectronic properties and photostability of the dyes. Also, functionalization of the outer NH of N-confused porphyrins can enhance the photophysicochemical properties of the dyes and improve their PDT and PACT efficiency.
- Conjugation of the dyes to up-conversion metallic nanoparticles or nano-assemblies, including conjugation with cancer receptors moieties or moieties that have specific affinities to the cancer cells or bacteria cell walls, can improve the performances of PS dyes.

REFERENCES

[1] Ormond AB, Freeman HS. Dye sensitizers for photodynamic therapy. *Materials (Basel)* 2013; 6: 817-840. doi: 10.3390/ma6030817

[2] Benov L. Photodynamic therapy: Current status and future directions. *Med Princ Pract* 24 *suppl 1. Karger AG* 2015, 14-28. doi: 10.1159/000362416

[3] Abrahamse H, Hamblin MR. New photosensitizers for photodynamic therapy. *Biochem J* 2016; 473: 347-364. doi: 10.1042/BJ20150942

[4] Gunaydin G, Emre Gedik M, Ayan S. Photodynamic Therapy for the Treatment and Diagnosis of Cancer-A Review of the Current Clinical Status. *Front Chem* 2021: 608. doi: 10.3389/fchem.2021.686303

[5] Plekhova N, Shevchenko O, Korshunova O, Stepanyugina A, Tananaev I, Apanasevich V. Development of Novel Tetrapyrrole Structure Photosensitizers for Cancer Photodynamic Therapy. *Bioengineering* 2022; 9: 82. doi: 10.3390/bioengineering9020082

[6] Correia JH, Rodrigues JA, Pimenta S, Dong T, Yang Z. Photodynamic therapy review: Principles, photosensitizers, applications, and future directions. *Pharmaceutics* 2021; 13. doi: 10.3390/pharmaceutics13091332

[7] Kashef N, Hamblin MR. Can microbial cells develop resistance to oxidative stress in antimicrobial photodynamic inactivation? *Drug Resist Updat* 2017; 31: 31-42. doi: 10.1016/j.drup.2017.07.003

[8] Mahmoudi H, Bahador A, Pourhajibagher M, Yousef Alikhani M. Antimicrobial Photodynamic Therapy: An Effective Alternative Approach to Control Bacterial Infections. *Laser Appl Med Sci Res Cent* 2018; 9: 154-160. doi: 10.15171/jlms.2018.29

[9] Gomes AT, Neves MG, Cavaleiro JA. Cancer, photodynamic therapy and porphyrin-type derivatives. *An Acad Bras Ciênc 90 (01 Suppl 2)* 2018; 90: 993-1026. doi: 10.1590/0001-3765201820170811

[10] Baskaran R, Lee J, Yang SG. Clinical development of photodynamic agents and therapeutic applications. *Biomater Res* 2018; 22: 1-8. doi: 10.1186/s40824-018-0140-z

[11] Hamblin MR. Special Issue Invited Review Photodynamic Therapy for Cancer: What's Past is Prologue. *Photochem Photobiol* 2020; 96: 506-516. doi: 10.1111/php.13190

[12] Dos Santos AF, De Almeida DRQ, Terra LF, Baptista MS, Labriola L. Photodynamic therapy in cancer treatment - an update review. *J Cancer Metastasis Treat* 2019; 5: 25. doi: 10.20517/2394-4722.2018.83

[13] Escudero A, Carrillo-Carrió C, Castillejos C, Romero-Ben E, Rosales-Barrios C, Khiar N. Photodynamic therapy: photosensitizers and nanostructures. *Mater Chem Front* 2021; 5: 3788-3812. doi: 10.1039/d0qm00922a

[14] Kwiatkowski S, Knap B, Przystupski D, Saczko J, Kędzierska E, Knap-Czop K, Kotlińska J, Michel O, Kotowski K, Kulbacka J. Photodynamic therapy-mechanisms, photosensitizers and combinations. *Biomed Pharmacother* 2018; 106: 1098-1107. doi: 10.1016/j.biopha.2018.07.049

[15] Van Straten D, Mashayekhi V, de Bruijn H, Oliveira S, Robinson D. Oncologic Photodynamic Therapy: Basic Principles, Current Clinical Status and Future Directions. *Cancers* 2017; 9(2): 19. doi: 10.3390/cancers9020019

[16] De Pinillos Bayona AM, Mroz P, Thunshelle C, Hamblin MR. Design features for optimization of tetrapyrrole macrocycles as antimicrobial and anticancer photosensitizers. *Chem Biol Drug Des* 2017; 89: 192-206. doi: 10.1111/cbdd.12792

[17] Shi X, Zhang CY, Gao J, Wang Z. Recent advances in photodynamic therapy for cancer and infectious diseases. *Wiley Interdiscip Rev Nanomed Nanobiotechnol* 2019; 11: e1560. doi: 10.1002/wnan.1560

[18] Ghorbani J, Rahban D, Aghamiri S, Teymouri A, Bahador A. Photosensitizers in antibacterial photodynamic therapy: An overview. *Laser Ther* 2018; 27: 293-302. doi: 10.5978/islsm.27_18-RA-01

[19] Sperandio FF, Huang YY, Hamblin MR. Antimicrobial Photodynamic Therapy to Kill Gram-negative Bacteria. *Recent Pat Antiinfect Drug Discov* 2013; 8(2): 108-120. doi: 10.2174/1574891x113089990012

[20] Hu X, Huang YY, Wang Y, Wang X, Hamblin MR. Antimicrobial photodynamic therapy to control clinically relevant biofilm infections. *Front Microbiol* 2018; 9: 1299. doi: 10.3389/fmicb.2018.01299

[21] Zgurskaya HI, López CA, Gnanakaran S. Permeability Barrier of Gram-Negative Cell Envelopes and Approaches to Bypass It. *ACS Infect Dis* 2016; 1: 512-522. doi: 10.1021/acsinfecdis.5b00097

[22] Youf R, Müller M, Balasini A, Thétiot F, Müller M, Hascoët A, Jonas U., Schönherr H, Lemercier G, Montier T, Le Gall T. Antimicrobial photodynamic therapy: Latest developments with a focus on combinatory strategies. *Pharmaceutics* 2021; 13: 1-56. doi: 10.3390/pharmaceutics13121995

[23] Cieplik F, Deng D, Crielaard W, Buchalla W, Hellwig E, Al-Ahmad A, Maisch T. Antimicrobial photodynamic therapy–what we know and what we don't. *Crit Rev Microbiol* 2018; 44: 571-589. doi: 10.1080/1040841X.2018.1467876

[24] Kashef N, Huang Y-Y, Hamblin MR. Advances in antimicrobial photodynamic inactivation at the nanoscale. *Nanophotonics* 2017; 6: 853-879. doi: 10.1515/nanoph-2016-0189

[25] Saxena P, Joshi Y, Rawat K, Bisht R. Biofilms: Architecture, Resistance, Quorum Sensing and Control Mechanisms. *Indian J Microbiol* 2019; 59: 3-12. doi: 10.1007/s12088-018-0757-6

[26] Jamal M, Ahmad W, Andleeb S, Jalil F, Imran M, Nawaz MA, Hussain T, Ali M, Rafiq M, Kamil MA. Bacterial biofilm and associated infections. *J Chin Med Assoc* 2018; 81: 7-11. doi: 10.1016/j.jcma.2017.07.012

[27] Singh S, Singh SK, Chowdhury I, Singh R. Understanding the Mechanism of Bacterial Biofilms Resistance to Antimicrobial Agents. *Open Microbiol J* 2017; 11: 53-62. doi: 10.2174/1874285801711010053

[28] Tautua A, Bamidele M, Songca SP, Oluwafemi OS. Application of porphyrins in antibacterial photodynamic therapy. *Molecules* 2019; 24. doi: 10.3390/molecules24132456

[29] Oyim J, Omolo CA, Amuhaya EK. Photodynamic Antimicrobial Chemotherapy: Advancements in Porphyrin-Based Photosensitize Development. *Front Chem* 2021; 9: 635344. doi: 10.3389/fchem.2021.635344

[30] Mesquita MQ, Dias CJ, Neves MGPMS, Almeida A, Amparo M, Faustino F. Revisiting Current Photoactive Materials for Antimicrobial Photodynamic Therapy. *Molecules* 2018; 23: 2424. doi: 10.3390/molecules23102424

[31] Zhang J, Jiang C, Figueiró Longo JP, Azevedo RB, Zhang H, Muehlmann LA. An updated overview on the development of new photosensitizers for anticancer photodynamic therapy. *Acta Pharm Sin B* 2018; 8: 137-146. doi: 10.1016/j.apsb.2017.09.003

[32] Klausen M, Ucuncu M, Bradley M, Barattucci A, Bonaccorsi P. Design of Photosensitizing Agents for Targeted Antimicrobial Photodynamic Therapy. *Molecules* 2020; 25(22): 5239. doi: 10.3390/molecules25225239

[33] Kou J, Dou D, Yang L. Porphyrin photosensitizers in photodynamic therapy and its applications. *Oncotarget* 2017; 8: 81591-81603. doi: 10.18632/oncotarget.20189

[34] Zhang Q, He J, Yu W, Li Y, Liu Z, Zhou B, Liu Y. A promising anticancer drug: a photosensitizer based on the porphyrin skeleton. *RSC Med Chem* 2020; 11: 427. doi: 10.1039/c9md00558g

[35] Shi Y, Zhang F, Linhardt RJ. Porphyrin-based compounds and their applications in materials and medicine. *Dyes Pigments* 2021; 188: 109136. doi: 10.1016/j.dyepig.2021.109136

[36] Snow AW. Phthalocyanine Aggregation 109. In *The Porphyrin Handbook: Phthalocyanines: Properties and Materials*. Vol. 17. Elsevier:Amsterdam 2003. doi: 10.1016/B978-0-08-092391-8.50009-1

[37] Lin AL, Fan PP, Liu SF, Chen JH, Zhao YY, Zheng BY, Ke MR, Huang JD. A phthalocyanine-based liposomal nanophotosensitizer with highly efficient tumor-targeting and photodynamic activity. *Dyes Pigments* 2020; 180: 108455. doi: 10.1016/j.dyepig.2020.108455

[38] Zhang Z, Yu HJ, Huang H, Wang HH, Wu S, Liu HY, Zhang HT. The photodynamic activity and toxicity evaluation of 5,10,15-tris(ethoxylcarbonyl)corrole phosphorus(V) *in vivo* and *in vitro*. Eur *J Med Chem* 2019; 163: 779-786. doi: 10.1016/j.ejmech.2018.12.031

[39] Teo RD, Hwang JY, Termini J, Gross Z, Gray HB. Fighting Cancer with Corroles. *Chem Rev* 2017; 117: 2711-2729. doi: 10.1021/acs.chemrev.6b00400

[40] Jiang X, Liu RX, Liu HY, Chang CK. Corrole-based photodynamic antitumor therapy. *J Chin Chem Soc* 2019; 66(9): 1090-1099.doi: 10.1002/jccs.201900176

[41] Lee SY, Lee R, Kim E, Lee S, Park Y Il. Near-Infrared Light-Triggered Photodynamic Therapy and Apoptosis Using Upconversion Nanoparticles with Dual Photosensitizers. *Front Bioeng Biotechnol* 2020; 8: 1-9. doi: 10.3389/fbioe.2020.00275

[42] Linares IAP, Martinelli LP, Moritz MNO, Selistre-de-Araujo HS, de Oliveira KT, Rodrigues Perussi J. Cytotoxicity of structurally-modified chlorins aimed for photodynamic therapy applications. *J Photochem Photobiol A* 2022; 425: 113647. doi: 10.1016/j.jphotochem.2021.113647

[43] Thomas AP, Saneesh Babu PS, Nair SA, Ramakrishnan S, Ramaiah D, Chandrashekar TK, Srinivasan A. Radhakrishna Pillai M. *meso*-Tetrakis(p-sulfonatophenyl)N-Confused Porphyrin Tetrasodium Salt: A Potential Sensitizer for Photodynamic Therapy. *J Med Chem* 2012; 55(11):5110-5120. doi: 10.1021/jm300009q

[44] Babu B, Mack J, Nyokong T. Sn(IV) N-confused porphyrins as photosensitizer dyes for photodynamic therapy in the near IR region. *Dalton Trans* 2020; 49: 15180-15183. doi: 10.1039/d0dt03296d

[45] Hiroto S, Miyake Y, Shinokubo H. Synthesis and Functionalization of Porphyrins through Organometallic Methodologies. *Chem Rev* 2017; 117(4): 2910-3043. doi: 10.1021/acs.chemrev.6b00427

[46] Mahammed A, Gross Z. Corroles as triplet photosensitizers. *Coord Chem Rev* 2019; 379: 121-132. doi: 10.1016/j.ccr.2017.08.028

[47] Jeong HG, Choi MS. Design and Properties of Porphyrin-based Singlet Oxygen Generator. *Isr J Chem* 2016; 56: 110-118. doi: 10.1002/ijch.201500026

[48] Kingsbury CJ, Senge MO. The shape of porphyrins. *Coord Chem Rev* 2021; 431: 213760. doi: 10.1016/j.ccr.2020.213760

[49] Nardis S, Mandoj F, Stefanelli M, Paolesse R. Metal complexes of corrole. *Coord Chem Rev* 2019; 388: 360-405. doi: 10.1016/j.ccr.2019.02.034

[50] Babu B, Mack J, Nyokong T. Photodynamic activity of Sn(IV) tetrathien-2-ylchlorin against MCF-7 breast cancer cells. *Dalton Trans* 2021; 50: 2177. doi: 10.1039/d0dt03958f

[51] Matsumoto J, Shiragami T, Hirakawa K, Yasuda M. Water-solubilization of P(V) and Sb(V) porphyrins and their photobiological application. *Int J Photoenergy* 2015; 2015. doi: 10.1155/2015/148964

[52] Matsumoto J, Suzuki K, Yasuda M, Yamaguchi Y, Hishikawa Y, Imamura N, Nanashima A. Photodynamic therapy of human biliary cancer cell line using combination of phosphorus porphyrins and light emitting diode. *Bioorganic Med Chem* 2017; 25: 6536-6541. doi: 10.1016/j.bmc.2017.10.031

[53] Matano Y. *Phosphorus-Based Porphyrins.* In *Main Group Strategies Towards Functional Hybrid Materials*. John Wiley & Sons:Hoboken, New Jersey 2017 p265-293.

[54] Vestfrid J, Kothari R, Kostenko A, Goldberg I, Tumanskii B, Gross Z. Intriguing Physical and Chemical Properties of Phosphorus Corroles. *Inorg Chem* 2016; 55: 6061-6067. doi: 10.1021/acs.inorgchem.6b00544

[55] Liang X, Mack J, Zheng LM, Shen Z, Kobayashi N. Phosphorus(V)-corrole: Synthesis, spectroscopic properties, theoretical calculations, and potential utility for in vivo applications in living cells. *Inorg Chem* 2014; 53: 2797-2802. doi: 10.1021/ic402347w

[56] Martins P, Jesus J, Santos S, Raposo LR, Roma-Rodrigues C, Baptista PV, Fernandes AR. Heterocyclic Anticancer Compounds: Recent Advances and the Paradigm Shift towards the Use of Nanomedicine's Tool Box. *Molecules*, 2015; 20: 16852-16891. doi: 10.3390/molecules200916852

[57] Fesatidou M, Petrou A, Athina G. Heterocycle Compounds with Antimicrobial Activity. *Curr Pharm Des* 2020; 26: 867-904. doi: 10.2174/1381612826666200206093815

[58] Pearce S. The importance of heterocyclic compounds in anti-cancer drug design. *Drug Discov World* 2017; 18: 66-70. ddw-online.com/media/32/(8)-the-importance-of-heterocyclic.pdf

[59] Petrov VA. *Fluorinated heterocyclic compounds*. John Wiley & Sons:Hoboken, New Jersey 2009.

[60] Mabkhot Y. N, Alatibi F, El-Sayed NNE, Al-Showiman S, Kheder NA, Wadood A, Rauf A, Bawazeer S, Hadda TB. Antimicrobial activity of some novel armed thiophene derivatives and petra/Osiris/Molinspiration (POM) analyses. *Molecules* 2016; 21(2): 222. doi: 10.3390/molecules21020222

[61] Li H, Li X, Lei H, Zhou G, Zhang W, Cao R. Convenient Immobilization of Cobalt Corroles on Carbon Nanotubes through Covalent Bonds for Electrocatalytic Hydrogen and Oxygen Evolution Reactions. *ChemSusChem* 2019; 12: 801-806. doi: 10.1002/cssc.201802765

[62] García Calavia P, Bruce G, Pérez-García L, Russell DA. Photosensitiser-gold nanoparticle conjugates for photodynamic therapy of cancer. *Photochem Photobiol Sci* 2018; 17: 1534-1552. doi: 10.1039/c8pp00271a

[63] Abrahamse H, Kruger CA, Kadanyo S. Nanoparticles for advanced photodynamic therapy of cancer. *Photomed Laser Surg* 2017; 35(11): 581-588. doi: 10.1089/pho.2017.4308

[64] Mitchell MJ, Billingsley MM, Haley RM, Wechsler ME, Peppas NA, Langer R. Engineering precision nanoparticles for drug delivery. *Nat Rev Drug Discov* 2021; 20: 101-124. doi: 10.1038/s41573-020-0090-8

[65] Sun J, Kormakov S, Liu Y, Huang Y, Wu D, Yang Z. Recent Progress in Metal-Based Nanoparticles Mediated Photodynamic Therapy. *Molecules* 2018; 23: 1704. doi: 10.3390/molecules23071704

[66] Mokwena MG, Kruger CA, Ivan MT, Heidi A. A review of nanoparticle photosensitizer drug delivery uptake systems for photodynamic treatment of lung cancer. *Photodiagnosis Photodyn Ther* 2018; 22: 147-154. doi: 10.1016/j.pdpdt.2018.03.006

[67] Cheng Z, Li M, Dey R, Chen Y. Nanomaterials for cancer therapy: current progress and perspectives. *J Hematol Oncol* 2021; 14. doi: 10.1186/s13045-021-01096-0

[68] Shariatzadeh S, Moghimi N, Khalafi F, Shafiee S, Mehrabi M, Ilkhani S, Tosan F, Nakhaei P, Alizadeh A, Varma RS, Taheri M. Metallic Nanoparticles for the Modulation of Tumor Microenvironment; A New Horizon. *Front Bioeng Biotechnol* 2022; 10: 847433. doi: 10.3389/fbioe.2022.847433

[69] Montaseri H, Kruger CA, Abrahamse H. Recent advances in porphyrin-based inorganic nanoparticles for cancer treatment. *Int J Mol Sci* 2020; 21: 1-24. doi: 10.3390/ijms21093358

[70] Sano K, Nakajima T, Choyke PL, Kobayashi H. Markedly enhanced permeability and retention effects induced by photo-immunotherapy of tumors. *ACS Nano* 2013; 7: 717-724. doi: 10.1021/nn305011p

[71] El-Hussein A, Mfouo-Tynga I, Abdel-Harith M, Abrahamse H. Comparative study between the photodynamic ability of gold and silver nanoparticles in mediating cell death in breast and lung cancer cell lines. *J Photochem Photobiol B* 2015; 153: 67-75. doi: 10.1016/j.jphotobiol.2015.08.028

[72] Vines JB, Yoon JH, Ryu NE, Lim DJ, Park H. Gold nanoparticles for photothermal cancer therapy. *Front Chem* 2019; 7: 167. doi: 10.3389/fchem.2019.00167

[73] Rai MK, Deshmukh SD, Ingle AP, Gade AK. Silver nanoparticles: the powerful nanoweapon against multidrug-resistant bacteria. *J Appl Microbiol* 2012; 112: 841-852. doi: 10.1111/j.1365-2672.2012.05253.x

[74] Kadish K, Smith KM, Guilard R. *The Porphyrin Handbook: Synthesis and Organic Chemistry*. Vol. 1. Academic Press:Cambridge, Massachusetts 2000

[75] Tahoun M, Gee CT, McCoy VE, Sander PM, Müller CE. Chemistry of porphyrins in fossil plants and animals. *RSC Adv* 2021; 11(13): 7552-7563. doi: 10.1039/d0ra10688g

[76] Kadish K, Smith KM, Guilard R. *Handbook of Porphyrin Science: With Applications To Chemistry, Physics, Materials Science, Engineering, Biology And Medicine*. Vol. 6–10. World Scientific: Singapore 2010.

[77] Senge MO, Sergeeva NN, Hale KJ. Classic highlights in porphyrin and porphyrinoid total synthesis and biosynthesis. *Chem Soc Rev* 2021; 50: 4730. doi: 10.1039/c7cs00719a

[78] Lebedeva NS, Gubarev YA, Koifman MO, Koifman OI. The application of porphyrins and their analogues for inactivation of viruses. *Molecules* 2020; 25. doi: 10.3390/molecules25194368

[79] Tsolekile N, Nelana S, Oluwafemi OS. Porphyrin as Diagnostic and Therapeutic Agent. *Molecules* 2019; 24: 2669. doi: 10.3390/molecules24142669

[80] Lin Y, Zhou T, Bai R, Xie Y. Chemical approaches for the enhancement of porphyrin skeleton-based photodynamic therapy. *J Enzyme Inhib Med Chem*, 2020; 1;35(1):1080-99. doi: 10.1080/14756366.2020.1755669

[81] Mahmood A, Hu JY, Xiao B, Tang A, Wang X, Zhou E. Recent progress in porphyrin-based materials for organic solar cells. *J Mater Chem A* 2018; 6: 16769-16797. doi: 10.1039/c8ta06392c

[82] Pyrzynska K, Kilian K, Pęgier M. Porphyrins as Chelating Agents for Molecular Imaging in Nuclear Medicine. *Molecules* 2022; 27: 3311. doi: 10.3390/molecules27103311

[83] Rabiee N, Tavakkoli Yaraki M, Mokhtari Garakani S, Mokhtari Garakani S, Ahmadi S, Lajevardi A, Bagherzadeh M, Rabiee M, Tayebi L, Tahriri M, Hamblin MR. Recent advances in porphyrin-based nanocomposites for effective targeted imaging and therapy. *Biomaterials* 2020; 232: 119707. doi: 10.1016/j.biomaterials.2019.119707

[84] Scherer J. Chemische-Physiologische Untersuchungen. *J Liebigs Ann Chem* 1841; 40(1): 1-64.

[85] Thudichum JLW. Report on Researches Intended to Promote an Improved Chemical Identification of Disease; *10th Report of The Medical Officer*. Privy Council, HMSO: London 1867; p 152-233.
[86] Hoppe-Seyler F. Das Hamatin. *Tubinger Med-Chem Untersuchungen*. 1871: 523-533.
[87] Soret JL. Recherches sur l'absorption des rayons ultra-violets par diverses substances. *C R Acad Sci* 1883: 1269-1270. doi: 10.1051/jphystap:018790080014500
[88] Küster W. Beiträge zur Kenntnis des Bilirubins und Hämins. *Hoppe Seylers Z Physiol Chem* 1912; 82: 463-483. doi: 10.1515/bchm2.1912.82.6.463
[89] Fischer H, Ziele K. Porphyrin Synthesis. XXII. Synthesis of Haematoporphyrin, Protoporphyrin and Haemin. *J Liebigs Ann Chem* 1929; 468: 98-116. doi: 10.1002/jlac.19294680104
[90] Fischer H, Orth H. Die chemie des pyrrols. Akademische Verlagsgesellschaft:Leipzig, Germany 1937.
[91] Fischer H, Stern A. Die Chemie des Pyrrols, II; Band, Pyrrolfarbstoffe, 2. Akademische Verlagsgesellschaft:Leipzig, Germany 1940.
[92] Merritt JE, Loening KL, Dixon HBF. UPAC-IUB Joint Commission on Biochemical Nomenclature (JCBN) Nomenclature of Tetrapyrroles Recommendations 1978. *Eur J Biochem* 1980; 108(1): 1-30. doi: 10.1111/j.1432-1033.1980.tb04691.x
[93] Koifman OI, Ageeva TA. Main Strategies for the Synthesis of *meso*-Arylporphyrins. *Russ J Org Chem* 2022; 58: 443-479. doi: 10.1134/s1070428022040017
[94] Da M, Vicente GH, Smith KM. Syntheses and Functionalizations of Porphyrin Macrocycles. *Curr Org Synth* 2014; 11(1): 3-28. doi: 10.2174/1385272003376346
[95] *The Porphyrin Handbook: Inorganic, organometallic and coordination chemistry*. Vol. 3. Kadish KM, Smith KM, Guilard R. (Eds), Academic Press:Cambridge, Massachusetts 2000.
[96] Babu B, Soy RC, Mack J, Nyokong T. Non-aggregated lipophilic water-soluble tin porphyrins as photosensitizers for photodynamic therapy and photodynamic antimicrobial chemotherapy. *New J Chem* 2020; 44. doi: 10.1039/d0nj01564d
[97] Lazarides T, Kuhri S, Charalambidis G, Panda MK, Guldi DM, Coutsolelos AG. Electron vs energy transfer in arrays featuring two Bodipy chromophores axially bound to a Sn(IV) porphyrin via a phenolate or benzoate bridge. *Inorg Chem* 2012; 51: 4193-4204. doi: 10.1021/ic2026472
[98] Biyiklioglu Z, Alp H. Electropolymerizable peripherally tetra-{2-[3-(diethylamino)phenoxy]ethoxy} substituted as well as axially (4-phenylpiperazin-1-yl)propanoxy-disubstituted silicon phthalocyanines and their electrochemistry. *Dalton Trans* 2015; 44: 18993. doi: 10.1039/c5dt03421c
[99] Rothemund P. Formation of porphyrins from pyrrole and aldehydes. *J Am Chem Soc* 1935; 57: 2010-2011. doi: 10.1021/ja01313a510
[100] Rothemund P, Menotti AR. Porphyrin Studies. IV.[1] The Synthesis of α,β,γ,δ-Tetraphenylporphine. *J Am Chem Soc* 1941; 63: 267-270. doi: 10.1021/ja01846a065

[101] Adler AD, Longo ER, Shergalis W. Mechanistic Investigations of Porphyrin Syntheses. I. Preliminary Studies on ms-Tetraphenylporphin. *J Am Chem Soc* 1964; 86: 3145-3149. doi: 10.1021/ja01069a035

[102] Adler AD, Longo FR, Finarelli JD, Goldmacher J, Assour J, Korsakoff L. A Simplified Synthesis for *meso*-Tetraphenylporphin. *J Org Chem* 1967; 32: 476. doi: 10.1021/jo01288a053

[103] Lindsey JS, Schreiman IC, Hsu HC, Kearney PC, Marguerettaz AM. Rothemund and Adler-Longo reactions revisited: synthesis of tetraphenylporphyrins under equilibrium conditions. *J Org Chem* 1987; 52: 827-836. doi: 10.1021/jo00381a022

[104] Lindsey JS, Hsu HC, Schreiman IC. Synthesis of tetraphenylporphyrins under very mild conditions. *Tetrahedron Lett* 1986; 27: 4969-4970. doi: 10.1016/S0040-4039(00)85109-6

[105] Lindsey JS. Synthetic routes to *meso*-patterned porphyrins. *Acc Chem Res* 2010; 43: 300-311. doi: 10.1021/ar900212t

[106] Mondal S, Pain T, Sahu K, Kar S. Large-Scale Green Synthesis of Porphyrins. *ACS Omega* 2021; 6: 22922-22936. doi: 10.1021/acsomega.1c03534

[107] Costa LD, Costa JI, Tomé AC. Porphyrin macrocycle modification: Pyrrole ring-contracted or-expanded porphyrinoids. *Molecules* 2016; 21(3): 320. doi: 10.3390/molecules21030320

[108] Roznyatovskiy VV, Lee CH, Sessler JL. π-Extended isomeric and expanded porphyrins. *Chem Soc Rev* 2013; 42(5): 1921-1933. doi: 10.1039/c2cs35418g

[109] Mack J. Expanded, Contracted, and Isomeric Porphyrins: Theoretical Aspects. *Chem Rev* 2017; 117: 3444-3478. doi: 10.1021/acs.chemrev.6b00568

[110] Orowski R, Gryko D, Gryko DT. Synthesis of Corroles and Their Heteroanalogs. *Chem Rev* 2017; 117: 3102-3137. doi: 10.1021/acs.chemrev.6b00434

[111] Gryko DT, Fox JP, Goldberg DP. Recent advances in the chemistry of corroles and core-modified corroles. *J Porphyrin Phthalocyanines* 2004; 8(09): 1091-1105. doi: 10.1142/S1088424604000465

[112] Iris AH, Gross Z. Aura of corroles. *Chem Eur J* 2009; 15: 8382-8394. doi: 10.1002/chem.200900920

[113] Kumar A, Yadav P., Majdoub M, Saltsman I, Fridman N, Kumar S, Kumar A, Mahammed A, Gross Z. Corroles: The Hitherto Elusive Parent Macrocycle and its Metal Complexes. *Angew Chem* 2021; 133(47): 25301-25307. doi: 10.1002/anie.202110964

[114] Aviv-Harel I, Gross Z. Coordination chemistry of corroles with focus on main group elements. *Coord Chem Rev* 2011; 255: 717-736. doi: 10.1016/j.ccr.2010.09.013

[115] Barata JFB, Neves MGPMS, Faustino MAF, Tomé AC, Cavaleiro JAS. Strategies for Corrole Functionalization. *Chem Rev* 2017; 117: 3192-3253. doi: 10.1021/acs.chemrev.6b00476

[116] Umasekhar B, Shetti VS, Ravikanth M. Heterocorroles: corrole analogues containing heteroatom (s) in the core or at a *meso*-position. *RSC Adv* 2018; 8(38): 21100-21132. doi: 10.1039/c8ra03669a

[117] Lemon CM. Corrole photochemistry. *Pure Appl Chem* 2020; 92: 1901-1919. doi: 10.1515/pac-2020-0703

[118] Mondal B, Sengupta K, Rana A, Mahammed A, Botoshansky M, Dey SG, Gross Z, Dey A. Cobalt corrole catalyst for efficient hydrogen evolution reaction from H_2O under ambient conditions: reactivity, spectroscopy, and density functional theory calculations. *Inorg Chem* 2013; 52(6): 3381-3387. doi: 10.1021/ic4000473

[119] Zhan X, Teplitzky P, Diskin-Posner Y, Sundararajan M, Ullah Z, Chen QC, Shimon LJ, Saltsman I, Mahammed A, Kosa M, Baik MH. Maximizing Property Tuning of Phosphorus Corrole Photocatalysts through a Trifluoromethylation Approach. *Inorg Chem* 2019; 58: 6184-6198. doi: 10.1021/acs.inorgchem.9b00436

[120] Mahammed A, Gross Z. Metallocorroles as Photocatalysts for Driving Endergonic Reactions, Exemplified by Bromide to Bromine Conversion. *Angew Chem* 2015; 127: 12547-12550. doi: 10.1002/ange.201503064

[121] Lai S-L, Wang L, Yang C, Chan M-Y, Guan X, Kwok CC, Che CM. Gold(III) Corroles for High Performance Organic Solar Cells. *Adv Funct Mater* 2014; 24: 4655-4665. doi: 10.1002/adfm.201400082

[122] Alemayehu AB, Day NU, Mani T, Rudine AB, Thomas KE, Gederaas OA, Vinogradov SA, Wamser CC, Ghosh A. Gold *tris*(carboxyphenyl)corroles as multifunctional materials: room temperature near-ir phosphorescence and applications to photodynamic therapy and dye-sensitized solar cells. *ACS Appl Mater Interfaces* 2016; 8(29): 18935-18942. doi: 10.1021/acsami.6b04269

[123] Higashino T, Kurumisawa Y, Alemayehu AB, Einrem RF, Sahu D, Packwood D, Kato K, Yamakata A, Ghosh A, Imahori H. Heavy Metal Effects on the Photovoltaic Properties of Metallocorroles in Dye-Sensitized Solar Cells. *ACS Appl Energy Mater* 2020; 3(12): 12460-12467. doi: 10.1021/acsaem.0c02427

[124] Agresti A, Berna BB, Pescetelli S, Catini A, Menchini F, Di Natale C, Paolesse R, Di Carlo A. Copper-Based Corrole as Thermally Stable Hole Transporting Material for Perovskite Photovoltaics. *Adv Funct Mater* 2020; 30(46): 2003790. doi: 10.1002/adfm.202003790

[125] Santos CI, Rodríguez-Pérez L, Gonçalves G, Pinto SN, Melle-Franco M, Marques PA, Faustino MA, Herranz MÁ, Martin N, Neves MG, Martinho JM. Novel hybrids based on graphene quantum dots covalently linked to glycol corroles for multiphoton bioimaging. *Carbon* 2020; 166: 164-174. doi: 10.1016/j.carbon.2020.04.012

[126] Paolesse R, Nardis S, Monti D, Stefanelli M, Di Natale C. Porphyrinoids for Chemical Sensor Applications. *Chem Rev* 2017; 117: 2517-2583. doi: 10.1021/acs.chemrev.6b00361

[127] Pribisko M, Palmer J, Grubbs RH, Gray HB, Termini J, Lim P. Cellular uptake and anticancer activity of Carboxylated gallium corroles. *Proc Natl Acad Sci USA* 2016; 113: E2258-2266. doi: 10.1073/pnas.1517402113

[128] Babu B, Prinsloo E, Mack J, Nyokong T. Synthesis, characterization and photodynamic activity of Sn(IV) triarylcorroles with red-shifted Q bands. *New J Chem* 2019; 43: 18805-18812. doi: 10.1039/c9nj03391b

[129] Hwang JY, Lubow J, Chu D, Ma J, Agadjanian H, Sims J, Gray HB, Gross Z, Farkas DL, Medina-Kauwe LK. A mechanistic study of tumor-targeted corrole toxicity. *Mol Pharm* 2011; 8: 2233-2243. doi: 10.1021/mp200094w

[130] Pohl J, Saltsman I, Mahammed A, Gross Z, Röder B. Inhibition of green algae growth by corrole-based photosensitizers. Journal of applied microbiology. *J Appl Microbiol* 2015; 118(2): 305-312. doi: 10.1111/jam.12690

[131] Preuß A, Saltsman I, Mahammed A, Pfitzner M, Goldberg I, Gross Z, Röder B. Photodynamic inactivation of mold fungi spores by newly developed charged corroles. *J Photochem Photobiol B* 2014; 133: 39-46. doi: 10.1016/j.jphotobiol.2014.02.013

[132] Johnson W, Kay IT. Corroles. Part I. Synthesis. *J Chem Soc* 1965: 1620. doi: 10.1039/jr9650001620

[133] Paolesse R, Mini S, Sagone F, Boschi T, Jaquinod L, Nurco DJ, Smith KM. 5, 10, 15-Triphenylcorrole: a product from a modified Rothemund reaction. *Chem Commun* 1999: 1307-1308. doi: 10.1039/A903247I

[134] Gross Z, Galili N, Saltsman I. The first direct synthesis of corroles from pyrrole. *Angew Chem Int Ed* 1999; 38: 1427-1429. doi: 10.1002/(sici)1521-3773(19990517)38:10<1427::aid-anie1427>3.0.CO;2-1

[135] Dogutan DK, Stoian SA, McGuire R, Schwalbe M, Teets TS, Nocera DG. Hangman corroles: Efficient synthesis and oxygen reaction chemistry. *J Am Chem Soc* 2011; 133: 131-140. doi: 10.1021/ja108904s

[136] Aviv I, Gross Z. Corrole-based applications. *Chem Commun* 2007: 1987-1999. doi: 10.1039/b618482k

[137] Bose S, Pariyar A, Biswas AN, Bandyopadhyay P. Selective olefin epoxidation catalyzed by metallocorroles in ionic liquid medium at room temperature. *J Mol Catal A* 2013; 378: 179-183. doi: 10.1016/j.molcata.2013.06.007

[138] Gryko DT, Jadach K. A Simple and Versatile One-Pot Synthesis of *meso*-Substituted *trans*-A_2B-Corroles. *J Org Chem* 2001; 66: 4267-4275. doi: 10.1021/jo010146w

[139] Gryko DT. A simple, rational synthesis of *meso*-substituted A_2B-corroles. *Chem Commun* 2000: 2243-2244. doi: 10.1039/b006734m

[140] Gryko DT, Koszarna B. Refined methods for the synthesis of *meso*-substituted A_3- and *trans*-A_2B-corroles. *Org Biomol Chem* 2003; 1: 350-357. doi: 10.1039/b208950e

[141] Koszarna B, Gryko DT. Efficient synthesis of *meso*-substituted corroles in a H_2O-MeOH mixture. *J Org Chem* 2006; 71: 3707-3717. doi: 10.1021/jo060007k

[142] Gryko DT. Adventures in the synthesis of *meso*-substituted corroles. *J Porphyrin Phthalocyanines* 2008; 12(08): 906-917. doi: 10.1142/S1088424608000297

[143] Taniguchi M, Ptaszek M, McDowell BE, Boyle PD, Lindsey JS. Sparsely substituted chlorins as core constructs in chlorophyll analogue chemistry. Part 3: Spectral and structural properties. *Tetrahedron* 2007; 63(18): 3850-3863. doi: 10.1016/j.tet.2007.02.040

[144] De Oliveira KT, Momo PB, De Assis FF, Ferreira MAB, Brocksom TJ. Chlorins: Natural Sources, Synthetic Developments and Main Applications. *Curr Org Synth* 2014; 11(1): 42-58. doi: 10.2174/15701794113106660085

[145] Borbas KE. BODIPYs and Chlorins: Powerful Related Porphyrin Fluorophores. In *Handbook of Porphyrin Science: With Applications to Chemistry, Physics, Materials Science, Engineering, Biology and Medicine*, Vol. 36. Kadish KM, Smith KM, Guilard R. (Eds), World Scientific:Singapore 2016, p1-149. doi: 10.1142/9789813149564_0001

[146] Taniguchi M, Lindsey JS. Synthetic chlorins, possible surrogates for chlorophylls, prepared by derivatization of porphyrins. *Chem Rev* 2017; 117: 344-535. doi: 10.1021/acs.chemrev.5b00696

[147] Taniguchi M, Bocian DF, Holten D, Lindsey JS. Beyond green with synthetic chlorophylls – Connecting structural features with spectral properties. *J Photochem Photobiol C* 2022; 52: 100513. doi: 10.1016/j.jphotochemrev.2022.100513

[148] Huang L, Asghar S, Zhu T, Ye P, Hu Z, Chen Z, Xiao Y. Advances in chlorin-based photodynamic therapy with nanoparticle delivery system for cancer treatment. *Expert Opin Drug Deliv* 2021; 18(10): 1473-1500. doi: 10.1080/17425247.2021.1950685

[149] Aronoff S, Calvin M. The porphyrin-like products of the reaction of pyrrole with benzaldehyde. *J Org Chem* 1943; 8: 205-223. doi: 10.1021/jo01191a002

[150] Calvin M, Ball RH, Aronoff S. α,β,γ,δ-Tetraphenylchlorin. *J Am Chem Soc* 1943; 65: 2259-2259. doi: 10.1021/ja01251a508

[151] Ball RH, Dorough GD, Calvin M. A Further Study of the Porphine-like Products of the Reaction of Benzaldehyde and Pyrrole. *J Am Chem Soc* 1946; 68: 2278-2281. doi: 10.1021/ja01215a046

[152] Dorough GD, Huennekens FM. The Spectra of α, β, γ, δ-Tetraphenylchlorin and its Metallo-Derivatives. *J Am Chem Soc* 1952; 74(16): 3974-3976. doi: 10.1021/ja01136a002

[153] Whitlock Jr HW, Hanauer R, Oester MY, Bower BK. Diimide reduction of porphyrins. *J Am Chem Soc* 1969; 91(26): 7485-7489. doi: 10.1021/ja01054a044

[154] Battersby AR, Fookes CJ, Snow RJ. Synthetic studies relevant to biosynthetic research on Vitamin B12. Part 2. Syntheses of C-methylated chlorins via lactams. *J Chem Soc Perkin Trans 1* 1984; 2733-2741. doi: 10.1039/P19840002733

[155] Battersby AR, Dutton CJ, Fookes CJ. Synthetic studies relevant to biosynthetic research on Vitamin B12. Part 7. Synthesis of (±)-bonellin dimethyl ester. *J Chem Soc Perkin Trans 1* 1988; 6: 1569-1576. doi: 10.1039/P19880001569

[156] Lindsey JS. *De novo* synthesis of gem-dialkyl chlorophyll analogues for probing and emulating our green world. *Chem Rev* 2015; 115(13): 6534-6620. doi: 10.1021/acs.chemrev.5b00065

[157] Pereira MM, Monteiro CJ, Simões AV, Pinto SM, Abreu AR, Sá GF, Silva EF, Rocha LB, Dąbrowski JM, Formosinho SJ, Simões S. Synthesis and photophysical characterization of a library of photostable halogenated bacteriochlorins: an access to near infrared chemistry. *Tetrahedron* 2010; 66: 9545-9551. doi: 10.1016/j.tet.2010.09.106

[158] Pereira MM, Abreu AR, Goncalves NP, Calvete MJ, Simoes AV, Monteiro CJ, Arnaut LG, Eusebio ME, Canotilho J. An insight into solvent-free diimide porphyrin reduction: a versatile approach for *meso*-aryl hydroporphyrin synthesis. *Green Chem* 2012; 14(6): 1666-1672. doi: 10.1039/c2gc35126a

[159] Nascimento BF, Gonsalves AM, Pineiro M. MnO_2 instead of quinones as selective oxidant of tetrapyrrolic macrocycles. *Inorg Chem Commun* 2010; 13: 395-398. doi: 10.1016/j.inoche.2009.12.032

[160] Harvey JD, Ziegler CJ. Developments in the metal chemistry of N-confused porphyrin. *Coord Chem Rev* 2003; 247: 1-19. doi: 10.1016/j.cct.2003.07.001

[161] Maeda H, Osuka A, Furuta H. Anion Binding Properties of N-Confused Porphyrins at the Peripheral Nitrogen. *J Incl Phenom Macrocycl Chem* 2004; 49: 33-36. doi: 10.1023/b:jiph.0000031110.42096.d3

[162] Maeda H, Furuta H. A dozen years of N-confusion: From synthesis to supramolecular chemistry. *Pure Appl Chem* 2006; 78: 29-44. doi: 10.1351/pac200678010029

[163] Toganoh M, Furuta H. Synthesis and Metal Coordination of N-Confused and N-Fused Porphyrinoids: In *Handbook of Porphyrin Science* (Synthesis and Coordination Chemistry). Vol. 2. Kadish KM, Smith KM, Guilard R. (Eds), World Scientific Publishing:Singapore 2010. doi: 10.1142/9789814280228_0010

[164] Toganoh M, Furuta H. Blooming of confused porphyrinoids - fusion, expansion, contraction, and more confusion. *Chem Commun* 2012; 8: 937-54. doi: 10.1039/c1cc14633e

[165] Toganoh M, Furuta H. N-Fused Porphyrin: A Maverick Member of the Porphyrin Family. *Chem Lett* 2019; 48: 615-622. doi: 10.1246/cl.190250

[166] Chmielewski PJ, Latos-Grażyński L, Rachlewicz K, Glowiak T. Tetra-*p*-tolylporphyrin with an Inverted Pyrrole Ring: A Novel Isomer of Porphyrin. *Angew Chem Int Ed* 1994; 33: 779-781. doi: 10.1002/anie.199407791

[167] Furuta H, Asano T, Ogawa T. "N-Confused Porphyrin": A New Isomer of Tetraphenylporphyrin. *J Am Chem Soc* 1994; 116(2): 767-768. doi: 10.1021/ja00081a047

[168] Furuta H, Ishizuka T, Osuka A, Dejima H, Nakagawa H, Ishikawa Y. NH tautomerism of N-confused porphyrin. *J Am Chem Soc* 2001; 123: 6207-6208. doi: 10.1021/ja010237a

[169] Geier GR, Haynes DM, Lindsey JS. An efficient one-flask synthesis of N-confused tetraphenylporphyrin. *Org Lett* 1999; 1: 1455-1458. doi: 10.1021/ol9910114

[170] Maeda H, Osuka A, Ishikawa Y, Aritome I, Hisaeda Y, Furuta H. N-confused porphyrin-bearing *meso*-perfluorophenyl groups: A potential agent that forms stable square-planar complexes with Cu(II) and Ag(III). *Org Lett* 2003; 5: 1293-1296. doi: 10.1021/ol034227l

[171] Fisher JM, Kensy VK, Geier III GR. Two-Step, One-Flask Synthesis of an N-Confused Porphyrin Bearing Pentafluorophenyl Substituents. *J Org Chem* 2017; 82(8): 4429-4434. doi: 10.1021/acs.joc.7b00195

[172] Gouterman M. Spectra of porphyrins. *J Mol Spectrosc* 1961; 6: 138-163. doi: 10.1016/0022-2852(61)90236-3

[173] Michl J. Magnetic Circular Dichroism of Cyclic π-Electron Systems. 2. Algebraic Solution of the Perimeter Model for the B Terms of Systems with a (4N+2)-Electron [n]Annulene Perimeter. *J Am Chem Soc* 1978; 100: 6812-6818. doi: 10.1021/ja00490a002

[174] Soy RC, Babu B, Mack J, Nyokong T. The photodynamic activities of the gold nanoparticle conjugates of phosphorus(V) and gallium(III) A_3 *meso*-triarylcorroles. *Dyes Pigments* 2021; 194: 109631. doi: 10.1016/j.dyepig.2021.109631

[175] Babu B, Sindelo A, Mack J, Nyokong T. Thien-2-yl substituted chlorins as photosensitizers for photodynamic therapy and photodynamic antimicrobial chemotherapy. *Dyes Pigments* 2021; 185: 108886. doi: 10.1016/j.dyepig.2020.108886

[176] Mack J, Kobayashi N. Low symmetry phthalocyanines and their analogues. *Chem Rev* 2011; 111: 281-321. doi: 10.1021/cr9003049

[177] Zhang A, Kwan L, Stillman MJ. The spectroscopic impact of interactions with the four Gouterman orbitals from peripheral decoration of porphyrins with simple electron withdrawing and donating groups. *Org Biomol Chem* 2017; 15: 9081. doi: 10.1039/c7ob01960b

[178] Valeur B, Berberan-Santos MN. *Molecular fluorescence: principles and applications*. John Wiley & Sons:Hoboken, New Jersey 2012.

[179] Polo AS, Frin KPM. Fundamentals of Photochemistry: Excited State Formation/Deactivation and Energy Transfer Processes. In *Springer Handbook of Inorganic Photochemistry*, Bahnemann D, Patrocinio AOT (Eds). Springer Handbooks, Springer International Publishing:New York 2022, p27-48. doi: 10.1007/978-3-030-63713-2_2

[180] Kasha M. Characterization of Electronic Transitions in Complex Molecules. *Discuss Faraday Soc* 1950; 9: 14-19. doi: 10.1039/DF9500900014

[181] Röder B, Büchner M, Rückmann I, Senge MO. Correlation of photophysical parameters with macrocycle distortion in porphyrins with graded degree of saddle distortion. *Photochem Photobiol Sci* 2010; 9: 1152-1158. doi: 10.1039/c0pp00107d

[182] Taniguchi M, Lindsey JS, Bocian DF, Holten D. Comprehensive review of photophysical parameters (ε, ϕ_f, τ_s) of tetraphenylporphyrin (H_2TPP) and zinc tetraphenylporphyrin (ZnTPP) – Critical benchmark molecules in photochemistry and photosynthesis. *J Photochem Photobiol C* 2021; 46: 100401. doi: 10.1016/j.jphotochemrev.2020.100401

[183] Azenha EG, Serra AC, Pineiro M, Pereira MM, De Melo JS, Arnaut LG, Formosinho SJ, Gonsalves AMd'AR. Heavy-atom effects on metalloporphyrins and polyhalogenated porphyrins. *Chem Phys* 2002; 280(1-2): 177-190. doi: 10.1016/S0301-0104(02)00485-8

[184] Ormond AB, Freeman HS. Effects of substituents on the photophysical properties of symmetrical porphyrins. *Dyes Pigments* 2013; 96: 440-448. doi: 10.1016/j.dyepig.2012.09.011

[185] Fery-Forgues S, Lavabre D. Are Fluorescence Quantum Yields So Tricky to Measure? A Demonstration Using Familiar Stationery Products. *J Chem Educ* 1999; 76. doi: 10.1021/ed076p1260

[186] Gentemann S, Medforth CJ, Ema T, Nelson NY, Smith KM, Fajer J, Holten D. Unusual picosecond $^{1}(\pi, \pi*)$ deactivation of ruffled nonplanar porphyrins. *Chem Phys Lett* 1995; 245(4-5): 441-447. doi: 10.1016/0009-2614(95)01030-D

[187] Karolczak J, Kowalska D, Lukaszewicz A, Maciejewski A, Steer RP. Photophysical Studies of Porphyrins and Metalloporphyrins: Accurate Measurements of Fluorescence Spectra and Fluorescence Quantum Yields for Soret Band Excitation of Zinc Tetraphenylporphyrin. *J Phys Chem A* 2004; 108: 4570-4575. doi: 10.1021/jp049898v

[188] Korínek M, Dědic R, Molnár A, Svoboda A, Hála J. A comparison of photosensitizing properties of *meso*-tetraphenylporphin in acetone and in dimethyl sulfoxide. *J Mol Struct* 2005; 744–747: 727-731. doi: 10.1016/j.molstruc.2004.11.036

[189] Gandra N, Frank AT, Le Gendre O, Sawwan N, Aebisher D, Liebman JF, Houk KN, Greer A, Gao R. Possible singlet oxygen generation from the photolysis of indigo dyes in methanol, DMSO, water, and ionic liquid, 1-butyl-3-methylimidazolium tetrafluoroborate. *Tetrahedron* 2006; 62(46): 10771-10776. doi: 10.1016/j.tet.2006.08.095

[190] Bonnett R, Martınez G. Photobleaching of sensitisers used in photodynamic therapy. *Tetrahedron* 2001; 57(47): 9513-9547. doi: 10.1016/S0040-4020(01)00952-8

[191] Da Silva EF, Pimenta FM, Pedersen BW, Blaikie FH, Bosio GN, Breitenbach T, Westberg M, Bregnhøj M, Etzerodt M, Arnaut LG, Ogilby PR. Intracellular singlet oxygen photosensitizers: on the road to solving the problems of sensitizer degradation, bleaching and relocalization. *Integr Bio* 2016; 8(2): 177-193. doi: 10.1039/c5ib00295h

[192] Demchenko AP. Photobleaching of organic fluorophores: Quantitative characterization, mechanisms, protection. *Methods Appl Fluoresc* 2020; 8. doi: 10.1088/2050-6120/ab7365

[193] Kim HS, Seo M, Park T-E, Lee DY. A novel therapeutic strategy of multimodal nanoconjugates for state-of-the-art brain tumor phototherapy. *J Nanobiotechnology* 2022; 20: 14. doi: 10.1186/s12951-021-01220-9

[194] Dougherty TJ, Gomer CJ, Henderson BW, Jori G, Kessel D, Korbelik M, Moan J, Peng Q. Photodynamic therapy. JNCI: *J Natl Cancer Inst* 1998; 90(12): 889-905. doi: 10.1093/jnci/90.12.889

[195] Loewen GM, Pandey R, Bellnier D, Henderson B, Dougherty T. Endobronchial photodynamic therapy for lung cancer. *Lasers Surg Med* 2006; 38: 364-370. doi: 10.1002/lsm.20354

[196] Akimoto J. Photodynamic therapy for malignant brain tumors. *Neurol Med Chir* 2016: ra-2015-0296. doi: 10.2176/nmc.ra.2015-0296

[197] Senge MO. MTHPC - A drug on its way from second to third generation photosensitizer? *Photodiagnosis Photodyn Ther* 2012; 9: 170-179. doi: 10.1016/j.pdpdt.2011.10.001

[198] Copper MP, Tan IB, Oppelaar H, Ruevekamp MC, Stewart FA. Meta-tetra(hydroxyphenyl)chlorin photodynamic therapy in early-stage squamous cell carcinoma of the head and neck. *Arch Otolaryngol - Head Neck Surg* 2003; 129: 709-711. doi: 10.1001/archotol.129.7.709

[199] Naim R. Photodynamische Therapie mit *m*-THPC (Foscan®). *HNO* 2008; 56, 490-492. doi: 10.1007/s00106-008-1750-x

[200] Arnold J, Barbezetto I, Birngruber R, Bressler NM, Bressler SB, Donati G, Fish GE, Flaxel CJ, Gragoudas ES, Harvey P, Kaiser PK, Koester JM, Lewis H., Lim JI, Ma C, Meredith TA, Miller JW, Mones J, Murphy SA, Pieramici DJ, Potter MJ, Reaves A, Rosenfeld PJ, Schachat AP, Schmidt-Erfurth U, Singerman L, Strong HA, Stur M, Williams GA. Verteporfin therapy of subfoveal choroidal neovascularization in age-related macular degeneration: two-year results of a randomized clinical trial including lesions with occult with no classic choroidal neovascularization-verteporfin in photodynamic therapy report 2. *Am J Ophthalmol* 2001; 131: 541-560. doi: 10.1016/S0002-9394(01)00967-9

[201] Verteporfin Roundtable Participants. Guidelines for using Verteporfin (Visudyne) in Photodynamic Therapy for Choroidal Neovascularization due to Age-related Macular Degeneration and Other causes: Update Verteporfin Roundtable Participants. *Retina* 2005; 25: 119-134. doi: 10.1097/00006982-200502000-00002

[202] Selman SH, Albrecht D, Keck RW, Brennan P, Kondo S. Studies of tin ethyl etiopurpurin photodynamic therapy of the canine prostate. *J Urol* 2001; 165: 1795-1801. doi: 10.1016/S0022-5347(05)66416-6

[203] Nanashima A, Hiyoshi M, Imamura N, Hamada T, Nishida T, Kawakami H, Ban T, Kubota Y, Nakashima K, Yano K, Wada T. Two cases of bile duct carcinoma patients who underwent the photodynamic therapy using talaporfin sodium (Laserphyrin®). *Clin J Gastroenterol* 2020; 13: 102-109. doi: 10.1007/s12328-019-01006-5

[204] Jeffes E. Levulan®: The first approved topical photosensitizer for the treatment of actinic keratosis*. J Dermatolog Treat* 2002; 13: s19-s23. doi: 10.1080/095466302317414663

[205] Apolikhin OI, Chernishov IV, Sivkov AV, Altunin DV, Kuzmin SG, Vorozhtsov GN. Adjuvant photodynamic therapy (PDT) with photosensitizer photosens for superficial bladder cancer. Experimental investigations to treat prostate cancer by PDT with photosens. *Opt InfoBase Conf Pap* 2007; 6632: 1-5. doi: 10.1117/12.730393

[206] Brilkina AA, Dubasova LV, Sergeeva EA, Pospelov AJ, Shilyagina NY, Shakhova NM, Balalaeva IV. Photobiological properties of phthalocyanine photosensitizers Photosens, Holosens and Phthalosens: A comparative *in vitro* analysis. *J Photochem Photobiol B* 2019; 191: 128-134. doi: 10.1016/j.jphotobiol.2018.12.020

[207] Senge MO, Brandt JC. Temoporfin (Foscan®, 5,10,15,20-tetra(*m*-hydroxyphenyl) chlorin)−a second-generation photosensitizer. *Photochem Photobiol* 2011; 87: 1240-1296. doi: 10.1111/j.1751-1097.2011.00986.x

[208] Douillard S, Olivier D, Patrice T. *In vitro* and *in vivo* evaluation of Radachlorin® sensitizer for photodynamic therapy. *Photochem Photobiol Sci* 2009; 8(3): 405-413. doi: 10.1039/b817175k

[209] Soy RC, Babu B, Oluwole DO, Nwaji N, Oyim J, Amuhaya E, Prinsloo E, Mack J, Nyokong T. Photophysicochemical properties and photodynamic therapy activity of chloroindium(III) tetraarylporphyrins and their gold nanoparticle conjugates. *J Porphyrin Phthalocyanines* 2019; 23: 34-45. doi: 10.1142/S1088424618501146

[210] Niu Y, Wang L, Guo Y, Zhu W, Soy RC, Babu B, Mack J, Nyokong T, Xu H, Liang X. Ga^{III}triarylcorroles with Push-Pull Substitutions: Synthesis, Electronic Structure and Biomedical Applications. *Dalton Trans* 2022: 10543-10551. doi: 10.1039/d2dt01262f

[211] Gwynne PJ, Gallagher MP. Light as a broad-spectrum antimicrobial. *Front Microbiol* 2018; 9. doi: 10.3389/fmicb.2018.00119

[212] Wang D, Kuzma ML, Tan X, He TC, Dong C, Liu Z, Yang J. Phototherapy and optical waveguides for the treatment of infection. *Adv Drug Deliv Rev* 2021; 179: 114036. doi: 10.1016/j.addr.2021.114036

[213] Tomb RM, White TA, Coia JE, Anderson JG, Macgregor SJ, Maclean M. Review of the Comparative Susceptibility of Microbial Species to Photoinactivation Using 380-480 nm Violet-Blue Light. *Photochem Photobiol* 2018; 94: 445-458. doi: 10.1111/php.12883

[214] Pajerski W, Ochonska D, Brzychczy-Wloch M, Golda-Cepa M, Sojka Z, Kotarba A. Attachment efficiency of gold nanoparticles by Gram-positive and Gram-negative bacterial strains governed by surface charges. *J Nanopart Res* 2019; 21: 186. doi: 10.1007/s11051-019-4617-z

[215] Openda YI, Ngoy BP, Muya JT, Nyokong T. Synthesis, theoretical calculations and laser flash photolysis studies of selected amphiphilic porphyrin derivatives used as biofilm photodegradative materials. *New J Chem* 2021; 45: 17320-17331. doi: 10.1039/d1nj02651h

[216] Wu J. The enhanced permeability and retention (EPR) effect: the significance of the concept and methods to enhance its application. *J Pers Med* 2021; 11(8): 771. doi: 10.3390/jpm11080771

[217] Zhou L, Wei S, Ge X, Zhou J, Yu B, Shen J. External Heavy-Atomic Construction of Photosensitizer Nanoparticles for Enhanced in Vitro Photodynamic Therapy of Cancer. *J Phys Chem B* 2012; 116: 12744-12749. doi: 10.1021/jp305137j

[218] Dube E, Oluwole DO, Nwaji N, Nyokong T. Glycosylated zinc phthalocyanine-gold nanoparticle conjugates for photodynamic therapy: Effect of nanoparticle shape. S*pectrochim Acta A* 2018; 203: 85-95. doi: 10.1016/j.saa.2018.05.081

[219] Barazzouk S, Bekalé L, Hotchandani S. Enhanced photostability of chlorophyll-a using gold nanoparticles as an efficient photoprotector. *J Mater Chem* 2012; 22: 25316-25324. doi: 10.1039/c2jm33681b

[220] Kolay S, Bain D, Maity S, Devi A, Patra A, Antoine R. Self-Assembled Metal Nanoclusters: Driving Forces and Structural Correlation with Optical Properties. *Nanomaterials* 2022; 12(3): 544. doi: 10.3390/nano12030544

[221] Piepho SB, Schatz PN. *Group Theory in Spectroscopy with applications to magnetic circular dichroism*. Wiley-Interscience:Hoboken, New Jersey 1983.

[222] Frisch MJ, Trucks GW, Schlegel HB, Scuseria GE, Robb MA, Cheeseman JR, Scalmani G, Barone V, Mennucci B, Petersson GA, Nakatsuji H, Caricato M, Li X, Hratchian HP, Izmaylov AF, Bloino J, Zheng G, Sonnenberg JL, Hada M, Ehara M, Toyota K, Fukuda R, Hasegawa J, Ishida M, Nakajima T, Honda Y, Kitao O, Nakai H, Vreven T, Montgomery JA, Jr Peralta JE, Ogliaro F, Bearpark M, Heyd JJ, Brothers E, Kudin KN, Staroverov VN,

Kobayashi R, Normand J, Raghavachari K, Rendell A, Burant JC, Iyengar SS, Tomasi J, Cossi M, Rega N, Millam JM, Klene M, Knox JE, Cross JB, Bakken V, Adamo C, Jaramillo J, Gomperts R, Stratmann RE, Yazyev O, Austin AJ, Cammi R, Pomelli C, Ochterski JW, Martin RL, Morokuma K, Zakrzewski VG, Voth GA, Salvador P, Dannenberg JJ, Dapprich S, Daniels AD, Farkas Ö, Foresman JB, Ortiz JV, Cioslowski J, Fox DJ. Gaussian 09, 2009.

[223] Yanai T, Tew DP, Handy NC. A new hybrid exchange-correlation functional using the Coulomb-attenuating method (CAM-B3LYP). *Chem Phys Lett* 2004; 393: 51-57. doi: 10.1016/j.cplett.2004.06.011

[224] Martin JML, Sundermann A. Correlation consistent valence basis sets for use with the Stuttgart-Dresden-Bonn relativistic effective core potentials: the atoms Ga-Kr and In-Xe. *J Chem Phys* 2001: 3408. doi: 10.1063/1.1337864

[225] Zhurko DA, Zhurko GA. ChemCraft 1.5, Plimus, San Diego, CA. Online: http://www.chemcraftprog.com 2017.

[226] Hanwell MD, Curtis DE, Lonie DC, Vandermeerschd T, Zurek E, Hutchison GR. Avogadro: An advanced semantic chemical editor, visualization, and analysis platform. *J Cheminform* 2012; 4: 1-17. doi: 10.1186/1758-2946-4-17

[227] Da Silva AR, Pelegrino AC, Tedesco AC, Jorge RA. Photodynamic activity of chloro(5,10,15,20-tetraphenylporphyrinato) indium(III). *J Braz Chem Soc* 2008; 19: 491-501. doi: 10.1590/s0103-50532008000300017

[228] Bajju GD, Ahmed A, Gupta D, Kapahi A, Devi G. Synthesis and spectroscopic characterization of some new axially ligated indium(III) macrocyclic complexes and their biological activities. *Bioinorg Chem Appl* 2014; 2014. doi: 10.1155/2014/865407

[229] Arnold DP. Aromatic ring currents illustrated - NMR spectra of tin(lV) porphyrin complexes: An advanced undergraduate experiment. *J Chem Educ* 1988; 65: 1111-1112. doi: 10.1021/ed065p1111

[230] Arnold DP, Blok J. The coordination chemistry of tin porphyrin complexes. *Coord Chem Rev* 2004; 248: 299-319. doi: 10.1016/j.ccr.2004.01.004

[231] Johnstone RAW, Luisa M, Nunes PG, Pereira MM, Gonsalves AR, Serrah AC. Improved Syntheses of 5,10,15,20-Tetrakisaryl- and Tetrakisalkylporphyrins. *Heterocycles* 1996; 43. doi: 10.3987/com-96-7436

[232] Gupta I, Hung C-H, Ravikanth M. Synthesis and Structural Characterization of *meso*-Thienyl Core-Modified Porphyrins. *Eur J Org Chem* 2003: 43924400. doi: 10.1002/ejoc.200300228

[233] Yuasa M, Oyaizu K, Yamaguchi A, Ishikawa M, Eguchi K, Kobayashi T, Toyoda Y, Tsutsui S. Structure and redox properties of electropolymerized film obtained from iron *meso-tetrakis*(3-thienyl)porphyrin. *Polym Adv Technol* 2005; 16: 616-621. doi: 10.1002/pat.633

[234] Rochford J, Botchway S, McGarvey JJ, Rooney AD, Pryce MT. Photophysical and electrochemical properties of *meso*-substituted thien-2-yl Zn(II) porphyrins. *J Phys Chem A* 2008; 112(46): 11611-11618. doi: 10.1021/jp805809p

[235] Berenbaum MC, Akande SL, Bonnett R, Kaur H, Ioannou S, White RD, Winfield UJ. *meso*-Tetra(hydroxyphenyl)porphyrins, a new class of potent tumour photosensitisers with favourable selectivity. *Br J Cancer* 1986; 54(5): 717-725. doi: 10.1038/bjc.1986.232

[236] Bonnett R, McGarvey DJ, Harriman A, Land EJ, Truscott TG, Winfield UJ. Photophysical properties of *meso*-tetraphenylporphyrin and some *meso*-tetra(hydroxyphenyl) porphyrins. *Photochem Photobiol* 1988; 48(3): 271-276. doi: 10.1111/j.1751-1097.1988.tb02820.x

[237] Banfi S, Caruso E, Caprioli S, Mazzagatti L, Canti G, Ravizza R, Gariboldi M, Monti E. Photodynamic effects of porphyrin and chlorin photosensitizers in human colon adenocarcinoma cells. *Bioorganic Med Chem* 2004; 12(18): 4853-4860. doi: 10.1016/j.bmc.2004.07.011

[238] Rojkiewicz M, Kuś P, Kozub P, Kempa M. The synthesis of new potential photosensitizers. *Dyes Pigments* 2013; 99: 627-635. doi: 10.1016/j.dyepig.2013.06.029

[239] Aly KI, Sayed MM, Mohamed MG, Kuo SW, Younis O. A facile synthetic route and dual function of network luminescent porous polyester and copolyester containing porphyrin moiety for metal ions sensor and dyes adsorption. *Microporous Mesoporous Mater* 2020; 298: 110063. doi: 10.1016/j.micromeso.2020.110063

[240] Paolesse R, Boschi T, Licoccia S, Khoury RG, Smith KM. Phosphorus complex of corrole. *Chem Commun* 1998: 1119-1120. doi: 10.1039/a801544i

[241] Bendix J, Dmochowski IJ, Gray HB, Mahammed A, Simkhovich L, Gross Z. Structural, Electrochemical, and Photophysical Properties of Gallium(III) 5,10,15-*Tris*(pentafluorophenyl)corrole. *Angew Chemie* 2000; 39: 4048-4051. doi: 10.1002/1521-3773(20001117)39:22<4048::aid-anie4048>3.0.CO;2-7

[242] Ghosh A, Lee W-Z, Ravikanth M. Synthesis, Structure and Properties of a Five-Coordinate Oxophosphorus(V) *meso*-Triphenylcorrole. *Eur J Inorg Chem* 2012; 2012: 4231-4239. doi: 10.1002/ejic.201200651

[243] Peng KM, Shao WL, Wang HH, Ying X, Wang H, Ji LN, Liu HY. Effects of solvents on the spectral properties of gallium corrole. *Acta Phys-Chim Sin* 2011; 27: 199-206. doi: 10.3866/pku.whxb20110129

[244] Rohand T, Dolusic E, Ngo TH, Maes W, Dehaen W. Efficient synthesis of aryldipyrromethanes in water and their application in the synthesis of corroles and dipyrromethenes. *Arkivoc* 2007; 10: 307-324. doi: 10.3998/ark.5550190.0008.a20

[245] Mironov AF, Moskalchuk TV, Shashkov AS. Formylation reaction in series of *meso*-tetraaryl substituted porphyrins and chlorins. *Russ J Bioorganic Chem* 2004; 30: 261-267. doi: 10.1023/b:rubi.0000030133.22914.8c

[246] Bonnett R, White RD, Winfield UJ, Berenbaum MC. Hydroporphyrins of the *meso*-tetra(hydroxyphenyl)porphyrin series as tumour photosensitizers. *Biochem J* 1989; 261(1): 277-280. doi: 10.1042/bj2610277

[247] Lee KS, El-Sayed MA. Gold and silver nanoparticles in sensing and imaging: Sensitivity of plasmon response to size, shape, and metal composition. *J Phys Chem B* 2006; 110: 19220-19225. doi: 10.1021/jp062536y

[248] Bürgi T. Nanoscale Properties of the gold-sulphur interface: from self-assembled monolayers to clusters. *Nanoscale* 2015; 7: 15553-15567. doi: 10.1039/c5nr03497c

[249] Nwaji N, Mack J, Nyokong T. Enhanced nonlinear optical response of benzothiazole substituted ball-type phthalocyanines in the presence of metallic nanoparticles. *Opt Mater* 2018; 82: 93-103. doi: 10.1016/j.optmat.2018.05.052

[250] Hansch C, Maloney PP, Fujita T, Muir RM. Correlation of biological activity of phenoxyacetic acids with Hammett substituent constants and partition coefficients. *Nature* 1962; 194: 178-180. doi: 10.1038/194178b0

[251] Oluwole DO, Prinsloo E, Nyokong T. Photophysical behavior and photodynamic therapy activity of conjugates of zinc monocarboxyphenoxy phthalocyanine with human serum albumin and chitosan. *Spectrochim Acta A* 2017; 173: 292-300. doi: 10.1016/j.saa.2016.09.032

[252] Sun B, Bte Rahmat JN, Zhang Y. Advanced techniques for performing photodynamic therapy in deep-seated tissues. *Biomaterials* 2022; 291: 121875. doi: 10.1016/j.biomaterials.2022.121875

[253] Kim MM, Darafsheh A. Light Sources and Dosimetry Techniques for Photodynamic Therapy. *Photochem Photobiol* 2020; 96: 280-294. doi: 10.1111/php.13219

[254] Magaraggia M, Visonà A, Furlan A, Pagnan A, Miotto G, Tognon G, Jori G. Inactivation of vascular smooth muscle cells photosensitised by liposome-delivered Zn(II)–phthalocyanine. *J Photochem Photobiol B* 2006; 82: 53-58. doi: 10.1016/j.jphotobiol.2005.08.010

[255] Qualls MM, Thompson DH. Chloroaluminum phthalocyanine tetrasulfonate delivered via acid-labile diplasmenylcholine-folate liposomes: Intracellular localization and synergistic phototoxicity. *Int J Cancer* 2001; 93: 384-392. doi: 10.1002/ijc.1339

[256] Gupta S, Dwarakanath BS, Muralidhar K, Koru-Sengul T, Jain V. Non-monotonic changes in clonogenic cell survival induced by disulphonated aluminum phthalocyanine photodynamic treatment in a human glioma cell line. *J Transl Med* 2010; 8: 43. doi: 10.1186/1479-5876-8-43

[257] Sindelo A, Kobayashi N, Kimura M, Nyokong T. Physicochemical and photodynamic antimicrobial chemotherapy activity of morpholine-substituted phthalocyanines: Effect of point of substitution and central metal. *J Photochem Photobiol A* 2019; 374: 58-67. doi: 10.1016/j.jphotochem.2019.01.025

[258] Wilson C, Lukowicz R, Merchant S, Valquier-Flynn H, Caballero J, Sandoval J, Okuom M, Huber C, Brooks TD, Wilson E, Clement B, Wentworth CD, Holmes AE. Quantitative and Qualitative Assessment Methods for Biofilm Growth: A Mini-review. *Res Rev J Eng Technol* 2017; 6(4): 1-42. http://www.rroij.com/open-access/quantitative-and-qualitative-assessment-methods-for-biofilm-growth-a-minireview-.pdf. Epub 2017 Oct 24.

[259] Lade H, Park JH, Chung SH, Kim IH, Kim JM, Joo HS, Kim JS. Biofilm formation by Staphylococcus aureus clinical isolates is differentially affected by glucose and sodium

chloride supplemented culture media. *J Clin Med* 2019; 8(11): 1853. doi: 10.3390/jcm8111853

[260] Dube E, Soy R, Shumba M, Nyokong T. Photophysicochemical behaviour of phenoxy propanoic acid functionalised zinc phthalocyanines when grafted onto iron oxide and silica nanoparticles: Effects in photodynamic antimicrobial chemotherapy. *J Lumin* 2021; 234. doi: 10.1016/j.jlumin.2021.117939

[261] Sen P, Soy R, Mgidlana S, Mack J, Nyokong T. Light-driven antimicrobial therapy of palladium porphyrins and their chitosan immobilization derivatives and their photophysical-chemical properties. *Dyes Pigments* 2022; 203: 110313. doi: 10.1016/j.dyepig.2022.110313

[262] Coffey BM, Anderson GG. Biofilm Formation in the 96-Well Microtiter Plate. In *Pseudomonas Methods and Protocols.* Methods in Molecular Biology, Vol. 1149, Springer:New York 2014.

[263] Santos I, Gamelas SR, Vieira C, Faustino MA, Tome JP, Almeida A, Gomes AT, Lourenco LM. Pyrazole-pyridinium porphyrins and chlorins as powerful photosensitizers for photoinactivation of planktonic and biofilm forms of E. coli. *Dyes Pigments* 2021; 193: 109557. doi: 10.1016/j.dyepig.2021.109557

[264] Cai S, Shokhireva TK, Lichtenberger DL, Walker FA. NMR and EPR studies of chloroiron(iii) tetraphenyl-chlorin and its complexes with imidazoles and pyridines of widely differing basicities. *Inorg Chem* 2006; 45: 3519-3531. doi: 10.1021/ic0515352

[265] Bürgi T. Properties of the gold-sulphur interface: from self-assembled monolayers to clusters. *Nanoscale* 2015; 7: 15553-15567. doi: 10.1039/c5nr03497c

[266] Menendez-Miranda M, Costa-Fernández JM, Encinar JR, Parak WJ, Carrillo-Carrion C. Determination of the ratio of fluorophore/nanoparticle for fluorescence-labelled nanoparticles. *Analyst* 2016; 141: 1266-1272. doi: 10.1039/c5an02405f

[267] Byrn MP, Curtis CJ, Hsiou Y, Khan SI, Sawin PA, Tendick SK, Terzis A, Strouse CE. Porphyrin sponges: conservative of host structure in over 200 porphyrin-based lattice clathrates. *J Am Chem Soc* 1993; 115: 9480-9497. doi: 10.1021/ja00074a013

[268] Chastain J, King Jr RC. *X-ray photoelectron spectroscopy (XPS)*. Vol. 40, 221. Perkin-Elmer Corporation; 1992. doi: 10.1002/0470014229.ch22

[269] Brückner C, Foss PC, Sullivan JO, Pelto R, Zeller M, Birge RR, Crundwell G. Origin of the bathochromically shifted optical spectra of *meso*-tetrathien-2'-and 3'-ylporphyrins as compared to *meso*-tetraphenylporphyrin. *Phys Chem Chem Phys* 2006; 8: 2402-2412. doi: 10.1039/b600010j

[270] Gupta I, Ravikanth M. Spectroscopic properties of *meso*-thienylporphyrins with different porphyrin cores. *J Photochem Photobiol A* 2006; 177: 156-163. doi: 10.1016/j.jphotochem.2005.05.020

[271] Zheng W, Shan N, Yu L, Wang X. UV-visible, fluorescence and EPR properties of porphyrins and metalloporphyrins. *Dyes Pigments* 2008; 77: 153-157. doi: 10.1016/j.dyepig.2007.04.007

[272] Mack J, Stillman MJ, Kobayashi N. Application of MCD spectroscopy to porphyrinoids. *Coord Chem Rev* 2007; 251: 429-453. doi: 10.1016/j.ccr.2006.05.011

[273] Mack J, Asano Y, Kobayashi N, Stillman MJ. Application of MCD Spectroscopy and TD−DFT to a Highly Non-Planar Porphyrinoid Ring System. New Insights on Red−Shifted Porphyrinoid Spectral Bands. *J Am Chem Soc* 2005; 127: 17697-17711. doi: 10.1021/ja0540728

[274] Thomas S, Nair SK, Jamal EMA, Al-Harthi SH, Varma MR, Anantharaman MR. Size-dependent surface plasmon resonance in silver silica nanocomposites. *Nanotechnology* 2008; 19: 075710. doi: 10.1088/0957-4484/19/7/075710

[275] Ghosh SK, Nath S, Kundu S, Esumi K, Pal T. Solvent and ligand effects on the localized surface plasmon resonance (LSPR) of gold colloids. *J Phys Chem B* 2004; 108: 13963-13971. doi: 10.1021/jp047021q

[276] Liu X, Mahammed A, Tripathy U, Gross Z, Steer RP. Photophysics of Soret-excited tetrapyrroles in solution. III. Porphyrin analogues: Aluminum and gallium corroles. *Chem Phys Lett* 2008; 459: 113-118. doi: 10.1016/j.cplett.2008.05.038

[277] Bag PP, Wang D, Chen Z, Cao R. Outstanding drug loading capacity by water stable microporous MOF: A potential drug carrier. *Chem Commun* 2016; 52: 3669-3672. doi: 10.1039/c5cc09925k

[278] Shen S, Wu Y, Liu Y, Wu D. High drug-loading nanomedicines: Progress, current status, and prospects. *Int J Nanomedicine* 2017; 12: 4085-4109. doi: 10.2147/ijn.S132780

[279] Ishizuka T, Sakashita R, Iwanaga O, Morimoto T, Mori S, Ishida M, Toganoh M, Takegoshi K, Osuka A, Furuta H. NH Tautomerism of N-confused porphyrin: Solvent/substituent effects and isomerization mechanism. *J Phys Chem A* 2020; 124(28):5756-69. doi: 10.1021/acs.jpca.0c04779

[280] Sripothongnak S, Ziegler CJ, Dahlby MR, Nemykin VN. Controllable and Reversible Inversion of the Electronic Structure in Nickel N-Confused Porphyrin: A Case When MCD Matters. *Inorg Chem* 2011; 50: 6902-6909. doi: 10.1021/ic102255k

[281] Doble S, Osinski AJ, Holland SM, Fisher JM, Geier III GR, Belosludov RV, Ziegler CJ, Nemykin VN. Magnetic Circular Dichroism of Transition-Metal Complexes of Perfluorophenyl-N-Confused Porphyrins: Inverting Electronic Structure through a Proton. *J Phys Chem A* 2017; 121: 3689-3698. doi: 10.1021/acs.jpca.7b02908

[282] Lipinski CA, Lombardo F, Dominy BW, Feeney PJ. Experimental and computational approaches to estimate solubility and permeability in drug discovery and development settings. *Adv Drug Deliv Rev* 2012; 64: 4-17. doi: 10.1016/j.addr.2012.09.019

[283] Feng C, Wang K, Xu Y, Liu L, Zou B, Lu P. Unique piezochromic fluorescence behavior of organic crystal of carbazole-substituted CNDSB. *Chem Commun* 2016; 52: 3836-3839. doi: 10.1039/c5cc09152g

[284] Yin J, Ma Y, Li G, Peng M, Lin W. A versatile small-molecule fluorescence scaffold: Carbazole derivatives for bioimaging. *Coord Chem Rev* 2020; 412: 213257. doi: 10.1016/j.ccr.2020.213257

[285] Frühbeißer S, Mariani G, Gröhn F. Porphyrin diacid-polyelectrolyte assemblies: Effective photocatalysts in solution. *Polymers* 2016; 8(5): 180. doi: 10.3390/polym8050180

[286] Pineiro M, Pereira MM, Gonsalves AD, Arnaut LG, Formosinho SJ. Singlet oxygen quantum yields from halogenated chlorins: potential new photodynamic therapy agents. *J Photochem Photobiol A* 2001; 138(2): 147-157. doi: 10.1016/S1010-6030(00)00382-8

[287] Gierlich P, Mucha SG, Robbins E, Gomes-da-Silva LC, Matczyszyn K, Senge MO. One-Photon and Two-Photon Photophysical Properties of Tetrafunctionalized 5,10,15,20-tetrakis(m-hydroxyphenyl)chlorin (Temoporfin) Derivatives as Potential Two-Photon-Induced Photodynamic Therapy Agents. *ChemPhotoChem* 2022; 6(4): e202100249. doi: 10.1002/cptc.202100249

[288] Silva EFF, Schaberle FA, Monteiro CJP, Dąbrowski JM, Arnaut LG. The challenging combination of intense fluorescence and high singlet oxygen quantum yield in photostable chlorins-a contribution to theranostics. *Photochem Photobiol Sci* 2013; 12:1187-1192. doi: 10.1039/c3pp25419d

[289] Babu B, Mack J, Nyokong T. A heavy-atom-free π-extended N-confused porphyrin as a photosensitizer for photodynamic therapy. *New J Chem* 2021; 45: 5654-5658. doi: 10.1039/d1nj00112d

[290] Poon CT, Zhao S, Wong WK, Kwong DWJ. Synthesis, excitation energy transfer and singlet oxygen photogeneration of covalently linked N-confused porphyrin-porphyrin and Zn(II) porphyrin dyads. *Tetrahedron Lett* 2010; 51: 664-668. doi: 10.1016/j.tetlet.2009.11.101

[291] Aleman EA, Joseph J, Modarelli DA. Solvent Effects on the UV-Vis Absorption Properties and Tautomerism of N-Confused Tetraphenylporphyrin. *J Org Chem* 2015; 80(21) : 11031-8. *J Org Chem* 2015; 80: 11031-11038. doi: 10.1021/acs.joc.5b02244

[292] Shabangu SM, Babu B, Soy RC, Oyim J, Amuhaya E, Nyokong T. Susceptibility of Staphylococcus aureus to porphyrin-silver nanoparticle mediated photodynamic antimicrobial chemotherapy. *J Lumin* 2020; 222: 117158. doi: 10.1016/j.jlumin.2020.117158

[293] Dos Santos FA, Pereira MC, de Oliveira TB, Mendonça Junior FJ, de Lima MD, Pitta MG, Pitta ID, de Melo Rêgo MJ, da Rocha Pitta MG. Anticancer properties of thiophene derivatives in breast cancer MCF-7 cells. *Anticancer Drugs* 2018; 29: 157-166. doi: 10.1097/CAD.0000000000000581

[294] Shabangu SM, Babu B, Soy RC, Managa M, Sekhosana KE, Nyokong T. Photodynamic antimicrobial chemotherapy of asymmetric porphyrin-silver conjugates towards photoinactivation of Staphylococcus aureus. *J Coord Chem* 2020; 73(4): 593-608 doi: 10.1080/00958972.2020.173927

[295] Naz H, Tarique M, Khan P, Luqman S, Ahamad S, Islam A, Ahmad F, Hassan M. Evidence of vanillin binding to CAMKIV explains the anti-cancer mechanism in human hepatic carcinoma and neuroblastoma cells. *Mol Cell Biochem* 2018; 438(1): 35-45. doi: 10.1007/s11010-017-3111-0

[296] Arya SS, Rookes JE, Cahill DM, Lenka SK. Vanillin: a review on the therapeutic prospects of a popular flavouring molecule. *Adv Trad Med* 2021; 21. doi: 10.1007/s13596-020-00531-w

[297] Gomes CA, Girão da Cruz T, Andrade JL, Milhazes N, Borges F, Marques MP. Anticancer activity of phenolic acids of natural or synthetic origin: a structure-activity study. *J Med Chem* 2003; 46: 5395-5401. doi: 10.1021/jm030956v

[298] Bouarab-Chibane L, Forquet V, Lantéri P, Clément Y, Léonard-Akkari L, Oulahal N, Degraeve P, Bordes C. Antibacterial properties of polyphenols: characterization and QSAR (Quantitative structure-activity relationship) models. *Front Microbiol* 2019; 10. doi: 10.3389/fmicb.2019.00829

[299] Drzewiecka-Matuszek A, Rutkowska-Zbik D. Application of TD-DFT Theory to Studying Porphyrinoid-Based Photosensitizers for Photodynamic Therapy: A Review. *Molecules* 2021; 26(23): 7176. doi: 10.3390/molecules26237176

[300] Babu B, Amuhaya E, Oluwole D, Prinsloo E, Mack J, Nyokong T. Preparation of NIR absorbing axial substituted tin (IV) porphyrins and their photocytotoxic properties. *Med Chem Commun* 2019; 10(1): 41-48. doi: 10.1039/c8md00373d

APPENDIX

Appendices

This section provides extra data obtained for Chapters 3 to 10.

12.0 Data for Chapter Three

This section provides extra data obtained during the structural characterization of the synthesized porphyrin and porphyrin analog dyes and those of the nanoconjugates.

12.1 Structural characterization data for porphyrin dyes.

12.1.1.1 ^{1}H NMR spectra for porphyrin dyes.

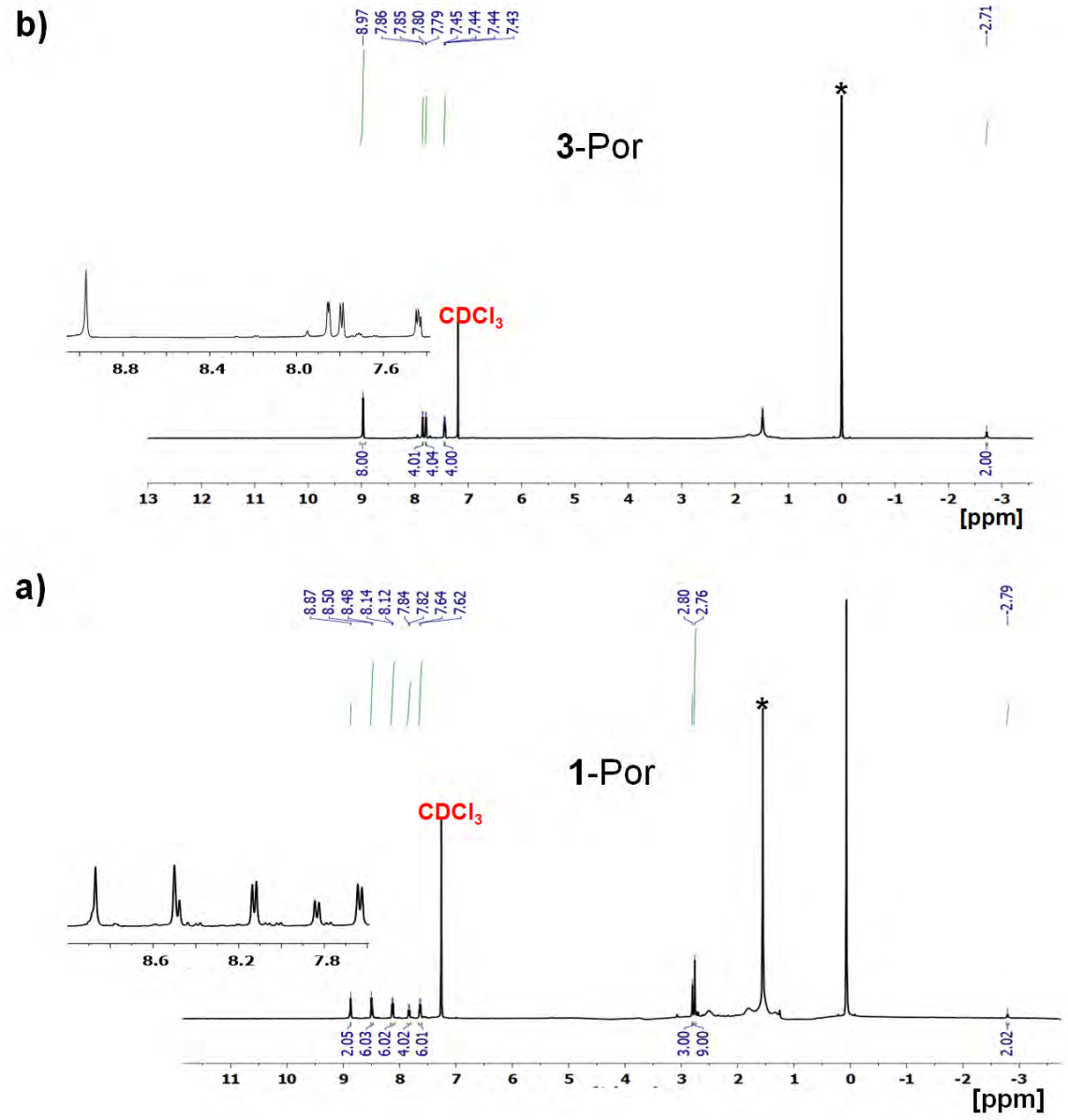

Figure A 1: ^{1}H NMR Spectra for a) **1**-Por and b) **3**-Por and black* asterisk highlight the residual water peak. The insets are expanded aromatic regions.

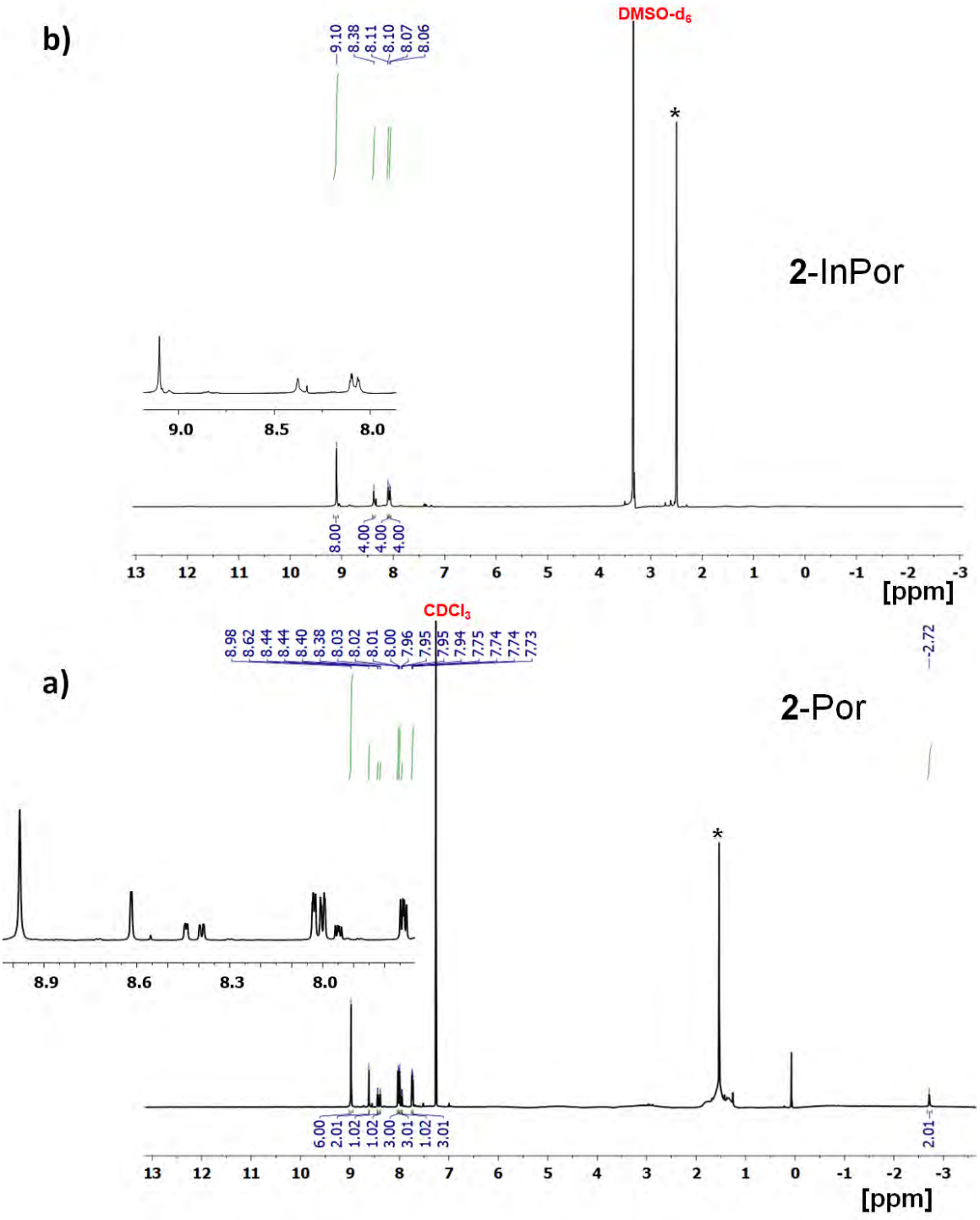

Figure A 2: ^{1}H NMR Spectra for a) **2**-Por and b) **2**-InPor and black* asterisk highlight the residual water peak. The insets provide expanded aromatic regions.

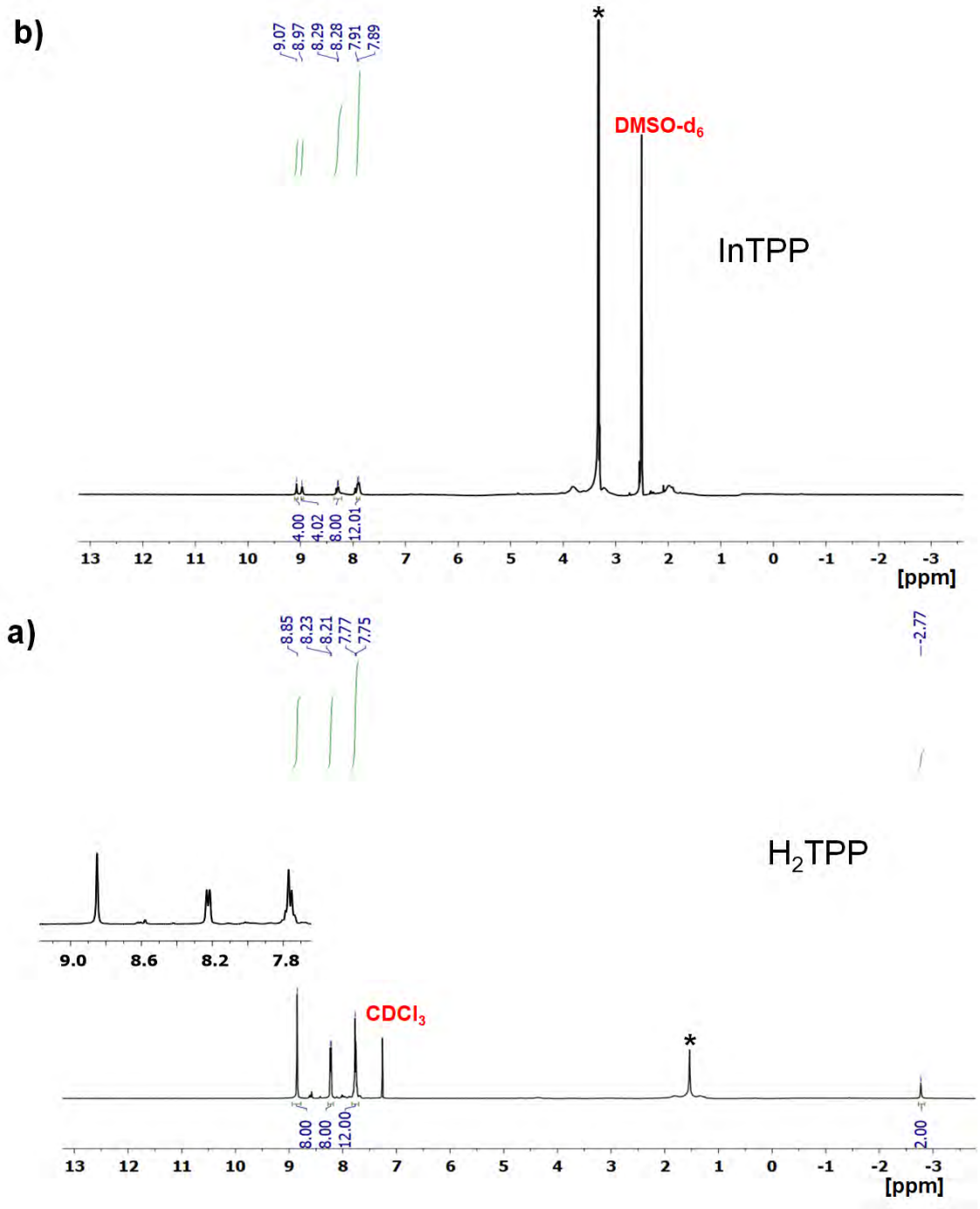

Figure A 3: ^{1}H NMR spectra for a) H_2TPP and b) InTPP and black* asterisk highlight residual water peak.

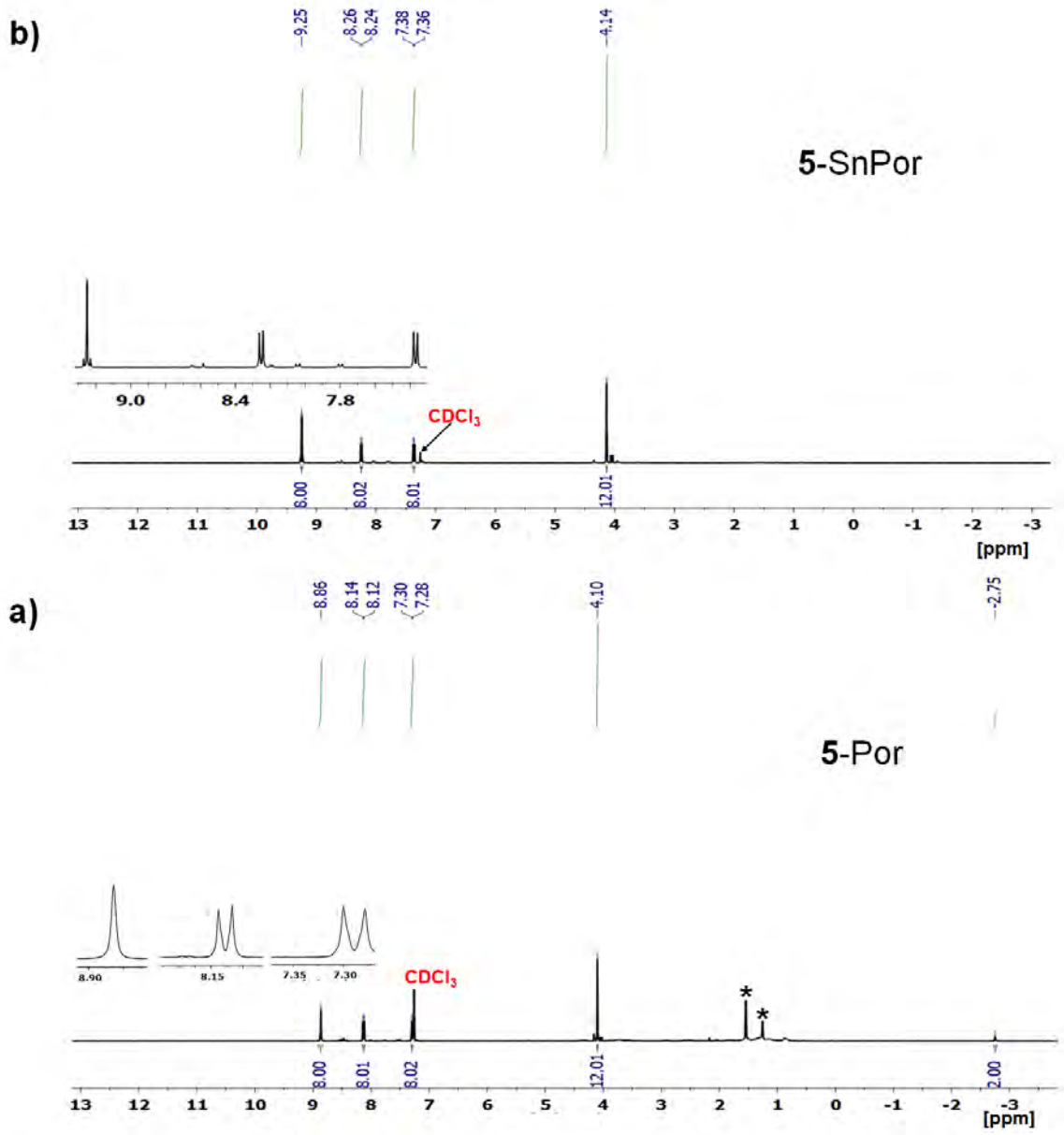

Figure A 4: ^{1}H NMR spectra for a) **5**-Por and b) **5**-SnPor and black* asterisk highlight residual water peak and solvent impurities.

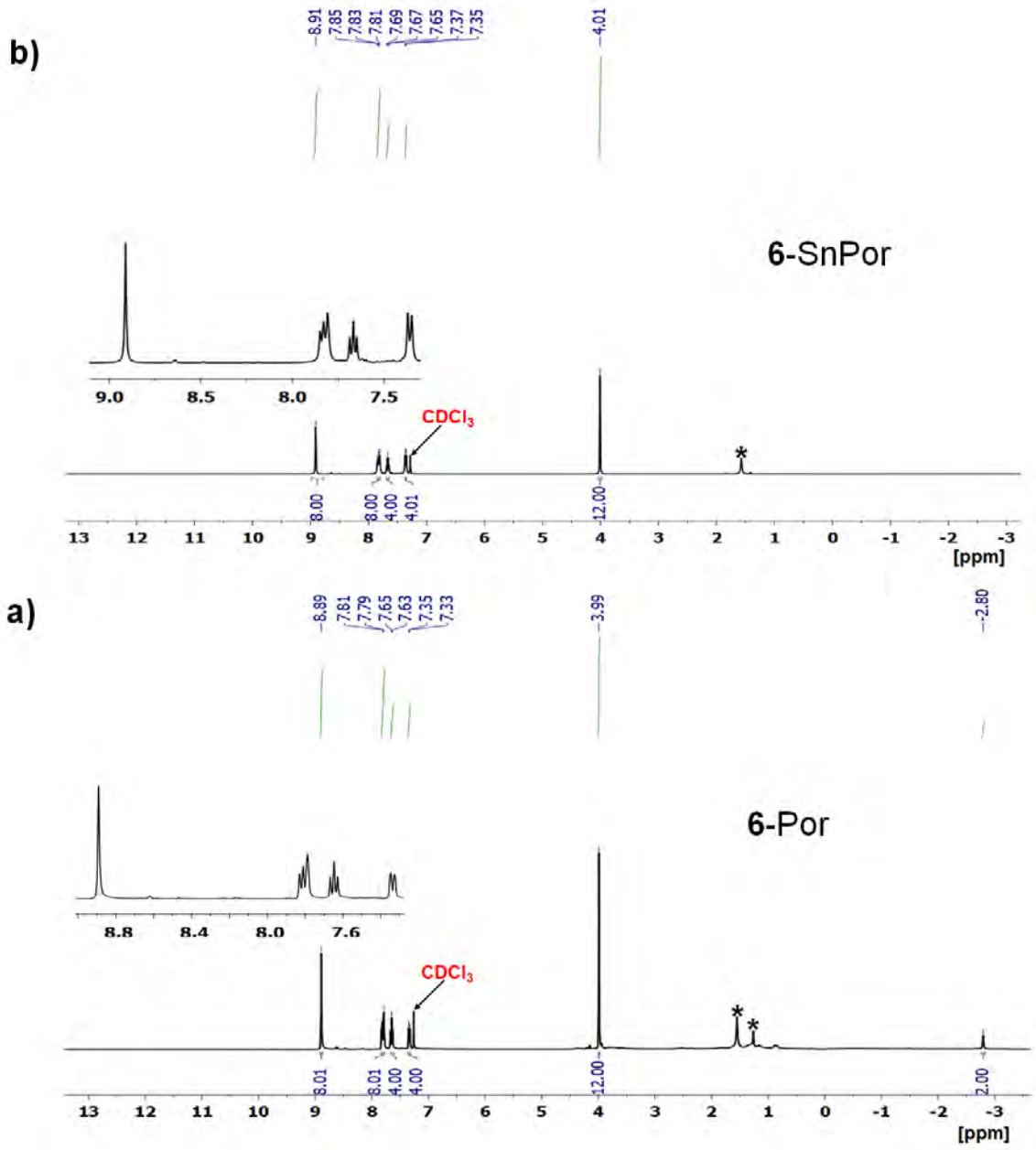

Figure A 5: ^{1}H NMR spectra for a) **6**-Por and b) **6**-SnPor and black* asterisk highlight residual water peak and solvent impurities.

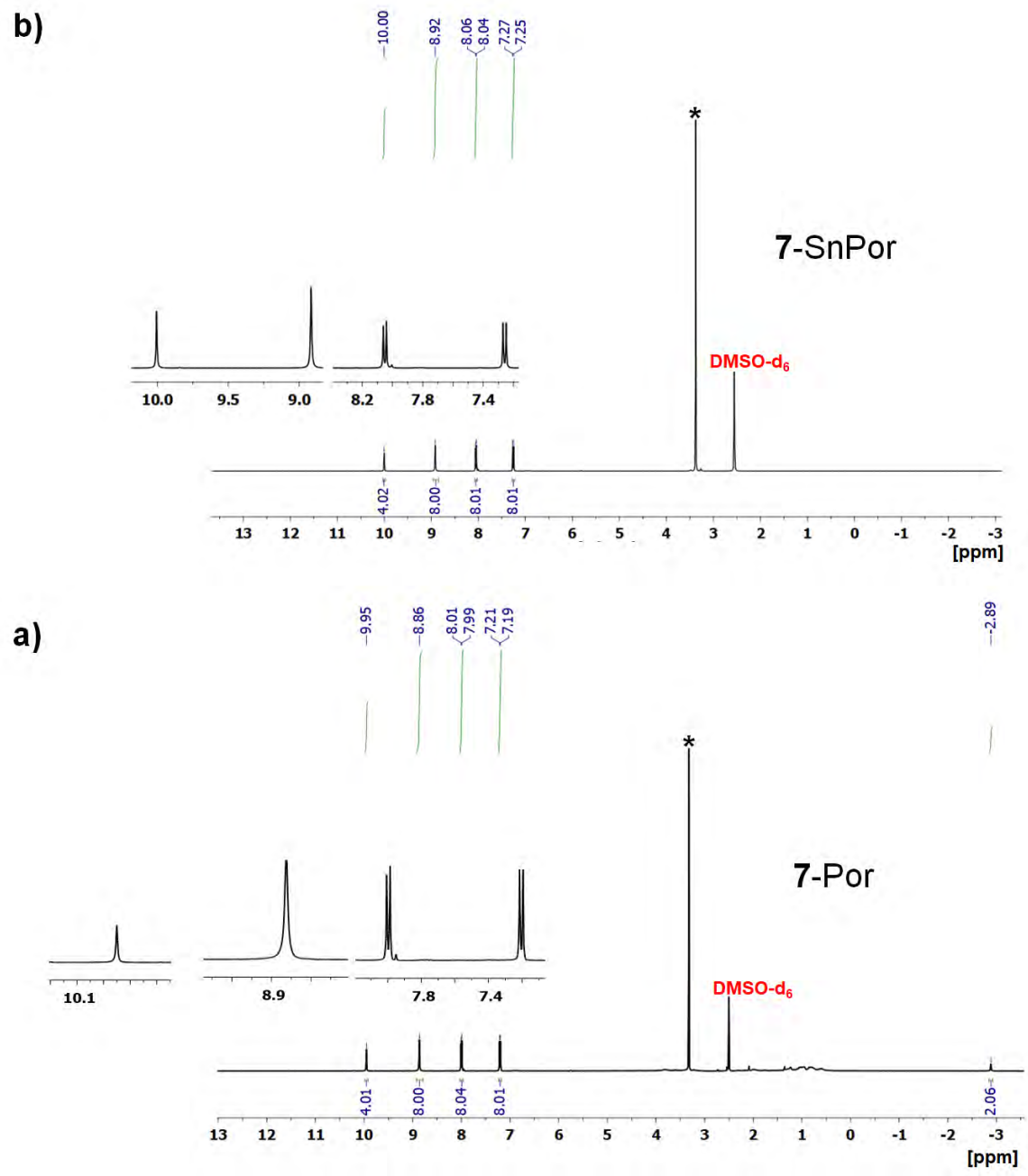

Figure A 6: ^{1}H NMR spectra for a) **7**-Por and b) **7**-SnPor and black* asterisk highlight residual water peak.

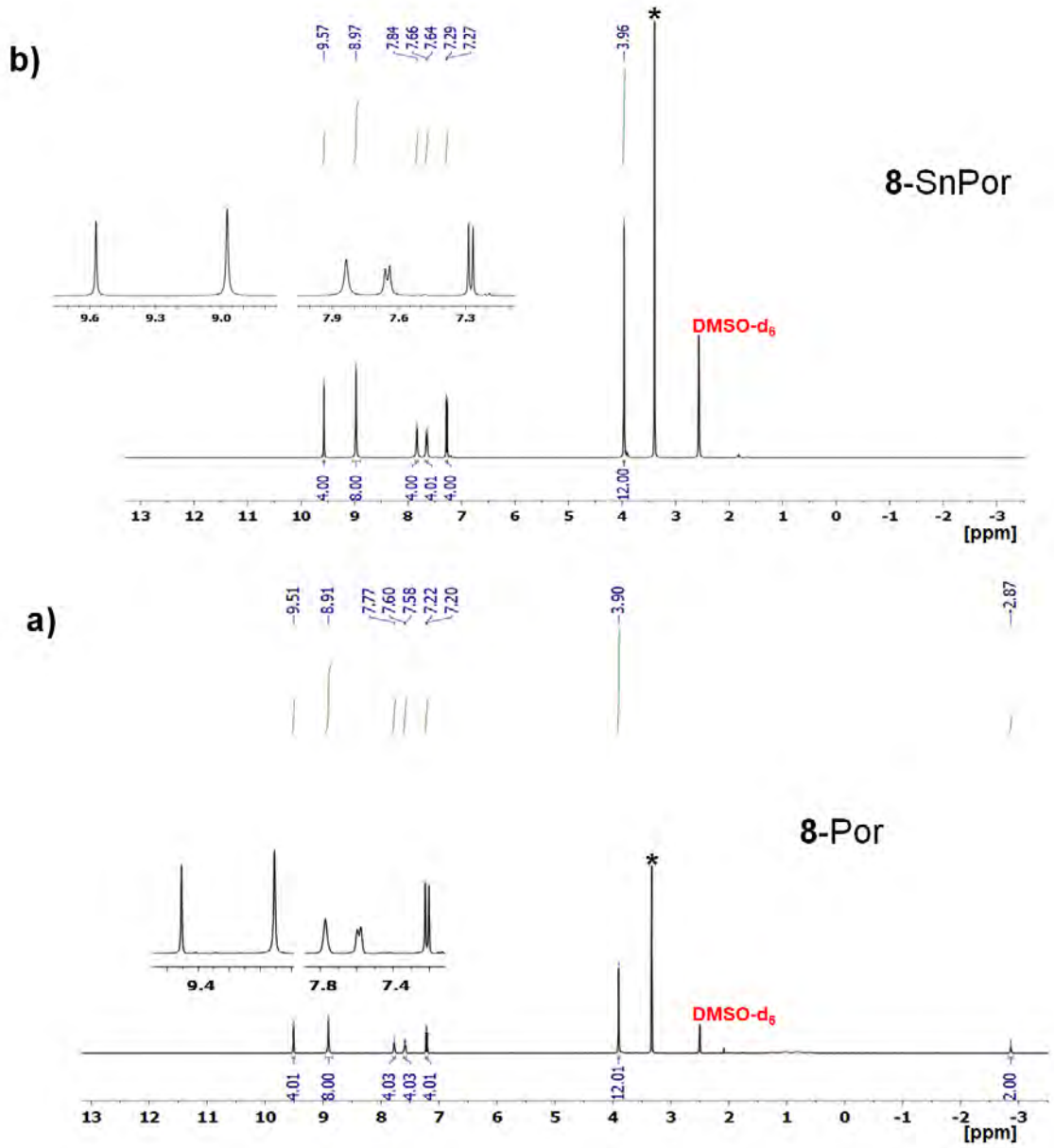

Figure A 7: ^{1}H NMR spectra for a) **7**-Por and b) **7**-SnPor and black* asterisk highlight residual water peak.

12.1.1.2 Mass spectra for porphyrin dyes using α-cyano-4-hydroxycinnamic acid as the matrix

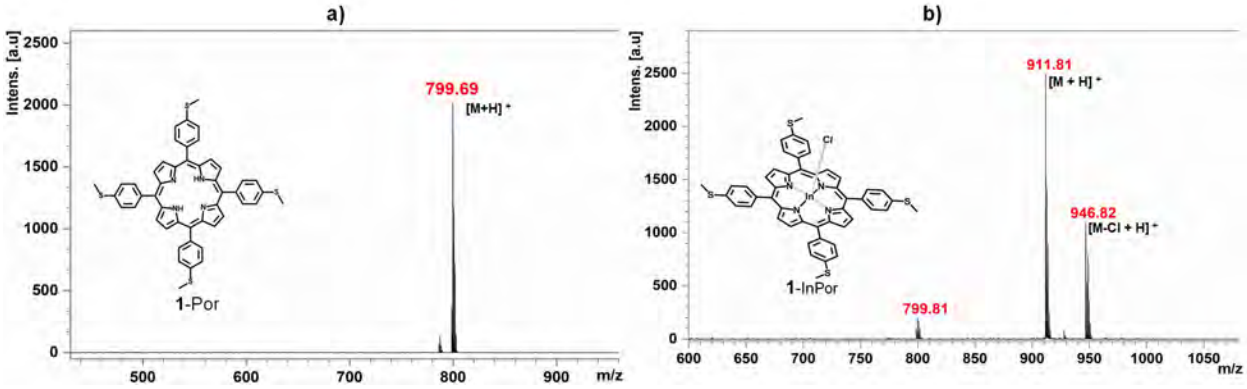

Figure A 8:MALDI-TOF MS data for a) **1**-Por and b) **1**-InPor.

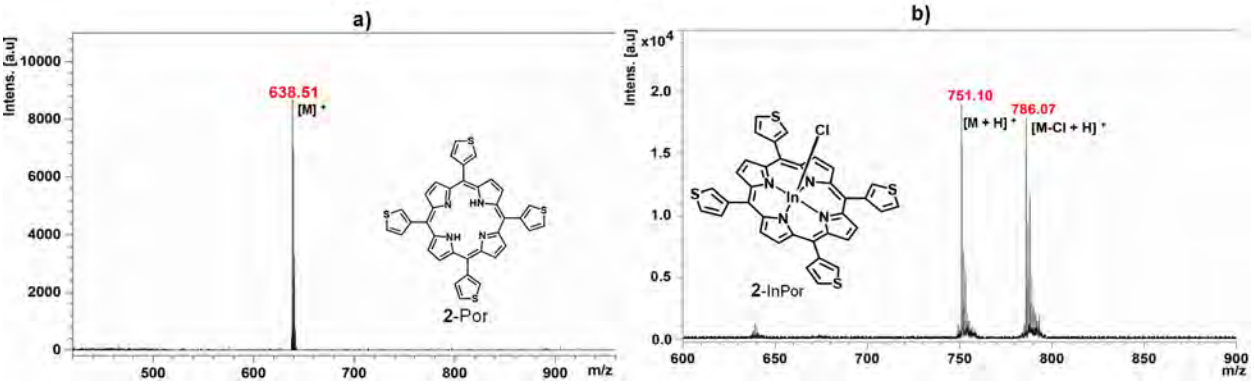

Figure A 9: MALDI-TOF MS data for a) **2**-Por and b) **2**-InPor.

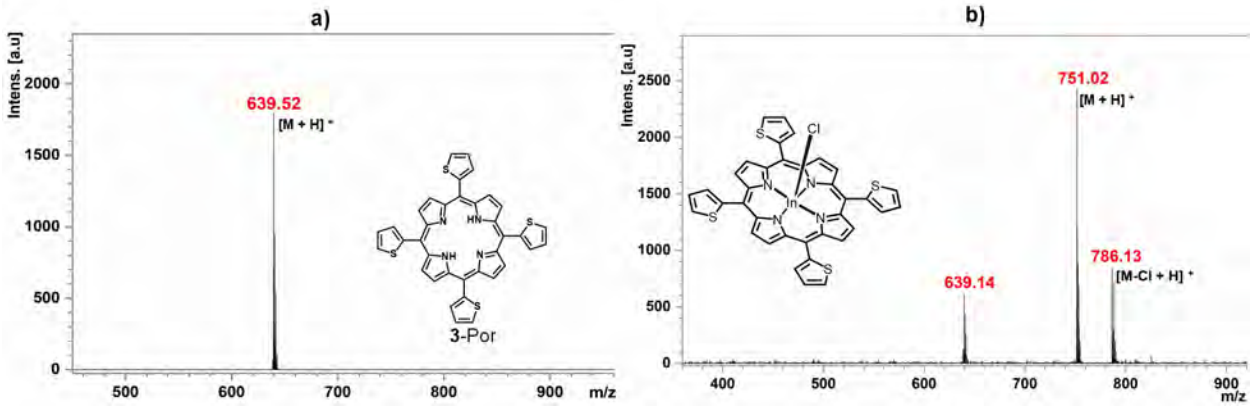

Figure A 10: MALDI-TOF MS data for a) **3**-Por and b) **3**-InPor.

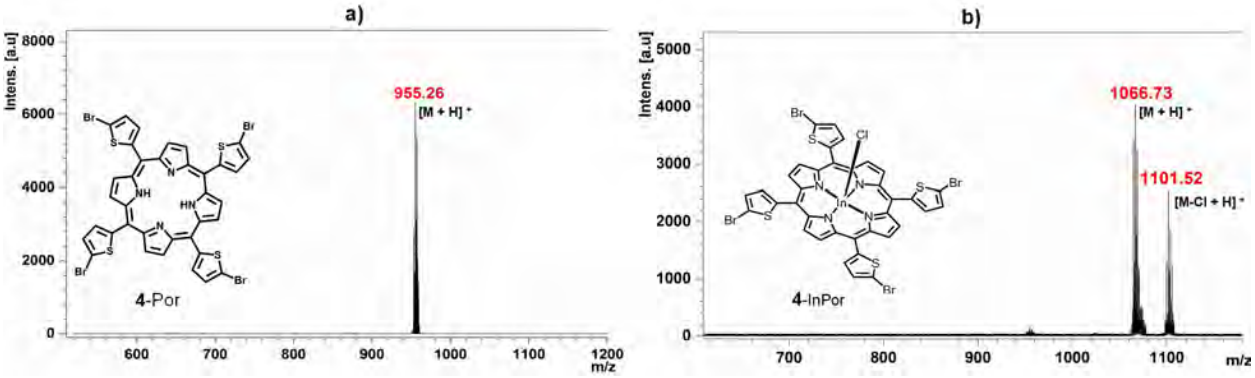

Figure A 11: MALDI-TOF MS data for a) **4**-Por and b) **4**-InPor.

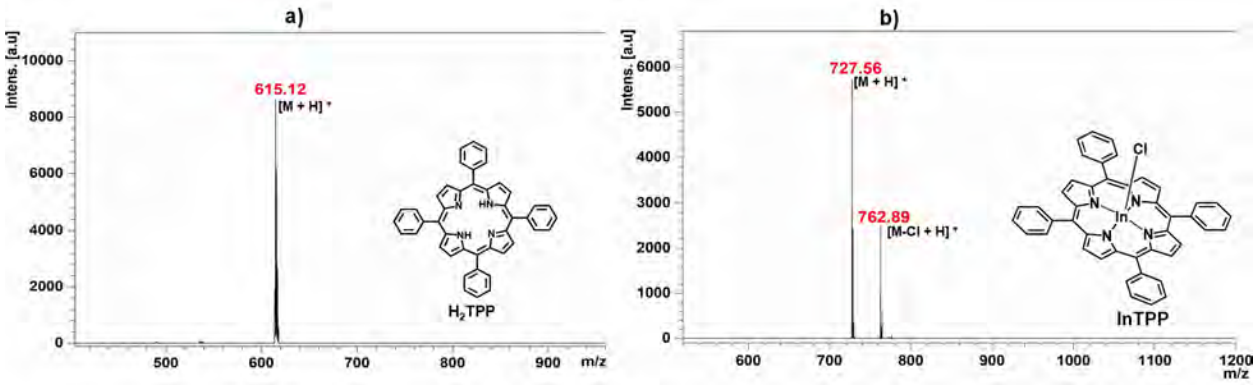

Figure A 12: MALDI-TOF MS data for a) H_2TPP and b) InTPP.

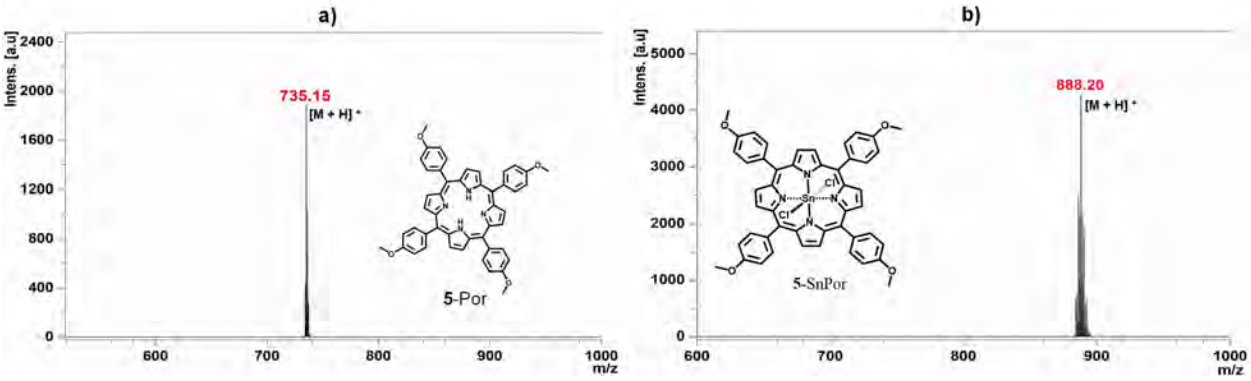

Figure A 13: MALDI-TOF MS data for a) **5**-Por and b) **5**-SnPor.

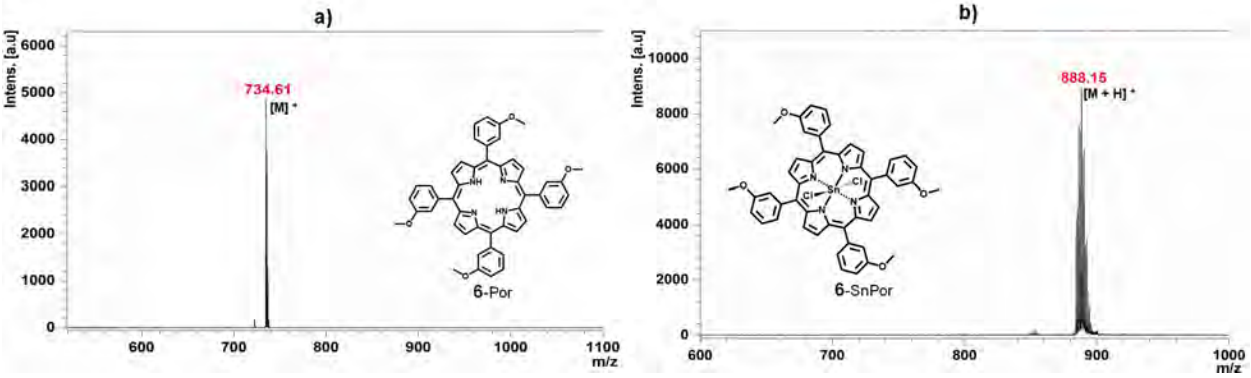

Figure A 14: MALDI-TOF MS data for a) **6**-Por and b) **6**-SnPor.

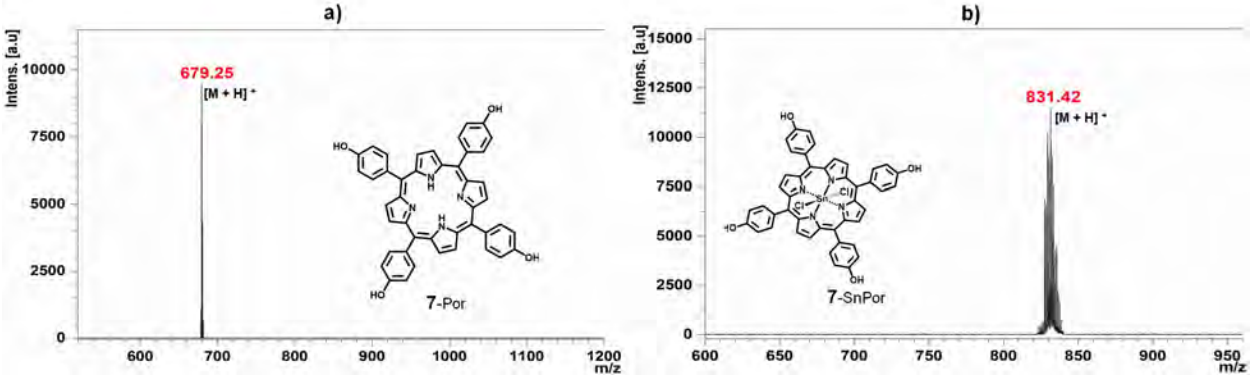

Figure A 15: MALDI-TOF MS data for a) **7**-Por and b) **7**-SnPor.

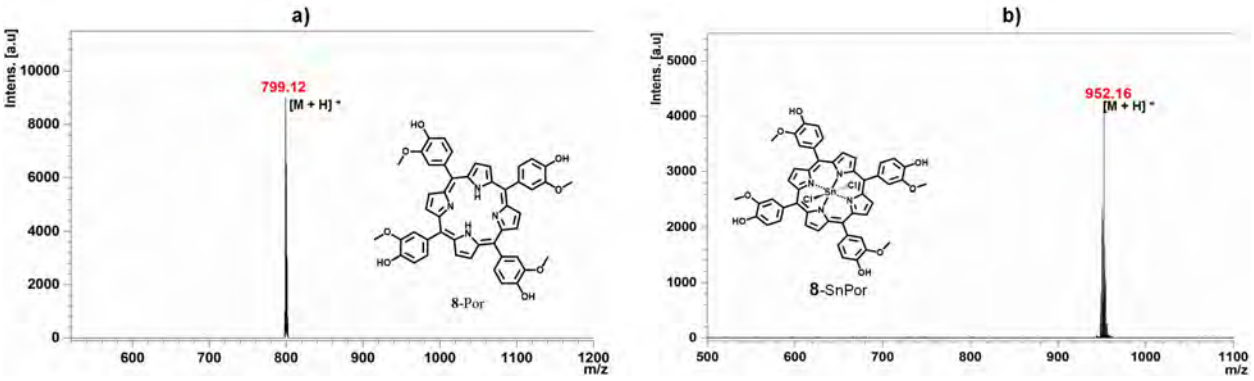

Figure A 16: MALDI-TOF MS data for a) **8**-Por and b) **8**-SnPor.

12.1.2 Structural characterization data for corrole dyes

12.1.2.1 ^{1}H NMR spectra for A_3 *meso*-triarylcorrole dye

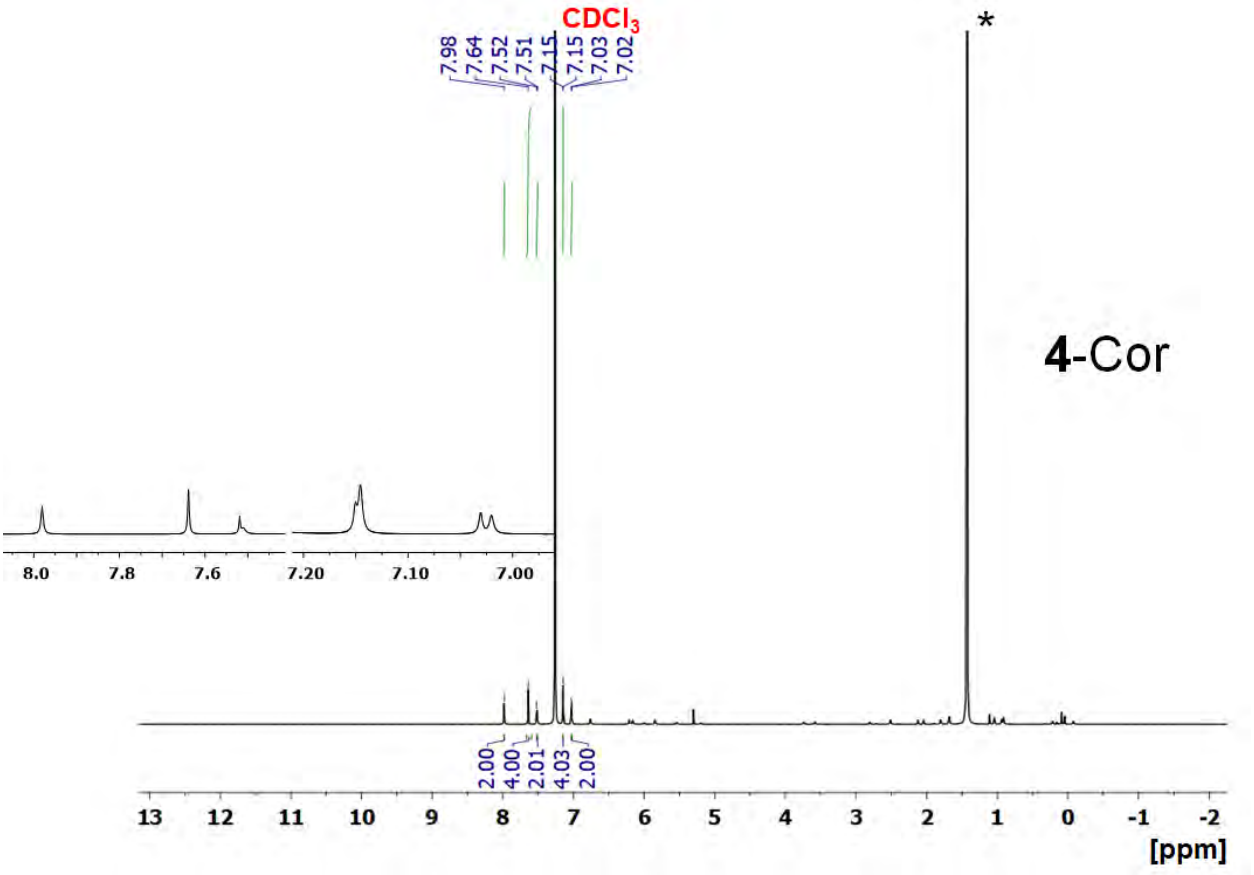

Figure A 17: ^{1}H NMR spectra for **4**-Cor and black* asterisk highlight the residual water peak.

12.1.2.2 Mass spectra for A_3 *meso*-triarylcorrole dyes using α-cyano-4-hydroxycinnamic acid as the matrix

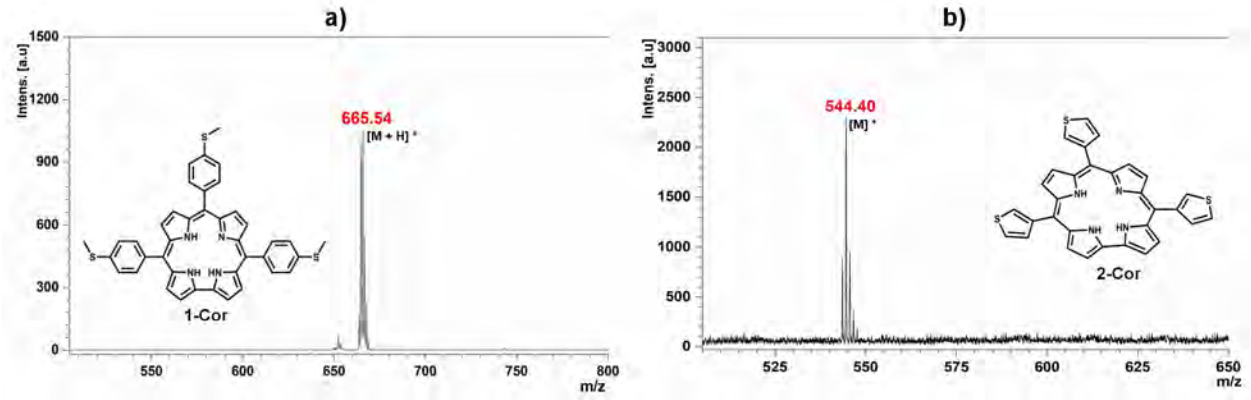

Figure A 18: MALDI-TOF MS data for a) **1**-Cor and b) **2**-Cor.

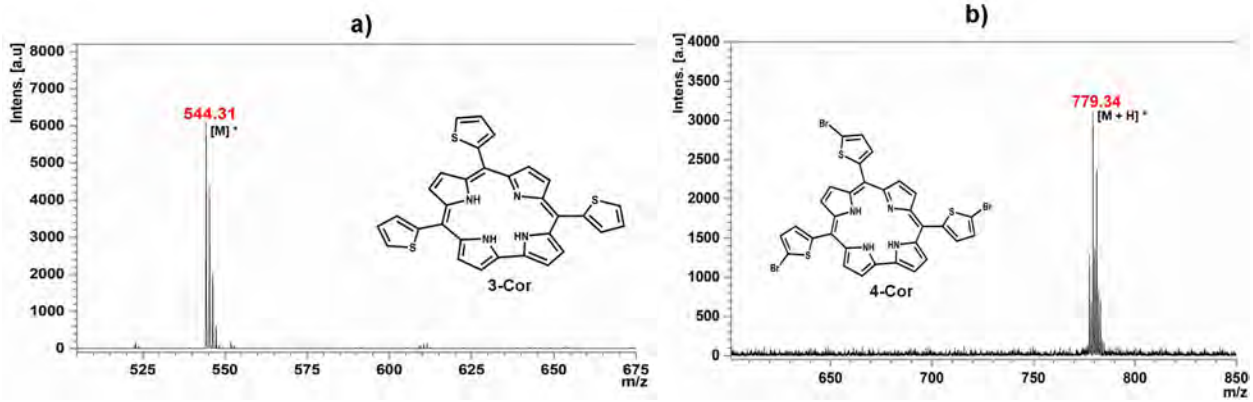

Figure A 19: MALDI-TOF MS data for a) **3**-Cor and b) **4**-Cor.

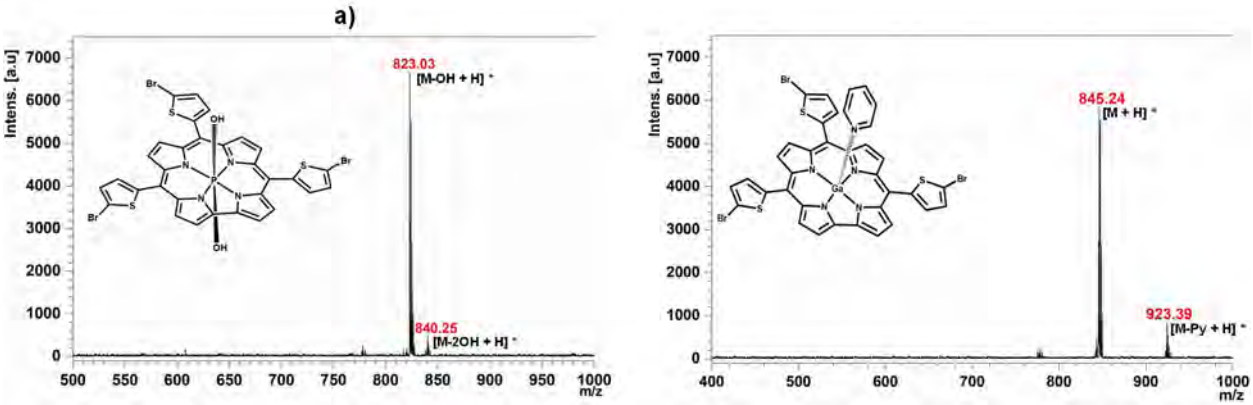

Figure A 20: MALDI-TOF MS data for a) **4**-P^{V}Cor and b) **4**-GaCor.

12.1.2.3 ^{1}H NMR spectra and MALDI-TOF MS data for A_2B *meso*-triarylcorrole dyes

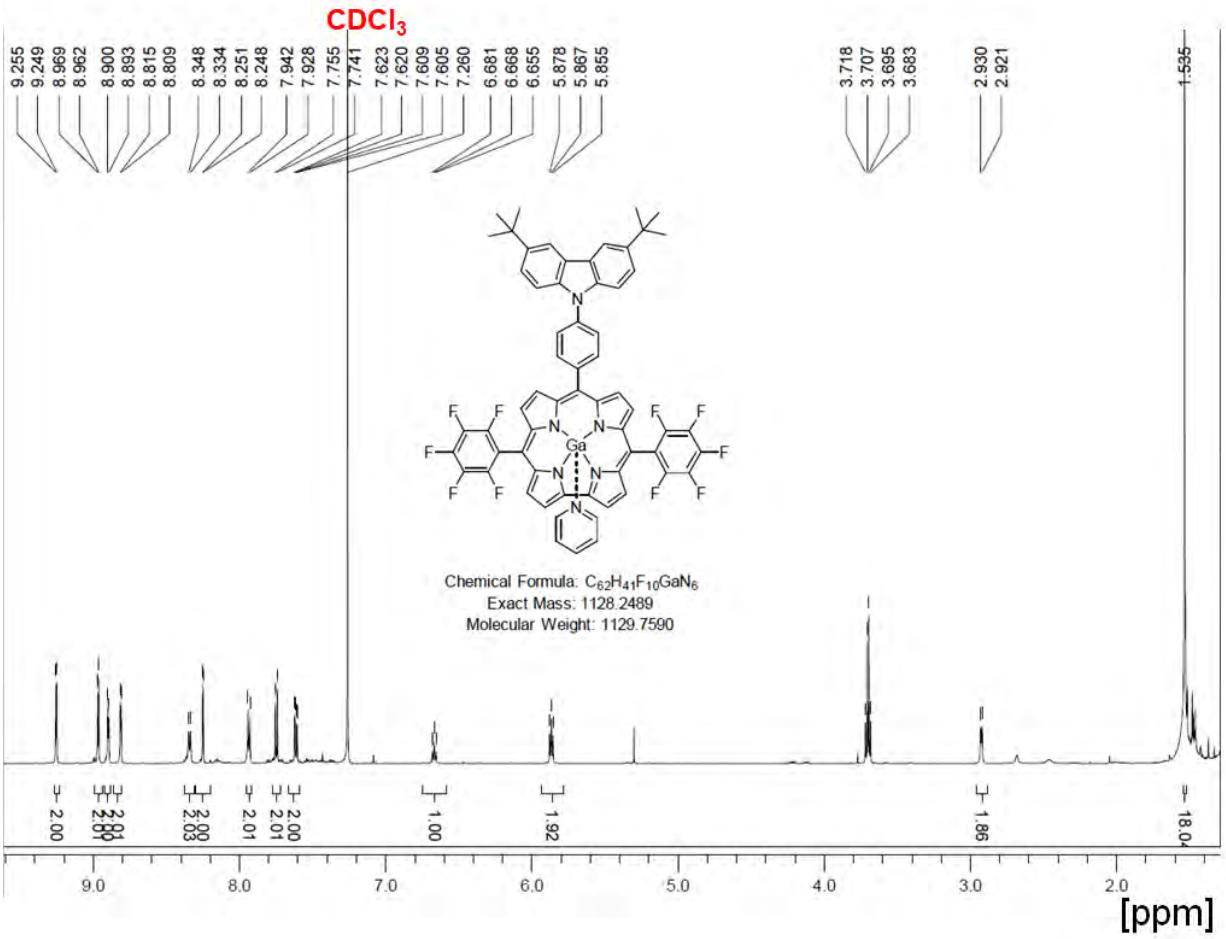

Figure A 21: ^{1}H NMR Spectra for **9**-GaCor.

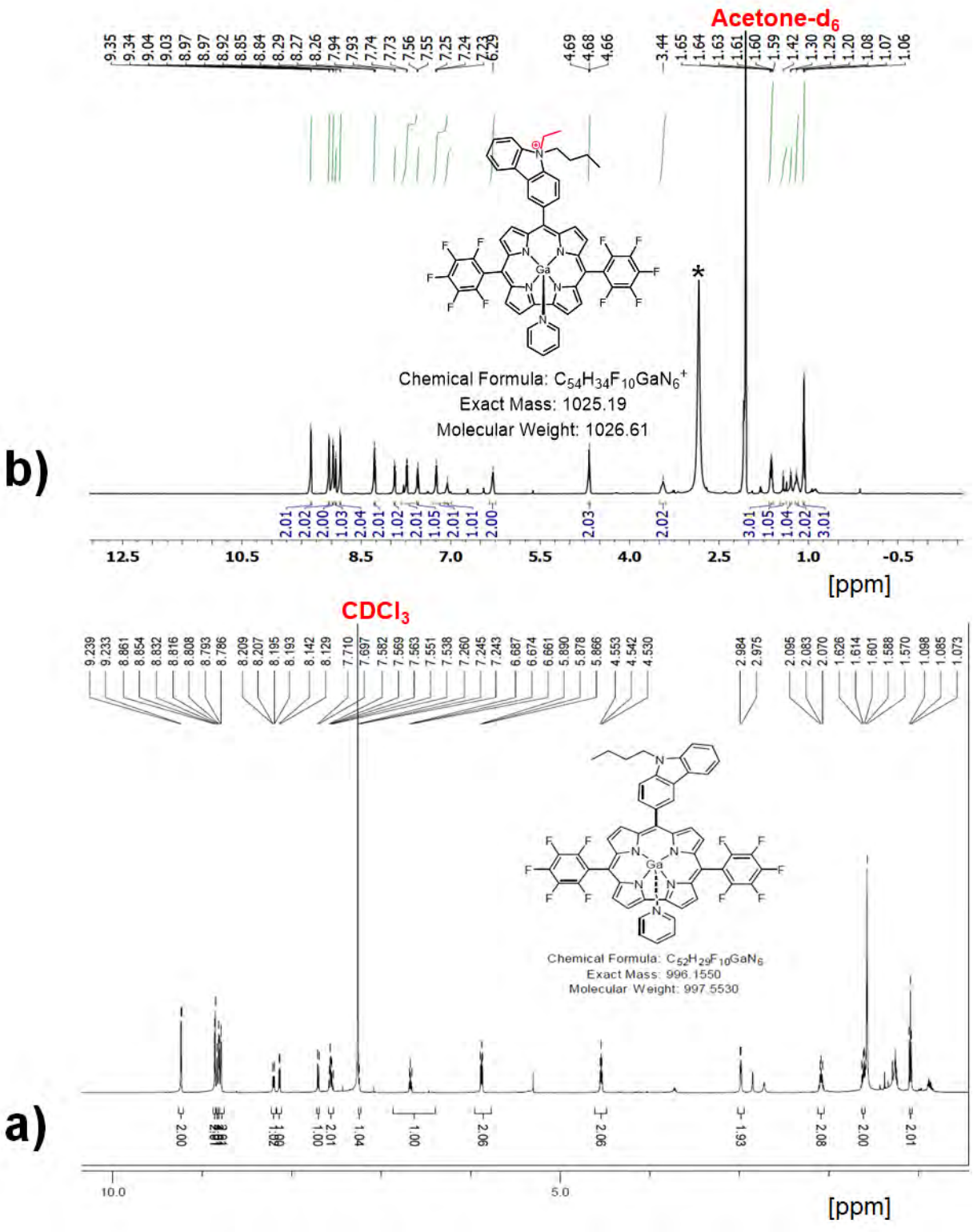

Figure A 22: ^{1}H NMR spectra for a) **10**-GaCor and b) **10**-GaCor-Q and black* asterisk highlight the residual water peak.

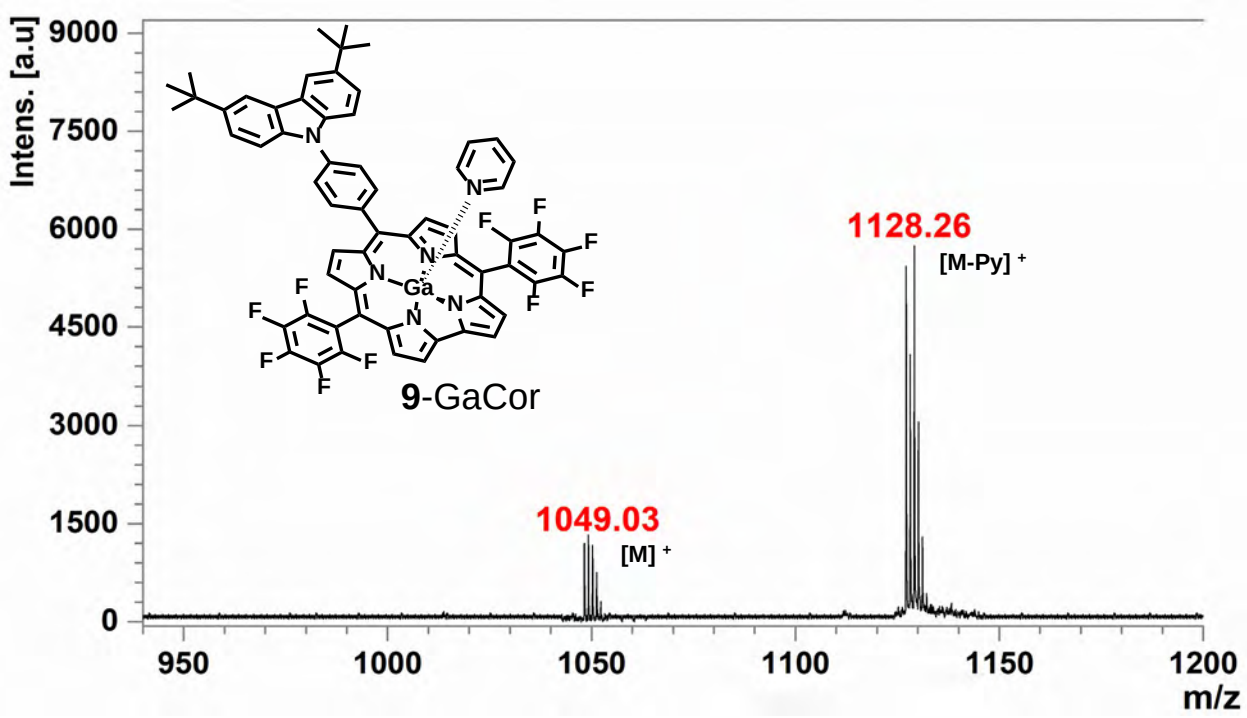

Figure A 23: MALDI-TOF MS data for **9**-GaCor using α-cyano-4-hydroxycinnamic acid as the matrix.

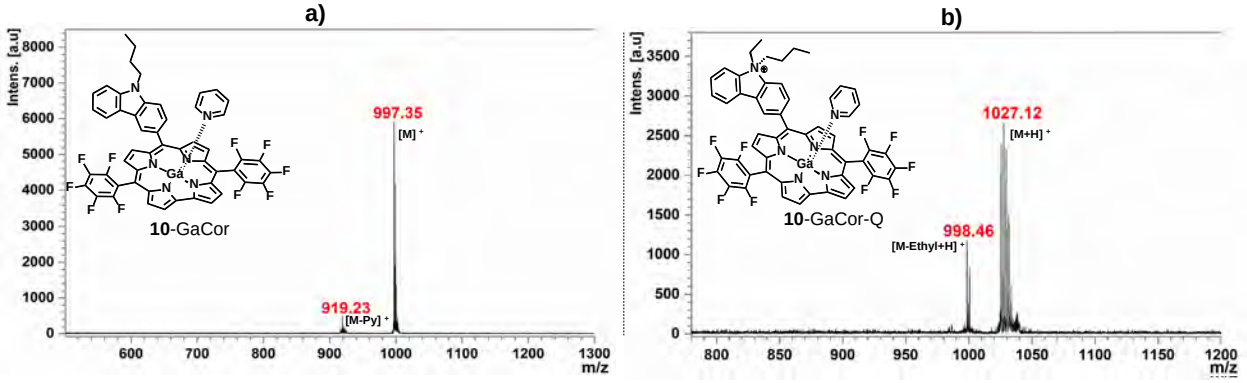

Figure A 24: MALDI-TOF MS data for a) **10**-GaCor and b) **10**-GaCor-Q using α-cyano-4-hydroxycinnamic acid as the matrix.

12.1.3 Structural characterization data for chlorin dyes

12.1.3.1 ^{1}H NMR spectra for chlorin dyes.

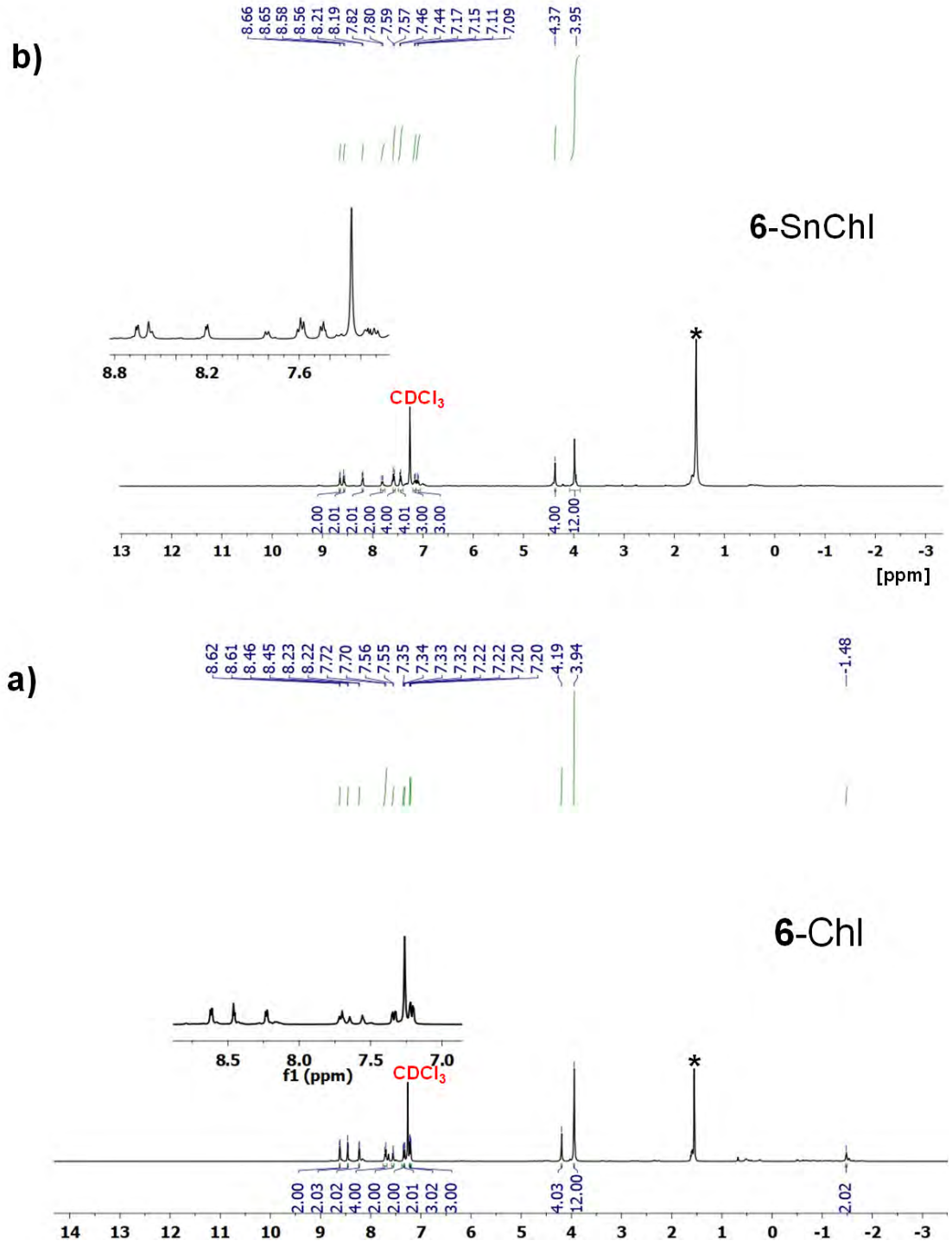

Figure A 25: ^{1}H NMR spectra for a) **6**-Chl and b) **6**-SnChl and black* asterisk highlight the residual water peak.

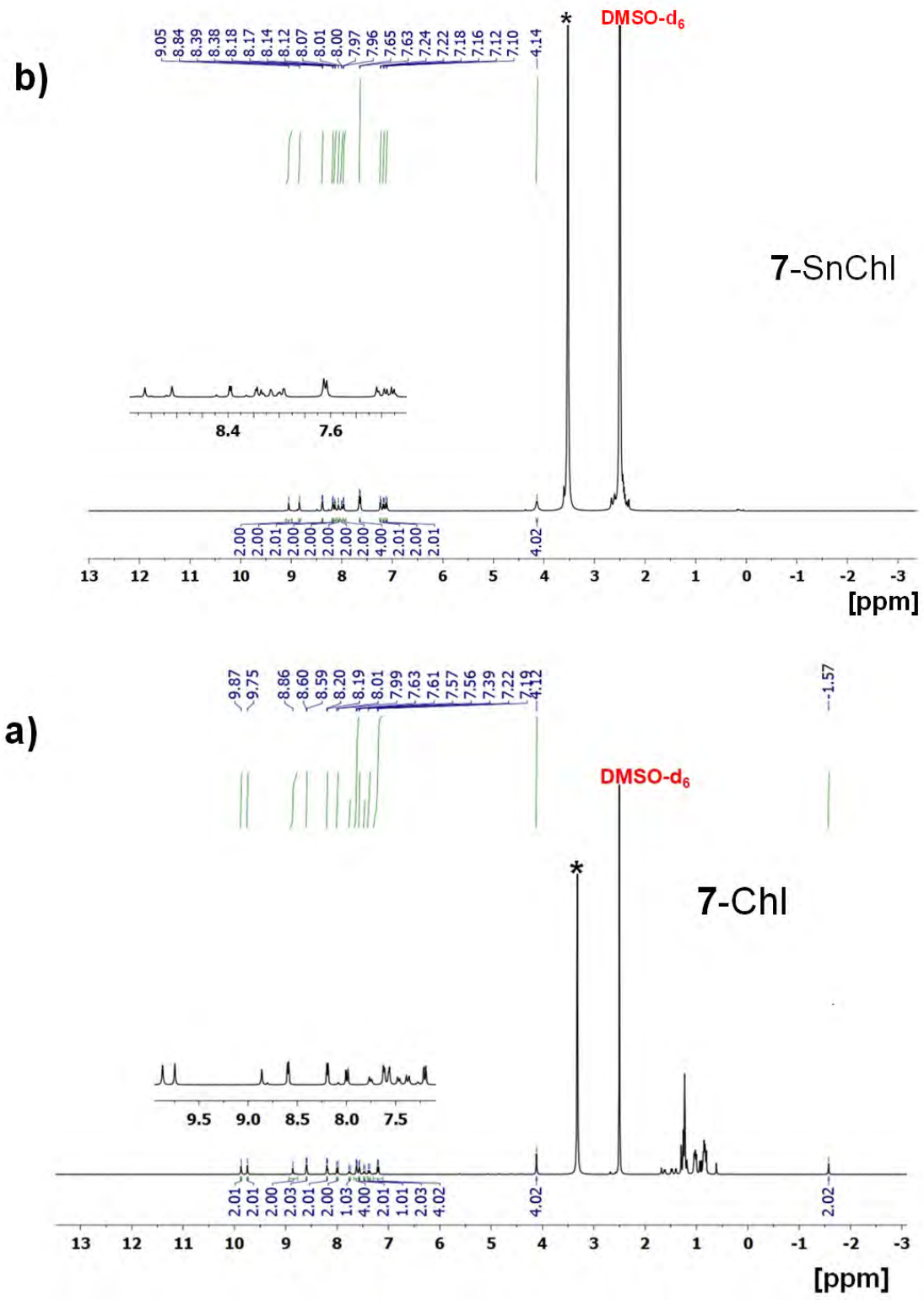

Figure A 26: ^{1}H NMR spectra for a) **7**-Chl and b) **7**-SnChl and black* asterisk highlight the residual water peak.

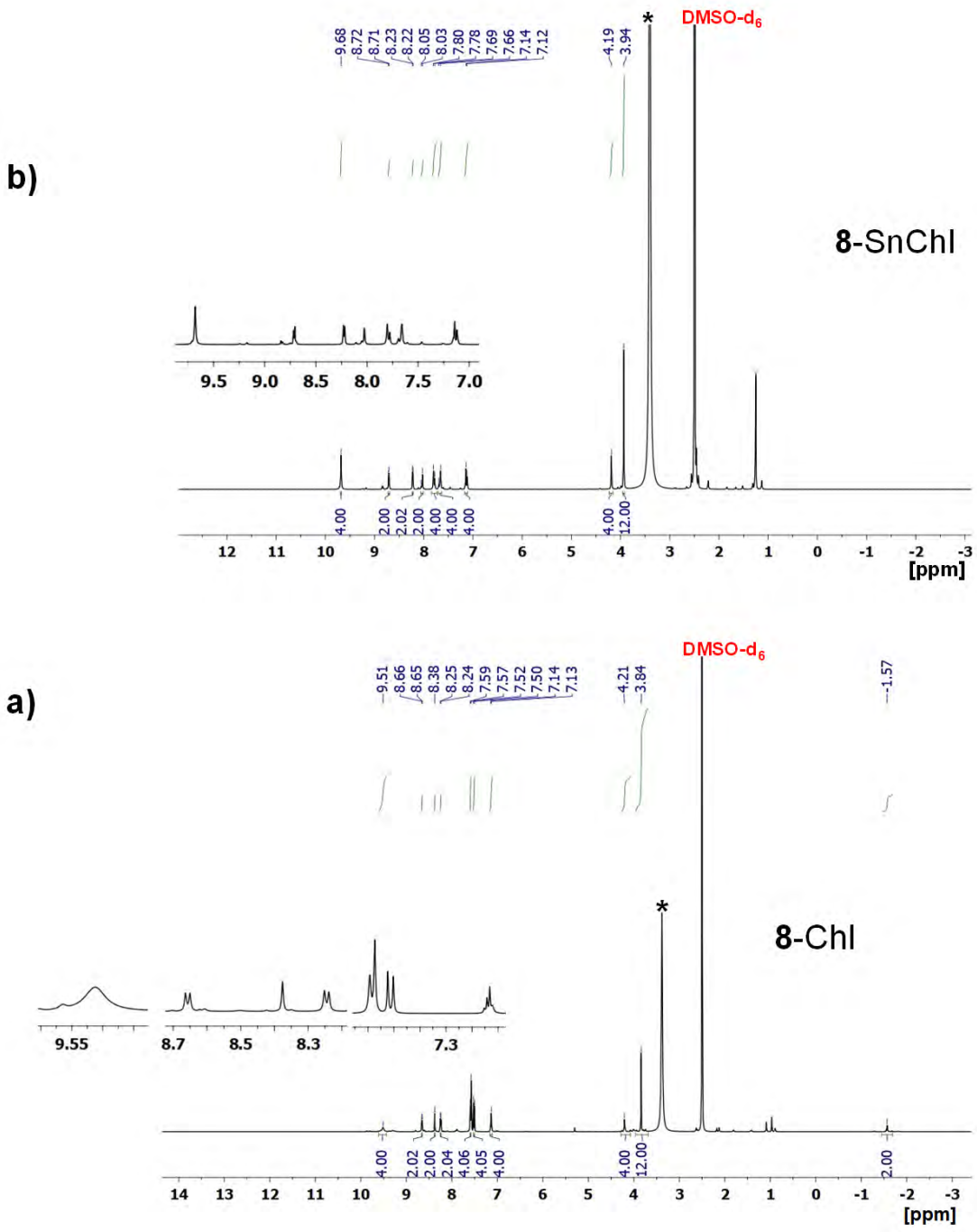

Figure A 27: ^{1}H NMR spectra for a) **8**-Chl and b) **8**-SnChl and black* asterisk highlight the residual water peak.

12.1.3.2 Mass spectra for chlorin dyes

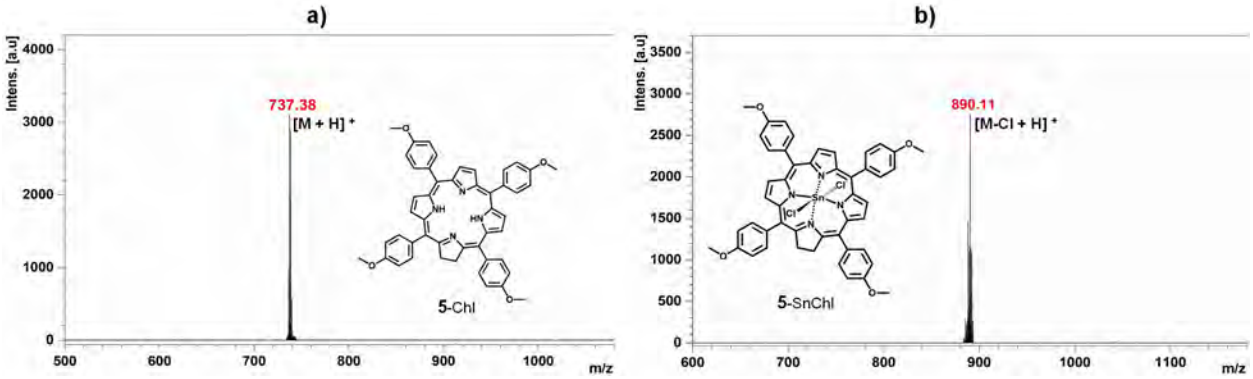

Figure A 28: MALDI-TOF MS data for a) **5**-Chl and b) **5**-SnChl.

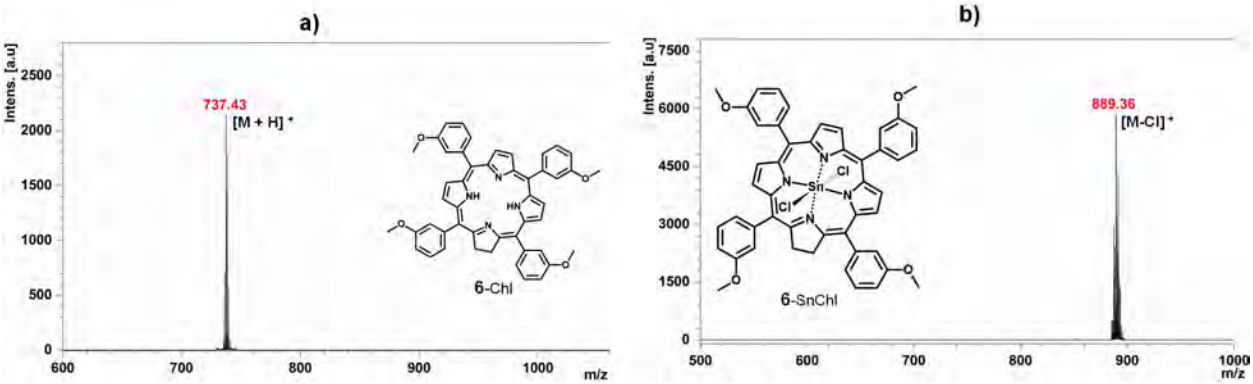

Figure A 29: MALDI-TOF MS data for a) **6**-Chl and b) **6**-SnChl.

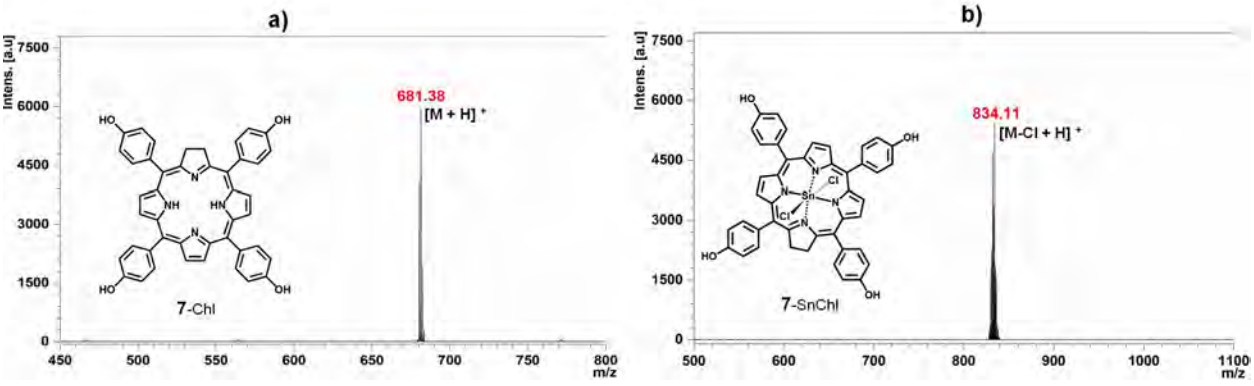

Figure A 30: MALDI-TOF MS data for a) **7**-Chl and b) **7**-SnChl.

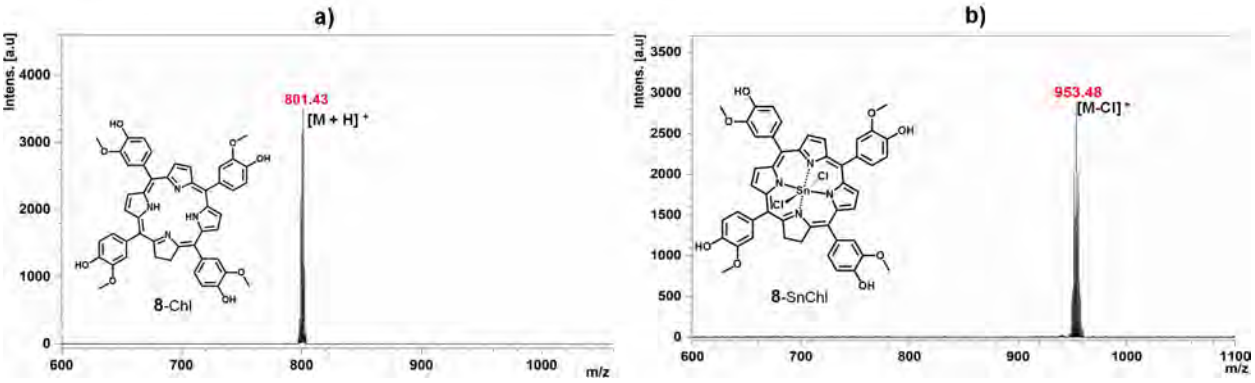

Figure A 31: MALDI-TOF MS data for a) **8**-Chl and b) **8**-SnChl.

12.1.4 Structural characterization data for N -confused porphyrin dyes

12.1.4.1 Mass spectra for N-confused porphyrin dyes

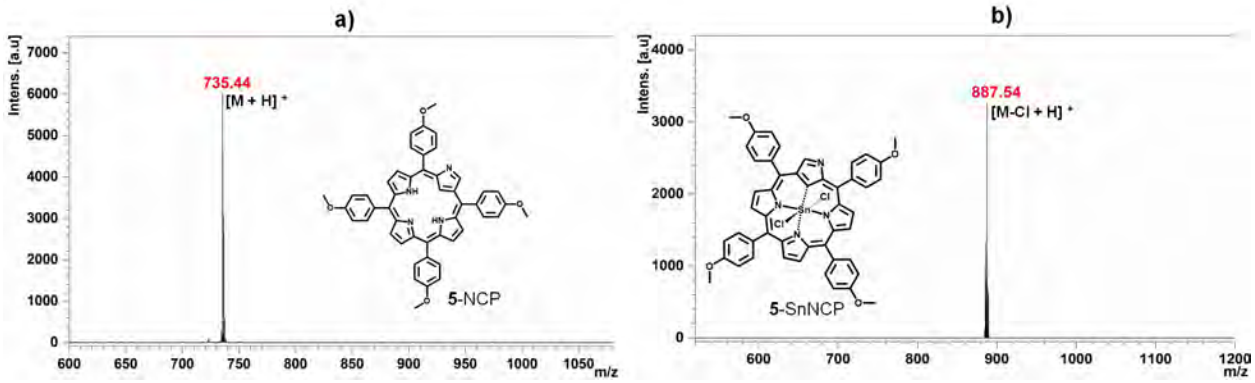

Figure A 29: MALDI-TOF MS data for a) **5**-NCP and b) **5**-SnNCP.

12.1.5 Characterization of gold and silver nanoparticles and nanoconjugates

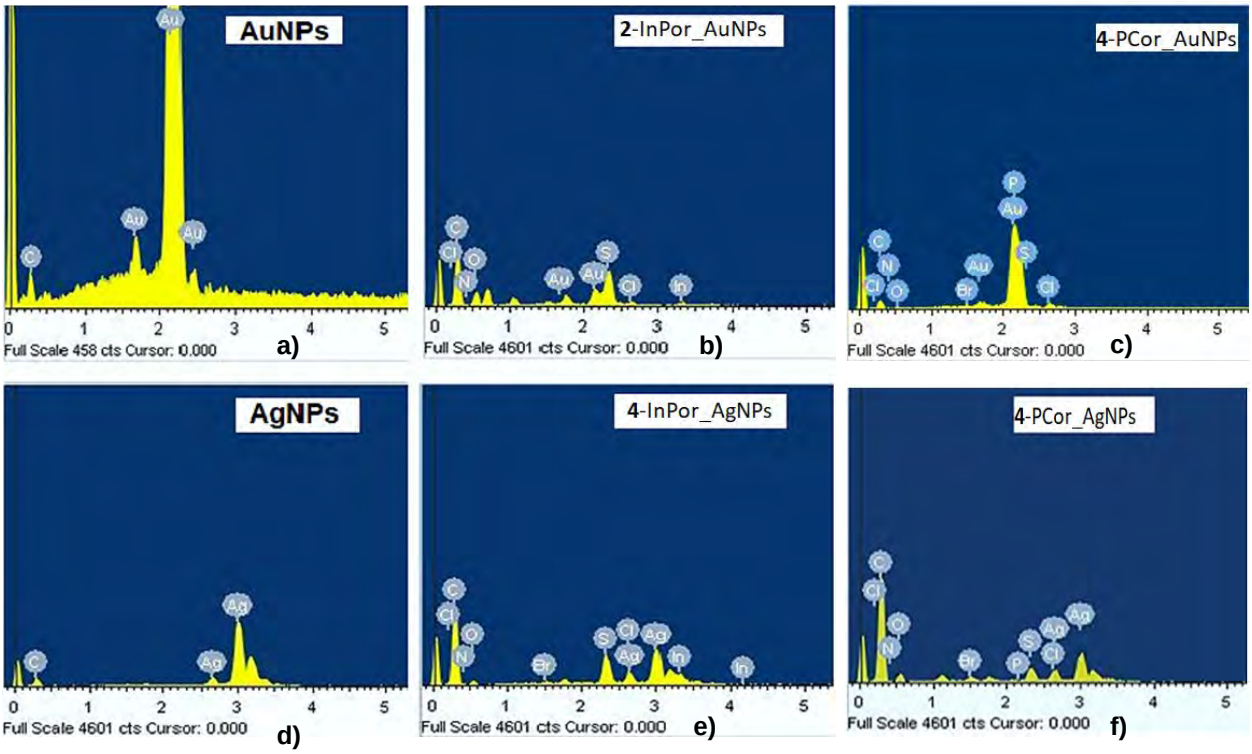

Figure A 32: Representative EDX spectra of a) AuNPs, b) **2**-InPor-AuNPs, c) **4**-P^{V}Cor-AuNPs, d) AgNPs, e) **4**-InPor-AgNPs and **4**-P^{V}Cor-AgNPs.

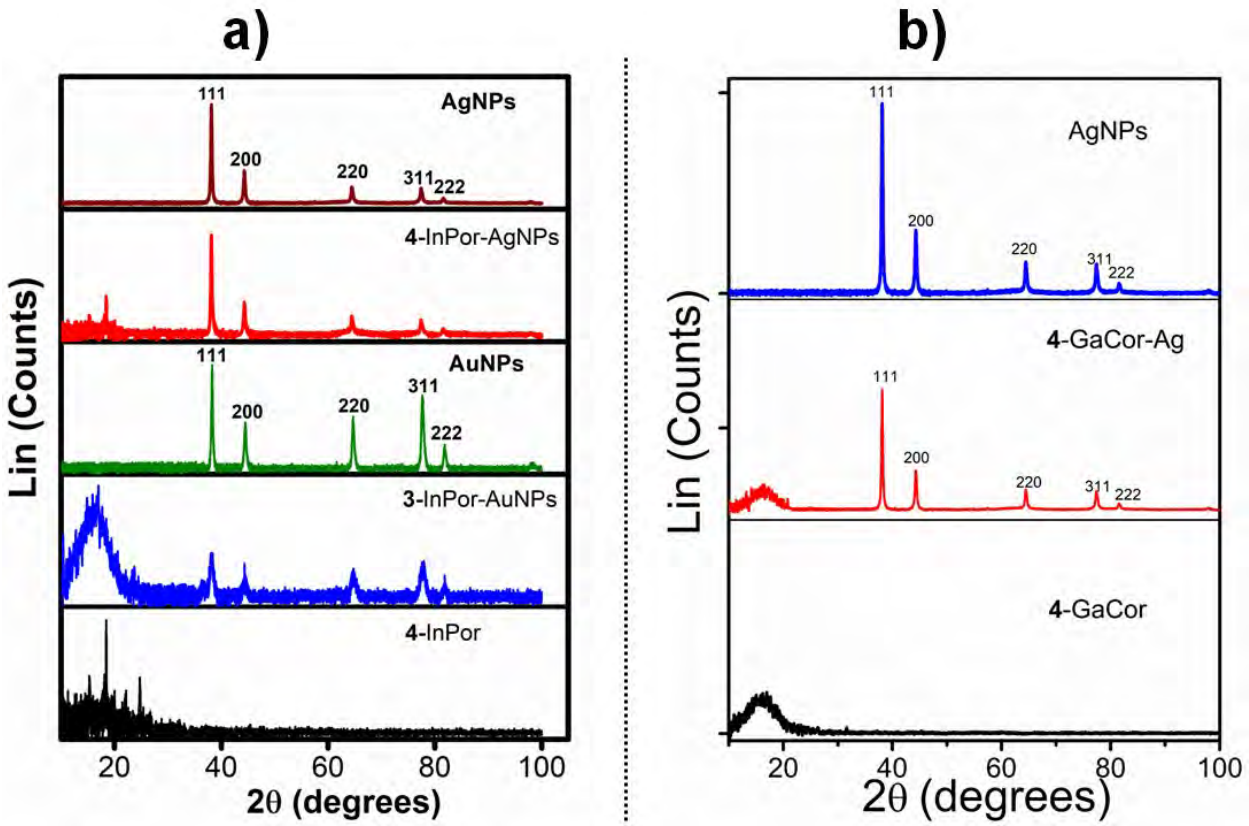

Figure A 33: Representative X-ray diffractograms of a) AgNPs, **4**-InPor-AgNPs, AuNPs, **3**-InPor-AuNPs, and **4**-InPor b) AgNPs, **4**-GaCor, and **4**-GaCor-AgNPs.

12.2 Data for Chapter Four

The extra data obtained during the optical spectroscopic analysis of the synthesized porphyrin and porphyrin analog dyes and those of the nanoconjugates are provided in this section.

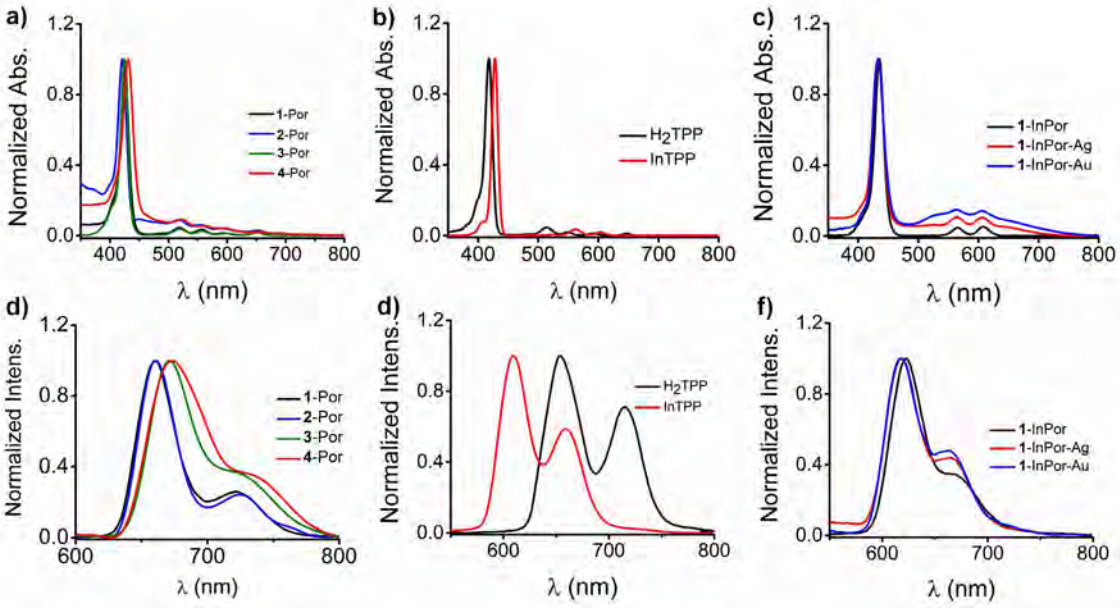

Figure A 34: UV-visible absorption spectra of (a) **1**-Por (black), **2**-Por (blue), **3**-Por (green), and **4**-Por (red); (b) H_2TPP (black), InTPP (red), and (c) **1**-InPor (black), **1**-InPor-Ag (red), **1**-InPor -Au (blue) in DMSO. Fluorescence spectra of the porphyrin dyes and nanoconjugates are provided at the bottom (d-f) with the same line types as in the absorption spectra.

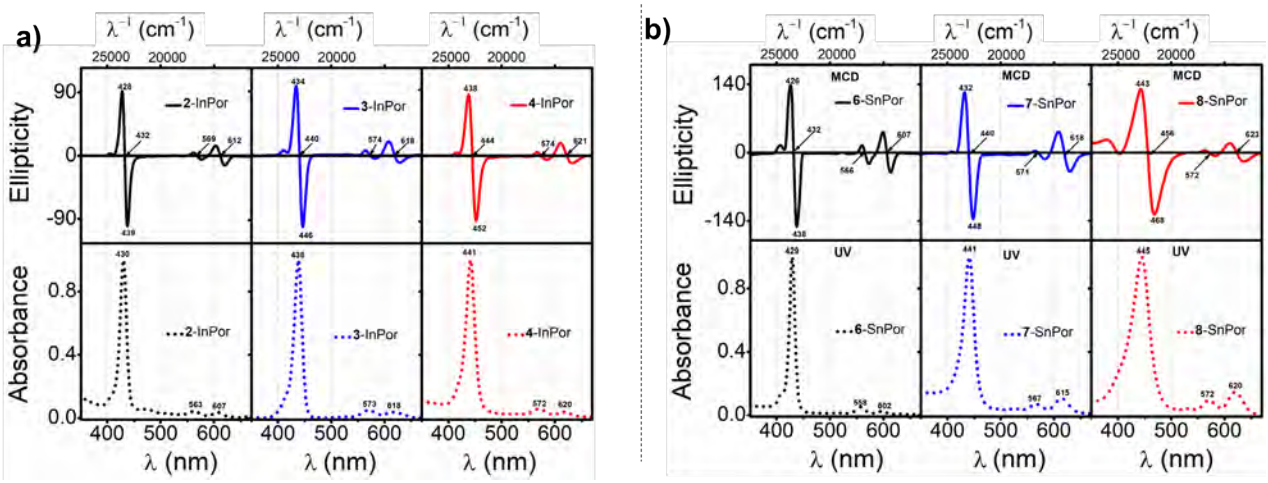

Figure A 35: MCD spectra (top) and absorption spectra (bottom) of a) **2**-InPor (black), **3**-InPor (blue), and **4**-InPor (red); b) **6**-snPor (black), **7**-SnPor (blue) and **8**-SnPor (red) in DMSO.

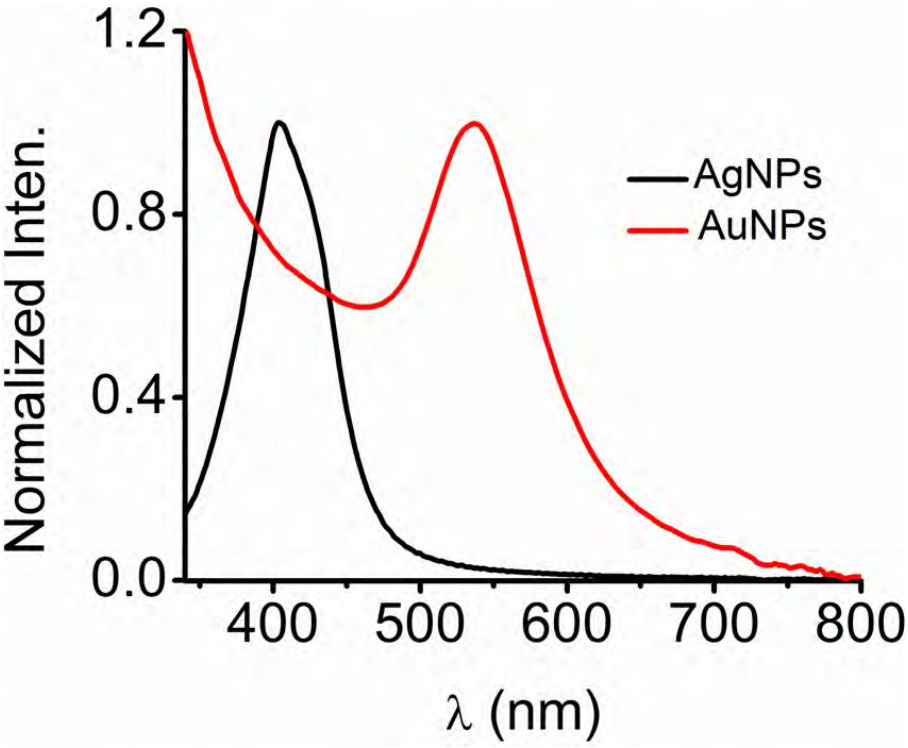

Figure A 36: Surface plasmon resonance (SPR) of AgNPs and AuNPs in $CHCl_3$.

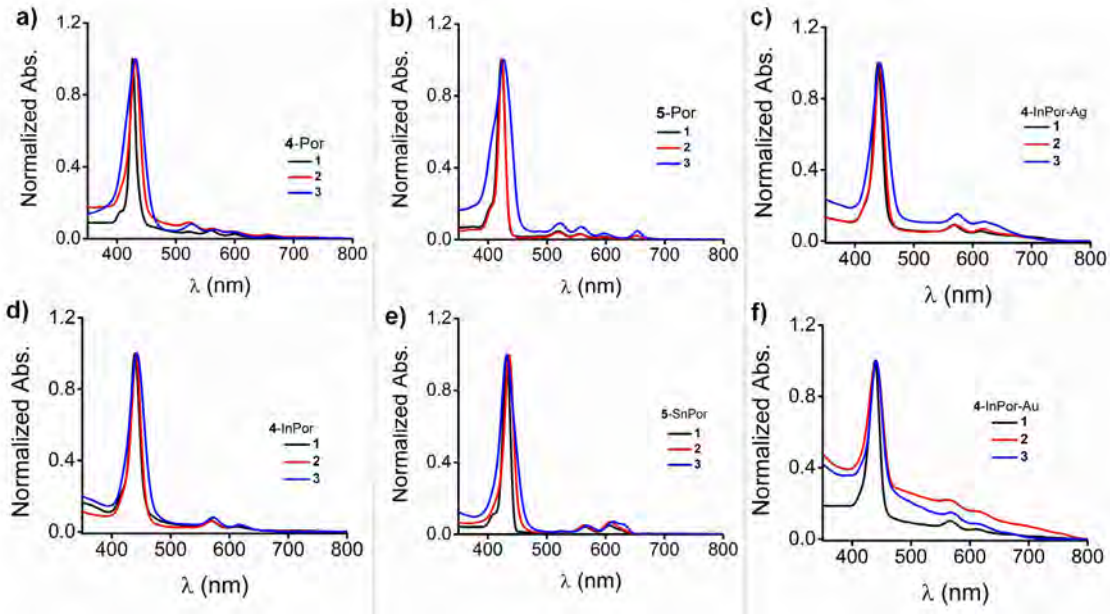

Figure A 37: UV-visible absorption spectra of (a) **4**-Por, (b) **5**-Por, (c) **4**-InPor-Ag, (d) **4**-InPor, (e) **5**-SnPor, and (f) **4**-InPor-Au in $CHCl_3$ (**1** black), DMSO (**2** red), and in 1% DMSO-water (**3** blue).

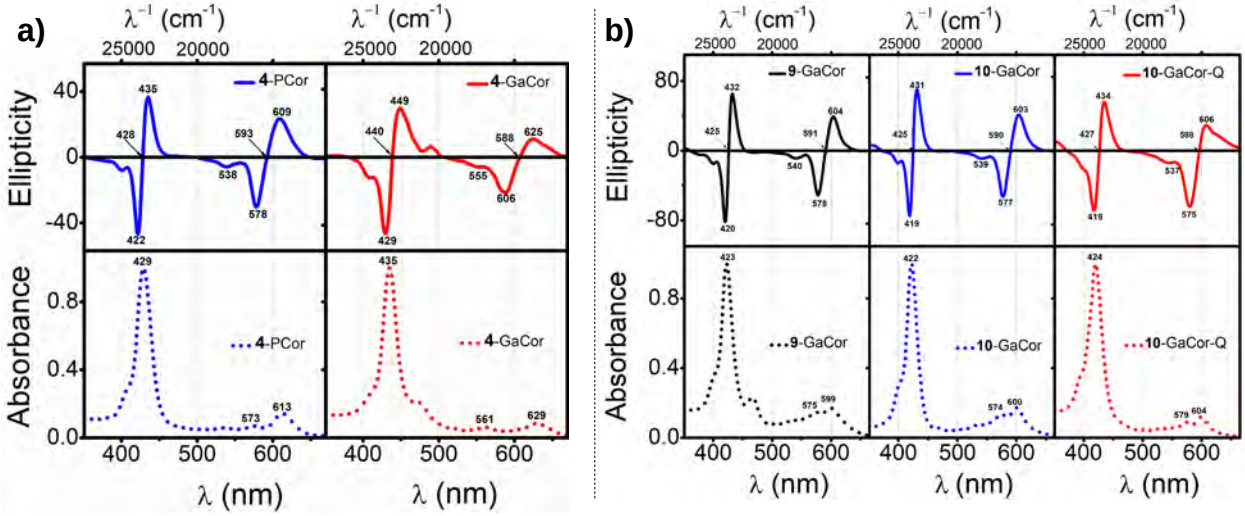

Figure A 38: MCD spectra (top) and absorption spectra (bottom) of a) **4**-P^{V}Cor, **4**-GaCor, and b) **9**-**10**-GaCor and **10**-GaCor-Q in DMSO.

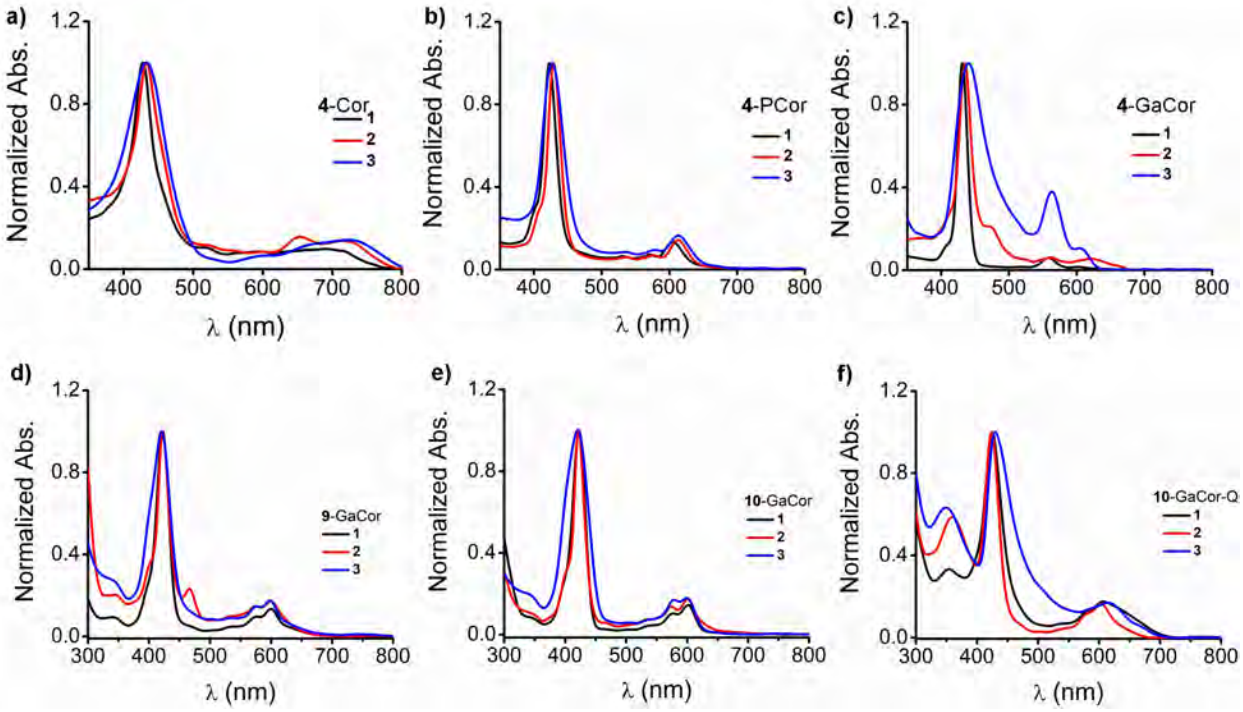

Figure A 39: UV-visible absorption spectra of (a) **4**-Cor, (b) **4**-P^{V}Cor, (c) **4**-GaCor, (d) **9**-GaCor, (e) **10**-GaCor, and (f) **10**-GaCor-Q in $CHCl_3$ (**1** black), DMSO (**2** red), and in 1% DMSO-water (**3** blue).

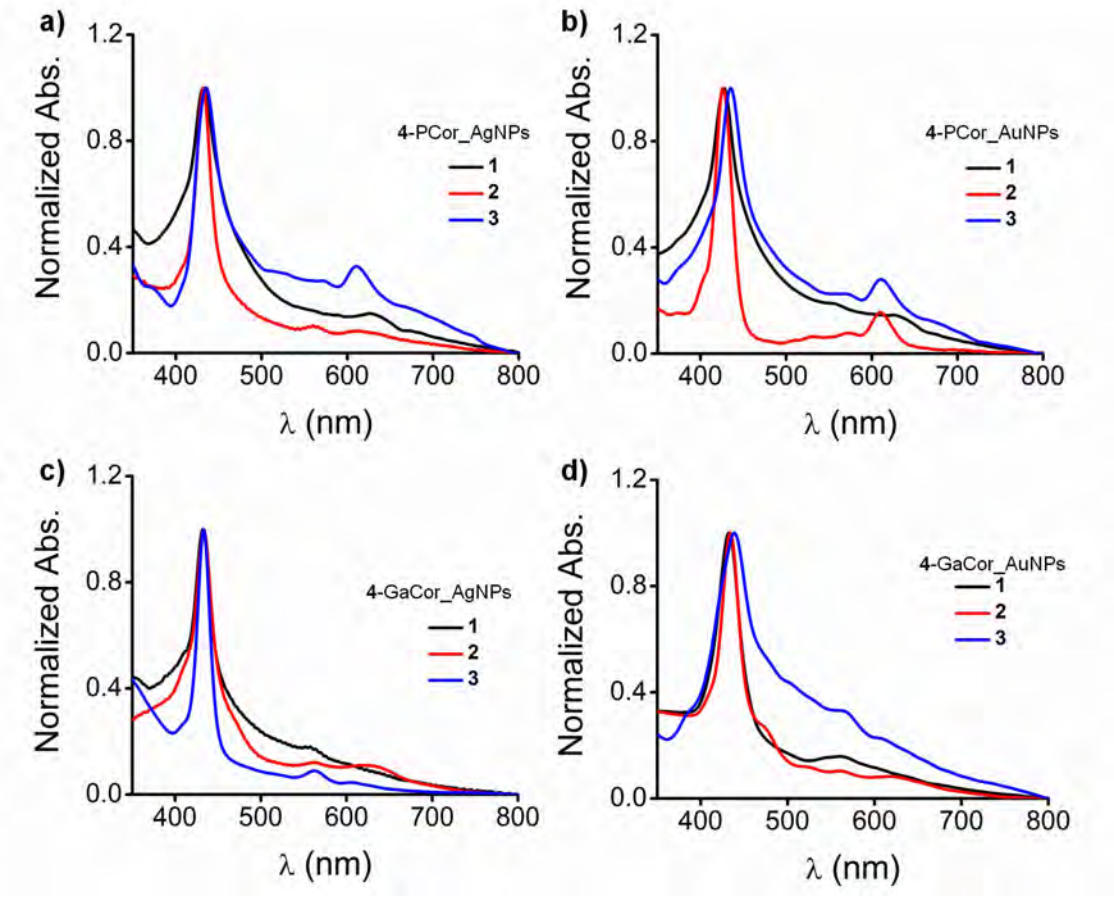

Figure A 40: UV-visible absorption spectra of (a) **4**-P^{V}Cor-AgNPs, (b) **4**-P^{V}Cor-AuNPs, (c) **4**-GaCor-AgNPs, and (d) **4**-GaCor-AuNPs, in $CHCl_3$ (**1** black), DMSO (**2** red), and 1% DMSO-water (**3** blue).

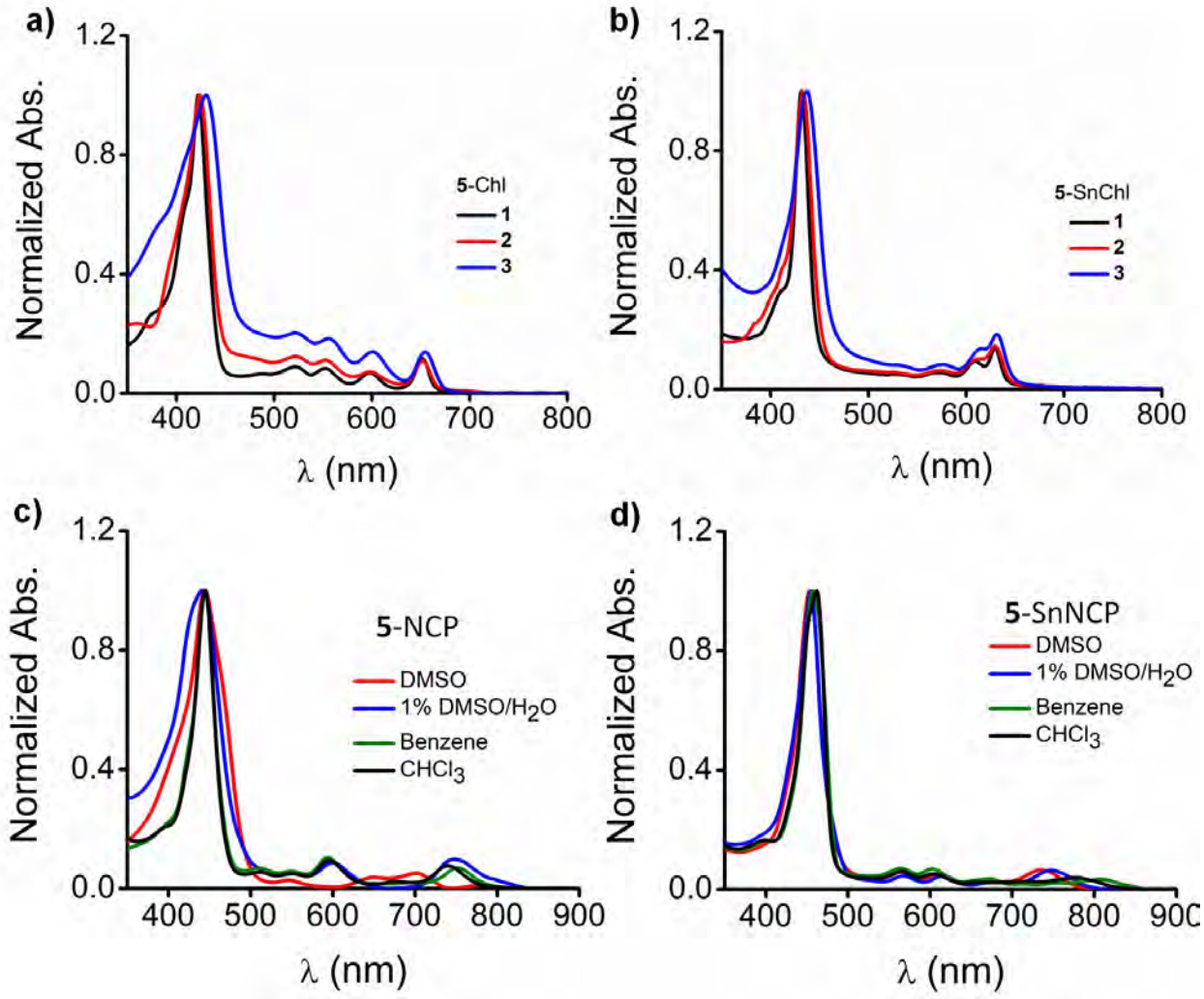

Figure A 41: UV-visible absorption spectra of (a) **5**-Chl, (b) **5**-SnChl, (c) **5**-NCP, and (d) **5**-SnNCP, in $CHCl_3$ (**1** black), DMSO (**2** red), 1% DMSO-water (**3** blue) and benzene (green).

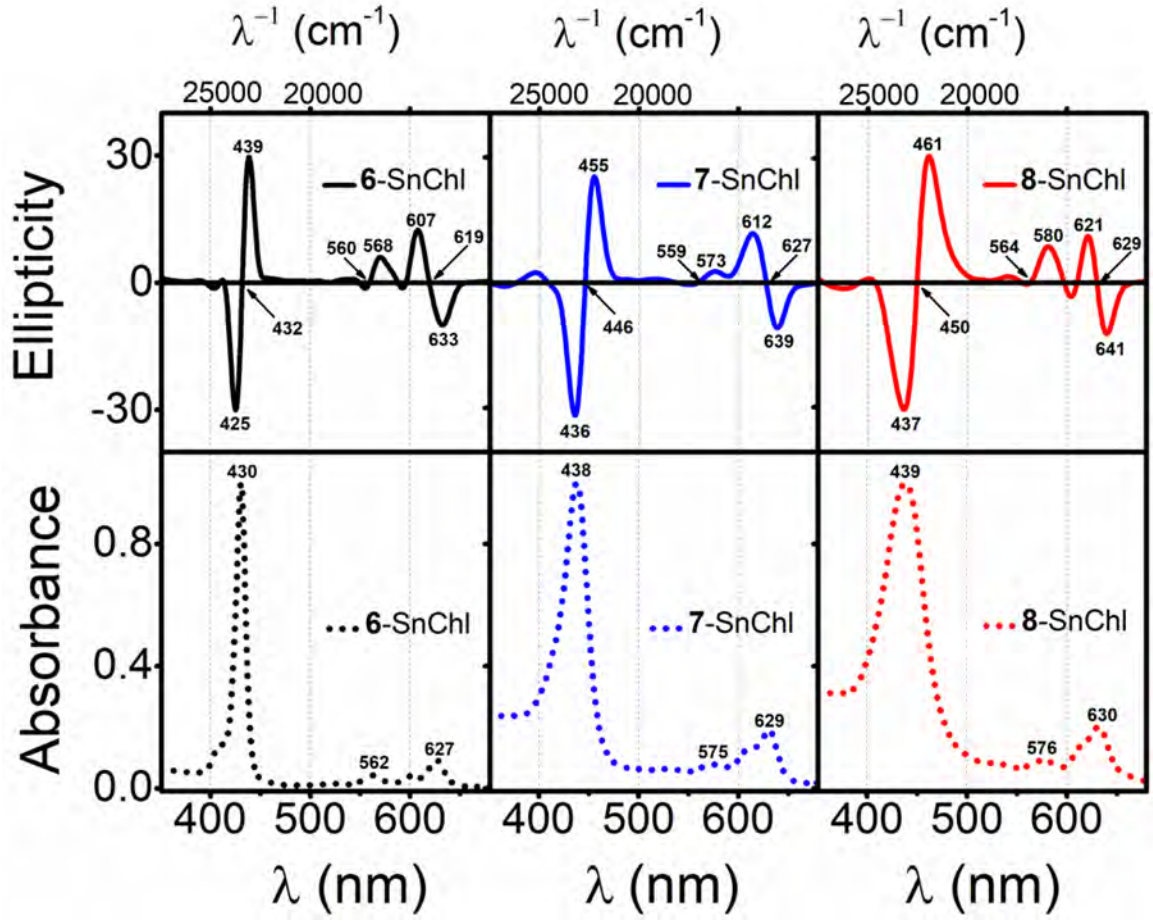

Figure A 42: MCD spectra (top) and absorption spectra (bottom) of **6**-SnChl (black), **7**-SnChl (blue), and **8**-SnChl (red) in DMSO.

Table A 1: Solvatochromic absorption data of porphyrin dyes in 1% DMSO/H_2O and $CHCl_3$.

Sample	**Solvent**	**λ_{Abs}** (nm)		
		B	Q_{01}	Q_{00}
H_2TPP	1% DMSO/H_2O	422	518, 551	592, 650
	$CHCl_3$	418	517, 550	590, 646
1-Por	1% DMSO/H_2O	426	522, 560	598, 657
	$CHCl_3$	423	520, 550	596, 650
2-Por	1% DMSO/H_2O	426	520, 560	600, 662
	$CHCl_3$	419	523, 555	599, 659
3-Por	1% DMSO/H_2O	426	522, 564	596, 660
	$CHCl_3$	425	521, 559	597, 660
4-Por	1% DMSO/H_2O	431	527, 569	600, 662
	$CHCl_3$	426	523, 560	599, 659
InTPP	1% DMSO/H_2O	423	560	600
	$CHCl_3$	422	559	598
1-InPor	1% DMSO/H_2O	433	570	612
	$CHCl_3$	430	562	603
2-InPor	1% DMSO/H_2O	429	556	609
	$CHCl_3$	427	562	604
3-InPor	1% DMSO/H_2O	438	570	616
	$CHCl_3$	435	567	607
4-InPor	1% DMSO/H_2O	442	573	618
	$CHCl_3$	438	567	612
1-**4**-InPor AuNPs and AgNPs nanoconjugates				
1-InPor-AgNPs	1% DMSO/H_2O	425	561	603
	$CHCl_3$	432	563	604
1-InPor-AuNPs	1% DMSO/H_2O	431	562	604
	$CHCl_3$	427	561	600
2-InPor-AgNPs	1% DMSO/H_2O	430	567	609
	$CHCl_3$	429	564	605
2-InPor-AuNPs	1% DMSO/H_2O	425	561	603
	$CHCl_3$	432	563	604
3-InPor-AgNPs	1% DMSO/H_2O	438	571	616
	$CHCl_3$	434	567	610
3-InPor-AuNPs	1% DMSO/H_2O	436	568	615
	$CHCl_3$	434	567	610
4-InPor-AgNPs	1% DMSO/H_2O	441	574	620
	$CHCl_3$	438	567	613
4-InPor-AuNPs	1% DMSO/H_2O	441	570	617
	$CHCl_3$	438	566	614
5-**8**-Por and their Sn(IV) complexes				

5-Por	1% DMSO/H_2O	426	523, 559	598, 654
	$CHCl_3$	422	519, 556	593, 650
6-Por	1% DMSO/H_2O	421	517, 552	591, 650
	$CHCl_3$	419	516, 551	589, 647
7-Por	1% DMSO/H_2O	426	525, 567	599, 660
	$CHCl_3$	422	519, 558	596, 650
8-Por	1% DMSO/H_2O	435	524, 562	597, 655
	$CHCl_3$	425	520, 560	595, 650
5-SnPor	1% DMSO/H_2O	432	569	614
	$CHCl_3$	431	565	608
6-SnPor	1% DMSO/H_2O	427	562	604
	$CHCl_3$	425	558	597
7-SnPor	1% DMSO/H_2O	439	570	616
	$CHCl_3$	435	567	610
8-SnPor	1% DMSO/H_2O	442	576	624
	$CHCl_3$	439	565	611

Table A 2: Solvatochromic absorption data for A_3 and A_2B *meso*-triaryl corrole dyes in 1% DMSO/H_2O and $CHCl_3$.

A_3 *meso*-triaryl corroles				
Sample	**Solvent**	**λ_{Abs}** (nm)		
		B	Q_{01}	Q_{00}
H_3TPCor	1% DMSO/H_2O	432	587	649
	$CHCl_3$	427	585	643
1-Cor	1% DMSO/H_2O	422	583	638
	$CHCl_3$	421	577	634
2-Cor	1% DMSO/H_2O	421	590	649
	$CHCl_3$	420	586	643
3-Cor	1% DMSO/H_2O	423	601	660
	$CHCl_3$	422	588	652
4-Cor	1% DMSO/H_2O	433	671	726
	$CHCl_3$	427	643	711
P^{V}TPCor	1% DMSO/H_2O	421	575	610
	$CHCl_3$	420	568	605
Ga^{III}TPCor	1% DMSO/H_2O	431	562	624
	$CHCl_3$	429	558	616
1-P^{V}Cor	1% DMSO/H_2O	417	569	608
	$CHCl_3$	415	566	603
2-P^{V}Cor	1% DMSO/H_2O	422	570	608
	$CHCl_3$	419	562	604
3-P^{V}Cor	1% DMSO/H_2O	424	573	609
	$CHCl_3$	422	571	610
4-P^{V}Cor	1% DMSO/H_2O	425	563	628
	$CHCl_3$	423	552	625
1-GaCor	1% DMSO/H_2O	433	578	621
	$CHCl_3$	426	576	615
2-GaCor	1% DMSO/H_2O	432	578	623
	$CHCl_3$	425	576	612
3-GaCor	1% DMSO/H_2O	428	563	610
	$CHCl_3$	423	558	603
4-GaCor	1% DMSO/H_2O	440	563	617
	$CHCl_3$	431	559	609

1-P^{V}Cor-AgNPs	1% DMSO/H_2O	416	567	603
	$CHCl_3$	412	565	600
1-P^{V}Cor-AuNPs	1% DMSO/H_2O	416	565	600
	$CHCl_3$	415	564	598
2-P^{V}Cor-AgNPs	1% DMSO/H_2O	434	569	614
	$CHCl_3$	423	566	606
2-P^{V}Cor-AuNPs	1% DMSO/H_2O	427	573	609
	$CHCl_3$	423	571	606
3-P^{V}Cor-AgNPs	1% DMSO/H_2O	426	579	613
	$CHCl_3$	421	547	608
3-P^{V}Cor-AuNPs	1% DMSO/H_2O	434	586	628
	$CHCl_3$	420	580	617
4-P^{V}Cor-AgNPs	1% DMSO/H_2O	435	572	626
	$CHCl_3$	430	565	610
4-P^{V}Cor-AuNPs	1% DMSO/H_2O	435	573	613
	$CHCl_3$	433	556	611
1-GaCor-AgNPs	1% DMSO/H_2O	428	582	624
	$CHCl_3$	407	577	623
1-GaCor-AuNPs	1% DMSO/H_2O	432	597	623
	$CHCl_3$	417	578	645
2-GaCor-AgNPs	1% DMSO/H_2O	432	565	622
	$CHCl_3$	429	558	612
2-GaCor-AuNPs	1% DMSO/H_2O	431	562	608
	$CHCl_3$	423	554	597
3-GaCor-AgNPs	1% DMSO/H_2O	433	556	628
	$CHCl_3$	430	552	625
3-GaCor-AuNPs	1% DMSO/H_2O	432	560	628
	$CHCl_3$	429	558	609
4-GaCor-AgNPs	1% DMSO/H_2O	433	563	608
	$CHCl_3$	432	557	606
4-GaCor-AuNPs	1% DMSO/H_2O	439	566	616
	$CHCl_3$	433	561	614
A_2B *meso*-triaryl Ga(III) corroles				
9-GaCor	1% DMSO/H_2O	423	573	600
	$CHCl_3$	422	572	600
10-GaCor	1% DMSO/H_2O	421	576	601
	$CHCl_3$	423	575	600
10-GaCor_Q	1% DMSO/H_2O	429	586	614
	$CHCl_3$	424	582	608

Solvent dependence of the B band λ_{max} values of 9-GaCor and 10-GaCor-Q.

Table A 3: Solvent dependence of the B band λ_{max} values of **9**-GaCor and **10**-GaCor-Q.

Solvent	Acetone	Benzene	Toluene	DMSO	MeCN	DMF	CH_2Cl_2	THF	Hexane	MeOH
λ_{max}**G-1**	422	425	425	426	421	425	422	422	419	422
λ_{max}**G-2**	420	423	424	424	420	424	422	422	420	422

G-1 and **G-2** denote **9**-**10**-GaCor and **10**-GaCor-Q previously reported in [210].

Table A 4: Solvatochromic absorption data for **5**-**8**-Chl, and **5**-NCP and their Sn(IV) complexes in 1% DMSO/H_2O and $CHCl_3$.

Sample	Solvent	λ_{Abs} (nm)		
		B	Q_{01}	Q_{00}
5-Chl	1% DMSO/H_2O	430	521, 556	600, 654
	$CHCl_3$	422	521, 552	597, 652
6-Chl	1% DMSO/H_2O	423	518, 547	598, 653
	$CHCl_3$	420	516, 547	595, 650
7-Chl	1% DMSO/H_2O	427	526, 557	600, 653
	$CHCl_3$	420	520, 549	597, 650
8-Chl	1% DMSO/H_2O	431	522, 559	600, 655
	$CHCl_3$	422	516, 553	594, 650
5-SnChl	1% DMSO/H_2O	437	574	631
	$CHCl_3$	431	571	629
6-SnChl	1% DMSO/H_2O	427	560	627
	$CHCl_3$	423	558	626
7-SnChl	1% DMSO/H_2O	432	571	629
	$CHCl_3$	427	569	628
8-SnChl	1% DMSO/H_2O	436	568	630
	$CHCl_3$	432	567	629
5-NCP	1% DMSO/H_2O	441	556, 600	749
	$CHCl_3$	445	551, 595	670, 739
	Benzene	445	546, 593	675, 752
5-SnNCP	1% DMSO/H_2O	455	566, 616	669, 749
	$CHCl_3$	457	564, 604	665, 713, 777
	Benzene	461	563, 602	672, 753, 809

12.3 Data for Chapter Five

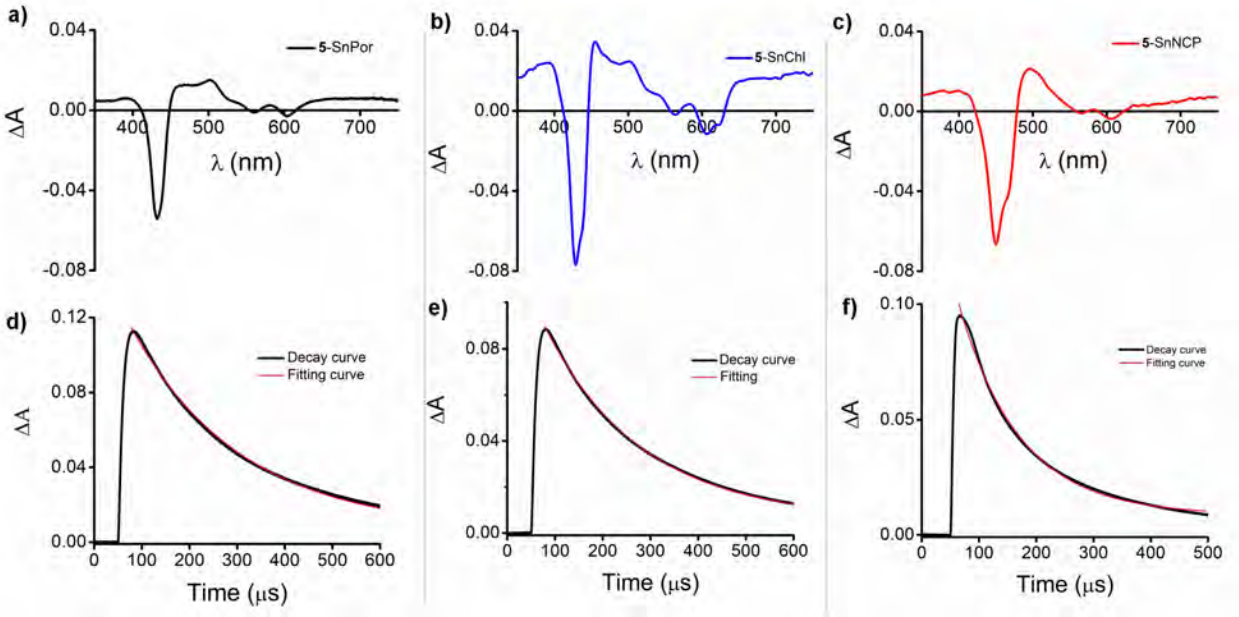

Figure A 43: Transient absorption spectra of **5**-SnPor (black), **5**-SnChl (blue), and **5**-SnNCP (red) and at the bottom (d-f) are the corresponding triplet decay curves in DMSO.

12.4 Data for Chapter Six

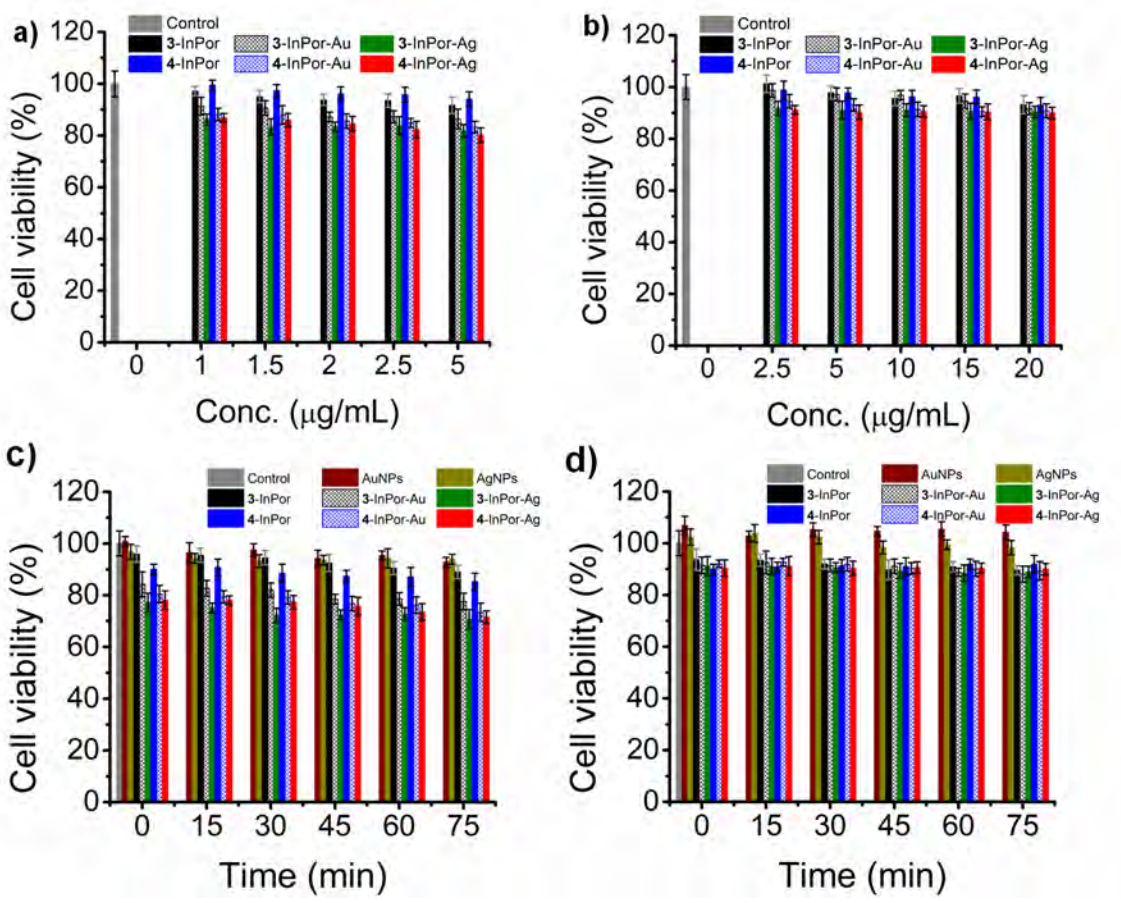

Figure A 44: Cell viability plots of planktonic cells of a, c) *S. aureus*, and b, d) *E. coli* in the dark upon treatment with gradient concentrations of **3**-InPor, **4**-InPor and their AgNP and AuNP nanoconjugates for 60 min; c-d) Cell viability plots upon treatment with c) 2.5 $\mu g.mL^{-1}$ and d) 10 $\mu g.mL^{-1}$ **3**-InPor, **4**-InPor, and their AgNP and AuNP nanoconjugates for 75 min.

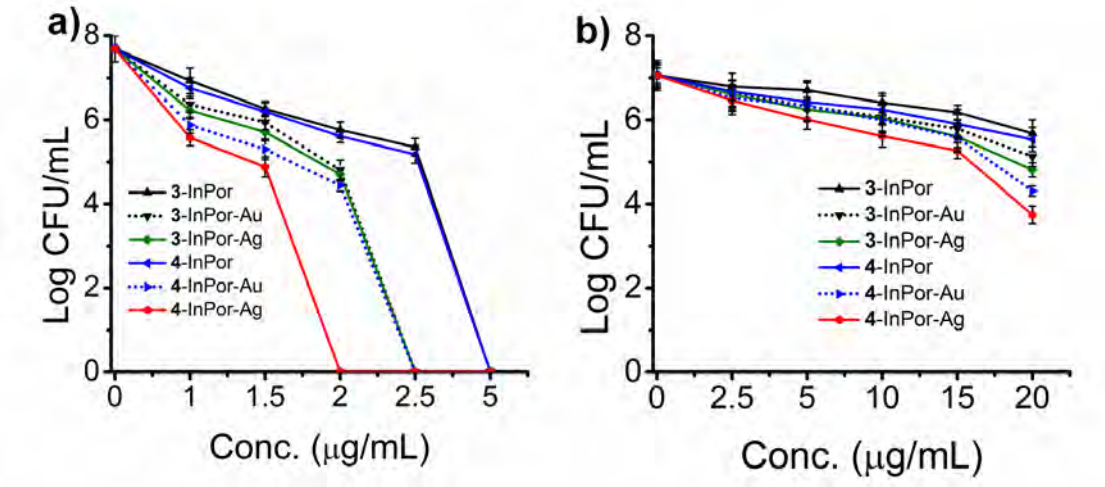

Figure A 45: The Log CFU.mL^{-1} plots of a) *S. aureus*, b) *E. coli* upon treatment with gradient concentrations of **3**-**4**-InPor In(III) porphyrin dyes and their AgNP (**3**-**4**-InPor-AgNPs) and AuNP (**3**-**4**-InPor-AgNPs) nanoconjugates after 60 min irradiation at 625 nm using a Thorlabs M625L3 LED.

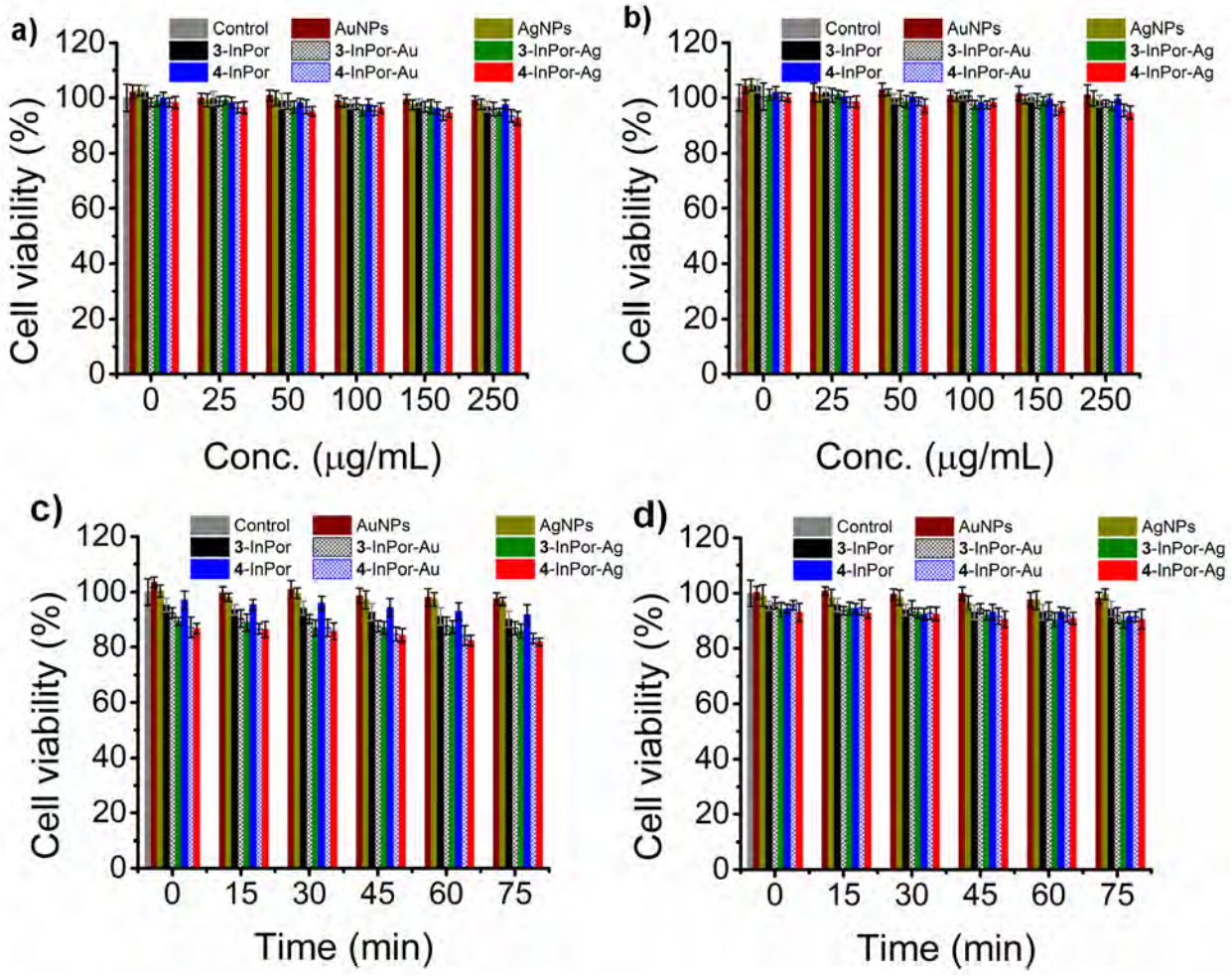

Figure A 46: Cell viability plots of biofilm cells of a, c) *S. aureus*, and b, d) *E. coli* in the dark upon treatment with gradient concentrations of **3**-InPor, **4**-InPor, and their AgNP and AuNP nanoconjugates for 30 min with cells quantification by crystal violet stain. c) upon treatment with 50 μg.mL^{-1} and d) 100 μg.mL^{-1} of the dyes for 75 min.

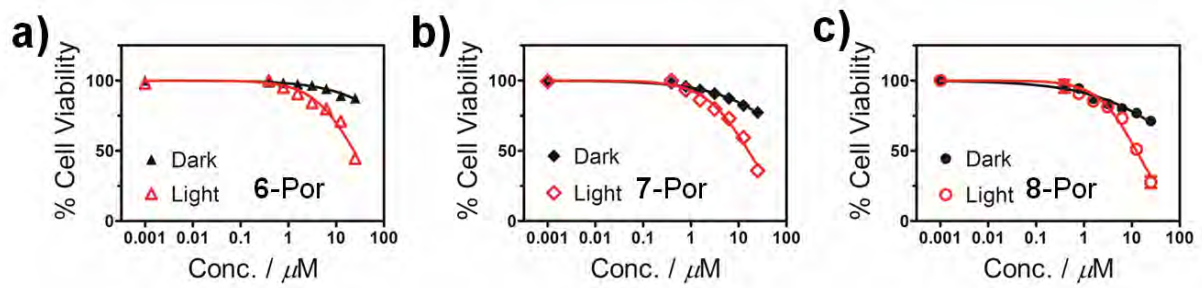

Figure A 47: Cytotoxicity plots of MCF-7 cancer cells in the dark (black line) and under illumination (red line) for 20 min with a Thorlabs M625L3 LED (240 mW.cm^{-2}) upon treatment with gradient concentrations of a) **6**-Por, b) **7**-Por and c) **8**-Por dyes.

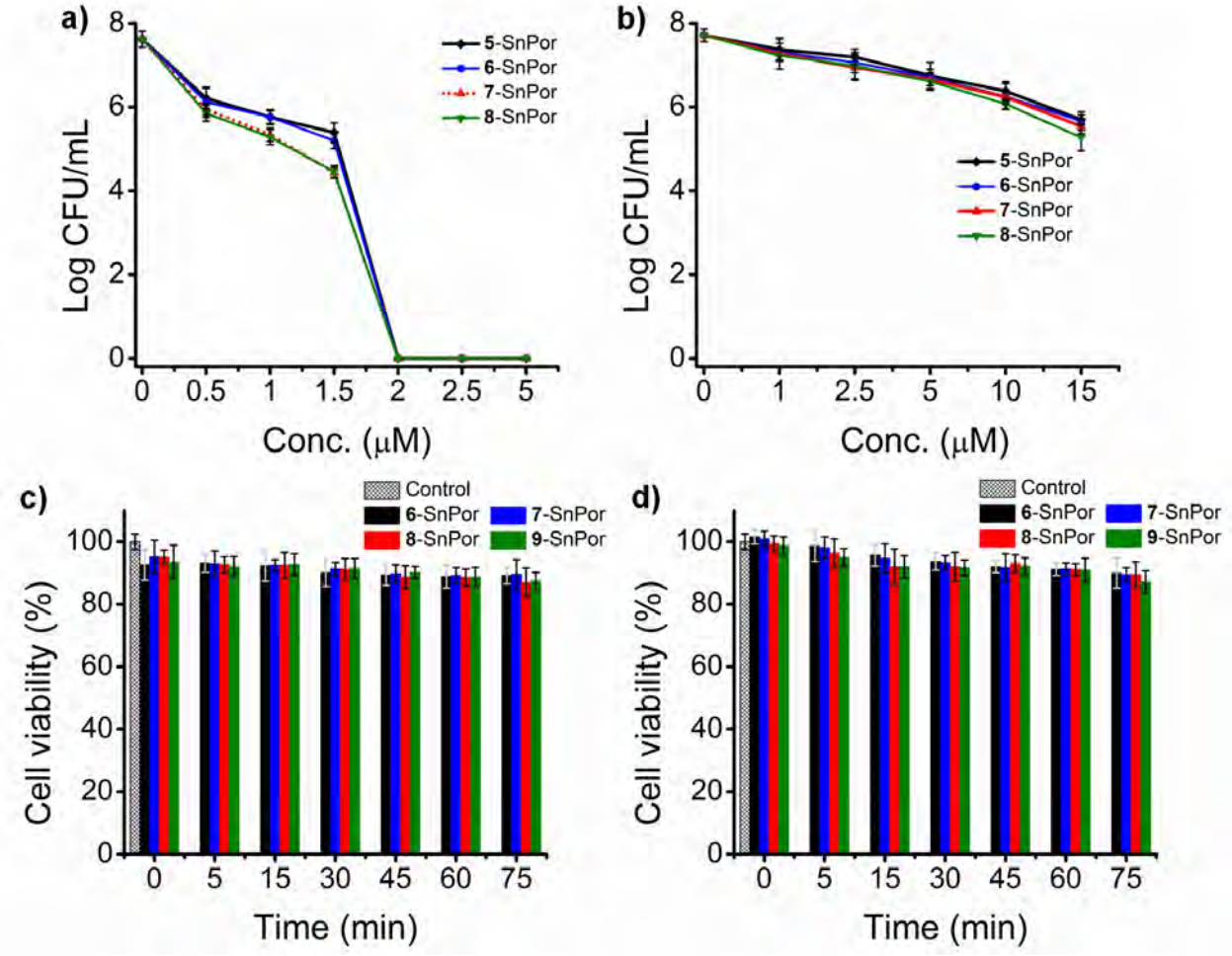

Figure A 48: Log CFU.mL^{-1} plots of a) *S. aureus* and b) *E. coli* upon treatment with gradient concentrations of **5**-**8**-SnPor dyes after 60 min irradiation at 625 nm using a Thorlabs

M625L3 LED (240 mW.cm^{-2}). c-d) Cell viability plots of planktonic cells in the dark of c) *S. aureus* and d) *E. coli* upon treatment with c) 1 µM and d) 5 µM **5**-**8**-SnPor for 75 min.

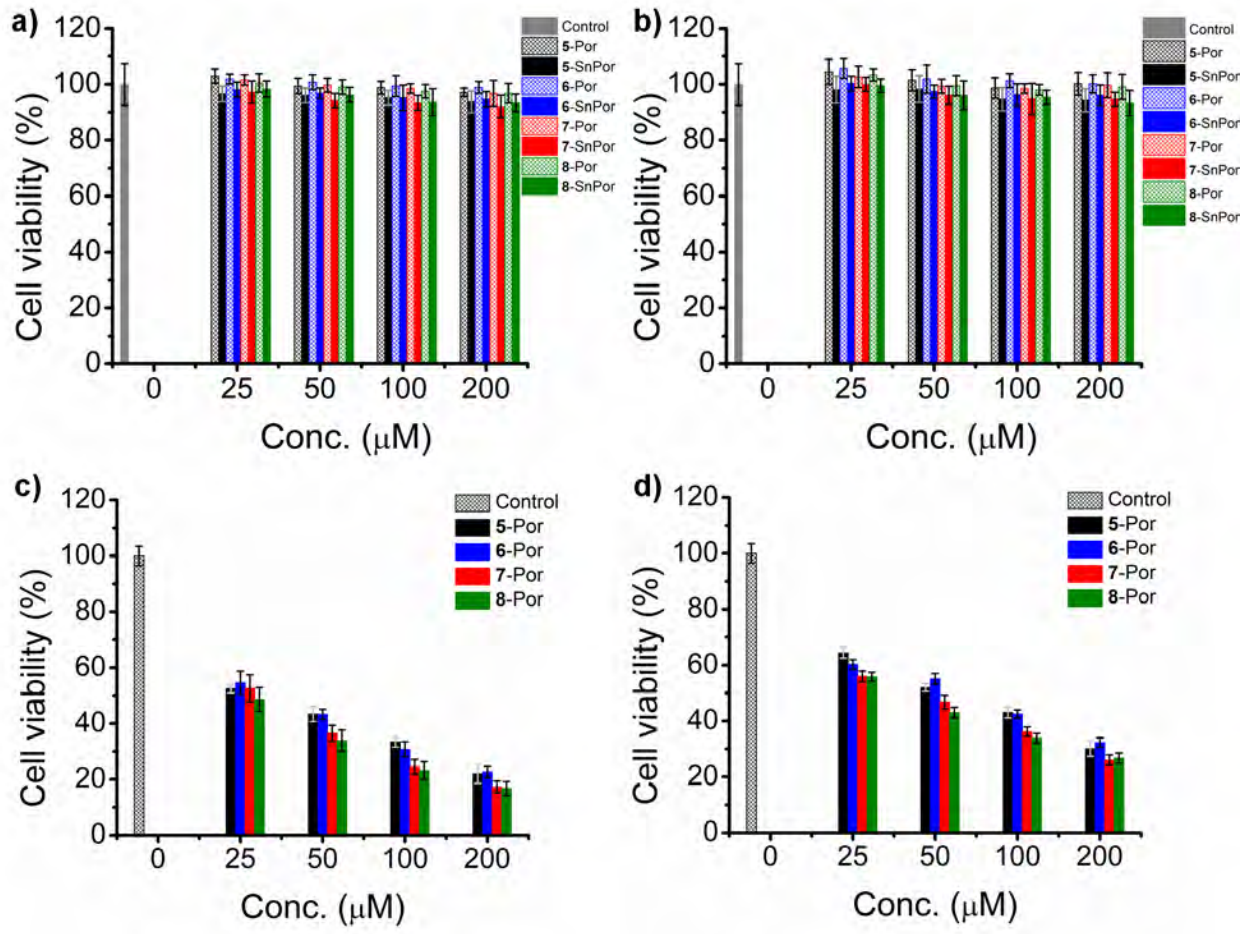

Figure A 49: Cell viability plots of biofilm cells of a, c) *S. aureus*, and b, d) *E. coli* a-b) in the dark and c-d) under illumination with a Thorlabs M625L3 LED (240 mW.cm^{-2}) for 30 min upon treatment with gradient concentrations of **5**-**8**-Por and their **5**-**8**-SnPor with cell quantification carried out with the Crystal violet assay.

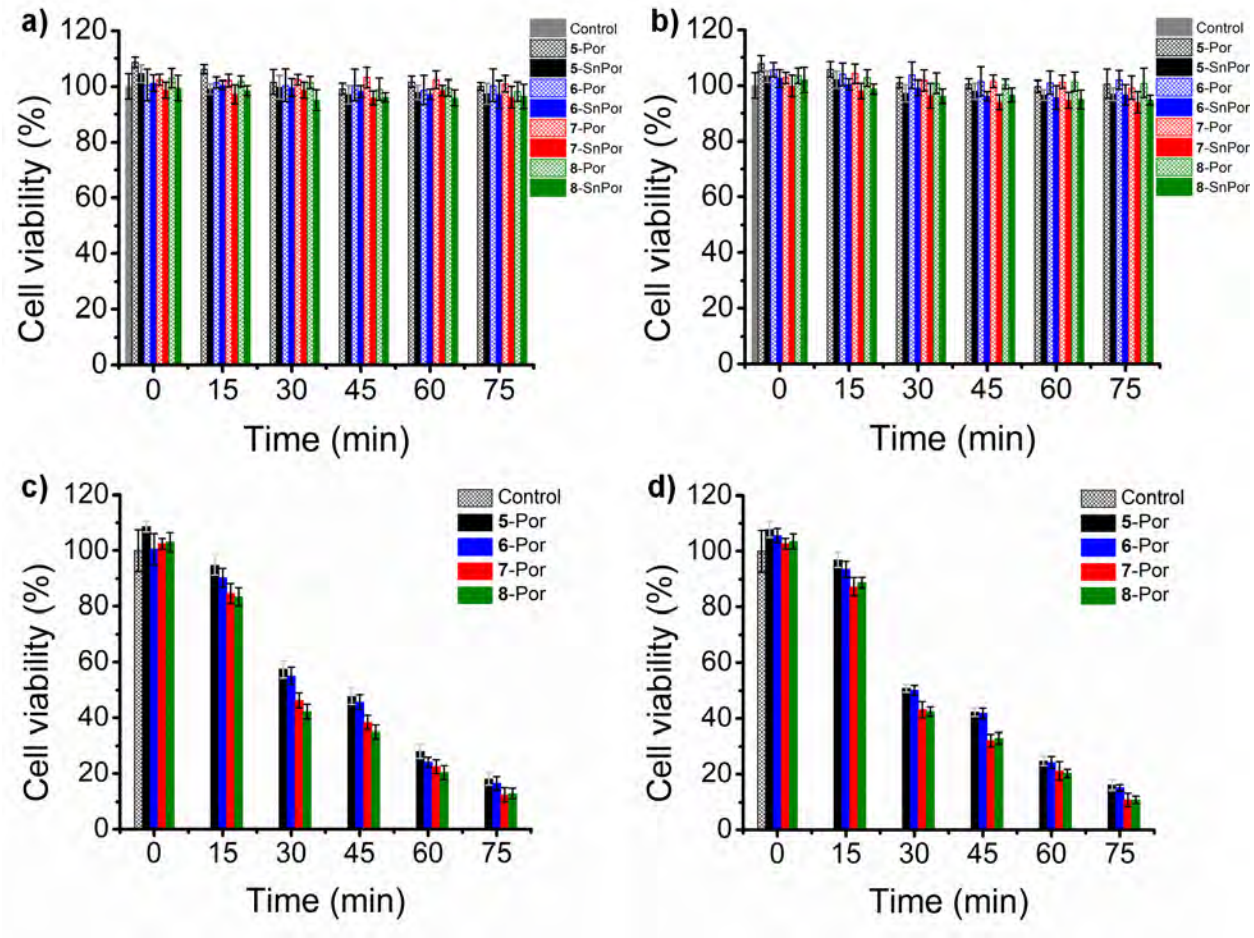

Figure A 50: Cell viability plots for biofilm cells of a, c) *S. aureus*, and b, c) *E. coli* upon treatment with a) 25 µM b) 50 µM of **5**-**8**-Por and **5**-**8**-SnPor dyes a-b) in the dark and c-d) after 75 min irradiations with a Thorlabs M625L3 LED. The viable colonies were estimated by using the viable cell count method.

12.5 Data for Chapter Seven

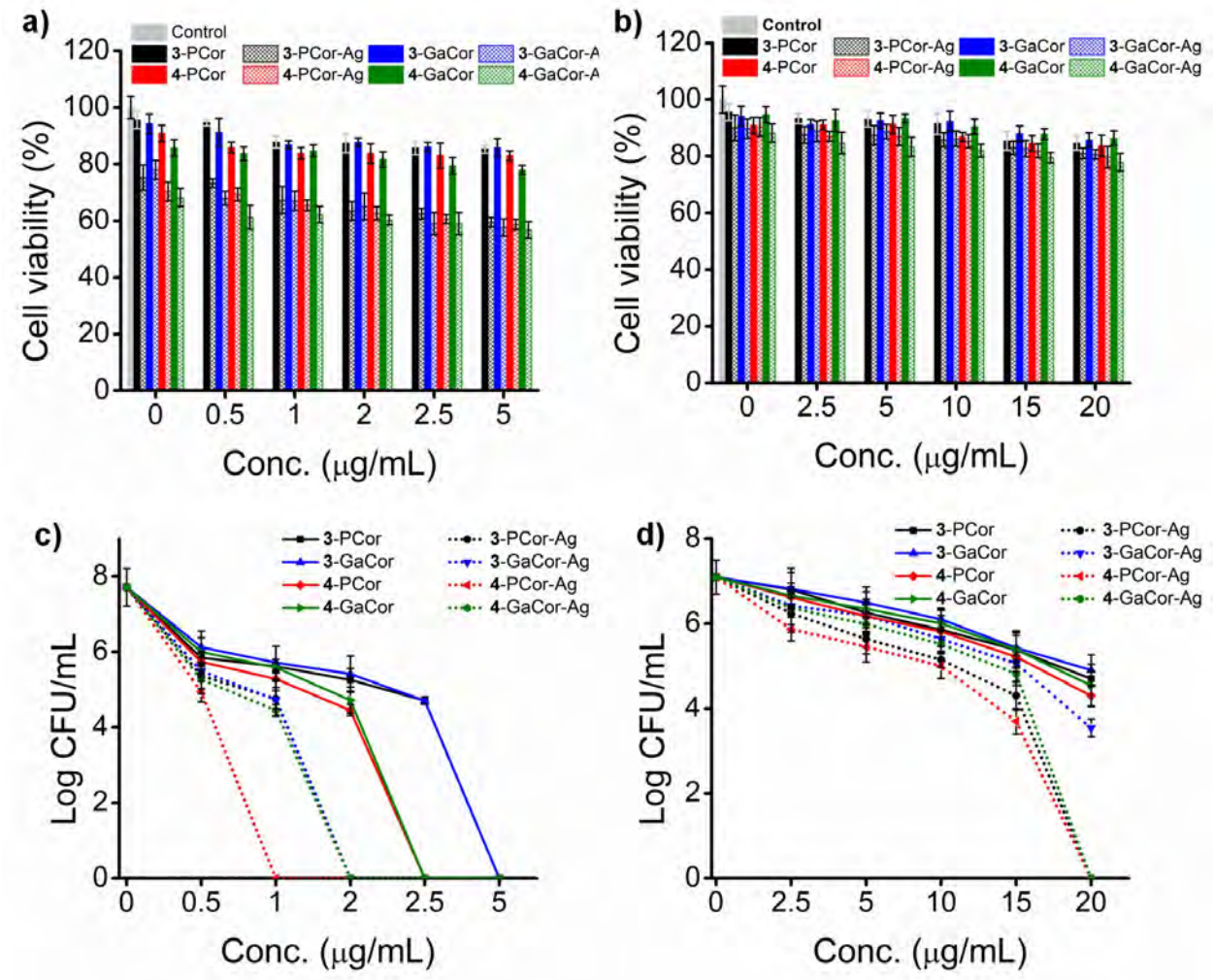

Figure A 51: a-b) Cell viability plots of planktonic cells of a) *S. aureus* and b) *E. coli* in the dark upon treatment with gradient concentrations of **3**-**4**-P^{V}Cor, **3**-**4**-GaCor, and their AgNP nanoconjugates. c-d) Log CFU.mL^{-1} plots of c) *S. aureus*, d) *E. coli* upon treatment with gradient concentrations of **3**-**4**-P^{V}Cor, **3**-**4**-GaCor, and their AgNP nanoconjugates under 60 min illumination at 625 nm using a Thorlabs M625L3 LED (240 $mW.cm^{-2}$).

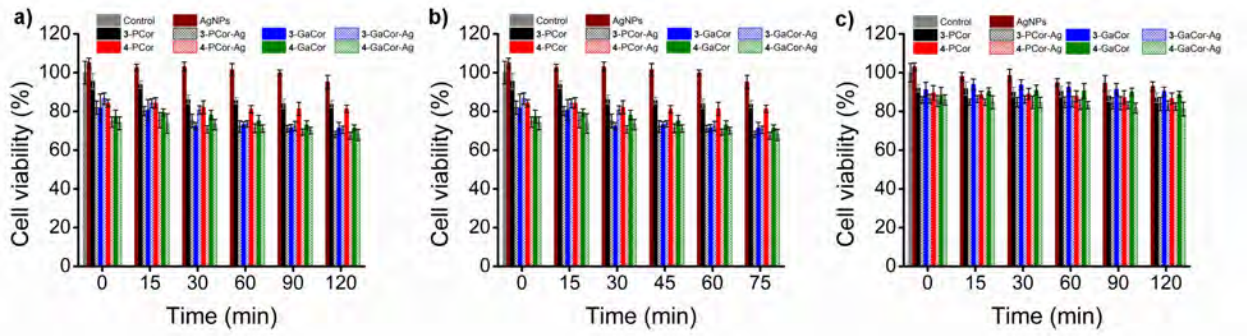

Figure A 52: Cell viability plots of planktonic cells of a-b) *S. aureus*, and c) *E. coli* in the dark upon treatment with a) 0.5 µg.mL^{-1}, b) 2.5 µg.mL^{-1} and c) 10 µg.mL^{-1}of **3**-**4**-P^{V}Cor, **3**-**4**-GaCor, and their AgNP nanoconjugates.

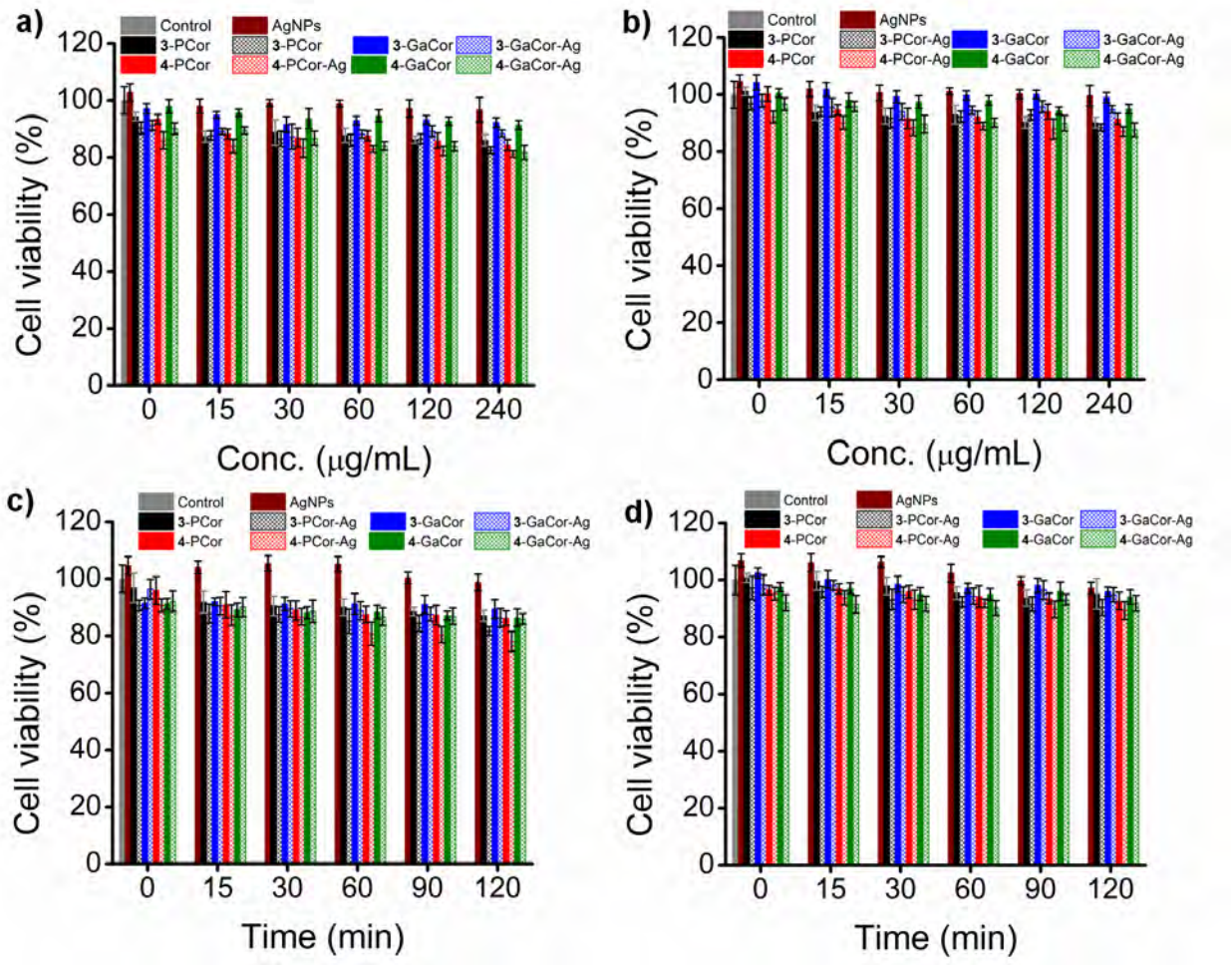

Figure A 53: Cell viability plots in the dark of biofilm cells of a, c) *S. aureus*, and b, d) *E. coli* upon treatment with gradient concentrations of AgNPs, **3**-**4**-P^{V}Cor, **3**-**4**-GaCor and their AgNP nanoconjugates for 30 min with viable cells quantified by crystal violet stain. c-d) upon treatment with 30 μg.mL^{-1} and d) 60 μg.mL^{-1} of the dyes for 120 min.

12.6 Data for Chapter Eight

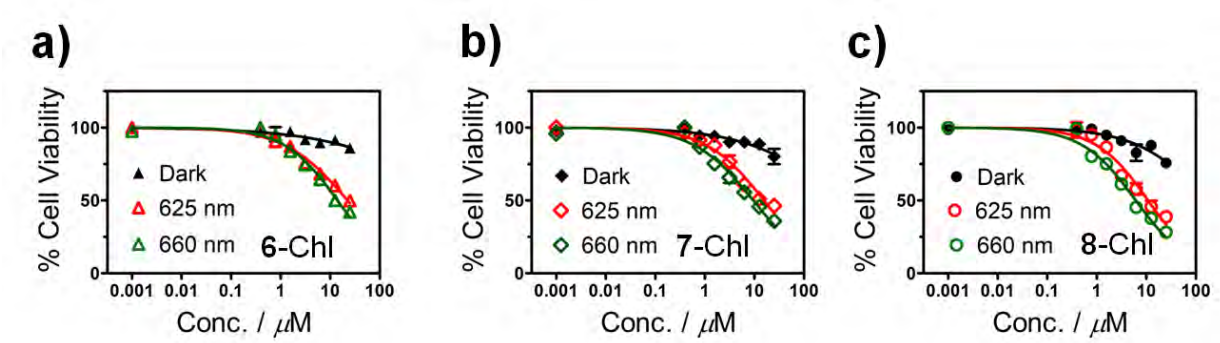

Figure A 54: Cytotoxicity plots for MCF-7 cancer cells in the dark (black line) and under illumination with a Thorlabs M625L3 LED (red line) and M660L3 LED (green line) for 20 min upon treatment with gradient concentrations of a) **6**-Chl, b) **7**-Chl and c) **8**-Chl free-base chlorin dyes.

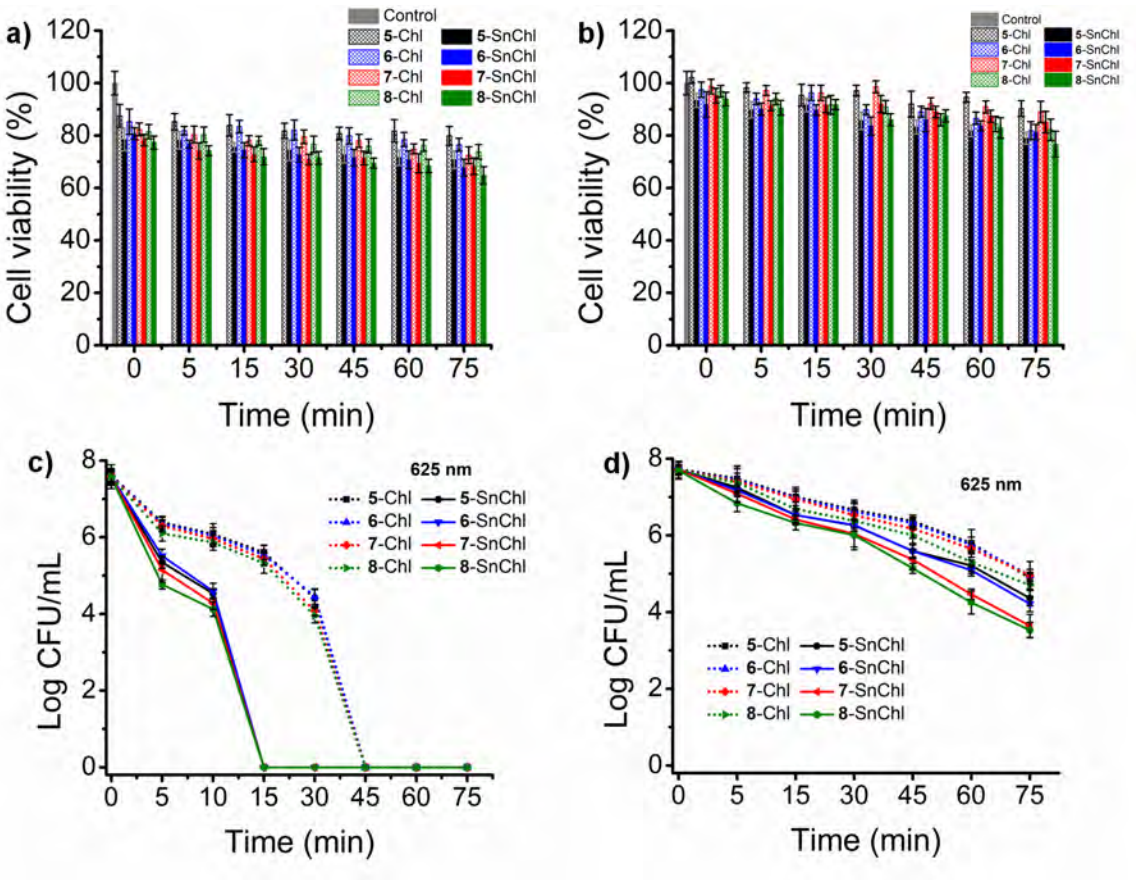

Figure A 55: Cell viability plots for planktonic a) *S. aureus* and b) *E. coli* upon treatment with a) 1 µM b) 5 µM of **5**-**8**-Chl and **5**-**8**-SnChl a-b) in the dark and c-d) Log CFU.mL^{-1} plots for planktonic a) *S. aureus* and b) *E. coli* upon treatment with a) 1 µM b) 5 µM of **5**-**8**-Chl and **5**-**8**-SnChl after 75 min irradiations with a Thorlabs M625L3 LED.

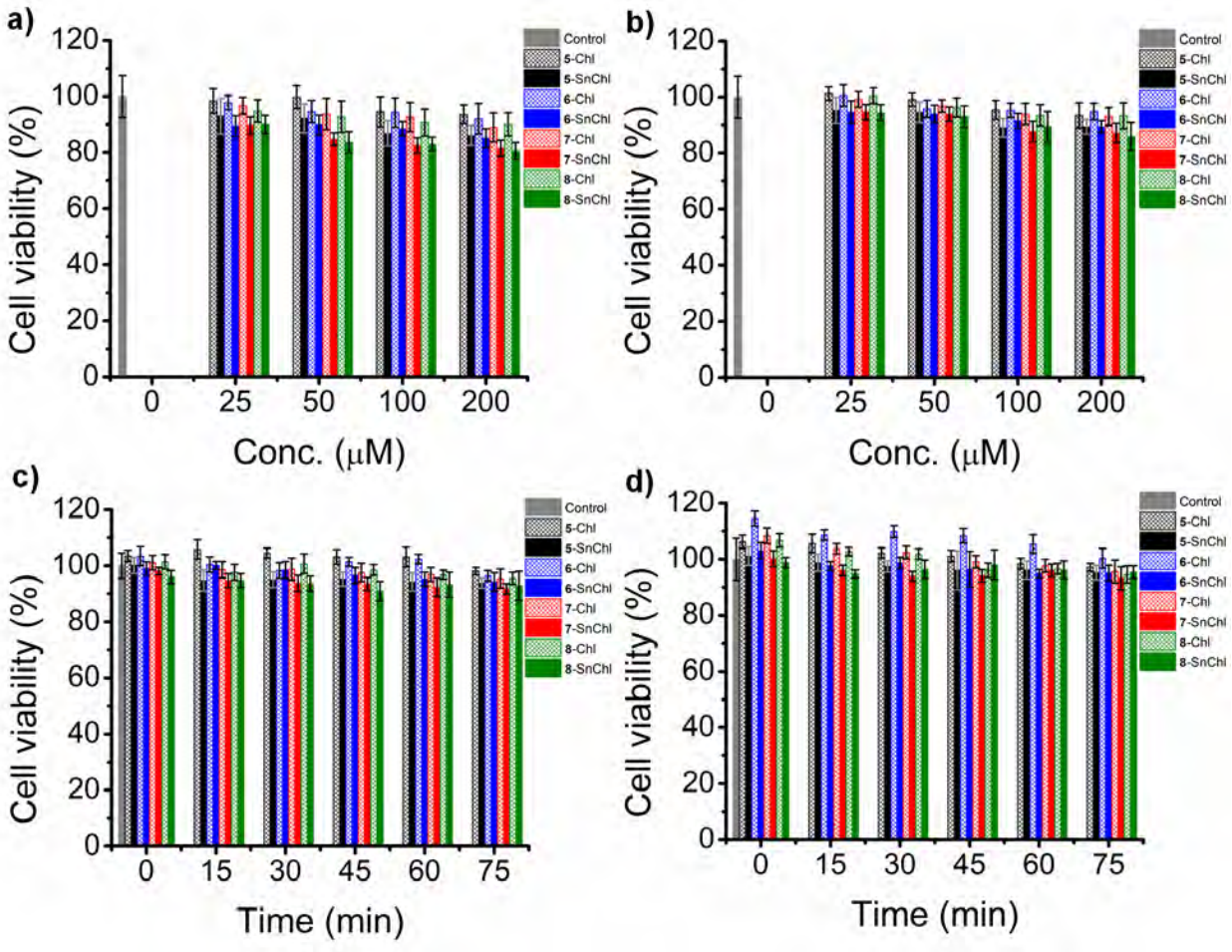

Figure A 56: Cell viability plots of biofilm cells of a, c) *S. aureus*, and b, d) *E. coli* in the dark upon treatment with gradient concentrations of **5**-**8**-Chl and **5**-**8**-SnChl for 30 min with viable cells quantified by crystal violet stain. c) upon treatment with 25 μM and d) 50 μM of the dyes for 75 min.

12.7 Data for Chapter Nine

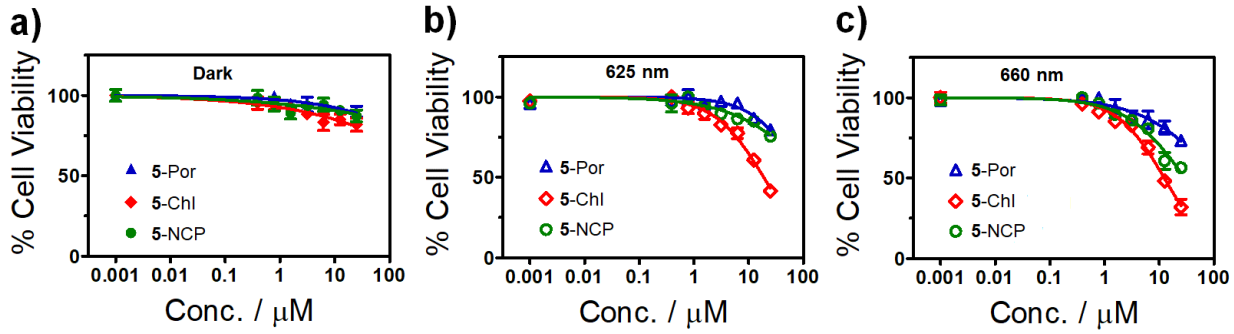

Figure A 57:Cytotoxicity plots for MCF-7 cancer cells in a) the dark (black line) and b-c) under illumination with b) a Thorlabs M625L3 LED and c) M660L3 LED for 20 min upon treatment with gradient concentrations of **5**-Por, **5**-Chl, and **5**-NCP free-base porphyrinoid dyes.

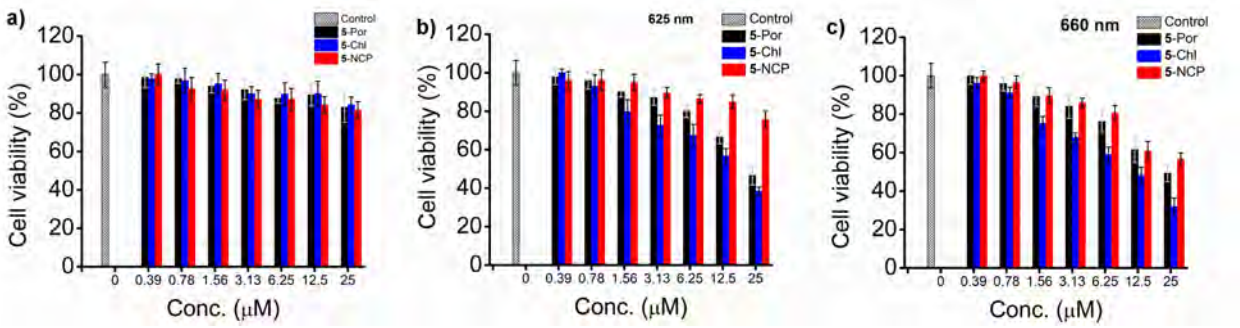

Figure A 58: Cell viability plots for MCF-7 cancer cells in the a) dark and b-c) under illumination with b) a Thorlabs M625L3 and c) a Thorlabs M625L3 LEDs for 20 min upon treatment with gradient concentrations of **5**-Por (black), **5**-Chl (blue) and **5**-NCP (red) free-base dyes.

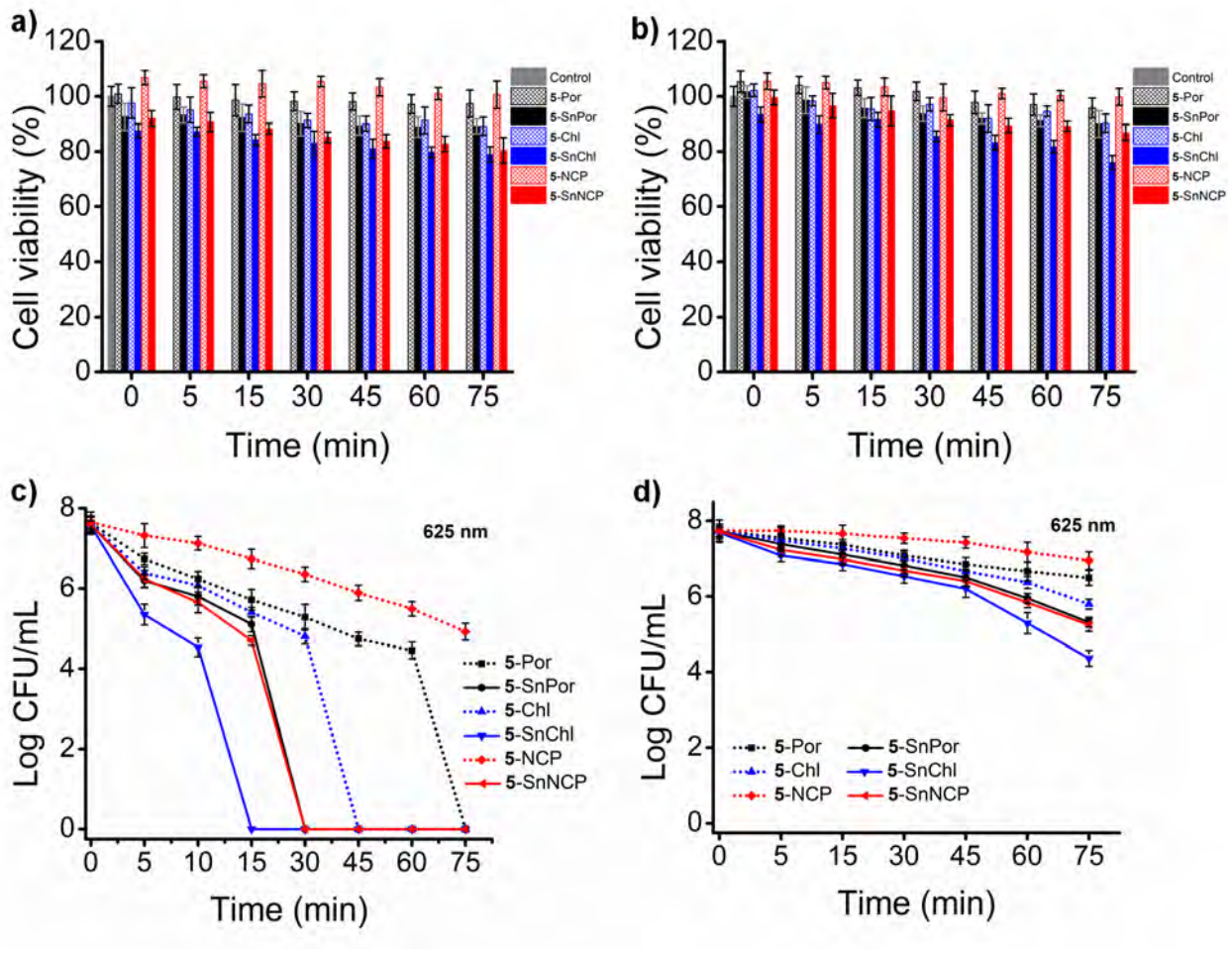

Figure A 59: a-b) Cell viability plots in the dark for planktonic a, c) *S. aureus*, and b, d) *E. coli* upon treatment with a, c) 1 µM b, d) 5 µM of **5**-Por, **5**-Chl, **5**-NCP, **5**-SnPor, **5**-SnChl, and **5**-SnNCP dyes and c-d) Log CFU.mL^{-1} plots after 75 min irradiation with a Thorlabs M625L3 LED.

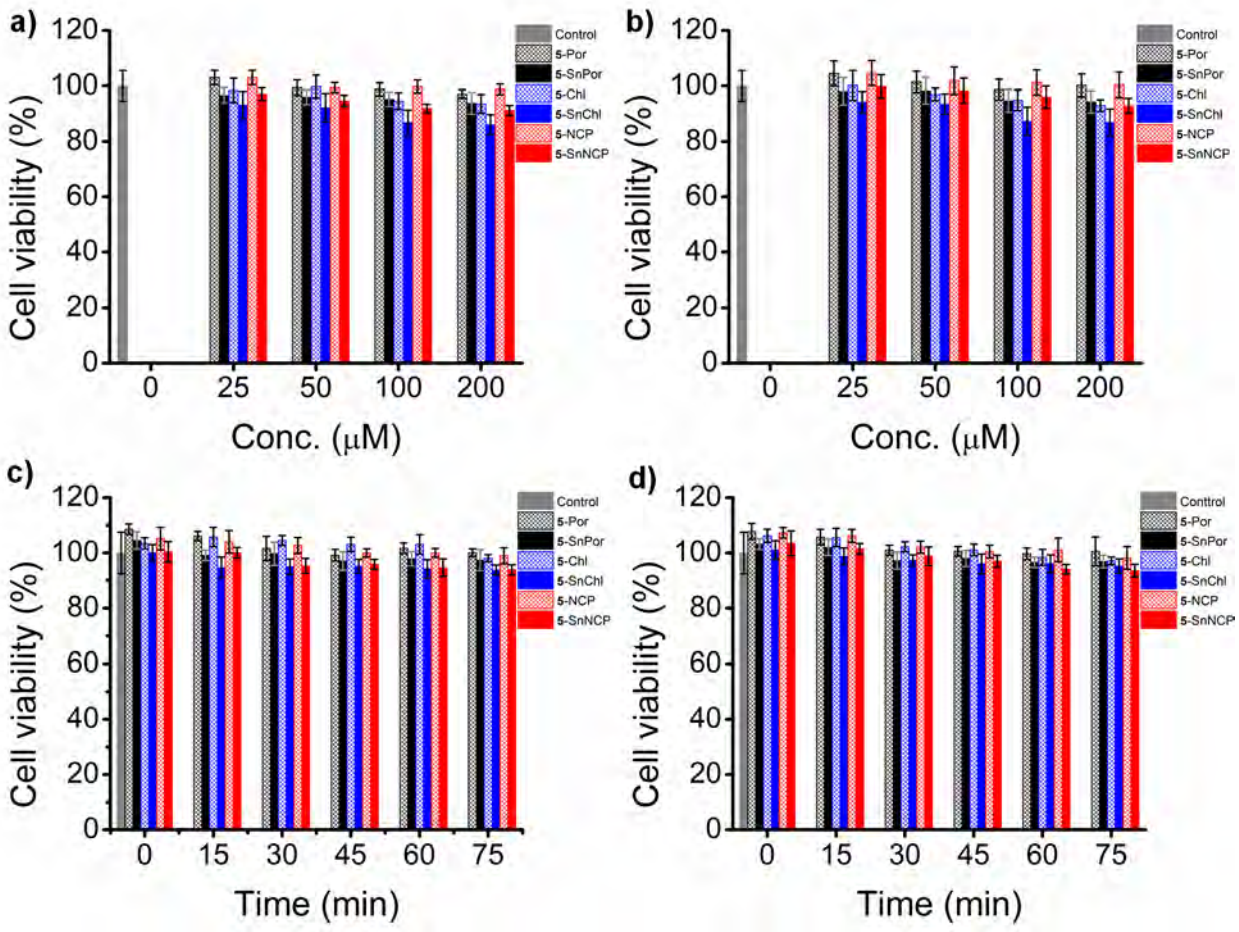

Figure A 60: Cell viability plots of biofilm cells of a, c) *S. aureus*, and b, d) *E. coli* in the dark upon treatment with gradient concentrations of **5**-Por, **5**-Chl, **5**-NCP and **5**-SnPor, **5**-SnChl, **5**-SnNCP for 30 min with viable cells quantified by crystal violet stain. c) upon treatment with 25 μM and d) 50 μM of the dyes for 75 min.

12.8 Data for Chapter Eleven

Optimized structures of porphyrins and porphyrin analog dyes

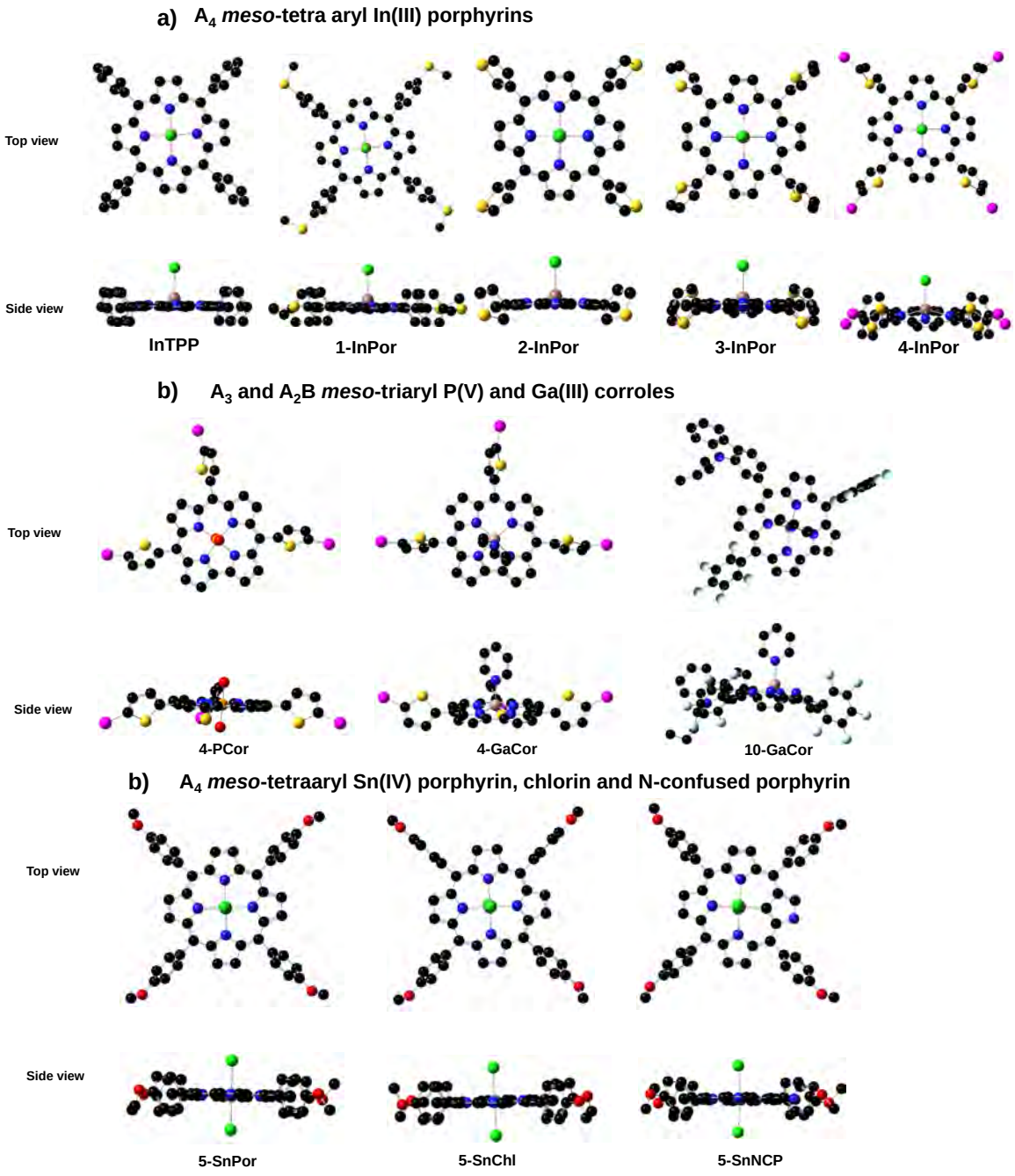

Figure A 61: Representative B3LYP/SDD optimized geometries for **a**) In(III) porphyrins and **b**) P(V) and Ga(III) A_3 corroles and A_2B triaryl Ga(III) corrole and **c**) Sn (IV) porphyrin, chlorin and

N-confused porphyrin showing the top and side views with hydrogens atoms omitted for clarity.

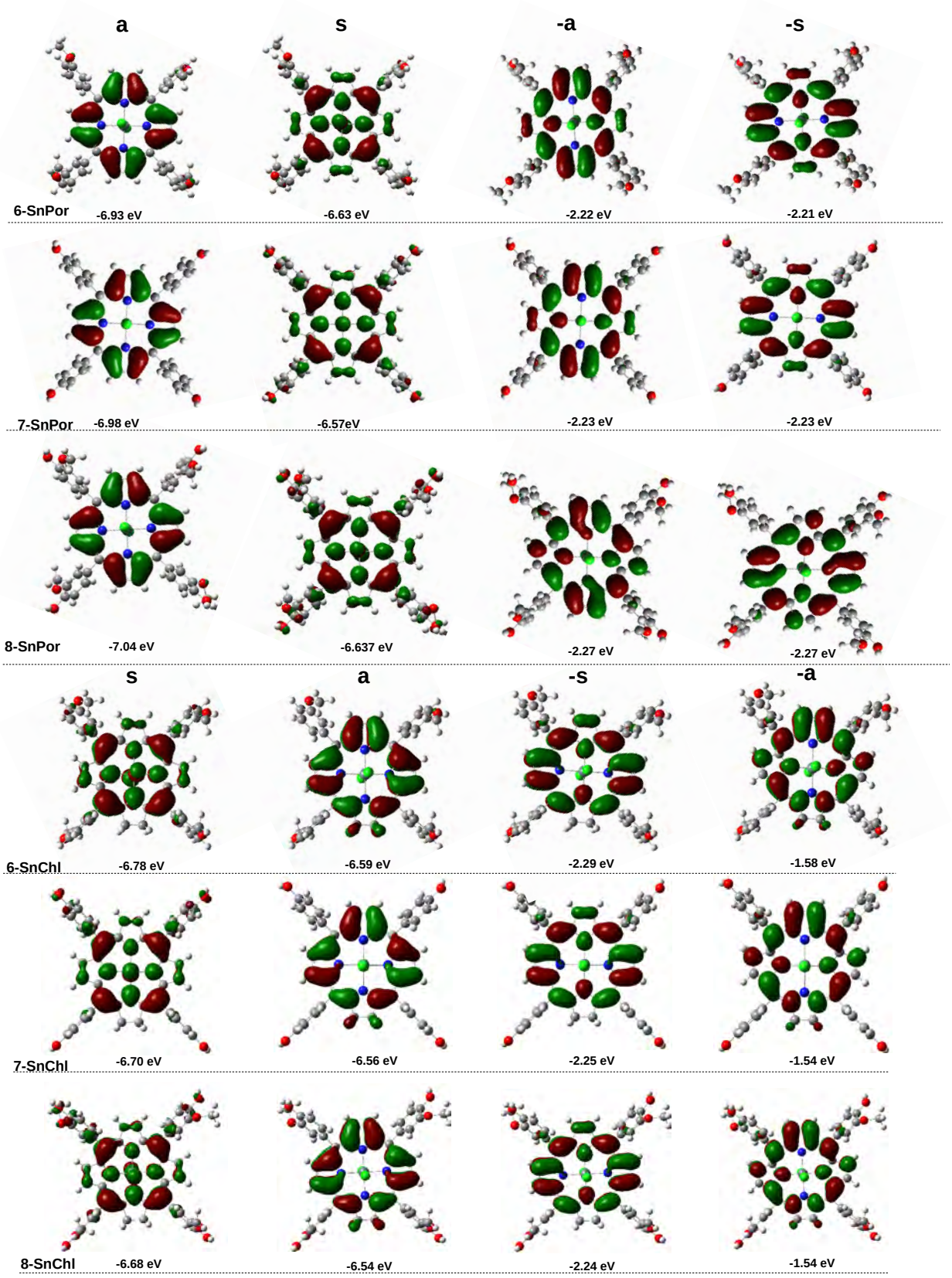
a
s
-a
-s
6-SnPor
-6.93 eV
-6.63 eV
-2.22 eV
-2.21 eV
7-SnPor
-6.98 eV
-6.57eV
-2.23 eV
-2.23 eV
8-SnPor
-7.04 eV
-6.637 eV
-2.27 eV
-2.27 eV
s
a
-s
-a
6-SnChl
-6.78 eV
-6.59 eV
-2.29 eV
-1.58 eV
7-SnChl
-6.70 eV
-6.56 eV
-2.25 eV
-1.54 eV
8-SnChl
-6.68 eV
-6.54 eV
-2.24 eV
-1.54 eV

Figure A 62: Angular nodal patterns and energies of **a**, **s**, **-a**, and **-s** MOs of **6**-**8**-SnPor and **6**-**8**-SnChl analogs.

Table A 5: Calculated TD-DFT UV-visible spectra of B3LYP optimized geometries of parent InTPP and **1**-**4**-InPor, parent P^{V}TPCor, Ga^{III}TPCor, Ga^{III}TPFPC, **1**-**4**-P^{V}Cor, and **1**-**4**-GaCor A_3 triaryl corroles and **9**-**10**-GaCor A_2B triaryl corroles, parent SnTPP, **5**-**8**-SnPor, **5**-**8**-SnChl, and **5**-SnNCP obtained using CAM-B3LYP functional with SDD basis sets.

A_4 *meso*-tetraaryl In(III) porphyrins

InTPP

Band[a]	#[b]		Calc[c]		Exp[d]		Wave Function[e] =
----	1	----	----	----	----	----	Ground State
Q	2	18.0	557	(0.03)	16.6	603	**65%s→-a; 34%a→-s; …**
	3	18.0	557	(0.03)	17.8	561	**64s→-s; 35%a→-a; …**
B	4	25.8	367	(1.14)	23.4	428	**59%a→-a; 32%s→-s; …**
	5	25.8	367	(1.12)			**59%a→-s; 31s→-a; …**

1-InPor

Band[a]	#[b]		Calc[c]		Exp[d]		Wave Function[e] =
----	1	----	----	----	----	----	Ground State
Q	2	17.7	564	(0.03)	16.4	609	**60%s→-a; 40%a→-s; …**
	3	17.8	563	(0.02)	17.7	566	**59%s→-s; 41%a→-a; …**
B	4	27.1	369	(1.59)	23	435	**33%a→-a; 25%a→-s; 23%s→-s;17%s→-a; …**
	5	27.1	369	(1.59)			**34%a→-s; 25%a→-a; 22%s→-a; 17%s→-s; …**

2-InPor

Band[a]	#[b]		Calc[c]		Exp[d]		Wave Function[e] =
----	1	----	----	----	----	----	Ground State
Q	2	17.5	572	(0.04)	16.5	607	**64%s→-a; 35%a→-s; …**
	3	17.6	567	(0.02)	17.8	563	**57%s→-s; 43%a→-a; …**
B	4	27	370	(1.34)	23.3	430	**63%a→-s; 36%s→-a; …**
	5	27	370	(1.44)			**57%a→-a; 43%s→-s; …**

3-InPor

Band[a]	#[b]		Calc[c]		Exp[d]		Wave Function[e] =
----	1	----	----	----	----	----	Ground State
Q	2	17.5	572	(0.02)	16.2	618	**57%s→-a; 42%a→-s; …**
	3	17.5	571	(0.02)	17.5	573	**55%s→-s; 44%a→-a; …**
B	4	26.6	376	(1.40)	22.8	438	**56%a→-s; 42%s→-a; …**
	5	26.6	375	(1.43)			**55%a→-a; 43%s→-s; …**

4-InPor

Band[a]	#[b]		Calc[c]		Exp[d]		Wave Function[e] =
----	1	----	----	----	----	----	Ground State
Q	2	17.4	574	(0.03)	16.1	620	**56%s→-a; 43%a→-s; …**
	3	17.5	572	(0.02)	17.5	572	**55%s→-s; 44%a→-a; …**
B	4	26.4	379	(1.57)	22.7	441	**55%a→-s; 42%s→-a; …**
	5	26.4	379	(1.62)			**54%a→-a; 44%s→-s; …**

A_3 triaryl P(V) and Ga(III) Corroles

P^VTPCor

Band[a]	#[b]		Calc[c]		Exp[d]		Wave Function[e] =
----	1	----	----	----	----	----	Ground State
Q	2	18.7	534	(0.22)	16.3	612	**79% s → -a; 20% a → -s;** …
	3	20.1	497	(0.01)	17.4	574	**57% a → -a; 41% s → -s;** …
B	4	28.2	355	(1.10)	23.5	425	**58% s → -s; 42% a → -a;** …
	5	29.1	343	(1.17)			**77% a → -s; 19% s → -a;** …

1-P^VCor

Band[a]	#[b]		Calc[c]		Exp[d]		Wave Function[e] =
----	1	----	----	----	----	----	Ground State
Q	2	18.5	540	(0.29)	16.4	610	**80% s → -a; 18% a → -s;** …
	3	20.0	499	(0.00)	17.5	570	**55% a → -a; 43% s → -s;** …
B	4	27.9	359	(1.20)	23.9	419	**56% s → -s; 43% a → -a;** …
	5	28.7	348	(1.39)			**76% a → -s; 19% s → -a;** …

2-P^VCor

Band[a]	#[b]		Calc[c]		Exp[d]		Wave Function[e] =
----	1	----	----	----	----	----	Ground State
Q	2	18.6	537	(0.21)	16.4	611	**79% s → -a; 20% a → -s;** …
	3	20.0	499	(0.01)	17.8	562	**57% a → -a; 41% s → -s;** …
B	4	28.0	356	(1.07)	23.6	423	**58% s → -s; 42% a → -a;** …
	5	29.0	345	(1.11)			**77% a → -s; 19% s → -a;** …

3-P^{V}Cor

Band[a]	#[b]		Calc[c]		Exp[d]		Wave Function[e] =
----	1	----	----	----	----	----	Ground State
Q	2	18.6	538	(0.21)	16.3	614	**77% s → -a; 21% a → -s;** …
	3	19.8	504	(0.01)	17.4	573	**59% a → -a; 39% s → -s;** …
B	4	27.8	360	(1.07)	23.4	427	**61% s → -s; 38% a → -a;** …
	5	28.5	351	(1.19)			**75% a → -s; 20% s → -a;** …

4-P^{V}Cor

Band[a]	#[b]		Calc[c]		Exp[d]		Wave Function[e] =
----	1	----	----	----	----	----	Ground State
Q	2	18.3	547	(0.20)	16.3	615	**77%s→ -a; 21%a→ -s;** …
	3	19.7	508	(0.00)	17.3	574	**59%a→ -a; 39%s→ -s;** …
B	4	27.3	366	(1.08)	23.3	429	**61%s→ -s; 39%a→ -a;** …
	5	27.9	359	(1.18)			**74%a→ -s; 22% s→ -a;** …

Ga^{III}TPCor

Band[a]	#[b]		Calc[c]		Exp[d]		Wave Function[e] =
----	1	----	----	----	----	----	Ground State
Q	2	18.4	543	(0.21)	16.1	622	**79% s → -a; 18% a → -s;** …
	3	19.9	503	(0.00)	17.6	567	**42% a → -a;** 29% s → L+1^{py}; **26% s → -s;** …
B	7	27.8	360	(1.13)	23.2	430	**58% s → -s; 39% a → -a;** …
	8	28.6	350	(1.17)			**76% a → -s; 18% s → -a;** …

1-GaCor

Band[a]	#[b]		Calc[c]		Exp[d]		Wave Function[e] =
----	1	----	----	----	----	----	Ground State
Q	2	18.4	544	(0.25)	16.3	615	**78% s → -a; 18% a → -s;** …
	3	19.9	503	(0.00)	17.2	581	**51% a → -a; 32% s → -s;** 15% s → L+1^{py}; …

B	7	27.6	363	(1.19)	23.3	429	**56% s → -s; 40% a → -a;** …
	8	28.3	354	(1.38)			**75% a → -s; 20% s → -a;** …

2-GaCor

Band[a]	#[b]		Calc[c]		Exp[d]		Wave Function[e] =
----	1	----	----	----	----	----	Ground State
Q	2	18.4	544	(0.21)	16.2	616	**79% s → -a; 18% a → -s;** …
	3	20.0	503	(0.01)	17.9	559	**53% a → -a; 31% s → -s;** 13% s → L+1^{py}; …
B	7	27.8	360	(1.07)	23.4	428	**60% s → -s; 38% a → -a;** …
	8	28.6	350	(1.07)			**76% a → -s; 20% s → -a;** …

3-GaCor

Band[a]	#[b]		Calc[c]		Exp[d]		Wave Function[e] =
----	1	----	----	----	----	----	Ground State
Q	2	18.3	547	(0.20)	16.1	622	**77% s → -a; 18% a → -s;** …
	3	19.7	508	(0.00)	17.3	578	**57% a → -a; 29% s → -s;** 12% s → L+1^{py}; …
B	6	27.3	366	(1.08)	23.1	433	**55% s → -s; 38% a → -a;** …
	7	27.9	359	(1.18)			**70% a → -s; 21% s → -a;** …

4-GaCor

Band[a]	#[b]		Calc[c]		Exp[d]		Wave Function[e] =
----	1	----	----	----	----	----	Ground State
Q	2	18.3	545	(0.22)	16.1	621	**76%s→ -a; 12%a→ L+1py; 10%a→ -s;** …
	3	19.7	509	(0.01)	17.9	560	**59%a→ -a; 22%s→ -s; 18%s→ L+1py;** …
B	6	27.3	366	(1.17)	23.0	435	**41%s→ L+1^{py}; 34%a→ -a; 16%s→ -s;** …
	7	27.8	360	(1.32)			**56%a→ L+1^{py}; 20%s→ -a;** …

A_2B triaryl Ga(III) Corroles

Ga^{III}TPFPC

Band[a]	#[b]		Calc[c]		Exp[d]		Wave Function[e] =
----	1	----	----	----	----	----	Ground State
Q	2	18.9	530	(0.11)	---	---	**70% s → -a; 28% a → -s;** …
	3	19.8	505	(0.02)	---	---	**64% a → -a; 33% s → -s;** …
B	6	27.8	359	(0.87)	---	---	**46% s → -s; 25% a → -a; 17% a → L+2^{py};** …

	7	28.2	354	(0.89)			**34% a → L+2^{py}; 32% a → -s; 17% s → -a;** …

9-GaCor

Band[a]	#[b]	Calc[c]			Exp[d]		Wave Function[e] =
----	1	----	----	----	----	----	Ground State
Q	2	18.5	541	(0.18)	16.6	604	**75% s → -a; 15% a → -s;** …
	3	19.5	512	(0.02)	17.4	574	**64% a → -a; 24% s → -s;** …
B	6	27.6	363	(1.34)	23.6	423	**34% a → L+2py; 31% s → -s; 31% a → -a;** …
	8	28.3	354	(1.03)			**47% a → L+2py; 27% a → -s; 21% s → -a;**

10-GaCor

Band[a]	#[b]	Calc[c]			Exp[d]		Wave Function[e] =
----	1	----	----	----	----	----	Ground State
Q	2	18.4	543	(0.21)	16.1	622	**79% s → -a; 18% a → -s;** …
	3	19.9	503	(0.00)	17.6	567	**42% a → -a;** 29% s → L+1^{py}; **26% s → -s;** …
B	7	27.8	360	(1.13)	23.2	430	**58% s → -s; 39% a → -a;** …
	8	28.6	350	(1.17)			**76% a → -s; 18% s → -a;** …

A$_4$ *meso*-tetraaryl Sn(IV) Porphyrins

SnTPP

Band[a]	#[b]	Calc[c]			Exp[d]		Wave Function[e] =
----	1	----	----	----	----	----	Ground State
Q	2	17.5	572	(0.03)	16.4	611	**63%s →-a; 37%a →-s;** …
	3	17.5	572	(0.03)			**63%s →-s; 37%a →-a;** …
B	4	26.7	375	(1.22)	23.0	434	**52%a →-a; 30%s →-s;** …
	5	26.7	375	(1.22)			**52%a →-s; 30%s →-a;** …

5-SnPor

Band[a]	#[b]	Calc[c]			Exp[d]		Wave Function[e] =
----	1	----	----	----	----	----	Ground State
Q	2	17.3	571	(0.04)	16.3	612	**64%s → -a; 35%a → -s;** …
	3	17.3	571	(0.04)	17.6	568	**64%s → -s; 35%a → -a;** …
B	4	26.4	379	(1.33)	22.8	438	**62%a → -s; 34%s → -a;** …

	5	26.4	378	(1.32)			**62%a → -a; 34%s → -s;** …

6-SnPor

Band[a]	#[b]		Calc[c]		Exp[d]		Wave Function[e] =
----	1	----	----	----	----	----	Ground State
Q	2	17.5	572	(0.02)	16.6	602	**61%s → -s; 38%a → -a;** …
	3	17.5	572	(0.02)	17.9	558	**62%s → -a; 37%a → -s;** …
B	4	26.5	377	(1.20)	23.3	429	**60%a → -s; 36%s → -a;** …
	5	26.5	376	(1.25)			**60%a → -a; 37%s → -s;** …

7-SnPor

Band[a]	#[b]		Calc[c]		Exp[d]		Wave Function[e] =
----	1	----	----	----	----	----	Ground State
Q	2	17.4	576	(0.03)	16.3	615	**64%s→-s; 35%a→-a;** …
	3	17.4	576	(0.04)	17.6	567	**64%s→-a; 35%a→-s;** …
B	4	26.5	377	(1.27)	22.7	441	**62%a→-a; 35%s→-s;** …
	5	26.5	377	(1.27)			**62%a→-s; 35%s→-a;** …

8-SnPor

Band[a]	#[b]		Calc[c]		Exp[d]		Wave Function[e] =
----	1	----	----	----	----	----	Ground State
Q	2	17.3	577	(0.04)	16.1	620	**62%s →-a; 35%a →-s;** …
	3	17.3	577	(0.04)	17.5	572	**62%s →-s; 35%a →-a;** …
B	4	26.2	381	(1.26)	22.5	445	**55%a →-a; 32%s →-s;** …
	5	26.3	380	(1.29)			**55%a →-s; 32%s →-a;** …

A_4 *meso*-tetraaryl Sn(IV) Chlorins

5-SnChl

Band[a]	#[b]		Calc[c]		Exp[d]		Wave Function[e] =
----	1	----	----	----	----	----	Ground State
Q	2	17.7	566	(0.10)	15.9	629	**76%s →-a; 23%a →-s;** …
	3	19.4	515	(0.10)	17.5	572	**75%a →-a; 23%s →-s;** …
B	4	27.1	369	(1.18)	23.1	433	**71%s →-s; 22%a →-a;** …
	5	27.5	363	(1.18)			**71%a →-s; 22%s →-a;** …

6-SnChl

Band[a]	#[b]		Calc[c]		Exp[d]		Wave Function[e] =
----	1	----	----	----	----	----	Ground State
Q	2	17.6	567	(0.11)	15.9	627	**77%s→-a; 22%a→-s;** …
	3	19.5	512	(0.07)	17.7	564	**73%a→-a; 25%s→-s;** …
B	4	27.2	367	(1.08)	23.3	430	**70%s→-s; 23%a→-a;** …
	5	27.8	360	(0.99)			**70%a→-s; 21%s→-a;** …

7-SnChl

Band[a]	#[b]		Calc[c]		Exp[d]		Wave Function[e] =
----	1	----	----	----	----	----	Ground State
Q	2	17.7	566	(0.10)	15.9	629	**76%s→ -a; 23%a → -s;** …
	3	19.5	514	(0.09)	17.4	576	**75%a → -a; 23%s→ -s;** …
B	4	27.2	368	(1.14)	22.8	438	**71%s→ -s; 22%a → -a;** …
	5	27.6	362	(1.05)			**71%a → -s; 22%s→ -a;** …

8-SnChl

Band[a]	#[b]		Calc[c]		Exp[d]		Wave Function[e] =
----	1	----	----	----	----	----	Ground State
Q	2	17.6	567	(0.10)	15.8	630	**76%s →-a; 23%a →-s;** …
	3	19.4	515	(0.09)	17.4	575	**74%a →-a; 23%s →-s;** …
B	4	27.1	370	(1.14)	22.8	439	**71%s →-s; 22%a →-a;** …
	5	27.6	363	(1.09)			**71%a →-s; 22%s →-a;** …

A_4 *meso*-tetraaryl Sn(IV) Porphyrins

5-SnNCP

Band[a]	#[b]		Calc[c]		Exp[d]		Wave Function[e] =
----	1	----	----	----	----	----	Ground State
Q	2	12.9	774	(0.13)	13.6	733	**92%s→-a;** …
	3	19.0	527	(0.03)	17.8	562	**67%s→-s; 31%a→-a;** …
B	6	25.2	396	(1.19)	22.0	454	**57%a→-a; 26% s→-s; 11%H-2→-a;** …
	8	27.2	368	(0.18)			**74%a→-s;** …

[a] Band assignment described in the main text. [b] States assigned in terms of ascending energy in the TD-DFT calculation. [c] Calculated band energies ($10^3.cm^{-1}$) and wavelengths (nm) with oscillator strengths in parentheses (f). [d] Observed energies ($10^3.cm^{-1}$) and wavelengths (nm) in DMSO, [e] The wave functions calculated from the eigenvectors predicted by TD-DFT. One-electron transitions associated with the **a**, **s**, **-**

a, and **-s** MOs are highlighted in bold. Only one-electron contributions > 10% are shown.